CHARACTERIZATION OF POROUS CONSTRUCTION MATERIALS USING ELECTROMAGNETIC RADAR WAVE

LAI WAI-LOK, WALLACE

Ph.D.

THE HONG KONG POLYTECHNIC UNIVERSITY

2006

THE HONG KONG POLYTECHNIC UNIVERSITY

DEPARTMENT OF BUILDING AND REAL ESTATE

CHARACTERIZATION OF POROUS CONSTRUCTION MATERIALS USING ELECTROMAGNETIC RADAR WAVE

LAI WAI-LOK, WALLACE

A thesis submitted in partial fulfillment of the requirements for the Degree of Doctor of Philosophy

January, 2006

Certificate of Originality

I hereby declare that this thesis is my own work and that, to the best of my knowledge and belief, it reproduces no material previously published or written, nor material that has been accepted for the award of any other degree or diploma, except where due knowledge has been made in the text.

LAI-WAI LOK, WALLACE

ABSTRACT

This thesis reports an experimental effort of characterizing three porous construction/geological materials (i.e. concrete, asphalt and soils) and the establishment and formulation of a set of novel unified constitutive models for these materials by utilizing electromagnetic (EM) radar waves of 0.4 to 1.5 GHz nominal frequencies. This research is recognized, as far as the author is aware, the first study of its kind (i.e. in terms of the technique of characterizing concrete, asphalt and soils based on an inter-disciplinary approach encompassing EM wave and engineering/geological properties). An important outcome of this piece of research is that the studied materials have been assigned successfully into their rightful positions corresponding to the different regimes governed by three different EM wave properties and two engineering/geological properties of the materials. The former refers to the real part of complex dielectric permittivity, energy attenuation and drift of peak frequency of the materials. The latter refers to porosity and permeability of the materials determined with forward models or conventional testing techniques.

In soil and asphalt, the material characterization was achieved by a novel in-house developed method called *Cyclic Moisture Variation Technique* (CMVT) which has been implemented successfully in a series of well-coordinated laboratory experiments. This CMVT is a non-invasive experimental material characterization technique for classifying material behaviour in laboratory, or as a non-invasive near-surface geophysical method in field applications. With this technique, water was used in CMVT as an enhancer or a tracer to allow differentiation of the studied materials which are difficult to differentiate when they are relatively dry. The technique is termed *cyclic* because the porous materials were subjected to change from partially

saturated states to a fully saturated state and vice versa, via a number of cycles of water-permeation and dewatering processes. Through the CMVT, soils and asphalt with different textures of their particulate constituents were characterized by different curves exhibited in the relationship between the real part of complex permittivities and degrees of water saturation (S_w).

The porosity of construction/geological materials is a subject of major concern in this research. It is a fundamental property of these porous materials, which has a bearing on their other major material behaviour. For mass manufactured materials such as concrete and asphalt, the presence of varying degrees, as well as the sizes of macro-pores and capillary pores within and between their particulate constituents affect their ultimate bulk physical behaviour, such as strength, permeability and durability. For natural particulate materials such as soils, the porosity is a useful measure to characterize the textures and compositions of soils.

Values of porosities (in the ranges of 0.38 to 0.63 in soils and 0.04 in asphalt) were estimated by fitting the data of real part of complex permittivities and S_w into the well-established Complex Refractive Index Model (CRIM). By using the findings in soils from this research and the referenced sources performed by others, the curves of the real part of complex permittivity versus degree of water saturation were found to be clearly divided into three regions: very low (i.e. existence of *transition moisture/wilting point*), intermediate (i.e. fitted by the CRIM) and very high degree of water saturation (i.e. existence of a *critical degree of water saturation*). In particular in these plots, *dielectric hysteresis* was observed (but rarely reported in the field of ground/surface penetrating radar) in soils and in asphalt. These observed phenomena are considered to provide profound influences on the behaviours as well as the understanding of these studied porous materials.

The different curing environment is known to affect both the porosity as well as the pore size distribution within mature concrete. By injecting water into concrete specimens under high pressure, the experimental technique advocated in this research allows the differentiation and non-destructive detection of the different curing history a concrete has gone through in fresh state. In particular, the curves (in the plots of the real part of complex permittivity against water saturation) for air-cured (AC) concrete were found to be very similar to those of soils. This similarity implies that the pore systems within air-cured concrete (but not normally cured concrete) and soils are rather similar.

Verification of the measurements of the properties investigated by other independent methods (such as mercury intrusion porosimetry test, soil test etc.) was undertaken as time and resource was allowed. However, there were circumstances in which other methods of measurements were considered to be either too time-consuming, disruptive (to the samples) or simply the instrument concerned was not available.

The presence of water in subsurface porous materials has usually been considered undesirable in most GPR applications and studies because of significant EM wave attenuation by water. However, the CMVT and the unified constitutive models advocated in this research have turned this drawback into a useful characterization technique of the porous construction and geological materials.

Also taking note that the findings were obtained in well-controlled laboratory conditions but not in field conditions. However, it is believed that they have already provided the fundamental and indispensable understanding of the materials and will be able to pave the ways for future field scale application. The research is believed to have advanced the fronts of both construction material research and geophysical explorations.

LIST OF PUBLICATIONS

Journal Papers:

Lai W. L., Tsang W. F., Fang H., Xiao D., 2006, Experimental Determination of Bulk Dielectric Properties and Porosity of Porous Asphalt and Soils using GPR and a Cyclic Moisture Variation Technique: *Geophysics*, 71(4), K93-K102.

Lai W. L. and Tsang W. F., Characterization of Pore Systems of Air/Water-cured Concrete Using Ground Penetrating Radar (GPR) through Continuous Water Injection (accepted by *Construction and Building Materials*)

Lai W. L. and Tsang W. F., Comparison of the Measurement of Real Permittivity on Differential and Homogeneous Distribution of Water in Soil (Manuscript is currently reviewed by *Water Resources Research*)

Lai W. L. and Tsang W. F., Characterization of Soil Textures by Ground Penetrating Radar based on a Cyclic Moisture Variation Technique (CMVT) (Manuscript is currently reviewed by *Geophysics*)

Lai W. L. and Tsang W. F., The Derivation of a Unified Constitutive Model for the Characterization of Porous Soil/Concrete/Asphalt Materials based on the Electromagnetic Wave Properties (Manuscript is currently reviewed by *Journal of ASTM International*, USA)

Papers published in Proceedings:

Lai W, Tsang S, 2005, Characterization of Soil Texture by Dielectric Properties using Ground Penetrating Radars operating at Different Frequencies of Cyclic Variation of Moisture Content of Soils, SEG International Exposition and Seventy-Fifth Annual Meeting, 1192-1195.

Lai, W.L. and Tsang, S., 2005, Experimental Evaluation of Honeycombed Concrete by Surface Penetrating Radar, ASNT Fall Conference & Quality Testing Show 2005, Columbus, Ohio, USA, p.435-438.

Shuang X. Z., Wong. K., Lai W. and Kwok Z., 2004, 'Pitfall of GPR Survey in Dielectric Property Calibration', 4th Asian Symposium on Engineering Geology and the Environment 2004.

Lai W, Tsang S and Chan F., 2003, 'A Preliminary Study of Data Fusion Techniques (DFTs) on Evaluation of Defective Concrete by Pulsed Radar and Ultrasonic System', BINDT Conference Proceedings 2003 p.139-144.

LIST OF INVITED PRESENTATIONS

Speaker of the Technical Seminar entitled 'Characterization of Porous Construction Materials by Cyclic Moisture Variation Technique and Ground Penetrating Radar' at *Department of Civil and Environmental Engineering, University of California, Berkeley* (4th Nov 2005)

Speaker of the Technical Seminar entitled 'Make or Break of the Method of Detection and Ranging of Underground Buried Utilities Using Ground Penetrating/Probing Radar' jointly organized by *Hong Kong Institute of Engineers (CAI & CVL)* and *Hong Kong Institute of Utility Surveyors* (20th May 2005)

Speaker of the Seminar and Workshop entitled 'Ground Penetrating Radar' organized by *Hong Kong Institute of Engineers (Materials)* (4th Dec 2004)

Speaker of the Technical Seminar entitled 'Condition Assessment of Asphalt Carriageway Network by Ground Penetrating Radar' jointly organized by *Hong Kong Institute of Engineers (CAI & CVL)* and *Hong Kong Institute of Utility Surveyors* (2nd Dec 2004)

Speaker of the seminar entitled 'Would Ground Penetrating Radar help in Underground Utility Survey?' jointly organized by *Hong Kong Institute of Engineers* (CAI & CVL) and *Hong Kong Institute of Utility Surveyors* (23rd April 2004)

ACKNOWLEDGEMENTS

I am indebted and most grateful to Dr. Steven Tsang for his continuous support over the past seven years. His enthusiasm, passion and knowledge in science inspired me to pursue new ideas and led my way on numerous occasions when I was at the crossroads of research. His ’British’ way of thinking was also vital in shaping my perspectives in research and manners of living. Geophysics was once a black box to me and it would not have been possible for me to finish this piece of difficult work without Steven’s beacon.

Mr. I.K. Chan and Mr. Kenneth Lai proved to be the best laboratory technicians. I.K. was invaluable in helping to establish all experimental setups, saving me months that would have otherwise been spent on connecting complicated pipe works and sieving soils. Kenneth, who taught and helped me to build and produce instrumentation and software control, was indispensable in my middle stage of research. Assistance was also offered to me most kindly by my fellow researchers in the laboratory, namely Fiona, Louis, Rolly and Janet. And there were Andrew, Undie, Faith, Thomas, Annie, Max, Eve and Yiu, C.H. Kwok, J., Leung and Hui who were past undergraduate students who worked alongside with me in this period. The pleasure is mine to have worked with all these wonderful people, the experience of which is one of the most gratifying parts of my research. I cherish the moments that we shared in our playground.

I would also like to thank Prof. Heng Li, Prof. Francis Wong, Dr. Paul Fox, Dr. Deric Drew and other administrative staff members in my department for the

constructive opinions they gave. They also provided my research with a stable environment that was free from administrative hurdles.

And I cannot forget the helping hands from other departments in PolyU. I owe my thanks to Mr. Leung and Mr. Dick Chu (Soil Mechanics Lab.), Dr. S.C. Kou and Mr. K.H. Wong (Concrete Lab.), Mr. Raymond Leung (Rock Lab.) for supplying to me essential laboratory facilities to conduct concrete and soil tests in Department of Civil and Structural Engineering. I also wish to acknowledge Ir. Albert Kwok, Mr. C.K. Kwok, Ir. Rex Lau and Mr. W.C. Lee from Industrial Centre for allowing me to access their concreting and soil sieving facilities on so many occasions. Thanks are also due to Dr. May Fan, Dr. Stephen Evans and Dr. Gillian Humphreys from Department of English, Dr. Steven Tsang's wife and my sister Anita for teaching me the way to write, as well as proofreading my manuscripts to journals and part of my thesis.

External collaborations were critical in my research. I appreciate very much the financial support from the Teaching Company Scheme supported by Innovation Technology Council, HKSAR Government and the industrial partner 'BUDA Engineers & Consultants Ltd.' Ir. King Wong, Dr. Shangxi Zhang, Bobby Li, Simon Chan and Wendy Lau of BUDA gave me backing in my two-year work in BUDA. Special thanks to Dr. Hui Fang and Mr. Du Xiao, scientists from Institute of Geophysical and Geo-chemical Exploration, Ministry of Land Resources, PRC. Both of them kindly lent me a radar system, conducted experiments with me and gave precious opinions about my experiments. Though there were times when we disagreed with one other, I cherish our friendship very much. Thanks are also given to Mr. Alex

AuYeung, S.F., my junior in secondary school and now a Ph.D. candidate of Department of Chemistry of Hong Kong University of Science and Technology, for providing X-ray diffraction facilities to conduct identification test of clay minerals.

The constructive comments given by the two external examiners, Dr. L.S. Chan of Department of Earth Science, University of Hong Kong, and Prof. Motoyuki Sato of Center for Northeast Asian Studies, Tohoku University are very helpful to the quality of my thesis. Their contributions in the examination process are highly appreciated.

Last but not least, I must express heartfelt gratitude to my warm and caring family and friends. The tremendous support that my parents, my late grandparents, and my girl friend Julia gave me over the past seven years, particularly when things were most difficult for me, was immeasurable and vital to the completion of this Ph.D. Being their companion and taking up an important part in their lives have made me the most fortunate man in this world.

TABLE OF CONTENTS

APPENDICES

LIST OF FIGURES

LIST OF TABLES

1. INTRODUCTION

1.1 GENERAL OVERVIEW

Porous Construction materials

This research investigates the characterization of three porous construction materials using electromagnetic (EM) radar. The studied porous construction materials are concrete, asphalt and soil. Traditionally, these porous materials are classified and characterized by their different solid structures, mineral compositions, and in particular, by a range of micro-structural properties. These properties refer to texture, porosity, specific surface and pore size distribution of the respective pore structures/systems such as the presence of varying degrees of inter-connected macro-pores, capillary pores and gel pores. These fundamental properties have a major bearing on a number of major phenomenological behaviours which are essential and central to the understanding of the material from the perspectives of engineering and material science. For mass manufactured materials such as concrete and asphalt, these phenomenological behaviour include strength, permeability and durability, etc. For natural materials such as soil, these phenomenological behaviours include strength, permeability, water-retaining and draining properties, and consolidation etc.

Characterization of Construction Materials by Traditional and the Advocated Methods/ Models

Traditional engineering/geological methods of material characterization, such as particle size distribution and the use of triangular diagrams (for soil only) depicting relative compositions of particle sizes (clay, silt and sand in soil), pore size distribution (inter-connected macro-pores, capillary pores and gel pores in concrete). Some of these methods are applicable to a particular material but not for the other materials, since their scopes of application are highly restricted and specially dedicated to a narrow range of materials. For example, the pore size distribution in fine-grained soil and asphalt cannot be determined by the Mercury Intrusion Porosimetry (MIP) method which is only applicable to concrete because of its high strength in resisting distortion during mercury intrusion.

Researchers in the EM field only focus on studying the EM wave properties of materials individually and in isolation; also only narrow and particular types of materials have been studied by particular researchers of distinct and isolated backgrounds. These backgrounds range from geophysics, civil engineering, soil science to hydrology and agriculture.

In this research, these three prominent construction materials are examined from the EM perspective using a unified approach. This approach is different from the traditional approach adopted in this field. It is realized by the establishment and the formulation of a set of unified constitutive models via data obtained from a series of coordinated experiments. These models characterize the three studied materials by using their EM wave properties and their engineering/geological properties. The former refers to the real part of complex dielectric permittivity (i.e. real permittivity in its short form or known as dielectric constant), energy attenuation and peak-frequency drift of the returned waveforms. The latter refers to porosity obtained by fitting data into dielectric and permeability models, as well as measurements following well-established methods.

Traditional, near-surface geophysical and non-destructive testing (NDT) techniques of investigation of sub-surface and man-made structures

Traditionally, engineers/geologists investigate the material’s sub-surface or structures (the latter refers to concrete and highway pavements) by retrieving the representative physical samples from the sub-surface/structures and putting these material samples through a series of traditional laborious laboratory tests. These methods are at times inaccurate and therefore the obtained data may not be representative of the actual sub-surface conditions. The inaccurate data is due to the restrictions in the sampling process which unavoidably disturbs the original physical state of the material. Results from laboratory tests on these disturbed samples do not represent the real in-situ sub-surface conditions and therefore render these laboratory results a certain degree of uncertainty.

Near-surface geophysical/Non-destructive testing (NDT) techniques offer an effective alternative for large scale and non-invasive investigations. Near-surface geo-physical techniques refer to those methods which cover a large scale of sub-surface materials, such as seismology, electrical resistivity, gravity, and geo-magnetics. Non-destructive testing techniques refer to those methods which cover a large mass of man-made materials and structures, such as ultra-sonic, infra-red thermography, eddy current, impact echo, shearography, and optics. Among these techniques, the Ground Penetrating Radar (GPR)/Surface Penetrating Radar (SPR) technique is preferred in a few particular aspects because of its high resolution and large depth of penetration when compared to many other geophysical and NDT methods, such as infra-red thermography which can only allow penetration to surface material. The GPR/SPR techniques provide an additional and perhaps a better insight into the subsurface strata/concrete structure conditions effectively without the need for retrieving a large amount of material samples and causing a lot of disturbance to the sub-surface/structures.

Traditional methods of characterization of sub-surface and structures by the EMCTL/TDR/GPR/SPR methods and the advocated Cyclic Moisture Variation Technique (CMVT)

Literature in this field reveals that most researchers adopted the Electromagnetic Coaxial Transmission Line (EMCTL) method and Time Domain Reflectometry (TDR) to characterize the subs-surface and concrete/asphalt structures. The former method can only be carried out on small extracted samples from the sub-surface, whereas the latter can only be applied to small masses of in-situ material. Doubt often remains whether the tested material is representative of the in-situ material. For large scale field investigations, researchers normally adopt GPR/SPR. Recently, large scale characterization of subsurface and man-made structures has been improved by enhancements in the capability and performance of advanced electronic hardware and software. This enhancement includes (1) minimizing the clutter, enhancing the signal to noise ratio, maximizing the antenna performance, (2) advancing the signal processing technique and mathematical algorithm, such as de-convolution, migration, etc., and (3) adopting dielectric models which were developed based on the traditional laboratory EMCTL method. However, the benefits of these enhancements are always undermined by the most fundamental and inherent difficulties in terms of the electromagnetic properties of the studied materials. These difficulties refer to (1) the inability of differentiating different material strata by GPR/SPR when contrast of dielectric permittivity of the studied materials is not sufficient (for example, they are relatively *dry*), and (2) the considerable differences of the prediction of real permittivity and water saturation due to the heterogeneous/layered distribution of solids, water and air, as well as geometries of the materials (Chan and Knight, 1999).

In this research, the limitations imposed by a small mass of material tested in the EMCTL/TDR methods and the inherent difficulties of GPR/SPR data interpretation (due to insufficient dielectric contrast of materials) are resolved by advocating a so-called Cyclic Moisture Variation Technique (CMVT). This technique subjects a large mass of materials to change from partially saturated states to a fully saturated state and vice versa, via a number of cycles of water-permeation and dewatering processes. GPR/SPR is designed to continuously track the changes of the EM wave properties. With this technique, water is used as an enhancer or a tracer to allow differentiation of the studied materials. This is difficult to perform when they are relatively dry.

Difficulties in Data Interpretation and Modeling of GPR/SPR's data

Engineers/geologists find GPR/SPR data interpretation difficult since the measured physical properties are not the resultant material properties (i.e. porosity, permeability, degree of water saturation and so on.) which are readily understood by engineers/geologists. Therefore forward modeling techniques have been developed to formulate relationships between a variety of physical properties obtained by geophysical methods and those resultant material properties for engineers/geologists.

In this research, three 'forward modelling' approaches are adopted. The well established Complex Refractive Index Model (CRIM) is used as a petrophysical model to relate the real permittivity (one of the EM wave properties), the porosity, and degree of water saturation of a porous material. Another renowned model, Debye's model (1929), is applied to explain the relaxation of permittivity and frequency-dependent characteristics of the measured real permittivity in this research. The last adopted model is the Kozeny-Carmen's permeability model (Kozeny, 1927; Carmen 1956) which depicts the relationships amongst permeability, porosity and specific surface in soils of near-spherical grains. These models allow the prediction of hydro-geological properties by means of measuring dielectric parameters, and the effects of different EM frequencies on these dielectric parameters.

1.2 HISTORICAL DEVELOPMENT FROM THE EVOLUTION OF ELECTROMAGNETISM THEORIES TO APPLICATION OF GPR/SPR

The development of the knowledge of electromagnetism has a long history. Michael Faraday (1791-1867) founded this science by observing and reporting the phenomena of electricity and magnetism through a series of experiments. James Clerk Maxwell (1831-1879) formulated and generalized these phenomena with mathematical expressions (collectively known as Maxwell's equations). Part of these mathematical expressions incorporates three constitutive parameters describing the behaviour of a medium when it is subject to external electric and magnetic fields. One of these three constitutive parameters is the dielectric permittivity of a material. During the early decades of the 20th century, different classical dielectric models and theories (such as the classic Debye's model, 1929, the volumetric mixing model by Lichtenecker-Rother, 1937, and Cole-Cole's model, 1941) were established over a wide range of EM frequencies (from kHz to GHz). From 1960 onwards, these theories and models have been used to characterize the dielectric properties of a large range of geological materials, such as rocks and soils (Birchak et al., 1974; Topp et.al., 1980; Wang, 1980; Knight and Nur, 1987a; Peplinski et.al., 1995). This advancement of knowledge of material characterization is attributed to the advancement and accuracy of modern electronic circuitry developed for the Electromagnetic Coaxial Transmission Line (EMCTL) method.

Since the 1970s, commercially available GPR/SPR systems have been developed as a near-surface geophysical instrument to survey the near-surface profiles and locate buried anomalies. Following the footsteps of the long-established seismic methods, the data collection methods (such as common-mid point method), data processing (such as migration and deconvolution) and interpretation methods (such as stacking of ray traces) of GPR/SPR were developed. Since the 1990s in the civil engineering discipline, the GPR/SPR technique has been increasingly utilized to inspect the quality of concrete in structures, such as Büyüköztürk (1998), McCann and Forde (2001) and Bungey (2003), as well as the thickness and structural integrity of asphalt pavements, such as Shang and Umana (1999) and Al-Qadi and Lahouar (2005). Also since the mid 1990s onwards, in the geophysical discipline, the majority of GPR/SPR applications have been in the locating and ranging of the buried anomalies (e.g. ancient buried constructions, underground mines, water tables, fracture detection, bedrock, aquifer and so on.) of the subsurface, such as Vaughan (1986), Davis and Annan (1989), Zeng and McMechan (1997), Nakashima et al. (2001), and Lu and Sato (2004). The more recent directions of research and applications are towards studying various engineering/hydro-geological parameters and petro-physical relationships of subsurface materials, such as Hubbard et al. (1997), Knoll (1996), Kowalsky et al. (2001) and Bevan et al. (2003). For large scale aquifer/soil transition zone characterization using GPR, as well as pumping-induced drainage, some successful case studies have been reported by Endres et al. (2000) and Bevan et al.

(2003). Table 1-1 summarizes chronologically the major milestones and achievements about the development of the science of GPR/SPR technology.

Table 1-1 Summary of the Era on Scientific Advancement of Understanding the Dielectric Properties of Materials, Advancing and Applying Investigation Techniques in the Field

Era	**Milestone and achievements**
Mid 19th century	Evolution of the theories of Electromagnetism
Mid 19th century	Formulation of Maxwell's equations
Early 20th century	Establishment of classic dielectric models and theories
1960s	Characterization of dielectric properties of soils and rocks
1970s	Development of more mature instrumentation of commercial GPR systems
	Formulation of mathematical models to establish relationship between electrical and other physical material properties by EMCTL method
1990s	Application in civil engineering, Hydro-geology, archaeology, forensics, precision farming, and so on.

To date, the applications of GPR/SPR are more involved in multi-disciplinary sciences and engineering, including near-surface geophysics, civil engineering, geotechnics, hydrology, mineralogy, archaeology, agriculture, electronics and so on.

1.3 RESEARCH OBJECTIVES

Three research objectives are identified as instrumental in the advancement in EM characterization techniques:

1. Characterization of three porous construction materials (i.e. concrete, asphalt and soil) in terms of the real part of dielectric permittivity, energy attenuation of the amplitudes of radar pulse reflections in time-domain and GPR/SPR reflection spectra in frequency domain over a wide range of degrees of water saturation utilizing GPR/SPR.

2. Formulation and establishment of a number of novel unified constitutive models of these three types of porous construction materials (i.e. concrete, asphalt and soil)

by amalgamating/association of two separate categories of material properties (i.e. dielectric properties and engineering/geological properties) by fusion of the experimental/empirical data obtained in the three materials.

3. Devising and pioneering the so-called Cyclic Moisture Variation Technique (CMVT) to characterize the three porous construction materials.

1.4 RESEARCH METHODOLOGY

An extensive literature search and review has been performed to identify the existing gaps of knowledge which help to justify the formulation of research approaches. A research plan was established and resulted in the instigation of an integrated and coordinated series of experiments on varying factors in concrete, asphalt and soil. These experiments were performed with the help of concurrent efforts in building an effective instrumentation system. This system was based on automation control by a number of in-house developed computer programs operating in the National Instrument™ hardware and the LabVIEW™ software environment. Data processing in both time- and frequency- domains were performed to obtain values of parameters of material properties. These sets of values were subsequently amalgamated to establish and formulate a number of unified constitutive models which assign the rightful positions of each studied material. These classifications have been verified and substantiated by sets of well-established tests.

1.5 ORGANIZATION STRUCTURE OF THE THESIS

This thesis starts with a fundamental review of literature in Chapter 2 and theories in Chapter 3. Chapter 4 and Chapter 5 introduce the development of the in-house effective instrumentation system and a range of data processing techniques adopted in this research respectively. To investigate the material properties of concrete, asphalt and soil, a series of coordinated experiments are given in Chapter 6, Chapter 7 and Chapter 8 respectively. Some findings from these chapters demonstrate dielectric hysteresis which is further elaborated in Chapter 9, with the basis established according to plots depicted in Chapter 7 and Chapter 8. The material properties obtained from the efforts reported from Chapter 6 to Chapter 8 will be further used to establish and formulate a number of unified constitutive models presented in Chapter 10 for characterizing the three studied materials. Chapter 11 describes a methodology of a hypothetical in-situ Cyclic Moisture Variation Technique (CMVT) which aims to extend and step forward from the laboratory CMVT advocated in Chapter 7 and Chapter 8 to the field CMVT. Chapter 12 summarizes the major contributions to knowledge achieved in this research. Chapter 13 suggests few recommendations for future research. Finally, Chapter 14 provides a conclusion to this research.

2. LITERATURE REVIEW

2.1 INTRODUCTION

This literature review is divided into four sections. Sections 2.2, 2.3 and 2.4 examine various factors of physical properties on dielectric properties of concrete, asphalt and soil respectively. These three materials are both porous and permeable and therefore allow various degrees of water saturation. The various material properties can be linked by a number of dielectric models/formulae (see Section 2.5) through experimental data in small scale homogeneous samples and derived from theories. With these models, the behaviour of some engineering/geological parameters of these porous materials can be modeled and therefore can be predicted in large scale investigations.

The determination of the material properties and the derivation of the dielectric/petrophysical models require accurate instrumentation. Section 2.6 reviews the experimental techniques to be applied in the laboratory and in the field. These techniques include Ground Penetrating Radar (GPR)/Surface Penetrating Radar (SPR), Electromagnetic Coaxial Transmission Line (EMCTL) method and Time Domain Reflectometry (TDR)/Portable Dielectric Probe (PDP). Their functions, working principles, advantages and disadvantages are introduced, compared and contrasted.

Section 2.7 provides several discussions on the inadequacy of the key studies covered from Sections 2.2 to 2.6. These discussions will summarize the development in this field, as well as identify the gaps in knowledge, which justify the formulation of research approaches on carrying out a series of experiments (described in Chapter 6 to Chapter 8) and the construction of the unified models (described in Chapter 10).

2.2 MAJOR FACTORS CONTRIBUTING TO THE DIELECTRIC PROPERTIES OF CONCRETE

Since the 1990s, there has been an increasing use of surface penetrating radar (SPR) to detect anomalies embedded in concrete structures (Bungey, 2003). In this non-destructive testing of structures, the depth range and detection of such anomalies are dependent on the accurate determination of the dielectric properties of the host material (i.e. concrete). The dielectric properties of concrete are influenced by a number of other physical properties possessed by the concrete.

In the past few decades, there has been little effort to investigate the relationship between dielectric properties and other physical properties of concrete (Gu and Beaudoin, 1997). The limited study of this relationship is attributed to the difficulty in differentiation and characterization of the physical properties of concrete components by SPR when concrete is relatively dry. A number of studies are summarized in Appendix A regarding this area of investigation. Some important factors listed in Appendix A on the dielectric properties will be discussed in subsequent sections. These major factors include water content, water to cement ratio, porosity and EM frequency, while other factors such as salt impregnation, cement type, pulverized fuel ash (PFA), ground granulated blast furnace slag (GGBS), high strength concrete (HSC), and temperature during testing are reported to be of minor significance or negligible (Soutsos et al., 2001).

2.2.1 THE FACTOR OF WATER CONTENT

It is well recognized that increasing water content is the major contributing factor to the increase of the dielectric permittivity of concrete. This increase comprises the real part as depicted in Fig. 2.2-1, as well as the imaginary part/the attenuation of EM transmission (Maierhofer and Wöstmann, 1998; Binda et al., 1998; Oota, 2000; Soutsos et al., 2001).

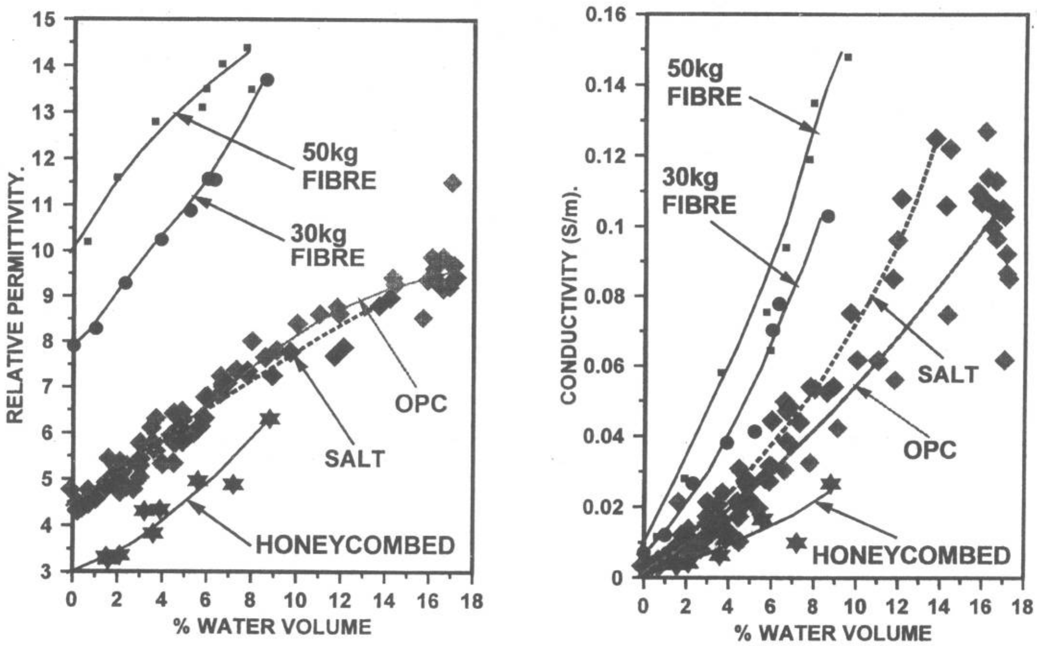

Remark: relative permittivity is the same as dielectric constant

Fig. 2.2-1 Relative Dielectric Permittivity and Conductivities for Fibre, Honeycombed and Salt Impregnated Concrete Specimens at 500MHz (Source: Soutsos et al., 2001)

Both the real and imaginary parts of dielectric permittivity increase with increased water content of concrete, but at very high levels of water content, the gradient of the dielectric permittivity curve decreases marginally, as reported by Soutsos et al., (2001) and Maierhofer and Wöstmann, (1998), as depicted in Fig. 2.2-1. This is possibly attributed to two issues:

1. a change of some free water to bound water (Soutsos et al., 2001), and hence the bounded water molecules absorbed in capillary pores is restricted in motion by electrostatic interaction with solid particles. This results in a smaller marginal increase of dielectric permittivity which is similar to the case in soil described by De Loor (1983), Huisman et al. (2003) and West et al. (2003).
2. the specimens may contain a small amount of un-hydrated cement which reacts with and consumes free water to form a new cement matrix. This change of the state of water reduces the bulk dielectric permittivity since less free water participates in the polarization process (Soutsos et al., 2001).

This phenomenon was also observed in the studies on soil described in Section 2.4, as well as the experimental findings reported in air-cured concrete and soil of various textures described in Chapter 6 and Chapter 8 respectively. However, this phenomenon cannot be observed in normal well-compacted concrete and asphalt layers, which will be shown in Chapter 6 and Chapter 7 respectively.

The role of water content on dielectric properties is equally apparent and important in mature and fresh concrete. This factor can be described by the controlled water to cement ratio which is determined during the mixing of concrete. This will be discussed in the following sub-section.

2.2.2 THE FACTOR OF POROSITY

Porosity is a measure of the ratio of the pore volume to the bulk volume. In concrete, it depends on the large voids/macro-pores and the small capillary/interstitial pores. The former refers to honeycombs which are normally caused by inadequate compaction and segregation, while the latter always exists between the solid constituents. The theory of these pores in concrete will be detailed in Chapter 3, whereas two representative studies (Soutsos et al., 2001; Gu and Beaudoin, 1997) related to the porosity of concrete and cement paste are described in this sub-section.

A. HONEYCOMB

The factor of honeycomb on dielectric properties in concrete was studied by Soutsos et al. (2001), as depicted in Fig. 2.2-1. In this work, it was found that the values of dielectric constant are reduced in the honeycombed concrete specimens, presumably due to a larger occupation of air voids which exhibit a low dielectric value. In particular for honeycomb concrete specimens, the marginal increase of ε’ in the plot of dielectric constant versus moisture content was steady, whilst that in the same plot for other normal concrete specimens is reduced. A similar phenomenon can also be observed in Maierhofer and Wöstmann (1998)’s work. However, both Maierhofer and Wöstmann (1998) and Soutsos et al., (2001) did not address the difference in gradients found in honeycomb and normal concrete. This difference is presumably caused by the reduced dielectric polarization in the bound form of water than free water when soils were the subject of investigation (De Loor, 1983; West et al., 2003; Huisman et al., 2003). In honey-combed concrete, most water molecules are effectively in its free state due to the existence of macro-pores, while in normal concrete, the water molecules absorbed by the very small capillary and gel pores are absorbed and bounded by the cement matrix. The polarization of bound water is limited by the electrostatic interaction with the very small gel particles, whereas that of free water is not restricted in motion to align with the external electric field. Therefore normal concrete contributes less ability of polarization (i.e. a measure of dielectric constant) than honeycombed concrete does.

Gu and Beaudoin (1997) investigated the porosity of cement paste and adopted an empirical equation established by Sen and Chew (1983). This equation relates the dielectric constant and the porosity of sedimentary rocks, as shown in Eq. [2.2-1]:

$$\varepsilon_e^{'} = 1.5\varepsilon_{cp}^{'} + P^{1.5}(\varepsilon_w^{'} - 1.5\varepsilon_{cp}^{'}) \text{ ....[2.2-1]}$$

where ε'_e is the measured real part of dielectric permittivity, ε'_{cp} and ε'_w are the real part of dielectric permittivity of cement paste and water respectively, P is the porosity of concrete.

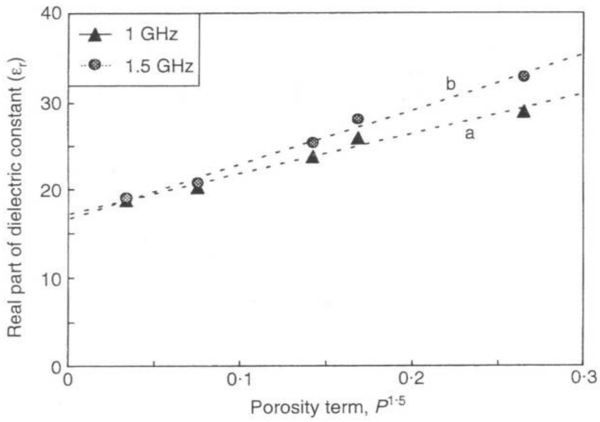

Fig. 2.2-2 Plot of the Effective Dielectric Constant obtained for Water Saturated Cement Pastes versus Porosity (Source: Gu and Beaudoin, 1997)

According to Eq. [2.2-1], a larger porosity increases the measured ε'_e. Gu and Beaudoin (1997)'s data was found to be in good agreement with Eq. [2.2-1], as shown in Fig. 2.2-2.

The porosity of concrete is a function of both isolated/inter-connected macro-pores in honeycombed concrete (i.e. a factor of degree of compaction) and the inter-connected capillary/gel pores (i.e. a factor of the degree of hydration and various aggregate to cement ratio). A relationship between the latter case and the dielectric permittivity was rarely reported in the literature and will be a major concern in Chapter 6.

B. WATER TO CEMENT RATIO

The factor of water to cement ratio on dielectric properties is commonly observable in cement paste (Taylor and Arulanandan, 1974; Wittmann et al., 1975; McCarter and Curran, 1984; Gu and Beaudoin, 1997). For water-saturated and hardened cement paste, a larger water to cement ratio is accompanied with a larger dielectric constant over a wide range of EM frequency (Gu and Beaudoin, 1997). It is presumably because the cement pastes with higher water to cement ratio have higher porosity values (Neville, 1995) and contain more evaporable water than that with a lower w/c ratio (Gu and Beaudoin, 1997). The evaporable water refers to the free water, absorbed water and intercalate water between solid matrix in concrete. As discussed in Section 2.2.1, water content is the dominant factor of the dielectric constant, and hence a cement paste with a higher w/c ratio (i.e. more water content during mixing) increases the dielectric constant. It is also noted that the cement type in this review and subsequent experimental chapters refer to ordinary portland cement (predominantly composed of calcium silicates).

The factors of w/c ratio found in cement paste were not identified in concrete specimens at either the mature state (Soutsos et.al., 2001) or the fresh state. In concrete, aggregate occupies as much as three-quarters of the bulk volume (Neville, 1995). Therefore due to the small porosity of aggregate, the dielectric constant of concrete is far smaller than that of cement paste, in which the latter contains no aggregate.

2.2.3 THE FACTOR OF ELECTROMAGNETIC FREQUENCY

The factor of EM frequency on dielectric permittivity was studied by Concrete Society (1997) and Soutsos et al. (2001). The behaviour of concrete under a range of EM frequencies follows the relaxation and dispersion theories of dielectric permittivity described in Debye's model (1929) which will be investigated in Section 3.2.

As illustrated in the plotted curves (Concrete Society, 1997) in Fig. 2.2-3 and the theory suggested in the Debye's model (1929), the real part of dielectric permittivity/dielectric constants (ε') is reduced along with increasing EM frequency within an intermediate region of frequency transition. At very high and very low frequencies, the change of ε' becomes less dependent of the EM frequency. Owing to the common theories corresponding to this phenomenon exhibited in both asphalt and concrete, a comprehensive discussion of this phenomenon will be collectively presented in Section 3.3.3.

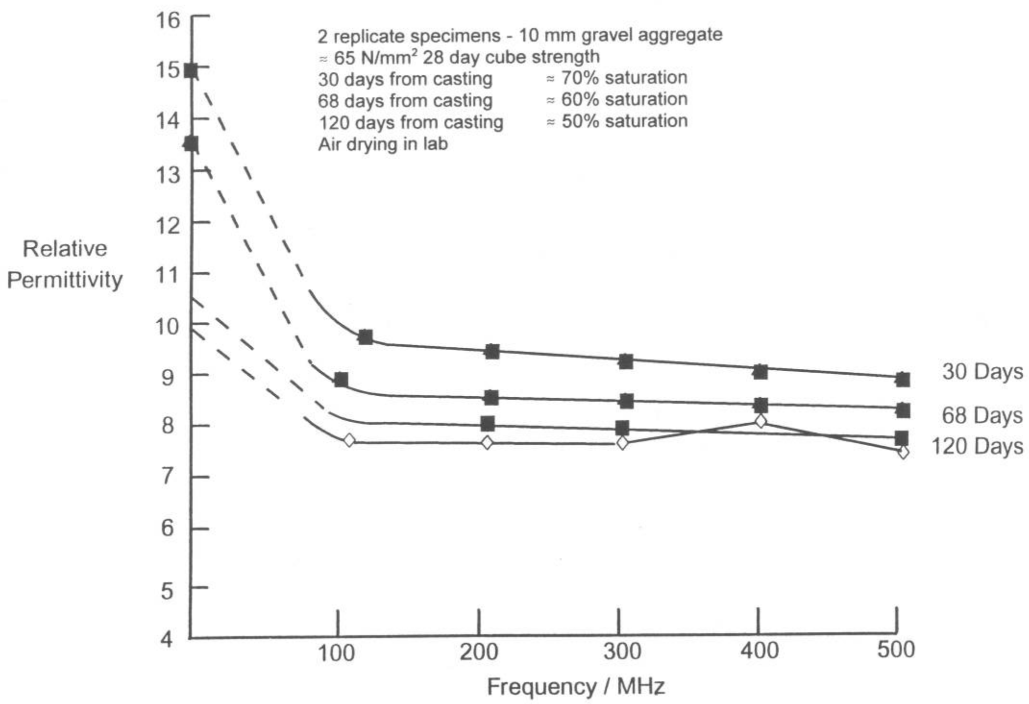

Fig. 2.2-3 Variation of Relative Dielectric Permittivity of Concrete with Frequency and Age (Source: Concrete Society, 1997)

In the following section, the literature works related to asphalt will be introduced. Asphalt is, together with concrete, a mass manufactured construction material. These two materials share the same factors affecting the dielectric properties and hence the resultant material properties described in Chapter 1, such as porosity and permeability.

2.3 MAJOR FACTORS CONTRIBUTING TO THE DIELECTRIC PROPERTIES OF ASPHALT

A large number of applications of Ground Penetrating Radar (GPR) have been reported with the depth ranging of asphalt thickness and the evaluation of structural integrity (Al-Qadi and Lahouar, 2004), but systematic studies on the dielectric properties of asphalt have rarely been reported (Shang and Umana, 1999). This may be attributed to the fact that the dielectric properties of asphalt can be inferred from studies of soil and concrete with a similar nature as reported elsewhere (see Appendixes A and B).

The study carried out by Shang and Umana (1999) is the most comprehensive study of the dielectric properties of asphalt. Hence the review in this section is based in general on this work. The following sub-sections describe two major factors of dielectric properties of asphalt, namely the water content of asphalt and the electromagnetic frequency. Some other effects, such as mix type, relative bulk density and asphalt cement content were found not to pose any significant effects on dielectric properties (Shang and Umana, 1999).

2.3.1 THE FACTOR OF WATER CONTENT

The dielectric properties of asphalt (represented as the marginal increase of the effective dielectric permittivity $\Delta\varepsilon_S$ and the marginal increase of Debye relaxation time $\Delta\tau$ as defined in Fig. 2.3-1) are controlled by the water content, as illustrated in Fig. 2.3-2. Both $\Delta\varepsilon_S$ and $\Delta\tau$ increased with water content after reaching a *characteristic volumetric water content* W_C (i.e. W_C = 1.2%). With the water content below this W_C, the values of the changes of dielectric permittivity and Debye relaxation time are in general constant, and are equal to 0.5 and 80ps respectively. This characteristic volumetric water content (W_C) is analogous to the transition water content (W_t) identified in the case of soil, as described in Section 3.2.5.7. In both cases the same phenomenon in the same plot are demarcated by initially a very slow increase of the dielectric constant/permittivity from very low water content up to the *transition moisture content* and increase rapidly afterwards (i.e. at the stage of intermediate degree of water saturation S_w). Shang and Umana (1999) attributed this phenomenon to the restricted polarization of bound water existing in the asphalt specimens over a range of small values of water content (i.e. W_C <1.2%). This explanation is analogous to the theory of soil's wilting point suggested by Wang (1980), as discussed in Section 3.2.5.4, as well as the building-up of mono-layers of water in sandstone suggested by Knight (1991).

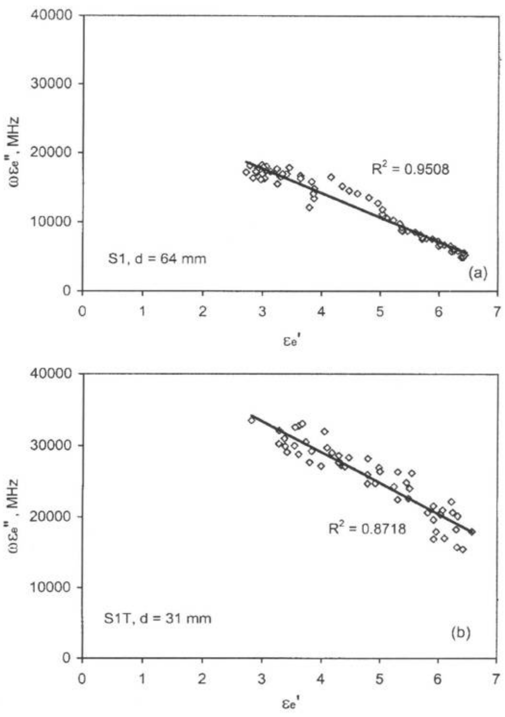

Fig.2.3-1 Determination of Relaxation Time from Complex Permittivity Measurement (Source: Shang and Umana, 1999)

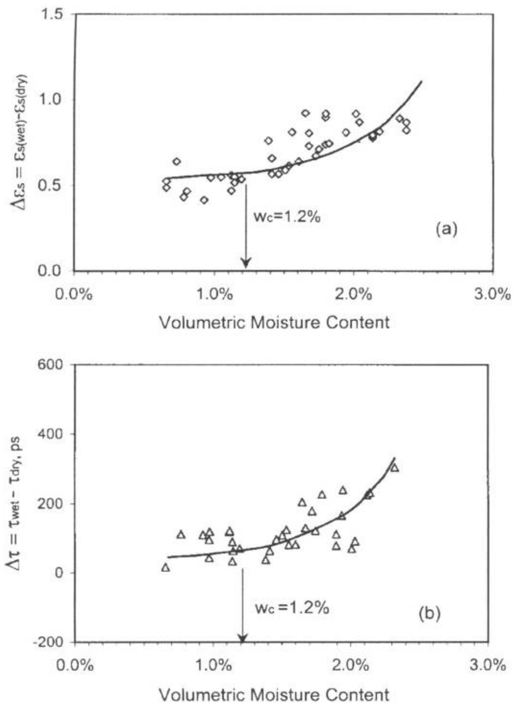

Fig. 2.3-2 Effect of Moisture Content on: (a) Dielectric Constant; (b) Relaxation Time (Source: Shang and Umana, 1999)

$$\Delta\varepsilon_S = \varepsilon_{S(wet)} - \varepsilon_{S(dry)} = 0.55 + \frac{6w^2}{0.03 - w} \ldots [2.3\text{-}1]$$

$$\Delta\tau = \tau_{wet} - \tau_{dry} = 60 + \frac{3500w^2}{0.03 - w} \text{ in ps } ...[2.3\text{-}2]$$

where

$\Delta\varepsilon_S$ is equal to $\varepsilon_{(wet)} - \varepsilon_{(dry)}$, $\Delta\tau$ is equal to $\tau_{(wet)} - \tau_{(dry)}$,

w is the volumetric moisture content

After exceeding the transition moisture content (i.e. W>1.2%), the marginal increases/decreases of dielectric permittivity and the relaxation time increase with water content. The mathematical relationship between these parameters is obtained by regression as shown in Eq. [2.3-1] and Eq. [2.3-2]. Both parameters were found to depend on water contents, but not any other material properties.

2.3.2 THE FACTOR OF ELECTROMAGNETIC FREQUENCY

Shang and Umana (1999) reported that the experimental findings over the frequencies ranging from 10MHz to 1.5GHz (depicted in Fig. 2.3-3) follow the classic Debye's model (1929). The real part of the dielectric permittivity decreases after reaching a frequency range from approximately 400MHz to 900MHz, while the imaginary part increases at the same range, as shown in Fig, 2.3-3. For the imaginary part, a peak was found at approximately 1GHz which is known as the relaxation frequency of the material. This relaxation frequency and its reciprocal value (known as relaxation time) quantify the dielectric dispersion in the real part of dielectric permittivity caused by sluggish motion of polar molecules in response to an external EM field. Owing to the established theories regarding this phenomenon exhibited in both soil and concrete, a comprehensive discussion of this phenomenon will be collectively presented in Section 3.3.3.

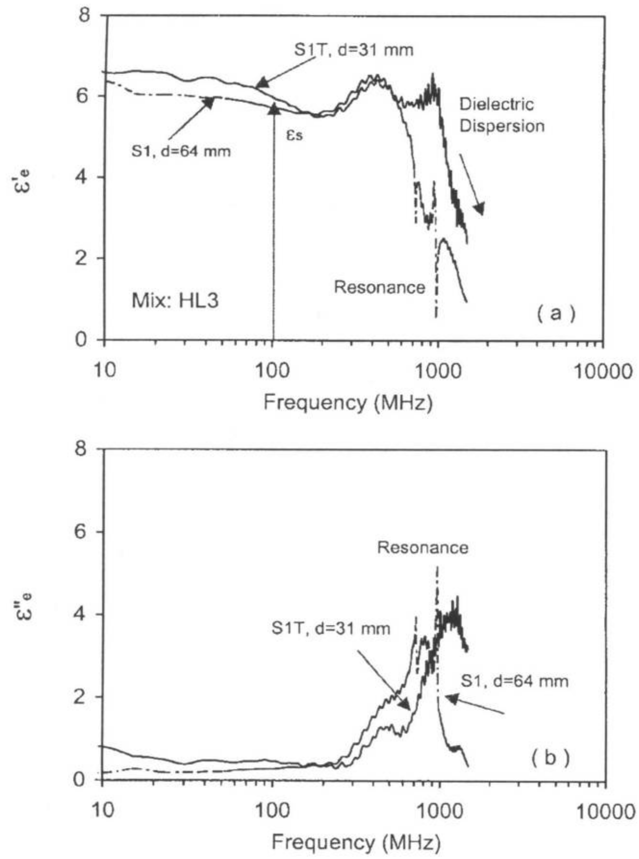

Fig. 2.3-3 Typical Results of Complex Permittivity Measurement: (a) Permittivity; (b) Loss Factor (Source: Shang and Umana, 1999)

Shang and Umana (1999) also reported that the curve should have included a leveled portion at very high frequencies, as predicted by Debye's model (1929). However, this portion cannot be observed because the maximum adopted EM frequency (i.e. 1.5GHz) did not reach the transition frequency which demarcates the downward portion (i.e. indicate a dielectric dispersion) and the leveled portion (i.e. demonstrate a minimum value of dielectric constant).

Water content and EM frequency were reported to be the only dominant factors affecting the dielectric properties of asphalt (Shang and Umana, 1999). Other factors are found to be not prominent, presumably due to the small ranges of both porosity (3-6%) and specific surface (0.06-2.18 m^2/g) exhibited in various types of asphalt. In the next section, the contributing factors on dielectric properties of soil will be discussed.

In soil, the number of contributing factors on dielectric properties is significantly more than that of asphalt, which can be attributed to wider ranges of porosity and specific surface exhibited in soils of widely varying types.

2.4 MAJOR FACTORS CONTRIBUTING TO THE DIELECTRIC PROPERTIES OF SOIL

The dielectric properties of soil determined in a wide range of microwave frequencies are influenced by a number of physical properties possessed in soil. In the past few decades, there have been numerous efforts in this area. Knoll (1996) summarized a large number of important research studies which investigate the relationships between a range of physical properties and the dielectric properties of soil. Knoll (1996) presented and tabulated these research studies in chronological order. In this research, the context in the original Knoll's table (1996) has been paraphrased, re-arranged and presented by putting the emphasis on physical properties instead of chronological order, as reported in Appendix B. Also, some further significant literature studies have been added and highlighted in this table.

With the table described in Appendix B, some important findings regarding a number of physical properties affecting the dielectric properties of soil are immediately apparent and will be discussed in the following sub-sections. These properties include water content, soil texture, EM frequency and clay mineralogy.

The majority of the research works described in Appendix B was based on the *Electro-Magnetic Coaxial Transmission Line* (EMCTL) method and/or the *Time Domain Reflectometry* (TDR) technique and only a minority adopted *Ground Penetrating Radar* (GPR). These techniques will be reviewed in Section 2.6.

2.4.1 THE FACTOR OF WATER CONTENT

Water is recognized as the major contributing factor to the increase of the dielectric properties of soil by many research studies (Hoekstra and Delaney, 1974; Topp et al., 1980; Wang, 1980; Dobson et al., 1985; Wang and Schmugge, 1980) since its permanent dipole structure of water molecules is easily polarized, as described in Section 3.3.3.

Within these studies, Topp et al. (1980) established a well-known and simple empirical equation. This equation is a simple third order polynomial function which describes the relationship between dielectric constants (ε') and volumetric water content (θ_v) as shown in Fig. 2.4-1:

$$\theta_v = -5.3x10^{-2} + 2.92x10^{-2}\varepsilon - 5.5x10^{-4}\varepsilon^2 + 4.3x10^{-6}\varepsilon^3 \text{ …….. [2.4-1]}$$

This simple relationship has been widely adopted in many applications of EMCTL, TDR, PDP and GPR's investigation of mapping in-situ soil moisture content using dielectric data at a multitude of frequencies. This equation will also be incorporated as one of the empirical models described in Section 2.5.1a.

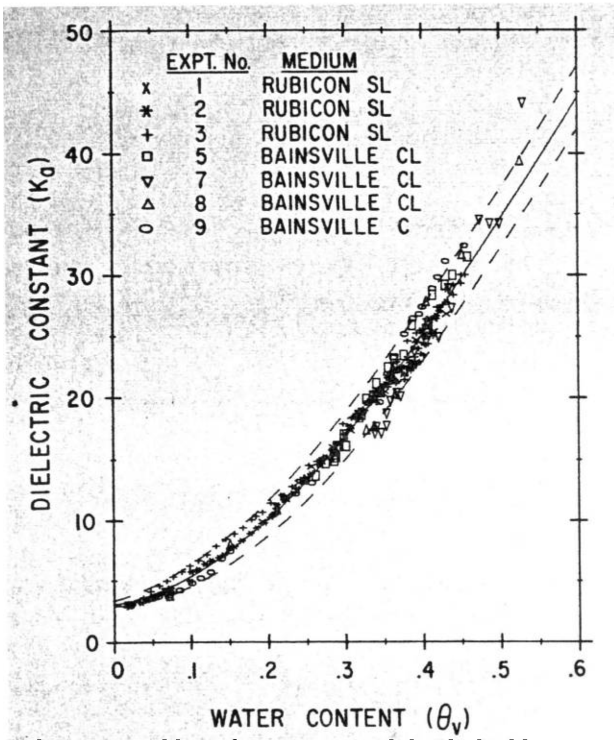

Remark: The solid line is the empirical best-fit equation and the dashed lines are shifted +/-0.025 in θ_v

Fig.2.4-1 Data and the fitted Curves in the Plots of K_a and θ_v for the Four Mineral Soils. (Source: Topp et al., 1980)

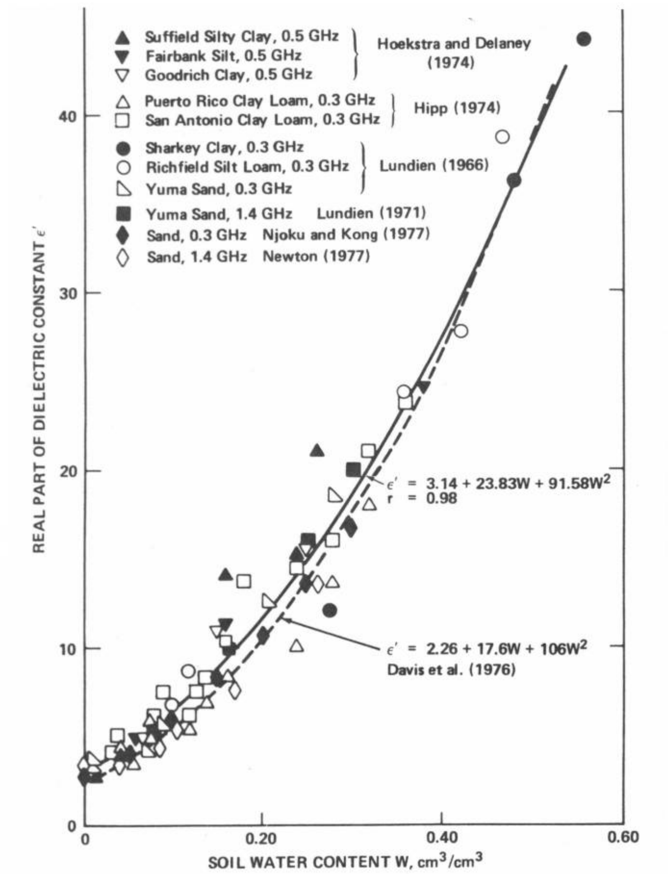

Remark: At 1.4GHz, only the results of sandy soil measurement are shown

Fig. 2.4-2 The Measured Real Part of Dielectric Constant as a function of Water Content for many Soils measured at the Frequencies 0.3GHz, 0.5GHz and 1.4GHz. (Wang, 1980)

Wang (1980) summarizes the studies conducted by a number of researchers, as shown in the data points obtained and curves summarized in their studies depicted in Fig. 2.4-2. These relationships relate the dielectric constant and water content over a large range of soil textures, using different microwave frequencies from 0.3GHz to 1.4GHz. As depicted in Fig. 2.4-1 and Fig. 2.4-2, the plots over a wide range of soil textures are represented as a single polynomial function over a wide range of frequencies. However in the following sub-section, these conclusions are in doubt according to the experimental studies conducted by other researchers, as discussed in Section 2.4.2a.

Wang and Schmugge (1980) reported another sets of results in their experiment, as shown in Fig. 2.4-3. . The curves at very high volumetric water contents shown in Fig. 2.4-3 show a transition from a relatively straight segment with constant increasing gradient to another segment with rapidly decreasing gradient after a turning point. Critical S_w is designated as the moisture corresponding to this *turning point*.

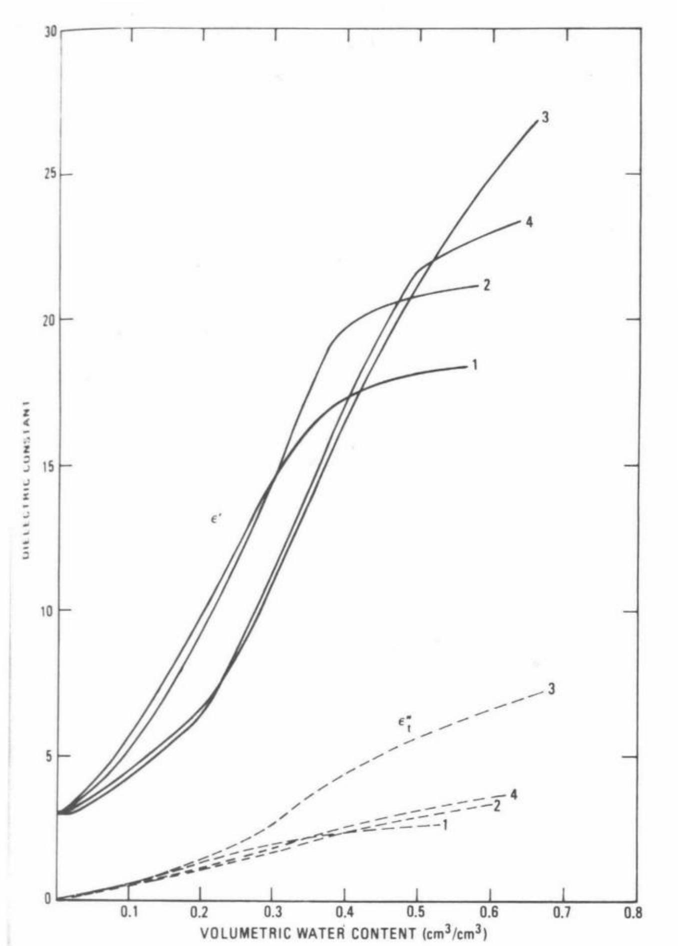

Curve	Texture (percent)			Wilting point WP (cm^3/cm^3)	Transition moisture θ_t (cm^3/cm^3)
	Sand	Silt	Clay		
1	88	7.3	4.7	0.034	0.2
2	56	26.7	17.3	0.115	0.22
3	19.3	46	34.7	0.220	0.31
4	2	37	61	0.358	0.31

Remark: This figure is the same as Fig. 2.5-2 and Fig. 3.2-15

Fig. 2.4-3 The Dielectric Constants versus Volumetric Water Content for Four Soils measured at 5GHz. Soil types are referred in Table 3.2-6 (Source Wang and Schmugge, 1980)

A similar phenomenon (i.e. changing curvature of curve in different segments) was also reported when experimenting on sandstone (Knight and Nur, 1987a) and on concrete (Soutsos et al., 2001 and Maierhofer and Wöstmann, 1998). The latter two studies have already been reported in Section 2.2. The theory related to this phenomenon in soil, concrete and asphalt will be collectively explained in Section 3.2.

Hoekstra and Delaney (1974) reported the relationship between attenuation in dB/m and water content for a wide range of sand, silt and clay at several frequencies from 0.5GHz to 26GHz as shown in Fig. 2.4-4. This figure depicts the trends of an increase of attenuation when water content increases for all frequencies from 0.5GHz to 26GHz.

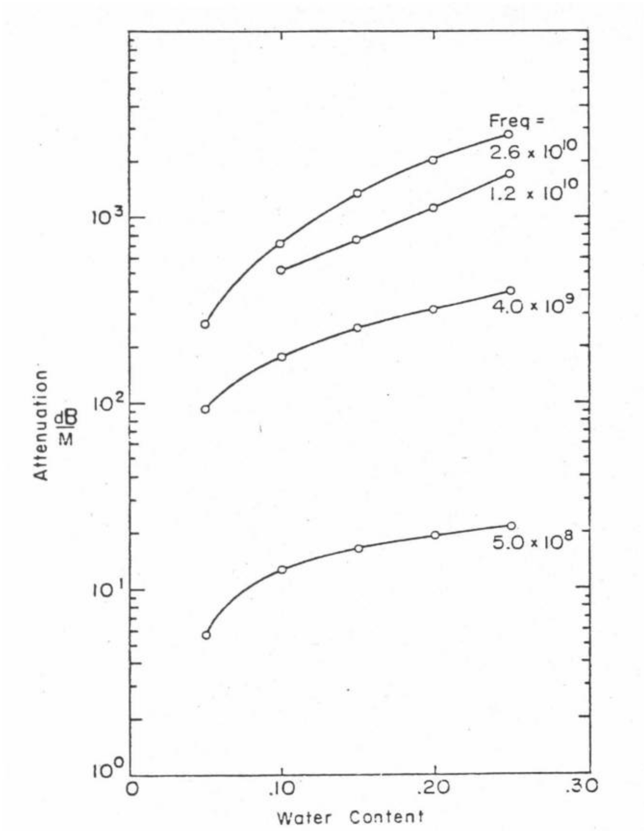

Fig.2.4-4 The Attenuation in Soil for Plane Electromagnetic Wave Propagation as a function of Volumetric Water Content at Several Frequencies
(Source: Hoekstra and Delaney, 1974)

2.4.2 THE FACTOR OF POROSITY

A. SOIL TEXTURE

It is noted from a number of research studies summarized in Appendix B that some confusion exists on the roles and effects of soil textures on the dielectric properties of soil in the presence of water amongst the studies of some investigators summarized in Appendix B. Specifically, Hoeskstra and Delaney (1974) and Topp et al. (1980) concluded that soil texture and composition have a very minor influence on the dielectric constant of wet soil. However, Wang and Schmugge (1980), Dobson et al. (1985) and Knoll (1996) suggested that significant dielectric differences were noted for different soil textures and compositions in the presence of water. Knoll (1996) recognized that this discrepancy is difficult to be reconciled and suggested that it may be due to non-unified sample compositions, sample preparation and measurement procedures.

To resolve this inconsistency, the theories of *wilting points* and *bound water* can be employed to investigate the effect of texture on dielectric properties. The use of *wilting point* proposed by Wang and Schmugge (1980) gives a more specific and plausible explanation of the dependence of the soil dielectric properties on soil texture (refer to Section 3.2.5.3). This work reports that

1. both wilting point (WP) and transition moisture content (W_t) (the latter is a characteristic in the relationship between dielectric constant and water content) are a function of soil texture and can be represented by a simple linear equation (see Eq. 3.2-1),

2. A large fraction of small sized soil particles (especially as clay) has a greater wilting point and a larger specific surface, and hence a greater contribution on dielectric permittivity.

Another theory based on the *bound water* in different soil textures and compositions was proposed by Dobson et al. (1985) (refer to Section 2.5.2b). The macroscopic dielectric behaviour of the soil system was modeled by the four components constructed in the soil physical model. The four components refer to dry solids, bound water, bulk water and air. Textures of soil affect the effects of each of these components on dielectric properties. For example, a soil of high clay content has a higher specific surface and therefore its effect of bound water on dielectric properties become more apparent than a soil of high sand content.

These two theories are collectively formulated and known as 'semi-empirical dielectric mixing models' (Knoll, 1996) and will be further elaborated in Section 2.5.2 to model the dielectric behaviour. These two independent theories provide a more comprehensive physical justification about the complex nature of soil dielectric and other properties than the simple equations provided in Topp's model (see Eq. [2.4-1]). A series of soil characteristics determined in the experimental works described in Chapter 8 will be explained on the basis of these two theories.

B. CLAY MINERALOGY

Clay possesses larger values of specific surface than coarser soil, as shown in Table 2.4-1. The values of specific surface of all particles (i.e. a function of soil texture and composition) determine the porosity, and hence determine the amount of water to be attracted to and adsorbed by the surfaces of the solid soil particles. It follows that a fine-textured soil (such as clay) results in larger values of dielectric permittivity than a coarse-textured soil.

Peplinski et al. (1995) illustrated the effects of the magnitude of specific surface (as reported in Table 2.4-1) in clay mineralogy on both the real and imaginary parts of the dielectric permittivity respectively, as depicted in Fig. 2.4-5. These effects are:

- West Bentonite, Kentucky Ball and Geogia Kaolin possess varying magnitudes (i.e. in decreasing order) of marginal increases of dielectric values of both the real and imaginary parts,
- The marginal increases of the real part are higher than that of the imaginary part,
- The marginal increases in the imaginary part are more differentiable in West Bentonite than Kentucky Ball and Georgia Kaolin in decreasing order.

Table 2.4-1 Specific Surface of Different Soil Textures (sand, silt and clay)
(Source: re-organized from Peplinski et al., 1995; Whitlow, 2001)

Soil texture		Specific Surface (m^2/g)	Sources
Sand		0.04-0.001	Whitlow (2001)
Silt		1-0.04	
Clay	Kaolinite	20	
	Illite	80	
	Montmorillonite	800	
	Georgia Kaolin	5-20	Peplinski et al. (1995)
	Kentucky Ball	20.9	
	Western Bentonite	~700	

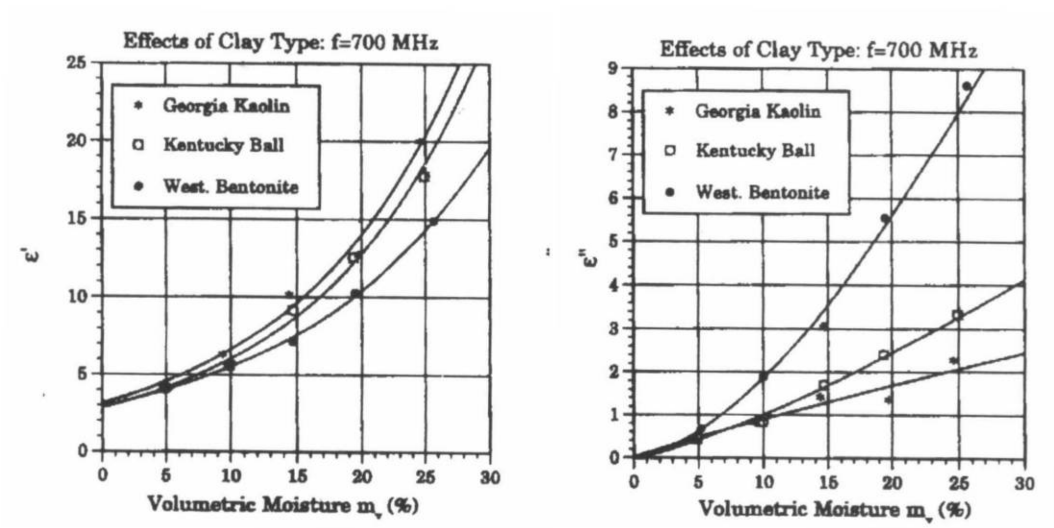

Fig.2.4-5 Measured Variations of ε' and ε" with Volumetric Moisture Content at 0.7GHz on different Clay Types (Source: Peplinski et al., 1995)

The values of specific surface in soil textures and clay mineralogy described in Table 2.4-1 have a important bearing on dielectric permittivity as shown in Fig. 2.4-5.

2.4.3 THE FACTOR OF ELECTROMAGNETIC FREQUENCY

Over the frequencies ranging from 100MHz to 10GHz and from 18GHz, two representative experimental results obtained by Hoeskstra and Delaney (1974), as well as Hallikainen et al. (1985) on variation of soil dielectric permittivity with water content, are shown in Fig. 2.4-6 and Fig. 2.4-8 respectively. The dielectric behaviour was found to agree in general with the classic Debye's model (1929) shown in Fig. 2.4-7.

A. THE REAL PART OF DIELECTRIC PERMITTIVITY

- It is noted that at low frequencies, the real part of soil remains constant, whereas at higher frequencies, dielectric constants of soil also remain constant but with lower values, as depicted in Fig. 2.4-7.

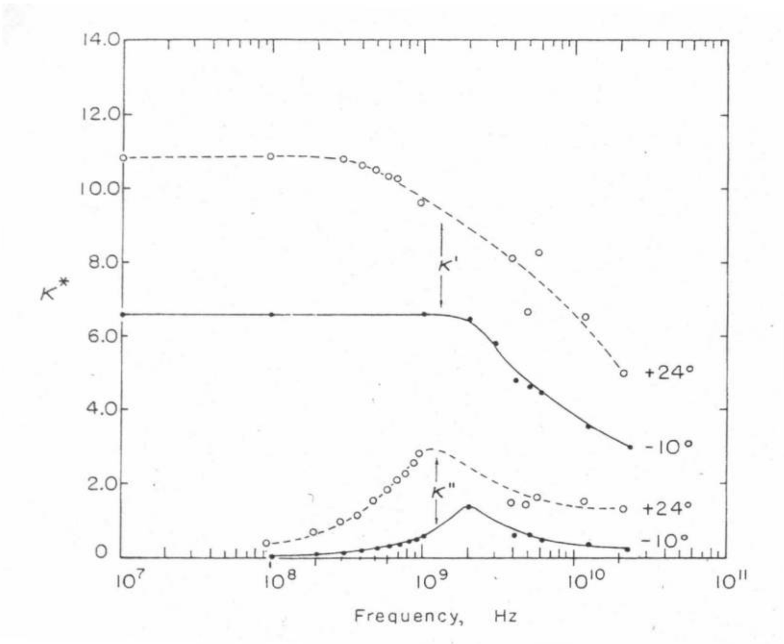

Fig. 2.4-6 The Complex Dielectric Constant of Goodrich clay at 24°C as a function of Frequency at two Water Contents (0.05 and 0.1) (Source: Hoeskstra and Delaney, 1974)

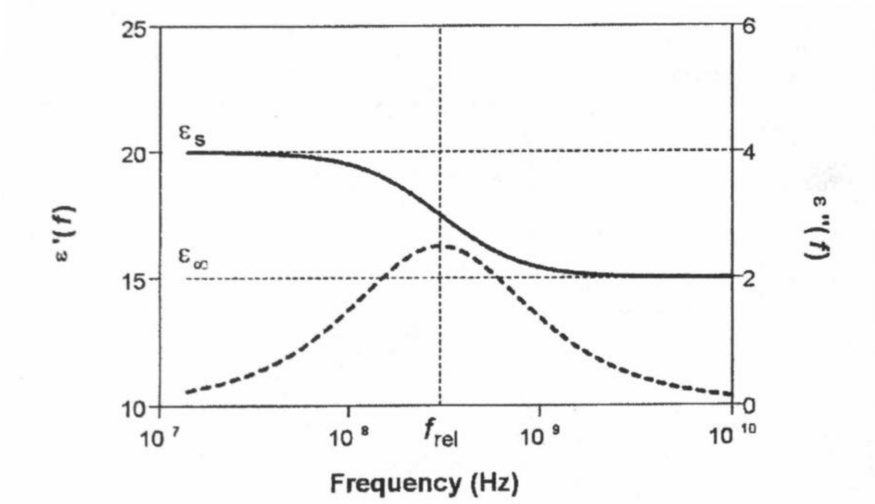

Fig. 2.4-7 Example of the Debye Model for the Real Part (solid line) and Imaginary Part (dashed line) of the Dielectric Permittivity (Source: Huisman et al., 2003)

- Within the intermediate frequencies called the *transition frequency band*, dielectric constant changes abruptly and becomes frequency-dependent. This phenomenon can be explained by the sluggish motions of the molecules and ions within the materials. At higher frequencies, the molecules and ions are not able to move fast enough to align themselves and reach equilibrium in response to the externally applied alternating electric field (i.e. polarization mechanism). Hence, the dielectric constant starts to decrease with increasing frequencies of the external electric field. The details of this related theory will be further elaborated in Section 3.3.3.

B. THE IMAGINARY PART OF DIELECTRIC PERMITTIVITY

- The imaginary part of complex dielectric constant remains at a rather low but constant values at both very high and very low frequencies at low moisture content, as shown in Fig. 2.4-8.

- Within the same *transition frequency band*, the imaginary part of complex dielectric permittivity rises rapidly from a small to a peak value and drops back abruptly to a small value again. The frequency at which the peak occurs is called the relaxation frequency of the material. This phenomenon is known as the dielectric relaxation as described in the classic Debye's model (1929). It can also be observed in the findings produced in the asphalt pavement experiment using a multitude of GPR frequencies as reported in Chapter 7, as well as the work by Shang and Umana (1999) reported in Section 2.3.

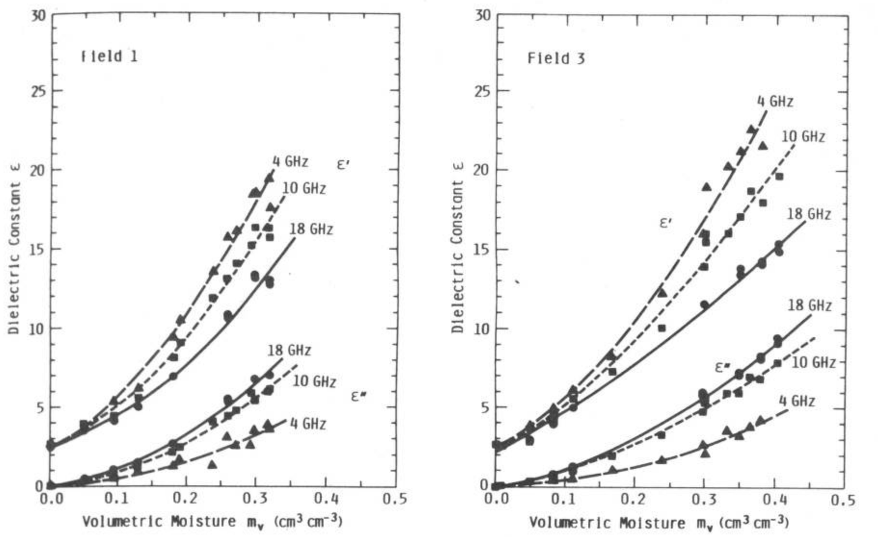

Fig. 2.4-8 Measured Dielectric Constant at 4, 10 and 18GHz with Polynomial Regression (Source: Hallikainen et al., 1985)

To complement Smith-Rose's (1935) results at the low frequency range (i.e. from 1000Hz to 100MHz), Hoeskstra and Delaney (1974) extended the database to the higher frequency range (i.e. from 100MHz to 10GHz) according to their experimental data. The full picture along a wide frequency range (i.e. 1000Hz to 10GHz) is shown in Fig. 2.4-9.

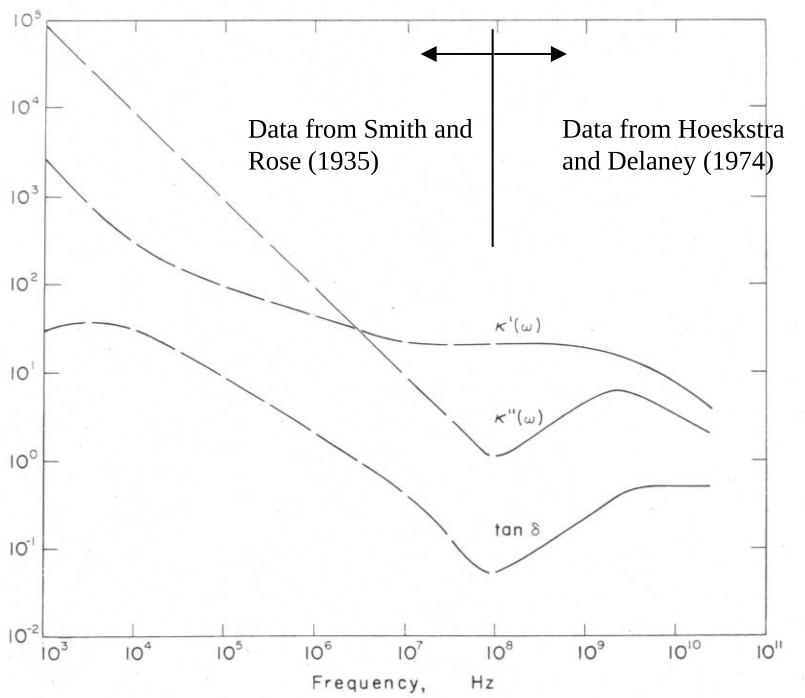

Fig. 2.4-9 The Complex Dielectric constant and the Loss Tangent of a Silty Clay soil at a Water Content of 15%. (Source: Hoeskstra and Delaney, 1974)

The more recent works by many researchers in this field have extended the knowledge and understanding of the correlation of the real permittivity of soil with the water content possessed in soil (Hubbard et al., 1997; Hubbard et al., 2002; Huisman et al., 2003; Lunt et al., 2005) and other petro-physical/soil properties such as porosity, permeability and dielectric hysteresis (Knight and Nur, 1987a; Endres and Knight, 1992; Knoll, 1996; Chan and Knight, 1999). In Chapter 7, Chapter 8 and Chapter 9, a number of these soil properties (i.e. porosity, permeability, specific surface, hysteresis) of a variety of soil textures will be investigated using different dielectric and petrophysical models, as well as experimental techniques. In the following two sub-sections, the former will be introduced in Section 2.5, whereas the latter will be reviewed in Section 2.6.

2.5 DIELECTRIC AND PETROPHYSICAL MODELS

Dielectric models and petrophysical models are a forward modeling approach which enables researchers to predict bulk dielectric constant of the composite materials based on a set of input parameters of material properties obtained from experimental data. Dielectric model is essential because it allows the determination or prediction of engineering/hydro-geological parameters such as porosity, permeability, volumetric moisture content and degree of water saturation through dielectric parameters. Many dielectric and petrophysical models have been widely summarized, and can be compared and categorized into the following five types (Knoll, 1996):

(1) Empirical

a. Logarithmic rule (Olhoeft and Strangway, 1975),

b. Polynomial rule (Topp et al., 1980)

(2) Semi-empirical

a. Wang’s model (Wang and Schmugge, 1980)

b. Four-Component Model (Dobson et al., 1985)

(3) Phenomenological

a. Debye’s model (Debye, 1929)

b. Cole-Cole plot (Cole and Cole, 1941)

(4) Volumetric

a. Litchetenecker-Rother,

b. Arithmetic Average,

c. Harmonic Average,

d. Complex Refractive Index Model (CRIM),

(5) Effective medium theory

a. Bruggeman-Hanai-Sen

The empirical and the semi-empirical models are obtained through curve-fitting of pairs of values of dielectric constants and volumetric water content to a prescribed polynomial curve (such as Topp et al., 1980, and Wang & Schmugge, 1980, in soil, as well as Shang and Umana, 1999, in asphalt). These experimentally determined models have been shown to be very useful to describe the changes of dielectric constants in various types of soils with volumetric water contents from 0 to 0.55 cm^2/cm^2 (Topp et al.,1980) and 0 up to 0.7 cm^2/cm^2 (Wang and Schmugge, 1980).

The phenomenological models (i.e. the Debye's model and the Cole-Cole's plot) describe the frequency-dependent characteristics of the complex dielectric permittivity of a dielectric material. The main feature of this model is *dielectric dispersion,* which describes a series of phenomena, such as the polarization and relaxation mechanism as described in Section 3.3.3. Most researchers adopt these models as a basis for describing the behaviour of porous construction materials, as tabulated in Appendix A and B.

The volumetric model and the effective medium model work for the widest range of material properties for more complex and heterogeneous composition of construction and geological materials. These models incorporate the factors of both the dielectric parameters of each individual constituent, as well as the engineering/geological parameters such as degree of water saturation and porosity of a material.

2.5.1 EMPIRICAL MODELS

A. TOPP'S MODEL

As discussed in Section 2.4.1, Topp's model (1980) is probably the most widely used model to establish the relationship between moisture content and effective dielectric constant. This work was based on the experimental results obtained from a coaxial transmission line method operating at frequencies ranging between 1MHz to 1GHz on various soil specimens (sandy loam to clay). The principal advantage of this model is its simplicity. This model is independent of porosity, texture, bulk density, temperature and soluble salt content (Topp et al., 1980), as shown in Eq. 2.5-1 and Fig. 2.4-1.

$$\theta_v = -5.3 \times 10^{-2} + 2.92 \times 10^{-2}\, \varepsilon_c - 5.5 \times 10^{-4} \varepsilon_c^{\,2} + 4.3 \times 10^{-6} \varepsilon_c^{\,3} \ldots\text{[2.5-1]}$$

This equation was determined by regression analysis on data from four mineral soils ranging in clay content from 9% to 66% by weight (Knoll, 1996). An error estimate was performed by Topp et al. (1980) which indicated that 93% of the measured data falls within the boundary shifted by +/-0.025 in the volumetric water content (θ_v).

Equation [2.5-1] has been commonly adopted in determining soil moisture content using time domain reflectometry (TDR) (Roth et al., 1990; Brisco et al.; 1992; Knoll, 1996), portable dielectric probe (PDP) (Brisco et al., 1992) and ground penetrating radar (GPR) (Hubbard, et al. 2002; Grote et al. 2002). The dielectric constant allows the measurement of the water content, irrespective of other parameters. However, this model does not have a theoretical basis and is therefore purely empirical.

In fact the third order polynomial in Topp's model predicts a change of curvature after a value of $\theta_v > 0.55\text{cm}^3/\text{ cm}^3$: from a steeply climbing curve with increasing gradient to a slowly climbing curve with decreasing gradient, as depicted in Fig. 2.5-6. After this value of θ_v, the equation was found not to be valid to describe the behaviour (Topp et al., 1980; Roth et al., 1990).

B. OLHOEFT'S MODEL

Another empirical relationship relating dielectric constant and dry bulk density was obtained by testing dry samples acquired from the moon (Olhoeft and Strangway, 1975):

$$\varepsilon = (\varepsilon_m)^{\frac{\rho}{G}} \text{ …………[2.5-2]}$$

where ε_m is the dielectric constant at density G and zero-porosity dielectric constant, ε is the dielectric constant at density p.

According to Eq. [2.5-2] and by regression analysis shown in Fig.2.5-1,

$$\varepsilon_m^{\frac{1}{G}} = 1.93 \pm 0.17 \text{ ………… [2.5-3]}$$

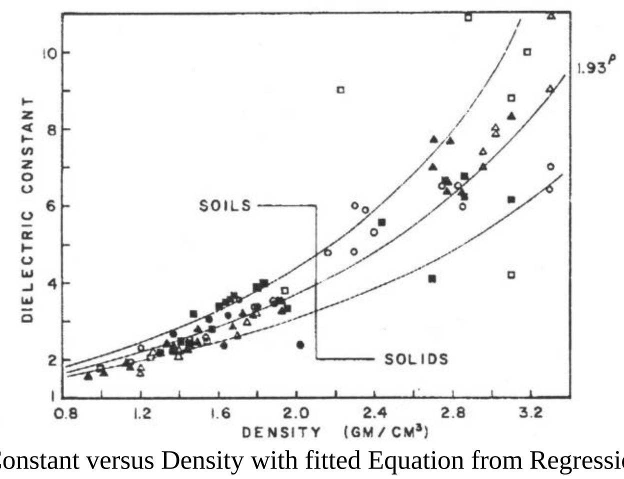

Fig.2.5-1 Dielectric Constant versus Density with fitted Equation from Regression Analysis (also known as curves for plus or minus one standard deviation). Open squares, triangles and circles are data from Apollo 11, 12 and 14 samples, respectively, and closed squares, triangles and circles are from Apollo 15, 16 and 17 samples, respectively. (Source: Olhoeft and Strangway, 1975)

Equation [2.5-2] may be useful to extract bulk density and porosity by dielectric measurement. However, Olhoeft and Strangway (1975) considered that this formula only works for dry rocks. Therefore, since Eq. [2.5-2] does not include the factor of water saturation obtained by data achieved from dry lunar samples, it is not applicable in most cases involving soil from the Earth.

2.5.2 SEMI-EMPIRICAL MODELS

A. WANG'S MODEL

A semi-empirical model was proposed by Wang and Schmugge (1980) to describe the dielectric behaviour of the soil-water mixtures. This model employs the mixing of the dielectric constant or ice water, rock and air, and introduced the parameter of the transition moisture value at the region of low moisture content which depends largely on the amount of clay content.

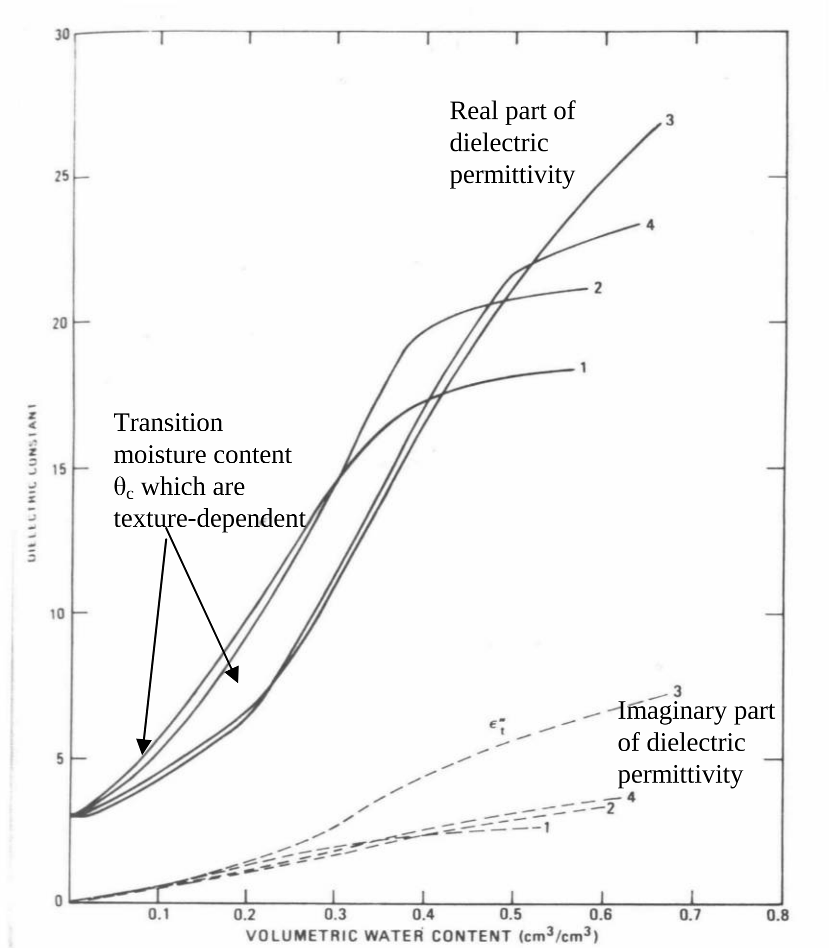

Fig. 2.5-2 Dielectric Constants versus Volumetric Water Content for Four Soils measured at 5GHz (Source: Wang and Schmugge, 1980)

Curve	Texture (percent)			Wilting point WP (cm^3/cm^3	Transition moisture θ_t (cm^3/cm^3)
	Sand	Silt	Clay		
1	88	7.3	4.7	0.034	0.2
2	56	26.7	17.3	0.115	0.22
3	19.3	46	34.7	0.220	0.31
4	2	37	61	0.358	0.31

Remark: this figure is the same as Fig. 2.4.3 and Fig. 3.2-15.

At $\theta_c \le \theta_t$, $\varepsilon = \theta_c \varepsilon_x + (\phi - \theta_c)\varepsilon_a + (1-\phi)\varepsilon_r$ ………………… [2.5-3]

with

$$\varepsilon_x = \varepsilon_i + (\varepsilon_w - \varepsilon_i)\frac{\theta_c}{\theta_t}.\gamma \quad \text{………………………..…} \ [2.5\text{-}4]$$

At $\theta_c > \theta_t$,

$$\varepsilon = \theta_t \varepsilon_x + (\theta_c - \theta_t)\varepsilon_w + (\phi - \theta_c)\varepsilon_a + (1-\phi)\varepsilon_r \quad \text{………} [2.5\text{-}5]$$

with

$$\varepsilon_x = \varepsilon_i + (\varepsilon_w - \varepsilon_i).\gamma \quad \text{……………………………} [2.5\text{-}6]$$

where

ε = composite dielectric constant

ε_x = dielectric constant of initially absorbed water

ε_a = dielectric constant of air

ε_r = dielectric constant of rock (Wang and Schmugge, 1980)/soil (Knoll, 1996)

ε_w = dielectric constant of water

ε_i = dielectric constant of ice

θ_c = volumetric moisture content at any instant

θ_t = volumetric moisture content at transition moisture content

ϕ = porosity

γ = best-fit coefficient of Eq. [2.5-6]

According to the experimental results plotted in Fig. 2.5-2, an empirical relationship between transition moisture and wilting point was established on the basis of soil texture information. Wang and Schmugge (1980) conducted linear regression analysis for the transition moisture content θ_t and the best-fit coefficient γ and relate these two parameters with the wilting point as follows:

$$\gamma = -0.57WP + 0.481 \ldots\ldots\ldots \text{[2.5-7]}$$

$$\theta_t = 0.49WP + 0.165 \ldots\ldots\ldots \text{[2.5-8]}$$

$$WP = 0.06774 - 0.00064xW_S + 0.00478xW_C \ldots\ldots \text{[2.5-9]}$$

where W_S and W_C is the percent of dry weight of sand and clay respectively.

The dielectric constant in this model according to Eq. [2.5-3] to [2.5-6] can be replaced by corresponding refractive indices of water, ice, air and rock/soil (Wang and Schmugge, 1980). This research concluded that both approaches (i.e. the original form and the form of replaced refractive indices of Eq. [2.5-3] to [2.5-6]) provide a similar outcome and are essentially equivalent for practical purposes.

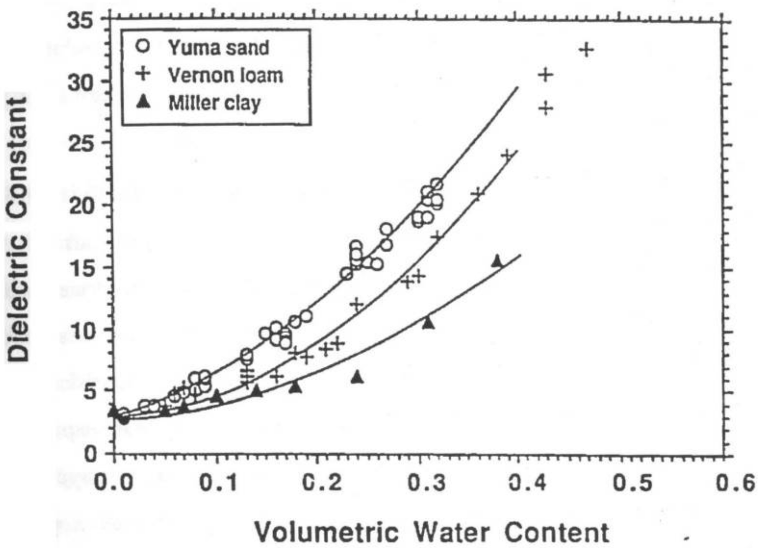

Remarks: Yuma sand has 100% sand and wilting point 0.4cm^3/cm^3; Vernon loam has 72% sand/silt and 28% clay, and wilting point 0.192cm^3/cm^3; Miller clay has 38% sand/silt and 62% clay, and wilting point 0.361 cm^3/cm^3.

Fig.2.5-3 Comparison of Wang and Schmugge (1980) Dielectric Model with equation [2.5-3] to [2.5-9] in the text (Source: Knoll, 1996)

Fig. 2.5-3 illustrates a plot (Knoll, 1996) depicting the Wang's model using Eq. [2.5-3] to [2.5-9] (i.e. the curves) and the experimental values of dielectric constant at 1.4GHz (i.e. the data in circles, crosses and triangles). In this figure, the Yuma sand, Vernon loam and Miller clay possess a wide range of sand/clay fractions and wilting points. The two factors determine the specific surface and the transition moisture content of the soil specimens. Both curves obtained from Wang's model and Knoll (1996)'s experimental data demonstrate the effect of soil texture on dielectric constant and therefore are better descriptions of soil than the Topp's model (1980). The better adaptability of this model to experimental data is attributed to

1. the consideration given to different dielectric properties of the initially absorbed water molecules (i.e. different to dielectric properties of free water) and
2. the consideration of correlating the transition moisture content and the wilting point in the model.

A further discussion of these models is referred to Section 2.7.1.

B. DOBSON'S MODEL

Dobson et al. (1985) developed another semi-empirical model which comprises essentially the dielectric constant of solid, air, bound water and free water. The equation is as follows:

$$\varepsilon^{\alpha} = V_s \varepsilon_s^{\alpha} + V_a \varepsilon_a^{\alpha} + V_{fw} \varepsilon_{fw}^{\alpha} + V_{bw} \varepsilon_{bw}^{\alpha} \text{..........} \quad [2.5\text{-}10]$$

where the subscripts of s, a, fw and bw refer to soil, air, free water and bound water respectively, V, ε and α are the volumetric fraction, dielectric constant and geometrical factor of each individual respectively.

Dobson et al. (1985) also estimated α = 0.65 by regression of data for different frequencies (1.4-18GHz) and soil types ranging from sandy loam to silty clay.

V_{bw} and V_{fw}, ε_{fw} and ε_{bw} were further approximated to avoid lengthy calculation. The latter two terms of Eq. [2.5-10] were therefore re-written as

$$m_v^{\beta}\varepsilon_{fw}^{\alpha} = V_{fw}\varepsilon_{fw}^{\alpha} + V_{bw}\varepsilon_{bw}^{\alpha} \text{ .... [2.5-11]}$$

where m_v is the volumetric moisture, β is a soil texture dependent factor and was determined empirically by regression, with

$$\beta_{\varepsilon'} = (127.48 - 0.519S - 0.152C)/100 \text{ ....[2.5-12]}$$

$$\beta_{\varepsilon''} = (1.33797 - 0.603S - 0.166C)/100 \text{ .... [2.5-13]}$$

where S and C are the percentage of sand and clay.

Dobson et al. (1985) found that the measured data worked reasonably well with this model at frequencies higher than 4GHz but not less than 4GHz, presumably because of the effects of bound water on a greater soil-dependent curvature to dielectric constant (Dobson et al., 1985).

2.5.3 PHENOMENOLOGICAL MODELS

This type of model relates frequency dependent behaviour with a distribution of characteristic relaxation time, in which data is modeled irrespective of component properties or geometrical relationship (Knoll, 1996). The original model was proposed by Peter Debye in 1929. According to his classic model (Debye, 1929) and its modified form by Cole and Cole (1941), dielectric constant (i.e. the real part of dielectric permittivity) remains constant at both very high and very low frequencies in the microwave band, as seen in Fig. 2.5-4 and formulated according to Eq. [2.5-14] and Eq. [2.5-15].

$$\varepsilon'(\omega) = \varepsilon_\infty + \frac{\varepsilon_S - \varepsilon_\infty}{1 + \omega\tau^2} \text{ ……….. [2.5-14]}$$

$$\varepsilon''(\omega) = \frac{(\varepsilon_S - \varepsilon_\infty)(\omega\tau)}{1 + (\omega\tau)^2} \text{ …….. [2.5-15]}$$

where

ω is the angular frequency,

ε_S and ε_∞ are the static and infinite dielectric constant of the mixture at $\mathrm{f} \rightarrow 0$ and $\mathrm{f} \rightarrow \infty$ respectively,

$\varepsilon'(\omega)$ and $\varepsilon''(\omega)$ are the real and imaginary part of dielectric permittivity respectively,

τ_r is the Debye's relaxation time

For a wide range of materials at intermediate frequencies (particularly for GPR/SPR operating between 25MHz to 2.5GHz), dielectric constant changes abruptly and becomes frequency-dependent. In this intermediate frequency, the motions of molecules and ions are not able to move fast enough to align and reach equilibrium with an external alternating electric field (i.e. polarization), the dielectric constant starts to decrease with increasing frequencies of the external electric field. Further discussions are referred to Section 3.3.3. At frequencies lower and higher than the GPR/SPR ranges, charge/Maxwell-Wagner polarization, and atomic polarization & electronic polarization occur respectively (Böttcher and Bordewijk, 1973). These phenomena were outside the GPR frequencies and are therefore beyond the scope of consideration of this research.

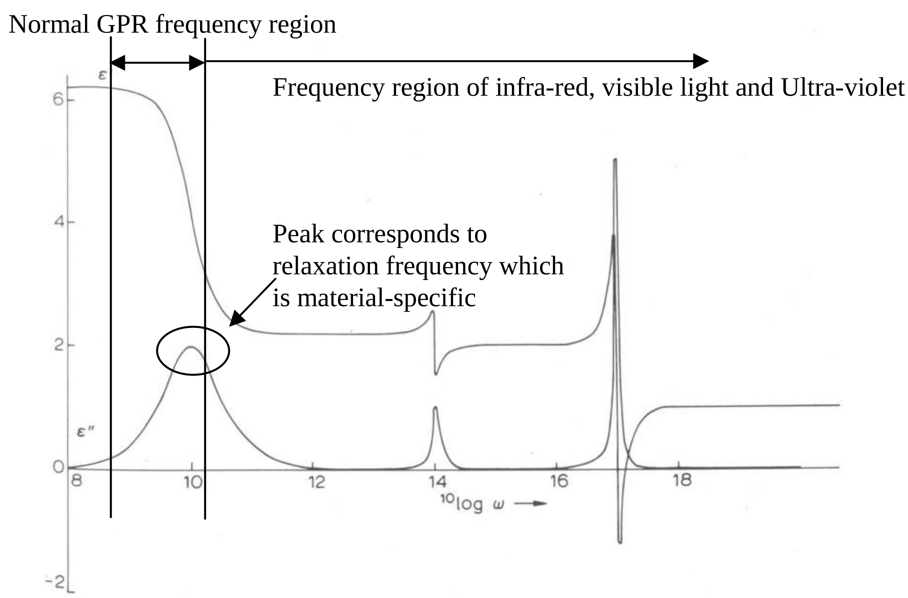

Fig. 2.5-4 Dielectric Dispersion and Loss for a Polar Compound (Source: Böttcher and Bordewijk, 1973)

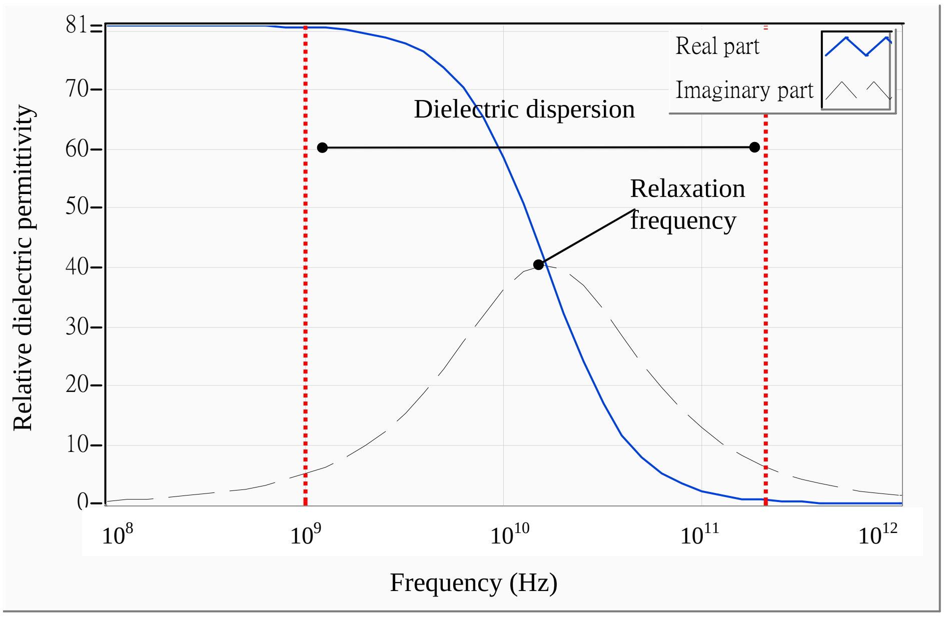

Figure 2.5-5 Graphical Presentation of Debye's Model in Liquid Water

For the experimental data obtained in the asphalt pavement experiment described in Chapter 7, the Debye's model was used to explain the behaviour of dielectric dispersion observed within three distinct groups of real permittivity determined, from three GPR frequencies, as shown in Fig. 7-11.

2.5.4 VOLUMETRIC MIXING MODELS

The forth approach to model the dielectric behaviour is to relate the composite dielectric constant of a multi-phase mixture to individual dielectric constant and its volumetric fractions. The most general form is from Lichtenecker-Rother (1937):

$$\varepsilon^{\alpha} = \sum_{i=1}^{n} V_i \varepsilon_i^{\alpha} \text{ ……………… [2.5-16]}$$

where V_i and ε_i are the volume fraction and dielectric constants of i^{th} component respectively, α is a ‘geometrical’ factor which relates the direction of effective layering of the components to the direction of the applied electric field. The electric field is parallel and perpendicular to the layering materials if α = 1 and -1 respectively (Brown, 1956). These extreme values of α represent the alignment of dielectric components.

Table 2.5-1 Types of Volumetric Models

Value α in the Lichtenecker-Rother (1937)	Arrangement of dielectric component	Type of volumetric model
-1	perpendicular	Harmonic average
+1	parallel	Arithmetic average
0.5	isotropic	Complex Refractive Index Model

The three volumetric mixing models, namely the Harmonic Average, the Arithmetic Average and the Complex Refractive Index Model, are the extended versions of the Lichtenecker-Rother equation (1937). The fundamental difference of these models is determined by the geometrical factor α. Table 2.5-1 summarizes the value of factor α in each model.

A. HARMONIC AVERAGE AND ARITHMETIC AVERAGE

For a two-phase mixture (e.g. soil and water), the volumetric mixing model becomes the harmonic average formula (α = -1):

$$\frac{1}{\varepsilon} = \frac{V_1}{\varepsilon_1} + \frac{V_2}{\varepsilon_2} \text{..........[2.5-17]}$$

For a two-phase mixture (e.g. soil and water), the volumetric mixing model becomes the arithmetic average formula (α =1):

$$\varepsilon = V_1\varepsilon_1 + V_2\varepsilon_2 \text{.......... [2.5-18]}$$

A parallel or perpendicular electric field to the layering materials represents that α in Eq. [2.5-20] should be 1 (i.e. the arithmetic average) or -1 (i.e. the harmonic average) respectively (Brown, 1956). In the plot of the real part of complex permittivity against water content, the Harmonic Average provides a flat slope until approaching saturation, while the Arithmetic Average provides a straight line as shown in Fig. 2.5-6. Both models generally do not corroborate well with most experimental data and are seldom applied (Knoll, 1996; Roth et al., 1990) to model the dielectric behaviour. This is attributed to the fact that no natural materials possess such a layering arrangement, except some clays such as interlaying illite and smectite.

B. COMPLEX REFRACTIVE INDEX MODEL (CRIM)

For porous geological and construction materials, the volumetric mixing model states that the ε’ of a composite material is a volumetric fraction of its porosity, state of S_w, respective ε’ of the individual constituent of pure air, water and solid matter. The widely used mixing model is known as the Power-Law (Sihvola, 1999) which is the most original form of the category of volumetric mixing models. By extending the Power-Law to a three-phase system to describe wet soil (Roth et al., 1990):

$$(\varepsilon')^{\alpha} = \theta_v(\varepsilon_w')^{\alpha} + (\phi - \theta_v)(\varepsilon_A')^{\alpha} + (1-\phi)(\varepsilon_S')^{\alpha} \text{ .... } [2.5\text{-}19]$$

where ε' , ε'_W , ε'_A, ε'_s = real permittivity of the composite and the constituents water (81 at 100MHz at room temperature), air (1) and solid matters forming the soil particle matrix respectively, ϕ = porosity and θ_v = volumetric water content, , α is a geometrical parameter and is dependent on soil types and the packing of the soil.

Also as $\theta_v = S_w\phi$ where S_w is the degree of water saturation (Alharthi and Lange, 1987), Eq. [2.5-19] can be re-written as:

$$(\varepsilon')^{\alpha} = S_w\phi(\varepsilon_w')^{\alpha} + (1-S_w)\phi(\varepsilon_A')^{\alpha} + (1-\phi)(\varepsilon_S')^{\alpha} \text{ .... } [2.5\text{-}20]$$

The values of exponent α in Eq. [2.5-20] has been investigated by many researchers (Birchak et al., 1974; Looyenga, 1965; Dobson et al., 1985; Roth et al. 1990). According to the experimental investigations conducted by Birchak et al. (1974) based on calculations of traveling time, as well as Roth et al. (1990) based on curve-fitting, it was found that α = 0.5 in [2.5-19] agrees well with the experimental data. For an isotropic two-phase medium (which is also the case in layering arrangement of asphalt pavement and soil described in Chapter 7 and Chapter 8), α in Eq. [2.5-20] is assigned the value of 0.5 to produce Eq. [2.5-21] (used in all analysis throughout this research). Hence Eq. [2.5-21] becomes the well-known CRIM.

$$\sqrt{\varepsilon'} = S_w\phi(\sqrt{\varepsilon_w'}) + (1-S_w)\phi(\sqrt{\varepsilon_A'}) + (1-\phi)(\sqrt{\varepsilon_S'}) \text{ ....} [2.5\text{-}21]$$

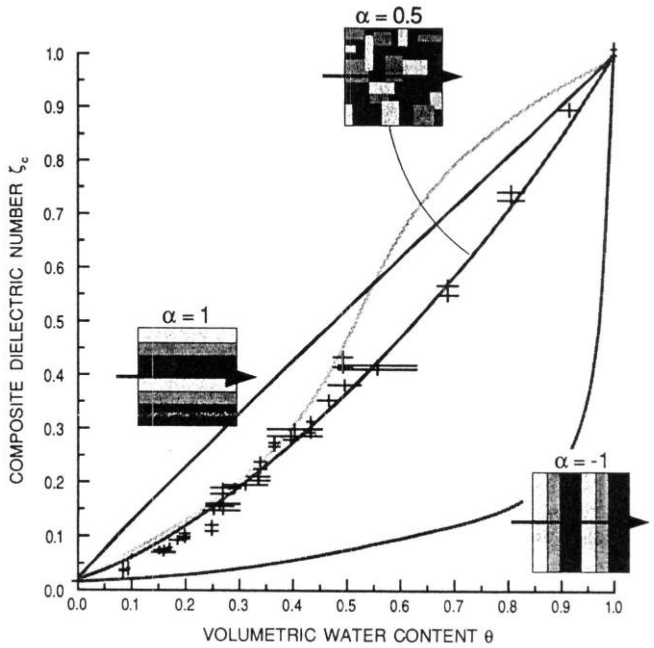

Remark: The light grey curve is obtained from the Topp's model (Topp et al., 1980)
Fig. 2.5-6 Measured Composite Dielectric Constant as a function of Volumetric Water Content θ and different Empirical Models. (Source: Roth et al., 1990)

The experimental data obtained in this research was found to be best-fitted by an exponent equal to 0.5 instead of 1/3 (Looyenga, 1965), -1 (the harmonic average) and +1 (the arithmetic average). The CRIM will be shown in Chapter 7 and Chapter 8 to be a useful model to explain and characterize the dielectric behaviour in air-cured concrete, asphalt and soil of various textures, at different ranges of GPR/SPR electromagnetic frequencies.

When ε' and S_w are measured independently and are plotted against each other using CRIM, the CRIM curve in Eq. [2.5-21] is found to fit a second order polynomial after some algebraic manipulations and inputs of constants such as the real permittivity of air and water, as shown in Eq. [2.5-22]. It is found that the second order polynomial coefficient 'a' of the curve provide a means to estimate the value of porosity (i.e. a fast-climbing/steeper curve indicates a larger porosity of the material).

$$\varepsilon_c = aS_w^{\ 2} + bS_w + c \ldots\ldots\ldots\ldots [2.5\text{-}22]$$

where a $=64\phi^2$, b = $16\phi[\phi(1-\sqrt{\varepsilon_S\,'})+\sqrt{\varepsilon_S\,'}]$ and c = $[\phi(1-\sqrt{\varepsilon_S\,'})+\sqrt{\varepsilon_S\,'}]^2$

By fitting experimental data of ε' and S_w into the CRIM, the coefficients 'a' will be used to determine the material porosity of asphalt and soil in Chapter 7 and Chapter 8 respectively.

2.5.5 EFFECTIVE MEDIUM THEORY (EMT)

Effective Medium Theory (EMT) is based on a physical model in which particles are coated with water and assembled together to construct a saturated porous media. (Alharthi and Lange, 1987). Through building this assembly repeatedly and using the dielectric properties of the coated particles, the composite dielectric constant of a composite material is yielded. The most common form of EMT to model dielectric properties of porous materials is the Bruggeman-Hanai-Sen (BHS) equation (Bruggeman, 1935; Hanai, 1961; Sen et al., 1981), i.e.

$$1-V = \left(\frac{\varepsilon_c - \varepsilon_s}{\varepsilon_F - \varepsilon_s}\right)\left(\frac{\varepsilon_F}{\varepsilon_c}\right)^d \ldots\ldots\ldots\ldots\ldots [2.5\text{-}23]$$

where ε_c , ε_S , ε_F are the dielectric constants of the composite material, solid constituents and pore fluid (e.g. water); d is the geometrical factor which vary from 0 to 1; V is the solid volume fraction.

The geometrical factor depends on the geometrical distribution of the matrix material and the saturating fluid within the pore system. When the matrix geometry is spherical, d equals to one-third (Knoll, 1996; Alharthi and Lange, 1987), and Eq. [2.5-23] can be modified as:

$$1 - V = \left(\frac{\varepsilon_c - \varepsilon_s}{\varepsilon_F - \varepsilon_s}\right)\left(\frac{\varepsilon_F}{\varepsilon_c}\right)^{\frac{1}{3}} \text{................[2.5-24]}$$

Application of the EMT requires a two-step procedure involving only two components in each step. In step 1, the three-component system existing in porous materials such as concrete, asphalt and soil is first treated as an air-soil system in which the volume of fluid is absent. In step 2, the composite dielectric constant of this air-soil system is then substituted into EMT again to a hypothetical material consisting of water and the first composite air-soil dielectric material (Alharthi and Lange, 1987).

Table 2.5-2 Parameters used to apply the EMT equation [2.5-24] to a Partially Water Saturated Soil (Source: Alharthi and Lange, 1987)

Step	Components	Volume fraction of fluid (1-V)
1	Air/solid	$1\text{-}V = (1\text{-}S_w)\phi = \phi - \theta$
2	Water/(air/solid)	$1\text{-}V = \theta = S_w\phi$

This model involves an iterative two-step procedures at every stage of material wetness. A disadvantage of this model is that the material wetness and porosity must be well-defined in advance. Also, this two-step procedure is too complicated to be implemented because it requires iterative process of computation in each stage of material wetness.

The basis for the selection of these models to model the experimental data obtained in this research will be justified in Section 2.7, whereas a number of technologies to determine the dielectric properties will be described in the following section.

2.6 ELECTROMAGNETIC TECHNOLOGIES TO DETERMINE THE DIELECTRIC PROPERTIES OF CONCRETE, ASPHALT AND SOIL

The dielectric properties of porous materials described in Section 2.2 to 2.4 have been investigated extensively by three electromagnetic (EM) technologies operating in the ranges of microwave frequencies, namely:

1. Ground Penetrating Radar (GPR)/Surface Penetrating Radar (SPR)
2. Electromagnetic Coaxial Transmission Line (EMCTL)
3. Time Domain Reflectometry (TDR)/Portable Dielectric Probe (PDP)

The GPR/SPR is a method using un-guided EM waves to investigate large masses of in-homogeneous material in laboratory experiments and field scales, whilst EMCTL make use of guided EM waves to measures small masses of homogeneous material in laboratory experiments. TDR/PDP is adopted to survey a localized area and also small masses of material in field application. In the following sections, the basic principles and instrumentation of these three technologies will be introduced.

2.6.1 GROUND PENETRATING RADAR (GPR)/SURFACE PENETRATING RADAR (SPR)

GPR/SPR has been recognized over the past two decades as one of the most promising non-destructive testing technologies in science and engineering discipline, including geophysics, civil engineering, soil science to hydrology and agriculture. Most of these research and applications focus on *detection* and *ranging* of construction anomalies/features embedded in concrete. Detection means the location (including orientation) of concrete anomalies such as voids, honeycombs as well as metallic and non-metallic bars, conduits and pipes. Ranging means the determination of concrete cover to these anomalies/features as well as the depth profile of the structural concrete elements. Ease of *detection* depends on the contrasts in dielectric properties between the embedded materials and concrete, as reflection coefficient is greater with larger dielectric contrasts. The accuracy of ranging depends on the accurate knowledge of the values of dielectric properties of the host materials, including both the real and the imaginary part of the complex dielectric permittivity, electromagnetic wave/pulse transmission and attenuation.

A. TYPES OF GPR/SPR ANTENNA

The antennae of GPR/SPR transmit short pulses of radio energy into a structure and records reflection of the reflected signals. The antennae types such as mono-static antenna (as in Fig. 2.6-1), bi-static antenna (as in Fig. 2.6-2), horn antenna (as in Fig. 2.6-3), and bore-hole antenna (as in Fig. 2.6-4) determine the transmission and reflection geometry of EM wave propagation. Mono-static antenna and horn antenna transmit and receive reflections from anomalies at one side of a surface. Tomographic antennae and bore-hole antenna are accommodated at the opposite sides of the structure and therefore enables full transmission of EM waves.

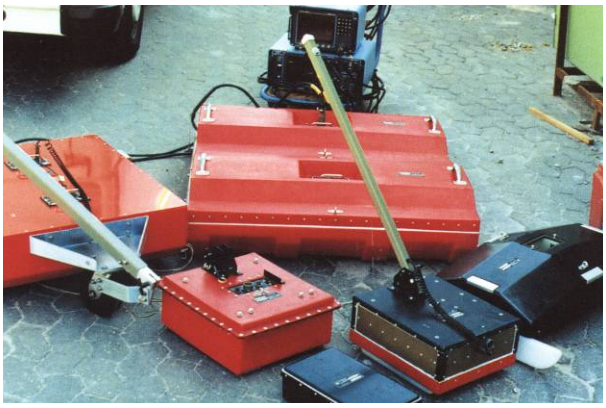

Fig. 2.6-1 A Selection of Some Available Antennas with Different Centre Frequencies. (Source: Concrete Society, 1997, Photo Courtesy Impulse Geophysics Ltd.)

Fig. 2.6-2 Bi-static Antenna (Source: Mala Geoscience web-page)

Fig. 2.6-3 Horn Antenna mounted at the back of a Vehicle to Survey a Asphalt Road Pavement (Source: Al-Qadi and Lahouar, 2005)

Fig. 2.6-4 Bore-hole Antenna (Source: Mala Geoscience web-page)

In most applications, the mono-static and horn antennae are usually more preferred than the other two counterparts due to their better resolution, greater mobility and easier assess to the surface of the material. However, the bi-static and bore-hole antennae are usually used particularly in geophysical explorations which usually involves large-scale survey and long range of investigations.

Table 2.6-1 Advantages and Dis-advantages of Different Types of GPR/SPR antennae

TYPE OF ANTENNA	ADVANTAGES	DISADVANTAGES	APPLICABLE ON	REMARK
Mono-static	1. No access to another side of surface is required 2. High frequency range enables a better resolution 3. The equipment is light in weight	The paths of EM wave propagation are restricted to be nearly vertical, hence a great deal of reflections from scattered objects/interfaces cannot be captured	Nearly all cases	Shielded, operates in the highest frequency range (250MHz to 3GHz)
Horn	It is the most effective antenna among the others since it can travel at highway speed, without disturbance to road traffic.	The penetrating path of horn is shallower than that of mono-static antenna since it is not coupled on the ground and hence some energy is dissipated in the air	Highway pavement, sub-surface	Shielded, operates in a high frequency range (300 to 600MHz)
Bi-static	1. Information of refraction between boundaries is available due to large separation distance of transmitting and receiving antennae 2. Survey modes like Common Mid Point (CMP), Wide Angle Reflection and Refraction (WARR) are available in this antenna types but not the others. 3. Low frequency range enables investigations upto 100m deep in some optimal cases	1. Time consuming to acquire data 2. The sampling density of sub-surface data is less than mono-static antenna	Geophysical exploration	Un-shielded, the mode of data acquisition is the same as seismic application
Bore hole	It provides far longer ranges of detection than mono-static and horn antenna since it is usually equipped with very low frequency antennae	Bore-hole is required.	Geophysical exploration	Un-shielded, operates in a low frequency range (20-250MHz)

B. TYPES OF WAVES IN GPR SURVEY

Thorough review of the types of waves and methods in GPR ray-traced diagram was conducted by Huisman et al. (2003). Some of the context of this work has been re-organized and tabulated in Table 2.6-2 in a different way, in terms of types of waves, antenna types and methods of survey. In particular the types of waves are depicted schematically in Fig. 2.6-5.

Table 2.6-2 Common Data Acquisition Methods in Ground Penetrating Radar

<table>
<tr><th>TYPES OF WAVES IN GPR SURVEY</th><th>RELATED TO MATERIAL PROPERTIES?</th><th>ANTENNA TYPES</th><th>METHODS OF SURVEY</th><th>REMARKS</th></tr>
<tr><td>Air wave</td><td>No</td><td rowspan="4">Bi-static</td><td rowspan="4">Common Mid-Point (CMP) and Wide Angle Reflection and Refraction (WARR)</td><td>Air wave is identified as the first and the uppermost slanted straight line extended from the origin. However it is not used for subsurface characterization</td></tr>
<tr><td>Ground wave</td><td>Yes</td><td>-</td></tr>
<tr><td>Refracted waves (including the critically refracted wave)</td><td>Yes</td><td>Refracted waves are split from the ground wave (i.e. the second slanted straight line) after a certain value of antenna separation.</td></tr>
<tr><td rowspan="2">Reflected wave from subsurface interface</td><td>Yes</td><td rowspan="2">The formulation is as Eq. 2.6[1] $v = f\lambda = \frac{c}{\sqrt{\varepsilon}}$</td></tr>
<tr><td>Yes</td><td>Mono-static</td><td>Direct reflection (DR)</td></tr>
<tr><td>Reflected wave from exposed ground surface materials</td><td>Yes</td><td>Horn</td><td>Surface reflection coefficient (SRC)</td><td>The formulation is as Eq. 2.6[2] $\varepsilon_{soil} = \left(\frac{1-\frac{A_0}{A_{\mathrm{int}}}}{1+\frac{A_0}{A_{\mathrm{int}}}}\right)^2$</td></tr>
<tr><td>Through wave transmission between boreholes</td><td>Yes</td><td>Bore-hole</td><td>Cross bore-hole transmission (CBHT)</td><td>The formulation is as Eq. 2.6[1] $v = f\lambda = \frac{c}{\sqrt{\varepsilon}}$</td></tr>
</table>

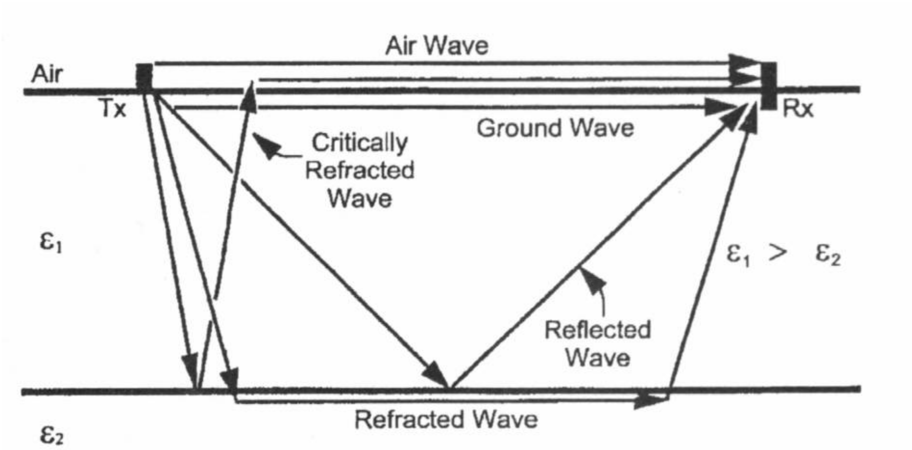

Fig.2.6-5a Propagation Paths of Electromagnetic Waves in a Soil with Two Layers of Contrasting Dielectric Permittivity ε_1 and ε_2 (Source: Huisman et al., 2003)

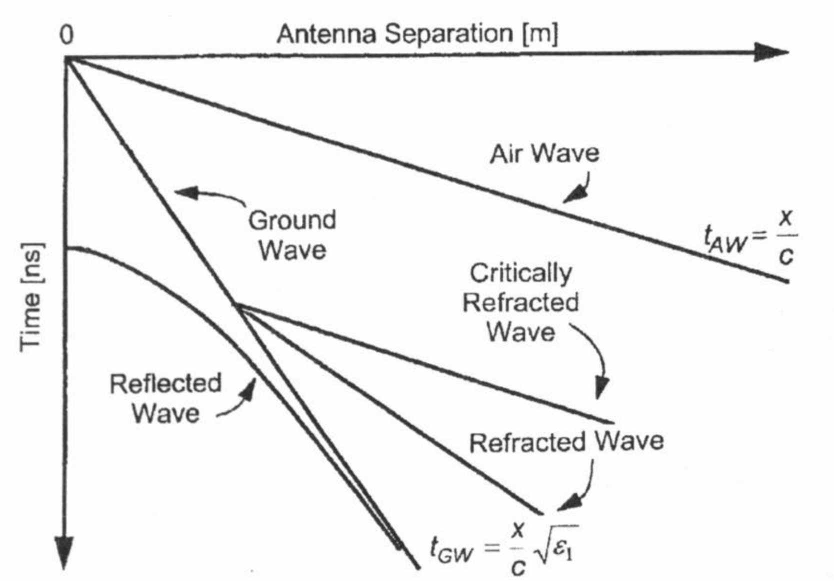

Fig.2.6-5b Wide Angle Reflection and Refraction (WARR) Measurement (Source: Huisman et al., 2003)

The following paragraphs describe the five types of waves (refer to Table 2.6-2) in detail (Huisman et al., 2003):

1. AIR WAVE:

This is the first-arrival wave which travels through air from the transmitter to the receiver at the speed of light and therefore does not yield any information related to the sub-surface material. The slope of the air wave serves as an independent check and verification of GPR’s timing circuitry/hardware using EM propagation velocities in air and the appearance of the air wave as a precursor of that of the ground wave.

2. GROUND WAVE:

In CMP and WARR methods, the ground wave is the second arrival wave from the transmitting antenna to the receiving antenna. The slope of the ground wave is directly related to the EM propagation velocities through the ground material near the exposed surface (i.e. to be governed by the surface dielectric constant ε of the ground material as shown in Eq. [2.6-1]

$$v_{ground\_wave} = f\lambda = \frac{c}{\sqrt{\varepsilon}} \text{ ....[2.6-1]}$$

3. REFRACTED WAVES (including critically refracted waves):

These waves are only obtained in the CMP and the WARR methods and allow the determination of layer thicknesses of the subsurface strata.

4. REFLECTED WAVES:

In the Common Mid Point (CMP)/Wide Angle Reflection and Refraction (WARR) method, the curve in the ray-traced diagram depicts the captured *interior* reflected wave from an interior boundary separating the ground material from the underlying material as shown in Fig. 2.6-5.

In the direct reflection (DR) method, the waves are reflected from the interfaces/objects with sufficient dielectric contrast, as depicted in Fig. 2.6-6. In this figure, the thickness and the structural integrity of asphalt can be determined by recording the two way transit time of wave forms and using a well-calibrated dielectric constant (Al-Qadi and Lahouar, 2004).

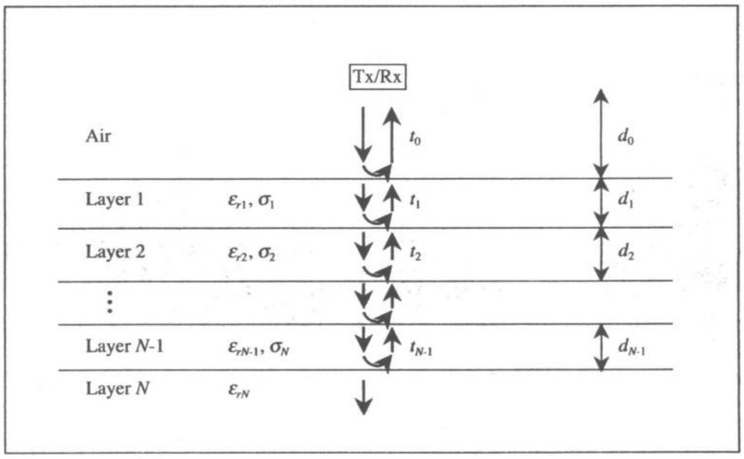

Fig. 2.6-6 GPR Reflected Signals from Multi-planar Layers at Normal Incidence
(Source: Al-Qadi and Lahouar, 2004)

The surface reflection coefficient (SRC) method is a particular case of the direct reflection (DR) method. A horn and mono-static GPR antenna is elevated from the ground to obtain amplitudes of *surface* reflections (i.e. the reflected wave) from the ground and the subsurface interface. These amplitudes are used to calculate the dielectric constant of exposed ground material according to Fig. 2.6-6 and Eq. [2.6-2] (Al-Qadi and Lahouar, 2004).

$$\varepsilon_{soil} = \left(\frac{1+\frac{A_0}{A_{\text{int}}}}{1-\frac{A_0}{A_{\text{int}}}}\right)^2 \text{………………..[2.6-2]}$$

where ε_{soil} is the dielectric constant of soil, A_0 is the amplitude of the surface reflection, A_{int} is the amplitude of the interface reflection.

5. THROUGH WAVES TRANSMISSION BETWEEN BOREHOLES

In the Cross Bore-hole Transmission (CBHT) method, the wave is transmitted from an emitting antenna placed in one bore-hole, through the body of material of subsurface strata, to another receiving antenna placed in another bore-hole, as depicted in Fig. 2.6-7.

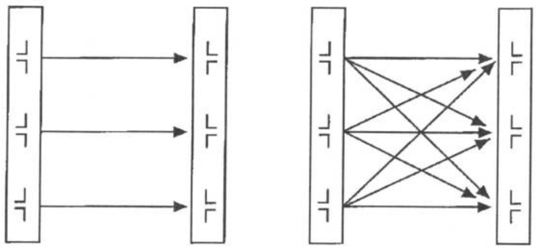

Fig.2.6-7 Wave Paths of Bore-hole Radar Transmission (Source: Huisman et al., 2003)

GPR/SPR is adopted to survey a large mass of material in field, whereas its counterpart, EMCTL is a long and well established technology which tests very small sized homogeneous samples. This technique is the subject of the next section.

2.6.2 ELECTROMAGNETIC COAXIAL TRANSMISSION LINE (EMCTL) METHOD

Electromagnetic Coaxial Transmission Line (EMCTL) is a traditional electromagnetic waveguide technique with operating frequencies ranging from the order of MHz to tens of GHz. It has been used to determine the complex dielectric properties and investigate the relationship of the complex dielectric properties and other physical properties. It has been widely adopted in nearly all studies related to dielectric properties of concrete, asphalt and soil. Soft samples (such as soil) and hardened samples (such as concrete and asphalt) can be accommodated in sample holders of various sizes. Normally sample holders for soil are in very small centimeter scale, whereas sample holders for hardened materials are in larger sizes.

Shaw et al. (1993) developed an electromagnetic coaxial transmission line (as in Fig. 2.6-8) to investigate concrete with sample size of 500mm in length and 101mm in diameter. This setup enables dielectric measurements with different frequencies ranging from 10MHz to 1GHz, which covers the normal frequency range used in radar systems.

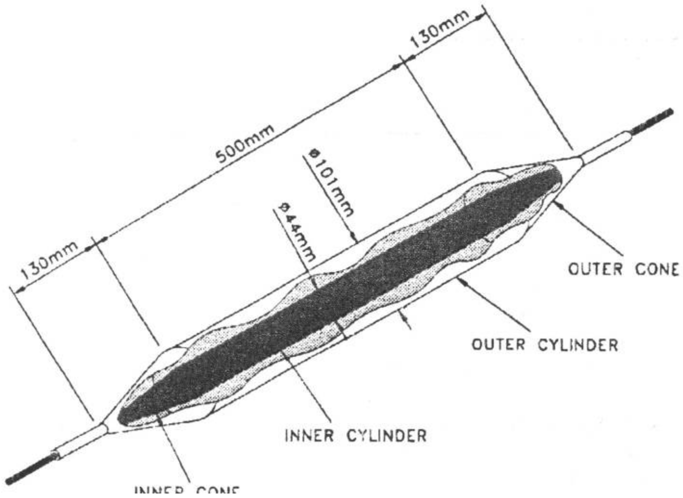

Fig. 2.6-8 The Transmission Line Connected to the Network Analyser (Source: Shaw et al., 1993)

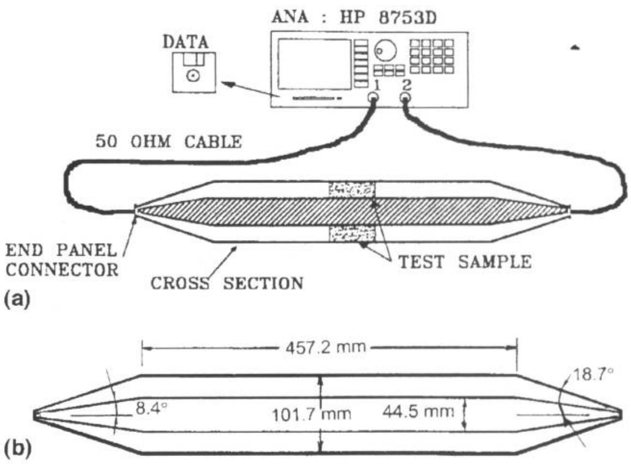

Fig.2.6-9 Schematic Diagram of Complex Permittivity Measurement Apparatus (Source: Shang and Umana ,1999)

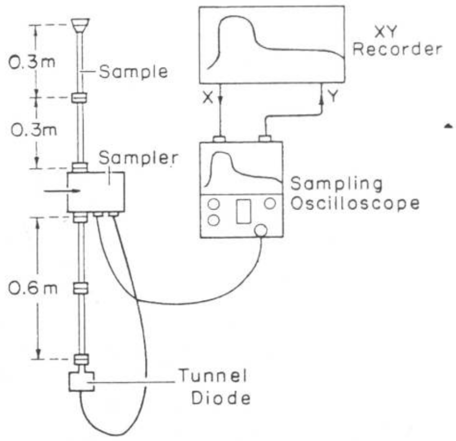

Fig. 2.6-10 Schematic Diagram of Experimental Apparatus used in Time Domain Measurements (Source: Hoekstra and Delaney, 1974)

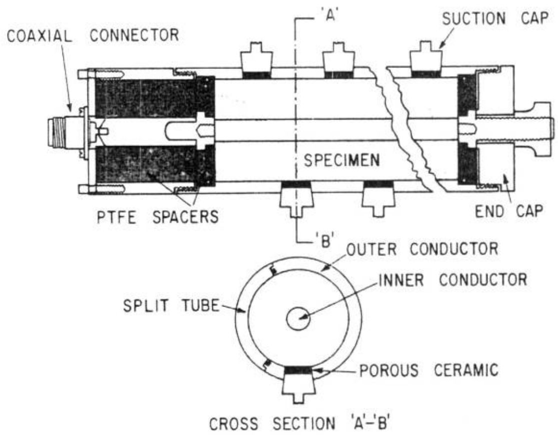

Fig. 2.6-11 Diagram of the Coaxial Transmission Line Soil Column (Source: Topp et al., 1980)

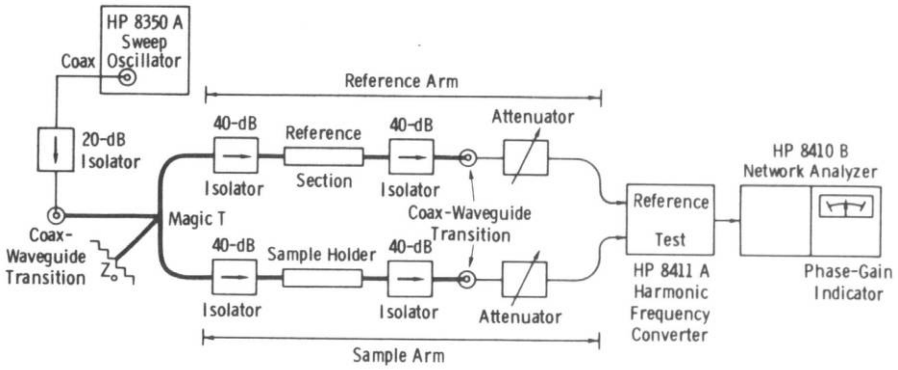

Fig. 2.6-12 Block Diagram of the 4GHz to 6GHz Waveguide Dielectric Measurement System Waveguide (Source: Hallikainen et al., 1985)

The schematics and block diagrams of a number of typical instrumentations developed by different researchers are shown in Fig. 2.6-8 (for concrete), Fig. 2.6-9 (for asphalt), and Fig. 2.6-10 to Fig. 2.6-12 (for soil). For example in the waveguide transmission line in Fig. 2.6-12, the amplitude and phase of the transmission coefficient for a dielectric sample are obtained by the network analyzer. The complex dielectric permittivity of a material is computed by using the attenuation coefficient α, phase factor β, free-space (i.e. air) wavelength and cut-off wavelength of the waveguide (Hallikainen et al., 1985).

While GPR is used to survey a large mass of in-situ materials and EMCTL measures a small mass of laboratory samples retrieved from the ground, TDR/PDP will be shown in the next section to offer another choice to measure the dielectric properties of in-situ materials but is limited to localized areas.

2.6.3 SURFACE DIELECTRIC MEASUREMENT TECHNOLOGIES: TIME DOMAIN REFLECTOMETRY (TDR) AND PORTABLE DIELECTRIC PROBE (PDP)

A number of in-situ field studies of soil moisture detection have been successfully conducted by Time Domain Reflectometry (TDR) and Portable Dielectric Probe (PDP) since the mid-1980s. (Roth et al., 1990; Herkelrath et al., 1991; Brisco et al., 1992; Sheets and Hendrickx, 1995). TDR systems make use of a waveguide inserted into a target medium, whereas PDP systems rely on a capacitance circuit at an open-ended coaxial cable probe (Brisco et al., 1992), as shown in Fig. 2.6-13.

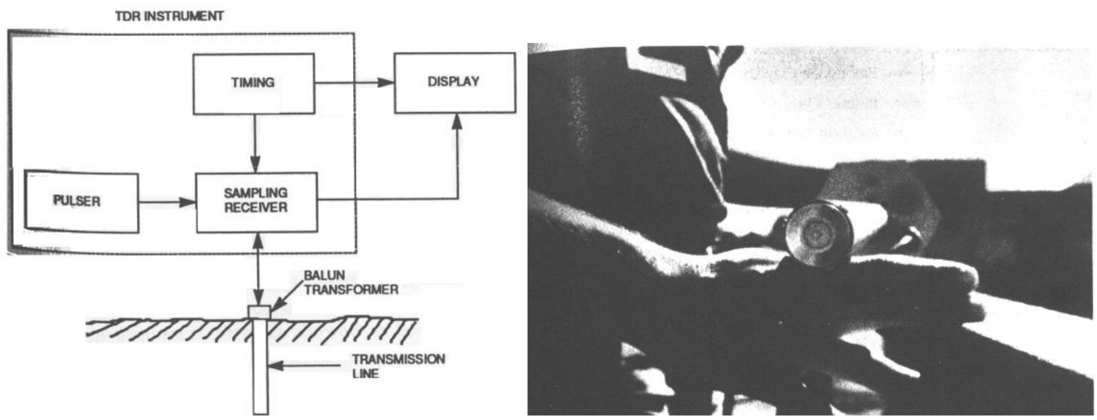

Fig. 2.6-13 A Schematic Diagram of the Time Domain Reflectometry Instrument (left) and a Dielectric Probe (right) (Source: Brisco et al., 1992)

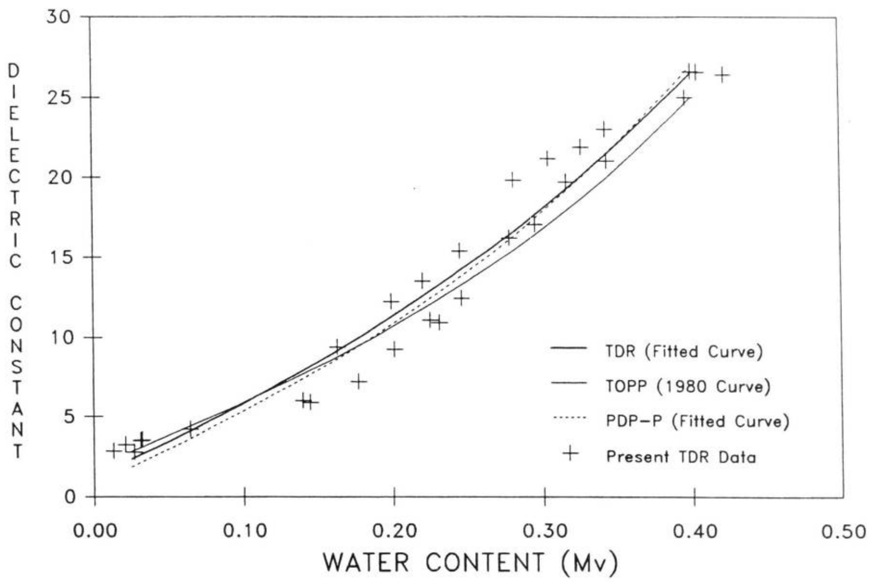

Fig. 2.6-14 A Comparison of the Dielectric Constant ε'_R versus Volumetric Soil Moisture for a P band Portable Dielectric Probe and TDR. (Source: Brisco et al., 1992)

The data from TDR and PDP was found to be generally in line with the Topp's empirical relationship as shown by Eq. [2.5-1] determined by the EMCTL method and depicted in Fig. 2.6-14. However, the depths of penetration of these technologies are limited to 0-5cm for TDR and 0-1cm for PDP (Brisco et al., 1992).

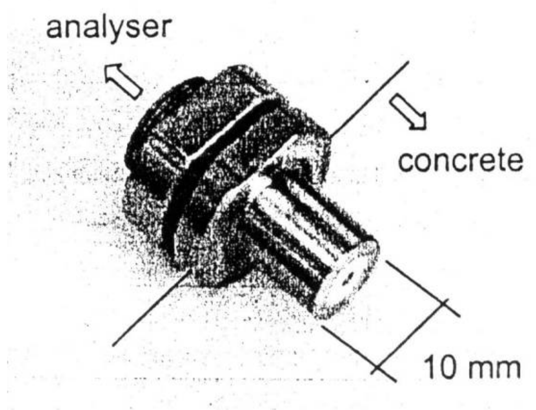

Fig. 2.6-15 Probe used for the 1-1000MHz Measurement (Source: Beek, 2000)

Beek (2000) utilized a cast-in dielectric probe (refer to Fig. 2.6-15) to determine dielectric permittivity, conductivity and temperature of fresh concrete simultaneously. Similar to the EMCTL method, the probe is connected to an impedance analyzer operating in the frequency range 1MHz to 1GHz. The design of the dielectric probe is close to the concept of Time Domain Reflectometry (TDR) method used to investigate moisture distribution in soil.

The pros and cons of these three EM technologies affect their scales of application. The following section compares and contrasts these technologies.

2.6.4 COMPARISON OF THE ELECTROMAGNETIC TECHNOLOGIES

A host of different technologies have been adopted in experimental determination of dielectric properties of material. These technologies include GPR/SPR, EMCTL and PDP which are derivatives of the EMCTL method. Amongst these three technologies, EMCTL is extensively and routinely used for measuring dielectric properties of concrete, cement paste, soil and asphalt.

The volume of material being tested by EMCTL, TDR and PDP is far less than that by GPR. Field applications of EMCTL and TDR methods are often hampered by difficulties and restrictions encountered in performing full-scale in-situ measurement. EMCTL can only be carried out on small extracted samples from the ground whereas TDR can only be applied to a small mass of in-situ material. In common with all test methods on a small mass of material/sample obtained in sampling process, two critical and un-desirable conditions are normally found:

1. the original physical states of the sampled material is usually disturbed, and
2. the in-situ ground conditions of the original material cannot be accurately reproduced in laboratory tests.

The test results are then shrouded in varying degrees of uncertainty. Hence, testing methods on larger masses of in-situ materials, such as GPR, are more effective and time-efficient in surveying a large area of soil dielectric properties, especially those soils saturated with water.

Apart from the coverage of large/small masses of materials, there exists another intrinsic difference among these technologies. In EMCTL, TDR and PDP, microwave transmission is wave-guided whilst the propagation of GPR waves is not. Therefore, GPR receives signals in a wide band of frequency exhibited in the sub-surface and the ambient environment. It is also noted that the commercially available GPR systems can only measure the propagation velocity of the EM wave and therefore only the real part of complex dielectric permittivity is concerned in this research and most practical applications, whilst the EMCTL methods yield information on both the real and imaginary parts.

Sections 2.2 to 2.6 have reviewed the literature in relation to the material properties, dielectric models and EM technologies. The formulations of the directions of this research are guided by the inadequacy identified in the literature review and gaps of knowledge, which will be given in Section 2.7.

2.7 SUMMARY AND DISCUSSIONS TO JUSTIFY THE FORMULATION OF RESEARCH APPROACHES

This chapter has reviewed and examined the following three aspects:

1. the major factors affecting the dielectric properties of three porous construction materials which are concrete (i.e. Section 2.2), asphalt (i.e. Section 2.3) and soil

(i.e. Section 2.4),

2. a number of well-known dielectric models to construct the relationships between the dielectric parameters and a number of physical properties (Section 2.5), and
3. a number of laboratory and field instrumentation methods for determination of the dielectric properties of these materials (Section 2.6).

The studies reviewed in this chapter have revealed that water content, porosity and the EM frequency are the primary factors and considerations to characterize the three porous materials. The water content and the EM frequency are the external factors in addition to the material properties, whereas the porosity is affected by a number of secondary factors. In concrete, these secondary factors are honeycombs, water to cement ratio, mix ratio and curing history, whereas in soil, these secondary factors are texture, specific surface and clay mineralogy. In asphalt, these secondary factors were not obvious, presumably because of the small influence by different combinations of mix constituents on their porosity and specific surface values.

Traditionally, research on concrete, asphalt and soil has been conducted by researchers from very distinct and separate backgrounds of civil engineering, transportation engineering, geotechnics and geophysics. It has been found that very few inter-disciplinary research efforts are noted. Therefore, a unified approach is advocated in this research to characterize these three important materials based on their similarity, as well as differences in their pore structures/systems. These primary and secondary factors exhibited in the porous structures/systems of the three studied porous materials are collectively studied from the electromagnetic perspective using GPR/SPR. Details will be further discussed in Section 2.7.1.

The use of appropriate dielectric and petrophysical models, as well as suitable instrumentation is critical in this research. Amongst the models described in Section 2.4, the CRIM and the Debye's model are considered to be the most appropriate models to model and shape the experimental data in this research. GPR/SPR was also considered as a preferred tool which is more appropriate than the EMCTL, TDR and PDP as it is the only method to characterize a large mass of material. Justification of the use of the CRIM and the Debye's model, as well as the use of GPR/SPR will be further elaborated in Section 2.7.2 and 2.7.3 respectively.

2.7.1 MATERIAL CHARACTERIZATIONS

A. DESIGN OF CONCRETE, ASPHALT AND SOIL SPECIMENS IN THIS RESEARCH

The factors discussed in the Section 2.2 to 2.4 and those to be investigated in the experimental sections (i.e. Chapter 6 to 8) in this research are summarized in Table 2.7-1.

Table 2.7-1 Factors Identified in Literature Review and Those Investigated in the Experiments of this Research

MATERIALS	FACTORS DISCUSSED IN CH.2	FACTORS TO BE INVESTIGATED AND REPORTED IN CH.6, 7 AND 8
Concrete	1. Water content, 2. Porosity (affected by water to cement ratio and honeycombs), and 3. EM frequency	1. Relationship of the real part of complex permittivity and degree of water saturation (S_w), 2. Relationship of the energy attenuation and degree of water saturation (S_w), 3. Relationship of the drift of radar peak frequency and degree of water saturation (S_w), 4. Porosity as a factor of aggregate to cement ratio, water to cement ratio, curing history and with/without compaction 5. Pore size distribution
Asphalt	1. Water content and, 2. EM frequency	1. Relationship of the real part of complex permittivity and degree of water saturation (S_w), 2. Relationship of the energy attenuation and degree of water saturation (S_w), 3. Relationship of the drift of radar peak frequency and degree of water saturation (S_w), 4. Porosity, 5. EM wave frequency
Soils	1. Water contents, 2. Porosity (affected by soil texture, EM frequency and clay mineralogy	1. Relationship of the real part of complex permittivity and degree of water saturation (S_w), 2. Relationship of the energy attenuation and degree of water saturation (S_w), 3. Relationship of the drift of radar peak frequency and degree of water saturation (S_w), 4. Porosity as a factor of texture of gravel, sand and silt in soil) 5. Specific surface, and 6. Permeability

- CONCRETE

To date, extensive and systematic studies of the effects of the concrete pore system/structure on its dielectric properties have been rarely reported. This leads to a series of experiments on concrete envisaged in this research to investigate the effects of different pore systems/structures (determined by porosity and pore size distribution) on the EM wave properties measured by SPR in Chapter 6. These EM wave properties refer to the real part of complex permittivity (ε’), energy attenuation and drift of peak frequency. This investigation will be shown to be achieved by varying the water to cement ratio, aggregate to cement ratio, curing history and compaction of the concrete specimens.

- ASPHALT

Studies of the factors affecting the dielectric behaviour of asphalt are also rare, with one exception of the work reported by Shang and Umana (1999). Their study concludes that the water content and the EM frequency are the only dominant factors affecting the dielectric properties of asphalt. In this research, an asphalt pavement section was constructed to investigate these factors, such as water content, EM frequency, as well as the three EM wave properties (mentioned in previous paragraph) and porosity. This investigation is to be performed by using GPR, and not the EMCTL method adopted by Shang and Umana (1999).

- SOIL

The literature review identifies a large number of in-depth and extensive studies found in soil. These studies utilized very small sized specimens (in centimetre scale) which were tested by the traditional EMCTL method. During the imbibition and drainage stages in these studies, water in the soil specimens was usually assumed to be homogenously distributed in the soil grains. This assumption is realistic because of using the very small sized specimens, as well as adopting techniques such as absorption of water vapour during imbibition stages (Knight and Nur, 1987a).

However, the assumption of homogeneous water distribution around soil grains is not valid particularly in field condition. It is because the soil mass in the field is far greater than that in the laboratory, so that part of the soil grains must be wetted (or drained) before some the remaining parts during either imbibition or drainage stages respectively. This phenomenon creates differential water distribution in soil, which can be defined as dry zone, transition zone, capillary fringe and fully saturated zone (i.e. water table) (Endres et al. 2000; Bevan et al., 2003). The differential distribution of water in soil can also be found in the experiments on concrete and asphalt. Subsequently, the associated dielectric behaviours due to changes of water content (as a result of differential water distribution) shall not adopt the assumption of homogeneous water distribution as reported in laboratory-based EMCTL studies.

In addition, among these studies, there exists a clear inconsistency of research findings about the effect of soil texture on dielectric properties. Contradictory findings were found to either support or to be against this statement, as described in Section 2.4.2a. Robinson (personal communication, 2005) attributed this inconsistency to the biased sampling of clay minerals: only those with relatively small specific surface were tested and included in the database depicting the well-known Topp et al. (1980)'s equation. Because the specific surface of the tested soil specimens in Topp et al. (1980)'s study was small and not representative enough of all possible soil types, soil texture was therefore found not a factor of consideration in the relationship of data between dielectric constant and volumetric water content.

In this research, soil of ten different textures will be envisaged to be tested to verify the validity of this statement, as well as to the three EM wave properties and the two engineering/geological properties (i.e. porosity and permeability) for soil characterization purposes.

B. A DIFFERENT BEHAVIOUR AT SMALL AND HIGH DEGREES OF WATER SATURATION (SW) IN THE CURVES OF REAL PERMITTIVITY AGAINST SW IN BOTH AIR-CURED CONCRETE AND SOIL

The literature review shows that in the plots of ε' vs S_w, the intermediate S_w is the region where many theoretical dielectric models (such as Topp's model, volumetric mixing models and effective medium theory) apply, and that porosity is the single most influential parameter to characterize the material's behaviour in this region. Much of the work (tabulated in Appendixes A and B) carried out in the past focused entirely on this intermediate range of S_w and ignored the 'peculiar' behaviours at very low and the very high S_w. The very low S_w is represented by the region before the *transition moisture content* θ_t, whereas the very high S_w is represented by the region after the *critical* S_w. Most researchers (except some studies such as Wang and Schmugge, 1980; Knight and Nur, 1987a; Shang and Umana, 1999; Soutsos et al., 2001) have overlooked the material behaviour in these two extreme S_w regions. This is presumably attributed to the following reasons:

1. in the region of low S_w values, the change of the curve gradient is not obvious due to a small range of the measured dielectric constants over a small range of S_w, and
2. in the region of high S_w values, Topp et al. (1980) and Wang and Schmugge (1980) attributed the non-compliance of the data to purely fitting and experimental errors respectively.

In microscopic scale of water distribution, the theoretical explanation of the existence of transition moisture content and critical S_w were not understood nor reported in many of previous studies, except the one carried out by Knight and Nur

(1987a). This study provides a systematic explanation of these phenomena at both small and high values of S_w in sandstone and will be discussed in Chapter 3. In this research, the peculiar behaviours in these two regions of S_w were also found in both air-cured concrete and soil of various textures, as will be described in Chapter 6 and Chapter 8 respectively. The theoretical explanations will then be explained by the theories adopted by Knight and Nur (1987a), Saarenketo, T. (1998), West et al. (2003) and Huisman et al. (2003) from the dielectric perspective, as well as Neville (1995) and Hillel (1998) from the perspective of concrete and soil respectively.

In macroscopic scale, the author has also furnished an alternative explanation to the microscopic point of view by attributing these phenomena to the existence of transition zone and capillary fringe which is based on differential distribution of water contained within the materials.

C. MEASUREMENT OF DEGREE OF WATER SATURATION INSTEAD OF VOLUMETRIC WATER CONTENT

The wetness of material in many studies was usually quantified either in terms of volumetric moisture content (θ_v in a ratio of water volume to bulk volume) or degree of water saturation (S_w). The former (θ_v) is adopted in the majority of studies because it enables the absolute amount of water possessed in materials to be quantified. This quantity is particularly useful and can be obtained accurately for the very small sized and homogeneous samples investigated in many studies. However, doubt remains for the accuracy of θ_v measurement, especially the local variation of water contents for relatively large scale experiments described in this research.

In view of the difficulty of obtaining accurate θ_v along the material profile in this research (no appropriate instrument other than GPR was available), the degree of water saturation (S_w) is to be adopted in this research as a measure of water content. This expression represents the degree of material wetness in a normalized scale ranging from an oven-dried state (S_w = 0) to the fully saturated state (S_w = 1). Linear/non-linear interpolation was applied between these two extremes to determine each intermediate S_w when a steady rate of flow was maintained in the permeation and pumping systems, as will be described in Section 7.4.1. Most importantly, the independent measures of both ε' and S_w enables coupling and fitting the data pairs into the Complex Refractive Index Model (CRIM) to obtain values of porosity, as described in Section 2.5.4B, Chapter 7 and Chapter 8. A justification of the use of S_w in lieu of θ_v is provided in Appendix L. An error estimation of S_w is also provided in Appendix M, based on the data and discussion covered in Appendix L.

D. DRIFT OF PEAK-FREQUENCY OF THE RETURNED WAVEFORMS DUE TO CHANGE OF WATER CONTENT

The EM wave properties have been well-documented in many studies. However, the drift of EM peak-frequency observed due to change of water saturation was mentioned in very few studies (Jol, 1995; Millard et al., 2001), but has not been reported systematically to date. These properties will be examined in the experimental chapters for characterization purposes.

E. THE FACTORS OF CONDUCTIVITY, TEMPERATURE AND PRESSURE

Many studies focused on both the behaviour of dielectric constant and conductivity of materials over a range of EM frequencies. In these studies, it was assumed that dielectric constant is independent/persists diminishing dependence of conductivity at high frequency at the GHz level (Sen and Chew, 1983; Davis and Annan, 1989; Daniels, 2004). The conductivity is assumed to be a fixed, frequency-independent, real value which is equal to the direct current conductivity (Keller, 1987; Xu and McMechan, 1997; Irving and Knight, 2003). This is attributed to the majority of cases that the energy storage mechanisms (i.e. polarization) overwhelm the energy loss mechanisms (i.e. conduction) in GPR/SPR frequency ranges (Irving and Knight, 2003). Details of the theory in this perspective will be investigated in Section 3.3.2.

The factors of temperature and pressure were also found to be negligible when the three EM constitutive parameters (i.e. ε, σ and μ as described in Section 3.2) are measured under a temperature range between 10^{o}C to 30^{o}C and subject to the atmospheric pressure (Topp et al., 1980; Garrouch and Sharma, 1994), in which the Section 3.3.2 is also referred. These factors are therefore also assumed to be negligible in the experiments described in Chapter 6, Chapter 7 and Chapter 8.

2.7.2 SELECTION OF THE DIELECTRIC/PETROPHYSICAL MODELS IN THIS RESEARCH

Researchers have continued to develop a wide range of models using their own experimental data. The following paragraphs provide some comments to dispute some of these methods as well as to justify the application of others adopted in this research.

Empirical models are obtained through a curve fitting process. These models describe the relationship between dielectric constants and moisture content in materials (particularly in soil) in a very simple way. They can easily be applied and have been found to be reasonably accurate in laboratory and field conditions. However, this type of models is not founded on any physical basis. Also, it has been shown in Section 2.4 that this type of models fails to consider the factor of soil texture, which affects porosity and specific surface.

In the semi-empirical models, they are founded on sound physical basis (such as wilting point) provided. However, several soil-specific parameters (determined by regression) still remain empirical. Also when these models are adopted, some unknown parameters (such as porosity and fraction of clay and sand) must be well-defined in advance. This type of models is generally believed to be useful only to model a particular set of data in the laboratory and may not be able to generalize.

Effective Medium Theory (EMT) incorporates the geometrical factor of the material and produces very similar results as predicted by the CRIM (Alharthi and Lange, 1987). However, the iterative two-step procedures in EMT make its applications to laboratory and field data more complicated than the CRIM.

Phenomenological models, such as the Debye (1929)'s model and the Cole-Cole (1941)'s plot, describe how dielectric permittivity is frequency-dependent across a wide range of micro-wave frequencies. They describe the different values of dielectric permittivity when different EM frequencies are adopted. The theories of these models will be discussed in Section 3.3.3.

The volumetric mixing model was found to be the most useful models amongst all for complex and heterogeneous composition of material investigated in this research. It is more effective than other models because it takes two fundamental factors (i.e.

the degree of water saturation and the porosity) possessed in a porous material into consideration, as a function of composite and individual dielectric constants. Among the various volumetric mixing models described in Section 2.5.4B, 'Complex Refractive Index Model (CRIM)' was found to provide the best agreement with the data obtained in this research, as well as the data obtained by many researchers, such as Knoll (1996) and Martinez (2001). Most importantly, the CRIM enables the porosity of a material to be derived and predicted from the dielectric measurement, as described in Section 2.5.4B. The determined values of porosity from the CRIM are essential to characterize and classify concrete, asphalt and soil as described in the material characterization models described in Chapter 10.

With the CRIM, two important engineering/geological properties (i.e. porosity and permeability) can be derived and determined by independent measurements of dielectric properties and degree of water saturation. With the Debye (1929)'s model, the frequency-dependent behaviour of dielectric dispersion can be explained. The success of the application of these models on the measured parameters is greatly dependent on the appropriate selection of measurement techniques, which will be discussed in the following section.

2.7.3 SELECTION OF THE EXPERIMENTAL TECHNIQUES IN THIS RESEARCH

Most studies reported in Appendix B were based on extracted samples to test under the wave-guided EMCTL method and/or probing a localized area by the wave-guided TDR/PDP technique. Only a relative minority of these studies adopted the non-wave-guided GPR method. However, field applications of the EMCTL and the TDR methods are often hampered by difficulties and restrictions encountered in performing full-scale in-situ measurement. EMCTL can only be carried out on small extracted samples from the ground whereas TDR can only be applied to small masses of in-situ material. The use of GPR advocated in Chapter 7 and Chapter 8 are considered to be more versatile and useful than EMCTL and TDR. This is because GPR/SPR provides information on larger masses of in-situ material so that local variations in material properties have been taken care of and evened out. Better still, the EMCTL method is a pre-cursor to the understanding of dielectric properties and large-scale applications of GPR/SPR.

2.7.4 CONFUSION OVER THE TERMINOLOGY 'DIELECTRIC CONSTANT'

It must be noted that dielectric constant is not a constant (Hilhorst, 1998), but varies with the externally applied EM frequency from a wide range of frequencies. It is a measure of the polarizability of a material and is a factor of a range of material properties, such as water content, conductivity, material textures, salinity, and so on. Researchers, scholars and practitioners describe this property in several terms, such as dielectric constants, relative dielectric permittivity and dielectric permittivity.

The term dielectric constant has a long history. It is customary to switch between the term 'dielectric constant' and the 'complex permittivity'. According to a private communication between the author with an anonymous paper reviewer of a world-renowned journal, this property was first discovered when experimenting with non-conductive dielectric materials and at those times neither the frequency dependence, nor its complex characteristics were understood. Hence the term "dielectric constant" was coined and has been used for many decades. However, since the phenomenon of frequency dependence has become well-known and well-established, the term "dielectric constant" seems to be contradictory and inappropriate. To account for this ambiguity caused by historical precedence, this property should be termed 'relative complex dielectric permittivity' which comprises of the real and imaginary parts. In this research, the term *real permittivity (ε')* will be selected to represent the 'real part of the relative complex permittivity', or the conventional term 'dielectric constant'. However, the term 'dielectric constant' is still used in the chapters of the Literature Review and Theory to maintain the convention and consistency of this terminology adopted by other researchers and scholars.

In the next chapter 'Theory', the material properties (as described in Sections 2.2 to 2.4) in terms of the pore system/structures possessed within the studied material will be further elaborated. Further to the material properties, Sections 3.2, 3.3 and 3.4 in the theory chapter serve as an extension of Sections 2.2, 2.3 and 2.4 respectively in this chapter. Also, the theories of the electromagnetics and some of the working principles of the GPR/SPR will be introduced in the final two sections of Chapter 3.

3. THEORIES

3.1 INTRODUCTION

This theory chapter is divided into five sections. Section 3.1 provides a very brief introduction. Section 3.2 reviews porous construction material through a range of material properties. These properties include a number of traditional and well-established physical properties, such as pore size, texture, and so on as well as the dielectric properties. Section 3.3 reviews the dielectric properties from the perspective of polarization mechanism, dielectric dispersion and dielectric relaxation over a wide range of EM frequencies experienced in lossy material. Section 3.4 reviews some important working principles of ground penetrating radar (GPR)/Surface Penetrating Radar (SPR). These principles include the energy loss and attenuation, as well as the vertical and horizontal resolutions achievable with different radar frequencies. Finally, Section 3.5 proides a brief conclusion of this chapter.

This chapter serves as an extension of the theoretical background of the material properties described from Chapter 2, as well as paving the way to establish the theoretical basis behind the findings obtained by a series of experiments in this research.

3.2 POROUS MATERIALS

3.2.1 CLASSIFICATION OF PORES

Porous material is defined as solid containing pores (Ishizaki et al., 1998). The porosity is a measure of the volumetric fraction of pores to that of the bulk volume possessed within a porous material. Ishizaki et al. (1998) provided a simple classification of pores, which is divided into two types: the open pores and the closed pores, as illustrated in Fig. 3.2-1. The former refers to the connected pores to the external media of a material. The latter refers to the isolated pores from the external media of a material. Penetrating pores, non-penetrating pores and ink-bottle pores are particular cases of open pores, as depicted in Fig. 3.2-1.

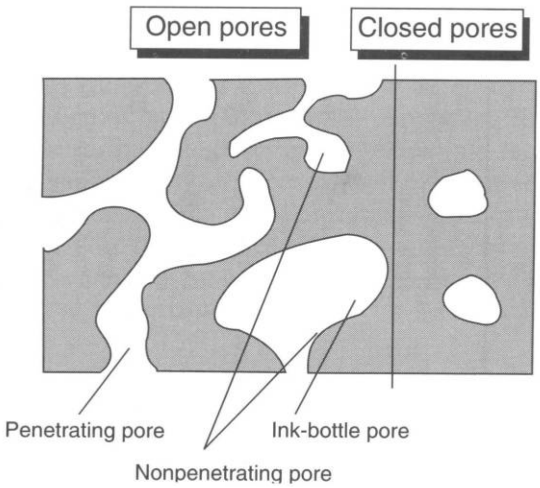

Fig.3.2-1 Schematic Illustration of Different Morphology of Pores (Ishizaki et al., 1998)

Pores can also be classified by different criteria, such as pore size, pore shape, material and production methods (Ishizaki et al., 1998). In this research, pore size is the primary and principal criteria to classify the studied porous material. The development of pore structures/system within the man-made materials (i.e. concrete and asphalt) and the natural material (i.e. soil) is mostly measured by the size of pores. The sizes of pores are classified differently in the conventional studies of these studied materials, such as gel pores (in nano-meter scale), capillary pores (in micro-meter scale) and macro-pores in concrete, as well as micro-pores (in micro-meter scale), capillary pores (from micro- to milli-meter scale) and macro-pores in soil. Details of these pores and their properties for each of these materials will be described in the next few sub-sections.

Fig. 3.2-2 illustrates different pore structures, whilst Table 3.2-1 lists these types of pore structures, as well as some of their examples, comments on the ranges of porosity and specific surface.

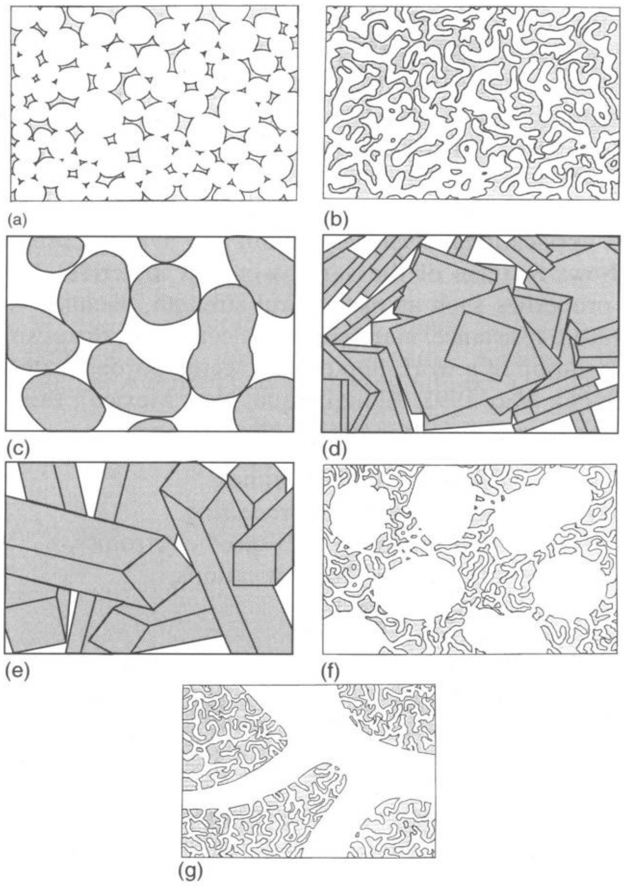

Fig. 3.2-2 Different Pore Structures (Source: Ishizaki et al., 1998)

Category	**Pore structures**	**Examples**	**PSD**	S_s
a	Foam	Ceramic material	Wide	Small
b	Interconnected	Glass	Very narrow	Small
c	Open among particles	Powder compact	Narrow	Large
d	Open among plates	Powder with plate-like particles	Narrow	Large
e	Open among fibres	Fibre	Wide	Small
f	Large-small pore network	Sintered porous material	Wide	Large
g	Large-small pore network	Porous material consisting of porous particles	Wide	Large

Remarks:
Category refers to the caption of Fig. 3.2-2
PSD: Pore Size Distribution
S_s: Specific surface area per unit volume

Table 3.2-1 Different Configurations of Pore Morphology of Porous Material
(Source: Ishizaki et al., 1998)

A large value of porosity indicates a significant contribution of specific surface within a porous material (Lowell et al., 2004). In the next section, the specific surface area (or specific surface) of the three studied porous materials will be the subject of concern.

3.2.2 SPECIFIC SURFACE

The values of specific surface of the studied material in this research vary largely, as tabulated in Table 3.2-2. Specific surface depends on both the sizes (i.e. shape and texture) and the shapes of the particles. For the latter, a sphere is known to exhibit a minimum area to volume ratio (i.e. specific surface) among all geometrical forms of material, whereas a chain of atoms bonded only along a chain axis exhibits a maximum specific surface (Lowell et al., 2004). All particulate matters with different geometries possess a surface area between these two extremes. For instance, gel particles in concrete (needle-shaped, plate-shaped, and foil-shaped), cement (powder-like appearance) and clay with very small grain size (flaky/plate-like shaped) yield a large specific surface (S_s). However, round/irregular shaped aggregate in concrete, asphalt, as well as spherical sand grains yield a comparatively small specific surface.

The specific surface (S_s) can be defined as the total surface area, A_S, of particle per unit mass (m^2/g), or per unit volume of particles (m^2/m^3), or per unit bulk volume of soil (m^2/m^3) (Hillel, 1998).

Table 3.2-2 Characteristic Values of Specific Surface and Porosity of Different Porous Construction Materials

<table>
<tr><th colspan="2" rowspan="2">Material</th><th colspan="2">Specific Surface (m^2/g)</th><th colspan="2" rowspan="2">Material</th><th colspan="2">Porosity (%)</th></tr>
<tr><th>Value</th><th>Source</th><th>Value</th><th>Source</th></tr>
<tr><td colspan="2">Concrete</td><td>-</td><td rowspan="7">Neville (1995)</td><td colspan="2">Concrete</td><td>5-28</td><td rowspan="7">Neville (1995)</td></tr>
<tr><td colspan="2">Cement</td><td>0.2-0.5</td><td colspan="2">Cement</td><td>-</td></tr>
<tr><td colspan="2">Gel</td><td>200</td><td colspan="2">Gel</td><td>28</td></tr>
<tr><td colspan="2" rowspan="4">Aggregate (rounded and irregular gravel/crushed granite)</td><td rowspan="4">0.01-0.0001</td><td rowspan="4">Aggregate</td><td>Granite</td><td>0-48</td></tr>
<tr><td>Quartzite</td><td>1.9-15.1</td></tr>
<tr><td>Limestone</td><td>0-37.6</td></tr>
<tr><td>Granite</td><td>0.4-3.8</td></tr>
<tr><td colspan="2">Asphalt</td><td>0.06 - 2.18</td><td>Anonymous product specification</td><td colspan="2">Asphalt</td><td>0.03-0.06</td><td>Anonymous product specification</td></tr>
<tr><td colspan="2" rowspan="2">Sand</td><td rowspan="2">0.04-0.001</td><td rowspan="6">Whitlow (2001)</td><td colspan="2">Coarse sand</td><td>30-40</td><td rowspan="9">Bell (2000)</td></tr>
<tr><td colspan="2">Medium to fine sand</td><td>25-35</td></tr>
<tr><td colspan="2">Silt</td><td>1-0.04</td><td colspan="2">Silt</td><td>40-50</td></tr>
<tr><td rowspan="6">Clay</td><td>Kaolinite</td><td>20</td><td colspan="2" rowspan="6">Clay</td><td rowspan="6">45-55</td></tr>
<tr><td>Illite</td><td>80</td></tr>
<tr><td>Montmorillonite</td><td>800</td></tr>
<tr><td>Georgia Kaolin</td><td>5-20</td><td rowspan="3">Peplinski et al. (1995)</td></tr>
<tr><td>Kentucky Ball</td><td>20.9</td></tr>
<tr><td>Western Bentonite</td><td>~700</td></tr>
</table>

* The characteristic values provided in this table are indicative and may be subject to great variation when different methods are used and/or different mixtures are provided.

In Section 3.2.5.5, the specific surfaces (S_s) of soil are derived and approximated by means of some basic physics and mathematics. This derivation and approximation should not be used to determine the specific surface of concrete and asphalt. It is due to the difficulties of approximating the specific surface of concrete and because of the variability in the shape of different aggregate particles (Neville, 1995). Instead, S_s should be obtained by indirect measurement (by methods such as water adsorption and X-ray scattering) which is beyond the scope and concern of this research. In the following three sub-sections, the solid structures and the pore structures/systems of concrete, asphalt and soil (as commonly referred to as a three-phrase system which comprises the solid, liquid and gas) will be briefly introduced.

3.2.3 SOLID STRUCTURES AND PORE STRUCTURES/SYSTEMS OF CONCRETE

3.2.3.1 SOLID STRUCTURES OF CONCRETE

Fresh cement paste is a network of cement particles surrounded by water. At every stage of cement hydration, the hardened cement matrix contains poorly crystallized hydrates, known as gel which is the crystals of $Ca(OH)_2$, as depicted in Fig. 3.2-3 Some minor components, such as un-hydrated cement and the residual water-filled spaces in the fresh cement paste form capillary pores which are 1.3μm (the median size) according to Glasser (1992). In an even smaller scale, interstitial voids exist within the porous cement gel and are known as gel pores. The nominal size of gel pores is about 3nm which is larger than water molecules by just one or two orders of magnitude (Neville, 1995).

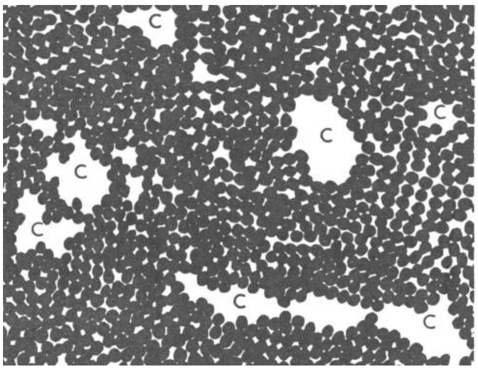

Remarks: Solid dots represent gel particles; interstitial spaces represent gel pores; Spaces marked with 'C' are capillary pores. Size of gel pores is exaggerated

Fig. 3.2-3 Simplified Model of Cement Paste Structure (Source: Neville, 1995)

Aggregate in concrete is not as porous as cement paste because the porosity of aggregate is generally very small. Since aggregate occupies as much as three quarters of the bulk concrete's volume, the overall porosity of concrete is also small so that the long-term durability can be sustained because of its excellent resistance to intrusion from water content and chloride content.

3.2.3.2 PORE STRUCTURES/SYSTEMS OF CONCRETE

The pore system in concrete is determined by factors such as the aggregate to cement ratio, the water to cement ratio, the cement content and the degree of hydration, and can be classified as macro-pores, capillary pores and gel pores according to their nominal sizes. Concrete can possess high porosity, as much as 40%, however these pores may not be inter-connected (Neville, 1995) as this is the case encountered in soil which behaves very differently. The different types of pores are briefly explained as follows:

- Macro-pores

Mature and hardened concrete contains different types of voids caused by trapped residual air bubbles resulting from inadequate compaction, imperfect cement particle packing or trapped free water not used up to complete hydration. These macro-pores are visible when they are at the concrete surface, such as cases in concrete with honeycombs and segregation.

All pores possessed in concrete are not truly spherical or cylindrical, except macro-pores; the diameter of pore represents a sphere which equals to the ratio of volume to surface area (Neville, 1995).

- Capillary pores

At any stage of hydration, the capillary pores represent the portion of the total volume within bulk concrete which has not been filled by the products of the hydration matrix. Most capillary pores have a median size smaller than 1.3µm (Glasser, 1992). They vary in shape and form an inter-connected water transport system randomly distributed throughout the cement paste. These inter-connected capillary pores allow the water saturation and permeation within the hardened cement matrix in concrete and therefore contribute to water permeability.

- Gel pores

The gel particles in concrete hold large quantities of evaporable water. The pores within the gel are inter-connected with interstitial spaces between the needle-plate and foil-shaped gel particles (Neville, 1995). The size of gel pores is less than 2 or 3 nm in nominal diameter and is only one order of magnitude larger than the size of molecules of water (Neville, 1995).

As hydration progresses, the solid content of the cement paste increases and the capillaries are blocked, segmented and therefore disconnected. Therefore, the capillary pores are only inter-connected solely by the gel pores. The reduced volume of inter-connected capillaries can be controlled by a suitable water to cement ratio and a complete degree of hydration, which is accomplished by water curing, as depicted in Fig. 3.2-4. The volume of the gel and capillary pores with a larger degree of hydration is considerably reduced when compared to that of a lesser degree of hydration.

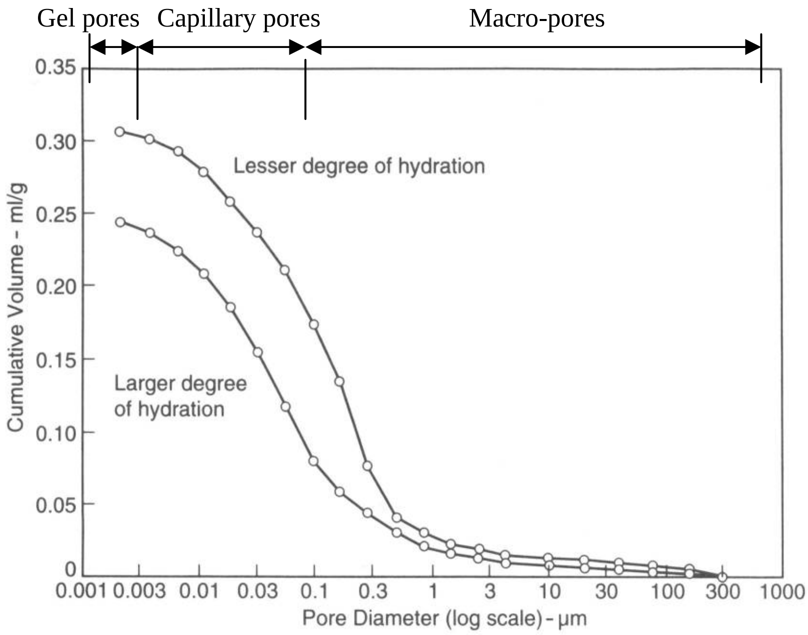

Fig. 3.2-4 Pore Distribution of More Hydrated Concrete, Mortar and Paste at a W/C ratio 0.45 (Source: Winslow and Liu, 1990)

The process to block the network of capillary pores is important because it is a prerequisite of producing concrete with high strength and high durability.

3.2.4 SOLID STRUCTURES AND PORE STRUCTURES/SYSTEMS OF ASPHALT

Asphalt pavement is a mixture of asphalt cement and aggregate. The asphalt cement acts as the binder phase in the asphalt mixture. Similar to the role of Portland cement as a binder in concrete, the asphalt cement governs most of the physical and mechanical properties (such as viscosity, elasticity, and so on.) (Young et al., 1998) in the asphalt pavement composite. The schematic structure of asphalt paving structure is depicted in Fig. 3.2-5 and Fig. 3.2-6.

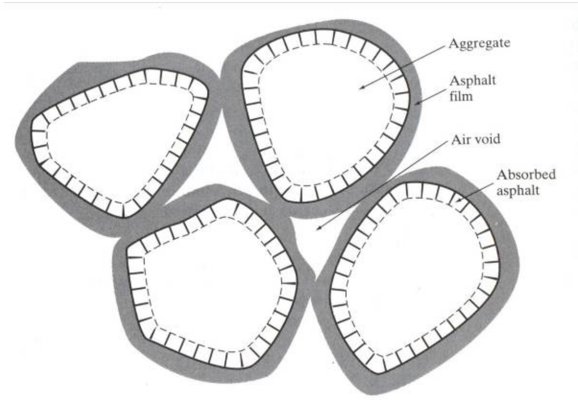

Fig. 3.2-5 Structure of Asphalt Concrete Paving Mixture (Source: Young et al., 1998)

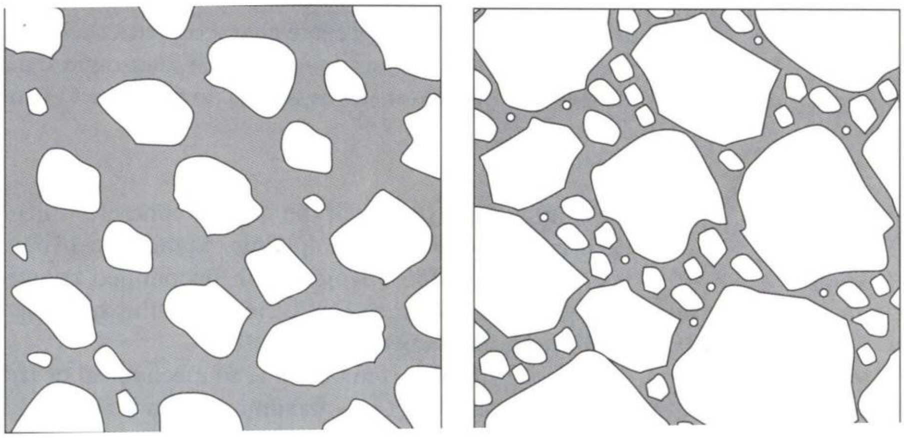

Fig. 3.2-6 Asphalt Concrete Mixture with (a) open-graded mixture and excess asphalt cement (b) dense-graded aggregate and sufficient asphalt cement (Source: Young et al., 1998)

As shown in Fig. 3.2-6, the proportion of asphalt cement and aggregate can be controlled to produce two different physical behaviours of asphalt concrete (Young et al., 1998). In Fig. 3.2-6a, the asphalt cement becomes the matrix and the aggregate is the filler, which results in a more viscous deformation behaviour. In Fig. 3.2-6b, the dominating aggregate particles acts as a continuous phase and the asphalt cement fills the void spaces between the aggregate. The bulk composite becomes less viscous and its behaviour is essentially that of a solid. The latter structure (i.e. Fig. 3.2-6b) is closer to the optimum structure than the former one (i.e. Fig. 3.2-6a) which consists of inter-locked and dense aggregate structure with asphalt cement filling the pore spaces for binding the aggregate matrix to resist the adverse environment (Young et al., 1998).

3.2.5 SOLID STRUCTURES AND PORE STRUCTURES/SYSTEMS OF SOIL

Soil is a three-phase system, which consists of essentially the solid phase, the liquid phase and the gaseous phase. A graphical illustration is depicted in Fig. 3.2-7. The solid phase comprises soil particles that exhibit various chemical compositions and organic matter, as well as size, shape and orientation. The liquid phase refers to the water possessed in a soil which dissolves substances. The gaseous phase corresponds to the soil atmosphere which represents the pores that are not occupied by water. This three-phase system governs all soil properties and is the most fundamental basis for subsequent discussion of other soil theories and experimental works in later chapters.

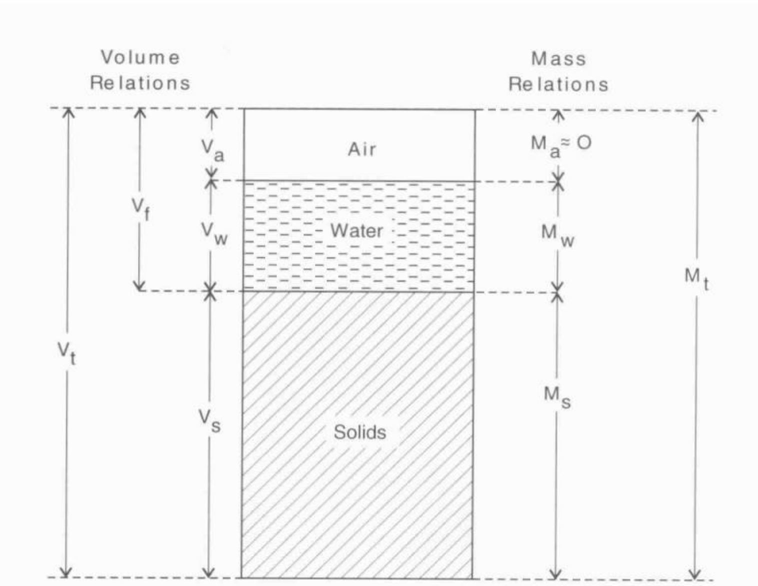

Fig. 3.2-7 Schematic Diagram of Soil as a Three-phase System (Source: Hillel, 1998)

The structure of soil (see Section 3.2.4) determines the geometrical characteristics of pore space which is an exchangeable fraction of air (gaseous phase) and water (liquid phase) occupied in the bulk volume. An increase in one of them is associated with a decrease in the others.

Texture and wilting points are two of the most common soil properties to characterize the solid portion in different types of soils. Most importantly, these two properties are mutually dependent and are highly related to electromagnetic wave properties which are part of the principal foci in this research. They will be discussed in Section 3.2.5.3 and 3.2.5.4. Also, soil permeability and hysteresis will be discussed in Section 3.2.5.6 and 3.2.5.8 respectively to provide insights on the effects of water on soil properties. Soil permeability is a measure of the transport of water between the solid particles, whereas in soil hysteresis, the effects of wetting and drying inside the menisci and capillarity established within the soil particles, as well as their associated effects on dielectric properties are concerned.

Furthermore, the relationships between dielectric constant and degrees of water saturation possessed in soil will be the subject of concern in Section 3.2.5.7. This section provides a theoretical basis to associate dielectric constant with above soil properties at various degrees of water saturation.

3.2.5.1 SOLID STRUCTURES OF SOIL

The solid phase of soil comprises soil particles of various shapes and sizes packed together in a number of ways (Marshall et al., 1996) and can be collectively classified by their soil structures. Soil structures can be divided into three broad and commonly accepted categories, namely single grained, massive and aggregated structures (Hillel, 1998). For soil particles entirely unattached to each other and the structure is therefore completely loose, it is considered to be single-grained or structure-less. Coarse-granular soil or an unconsolidated deposit of desert dust is examples of this category. One typical packing arrangement of the single-grained structure is shown in Fig. 3.2-8, where a gradual distribution of grain size constitutes the soil structure. Smaller grains fill the voids between larger grains and this packing of soil particles is known as ‘poly-disperse’, whereas a packing with uniform soil particles is known as ‘mono-disperse’ which is unreal theoretical packing type.

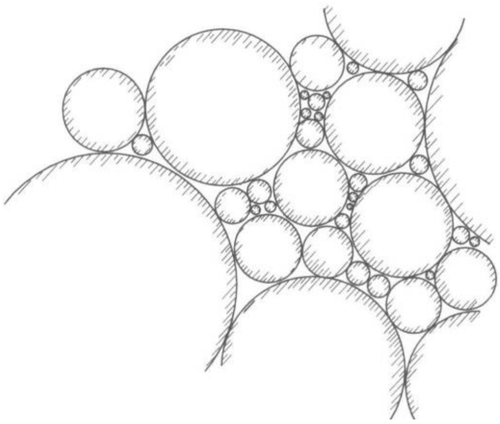

Fig. 3.2-8 Hypothetical Packing of Poly-disperse Particles (Source: Hillel, 1998)

On the other hand, a soil which is tightly packed in large cohesive blocks can be termed as a massive structure, such as dried clay. Between these two extremes the soil is said to contain quasi-stable small clods which is considered to be an aggregated structure, as depicted in Fig. 3.2-9 (Hillel, 1998).

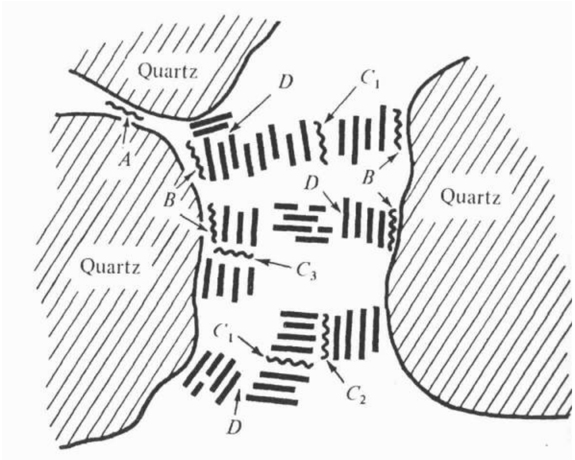

Remark: Type of bond: A, quartz-organic matter-quartz; B, quartz-organic matter-domain; C, domain-organic matter-domain (C_1, face-face; C_1, edge-face; C_1, edge-edge); D, domain edge-domain face

Fig. 3.2-9 Possible Arrangement of Quartz, Clay Domains, and Organic Matter in an Aggregate. (Source: Emerson, 1959)

3.2.5.2 PORE STRUCTURES/SYSTEMS OF SOIL

In a three-phase system exhibited in soil described previously, the soil structure (single-grained/massive/aggregate) determines the geometrical characteristics of the pore spaces, in which water and air are transported and retained (Hillel, 1998). These geometrical characteristics of the pores can be classified and summarized in Table 3.2-3.

Table 3.2-3 Pore Classification in Soil in terms of Pore Size

	MICRO-PORES	CAPILLARY PORES	MACRO-PORES
SIZE	Less than micro-meter in width	Several micro-meters to a few milli-meters wide	Several milli-meters or even centimeters wide, visible by naked eye
TYPE OF SOIL	Clayey soil	Medium-textured soil	Coarse and fine-textures of soils. In particular it appear as cracks or fissures in clayey soil upon drying
LAWS TO BE OBEYED BY WATER HELD IN THIS TYPE OF PORE	Cation absorption and hydration, and anion exclusion	Capillarity and Darcy's law, laminar water flow	Turbulent water flow
CONNECTIVITY	Isolated and does not participate in ordinary liquid flow, and is therefore referred to as absorbed water or bound water	Inter-connected	Inter-connected

Remark: this table is a summary of several paragraphs of text abstracted from 'Fundamental of Soil Physics' written by Hillel (1998).

In addition, the pores can be classified by their locations within and between neighbouring soil particles. In a strongly aggregated soil which contains relatively narrow pore width as shown in Fig. 3.2-9, the pores are *within* adjacent particles and are known as *intra-aggregate* pores which are analogous to the gel pores in concrete. Since the sizes of these pores are very small, these pores also fall into the categories of micro-pores and capillary pores as described in Table 3.2-3. However, *inter-aggregate* pores refer to wider spaces and cavities *between* adjacent soil particles. The size of this type of pore lies partly in that of capillary pores and partly of macro-pores.

The soil texture also determines the pore size distribution. In coarse-grained soil, macro-pores form inter-aggregate cavities which serve as the principal paths for the permeation and drainage of water. In fine-grained soil, micro-pores form the intra-aggregate capillaries which retain water during drainage (Hillel, 1980).

Porosity is the measure of the total intra-aggregate pores and inter-aggregate pores possessed in a soil. Some characteristic values obtained from a number of studies in a range of different soil types are reported in Table 3.2-4, Table 3.2-5 and Fig. 3.2-10. These values were compared with the experimental findings reported in Chapter 8.

Table 3.2-4 Range of Values found in Bulk Density, Porosity and Void Ratio in different Soils. (Source: Marshall et al. 1996)

DESCRIPTION	BULK DENSITY (Mg/m^3)	POROSITY	VOID RATIO
SURFACE SOIL OF WET CLAY	1.12	0.58	1.37
SURFACE SOIL OF LOAM TEXTURE	1.28	0.52	1.07
SPHERES OF UNIFORM SIZE IN OPEN PACKING	1.39	0.48	0.91
SUBSOIL OF SANDY TEXTURE	1.61	0.39	0.65
SANDY LOAM SOIL COMPACTED BY HEAVY TRAFFIC	1.90	0.28	0.39
SPHERES OF UNIFORM SIZE IN CLOSEST PACKING	1.96	0.26	0.35
SANDSTONE	2.12	0.20	0.25

Remark: Particle Density if taken as $2.65Mg/m^3$

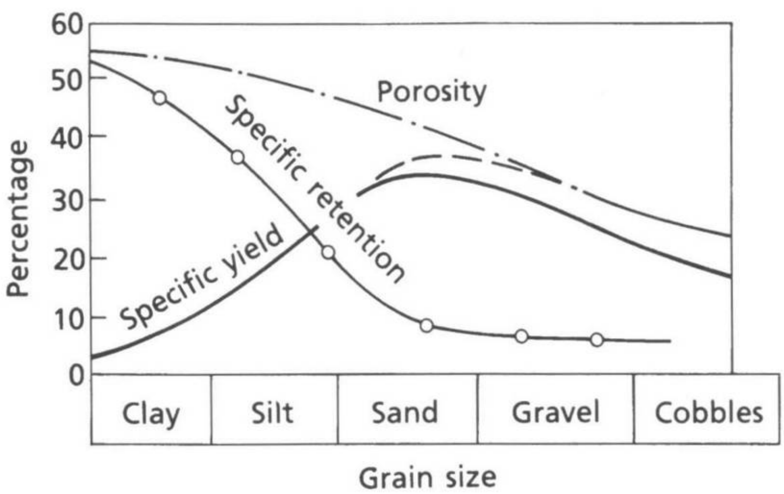

Fig. 3.2-10 Relationship between Grain Size, Porosity, Specific Retention and Specific Yield (Bell, 2000)

Table 3.2-5 Summary of Measured Data of Clay Volume, Porosity, Permeability and Dielectric Constant at 1MHz (Source: Knoll, 1996)

CLAY WEIGHT FRACTION	CLAY VOLUME FRACTION	POROSITY	PERMEABILITY (cm^2)	Dielectric Constant at 1MHz	
				Dry	**Saturated**
0.000	0.000	0.399	4.4×10^{-6}	2.62	26.5 (0.99)
0.062	0.063	0.359	7.5×10^{-9}	3.00	20.4 (0.80)
0.129	0.130	0.308	1.6×10^{-10}	3.51	21.3 (0.82)
0.209	1.211	0.238	5.4×10^{-12}	4.34	21.5 (0.85)
0.372	2.375	0.359	7.1×10^{-12}	4.27	33.9 (0.90)
0.613	0.615	0.480	6.4×10^{-12}	4.27	44.7 (0.85)
1.000	1.000	0.599	1.5×10^{-11}	4.08	58.5 (0.88)

This section reviews the two fundamental parameters (i.e. porosity and specific surface) which are governed by the pore structures/systems of a porous material. The following section investigates some of the important properties affecting the pore structures/systems of soil.

3.2.5.3 TEXTURES AND PARTICLE SIZE DISTRIBUTION OF SOIL

The texture of a soil is represented and expressed as a weighed proportion of sand, silt and clay. The mixture of different sizes of soil can be defined according to the triangular diagram illustrated in Fig. 3.2-11. There are several conventional schemes of the classification of soil fractions according to the ranges of particle diameters. These schemes are basically the same with minor differences. In this research, the convention suggested by BS1377-2:1990 is adopted.

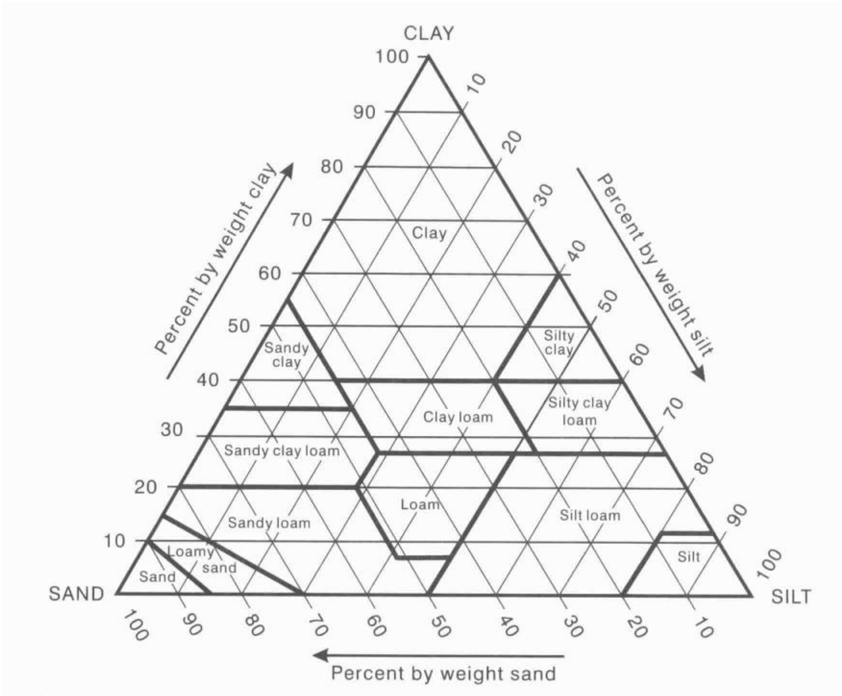

Fig. 3.2-11 Soil Texture Triangle, showing the Percentages of Clay (below 0.002mm), silt (0.002-0.05mm), and sand (0.05-2mm) (Hillel, 1998)

A more convenient and comprehensive description of the soil texture in a soil can be determined by the particle size distribution (PSD) using methods of dry sieving, wet sieving and sedimentation. An example of PSD graphs obtained from the specimens of soil in this research is referred to Fig. 8-1.

3.2.5.4 WILTING POINT AND FIELD CAPACITY OF SOIL

Water content possessed in a soil ranges from the oven-dried state to the fully saturated state. Between these two extremes, two more intermediate states can be defined in accordance with two particular phenomena in soils. The first state is termed *field capacity*. It is a property and measure of soil wetness when a saturated soil has been drained for about two days (Marshall et al., 1996). However, it is not easy to be determined in the field since the required conditions of good drainage and absence of evaporation are difficult to fulfill. The second state is termed *wilting point* which is defined based on the aspect of planting. During a drying process and until the wilting point of a soil is reached, a plant is considered to be unaffected by any decrease of soil wetness (Hillel, 1998). However, any water content below the wilting point would abruptly curtail the plant's activity. A conceptual model suggested by Hillel (1998) is illustrated in Fig. 3.2-12 to demonstrate the full range of soil wetness that is possible for a soil to possess.

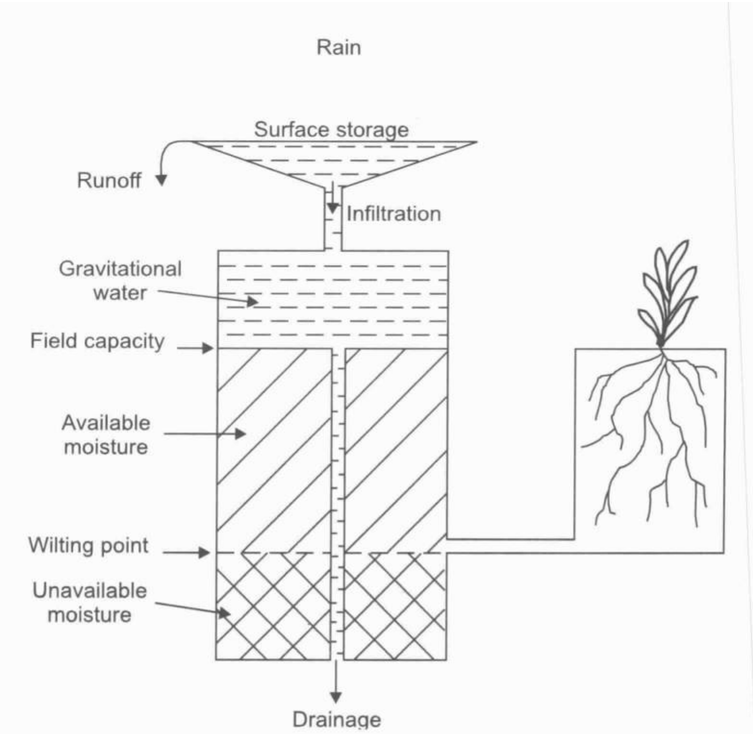

Fig. 3.2-12 The 'Bucket Model': A Simple Representation of Soil Moisture Availability, between Field Capacity and Wilting Point (Source: Hillel, 1998)

Also, the benchmarks of the wilting point (WP) and the field capacity (FC) can be presented in terms of the water-bearing ability of soil as depicted in the model in Fig. 3.2-13 (Wang and Schmugge, 1980). This figure depicts different successive layers of water surrounding a particle: from the innermost mono-layer to the intermediate layer (corresponding to wilting point) and the outer-most layer (marked by the field capacity). Water is tightly held in tension by solid particles at a pressure of 10^4 bars for the innermost mono-layer, and 1/3 bar for the outer-most layer. Beyond the field capacity surface, water is free to flow under gravity. A certain thickness of water layer was held by a solid particle by hygroscopic forces (inside the space marked by the hygroscopic surface) which do not allow the escape of water even by oven drying.

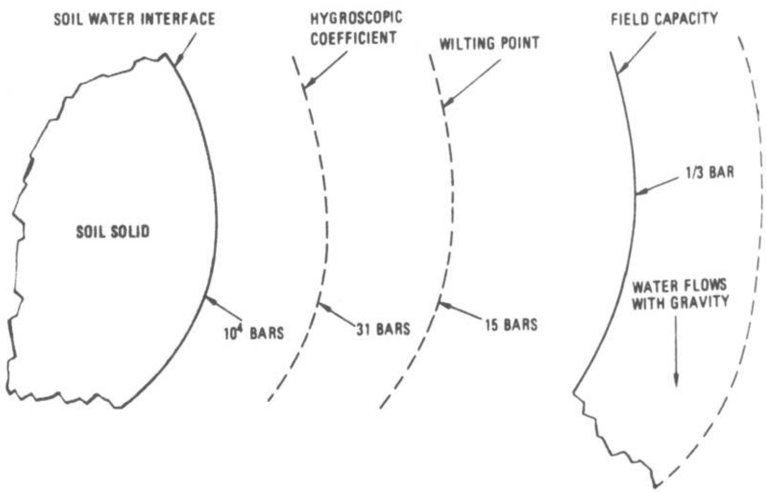

Remark: The Wilting Point and Field Capacity are defined as the Volumetric Content of Water held in Tension by Solid Particles at the 15 bars and 1/3 bars, respectively.

Fig. 3.2-13 The Model of a typical Soil-water System. (Source: Wang and Schmugge, 1980)

Higher clay content of a soil attributes to a larger value of WP (Marshall et al., 1996). Schmugge et al. (1976) determined the relationship between clay content and WP according to over 100 data sets of soil with different moisture characteristics and by performing multiple regressions (Wang and Schmugge, 1980), as follows:

$$WP = 0.06774 - 0.00064xW_S + 0.00478xW_C \;\ldots.. \; [3.2\text{-}1]$$

where W_S and W_C are the weight of sand and clay respectively. Some soil types are illustrated in Table 3.2-6.

According to Eq. [3.2-1] and Table 3.2-6, higher clay content of a soil yields a larger wilting point, and vice versa.

Table 3.2-6 Different types of Soils used for the Dielectric Measurements as a function of Water Content at 1.4GHz and 5GHz (Source: Wang and Schmugge, 1980)

No.	Soil type	Texture (percent) Sand	Silt	Clay	Wilting[1] point WP (cm^3/cm^3)	Transition[2] moisture W_t (cm^3/cm^3)	γ^+	α[3]	Remarks
1	M5	88.0	7.3	4.7	0.034	0.20	0.40	0	Measurement frequency = 5 GHz (Wang *et al.*, 1978)
2	F2	56.0	26.7	17.3	0.115	0.22	0.40	0	
3	H7	19.3	46.0	34.7	0.220	0.31	0.35	0	
4	Harlingen clay	2.0	37.0	61.0	0.358	0.31	0.30	0	
5	Yuma sand	100.0	0	0	0.004	0.17	0.50	0	Measurement frequency = 1.412 GHz (Lundien, 1971)
2	Eufaula fine sand	90.0	7.0	3.0	0.024	0.16	0.50	0	
3	Dougherty fine sand	82.0	14.0	4.0	0.034	0.17	0.50	0	
4	Minco very fine sand	70.0	22.0	8.0	0.051	0.17	0.50	0	
5	Openwood street silt	22.0	70.0	8.0	0.092	0.23	0.50	8	
6	Chickasha loam	58.0	28.0	14.0	0.098	0.22	0.40	8	
7	Zaneis loam	48.0	36.0	16.0	0.114	0.22	0.40	8	
8	Collinville loam	45.0	39.0	16.0	0.115	0.23	0.40	8	
9	Kirkland silt loam	26.0	56.0	18.0	0.137	0.20	0.40	8	
10	Tabler silt loam	22.0	56.0	22.0	0.159	0.19	0.40	8	
11	Vernon clay loam	16.0	56.0	28.0	0.192	0.28	0.45	26	
12	Long lake clay	6.0	54.0	40.0	0.255	0.26	0.40	26	
1	Sand	86.0	7.0	7.0	0.046	0.20	0.40	0	Measurement frequency = 1.4 GHz (Newton, 1977)
2	Samples 4 and 5	40.0	26.0	34.0	0.205	0.30	0.30	22	
3	Samples 7 and 18	36.0	29.0	35.0	0.212	0.28	0.30	16	
4	Samples 14 and 15	52.0	9.0	39.0	0.221	0.30	0.30	18	
5	Sample 13	44.0	12.0	44.0	0.250	0.31	0.30	22	
6	Miller clay	3.0	35.0	62.0	0.361	0.33	0.30	20	

[1]Computed from (1).
[2]Determined from (2)–(5).
[3]Determined from (6).

The existence of a wilting point in a soil is highly correlated with the cause of the initial change of curvature at the early S_w exhibited in the plots between dielectric constants and degree of water saturation. This phenomenon will be examined in detail in Section 3.2.5.7.

3.2.5.5 DERIVATION OF SPECIFIC SURFACE OF SOIL

For soil with a large S_s, a fine-grained soil attracts more water molecules and therefore becomes more porous than a coarse-grained soil. For example, clay hydrates to form electrostatic double layers with exchangeable ions in the surrounding solution (Hillel, 1980).

A well-known approximation of S_s (m^2/g), nominal diameter of spherical soil grains and specific gravity is shown as follows (Whitlow, 2001):

$$S_S = \frac{0.006}{d\rho_S} \text{ ....[3.2-2]}$$

where d is the nominal diameter of the soil grain and ρ_s is the specific gravity of the soil grain.

Another formulation of specific surface in soil also assumes that the soil grains are in the form of spherical shapes which comprise size fractions 'N', with each size fraction comprising N_i spheres of radius r_i (Knoll, 1996) and presented in the form of m^3/m^2.

$$S_S = \frac{\sum_{i=1}^{m} 4\pi r_i^2 N_i}{\sum_{i=1}^{m} \frac{4}{3}\pi r_i^3 N_i} = 3\sum_{i=1}^{m} \frac{V_i}{r_i} \text{ ....[3.2-3]}$$

where

S_s is the specific surface

N_i is the quantity of grain spheres of the i th component

r_i is the radius of grain spheres of the i th component

V_i is the volume fraction of the i th component (such that $\Sigma V_i = 1$)

Soil particles with smaller grain sizes possess greater specific surface (S_s) than larger sized particles if the particle is more or less spherical, in which the specific surface can be determined by Eq. [3.2-2] and Eq. [3.2-3]. However, small particles, such as clay, are rarely spherical and possess plate-like molecular structures. Fig. 3.2-14 depicts the fact that plate-like clay particles possess the highest specific surface areas compared to coarse spherical particles with nearly cylindrical pores.

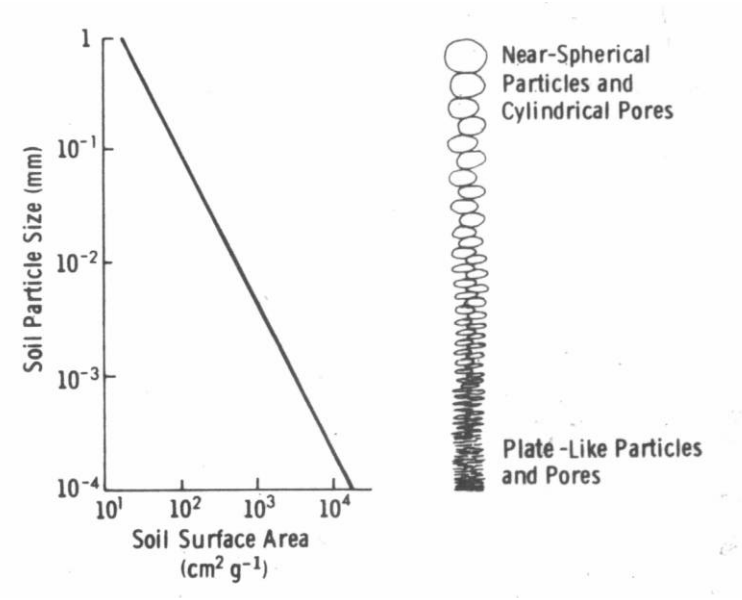

Fig. 3.2-14 Relationship among Particle Size, Shape and Surface Area of Soil
(Source: Dobson et al., 1985)

Clay particles are usually charged and when two neighbouring particles hydrate, they form electrostatic double layers of exchangeable ions from the surrounding solution between them (Hillel, 1980). Thus, clay fraction of the soil mixture and the mineralogy of the clay particles determine the specific surface area of soil (Peplinski et al., 1995).

3.2.5.6 SOIL PERMEABILITY MODEL: KOZENY-CARMEN'S MODEL

Kozeny-Carmen's model (Kozeny, 1927 and its modification by Carmen, 1956) is one of the most widely accepted models to predict soil permeability. It is approximated by the prior information of the specific surface and the porosity of soils. This theory is a statistical characterization based on the concept of hydraulic radius (Carmen, 1956; Knoll, 1996). The hydraulic radius is defined as the average ratio of the cross-section area to the average circumferences of the complicated pore network, and is equivalent to the ratio of pore volume to surface area (Hillel, 1980), as shown in Eq. [3.2-4]:

$$k = \frac{\phi^3}{cS_t^{\ 2}} = \frac{\phi^3}{5(1-\phi)^2 S_S^{\ 2}} \text{ ………..... [3.2-4]}$$

where k is the coefficient of permeability,, ϕ is the porosity, S_s is the specific surface (i.e. surface area per unit volume) and the constant '5' is a dimensionless constant which is dependent on the shape and orientation of capillary tubes possessed within the soil grain. The constant '5' is commonly accepted for general application (Carmen, 1956; Knoll, 1996).

The values of S_s can be derived and predicted from the basic definitions (i.e. ratio of surface area to the volume fractions of the soil). The bulk volume of soil can be divided into that of sand and clay (Yin, 1993; Knoll, 1996). By further substituting the value of S_S obtained from Eq. [3.2-3] into Eq. [3.2-4], Eq. [3.2-5] is obtained:

$$k = \frac{\phi^3}{45(1-\phi)^2 (\frac{V_S}{r_S} + \frac{V_{cl}}{r_{cl}})^2} \text{ ……………..[3.2-5]}$$

where V_S and V_{cl} are the volumetric fractions of sand and clay respectively, and r_s and r_{cl} are the radii of the sand and clay grain spheres respectively.

If the size distribution of soil is known, Eq. [3.2-5] can be further modified as:

$$k = \frac{\phi^3}{45(1-\phi)^2 (\sum_{i=1}^{m} \frac{V_i}{r_i})^2} \text{ ……………..[3.2-6]}$$

More representative values of S_S can be obtained in Eq. [3.2-6] than in Eq. [3.2-5] when each particle size and its fraction are incorporated in Eq. [3.2-6] than those of only two generic sizes (i.e. sand and clay) employed in Eq. [3.2-5].

A word of caution must be noted that this theory is not valid when it is used to describe structured soil bodies (Hillel, 1980) like fissured fine particles in silt/clay, as reported in the experimental findings described in Section 8.4.4.

3.2.5.7 RELATIONSHIP BETWEEN DIELECTRIC CONSTANT AND WATER CONTENT IN SOIL

Water content is commonly known to be the dominant factor of dielectric constant in soil. In the relationship between dielectric constant and water content, three different curvatures are recognized in the plots between dielectric constant and S_w in a wide range of soil textures investigated by many researchers (but rarely reported systematically), as described in Table 3.2-7. These curvatures are commonly found in previous studies tabulated in Appendix B and explained in a number of ways, but have not been organized and summarized in the format of Table 3.2-7 yet. They are correspondent to different theories and can generally be classified by three distinct ranges of degrees of water saturation (S_w)/ volumetric moisture content θ_v as follows:

Table 3.2-7 Characteristics of Different Curvatures reported in the Relationship describing Soil Real Permittivity ε' and degrees of water saturation S_w /Volumetric Moisture Content θ_v of Soils

Increasing/ Decreasing water content	**Stages at the plot of ε vs S_w/θ_v**	**Characteristics of curvature in the plot of ε vs S_w/θ_v**	**Theories/Models to describe these characteristics**	**Similar characteristics reported by other authors**
Permeation/ Imbibition (i.e. Increasing water content)	Early S_w stage (such as S_w<0.12 or θ_v<0.15cm^3/ cm^3)	The slow-climbing region	Wilting point/transition moisture content by Wang (1980)	Davis et al. (1976), Wang (1980), Wang and Schmugge (1980) Topp et al. (1980), Knoll (1996), Hallikainen et al. (1985), Knight and Nur (1987a) and Peplinski et al. (1995), Saarenketo (1998), West et al. (2003)
	Intermediate S_w stage (such as 0.12<S_w<0.7 or 0.15<θ_v<0.5 cm^3/ cm^3)	The fast-climbing region	Complex Refractive Index Model, of which its most general form was by Lichtenecker-Rother (1937)	Brown (1956), Birchak et.al. (1974), Topp et.al. (1980), Roth et.al. (1990), Chan and Knight (1999), Saarenketo (1998) , West et al. (2003)
	High S_w (such as S_w>0.7 or θ_v>0.15) stage	The slow-climbing region	loss of connectivity in the gas phase contribution of the capacitance of water-gas arrangement by Knight and Nur (1987a) (Remark: sandstone is used in this work)	Wang (1980)
de-watering/ drainage (i.e. Decreasing water content)	From high S_w to low S_w	Different pathway when compared to that of the increasing water content (known as *dielectric hysteresis*)	Micro-geometry of the pore space by Knight and Nur (1987a) and Endres and Knight (1992) (Remark: sandstone is used in their work)	Hysteresis in the relationship between matric suction and water content in soil is reported by Baver, et al. (1972), Marshall and Holmes (1979), and Hillel (1980), West et al. (2003)

Remarks:
1. Maximum value of S_w = 1 (fully saturated state), minimum value of S_w = 0 (oven-dried state)
2. Values of S_w and θ_v are dependent on soil texture and vary in different studies

As an example, the three stages (i.e. three curvatures in the curve) defined during permeation/imbibition stage identified in Table 3.2-7 are depicted in Fig. 3.2-15. Each of these stages will be detailed in the following sections.

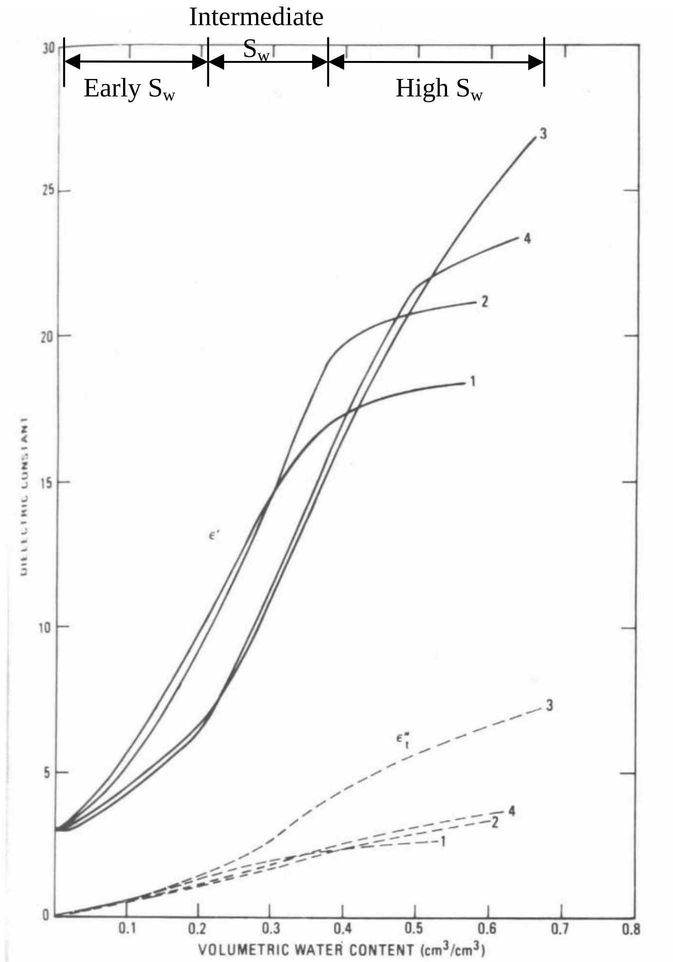

Curve	Texture (percent)			Wilting point WP (cm^3 /cm^3)	Transition moisture θ_t (cm^3 /cm^3)
	Sand	Silt	Clay		
1	88	7.3	4.7	0.034	0.2
2	56	26.7	17.3	0.115	0.22
3	19.3	46	34.7	0.220	0.31
4	2	37	61	0.358	0.31

Remark: this figure is the same as Fig. 2.5.2 and Fig. 2.4-3

Fig. 3.2-15 The Dielectric Constants versus Volumetric Water Content for Four Soils measured at 5GHz. (Source: Wang and Schmugge, 1980)

A. LOW DEGREE OF WATER SATURATION

For low S_w, a '*transition moisture content*' is recognized to demarcate two different but important phenomena: i.e. a very slow increase of the observed dielectric constant from very low moisture content up to the *transition moisture content* and rapid increase afterwards (i.e. the intermediate S_w), as depicted in Fig. 3.2-16.

This transition moisture content (W_t) is found to be texture-dependent (i.e. larger W_t for fine-grained soil than coarse-grained soil). For values below W_t, a soil of high clay content contains a larger fraction of tightly bound water molecules on the surface of soil grains than a soil of high sandy content (Wang and Schmugge, 1980; Knight, 1991).

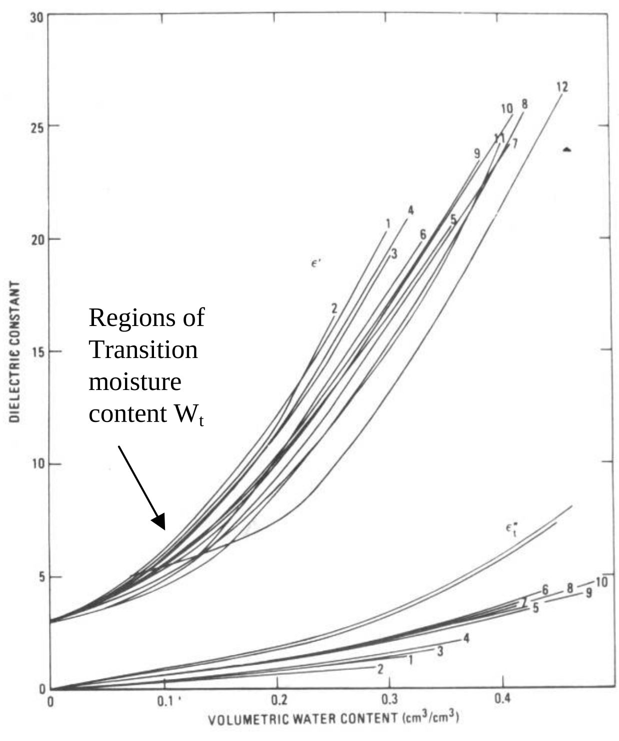

Remark: Soil types cover a wide range of soil texture, including clay, clay loam, silt, silt loam and sand.

Fig.3.2-16 The Dielectric Constants versus Volumetric Water Content (for 12 different types of soils described in Table 3.4-1) measured at 1.412 GHz. (Source: Wang and Schmugge, 1980)

The existence of this transition moisture content was also recognized with sandstone (Knight and Nur, 1987a), but the adopted frequency range is much lower than that used by Wang (1980). The existence of this transition moisture content was attributed to the existence of a single mono-layer of absorbed water (3.5Å in thickness) coated on the pore surface at low S_w (Knight and Nur, 1987a). This polarization of this mono-layer of water by external EM field was restricted since it is tightly bound to the surface (Knight and Nur, 1987a). Hence its contribution of polarization is reduced, in comparison to that exhibited in free water which gives a larger value of dielectric constant.

Both wilting point (WP) and transition moisture content (W_t) were found to be a function of soil texture, as demonstrated by a relationship obtained through a linear regression of data according to Eq. [3.2-7] (Wang and Schmugge, 1980). Furthermore, no significant difference between the two adopted EM frequencies (i.e. 1.4GHz and 5GHz) on this relationship is noticed in Wang and Schmugge (1980)'s work.

$$W_t = 0.49WP + 0.165 \text{ .... [3.2-7]}$$

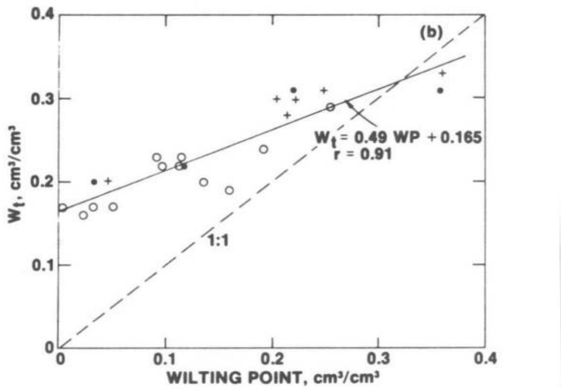

Remarks: data expressed with hollow circle and cross was collected using 1.4GHz, while data expressed with solid circle was acquired using 5GHz

Fig.3.2-17 The Variations of the Transition Moistures with the Wilting Points of Soil. (Source: Wang and Schmugge, 1980)

The theories suggested by Wang (1980) and Knight and Nur (1987a) are corresponding to the same phenomenon: less contribution of dielectric constant of bound water at small S_w. When water continues to accumulate to reach the intermediate S_w, The phenomenon of bound water vanishes and the water in these porous materials will behave differently, as described in the following section. In particular according to Wang (1980) and Wang and Schmugge (1980), the wilting point of a soil can be determined if the transition moisture content in the plot of dielectric constant versus water content is known. The value of the wilting point can be subsequently used to estimate the texture of the soil. Detailed investigations of the model derived by Wang and Schmugge (1980) were referred to in Section 2.5.2a.

For soils composed of coarse texture, most water molecules are effectively in its liquid state and are known as ‘free water’. However, for soils composed of fine texture, bound and capillary water is physically absorbed by soil particles in the capillary pores. Hence, the contribution to dielectric constant (i.e. a measure of polarization) by free water is larger than that by bound water.

B. INTERMEDIATE DEGREE OF WATER SATURATION

After a water content exceeding W_t, water is essentially in its free state, and therefore the contributions of water to polarization are higher at values above the transition moisture content. The portion of the curve in this stage possesses the largest climbing rate among the other two counterpart stages. The data in this region was found to be best-fitted by the Complex Refractive Index Model (CRIM), which in its most general form was contributed by Lichtenecker-Rother (1937), as discussed in Section 2.5.4B.

Knight and Nur (1987a) attributed the remarkable increase of dielectric constant at the intermediate S_w to the conductive paths constructed by adsorption of two to three additional mono-layers of water. These mono-layers of water were considered to act as a thin capacitor, whereas the solid grains or gas act as the insulating medium. As S_w increases, the quantities of these water-solid grain and water-gas capacitors increase. The existence of these conducting fluids and capacitors increases the contribution of dielectric constant at intermediate S_w (Sen, 1980) and therefore manifests the fast-climbing region as depicted in Fig. 3.2-16 and Fig. 3.2-18.

C. HIGH DEGREE OF WATER SATURATION

In the region of high S_w, the curve shows a transition from the relatively straight segment (i.e. the intermediate S_w) before a particular *turning point* to another segment with rapidly decreasing gradient, as annotated in Fig. 3.2-19. Critical S_w is designated as the moisture corresponding to this *turning point*.

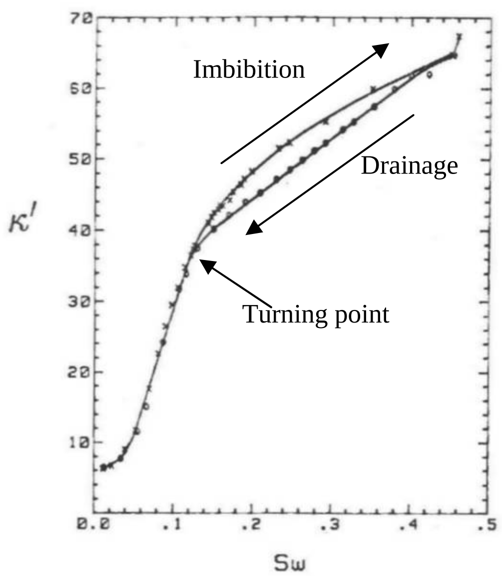

Remark: data in cross and in circle were obtained from adsorption and desorption of water respectively)

Fig.3.2-18 Dielectric Constant versus Degree of Water Saturation at 30kHz (Source: Knight and Nur, 1987a)

When water content reaches the critical S_w, the weaker polarization effect caused by bound water becomes more significant again, as illustrated by the smaller contribution to dielectric constant according to Fig. 3.2-15 and Fig. 3.2-18. This dramatic drop after the turning point can be attributed to the loss of connectivity in the gas pockets (Knight and Nur, 1987a). As the surface layers of a soil are absorbing water (i.e. S_w increases progressively), the capacitance of the water-gas mixture increases and the thickness of gas pocket decreases. When a *critical S_w* is reached, the capacitance in the gas phase of pores is considered to be 'short-circuited' and contributes to a smaller capacitance value which leads to smaller dielectric constants at high S_w.

3.2.5.8 HYSTERESIS OF SOIL-WATER RELATIONSHIP

Hysteresis of porous material is described by the different path-ways identified by material properties under cyclic wetting and drying processes. This phenomenon manifests loops in *matric suction* versus water content plots (as described by Baver et al., 1972; Marshall and Holmes, 1979 and Hillel, 1998), and some others as found in the loops with dielectric constant (Knight and Nur, 1987a; Endres and Knight, 1992), electrical resistivity (Longeron et al., 1989), elastic wave velocities (Knight, R.J. and Nolen-Hoeksema, R. 1990), and elastic wave attenuation (Bourbie and Zinszner, 1984). The first two properties (i.e. matric suction and dielectric constant) will be discussed in the following sections. They are selected because the former is the most fundamental property to start with the understanding of soil hysteresis, whereas the latter is observed from the dielectric perspective which is related to this research.

A. MATRIC SUCTION VS WATER CONTENT

According to Baver et al. (1972), Marshall and Holmes (1979) and Hillel (1998), a pore structure of a porous material produces a so-called *ink-bottle effect*. For a given matric suction, this hysteresis phenomenon, as depicted in Fig. 3.2-19, can be explained by the characteristics of having many capillary pores which are larger than their openings. It results in a limitation of the passage of water by a channel of an effective radius r_t which is narrower than the pores with an internal effective radius R_t, as shown in Fig. 3.2-20.

$$s = \frac{2\gamma}{\rho g r} \quad \text{……..[3.2-8]}$$

where

s = matric suction (m)

γ = surface tension of water (mNm^{-1})

ρ = gravitational constant (m/s^2)

r = effective radius (m)

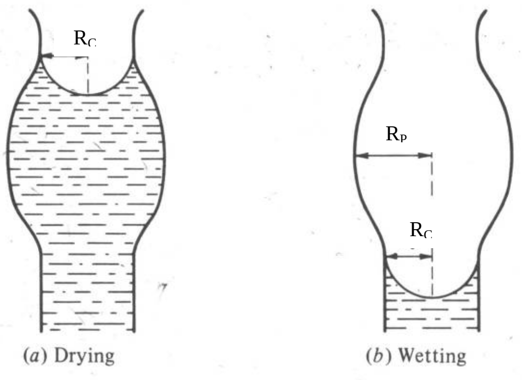

Fig.3.2-19 Hysteresis in the Amount of Water contained in a Pore at a given Suction due to the 'ink-bottle' effect (Source: Marshall et al.,1996)

Table 3.2-8 summarizes the effects of the effective radii within a pore on the suction force during drying and wetting/re-wetting described in Fig. 3.2-20. Both R_C and R_P affect the suction force required to mobilize water molecules during the respective drying and wetting processes. During drying, the matric suction is dependent on and inversely proportional to the radius of the ink-bottle channels (i.e. R_C), whereas during wetting, the matric suction is dependent on and inversely proportional to R_P (Hillel, 1998). Since R_P is always larger than R_C, it follows that S_P is smaller than S_C (i.e. suction force required during drying is larger than that of wetting) as according to Eq. [3.2-8]. Therefore this difference in the magnitudes of suction force (i.e. $S_P < S_C$) leads to dielectric hysteresis (in the relationship between suction force and water content) during cyclic wetting and drying of soil.

Table 3.2-8 Effects of the Effective Radii within a Pore on the Suction Force required in the drying/wetting process in a Porous Material

	Influential factors	Suction force (i.e. equals sρg according to Eq.[3.2-8]) in the drying/wetting process
Drying	R_C but not R_P	$S_C > \frac{2\gamma}{R_C}$
Wetting/ Re-wetting	R_P but not R_C	$S_P < \frac{2\gamma}{R_P}$

Remarks:
*R_C is radius of a channel in the ink-bottle neck of a pore, and
R_P is the maximum radius inside this pore.

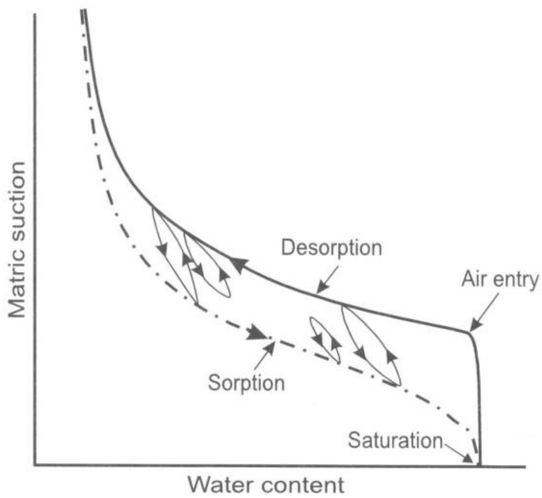

Fig.3.2-20 Suction vs Water Content curves in Sorption and Desorption (Source: Hillel, 1998)

Hysteresis in soil is not only measurable by observing the relationship between matric suction and water content, but also a number of material properties, such as resistivity, elasticity and dielectric constant. The last one is the subject of concern of our next section. The experimental data obtained in this research regarding to this phenomenon will be illustrated and investigated in Chapter 9.

B. DIELECTRIC CONSTANT VS WATER CONTENT

The soil-water interaction during wetting and during processes can also be observed from the dielectric perspective. Starting from the geometries of the gas phase during imbibition and drainage of water in soil, Knight (1991) proposed a simple model which was based on another model suggested by Foster (1932) in a study of condensation in silica gel, as depicted in Fig. 3.2-20.

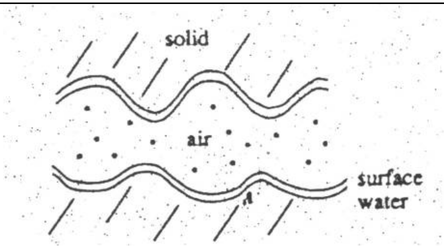

Geometry A (imbibition): A thin layer coats the solid particles

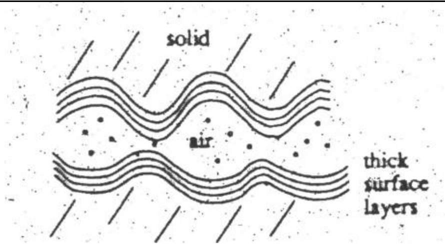

Geometry B (imbibition): Thick and metastable surface layers of water develop

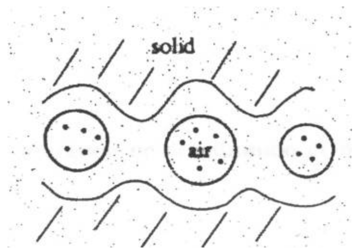

Geometry C (imbibition): Linkage of air breaks and formation of spherical bubbles and water accumulates to fill the narrow region of pore spaces

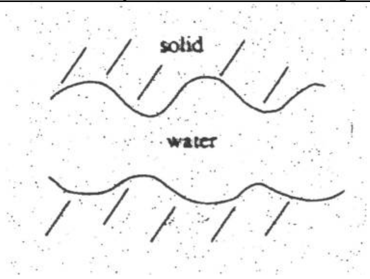

Geometry D (imbibition): The pore space is fully saturated with water

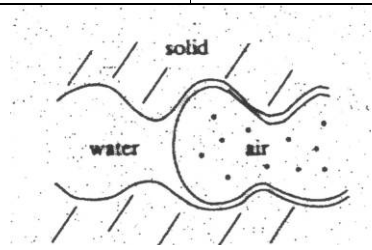

Geometry E (drainage): The thin air and thick surface water layers are not recreated. Thin layers of water remain at the surface of solids, others are drained.

Fig.3.2-20 Schematic Illustration of the Fluid Geometries at Various Saturation Stages during Imbibition and Drainage (Source: Knight, 1991)

The illustrations given in Fig. 3.2-20 can be used to explain the features of curves found in sandstone during cyclic water imbibition and drainage as reported by Knight and Nur (1987a). The experimental investigation conducted by EMCTL covered a frequency ranging from 10kHz to 1MHz. In these experiments, the values of dielectric constant were found to be generally lower during the drainage stage than those of the imbibition stage, as depicted in Fig. 3.2-18. Endres and Knight (1992) further developed a theoretical model which incorporated geometrical microscopic fluid distributions of water and gases to interpret and model the experimental results obtained by Knight and Nur (1987a).

Knight and Nur (1987a) attributed this dielectric hysteresis (see Fig. 3.2-18) to the water-filling (vapor absorption/imbibition) and -emptying (evaporation/drainage) of the central pore volume, which was based on a model describing water adsorption in the capillaries of silica gel proposed by Foster (1932). In Foster's (1932) model, meniscus is assumed to be present inside a pore during these water-filling and -emptying processes and its formation is regarded as a prerequisite before water-filling. When vapor absorption/imbibition begins in the water-filling process, a meniscus can be created firstly by vapor condensation and aided by the blockage of water at a narrow end of the pore. However, a meniscus may not be successfully built in some pores and therefore this leads to a delayed initiation of vapour condensation. The accumulation of water vapor and thus the establishment of meniscus still continues until a sufficient thickness of surface water forms to fill up the narrow end of the pore. When this process of building a meniscus finishes, the pore can then be filled with water as a result.

A major difference of water-filling and -drying processes is that a meniscus is always present in the drying stage, but may be absent in the water-filling stage as described previously. In the drying process, the meniscus moves down the pore as the pore is emptied. At the same time, the meniscus takes away all the water inside the pore, except the first few mono-layers of water, which are tightly-held in the pore (Knight and Nur, 1987a).

Foster (1932) and Knight and Nur (1987a) concluded that during the water-filling stage, the layers of surface water are thicker and gas pockets formed between the water layers are thinner than that during the drying stage. This water and gas (i.e. air) mixture was termed the thin *insulating water-coated gas pockets*. Their presence raises the values of the dielectric constant. They only exist during the water-filling stage but not the drying stage, and thus the dielectric constants obtained during imbibition stage are larger than those of drying stage. This phenomenon is termed dielectric hysteresis in the plot of dielectric constant against degree of water saturation.

Section 3.2 reviews porous material from the perspective of solid and pore structures. In the following section, porous material will be examined using only the electromagnetic perspective.

3.3 ELECTROMAGNETICS

3.3.1 MAXWELL'S EQUATIONS

In 1891, James Clerk Maxwell established, summarized and published a collection of four fundamental equations to establish the foundations of electromagnetics. These equations are based on the earlier experiments and the associated findings by Michael Faraday. These equations describe the macroscopic behaviour of electric and magnetic fields which are orthogonal to each other. These equations have been widely adopted in many disciplines of science and technology. These equations are as follows:

$\nabla \cdot D = \rho_V$	(Gauss' law for E-field)	…….. [3.3-1]
$\nabla \cdot B = 0$	(No magnetic charges)	…….. [3.3-2]
$\nabla \times E = -\dfrac{\partial B}{\partial t}$	(Faraday's law)	…….. [3.3-3]
$\nabla \times H = J + \dfrac{\partial D}{\partial t}$	(Extension of Ampere's law)	…….. [3.3-4]

where

D is the electric flux density (Coulumb/m), E is the E-field intensity (Volt/m^2),

B is the magnetic flux density (Tesla), H is the magnetic field intensity (Wb/Hm),

ρ_V is the electric charge density per unit volume, J is the current density (A/m^2)

The divergence of a vector field D and B (i.e. $\nabla \cdot D$ and $\nabla \cdot B$) is a measure of the net outward flux per unit volume through a closed surface (Ulaby, 2001) surrounding the unit volume, whereas the curl of a vector field E and H ($\nabla \times E$ and $\nabla \times H$) is a measure of the circulation of the vector field per unit area $\triangle$s, with the orientation of $\triangle$s selected such that the circulation is maximum.

The first Maxwell equation is also called Gauss' Law. It states that the total electric flux through any closed surface is equal to the total charge enclosed by that surface. In other words, the density of charge in a region is equal to the divergence of electric flux density ($\nabla \cdot D$) (Knoll, 1996)

The second equation states that the divergence of magnetic flux density (i.e. the net magnetic flux through a closed surface) is always zero. It follows that there are no isolated magnetic 'charges' analogous to the source of electro-static fields so that all magnetic field lines form closed paths.

The third equation is called the Faraday's Law. Different to Eq. [3.3-1] and Eq. [3.3-2], this equation demonstrates the fundamental inter-dependence of electric and magnetic fields. It states that the induced electromagnetic force/voltage in the circuit is equal to the time-rate of change of the magnetic flux linkage within the circuit.

The forth equation is known as the extension of Ampere's Law. This equation states that the line integral of H around a closed path is equal to the current traversing the surface bounded by that path (Ulaby, 2001).

3.3.2 CONSTITUTIVE PARAMETERS OF EM WAVE PROPAGATION IN MATERIALS

The Maxwell's equations described in Section 3.3.1 do not entail any material parameters of the media. Three constitutive parameters were assigned to relate the electrical and magnetic fields. These parameters include electrical conductivity, dielectric permittivity and magnetic permeability.

The three constitutive parameters given in the equations [3.3-5] to [3.3-7] characterize the materials by measuring the values of dielectric constant (ε), conductivity (σ) and magnetic permeability (μ).

- CONDUCTIVITY

On the electrical side, dielectric constant (ε) and conductivity (σ) classify the materials as conductors (metals) and dielectrics (insulators) according to their magnitude of conductivities. In a conductor subject to an external E-field, electrons in the outermost shell of the atoms move from one atom to the next in the opposite direction to that of the external E-field. This move gives rise to *conduction current*. In a dielectric, electrons are tightly bound to the atoms and are hardly able to be detached when subjected to an external E-field and therefore do not produce a conduction current. Conductivities of any material are within a wide range from the perfect conductors (i.e. $\sigma = \infty$) to the perfect dielectric ($\sigma = 0$).

$$J = \sigma E \text{ ………………[3.3-5]}$$

where J is the conduction current density (Ampere/m^2), E is the E-field intensity (Volt/m^2), and σ is the conductivity (Siemens/m)

- DIELECTRIC CONSTANT

In a dielectric material, an electron in an atom is not free to drift to another under the influence of an E-field. However, an atom can be polarized by distorting the center of the electron cloud and the location of the nucleus. The polarized atom is said to be an electrical dipole consisting of charge +q at the center of the nucleus and the charge –q at the center of the electron cloud.

$$D = \varepsilon E \text{ ………………[3.3-6]}$$

where D is the electric flux density (Coulumb/m), E is the E-field intensity (Volt/m^2), and ε is the dielectric constant (Farad/m),

In particular, the dielectric constant/real permittivity (ε') measured in this research is real, effective and does not involve the imaginary part. However, this fact was not emphasized or stated clearly in many research studies related to GPR (Knoll, 1996).

- MAGNETIC PERMEABILITY

A material can usually be classified as diamagnetic, paramagnetic and ferromagnetic material in the aspect of magnetic properties. Diamagnetic and paramagnetic materials are normally dielectric materials and most metals. Their values of the relative magnetic permeabilities are very close to unity. However, ferromagnetic materials, such as iron, nickel and cobalt, exhibit large values of μ (such as μ equals to 200,000 in the case of purified iron)

$$B = \mu H \quad \text{………..……[3.3-7]}$$

where B is the magnetic flux density (Tesla), H is the magnetic field intensity (Wb/Hm) and μ is the relative magnetic permeability (Henry/m)

In this research, five assumptions related to these three constitutive parameters were made, whilst the first four assumptions were directly adopted from Knoll (1996):

- 1ST ASSUMPTION: HOMOGENEITY

A material is assumed to be homogeneous if its constitutive parameters do not vary from point to point. At the microscopic scale, engineering/geological materials are always heterogeneous. However, this effect of heterogeneity has been effectively averaged during the measurement process over some finite volume (Knoll, 1996). Therefore, the measurement of the constitutive parameters of a heterogeneous material is said to be essentially representative to that of a homogeneous material.

- 2ND ASSUMPTION: ISOTROPIC MEDIUM

A material is said to be isotropic if its constitutive parameters are independent of direction. Therefore, these parameters become a scalar function such that J is parallel to E, D is parallel to E and B is parallel to H. Most materials possess this property, except some crystals (Ulaby, 2001). This assumption also enables the adoption of the square root as an exponent of the Complex Refractive Index Model (CRIM), as depicted in Fig. 2.5-6 and Eq. [2.5-21].

- 3RD ASSUMPTION: LINEARITY

A material is said to be linear if its constitutive parameters are independent of the magnitudes of the externally applied field/applied voltage. Voltages in GPR/SPR systems are within the ranges 10^{-6} to 10^{3} V, in which engineering/geological materials are assumed to exhibit linear behavior in this range. If the applied E-field/voltage exceeds the upper limit of a dielectric material (i.e. reaching the dielectric strength), the electrons are freed completely from the molecules and a conduction current is formed as a result. This phenomenon is known as 'dielectric breakdown' (Ulaby, 2001). For commercial systems, such as the two systems (Japan Radio Company (JRC) radar and Geophysical Survey System Instrument (GSSI) radar) adopted in this research, the maximum voltage is assumed to be within the acceptable range (i.e. 10^{-6} to 10^{3} V), even though its exact values are not known.

- 4TH ASSUMPTION: NO SIGNIFICANT MAGNETIC RESPONSE

Magnetic permeability of most engineering and geological material was reported to be negligible (Daniels, 2004; Knoll, 1996), except those possessing a large amount of iron, nickel, or cobalt (Strangway, 1972). In all studied materials in this research, the magnetic content was insignificant in general and the effect of magnetic permeability was therefore assumed to be negligible. Also referring to the assumption related to magnetic properties made by Knoll (1996) on his study, the magnetic permeability of a large range of soil is assumed to be real, frequency independent and equivalent to that of free space, i.e. $\mu_0 = 1.257 \times 10^{-6}$H/m. These few assumptions are also assumed to be valid in this research.

- 5TH ASSUMPTION: INSIGNIFICANT EFFECTS OF CONDUCTIVITY

The electric conduction behaviour is mainly determined at lower frequency regions and its effect on dielectric permittivity reduces rapidly towards regions at high frequency (Poley et al., 1978). More specifically, the effect of conductivity on the dielectric permittivity is small and commonly negligible if the conductivity is below 10^{-1} S/m and at frequencies after 1GHz (Daniels, 2004), or persists with diminishing dependence (Sen and Chew, 1983) at the GHz level. This characteristic is also presented graphically in Fig. 3.3-1.

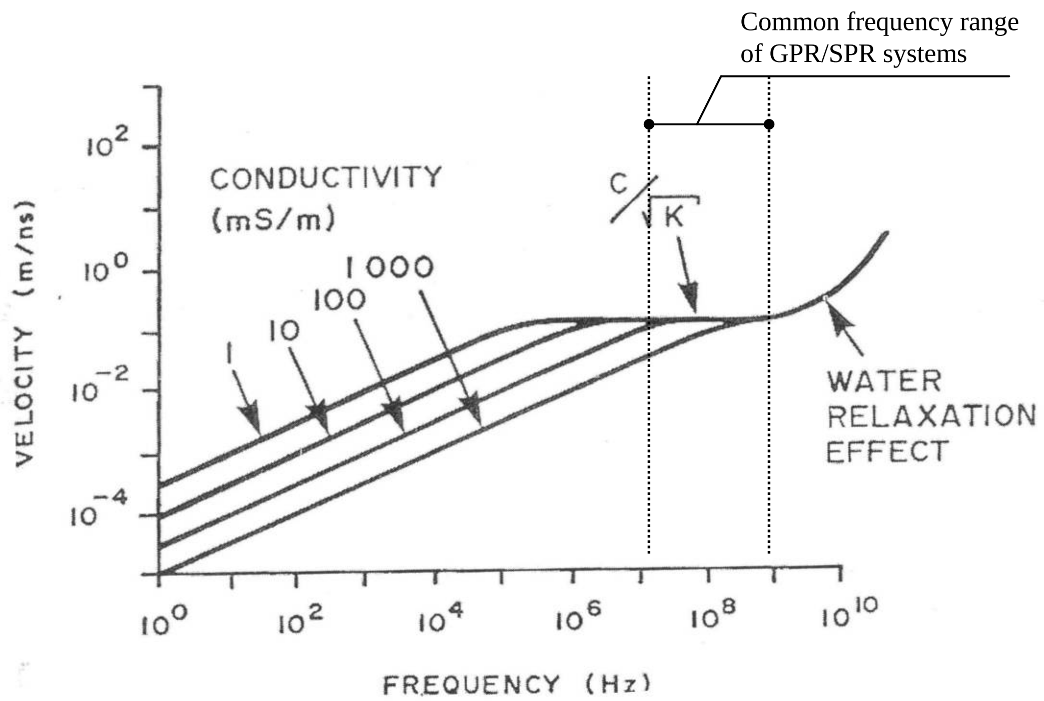

Fig. 3.3-1 Effects of Conductivity on EM Wave Velocity/Dielectric Constant over a Wide Range of Frequencies (Source: Davis and Annan, 1989)

According to Table 3.3-2, the maximum conductivities of most engineering/geological materials are below 10^{-3} mS/m. Hence according to Fig. 3.3-1, the effect of conductivities on velocity (and therefore dielectric permittivity) at the common GPR/SPR frequency range is insignificant.

3.3.3 POLARIZATION

The polarization of a dielectric material describes a phenomenon of how dipoles can be established. When an external E-field is applied, the charges of opposite polarity repel each other and are displaced relative to their position in equilibrium state. If there are n dipoles in a dielectric, the total polarization becomes the summation of the moments of these dipoles: $q_1d_1 + q_2d_2 + \ldots\ldots + q_nd_n$. Then the polarization vector is defined as the total dipole moment per unit volume of a dielectric.

$$P = \lim_{\Delta v \to 0} \frac{\sum_{i=1}^{n} q_i d_i}{\Delta v} \text{............[3.3-8]}$$

where d is the distance vector from –q to +q of each dipole per unit volume Δv.

More explicitly, the dipole moment is defined by the degree of separation of positive and negative charges in this dipolar molecular structure (Ulaby, 2001). It is a measure of the ability of polarization of a molecule to orient itself along the externally applied E-field (Hillel, 1998). Through this polarization process, electrical energy is stored and is measured by the relative permittivity/dielectric permittivity which is a ratio of the capacitance of a dielectric to that of free space/air (ASTM D6432-99).

3.3.3.1 MECHANISMS OF POLARIZATION

In a dielectric material, polarization can be characterized by four mechanisms, namely electronic, atomic, dipole/orientation and space charge polarization over a wide range of frequency (i.e. 10^3 to 10^{15} Hz), as depicted in Fig. 3.3-2 (Von Hippel,

1995) and Fig. 3.3-3 (Poley et al., 1978). The existence of these mechanisms was found to depend on

1. whether the material possesses a polar or non-polar molecular structure,
2. how many dipoles exist, and
3. how far these dipoles are separated from each other.

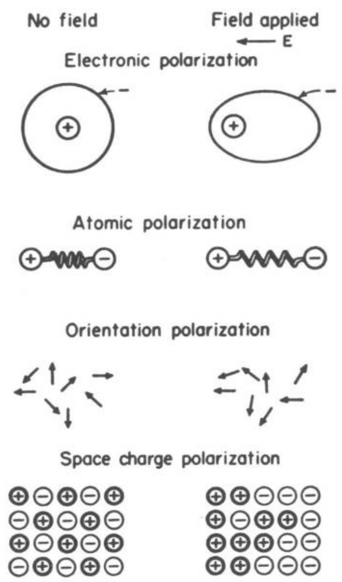

Fig. 3.3-2 Polarization Mechanism (Source: von Hippel, 1995)

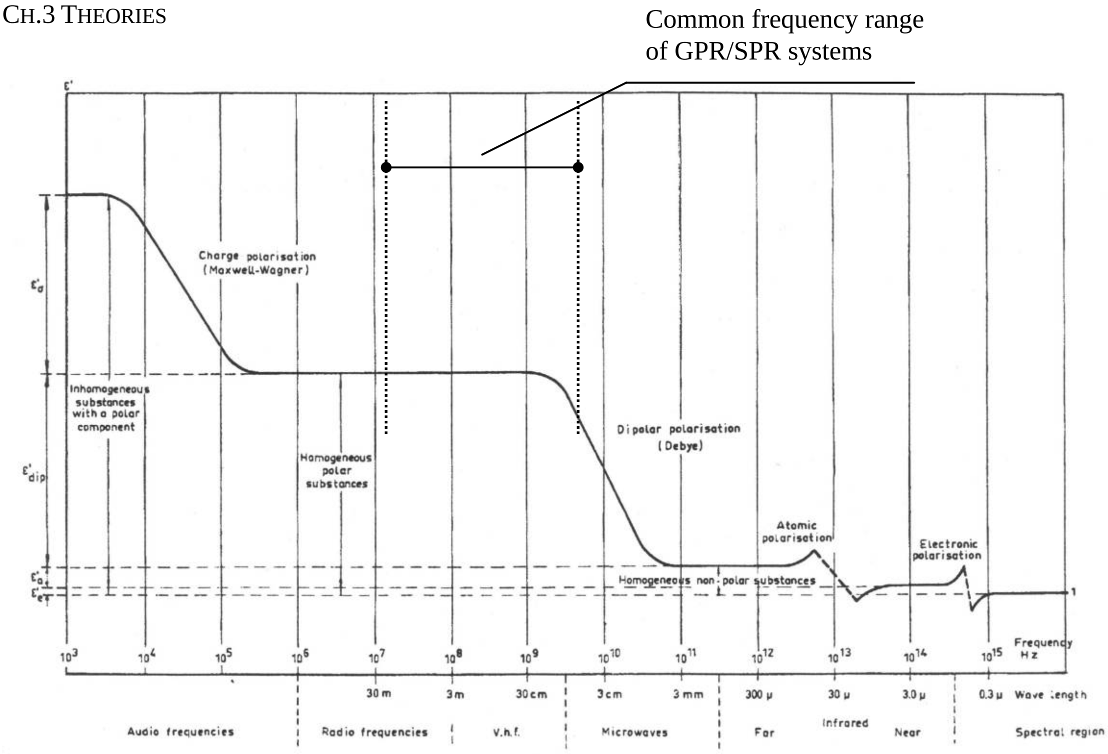

Fig. 3.3-3 Dielectric Dispersion of Various Types of Induced Polarization (Schematic)
(Source: Poley et al., 1978)

A. DIPOLE/ORIENTATION POLARIZATION IN POLAR MOLECULES

The mechanism of polarization in polar molecules is the dipole/orientation type. Water, which is made up of permanent dipolar structures and polar molecules, possesses permanent dipole moments due to the asymmetry of their electron distribution (Poley et al., 1978). Table 3.3-1 and Fig. 3.3-4 provide some basic information of water molecules and a diagrammatic model respectively. When no external E-field is applied, the molecules/dipoles orients randomly. When an external E-field is applied, the molecules/dipoles experience an additional dipole moment to align with the E-field, as depicted in Fig. 3.3-2.

Table 3.3-1 Basic Information of Water Molecules (summarized after Hillel, 1998)

Diameter		0.3nm
Chemical formula		H_2O
Type of bonding		Covalent bond
Dielectric Constant		81 at 100MHz
Number of Atoms	Hydrogen	2
	Oxygen	1 (with a negatively charged electron)
Molecular structure	Hydrogen	a positively charged proton and a negatively charged electron
	Oxygen	a nucleus having a positive charge of eight protons, surrounded by eight electrons, of which six are in the outer shell

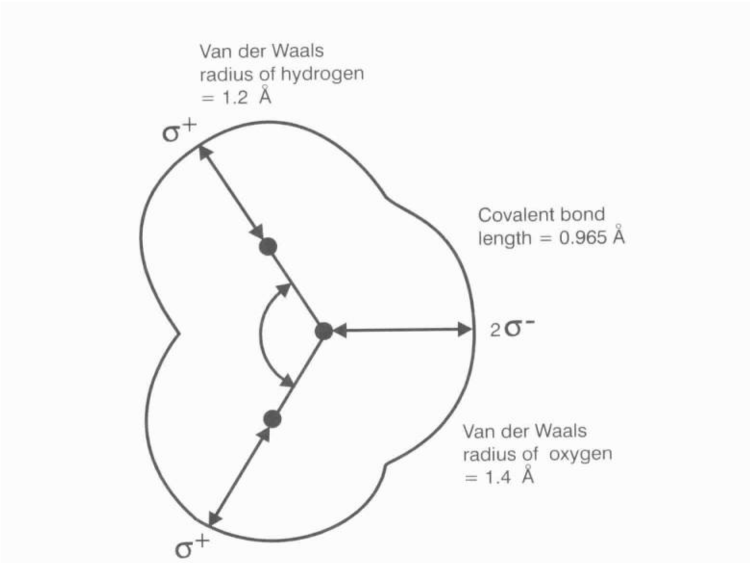

Remark: The curved lines represent the borders at which van der Waals attractions are counter-balanced by repulsive forces

Fig. 3.3-4 Model of a Water Molecule (Source: Hillel, 1998)

The Van der Waals forces within water are due to the existence of electrical asymmetry which is manifested by the deficiency of electron at the outer-shell of the oxygen atom. Therefore, the oxygen atom attracts the single electron of each of the two hydrogen atoms and is therefore positively charged.

B. ELECTRONIC, ATOMIC AND SPACE CHARGE POLARIZATION IN NON-POLAR MOLECULES

In non-polar molecules, the externally applied E-field creates the dipole in a variety of polarization mechanisms. These mechanisms include the electronic polarization (locally bound in atom), the atomic polarization (bound in molecules), and the space charge polarization (resulting in the Maxwell-Wagner effect, as resulted when charges are trapped in the material or on the interfaces). Unlike the dipolar/orientation polarization found in polar molecules, non-polar molecules contain no permanent dipole. Therefore the polarized charges return to their equilibrium position when the externally applied E-field is removed (Von Hippel, 1995).

Most engineering/geological materials possess non-polar molecules. With absence of water, their polarizations are of the electronic, the atomic and the space charge types. With the presence of water, the degrees of polarization shown in Eq. [3.3-8], or the range of the values of the relative permittivity/dielectric permittivity are essentially a function of water which possesses a permanent polar structure (i.e. dipole/orientation polarization), as shown in Table 3.3-2. It follows that water is the most dominant factor affecting dielectric behaviour of porous construction materials, as discussed in Section 2.2 to 2.4.

Table 3.3-2 Typical Ranges of Conductivities and Dielectric Constants at 100MHz (Daniels, 2004)

MATERIAL	RANGE OF CONDUCTIVITY (mS/m)	RANGE OF RELATIVE PERMITTIVITY/DIELECTRIC CONSTANT
Air	0	1
Fresh water	10^{-9} to 10^{-5}	81
Fresh water ice	10^{-7} to 10^{-6}	4
Sea water	10^{-1}	81
Sea water ice	10^{-5} to 10^{-4}	4-8
Dry sand	10^{-10} to 10^{-6}	2-6
Wet sand	10^{-6} to 10^{-5}	10-30
Dry sandy soil	10^{-7} to 10^{-5}	4-10
Wet sandy soil	10^{-5} to 10^{-4}	10-30
Dry loam soil	10^{-7} to 10^{-6}	4-10
Wet loam soil	10^{-5} to 10^{-4}	10-30
Dry clay	10^{-5} to 10^{-4}	4-10
Wet clay	10^{-6} to 10^{-3}	10-30
Dry sandstone	10^{-9} to 10^{-8}	2-5
Wet sandstone	10^{-7} to 10^{-5}	5-10
Dry concrete	10^{-6} to 10^{-5}	4-10
Wet concrete	10^{-5} to 10^{-4}	10-20
Dry asphalt	10^{-5} to 10^{-4}	2-4
Wet asphalt	10^{-6} to 10^{-4}	6-12
Permafrost	10^{-8} to 10^{-5}	4-8
Dry granite	10^{-11} to 10^{-9}	5
Wet granite	10^{-6} to 10^{-5}	7
Dry limestone	10^{-11} to 10^{-9}	7
Wet limestone	10^{-5} to 10^{-4}	8

The characteristic/nominal frequencies of wide band GPR/SPR systems normally range from 25MHz to 3GHz, whilst in this research study, the GPR operates at the characteristic/nominal frequencies 400MHz, 1GHz and 1.5GHz. This range overlaps the range of dipolar/orientation polarization which will be discussed in Section 3.3.3.2. It follows that other types of polarizations are out of consideration in most GPR/SPR studies, as well as in this research study.

3.3.3.2 DIELECTRIC DISPERSION AND RELAXATION IN DIPOLAR/ORIENTATION POLARIZATION

At very high frequencies of the applied alternating external E-field, the frictional and the inertial effects cause the polarization to lag behind the applied E-field (i.e. a phase difference), so that the response of the polarization becomes no longer instantaneous (Knoll, 1996), or in other words the in-phase components are small.

Hence the dipole orientation does not fully contribute to the total polarization (Poley et al., 1978). This phenomenon is known as a dielectric dispersion of the dipolar/orientation polarization (Von Hippel, 1995). At this moment, a dielectric dispersion of the dipolar/orientation polarization can be found approximately at a center frequency 'f' and the respective dielectric relaxation time τ_r, as governed by Eq. [3.3-9] (Poley et al., 1978; Shang and Umana, 1999).

$$2\pi f\tau_r = 1 \text{...........[3.3-9]}$$

The effect of the dipolar/orientation polarization can be best described by Debye's (1929) and Cole and Cole's (1941) models. The existence of dielectric dispersion and relaxation time in a dielectric material results in an in-phase and an out-of-phase component in the polarization vector P and is represented by the complex values of ε (i.e. ε = ε'(ω)-iε''(ω)). For a pure material that exhibits a single, well-defined polarization mechanism with a corresponding relaxation time τ_t (such as water), the effect of frequency dependence on dielectric permittivity can be modeled by the famous Debye (1929)'s model, as described in Section 2.5.3.

$$\varepsilon(\omega) = \varepsilon_\infty + \frac{\varepsilon_S - \varepsilon_\infty}{1 + i\omega\tau_r} \text{.......... [3.3-10]}$$

where

ω is the angular frequency,

ε_S and ε_∞ are the static and infinite dielectric constant of the mixture at $f \to 0$ and $f \to \infty$ respectively

$\varepsilon(\omega)$ comprises $\varepsilon'(\omega)$ and $\varepsilon''(\omega)$ which are the real and imaginary part of dielectric permittivity respectively,

τ_r is the Debye's relaxation time

For most other materials which do not exhibit well-defined polarization mechanisms, there may exist different polarization mechanisms and different regions of dielectric dispersion and a spectrum of relaxation time, as depicted in Fig. 3.3-3. In this case, the dielectric behaviour of a material can be modeled as follows (Cole and Cole, 1941):

$$\varepsilon'(\omega) = \varepsilon_{\infty} + \frac{(\varepsilon_S - \varepsilon_{\infty})}{1 + (i\omega\tau_r)^{1-c}} \;\textbf{........}\; [3.3\text{-}11]$$

where c is the Cole-Cole distribution parameter ($0<c<1$) which indicates the distribution of relaxation time.

Eq. [3.3-11] was widely adopted to model the effects of a wide range of applied EM frequencies on dielectric behaviour. However, the single-dispersion Cole-Cole model is adequate to describe the dielectric behaviour over a small range of frequency in most research work (Knoll, 1996), including the application of GPR/SPR which operates at frequency ranges of MHz and GHz depicted in Fig. 2.5-4 and Fig. 2.5-5 previously.

Ranges of dielectric relaxation frequency are given in Fig. 3.3-5 (De Loor, 1983). The relaxation frequency of free liquid water is the highest compared to other composite materials containing water in the microwave region (De Loor, 1983). Its value is reported to be 17.1GHz at 25^0C by Hasted (1973).

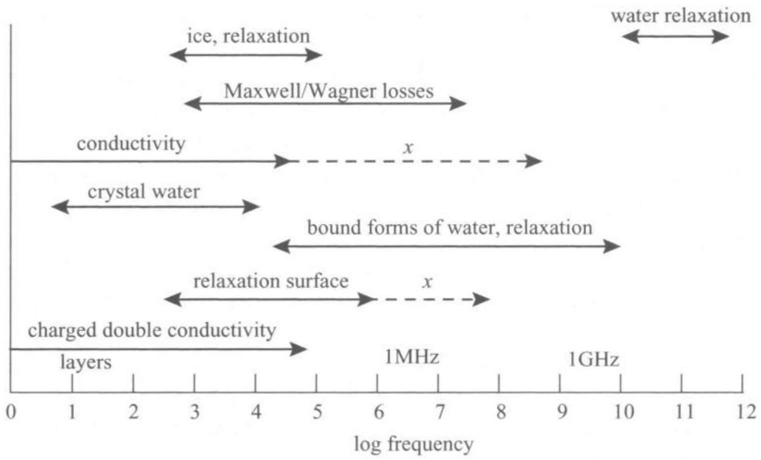

Fig. 3.3-5 Origin of Dielectric Loss in Heterogeneous Materials Containing Water (Source: De Loor, 1983)

Composite materials with a bound form of water (such as clayey soil) possess smaller values of relaxation frequency than that with a free state of water (such as sandy soil) (Wang and Schmugge, 1980; Huisman et al., 2003; West et al. 2003). The bound water is limited in motion by electrostatic interaction with clay particles, while the free water in the latter is not restricted by any neighbouring solid particles (Huisman et al., 2003), as discussed in Section 3.2.5.7. It follows that the dielectric dispersion and relaxation frequency of a material is determined by the forms of water (i.e. bounded or free) in a material.

3.3.4 PROPAGATION OF ELECTROMAGNETIC WAVES IN DIELECTRIC MATERIALS

Maxwell's equations are the fundamental rules governing the propagation of electromagnetic waves. The time-varying electric field E(t) produces a time-varying magnetic field H(t), and vice versa. This inter-dependent behaviour enables the propagation of EM waves in free space and in materials, as illustrated in Fig. 3.3-6.

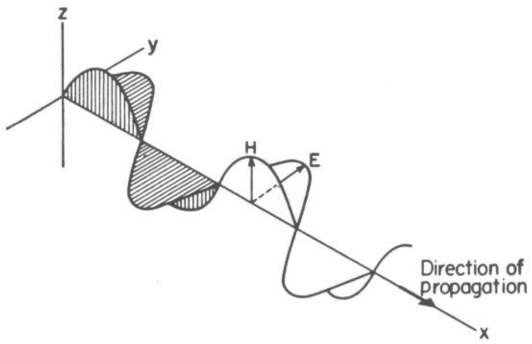

Fig. 3.3-6 Propagation of Orthogonal Electric (E) and Magnetic (H) Fields
(Source: Von Hippel, 1995)

3.3.4.1 LOSS-LESS MEDIUM

In free space the constitutive parameters described in Section 3.3.3, ε and μ are constant and are independent of frequency. In a perfect dielectric material (i.e. σ = 0), there is no attenuation during EM wave propagation, but this ideal condition does not exist in real dielectric materials.

The EM wave propagation can be represented by a one-dimensional wave equation [3.3-12].

$$\frac{\partial^2 E}{\partial z^2} = \mu\varepsilon \frac{\partial^2 E}{\partial t^2} \text{ .... [3.3-12]}$$

where the z-axis is the direction of EM wave propagation, in which the velocity of propagation is

$$v = \frac{1}{\sqrt{\mu\varepsilon}} \text{ where } \varepsilon = \varepsilon_r \varepsilon_0 \text{ .... [3.3-13]}$$

and the velocity at free space ‘c’ is

$$c = \frac{1}{\sqrt{\mu_0 \varepsilon_0}} \text{ where } \mu = \mu_r \mu_0 \text{ .... [3.3-14]}$$

where ε_0 is the dielectric permittivity of free space, 8.854 x 10^{-6} F/m and

μ_0 is the dielectric permittivity of free space, 1.26 x 10^{-6} H/m

By dividing Eq. [3.3-13] by Eq. [3.3-14] and assuming that the studied materials do not contain significant content influencing the magnetic field (such that $\mu = \mu_0$ as discussed in the 4th assumption in Section 3.3.3),

$$v = \frac{c}{\sqrt{\varepsilon_r}} \text{ …….. [3.3-15]}$$

From Eq. [3.3-15], The propagation velocity is governed by the relative dielectric permittivity/ dielectric constant.

3.3.4.2 LOSSY MEDIUM

The propagation of EM waves originating from z = 0, t = 0 in a conducting dielectric can be described by Eq. [3.3-16].

$$E(z) = E_0 e^{-\alpha z} e^{-j\beta z} \text{ …….. [3.3-16]}$$

The first exponential function is the attenuation term and the second is the propagation term. When the distance z is equal to 1/α in the attenuation term, the attenuation becomes 1/e. The distance z is termed 'skin depth' which is one of the factors to determine the depth of penetration reached by the EM wave.

In a real dielectric material, a wave number/propagation factor 'k' is a ratio of the angular frequency to the propagation velocity. It can be defined as the change in phase per unit length, which is considered as a constant of a material under a particular frequency.

$$k = \frac{\omega}{v} = \omega\sqrt{\mu\varepsilon} \text{ (rad/m) …….. [3.3-17]}$$

In a real dielectric material, k is complex and can be written as Eq. [3.3-18] and separated into real and imaginary parts as Eq. [3.3-19] (Daniels, 2004):

$$k = \omega\sqrt{\mu(\varepsilon' - j\varepsilon'')} \text{ where } j = \sqrt{-1} \text{ …….. [3.3-18]}$$

$$ik = \alpha + i\beta = j\omega\sqrt{\mu\varepsilon'(1 - j\frac{\varepsilon''}{\varepsilon'})} \text{ …….. [3.3-19]}$$

$$\text{where } \alpha = \omega\sqrt{[\frac{\mu\varepsilon'}{2}\sqrt{1+(\frac{\varepsilon''}{\varepsilon'})^2} - 1]},\ \beta = \omega\sqrt{[\frac{\mu\varepsilon'}{2}\sqrt{1+(\frac{\varepsilon''}{\varepsilon'})^2} + 1]}$$

α is known as the attenuation constant, β is known as the phase constant and the dimension-less ratio $\varepsilon''/\varepsilon'$ is known as the loss tangent. The parameters and their formulations in each of these materials are summarized in Table 3.3-3.

Table 3.3-3 Expressions for α, β, η_c and v for Various Types of Media (Source: Ulaby, 2001)

	ANY MEDIUM	**LOSS-LESS MEDIUM (σ = 0)**	**LOW-LOSS MEDIUM * (ε''/ε' << 1)**	**GOOD CONDUCTOR ** (ε''/ε' >>1)**	**UNITS**
α	$\omega\sqrt{[\frac{\mu\varepsilon'}{2}\sqrt{1+(\frac{\varepsilon''}{\varepsilon'})^2} - 1]}$	0	$\frac{\sigma}{2}\sqrt{\frac{\mu}{\varepsilon}}$	$\sqrt{\pi f\mu\sigma}$	(Np/m)
β	$\omega\sqrt{[\frac{\mu\varepsilon'}{2}\sqrt{1+(\frac{\varepsilon''}{\varepsilon'})^2} + 1]}$	$\omega\sqrt{\mu\varepsilon}$	$\omega\sqrt{\mu\varepsilon}$	$\sqrt{\pi f\mu\sigma}$	(rad/m)
η_c	$\sqrt{\frac{\mu}{\varepsilon'}}(1 - j\frac{\varepsilon''}{\varepsilon'})^{-1/2}$	$\sqrt{\frac{\mu}{\varepsilon}}$	$\sqrt{\frac{\mu}{\varepsilon}}$	$(1+j)\frac{\alpha}{\sigma}$	(Ω)
v	$\frac{\omega}{\beta}$	$\frac{1}{\sqrt{\mu\varepsilon}}$	$\frac{1}{\sqrt{\mu\varepsilon}}$	$\sqrt{\frac{4\pi f}{\mu\sigma}}$	(m/s)

Remarks:
* A medium is said to be low-loss when the loss tangent ε''/ε' = σ /ωε < 0.01
** A medium is said to be a good conductor when the loss tangent ε''/ε' > 100.
α is the attenuation constant (dB/m),
β is the phase constant (rad/m)
η_c is the intrinsic impedance (Ω)

By adopting the values of loss tangent (ε''/ε') to demarcate the loss-less, low-loss and conducting medium (i.e. the value of σ/ωε), most engineering/geological materials are found to belong to the category of low-loss materials, subject to an EM frequency ranging from MHz to GHz.

3.4 GROUND PENETRATING RADAR/SURFACE PENETRATING RADAR

3.4.1 ENERGY LOSS AND ATTENUATION

A successful Ground Penetrating Radar (GPR)/Surface Penetrating Radar (SPR) survey is essentially controlled by the material properties which permit the transmission of radar waves, the efficiency of the antenna and the antenna frequency. These three factors govern the energy loss and attenuation during the propagation of radar waves. The sources of the energy loss and attenuation are depicted schematically in Fig. 3.4-1 and are a function of a number of factors described as follows:

1. antenna loss,
2. transmission loss between the air and the ground,
3. geometrical spreading through the beam width/cone angle, which causes a reduction in energy per unit area at a rate 1/r2, where r is the propagation distance,
4. absorption which turns the electromagnetic energy into heat,
5. attenuation as a function of dielectric and electrical properties of the ground and the propagation frequency of the radar wave,
6. scattering of the radar signal from a target with dimension of the same order as the wavelength of radar signal, which induces ‘clutter’ noise in the radar signal, and,
7. reflection and transmission across boundaries with electrical contrast.

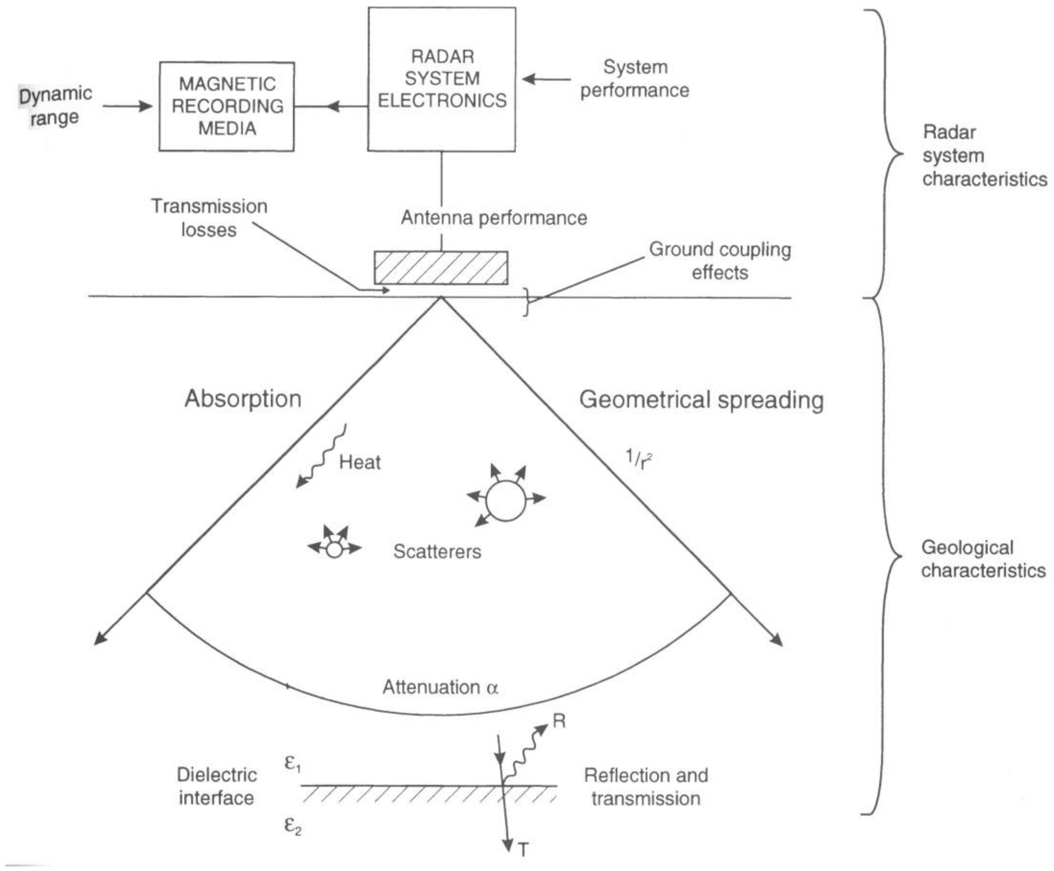

Fig. 3.4-1 Schematic Diagram of the Energy Loss and Attenuation of a GPR/SPR Survey
(Source: Reynolds, 1997)

The range of radar signal (in dB) was formulated as in Eq. [3.4-1] and depicted in Fig. 3.4-2, as a function of both attenuation of material and radar system performance (Q) (Davis and Annan 1989):

$$Q = \frac{E_{TX} E_{RX} G_{TX} G_{RX} (gF) \exp(-4\alpha z)}{64\pi^3 f^2 z^4} \qquad \text{…………Eq. [3.4-1]}$$

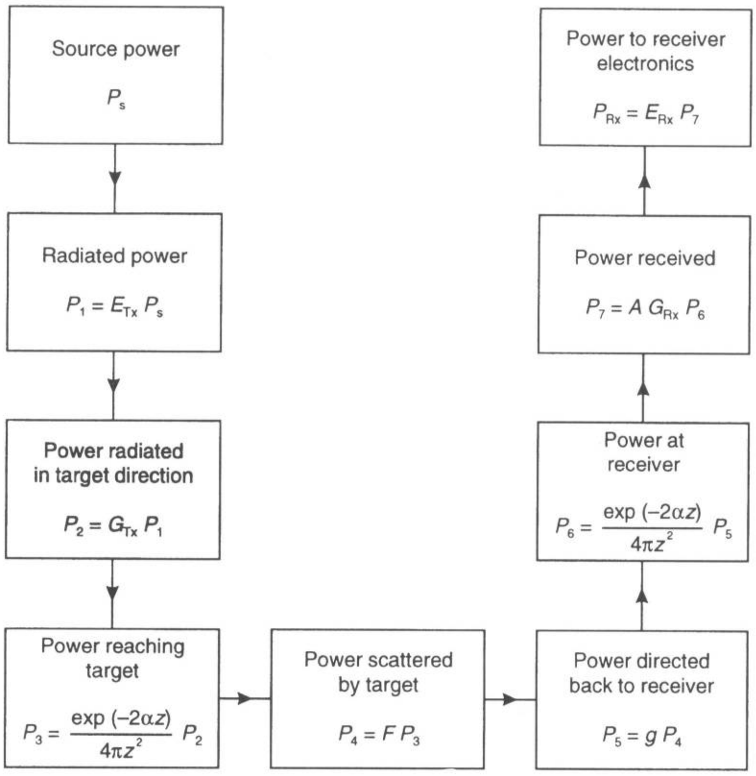

where

ETX, RX	Efficiency of transmitter/receiver antenna	α	Attenuation coefficient of medium
GTX, RX	Transmitter/receiver gain	V	Radio-wave velocity of medium
g	Backscatter gain of target	A	Effective area of receiver antenna
F	Target scattering cross-sectional area	f	Frequency
z	Distance of target from antenna	R	Power reflection coefficient at a boundary

Fig. 3.4-2 Block Diagram of the Radiated and Returned Power of a GPR System
(Source: Davis and Annan, 1989)

The last factor contributing to the energy loss and the attenuation is the reflection and transmission across boundaries with sufficient dielectric contrast. This factor can be described by the reflection coefficient determined according to Eq. [3.4-2].

$$RC = \frac{\sqrt{\varepsilon_{r1}} - \sqrt{\varepsilon_{r2}}}{\sqrt{\varepsilon_{r1}} + \sqrt{\varepsilon_{r2}}} \text{ .... Eq. [3.4-2]}$$

where ε_{r1} and ε_{r2} are the dielectric constants of the first and the second underlying material and RC is the reflection coefficient of the interface separating two materials with different magnitude of dielectric contrast.

The value of RC is negative when $\varepsilon_{r2} > \varepsilon_{r1}$, and vice versa. Its effect on the GPR/SPR reflected waveform is the phase difference of a particular reflected wavelet. The contrast of the dielectric constants of the objects/interfaces compared to those of the host material cause different phase patterns and polarities (+/- amplitude) possessed in a wavelet. Also, a larger value of RC represents a larger dielectric contrast separating the material interface, and hence a stronger magnitude of the reflection signal.

3.4.2 DEPTH RESOLUTION

Depth resolution refers to the ability for two adjacent signals (i.e. from interface/point targets) contained in a reflected waveform to be differentiated and resolved. The depth resolution is affected by two factors: nominal/characteristic frequency of a GPR signal and the dielectric constant of a material. For the former, an increase of the nominal/characteristic frequency reduces the wavelength and the depth penetration, increases the depth resolution according to a rule of thumb: depth resolution is one-quarter of the nominal/characteristic wavelength (Yilmaz and Doherty, 1987; Reynolds, 1997; ASTM D6432-99). For the second factor (i.e. dielectric constant), Fig. 3.4-3 illustrates that the larger the dielectric constant of a material, the better the depth resolution is, based on the afore-mentioned rule of thumb.

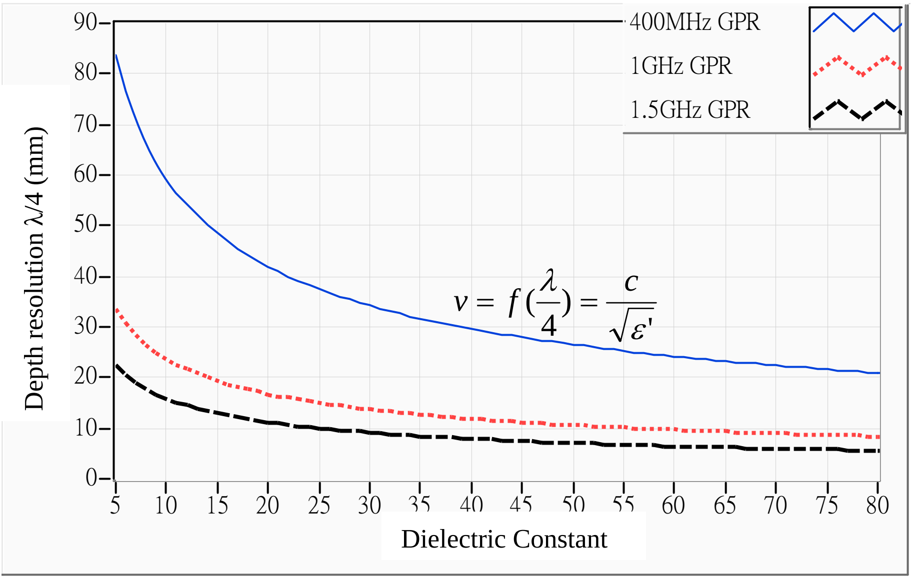

Fig. 3.4-3 Vertical Resolution at Different GPR Frequencies and Different Dielectric Constants

An example of the calculation of the relationships among velocity, frequency, wavelength and the depth resolution is reported in Table 3.4-1 (also see a similar table made by Jol, 1995). This table is extracted from Table 7-3 which abstracts some of the data obtained in the soil texture experiments described in Chapter 7. Table 3.4-1 summarizes the velocities of EM wave propagation and the returned peak frequencies of GPR waveforms captured using three antenna frequencies (i.e. 400MHz, 1 GHz and 1.5 GHz) adopted in the experiments described in Chapter 7.

Table 3.4-1 Depth Resolutions (calculated according to one-forth of nominal wavelength) obtained in the Dry and Saturated States of Asphalt Specimen

Nominal/centre frequencies of the GPR antennae		**400MHz**	**1GHz**	**1.5GHz**
Dry state	Propagation velocity of GPR wave (v)	0.129 m/ns	0.134 m/ns	0.143 m/ns
	Returned nominal/characteristic peak frequency (determined from the frequency spectrum)	323 MHz	645 MHz	1.39 GHz
	Nominal/characteristic wavelength λ (=v/f)	400mm	208mm	103mm
	Depth resolution (one quarter of λ)	**100mm**	**52mm**	**26mm**
Saturated state	Propagation velocity of GPR wave (v)	0.0916 m/ns	0.117 m/ns	0.121 m/ns
	Returned nominal/characteristic peak frequency (determined from the frequency spectrum)	292MHz	567MHz	1.30 GHz
	Nominal/characteristic wavelength λ (=v/f)	313mm	206mm	92mm
	Depth resolution (one quarter of λ)	**78mm**	**52mm**	**23mm**

Remark: This table is the same as Table 7-3

A word of caution must be noted that the depth resolution determined based on the rule of thumb is an ideal case that could be obtained theoretically. It is a good reference but is only indicative to the actual condition because of the complex nature of the source waveform and the complicated ground response (Reynolds, 1997).

3.4.3 HORIZONTAL RESOLUTION

The signal transmitted by radar appears as a cone of radiation with a finite-sized footprint, as depicted in Fig. 3.4-4. This cone is known as the First Fresnel Zone (FFZ) which describes the area of the footprint illuminated by the radar antenna. This zone was defined in a way that objects/interfaces with dimensions smaller than this footprint cannot be imaged. The radius described by FFZ is determined by Eq. [3.4-3] as illustrated in Fig. 3.4-5 (Reynolds, 1997):

$$r = \sqrt{\left(\frac{\lambda^2}{16} + \frac{\lambda z}{2}\right)} = \sqrt{\left(\frac{v^2}{16 f^2} + \frac{vz}{2f}\right)} \quad \text{...........} \ [3.4\text{-}3]$$

where r is the First Fresnel Zone footprint, λ is the wavelength which depends on dielectric properties, z is the depth of penetration, f is the frequency, and v is the propagation velocity.

From Eq. [3.4-3], the radius of FFZ increases with a larger propagation velocity, a longer distance from the target to the antenna, but with smaller antenna frequencies. The latter two relations are depicted in Fig. 3.4-5 according to Eq. [3.4-3].

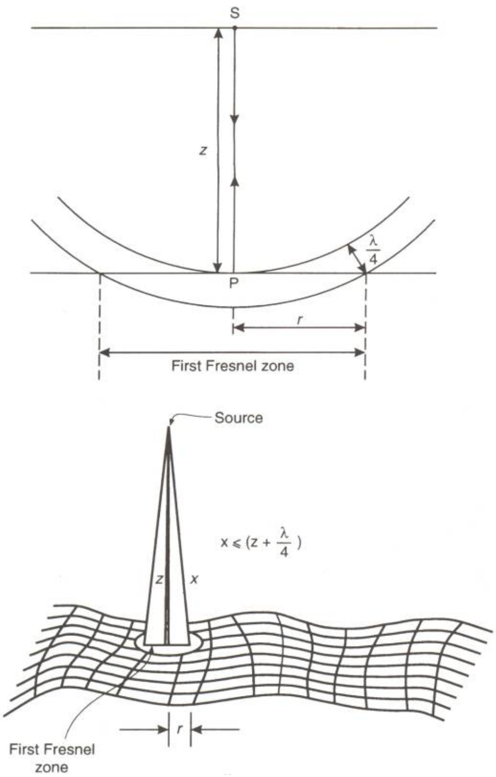

Fig. 3.4-4 Reflection from a Rough Interface; the Target Cross-section Area is Equivalent to the Area of the First Fresnel Zone (Source: Reynolds, 1997)

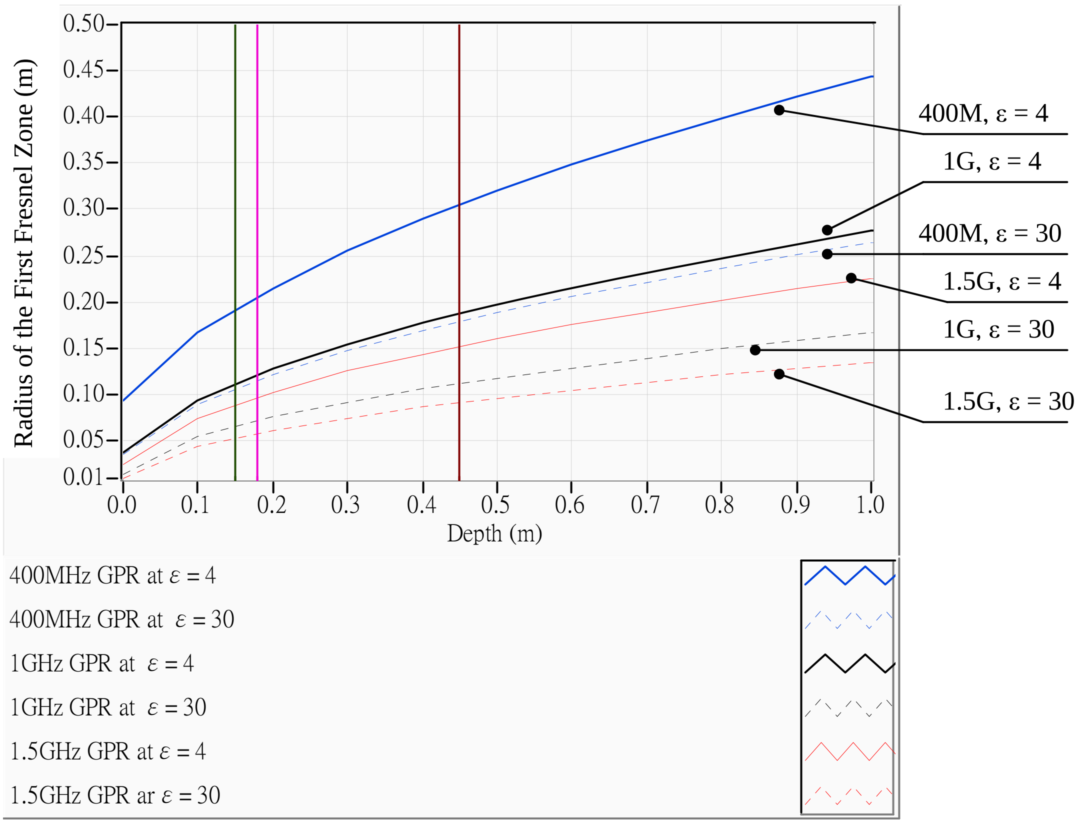

Remarks: The vertical lines 'Thickness of concrete', 'Thickness of soil textures A to I', 'Thickness of asphalt' refer to the sample thickness described in Chapter 6,.8 and.7 respectively.

Fig. 3.4-5 Radius of First Fresnel Zone (FFZ) at Different GPR Frequencies and Different Dielectric Constants

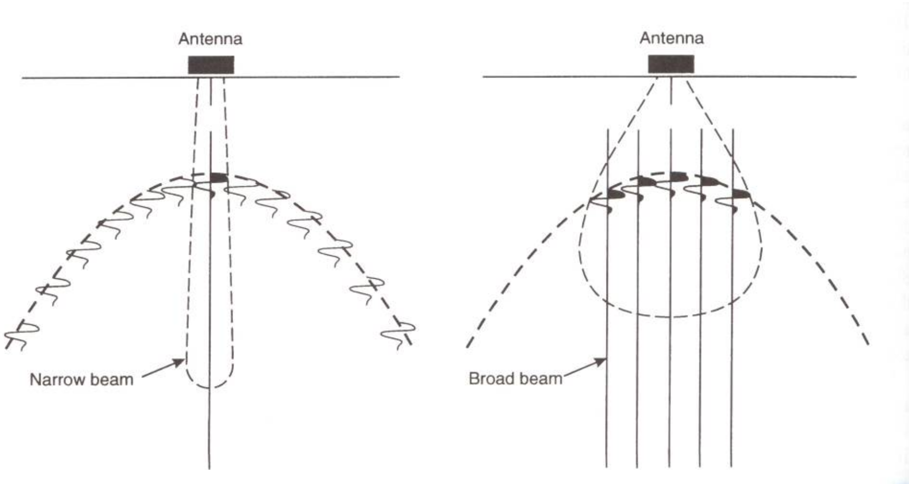

Fig. 3.4-6 Horizontal Resolution due to Beam Width (Source: Reynolds, 1997)

A larger radius in FFZ (to the right of Fig. 3.4-6) causes a smaller horizontal resolution (i.e. the adjacent objects are much more difficult to be resolved) than a smaller radius in FFZ (to the left of Fig. 3.4-6). In addition, a material with a larger dielectric constant also decreases the radius in FFZ and hence improves the horizontal resolution, as shown in Fig. 3.4-5.

3.5 SUMMARY AND DISCUSSION

This chapter examines and reviews several fundamental and theoretical issues from the perspectives of porous materials (Section 3.2), electromagnetics (Section 3.3) and ground penetrating radar (GPR)/surface penetrating radar (SPR) (Section 3.4), which underpin the methodology adopted in this research. In particular, Section 3.2 reviews some fundamental properties of porous concrete, asphalt and soil. Section 3.3 reviews the electromagnetics section describes a range of EM behaviour (polarization, dielectric dispersion, and so on.) exhibited in lossy material. Section 3.4 reviews a number of working principles of GPR/SPR.

The theories given in this chapter are extensions of the literature studies reviewed in Chapter 2, as to provide more in-depth coverage of the technical issues.

They form the most central and essential elements to the understanding of porous construction materials and pave the way for the subsequent chapters which detail the series of experiments.

In the following two chapters, the instrumentation of the radar systems and the data processing techniques used in this research will be discussed.

4. INSTRUMENTATION

4.1 INTRODUCTION

This chapter introduces the technical and operational basis of two radar instrumentation systems and their characteristics/performance in time- and frequency-domains. The most essential components of these instrumentation systems include two commercially available Ground Penetrating Radar (GPR)/Surface Penetrating Radar (SPR):

(1) A JEJ-60BF (manufactured by Japan Radio Company Limited) radar system equipped with a 1GHz mono-static antenna (abbreviated as JRC radar), and

(2) A GSSI (manufactured by Geophysical Survey System Inc.) SIR-20 GPR system equipped with a 400MHz and a 1.5GHz mono-static antenna (abbreviated as GSSI radar).

For the JRC Radar system, data captured by this system is presented in the form of superimposed wavelets and is represented in the form of ray-traces which are commonly known as ‘wiggle waveform’ or simply ‘waveform’. These waveforms are produced by three essential and connected components in the instrumentation system: (1) the JRC radar system (2) the ‘National Instrument’ (NI) hardware including data acquisition card and connection board and, (3) an in-house developed program established in the ‘Laboratory Virtual Instrument Engineering Workbench’ (LabVIEW) programming environment.

For the GSSI radar system, data acquisition and control are built as a ‘black box’ which can only be run and controlled by the proprietary GSSI hardware and software.

Tampering the source code of the proprietary software and hardware interface is not allowed.

A schematic diagram describing the instrumentation systems is illustrated in Fig. 4-1. After acquiring the raw data/waveforms, the acquired data from these two instrumentation systems was then processed and transferred to another LabVIEW computer program for subsequent data analysis in both time- and frequency- domains, which will be described in Chapter 5.

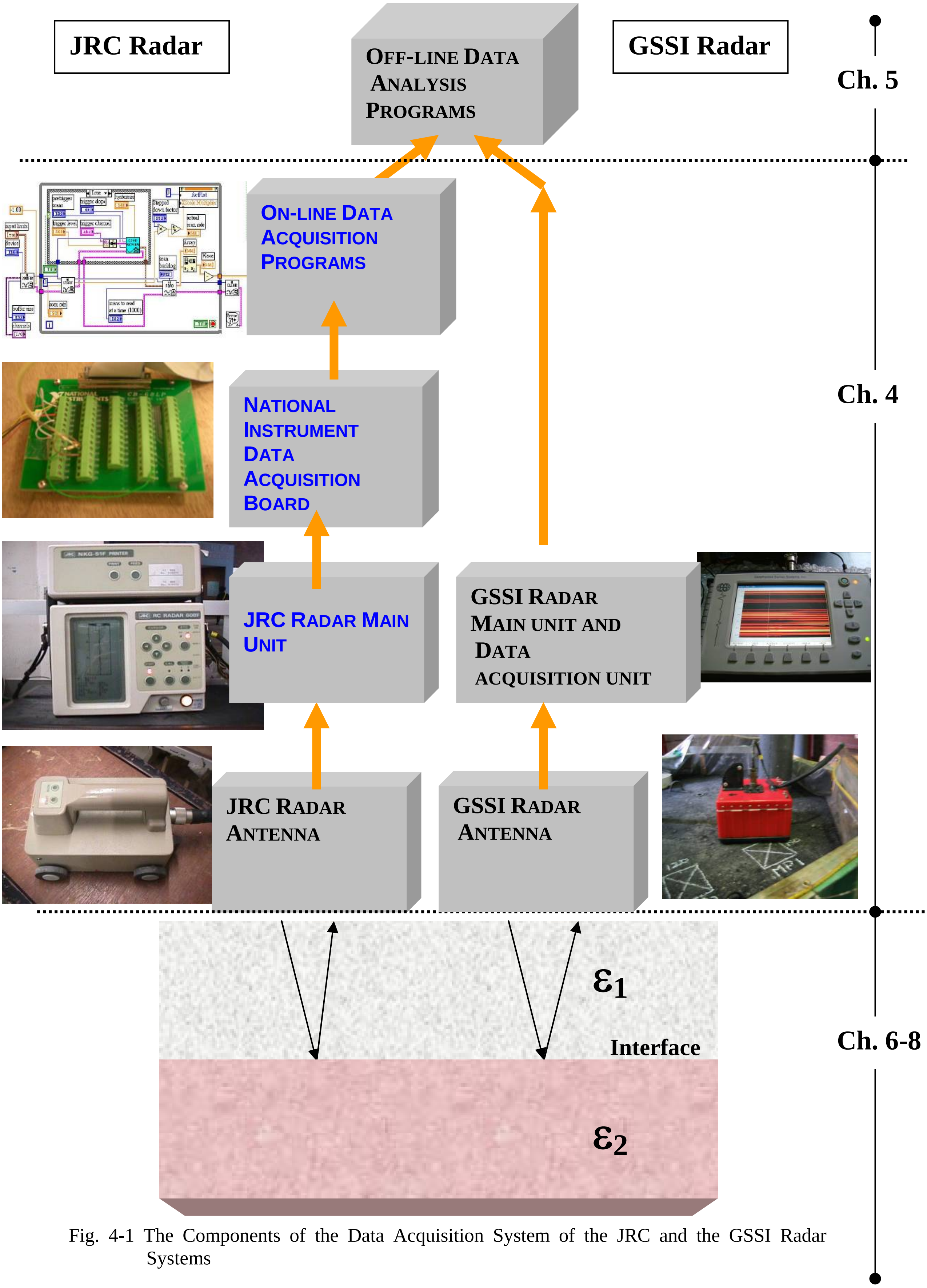

Fig. 4-1 The Components of the Data Acquisition System of the JRC and the GSSI Radar Systems

4.2 DIGITAL DATA ACQUISITION SYSTEM BASED ON THE JRC 1GHZ RADAR

4.2.1 SAMPLING OF SIGNALS

The rate of sampling determines how frequent an Analog-to-Digital (A/D) signal conversion takes place. A fast sampling rate acquires more data in a fixed period and performs better representation of the original signal than a slow sampling rate does. Under-sampling of a signal (known as 'alias') distorts the original signal and appears as if it would contain other frequency contents, as illustrated in Fig. 4-2. The classic Nyquist theorem (Baher, 2001) states that the sampling rate must be at least twice that of the highest frequency component of the signal. This theorem is followed for all tasks involving signal sampling in this research.

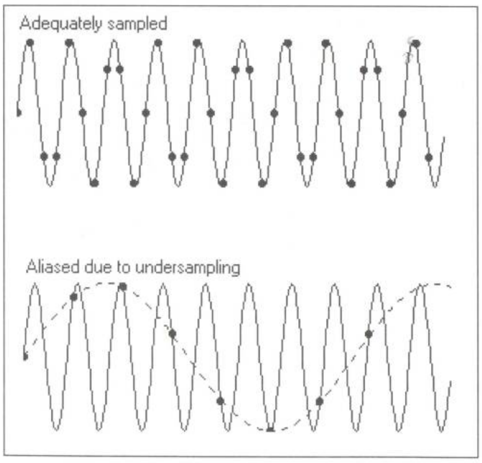

Fig.4-2 Aliasing Effects of an Improper Sampling Rate

Alias of signals can be prevented by adopting an appropriate sampling rate for the radar system. For the JRC radar system, the output terminal provides waveforms not in the original time base in nano-seconds, but in a re-scaled milli-second time base. It will be shown in Section 4.2.4.1 that a scaling factor was determined in this research to obtain the true nano-second time base, through performing an experiment with the known real permittivity of air.

4.2.2 INPUT/OUTPUT CONNECTIONS OF THE HARDWARE INTERFACE

The signal outputs of the JRC radar system are analogue. They are connected to the NI data acquisition device NI6013 DAQ board with sixteen on-board input channels. Each output acquired from the radar system is based on a positive and a negative input channel of the DAQ board. For each of these input channels, the positive one connects to the input channel of the board, and the negative one connects to a common ground on the board. Table 4-1 reports the functions and operational characteristics of each of these input channels used in the JRC radar system.

Table 4-1 Channel Register of the Analog Signal Outputs of the JRC Radar System

JRC radar channel	**Designated NI DAQ board connection channel**	**Analog input**	**Sampling rate (Samples per second)**	**Voltage range (V)**	**Functions**
Start pulse (Channel 0)	pin 68 (ACH<0>) to pin 34 (ACH<8>)	Constant trigger	125,000	0 or +1V	When the start pulse is triggered to +1V (0V is the initial stage), channel 1is controlled to record the transmitted and reflected waveforms
Waveform (Channel 1)	pin 66 (ACH<9>) to pin 33 (ACH<1>)	JRC radar waveforms	125,000	+5V to -5V	Reflected pulse captured by the antenna and output as waveforms in the form of voltage versus time

* Channels 31, 33 and 34 are connected to a common ground (GND)
** ACH stands for Analog Channel

4.2.3 DATA ACQUISITION PROGRAMS

While NI hardware serves as an analogue-to-digital (A/D) interface to channelize the digitized radar signals to the computer, an in-house computer program was developed to process these signals. This program was designed to enable continuous capturing of the radar waveforms in a designated period of time, which was essential and central to the experiments described from Chapter 6 to Chapter 8. Five essential stages/communication protocols (i.e. Virtual Instrument (VI) pre-set in the LabVIEW program) work in sequential order in this program as shown in Table 4-2. The front panel and the block diagram of this program are illustrated in Appendix F.

Table 4-2 Five Essential Data Acquisition Virtual Instruments (VI)

Five stages / communication protocol ofs data acquisition	**Functions**
Analog (AI) Config	Configures an analog input operation for a specified set of channels. This VI configures the hardware and allocates a buffer for a buffered analog input operation.
Conditional Retrieval	Retrieves data in a fixed window for Analog (AI) Read under prescribed controls specifying trigger channel, trigger level, trigger slope, pre-trigger scan and hysteresis
Analog (AI) Read	Reads data from a buffered data acquisition.
Analog (AI)Start	Starts a buffered analog input operation. This VI sets the scan rate, the number of scans to acquire, and the trigger conditions. The VI then starts an acquisition.
Analog (AI) Clear	Stops an acquisition and releases associated internal resources, including buffers.

The five stages/communication protocols of data acquisition are described as follows and summarized in Appendix C:

1. In stage 1 ‘Analog Input (AI) Configuration’, the program initiates the communication with the hardware (DAQ board) through setting input limits, channel string, buffer size and so forth.,
2. In stage 2 ‘Conditional Retrieval’, the program determines the timing to trigger the waveform according to a number of pre-determined parameters, such as trigger channel, trigger slope, trigger level, and so on,
3. In stage 3 ‘AI Start’, the program defines the sampling rate being adopted in each input channel. This sampling rate is designed according to Table 4-1,
4. In stage 4 ‘AI Read/Write’, the program acquires or generates the data and performs signal input or output, and
5. In stage 5 ‘AI Clear’, the program terminates the communication with the hardware by releasing all parameter settings. (Beyon, 2001)

4.2.4 TIME DOMAIN DATA CONVERSION

4.2.4.1 DETERMINATION OF APPROPRIATE RE-SCALING FACTOR OF THE TIME BASE

Since the original time base acquired from the output interface of JRC radar is in the order of milli-seconds and not in the original nano-seconds, as stated in Section

4.2.1, an accurate 're-scaling factor' for the waveforms must be established to obtain an accurate two-way-transit-time (TTT) of reflections in the time-domain. This was achieved by calibrating a media (i.e. air) with a known value of real permittivity (i.e. unity).

A metal plate was placed at specified distances from the antenna, as shown in Fig. 4-3. By varying the specified distances from the antenna to the metal plate, the corresponding reflections from the metal plate were obtained as depicted in Fig. 4-4 in the form of a radargram and stacked wiggle ray-traces. A particular and typical waveform captured at a particular separation distance is depicted in Fig. 4-5. The calculation of the re-scaling factor is shown in Appendix D and the estimated error of real permittivity due to this re-scaling factor is reported in Appendix K2. The determined and empirical re-scaling factor is $515{,}697 \pm 1000$ (i.e. the true nano-second TTT in a waveform is equal to the multiplication of the re-scaling factor and the detected TTT in the scale of milli-seconds).

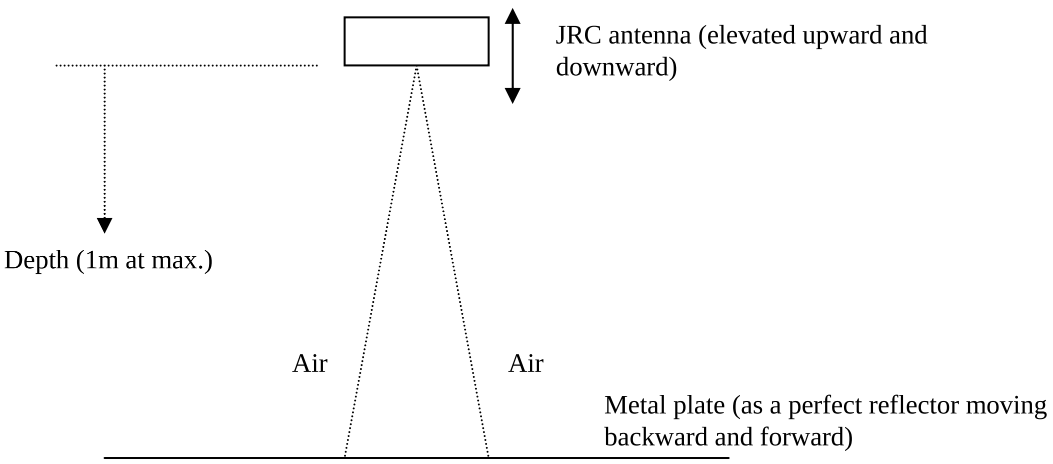

Fig. 4-3 Experimental setup to calibrate the Re-scaling Factor built in the JRC Radar System

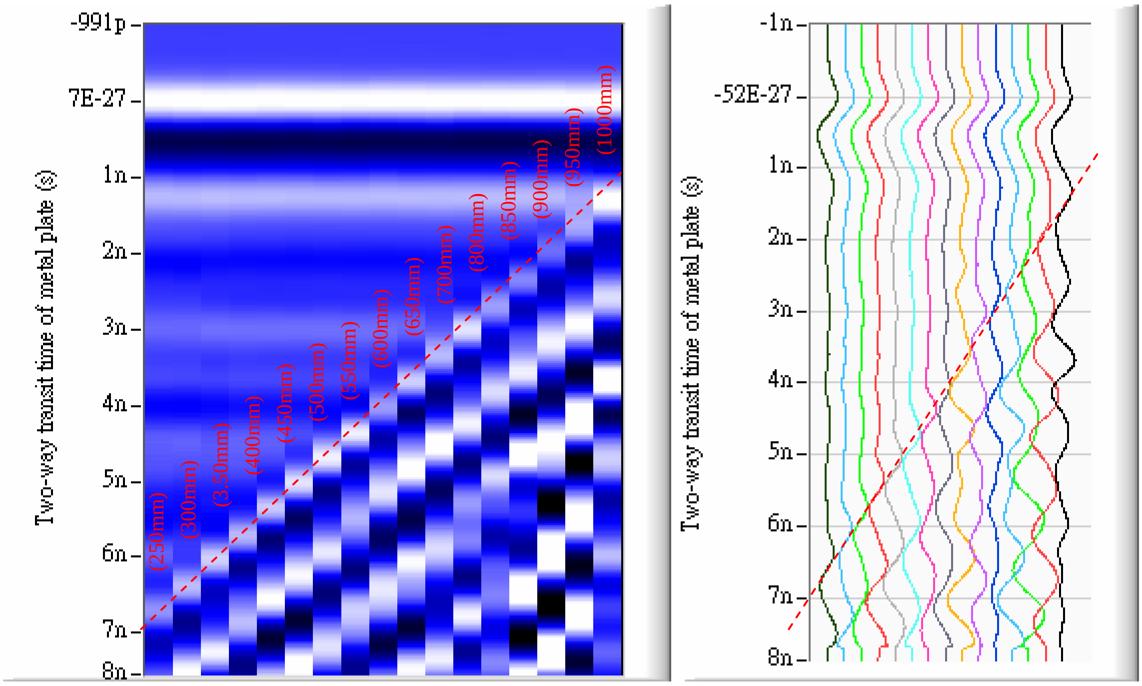

Remark: the distance enclosed by brackets inside this figure is the distance separating the antenna to the metal plate. The latter is represented by the dotted red line

Fig. 4-4 Radargram (left) and Stacked Waveforms (right) of Metal Plate Reflections Recorded from Variable Distances to the JRC Radar Antenna

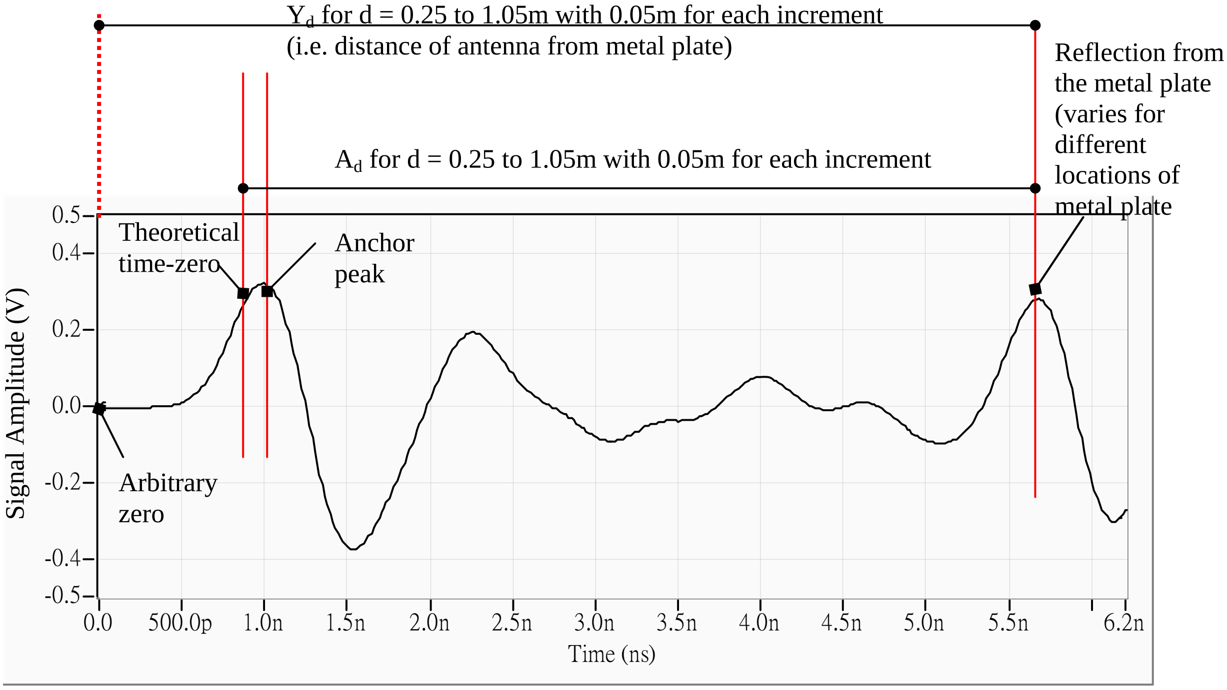

Remark: Detail calculation is reported in Appendix D.

Fig. 4-5 One of the Waveforms obtained from the Experiment Calibrating the Re-scaling Factor in a Typical Waveform acquired in the JRC Radar System

This adapted re-scaling factor was applied on all time-domain and frequency-domain data analysis from Chapter 6 to Chapter 8, so that the measured milli-second time base can be converted to the original nano-second time base.

4.2.4.2 LOCATION AND STANDARDIZATION OF THE THEORETICAL TIME-ZERO AT THE RADAR WAVEFORMS

The position of the so-called ‘theoretical time-zero’ located in a waveform represents the common start–time of the pulse. The common theoretical time-zero must be determined in a GPR waveform to provide consistent timing and depth ranging of embedded objects/interfaces. For practical purposes, the theoretical time-zero was commonly assumed to be either the so-called anchor peak or the anchor valley in a waveform by many GPR systems and GPR users.

The method and data obtained in the experiment of determination of theoretical time-zero were the same as those in Section 4.2.4.1 (i.e. determination of the re-scaling factor). The position of the theoretical time-zero in a reflected waveform was back-calculated from the known propagation velocity of EM waves in free space (i.e. approximately 3 x 10^8 m/s) and the designated distances separating the metal plate and the antenna as shown in the experimental setup depicted in Fig. 4-3. The steps of calculation are shown in Appendix E1.

In the table of Appendix E1, the negative sign in the column "Time difference" indicates that the theoretical time-zero is at the right of the anchor peak of the waveform, and vice versa. The magnitude of these differences is 15ps which was taken into account in all experiments described from Chapter 6 to Chapter 8.

4.2.5 VERIFICATION AND DETERMINATION OF THE CHARACTERISTIC/NOMINAL ANTENNA FREQUENCY IN AIR

The characteristic/nominal antenna frequency was calibrated by capturing a time-domain waveform through exposing the radar antenna to air, without any neighbouring reflectors. This waveform (as illustrated in Fig. 4-6) was then transformed to a frequency spectrum, as shown in Fig. 4-7, after adopting five signal processing techniques which will be described in Table 5-1.

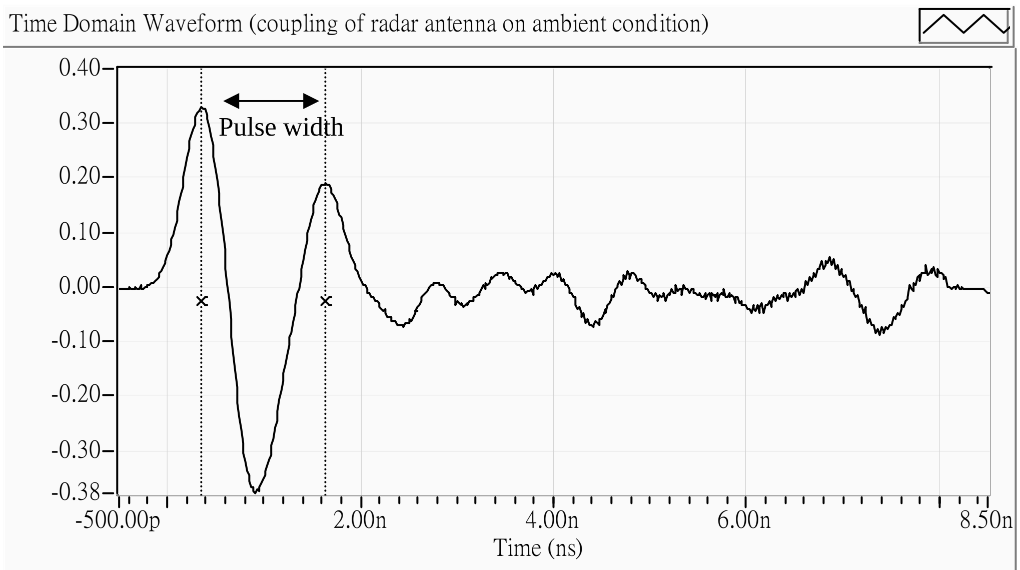

Fig.4-6 Time-domain Waveform (obtained during Coupling of the JRC 1GHz Antenna to Ambient Environment)

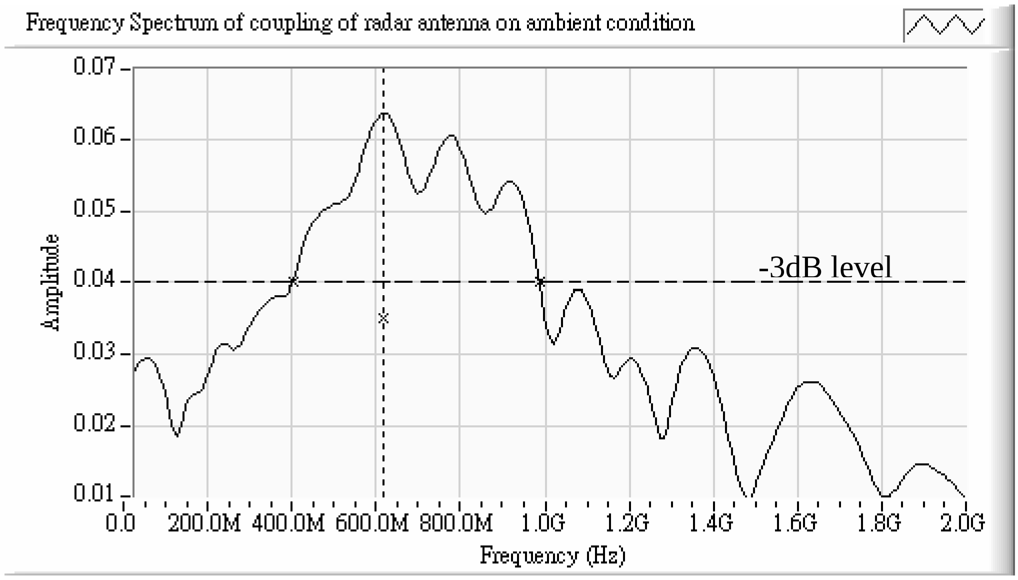

Fig.4-7 Frequency Spectrum (obtained during coupling of the JRC 1GHz Antenna to Ambient Environment)

The characteristic/nominal frequency was found to be approximately 650MHz which is 350MHz lower than the nominal peak frequency suggested by the manufacturer. This characteristic/nominal frequency can also be estimated by using the reciprocal value of pulse width in the time-domain waveform (i.e. the time interval from the anchor peak to the second peak). The pulse width determined by this method is 1.3ns, accompanied with a nominal frequency 775MHz. Furthermore, the frequency bandwidth at -3dB was used to describe the spread of the frequency content distributes (ASTM D6432-99; Millard et al, 2001). This value was determined by reducing the maximum spectrum power by 3dB (i.e. 70.79% of the maximum amplitude in the spectrum).

4.3 DIGITAL DATA ACQUISITION SYSTEM BASED ON THE GSSI 400MHZ AND 1.5GHZ RADAR

4.3.1 SAMPLING OF SIGNALS

The sampling rate for the GSSI radar system is dependent on the pre-determined number of sample points in a waveform and the designated time windows. For a waveform comprising 512 nos. sample points and a designated time window of 30ns (for 400MHz radar) and 15ns (for 1.5GHz radar), the sampling rates becomes

Sampling rate for 400MHz radar system= 512/30ns=17.1G samples per second……. [4-2]

Sampling rate for 1.5GHz radar system=512/15ns=34.1G samples per second……… [4-3]

The sampling rates (i.e. 17.1G and 34.1G) of the GSSI GPRs are many times faster than the nominal frequency (i.e. 400MHz and 1.5GHz) of the antenna systems and are therefore considered to be appropriate and adequate to sample the signal acquired by the radar. These sampling rates will be used as a typical setting in the experiments described in Chapter 7 (Remark: not in Chapter 6 and Chapter 8 since GSSI radar systems were not used in the experiments in these two chapters).

4.3.2 TIME DOMAIN DATA CONVERSION

4.3.2.1 LOCATION AND STANDARDIZATION OF THE THEORETICAL TIME-ZERO AT THE RADAR WAVEFORMS THROUGH KNOWN REAL PERMITTIVITY OF AIR

The importance of the determination of theoretical time-zero has been discussed in Section 4.2.4.2. To determine the theoretical time-zero of the GSSI radar system as that in the JRC system, the experiment described in Section 4.2.4.1 was repeated and the JRC radar was replaced by the GSSI radar. In this experiment, the distance between the antenna and metal plate was varied. These values of distance, as well as the respective two way transit times (TTT) determined in the waveforms and the known real permittivity value of air (i.e. unity), were used to determine the location of the theoretical time-zero. The radargrams and the stacked ray-traces of the 400MHz and 1.5GHz antennae are depicted in Fig. 4-8 and Fig. 4-9.

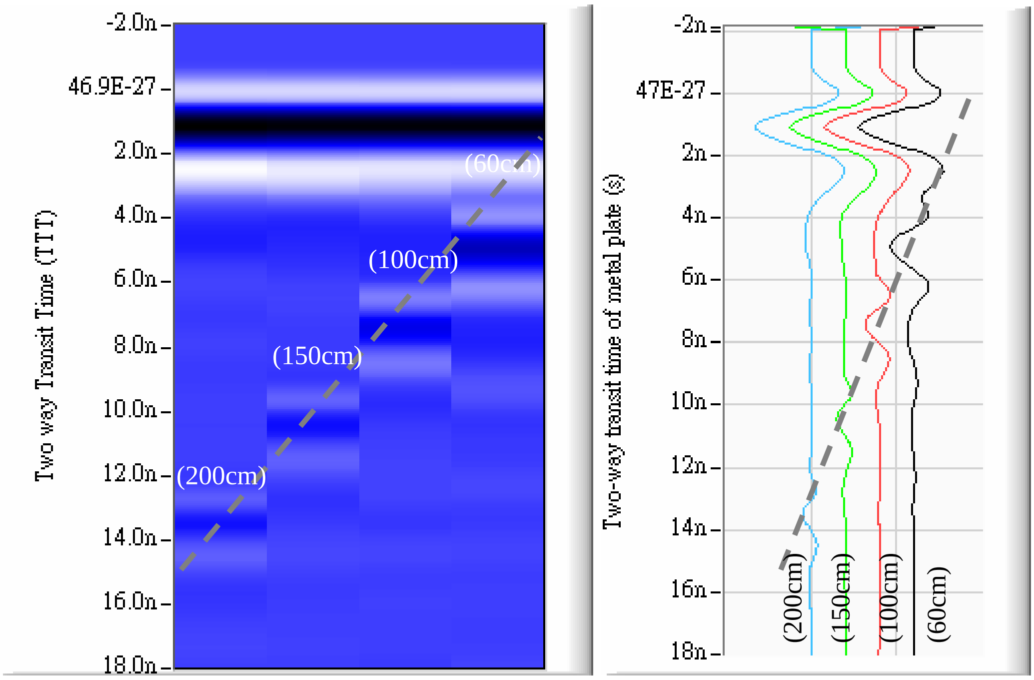

Remark: the distance enclosed by brackets inside this figure is the distance separating the antenna to the metal plate. The latter is represented by the dotted grey line

Fig.4-8 Radargram (left) and Stacked Waveforms (right) of Metal Plate Reflections Recorded from Variable Distances to the 400MHz GSSI Radar Antenna

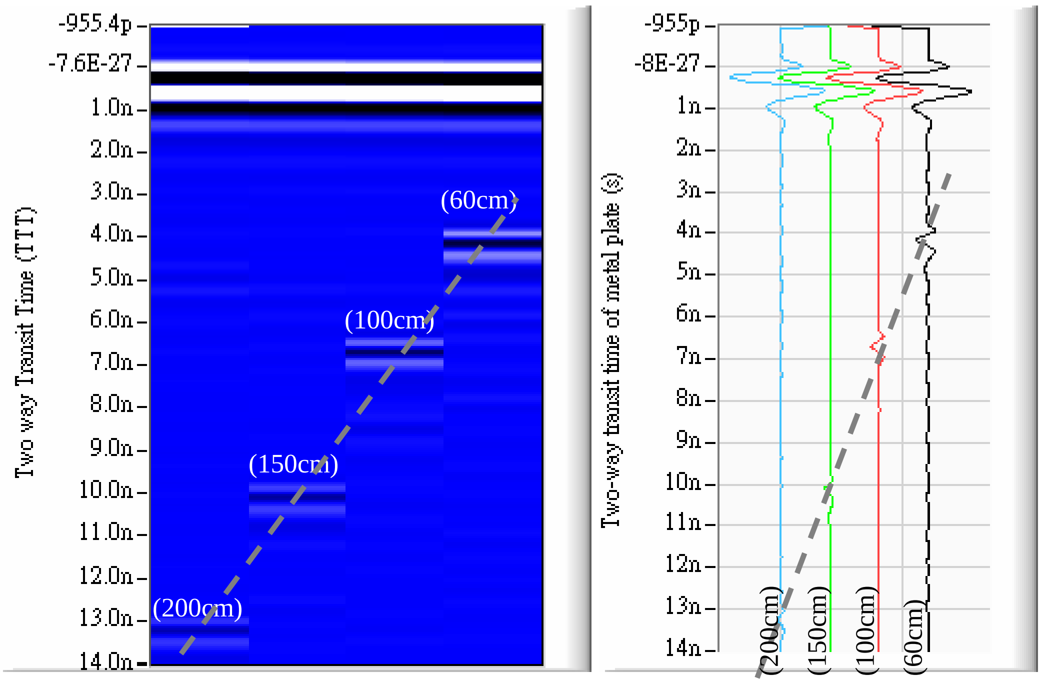

Remark: the distance enclosed by brackets inside this figure is the distance separating the antenna to the metal plate. The latter is represented by the dotted grey line.

Fig. 4-9 Radargram (left) and Stacked Waveforms (right) of Metal Plate Reflections Recorded from Variable Distances to the 1.5GHz GSSI Radar Antenna

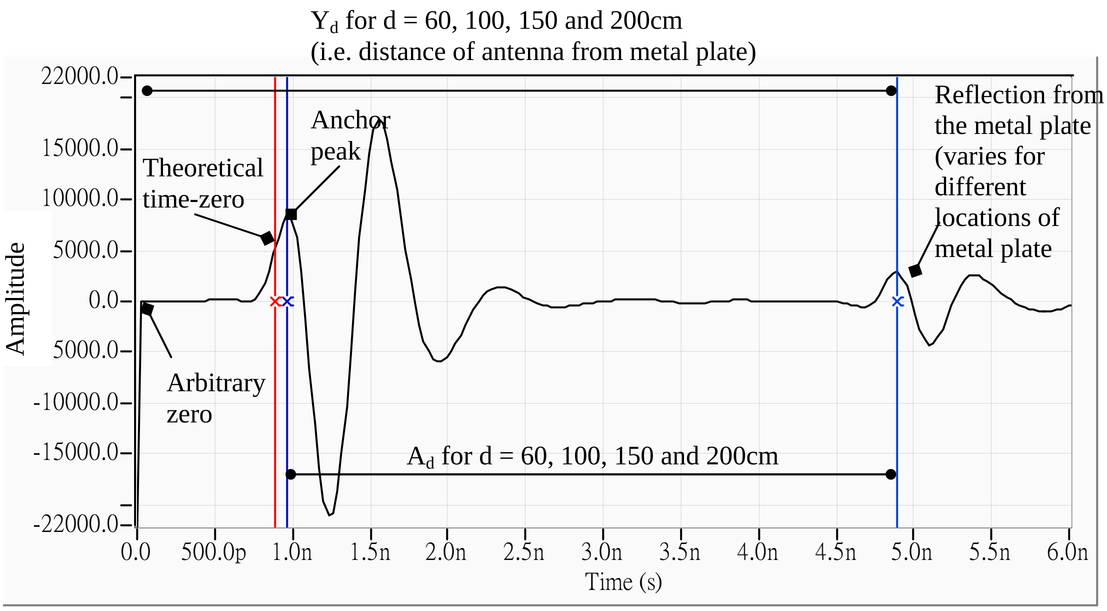

Fig. 4-10 One of the Waveforms obtained from the Experiment Calibrating the Theoretical Time-Zero in a Typical Waveform Acquired in the GSSI Radar System

As shown in Appendix E2, a positive sign of the difference between T_d'-A_d indicates that the theoretical time-zero is at the left of the anchor peak of the waveform, and vice versa. The magnitude of these differences in 400MHz and 1.5GHz antennae are 330.5ps and 174.2ps respectively. These differences will be taken into account in all experiments involving these two antenna frequencies described in Chapter 6.

4.3.2.2 SELECTION OF TIME WINDOW

Unlike the fixed time window of approximately 8.5ns in the JRC radar system, the range of time window in the GSSI radar system can be calculated and pre-selected. This selection of time window was based on the approximate and assumed maximum real permittivity of the material, as well as the target depth range of target/interface, as in Eq. [4-4].

$$v = \frac{2d_r}{T_{max}} = \frac{c}{\sqrt{\varepsilon_{max}'}} \quad \ldots\ldots\ldots\ldots\ldots [4\text{-}4]$$

where v is the radar wave propagation velocity, d_r is the depth range of investigation, T_{max} is the maximum time of flight (i.e. time window of a waveform), c is the traveling speed of light and ε_{max} is the maximum real permittivity encountered in the material.

For instance, if a saturated silt (with ε_{max}' = 40 approximately) of thickness 200mm would be ranged, then the prescribed maximum time window must not be smaller than 8.4ns.

4.3.3 VERIFICATION AND DETERMINATION OF THE CHARACTERISTIC/NOMINAL ANTENNA FREQUENCY IN AIR

Time-domain waveforms in the GSSI radar system were obtained through coupling the antenna in ambient conditions, as illustrated in Fig. 4-11. This waveform was then transformed to a frequency spectrum as depicted in Fig. 4-12, after adopting the five signal processing techniques which will be described in Table 5-1. The characteristic/nominal peak frequencies were found to be 296MHz and 1.33GHz for 400MHz and 1.5GHz respectively, as depicted in Fig. 4-12. These values are found to be lower than those given by the manufacturer.

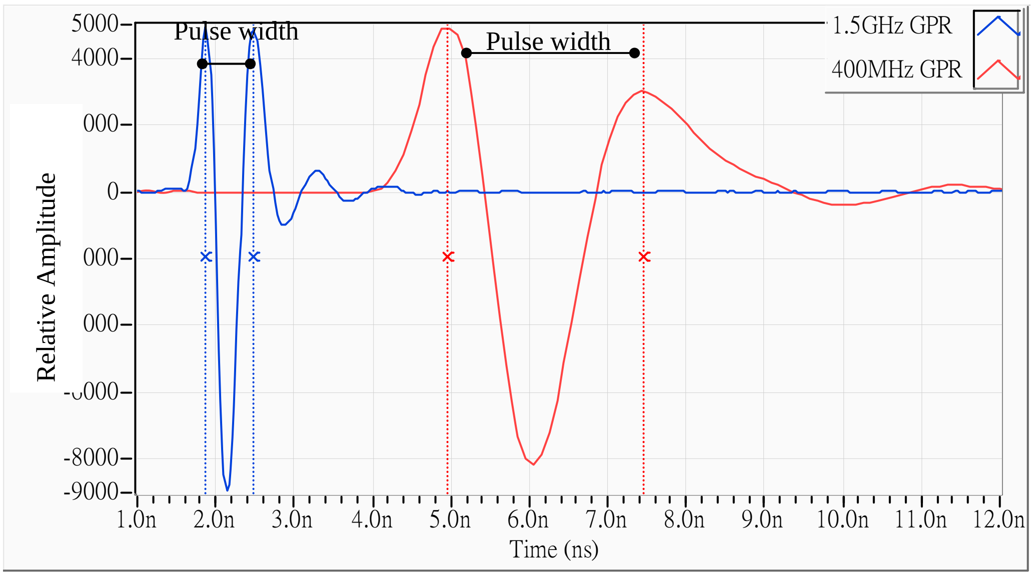

Fig.4-11 Time Domain Waveform (obtained during coupling of the GSSI 400MHz and 1.5GHz Antenna to Ambient Environment)

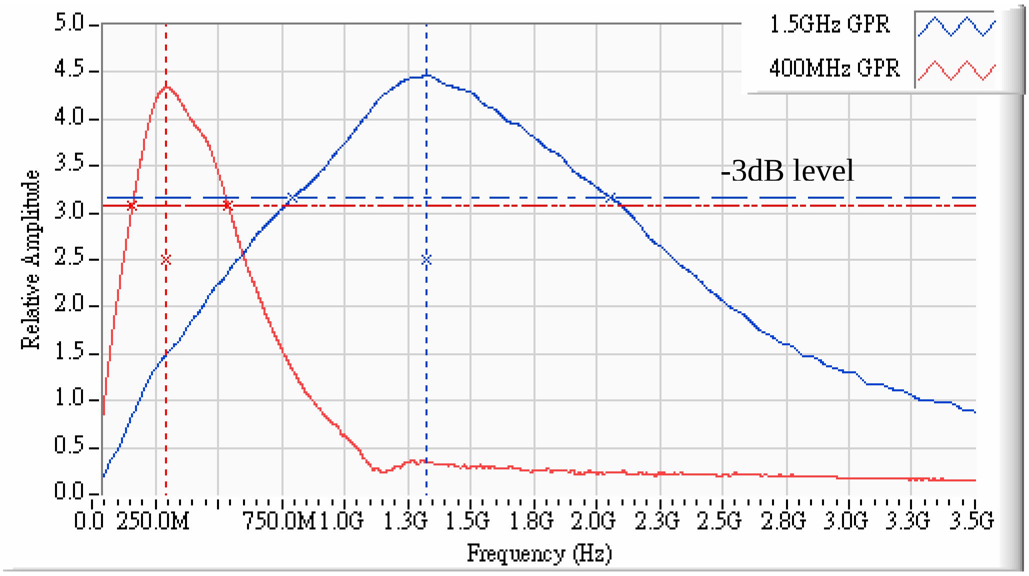

Fig.4-12 Frequency Spectrum (obtained during coupling of the GSSI 400MHz and 1.5GHz Antennae to Ambient Environment)

Following the same method adopted in the JRC radar system described in Section 4.2.5, the characteristic/nominal peak frequency was also determined by measuring the reciprocal values of the pulse widths between the anchor peak and the second peak in Fig. 4-11. Furthermore, the frequency bandwidths at -3dB were measured by reducing the maximum spectrum power by 3dB (i.e. 70.79% of the maximum amplitude in the spectrum) (ASTM D6432-99; Millard et al., 2001). These values are summarized in Table 4-3.

4.4 A COMPARISON OF THE OPERATING CHARACTERISTICS OF THE JRC AND THE GSSI RADAR SYSTEMS

Some important characteristics about the time domain waveforms and the frequency spectra of both the JRC radar and the GSSI instrumentation systems are summarized in Table 4-3.

Table 4-3 Comparison of the Operational Characteristics of the JRC Radar and the GSSI Radar system

Domain	**Items**	**JRC radar (1GHz antenna)**	**GSSI radar**	
			400MHz antenna	**1.5GHz antenna**
Time	Time window	8.5ns (fixed)	Variable up to 200ns	
	Re-scaling factor	515697	Nil	Nil
	Position of theoretical time-zero	14ps ahead of the anchor peak	6ps behind the anchor peak	6ps behind the anchor peak
	Error in determination of real permittivity (refer to Appendixes K2 and K3 for the calculation)	+/- 0.05	+/- 0.79	+/- 0.62
Frequency	Nominal frequency (suggested by the manufacturer)	1GHz	400MHz	1.5GHz
	Characteristic/nominal peak frequency in frequency spectrum (the upper bound of the low-pass filter is decided by halving the sampling frequency)	619MHz in a wide low-pass filter (upper bound 32.23G)	296MHz in a wide low-pass filter (upper bound 5.12G)	1.33GHz in a wide low-pass filter (upper bound 17G)
	Characteristic/nominal frequency by using the reciprocal value of pulse width in the time-domain waveform	775MHz	397MHz	1.61GHz
	Frequency bandwidth at -3dB (the higher frequency minus the lower frequency in -3dB)	986M -403M = 583M	541M -160M = 381M	2.06G -796M = 1.26G

All characteristic/nominal peak frequencies of the three radar antennae were determined and verified using the two methods: peak at the frequency spectrum and the reciprocal of pulse width. All these characteristic/nominal peak frequencies were found to be smaller than the nominal values (i.e. 400MHz, 1GHz and 1.5GHz) suggested by the manufacturers, except the frequency found at GSSI 1.5GHz GPR (i.e. 1.61GHz) using the pulse width method. The error analyses of real permittivity based on the two systems are referred to Appendixes K2 and K3.

After a series of trials and calibrations using time- and frequency- domain analysis, the GSSI radar system was found to be more versatile than the JRC system based on the following two aspects:

1. The time window in the GSSI system can be pre-selected based on the assumed real permittivity of material and the depth range of subsurface target/interface, as described in Eq. [4-4], whereas the JRC system only provides a fixed time window.

2. The background noise of the time domain waveforms in the GSSI system is well-suppressed when the antenna was coupled to ambient conditions. This leads to a smoother frequency distribution in the frequency spectrum, as depicted in Fig. 4-12.

4.5 WATER LEVEL/WATER HEAD MEASUREMENT BY A STRAIN GAUGE BASED PRESSURE GAUGE

In the asphalt pavement experiment described in Chapter 7, a strain-gauge based pressure gauge (as seen in Fig. 4-13) was put inside the pump well to measure the water level. The data of water level was used to predict the overall degrees of water saturation of the material, as will be shown in Section 7.4.1.

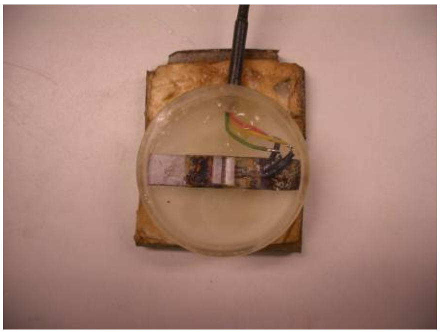

Fig. 4-13 Photo of the Strain-gauge Based Pressure Gauge

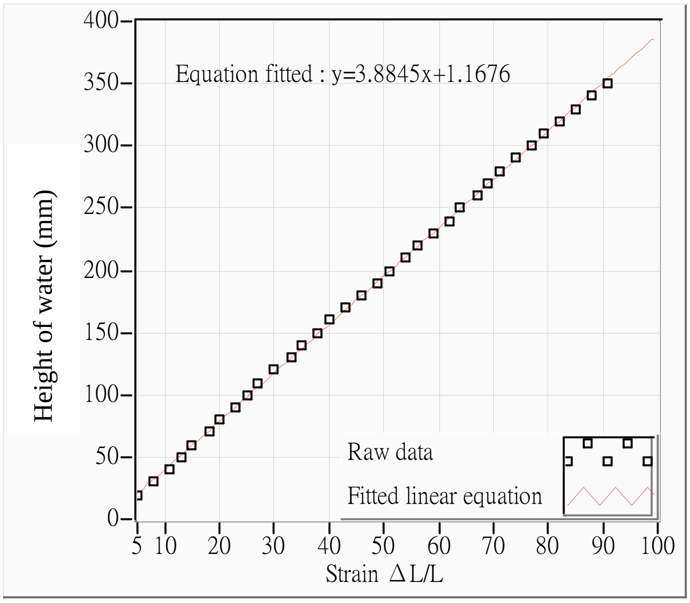

Fig. 4-14 The Linear Relationship between the Controlled Water Level and the Measured Strain in the Strain-gauge Based Pressure Gauge

When the gauge was placed at the bottom of a free water head, the changes of water level/water head exert different static water pressures on the gauge (i.e. by $P = h\rho g$ where P is the static pressure, ρ is the water density and g is the gravitational constant). The gauge responds quite linearly with the change of water level/water head, as depicted in Fig. 4-14 which was obtained by performing a calibration experiment. A best-fit linear equation was obtained according to the paired data comprising water level and strain obtained by the gauge. Therefore, measuring strain enables a direct computation of the water level/water head according to the equation shown in Fig. 4-14.

After examining the technical and operational basis of the two instrumentation systems, the next chapter will provide an insight into the data processing techniques.

5. DATA PROCESSING

5.1 TIME-DOMAIN METHODS

In the time-domain data processing, the real permittivity and the energy attenuation of the material are the two essential material properties to be measured. Both these two material properties are determined in the time-domain reflected waveform and are acquired by the methods described in the following sections.

5.1.1 REAL PERMITTIVITY

The real permittivity of a material was determined according to the following steps:

1. identification of the peak/valley in the reflected waveforms, as depicted in a material layering configuration shown in Fig. 5-1a and Fig. 5-1b, as well as the corresponding waveforms depicted in Fig. 5-1c,

2. determination of the two-way-transit-time (TTT) by calculating the differences between the theoretical time-zero reported in Chapter 4 and the peak/valley of the interfaces in the waveform and,

3. determination of the real permittivity according to Eq.[5-1]

$$v = \frac{2d}{T} = \frac{c}{\sqrt{\varepsilon^{'}}} \Rightarrow \varepsilon^{'} = (\frac{cT}{2d})^2 \text{ …………[5-1]}$$

where d = thickness of the layer, T = two way transit time (TTT), c = speed of light and ε = real permittivity. Accuracies of the real permittivities are referred to the error analysis described in appendices K1 to K3.

5.1.2 ENERGY ATTENUATION

Energy attenuation was extracted and measured from the peak/valley identified in the waveforms, based on the reductions of signal amplitudes due to energy absorption by the dielectric material. The amplitudes (i.e. Volts) acquired in the different GPR/SPR data acquisition systems (i.e. JRC radar and GSSI radar systems) are expressed in a dB/m scale. In this scale the amplitudes of the reflected signals are divided by the amplitudes of the anchor peak reflection, according to Eq. [5-2].

$$\text{Energy attenuation expressed in dB/m} = (20x\log\frac{A_{reflection}}{A_{anchor}})\,/\,T\ldots\ldots\ldots\ldots[5\text{-}2]$$

where $A_{reflection}$ = amplitude of the material interface, A_{anchor} = amplitude of reflection of the anchor peak (refer to Fig. 4-5), T = the thickness of the specimen.

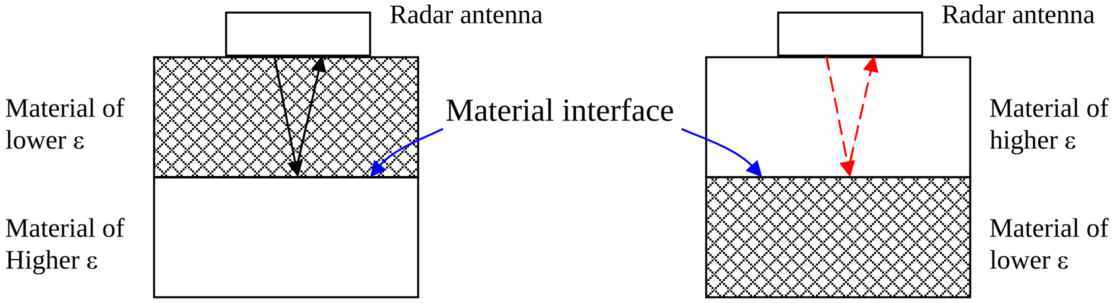

Fig.5-1a Material Interface Separating Materials from Lower to Higher ε'

Fig.5-1b Material Interface Separating Materials from Higher and Lower ε'

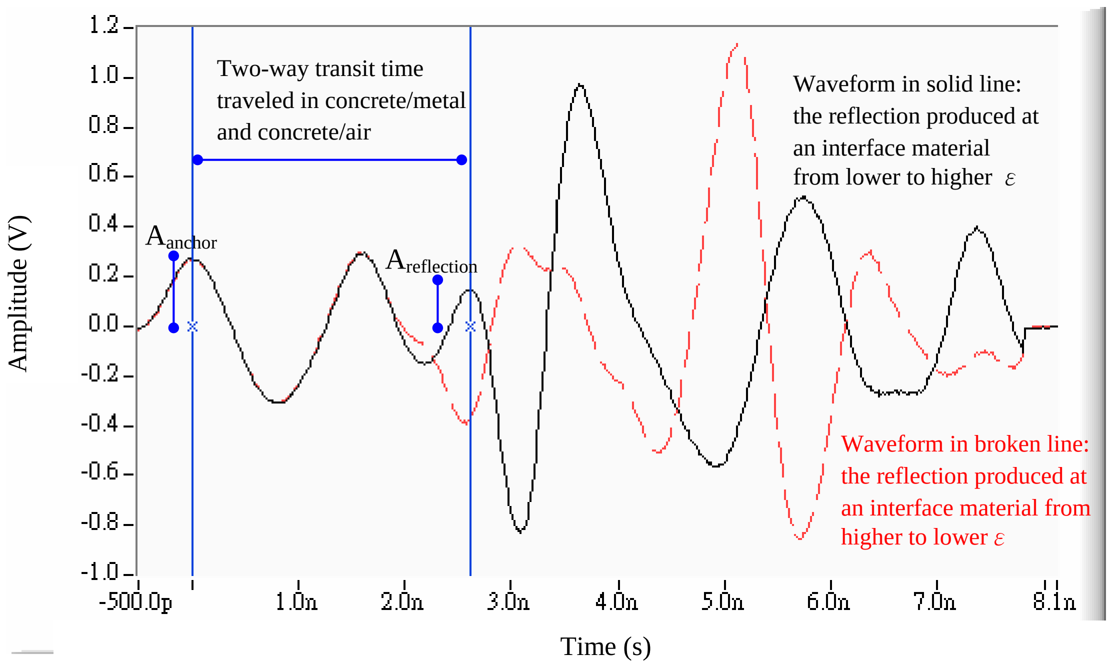

Fig.5-1c Reflected Waveforms obtained from the Material Configuration in Fig. 5-1a and Fig. 5-1b

The energy attenuation expressed in the dB/m scale provides a common basis for characterization of different energy absorption levels in different materials as described in subsequent chapters.

A *differential*, but *un-traceable* and *un-controllable* signal transmission control (STC) (i.e. an automatic gain setting) at different TTT of reflections along the time-axis was built in the JRC radar system (personal communication, Corcoran 2005). It is *differential* because the amplitudes of reflections existed at a later part of the time window are automatically magnified and are therefore larger than those existing at earlier TTTs. This automatic magnification makes weak reflections existing at later parts of the time window more observable, but at the same time the true values of amplitudes are not measurable.

The STC is also *un-traceable* because the level of amplitude cannot be restored to the original levels as the original setting of the amplitude magnification is not understood. Finally, this STC is *un-controllable* since the JRC radar instrumentation system is a ‘black box’ which does not allow control of electronic circuitry and algorithms, as described in Chapter 4.

5.1.3 REFLECTION COEFFICIENTS

Fig. 5-1 depicts the transmission of EM waves in two layered materials from low to high ε (as in Fig. 5-1a) and vice versa (as in Fig. 5-1b). Fig. 5-1c shows the two waveforms corresponding to the material interfaces depicted in Fig. 5-1a and Fig.1b. In Fig. 5-1c, the polarity of the reflection coefficients (RC) is governed by the relative magnitude of the real permittivity as shown in Eq. [5-3].

$$RC = \frac{\sqrt{\varepsilon_1} - \sqrt{\varepsilon_2}}{\sqrt{\varepsilon_1} + \sqrt{\varepsilon_2}} \quad \text{...............[5-3]}$$

where RC is the reflection coefficient, ε_1 is the real permittivity of the material in the first underlying layer, ε_2 is the real permittivity of the material in the second underlying layer.

5.1.4 RADARGRAM

The time-domain waveforms were stacked together along an axis of elapsed time to produce a colored radargram which depicts explicitly any changes of TTT of the echoes over the elapsed time. An example of such a radargram and a particular waveform captured at a particular instant are shown in Fig. 5-2.

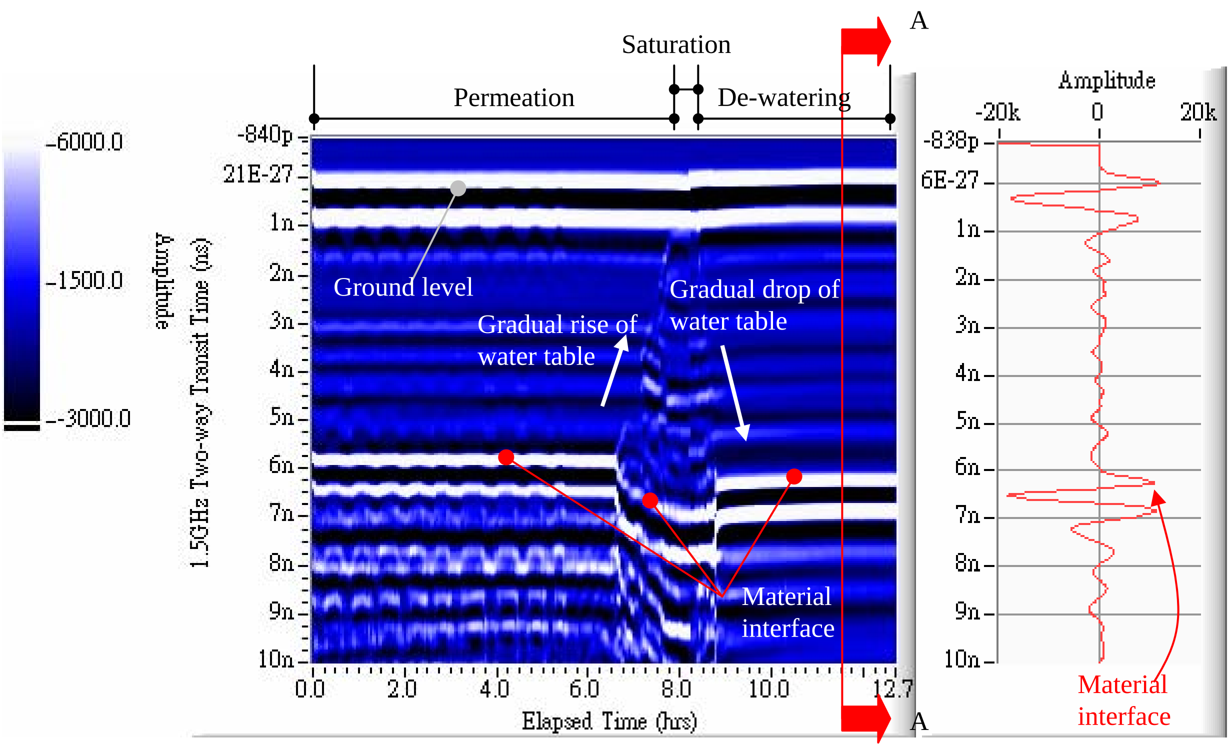

Fig.5-2 A Radargram obtained by Stacked Time-Domain Waveforms Using 1GHz Radar (left) and a Correspondent Waveform (A-A) at a Particular Elapsed Time (right)

In the radargram depicted in Fig. 5-2, an asphalt specimen (described in Chapter 7) was subjected to a cycle of water permeation and de-watering. This radargram is illustrated as an example to depict the stacked reflections against the elapsed time. The amplitudes of reflection shown in the radargrams (Fig. 5-2) are encoded based on the color chart at the upper left corner of the radargram (i.e. from white positive to black negative respectively). The white lines at 5.8ns represent the location of an interface. The white lines remain constant from the start to 6 hours and 30 minutes because the water table did not reach the interface and was out of the detection range of the radar. As time progressed and when the water table was raised above the interface (i.e. after 6 hours and 30 minutes), the reflection from the rising water table was clearly observable and was indicated by an inclined and straight white line. Simultaneously, the TTT from the interface was lengthened continuously and appears as a parabolic locus. The TTT reaches a maximum until the water level raised to the top of ground level. After saturation, de-watering started and the entire process was reversed.

5.2 FREQUENCY-DOMAIN METHODS

5.2.1 TRANSFORMATION FROM TIME-DOMAIN WAVEFORMS TO FREQUENCY-DOMAIN SPECTRA

Frequency spectra reflect the overall distribution of frequency which are embedded and therefore not observable in the time-domain waveforms. To transform the time-domain waveforms to their frequency spectra, some signal processing techniques were applied, as summarized in Table 5-1.

Table 5-1 Five Data Processing Techniques adopted to transform Time-domain Waveforms to Frequency-domain Spectra

Stage	Data processing technique	Description	Function
1	Dummy zero padding	In a typical waveform comprising 1024 nos. data points, 7168 nos. extra zeros are padded at the rear of a waveform to obtain a ray-trace with 8192 nos. (a higher power of 2) data points.	Provide frequency domain interpolation to increase its resolution in the frequency spectrum (Chugani, et.al., 1998)
2	Transformation of Δt in the time domain to Δf in the frequency domain	Determination of each time increment of data point (Δt) in the time domain which is a function of the sampling frequency. (i.e. $\Delta f = \frac{f_s}{N} = \frac{1}{N\Delta t}$)…..[5-4]	Determine the increment of each frequency in the frequency domain (Δf)
3	Exponential windowing	Apply exponential window by an equation in the form of $w[n] = e^{\frac{n}{N-1} \times \ln(f)}$ …..[5-5] for n = 0, 1, 2,……., N-1.	Prevent spectral leakage (particularly in the high frequency region), as shown in Fig. 5-3
4	FFT algoithm	Apply the FFT algorithm with the processed time-domain waveform. The FFT algorithm is as $X[k] = \sum_{i=0}^{N-1} x[i] e^{-j2\pi(ik)/N}$ …..[5-6] for k=0, 1, 2….., N-1, where N is a power of 2.	Determine the frequency spectra of the reflected time-domain waveform
5	Butterworth filter	Apply low-pass "Butterworth" filter	Remove the unwanted frequency content

In particular, before adopting the algorithm of Fast Fourier Transform (i.e. Stage 4 in Table 5-1), an exponential window (i.e. Stage 3 in Table 5-1) was applied to prevent spectral leakage at the end of the designated time window, as shown in Fig. 5-3.

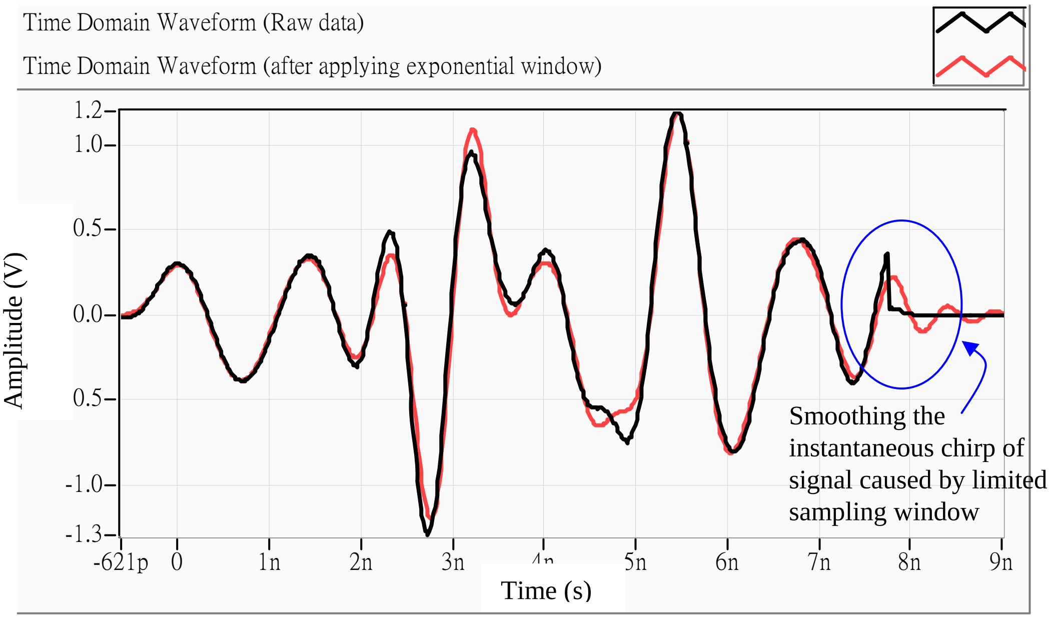

Remark: the waveform was acquired from one of the concrete specimens.

Fig.5-3 Time Domain Waveforms obtained before and after Applying the Exponential Window

Fig. 5-4a depicts five time-domain waveforms, whereas Fig. 5-4b shows the respective frequency spectra transformed from the time-domain waveforms, after processing with the five data processing techniques reported in Table 5-1. These waveforms and frequency spectra were obtained when the JRC antenna was coupled to a number of media which include air, a metal plate and concrete specimens of various degrees of water saturation.

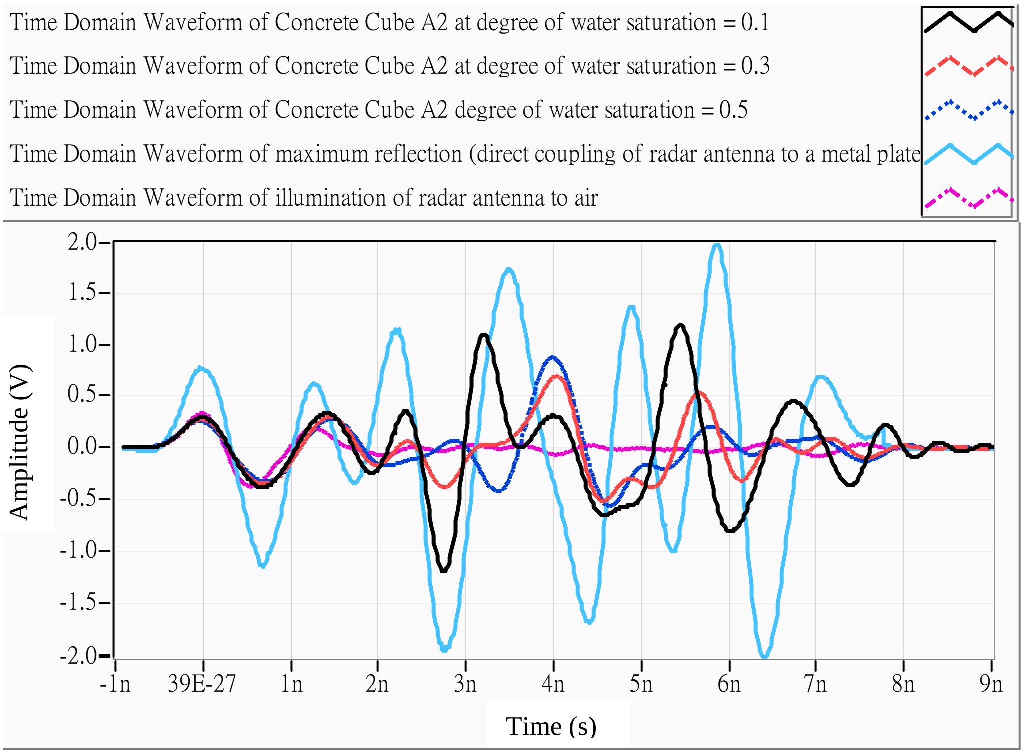

Fig.5-4a Time Domain Waveforms obtained when the Antenna is Coupled to Different Materials

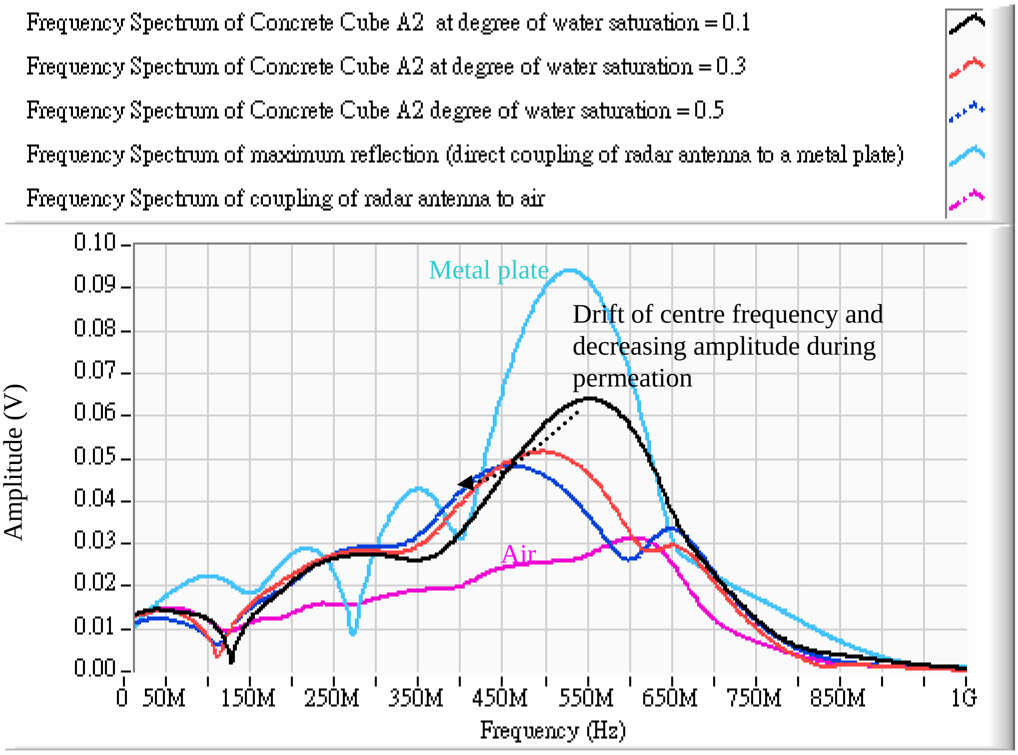

Fig.5-4b Frequency Spectra transformed from the Time-domain Waveforms depicted in Fig. 5-4a

When the antenna was coupled to air, the frequency spectrum possesses the largest peak-frequency, followed by the smaller values achieved for concrete specimens in drier conditions (i.e. a smaller S_w) and the smallest with moist conditions (i.e. a larger

S_w). This order is to be explained through a simple simulation detailed in Section 5.2.3.

When the antenna was coupled to a metal plate, the amplitude of frequency spectra was the greatest, followed by the smaller value achieved for concrete specimens with various S_w and the smallest when the antenna was coupled to air. This order in the frequency spectra reflects the different amplitudes of energy reflection in the time-domain waveform.

5.2.2 SPECTRAGRAM

The frequency spectra transformed from the time-domain waveforms can also be presented in the form of a so-called '*spectragram*' which was obtained by stacking and aligning sets of frequency spectra, as shown in Fig. 5-5.

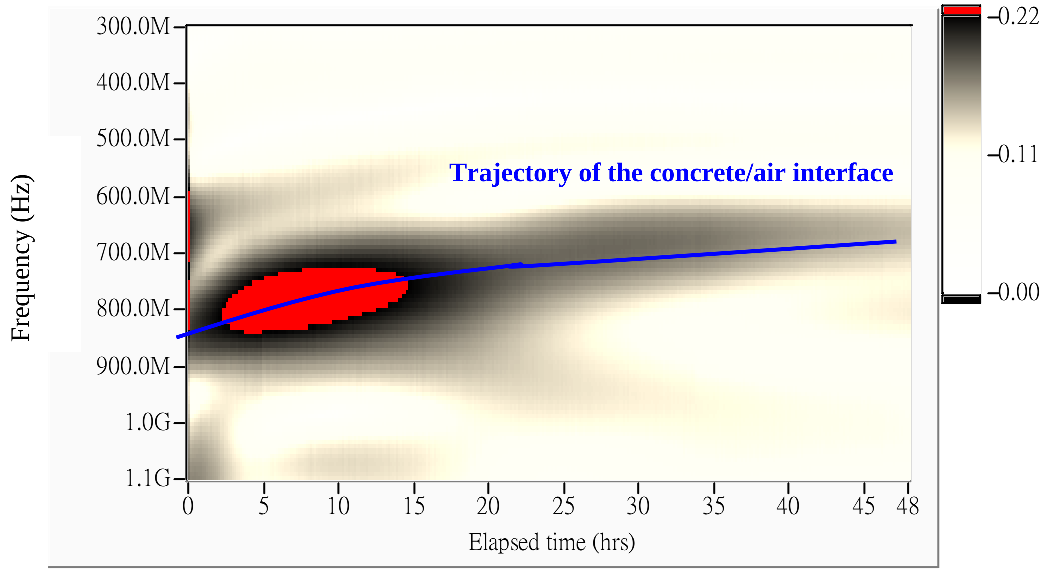

Fig. 5-5 A Spectragram obtained by Stacked Frequency Spectra transformed from Time-Domain Waveforms Using 1GHz Radar in One of the Concrete Experiments

Similar to the case in the radargram, each spectragram depicts explicitly any changes of the stacked frequency spectra over the elapsed time in the experiments described from Chapter 6 to Chapter 8.

5.2.3 A SIMPLE SIMULATION OF THE RELATIONSHIPS AMONGST THE NUMBER OF ECHOES, TIME WIDTH SEPARATING THE ECHOES IN TIME-DOMAIN WAVEFORMS AND THE DRIFT OF PEAK-FREQUENCY IN FREQUENCY SPECTRA

A so-called 'peak-frequency drift' is observed in Fig. 5-4b and was commonly found in the experimental findings in this research. This drift refers to the reduction or the increase of the peak-frequency found in the frequency spectra. This phenomenon has been reported in only a few literature. Millard et al. (2001) attributed this drift to absorption of high frequencies in material with a larger real permittivity. Daniels (2004) describes the dielectric materials as a low-pass filter in the frequency spectra. However, these investigations are found to be not sufficient to describe and explain the phenomena of peak-frequency drift found in the experimental findings of this research. Hence a simple simulation was conducted to simulate the results obtained in these experiments. A number of time-domain waveforms were defined in advance (as shown in Fig. 5-6a and Fig. 5-7a), and were subsequently processed with the five data processing techniques (as described in Table 5-1) to determine the frequency spectra (as shown in Fig. 5-6b and Fig. 5-7b). The characteristics in both the time- and frequency- domains are summarized in Table 5-2.

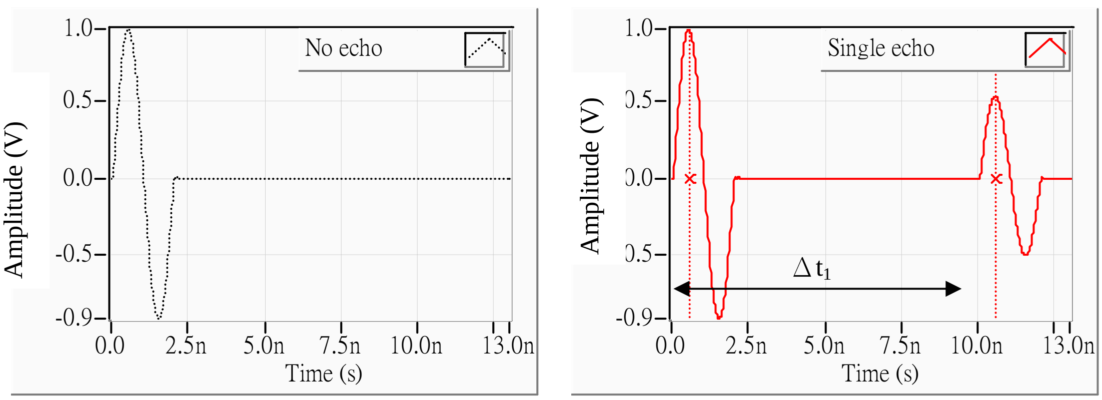

(1) No echo (2) One echo

Fig. 5-6a Different Quantities and Separation Distances of Repetitive Echoes in a Fixed Time Window

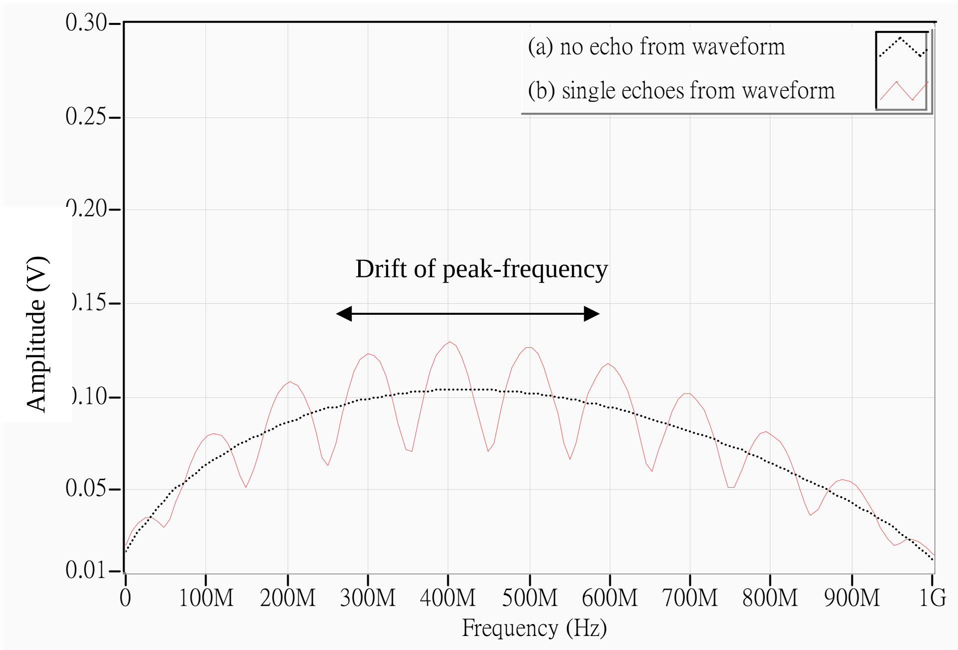

Fig. 5-6b Drift of Peak-frequency in Frequency Spectra due to the Number of Echoes and the Spacing of Echoes in Time-Domain Waveforms depicted in Fig. 5-5 (a), (b) and (c)

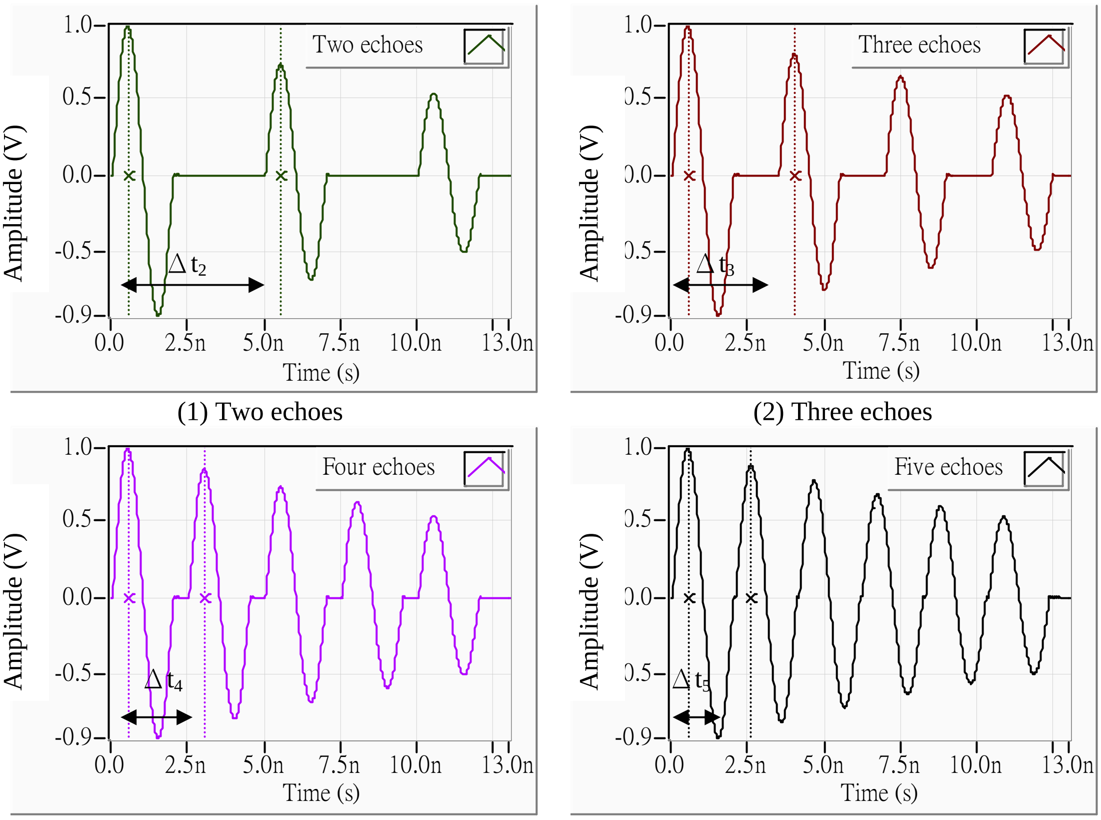

Remark: Echo refers to a complete cycle of a sinusoid with pre-determined amplitude and frequency

Fig. 5-7a Different Quantities and Separation Distances of Repetitive Echoes in a Fixed Time Window

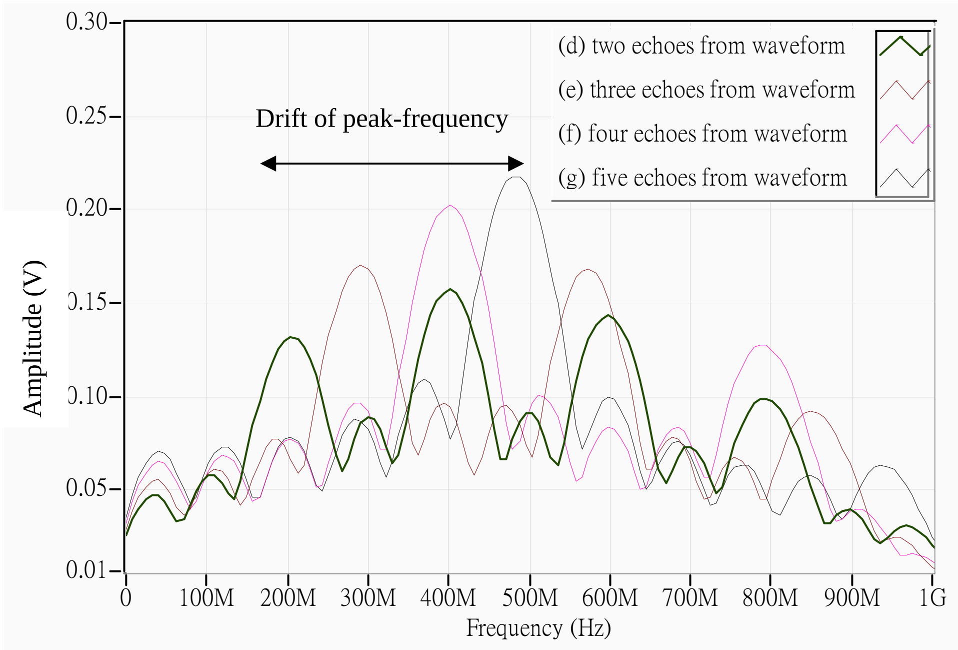

Fig. 5-7b Drift of Peak-frequency in Frequency Spectra due to the Number of Echoes and the Spacing of Echoes in the Time-Domain Waveforms depicted in Fig. 5-7(a)

Table 5-2 Relationships of the Number of Echoes, Time Width separating Echoes and the Drift of Peak-frequency in a Fixed Time Window

Figure	Time-domain		Frequency-domain
	No. of repetitive echoes	Δt of peak to peak or valley to valley (ns)	Peak-frequency (MHz)
5-5a (1)	No echo	-	425
5-5a (2)	One echo	$\Delta t_1 = 10$	401
5-6a (1)	Two echoes	$\Delta t_2 = 5.0$	205
5-6a (2)	Three echoes	$\Delta t_3 = 3.5$	291
5-6a (3)	Four echoes	$\Delta t_4 = 2.5$	401
5-6a (4)	Five echoes	$\Delta t_5 = 2.1$	480

For a waveform comprising multiple echoes, as depicted in Fig. 5-7a, a longer Δt_i in a fixed time window gives rise to a result of fewer repetitive echoes. Those waveforms with a longer Δt_i also corresponds to a decrease of peak-frequency in the frequency-domain (i.e. the left-drift of peak-frequency), and vice versa for the right drift of peak-frequency, as reported in Table 5-2.

The phenomena of peak-frequency drift were found in all experimental findings described in Chapter 6 to Chapter 8. During the permeation stages, an increase of water contributes to an increase of real permittivity of materials and a decrease in pulse velocity, and vice versa for the de-watering stages. Thus for a fixed time window prescribed in each GPR/SPR system (as described in Chapter 4), Δt_i of each reflected pulse was prolonged and the number of repetitive echoes in the fixed time window (i.e. the ringing or the reverberant signals) was reduced. As a result, the peak-frequency was found to be left-drifted (i.e. reduction of peak-frequency) for the permeation stages, and vice versa for the de-watering stages. These phenomena identified in the permeation and the de-watering stages were found to be in agreement with the results of the simulation depicted in Fig. 5-6, 5-7 and reported in Table 5-2.

5.3 SUMMARY AND DISCUSSION

This chapter reviews and examines the methods to process and analyze the data through both time- and frequency-domain methods. These methods will be adopted for all data analysis reported in the following chapters (Chapter 6 to Chapter 8) which details a series of experiments on concrete, asphalt and soil.

6. EXPERIMENTS TO CHARACTERIZE MATURE CONCRETE BY DETERMINATION OF THE ELECTROMAGNETIC WAVE PROPERTIES

6.1 INTRODUCTION

This chapter describes a series of experiments in characterizing the EM wave properties within matured concrete shed some light on the pore structure/systems possessed within concrete. The concrete specimens were cast by varying curing methods, with/without compaction, aggregate to cement mix ratios and water-to-cement ratios. The characterization methodologies were based on determining the changes of the real permittivity ($\Delta\varepsilon'$), the energy attenuation (expressed as dB scale) and the peak-frequency drift (Δf) in the spectragram with increasing degrees of water saturation (S_w). In all these test runs, water was allowed to permeate through traditional 150mm sized cubes and some concrete specimens of different sizes over different periods of 24, 48 or 72 hours under the influence of two pressure conditions: i.e. an externally applied pneumatic pressure of 200kPa and a small 1.5m hydrostatic pressure head. The continuous water permeation subjected the specimens to a series of moisture changes from the initial oven-dried state to a partially saturated state or even a fully saturated state at the end of the test runs. The specimens were also tested by a number of traditional tests, including the mercury intrusion porosimetry (MIP), the ultra-sonic pulse velocity (UPV) and the initial surface absorption test (ISAT) to obtain information on the pore size distribution (PSD)/porosity, indicator of the compressive strength and the degree of surface absorption/permeability respectively. The determined EM wave properties (i.e. ε', dB and f) and the traditional tests were used to differentiate the pore structures within these concrete specimens.

6.2 DESIGN AND CONSTRUCTION OF THE EXPERIMENTAL RIG

The experimental rig consisted of a rigid cylindrical steel pipe section (of internal diameter 100mm). This pipe section imposed a standing water column up to 1.5m high with different schemes of pneumatic pressure during all test runs, as reported in Table 6-1 and shown schematically in Fig. 6-1.

The concrete specimens (most are 150mm cubes but some have different widths) were cast and cured by immersion in fresh water (except the air-cured specimens D1, D2 and D3) for a period of at least 28 days to allow sufficient cement hydration (in accordance with BS 1881-111:1983).

Specimens with special widths (as reported in Table 6-1) were also cast to investigate how the boundaries/edge effects affect the data analysis in both the time and frequency domains. These boundaries/edge effects refer to the unwanted side reflections picked by the radar antenna. These effects are caused by the sides of concrete in contact with both the water column inside the cylindrical pipe, as well as the metal flange for clamping the specimens, as shown in Fig. 6-1. For ε’ and energy attenuation in the time domain analysis, the effects of the boundaries/edges on these parameters were insignificant because the major reflections from the back wall were un-affected. For frequency domain analysis, the effects were found significant and will be discussed in detail in Section 6.4.1B.

Before the test runs were started, the specimens had been oven-dried for at least 24 hours to ensure that initially the specimens contained no free water. The specimens were then wrapped with polythene sheets before the test runs so that evaporation and ingress of atmospheric moisture could be avoided during the test runs. Sets of different durations of these test runs are tabulated in Table 6-1, under the designation of D-series.

Throughout all test runs, the 1GHz radar antenna was placed on one side of the specimen, and the opposite side was a back wall which served as a reference reflector. During each test run, acquisition of the radar waveforms started five minutes before water permeation. Then water was filled in the pipe to penetrate into the specimens. With the constant water column and the 200kPa pneumatic pressure, water continued to permeate the specimens. The radar system continued to acquire a waveform per minute over a period of 24, 48 or 72 hours. To observe and measure the amount of water ingress into the specimens, an external observation glass tube was taped alongside the cylindrical pipe. Graduated markings on the glass tube allowed visual readings collected by a camera to the nearest milli-meter. The visual images of the reduced water levels were also captured per minute and programmed continuously throughout the test runs. The gravimetric measurements of the specimens were obtained at the beginning and at the completion of each test run. This data was used to compute the intermediate degree of water saturation of concrete at any particular moment, as will be discussed in Section 6.4.1A.

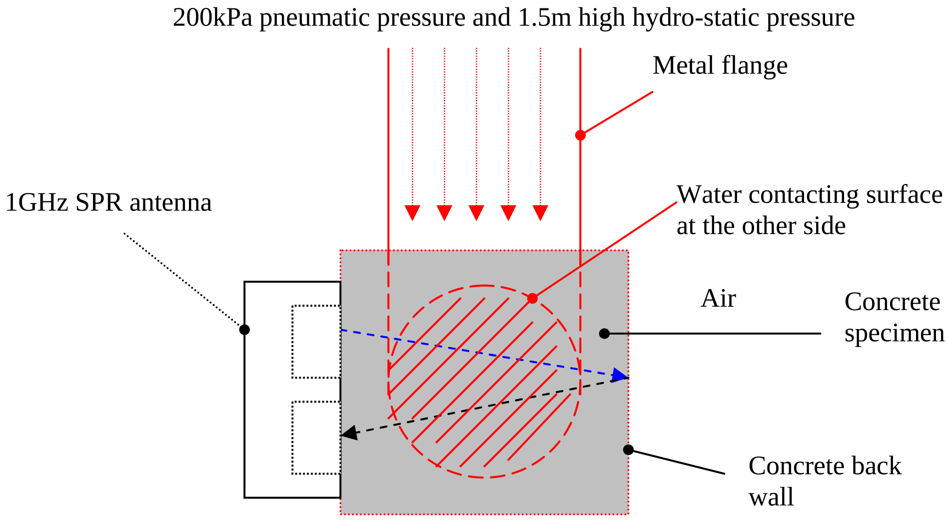

Fig. 6-1a Schematic Experimental Setup of the Experiments on Concrete

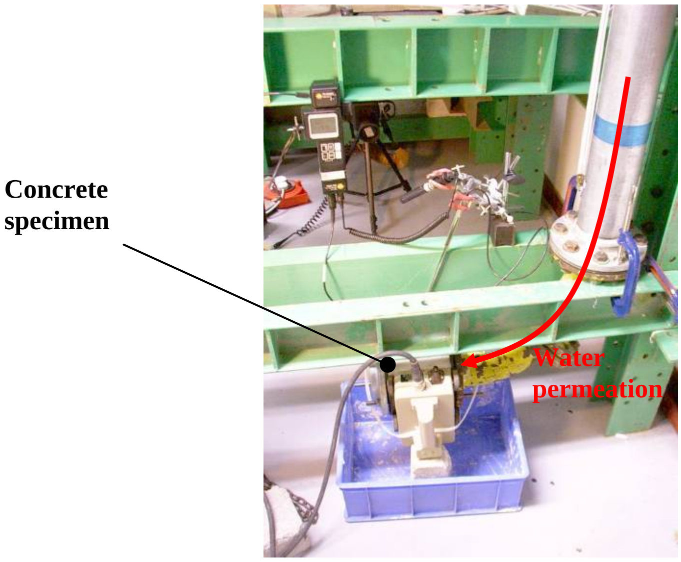

Fig. 6-1b Photo of the Experimental Setup

Table 6-1 reports the designation of concrete specimens, design mixes and some background information about the specimens. Fig. 6-2 shows the specimens marked with the respective final wetted-fronts after the test runs. The correct positions of these wetting fronts were determined by the use of a protimeter to demarcate the wetted and dried regions on the concrete’s surface. The central part of the concrete specimens (approximately 22mm thick and 11mm in radius) were cored and cut from the specimens to carry out the MIP tests, as depicted in Fig. 6-2f.

		
(a) Cube Specimen A2 (water-cured, not compacted)	(b) Cube Specimen A5-2 (water-cured, well- compacted)	(c) Cube Specimen B4 (water-cured, well- compacted)
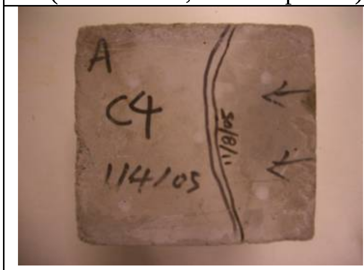	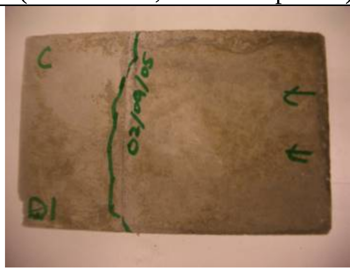	
(d) Cube Specimen C4 (water-cured, well- compacted)	(e) Specimen D1 (air-cured, well-compacted)	(f) A sample for MIP test cored from a cube specimen

Remark:

1. All specimen photos are incorporated in Appendix G.
2. Water fronts were determined using a protimeter and were drawn on the surface of the specimens after test runs.

Fig. 6-2 Some Representative Concrete Specimens after Test Runs and a cored sample for MIP Test

Table 6-1 Design Specifications of Concrete Specimens

<table>
<tr><th>Specimen designation *</th><th>A/C ratio</th><th>W/C ratio</th><th>Mix ratio **</th><th>Slump (mm)</th><th>Method of curing</th><th>Method of compaction ***</th><th>Visual inspection at mature state</th><th>Designation of Sizes of specimens****</th><th>Duration of test runs</th></tr>
<tr><td>A1</td><td rowspan="6">6:1</td><td>0.6</td><td rowspan="6">1:2:4</td><td>15</td><td rowspan="6">Water</td><td rowspan="2">NC</td><td rowspan="2">HC</td><td rowspan="6">1</td><td rowspan="2">1.5m high constant water head applied for first 48 hours and 200kPa applied for next 24 hours *****</td></tr>
<tr><td>A2</td><td>0.4</td><td>15</td></tr>
<tr><td>A3</td><td>0.8</td><td>194</td><td rowspan="4">WC</td><td rowspan="4">Normal</td><td rowspan="4">24 hours for 200kPa ******</td></tr>
<tr><td>A4</td><td>0.6</td><td>158</td></tr>
<tr><td>A5-1</td><td>0.5</td><td>78</td></tr>
<tr><td>A5-2</td><td>0.5</td><td>78</td></tr>
<tr><td>C4</td><td rowspan="3">6:1</td><td>0.75</td><td rowspan="3">1:3:3</td><td>65</td><td>Water</td><td rowspan="3">WC</td><td rowspan="3">Normal</td><td rowspan="3">1</td><td rowspan="3">24 hours for 200kPa ******</td></tr>
<tr><td>C5</td><td>0.8</td><td>150</td><td rowspan="2">Water</td></tr>
<tr><td>C6</td><td>0.85</td><td>185</td></tr>
<tr><td>D1</td><td rowspan="7">4.3:1</td><td rowspan="7">0.41</td><td rowspan="7">1:2.2:2.1</td><td rowspan="7">132</td><td rowspan="3">Air</td><td rowspan="5">WC</td><td rowspan="5">Normal</td><td>2</td><td rowspan="7">48 hours for 200kPa</td></tr>
<tr><td>D2</td><td>3</td></tr>
<tr><td>D3</td><td>4</td></tr>
<tr><td>D4</td><td rowspan="4">Water</td><td rowspan="4">1</td></tr>
<tr><td>D5</td></tr>
<tr><td>D6</td><td rowspan="2">NC</td><td rowspan="2">HC</td></tr>
<tr><td>D7</td></tr>
<tr><td>B2</td><td rowspan="4">3:1</td><td>0.45</td><td rowspan="4">1:1:2</td><td>59</td><td rowspan="4">Water</td><td rowspan="4">WC</td><td rowspan="4">Normal</td><td rowspan="4">1</td><td rowspan="4">48 hours for 200kPa</td></tr>
<tr><td>B4</td><td>0.55</td><td>216</td></tr>
<tr><td>B5</td><td>0.6</td><td>219</td></tr>
<tr><td>B6</td><td>0.6</td><td>214</td></tr>
</table>

* Specimens B1, C1 to C3 are excluded since the shapes of concrete cannot be formed corresponding to too small water to cement ratio; No experiment was conducted on cube B3.

** The mix ratio is the ratio of Ordinary Portland Cement (OPC): fine aggregate (river sand): coarse aggregate (10mm and 20mm aggregate in the ratio of 1:2)

*** NC: Not compacted; WC: Well-compacted

**** Size Designation 1: 150mm cube, Designation 2: 236(W) x 150(L) x 150mm (D), Designation 3: 201(W) x 150(L) x 150mm (D), Designation 4: 182(W) x 150(L) x 150mm (D).

***** This designated period of test runs caters for the very permeable nature of the specimens. If a high pressure (such as 200kPa) was exerted on the specimens, water would have seeped through some inter-connected macro-pores possessed within the specimens and flowed freely outside the experimental rig. This would lead to a un-controllable flow of water and un-measurable S_w. Therefore the specimens were designed to receive a lower and optimal pressure (i.e. 1.5m water head) for the first 48 hours to partially saturate the specimens. After this partial saturation, a pressure of 200kPa was exerted to increase the range of S_w.

****** This designated period of test runs caters for a shorter duration to reach the saturation state of the specimens, presumably due to the more permeable nature of the concrete specimens possessed in A- and C-series than the B- and D-series.

6.3 INSTRUMENTATION AND SPR ANTENNA FREQUENCIES

The SPR system adopted in these experiments is a JEJ-60BF (manufactured by Japan Radio Company Limited) radar system equipped with a 1GHz antenna. The data acquisition and processing units of the 1GHz antenna were assembled by the 'National Instrument ™' hardware and an in-house developed software program in the 'LabVIEW ™' environment. The latter performed all the automated data acquisition and the signal processing tasks in the time domain and frequency domain reported in this chapter. The details of this instrumentation system are referred to Chapter 4.

Fig. 6-3 illustrates the frequency spectra obtained at various S_w of concrete specimen D1, as well as the respective peak-frequency drift and reduced amplitude due to increasing S_w. Table 6-2 summarizes the information of returned peak frequencies, velocities, wavelength and depth resolution under different S_w.

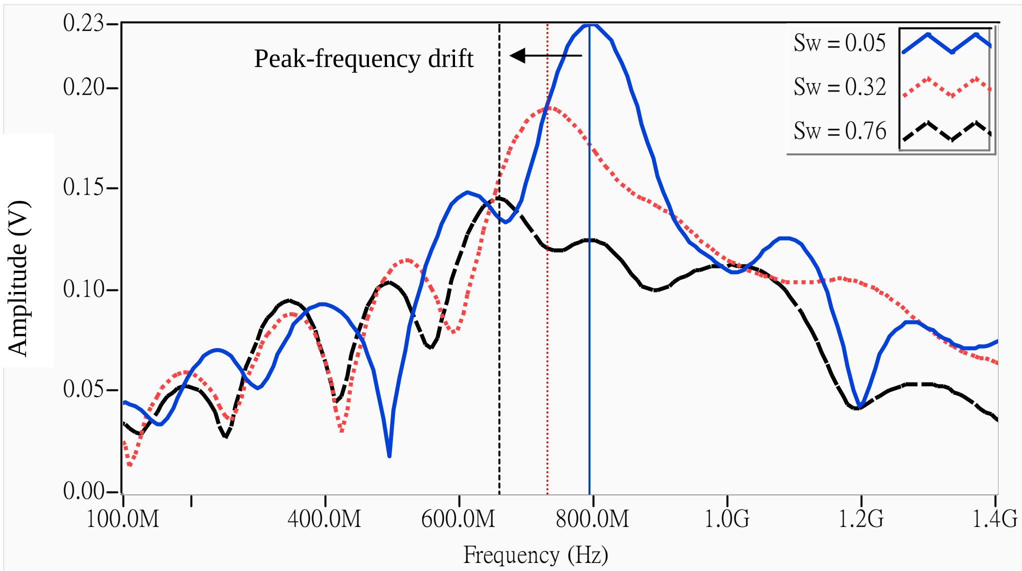

Fig.6-3 Frequency Spectra of the Returned Radar Wave Signals processed with 2GHz low-pass filter for the Antennae coupled on Concrete Specimen D1 during Partially Saturated States

Table 6-2 Depth Resolutions (calculated according to one-forth of nominal wavelength) obtained in different Partially Saturated States of Concrete Specimens

Nominal/characteristic frequencies of the GPR antenna		**1GHz**
Concrete Specimen		**D1**
At S_w = 0.05	Propagation velocity of GPR wave (v)	0.148m/ns
	Returned nominal/characteristic peak frequency (determined from the frequency spectrum)	785MHz
	Nominal/characteristic wavelength λ (=v/f)	186mm
	Depth resolution (one quarter of λ)	**47mm**
At S_w = 0.32	Propagation velocity of GPR wave (v)	0.140m/ns
	Returned nominal/characteristic peak frequency (determined from the frequency spectrum)	732MHz
	Nominal/characteristic wavelength λ (=v/f)	191mm
	Depth resolution (one quarter of λ)	**48mm**
At S_w = 0.76	Propagation velocity of GPR wave (v)	0.100m/ns
	Returned nominal/characteristic peak frequency (determined from the frequency spectrum)	661MHz
	Nominal/characteristic wavelength λ (=v/f)	152mm
	Depth resolution (one quarter of λ)	**38mm**

The ultra-sonic system adopted is *TICO* Ultrasonic Instrument with a nominal acoustic frequency 54kHz. Mercury Intrusion Porosimetry (MIP) (model *PoreSizer* 9320 manufactured by Micromeritics) was used to measure the pore size distribution, porosity and the respective volume fraction of each specimen. Gravimetric measurement was also used to determine the values of porosity and compared with the values obtained from MIP. This method determines the differences in weights obtained through oven drying and fully submerging the specimens in water until no further increase of weight was noticed. The Initial Surface Absorption Test (ISAT) provides the degree of surface water absorption and serves as an indicator of permeability of the concrete (Concrete Society, 1987). The MIP and the gravimetric method were carried out according to the standard procedures described in BS7591-1:1992 and BS1881:114 1983 respectively, whereas the ISAT was carried out in accordance with BS1881:208 1996.

6.4 FINDINGS AND DATA ANALYSIS

It is known that the methods of treatment at the fresh/early state and the design mixes of concrete affect the pore structures, as discussed in Section 3.2.3.2. The former refers to the curing history and the conditions of compaction immediately after mixing, while the latter refers to different aggregate to cement (A/C) ratios, as well as the water to cement (W/C) ratio. The factors affecting the pore structures of individual specimens are summarized and reported in Table 6-3 to Table 6-5.

6.4.1 DETERMINATION OF REAL PERMITTIVITY, ENERGY ATTENUATIONS AND PEAK-FREQUENCY DRIFT AND THEIR CONSTITUTIVE RELATIONSHIPS WITH DEGREE OF WATER SATURATION

The determined material properties are the three EM wave properties obtained in time and frequency domains, as well as with the pore size distribution (PSD), the porosity (ratio of the total pore volume to the bulk volume) and the degrees of surface absorption. The EM wave properties refer to the real permittivity (ε'), the energy attenuation (dB) and the drift of the peak frequency (f) in frequency spectrum, as reported in Table 6-3 to Table 6-5. The methods of determination of these properties in both time and frequency domains were described in Chapter 5. These properties were subsequently normalized to $\Delta\varepsilon$, ΔdB and Δf (based on their initial values) so that their marginal changes after various stages of water saturation were immediately apparent. These values were also plotted against S_w to determine their constitutive relationships, as depicted from Fig. 6-9 to Fig. 6-11 and Fig. 6-13 to Fig. 6-15. The values of S_w at the intermediate state of the experiment are determined using Eq. [6-1] and Eq. [6-2]. A schematic diagram is depicted in Fig. 6-4 to describe the hierarchy and conceptual data flow of various material properties examined in the data analysis.

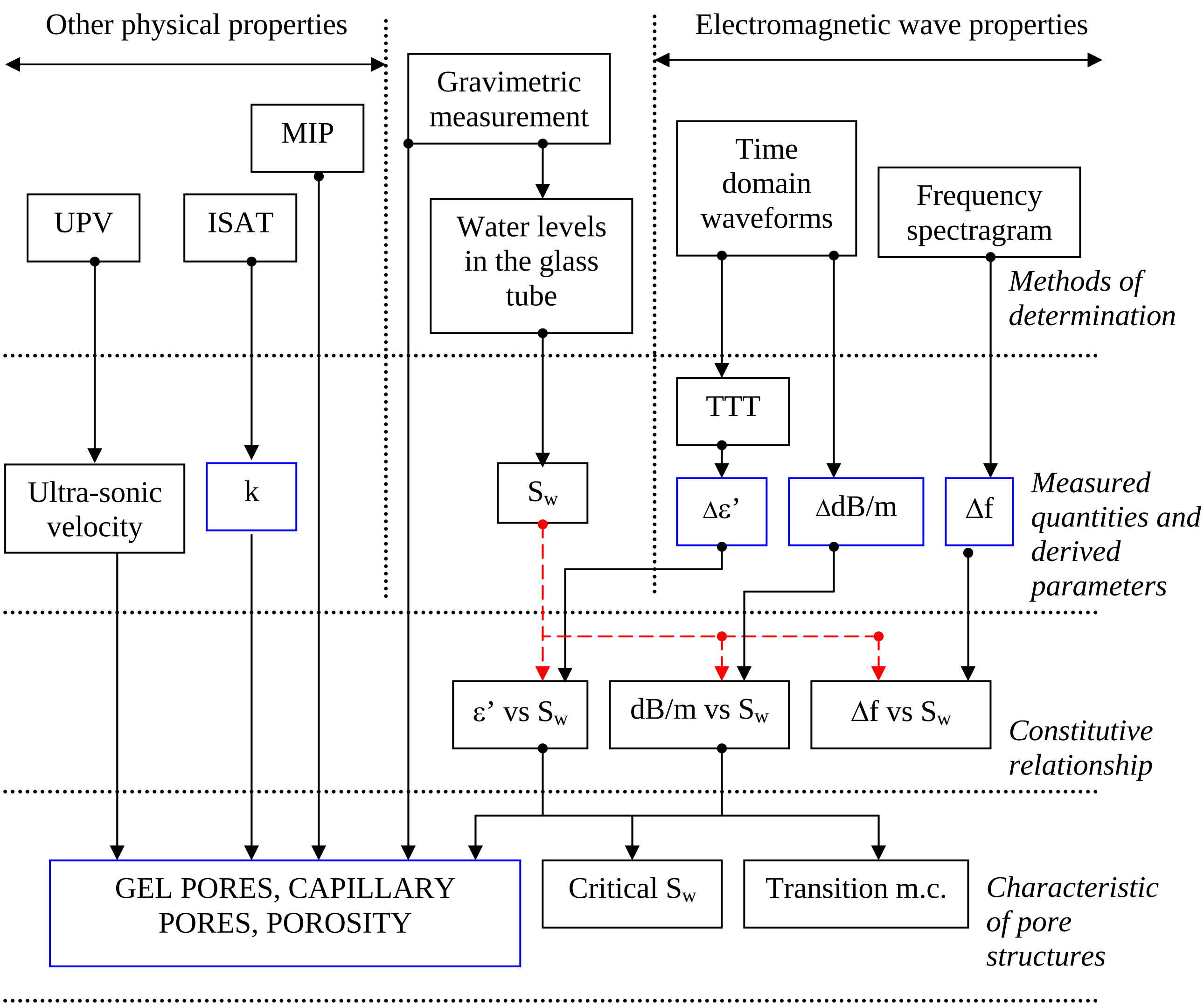

UPV: Ultrasonic pulse velocity
ISAT: Initial Surface Absorption Test
MIP: Mercury Intrusion Penetration
k: Surface absorption/diffusion ($mL/m^2/s$)
S_w: Degree of water saturation
TTT: Two-way-transit-time of radar wave from antenna to the base interface (ns)
Δε': Change of real permittivity at partially saturated state relative to real permittivity at dry state
ΔdB: Change of energy attenuation at partially saturated state relative to energy attenuation at dry state
Δf: Change of peak-frequency at partially saturated state relative to peak-frequency at dry state

Remark: The values of material properties determined in the blue boxes were used in the characterization models constructed in Ch. 10

Fig. 6-4 Schematic Diagram of Hierarchy and Conceptual Data Flow of Different Methods of Data Analysis in Concrete Experiments

A. ASSUMPTION OF OVERALL AND SINGLE DEGREE OF WATER SATURATION AND DETERMINATION OF INTERMEDIATE DEGREE OF WATER SATURATION

The water distribution in each test run was differential along the entire profile of the concrete specimens, in which the distribution consisted of a dry zone, a transition zone and a saturated zone, as depicted in Fig. 6-5.

An overall and single S_w was assumed to represent the differential S_w along the entire profile of concrete at a particular instant, as if it would be essentially representing a homogeneous sample mass with evenly distributed water contents. This overall and single S_w (denoted by S_w afterwards for simplicity) was used to pair with the real permittivity determined from the TTTs which are the ray-path averages of the reflections from the back wall of the concrete specimens.

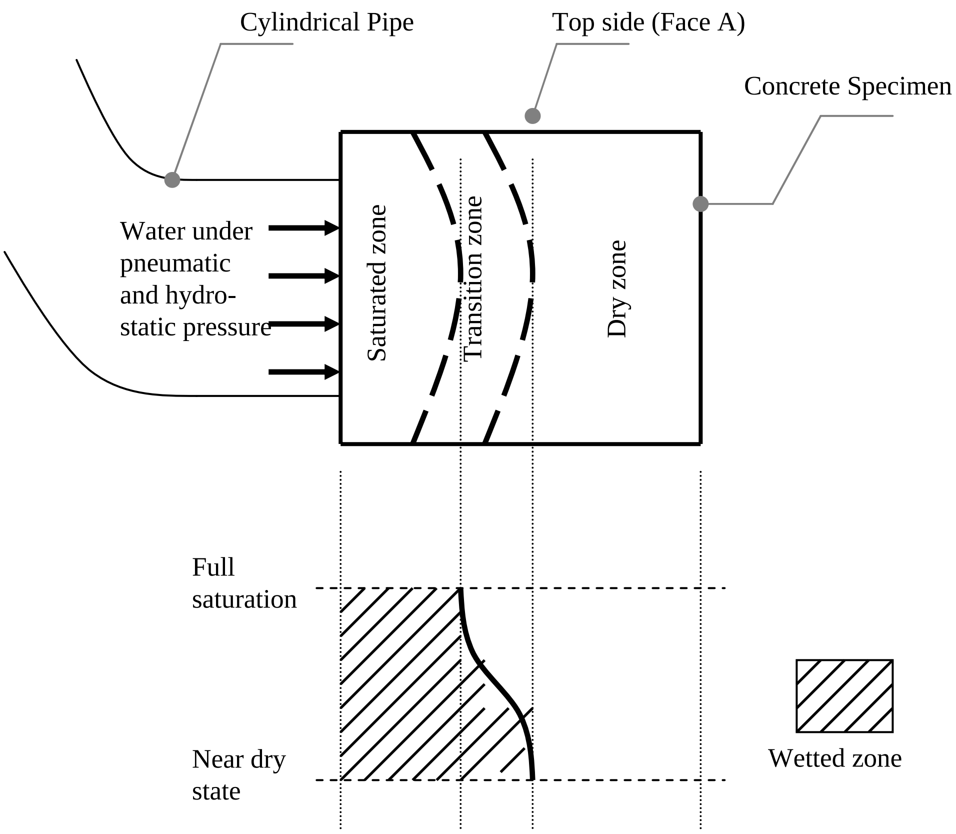

Fig. 6-5 Hypothetical Water Distribution (top) and Saturation Profile (bottom) at Various Points of the Concrete Specimens

The overall and single S_w at any instant of the test runs (or termed as intermediate S_w) was determined by interpolating the initial S_w (i.e. approach to zero) and the final S_w at the end of each test run. This interpolation is determined by the gradual increments of water levels tracked by the graduated marks of the external glass tube taped alongside the cylindrical pipe. An example is shown in Fig. 6-6.

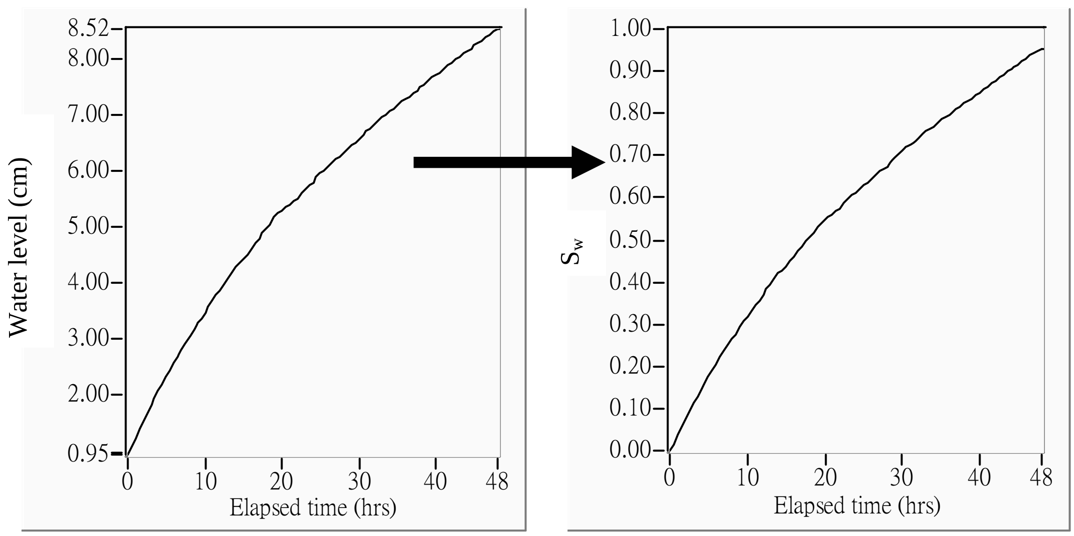

Fig.6-6 Water Level (left) and Degree of Water Saturation (right) against Elapsed Time of each Experiment

The calculation is based on assuming that the reduced water level is proportional to the increased degree of water saturation of concrete specimen.

$$S_{w(\text{int})} = \frac{(WL_{\text{int}} - WL_i)}{(WL_{final} - WL_i)} \times (S_{w(final)} - S_{w(i)}) + S_{w(i)} \text{ ....[6-1]}$$

where

$S_{w(int)}$ = intermediate degree of water saturation

$S_{w(final)}$ = final degree of water saturation

$S_{w(i)}$ = initial degree of water saturation = 0

$WL_{w(int)}$ = intermediate water level

$WL_{(final)}$ = final water level

$WL_{(i)}$ = initial water level

The initial S_w is equal to zero because all specimens were oven-dried before the commencement of each test run, whereas the final S_w of each concrete specimen was determined by the gravimetric method, according to Eq. [6-2]:

$$S_{w(final)} = \frac{(M_{final} - M_{oven-dried})}{(M_{saturate} - M_{oven-dried})} \quad \text{.........[6-2]}$$

where

M_{final} = final mass of specimen after each test run

$M_{oven-dried}$ = initial oven-dried mass of specimen before each test run

$M_{saturate}$ = saturated mass of specimen

B. DETERMINATION OF FREQUENCY SPECTRA AND SPECTRAGRAM

To make the variation of the peak-frequencies immediately apparent, the frequency spectra transformed from the time-domain waveforms obtained in each concrete specimen were stacked and aligned to create sets of so-called *spectragram*. Each spectragram depicts the stacked frequency spectra over elapsed time obtained in each concrete specimen. Over the entire period of elapsed time, the degree of water saturation increases with the continuous permeation of water into the specimen. The peak-frequency drift (Δf) is quantified based on tracking the decreases of the peak-frequency in the spectragram. Fig. 6-7 depicts two spectragrams obtained during the test runs on specimens D1 and D4, which illustrates a drift of peak-frequency over the period of the test run. A full set of these spectragrams obtained from all specimens in all test runs are given in Appendix H1.

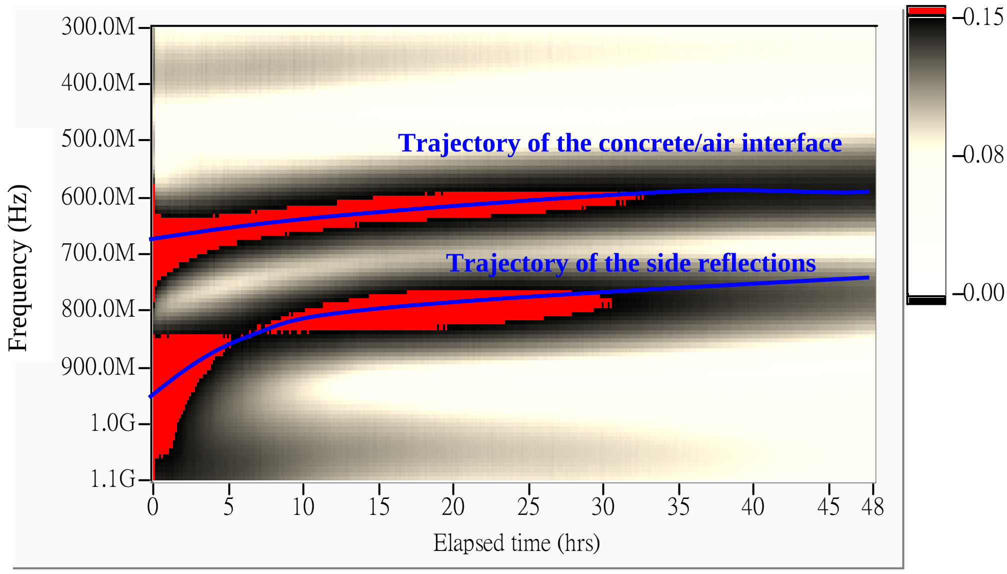

Fig.6-7a Spectragram obtained in Concrete Specimen D4 using 1GHz SPR and processed with a 2GHz Low-pass filter (the width of D4 covered by the antenna is 150mm)

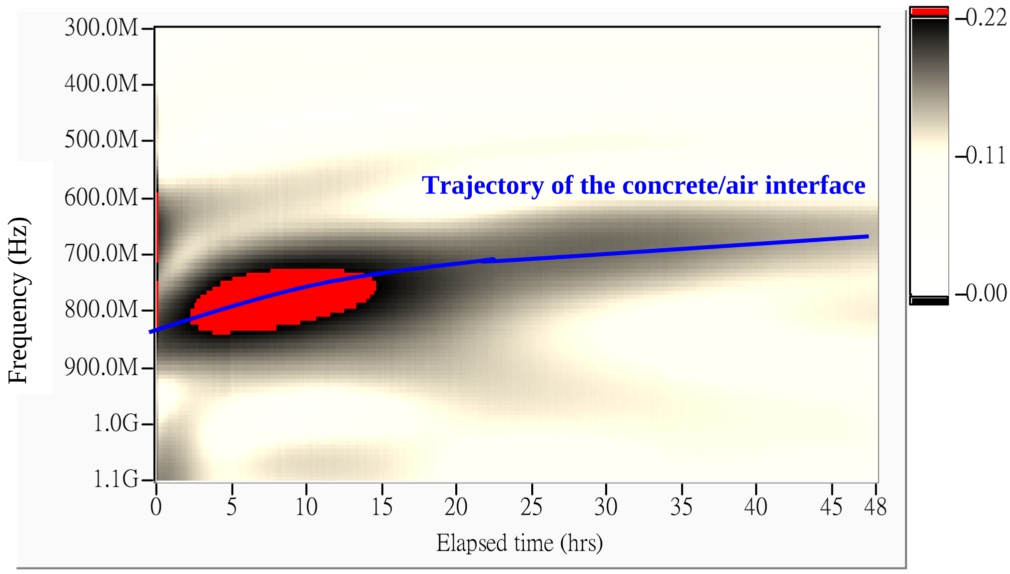

Fig.6-7b Spectragram obtained in Concrete Specimen D1 using 1GHz SPR and processed with a 2GHz Low-pass filter (the width of D1 covered by the antenna is 236mm)

As mentioned earlier in Section 6.2, the boundaries/edge effects picked by the radar antenna were caused by the water column within the cylindrical pipe and the metallic flange. These boundaries/edge effects do not pose any influence on the determination of the Δε' and the ΔdB/m in the time-domain analysis. However in the frequency domain analysis, these effects are apparent for those specimens of width 150mm. This is illustrated in the spectragram obtained from the specimen D4 as depicted in Fig. 6-7a. In this figure, two parallel trajectories are found to progress over the entire period of testing. The trajectory with higher frequency is associated with the side reflections, whilst the one with lower frequency is corresponding to the back wall interface which is the main subject of concern. For the specimens with sufficiently large width (such as specimen D1 of width 236mm depicted in Fig. 6-2e), the effect of the side reflections vanishes and one peak remains, as shown in Fig.6-7b.

6.4.2 FACTOR OF CURING METHODS ON THE CONSTITUTIVE RELATIONSHIPS

In actual construction site practice, doubt remains whether a thorough water/moist curing scheme is implemented on the concrete components by the contractors. For a variety of reasons, it is not unusual to allow the structural concrete members to be exposed to the air (i.e. air-cured) during the early stage after mixing and placing. This air-cured concrete is thus more vulnerable than water/moist cured concrete when they are subjected to external intrusion. However, the appearance of air-cured concrete and water-cured concrete is hardly to be distinguishable to the naked eye.

In this experiment, air-cured specimens (i.e. D1 to D3) were designed to allow the formation and development of the inter-connected capillary pore structure/system in concrete, as discussed in Section 3.2.2.3. This pore structures/systems possessed in the air-cured specimens are more vulnerable to water permeation and more porous than those possessed in the water-cured specimens. This is because these air-cured specimens do not allow for sufficient cement hydration to form enough of solid matrix to fill up the pores at an early age. Hence throughout the first 28 days after the mixing of concrete, the air-cured concrete lost weight and bulk density, as shown in Fig. 6-8. Therefore larger amounts of gel pores and inter-connected capillary pores were formed in air-cured concrete than in water-cured concrete.

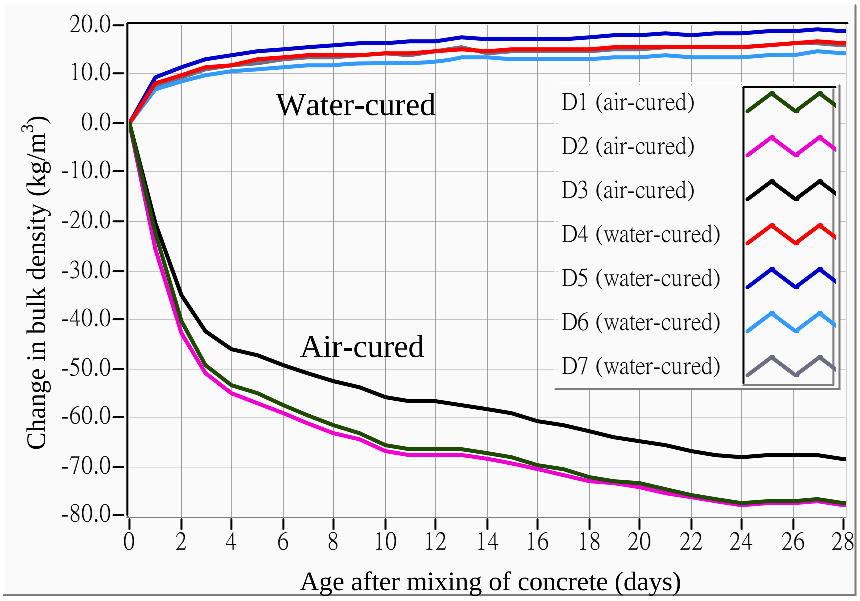

Remark: the definitions of bulk density in air-cured and water-cured concrete are different

Fig. 6-8 Change of Concrete Bulk Density in the First 28 days after Mixing and Placing of Concrete

The Δε', ΔdB/m and Δf caused by increasing water content identified in the air-cured specimens are significantly larger than those attained by other water-cured specimens in D-series, as depicted in Fig. 6-9 to Fig, 6-11. The *transition moisture content* and the *critical* S_w are found to exist in air-cured concrete but not in water-cured concrete (i.e. the specimens D4 to D7), as shown in Fig. 6-9. It is presumably attributed to the fact that air-cured concrete possesses a far greater volumetric fraction of gel pores (less than 2-3nm diameter) and inter-connected capillary pores (median diameter 1.3μm) than water-cured concrete does, as illustrated in the MIP results depicted in Fig. 6-12. These gel pores and inter-connected capillary pores established a pore structure which is similar to that found in soil, as explained in Section 3.2.5.2 and Chapter 8. Further interpretation of the fast-climbing and slow-climbing regions observed in concrete (from Fig. 6-9) and in soil will be jointly elaborated in Section 8.4.2B and Section 10.3.1.

At a higher value of S_w in the plots of ε' vs S_w, the pathways of the curves depicted in the air-cured specimens are very similar to those depicted in Fig. 8-8 and Fig. 8-9 (identified in another series of experiments on soil in Chapter 8), as well as Fig. 3.2-15 by Wang and Schmugge (1980) and Fig.3.2-18 from Knight and Nur (1987a) on sandstone.

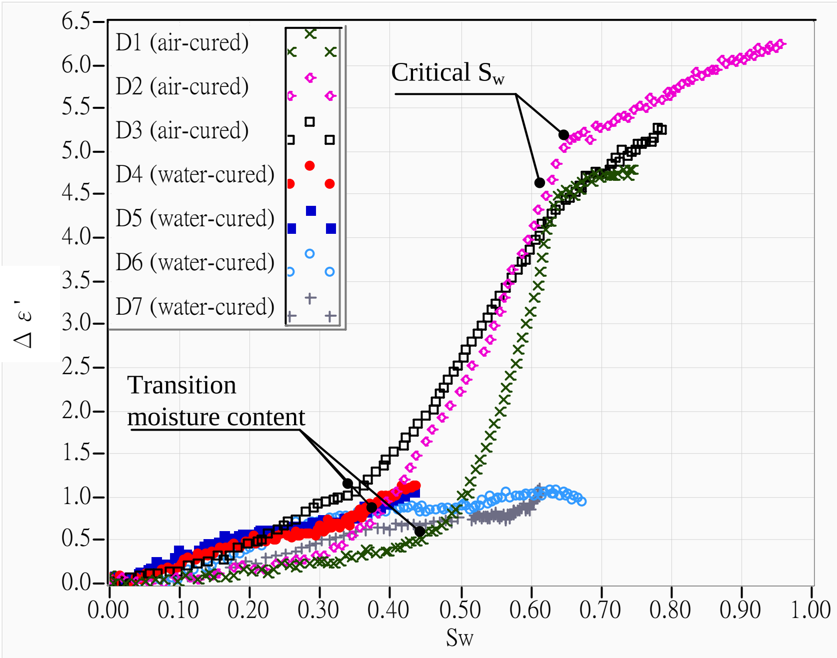

Fig. 6-9 Plots of ε' against S_w using 1GHz SPR on D-series Concrete Specimens

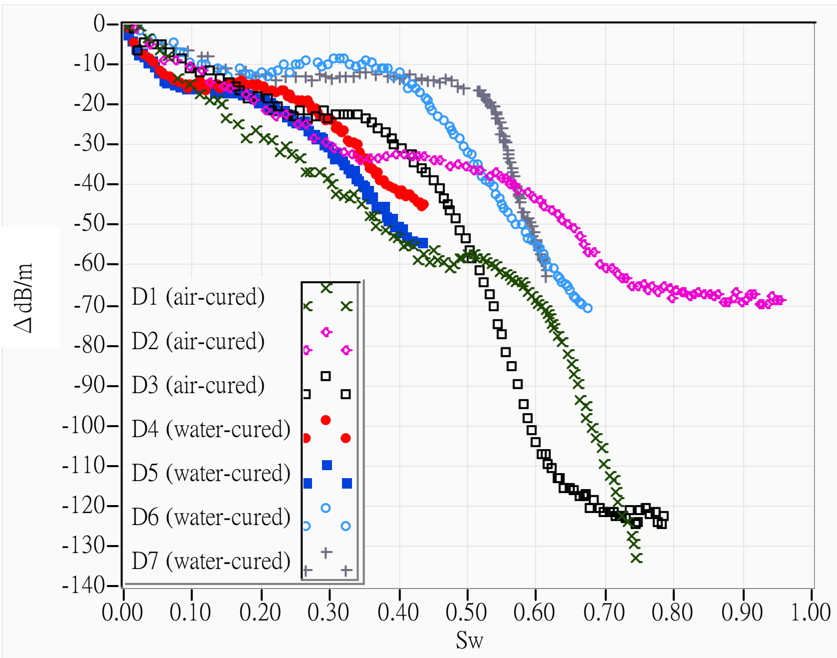

Fig. 6-10 Plots of Energy Attenuation against S_w using 1GHz SPR on D-series Concrete Specimens

Energy was attenuated with increasing S_w, as shown in Fig. 6-10. In this figure, the curves of the air-cured concrete possess both the demarcation points and the correspondent S_w identified in the plots of $\Delta\varepsilon$' and S_w, as shown in Fig. 6-9. This correspondence is possibly attributed to the similar effects of bound water and free water posed on both real permittivity and energy attenuation in concrete, as explained previously. However, a word of caution must be stated that there is no further physical justification to explain this correspondence.

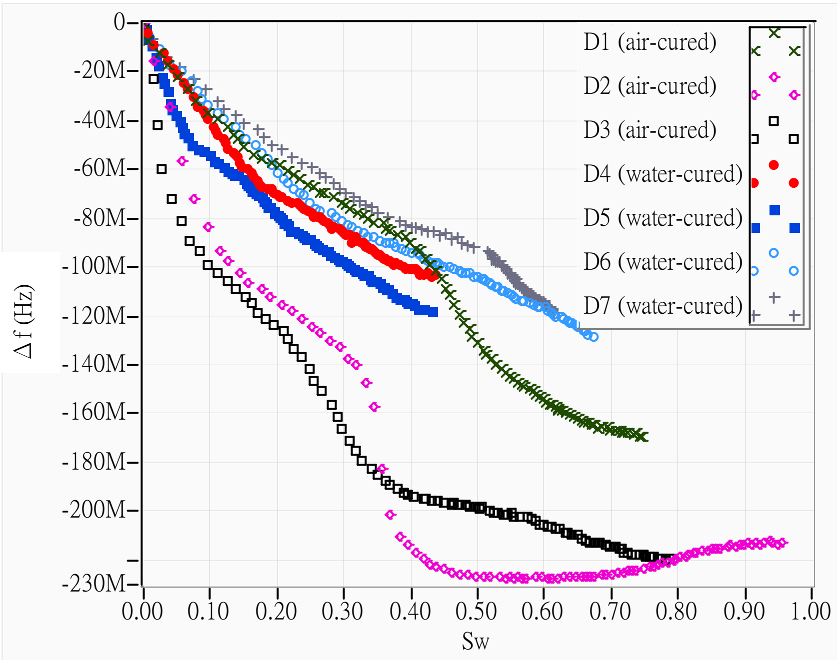

Fig. 6-11 Plots of Peak Frequency against S_w using 1GHz SPR on D-series Concrete Specimens

A larger peak-frequency drift is found with increasing S_w. Also some transitions in these curves were observed. However, these transitions are not as apparent as those identified in ε' vs S_w and dB/m vs S_w. Therefore over-interpretation of these transitions of curvatures should be avoided.

Table 6-3 reports the sets of values obtained from the tests of EM wave properties, porosity, UPV and ISAT. The air-cured specimens possess smaller UPV values (inferring a weaker compressive strength) and faster rates of water absorption in ISAT (inferring a larger permeability) than the water-cured specimens do. These characteristics are attributed to the more porous nature of the air-cured than the water-cured concrete. The results substantiate the findings obtained by the EM wave properties.

Table 6-3 Summary of Real Permittivity, Energy Attenuation and Peak-frequency Drift determined in Different Groups of Curing Methods

Curing history	**Specimen designation**	**EM wave properties determined by SPR**						**Porosity (%) measured by**		**S_w after the permeation test runs**	**Ultra- sonic pulse velocity (m/s) at oven-dried state (Grade) ****	**ISAT values (mL/m^2/s) at 10 min (Grade) *****
		Real permittivity		**Signal attenuation (dB)**		**Peak frequency (MHz)**						
		at oven-dried state	after the test runs	at oven-dried state	after the test runs	at oven-dried state	after the test runs	**Gravimetric method**	**MIP ***			
Air cured	D1	4.1	9	5.4	-15.5	825	654	21.0	19.85	0.75	3830 (G)	1.54(H)
	D2	4.0	10.2	6.3	-4.2	731	519	20.8	16.45	0.95	3890 (G)	0.71(H)
	D3	4.0	9.2	7.9	-10.8	746	526	18.9	22.71	0.79	4140 (G)	1.03(H)
Water cured for 28 days	D4	4.5	5.7	5.5	-1.3	684	579	17.1	12.13	0.44	4460 (G)	0.62(H)
	D5	3.9	5.0	6.3	-2.2	695	576	19.9	11.61	0.43	4430 (G)	0.56(H)
	D6	4.0	5.1	7.6	-3.3	672	542	16.6	12.71	0.67	4310 (G)	0.60(H)
	D7	4.0	5.0	8.1	-1.3	680	561	17.3	16.34	0.61	4390 (G)	0.86(H)

* MIP: Mercury Intrusion Porosimetry (measures gel and capillary pores effectively but not macro-pores)

** Grades for ultra-sonic pulse velocity
E: Excellent (Above 4575m/s)
G: Good (3660-4575m/s)
Q: Questionable (3060-3660m/s)
P: Poor (2135-3050m/s)
VP: Very Poor (Below 2135m/s)
(Source: http://www.mint.gov.my/PRODUCTS/BTI/nde/Ndt_Concrete_details.html)

*** Grades for permeability/absorption/diffusion
L: Low permeability/absorption/diffusion (Concrete Society 1987)
A: Average permeability/absorption/diffusion (Concrete Society 1987)
H: High permeability/absorption/diffusion (Concrete Society 1987)
The Initial Surface Absorption Test (ISAT) was carried out according to BS1881:208 1996

Remark: The uncertainty analysis of real permittivity is referred to Appendix K2.

The differences in air-cured and water-cured concrete are revealed according to the overall porosity, as well as the larger contributions of inter-connected capillary and gel pores in air-cured compared to the water-cured specimens. The overall porosity was measured by the gravimetric method and supplemented by the MIP, as reported in Table 6-3, whereas the distribution of capillary, gel and macro-pores was measured and illustrated by the MIP, as shown in Fig. 6-12.

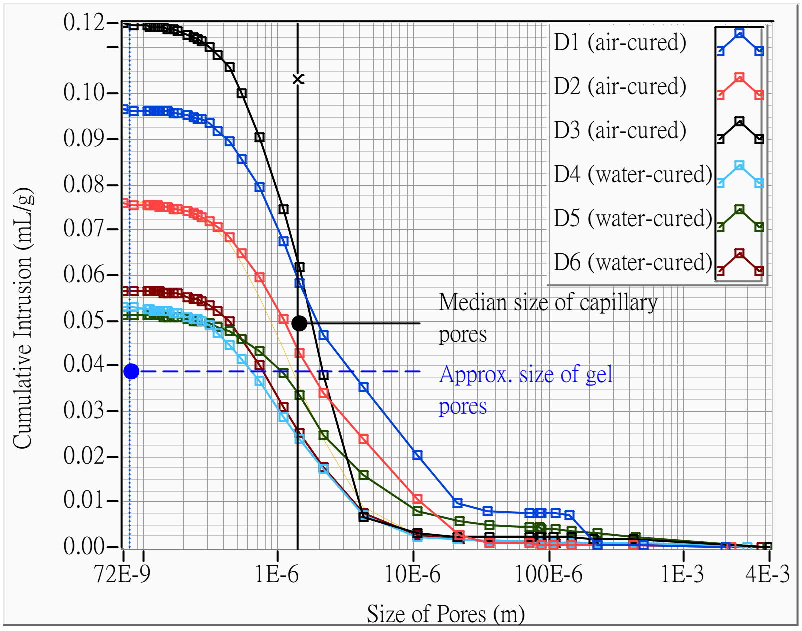

* Size of capillary pore: diameter 1.3μm median size (Glasser, 1992)
** Size of gel pore: less than 2-3nm diameter (Neville, 1995)

Fig. 6-12 Pore Size Distribution of D-series Concrete Cube Specimens Measured by Mercury Intrusion Porosimetry (MIP) Method

The findings in this section have proven that the air-cured concrete possesses the following characteristics of material properties, in comparison to water-cured concrete:

1. more porous (determined by the curves in $\Delta\varepsilon'$ vs S_w, ΔdB/m vs S_w and Δf vs S_w, MIP and gravimetric method),
2. existence of two demarcation points in the plots of $\Delta\varepsilon'$ vs S_w which are similar to those obtained in soil,
3. larger volumetric fraction of gel and capillary pores (determined by MIP),
4. weaker compressive strength (inferred by UPV values), and
5. more permeable (inferred by ISAT values).

The factor of compaction was found not to be an important factor on the two EM wave properties, as well as the results obtained from MIP and gravimetric method, as shown in the specimens D6 and D7. This is because degree of compaction affects the formation of macro-pores/honeycombs only, which are not readily detectable by EM wave properties and the MIP test. However, smaller UPV and larger ISAT values were obtained in specimens D6 and D7 than in specimens D4 and D5, as reported in Table 6-3. It follows that the factor of compaction can be identified under the UPV and ISAT tests, but not the EM wave properties and porosity tests.

6.4.3 FACTORS OF AGGREGATE TO CEMENT (A/C) RATIOS ON THE CONSTITUTIVE RELATIONSHIPS

Concrete with a larger aggregate to cement (A/C) ratio has a smaller value of both the overall porosity and the specific surface than concrete with a smaller A/C ratio does, as reported in Table 3.2.2. This is because aggregate is far less porous than cement gel. In this series of experiments, the designated A/C ratios in the B-series (3:1) and the D-series (4.3:1) are smaller than those in the A-series (6:1) and the C-series (6:1), as reported in Table 6-1. This corresponds to a larger porosity value measured in the B- and D-series than in the A- and C-series, according to the gravimetric and MIP methods which are reported in Table 6-4.

It was found that the B- and the D-series possess larger ranges of $\Delta\varepsilon'$ and ΔdB (but not Δf) than those of the A- and the C-series do, given the same fixed range of S_w (i.e. from zero to unity), as depicted in Fig. 6-9 and Fig. 6-10 respectively. As a result, the curves in the B- and D- series have larger gradients in the plots of ε' and S_w than those in the A- and C-series. According to the Complex Refractive Index Model (CRIM) described in Eq. 2.5-22, a larger gradient in the plots of ε' and S_w implies that the specimens in the B and D-series are more porous than those in the A- and C-series. This observation is also substantiated by the larger values of porosities (determined by the gravimetric method) found in the B- and D-series than in the A- and C-series.

However, the data in the plots of ε' and S_w are found not to conform to the CRIM in general and no sensible porosity can be determined according to Eq. 2.5-22. This is because the CRIM curve possesses an ever-increasing gradient, in which a considerable amount of data shown in Fig. 6-9 does not comply with this essential requirement of CRIM. In the experiments on asphalt and soil described in Chapter 7 and Chapter 8 respectively, the experimental data will be shown to exhibit an increasing gradient along the range of S_w to be fitted in the CRIM. Therefore the values of porosity of asphalt and soil can be determined according to the derivation reported in Eq. [2.5-22].

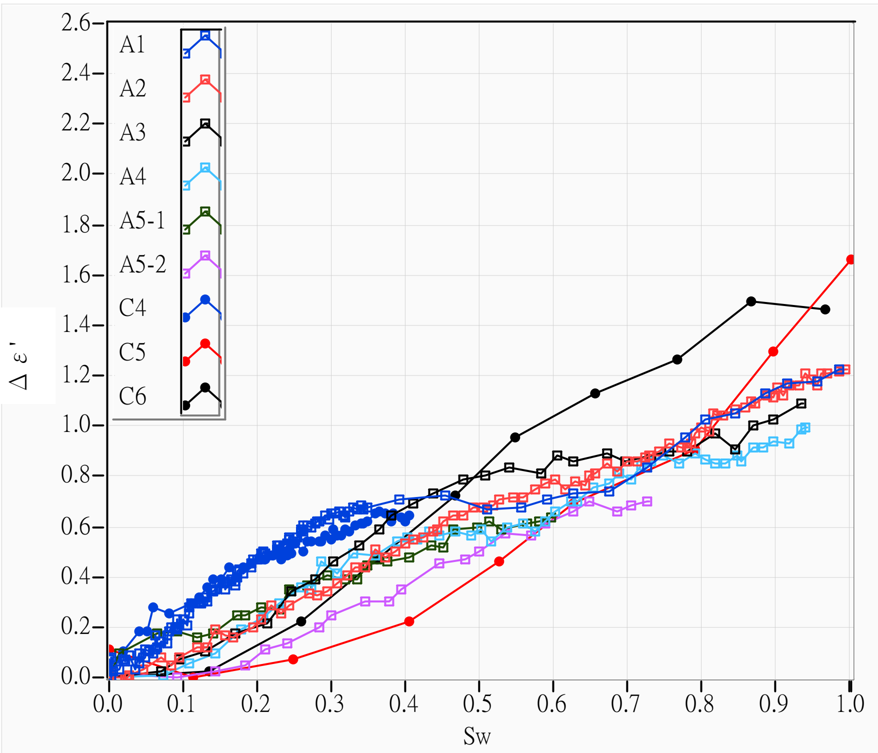

Fig. 6-13a Plots of ε' against S_w using 1GHz SPR on A- and C-series Concrete Specimens

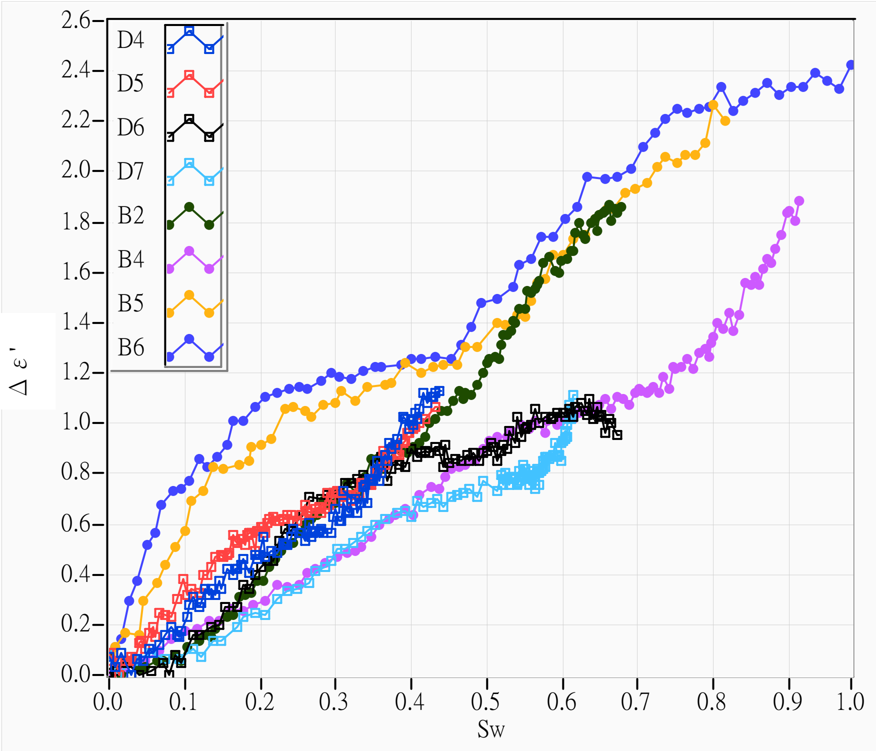

Fig. 6-13b Plots of ε' against S_w using 1GHz SPR on B- and D-series Concrete Specimens

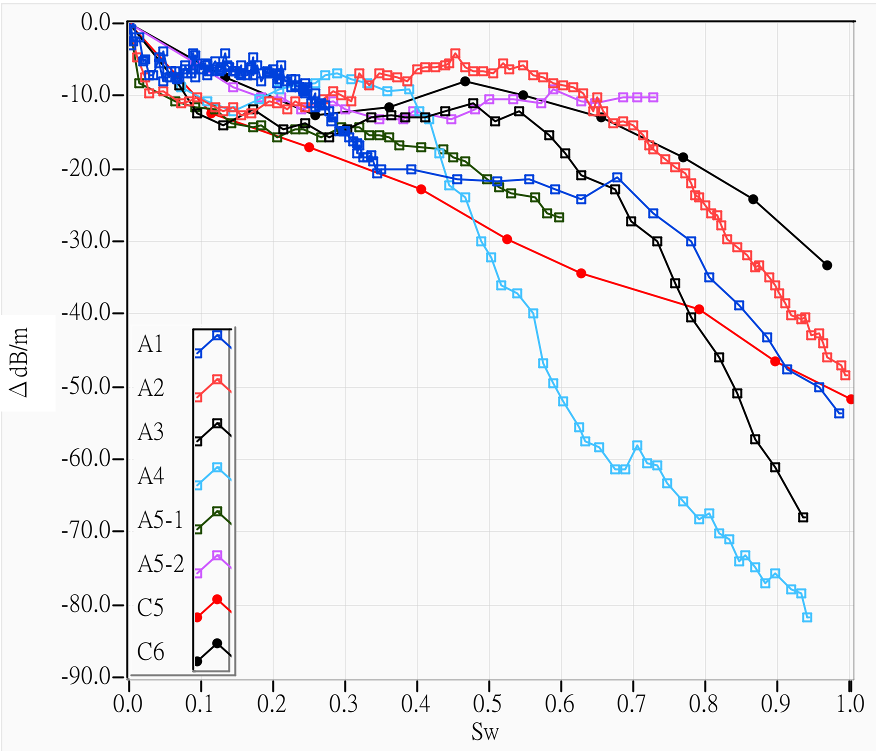

Fig. 6-14a Plots of Energy Attenuations against S_w using 1GHz SPR on A- and C-series Concrete Specimens

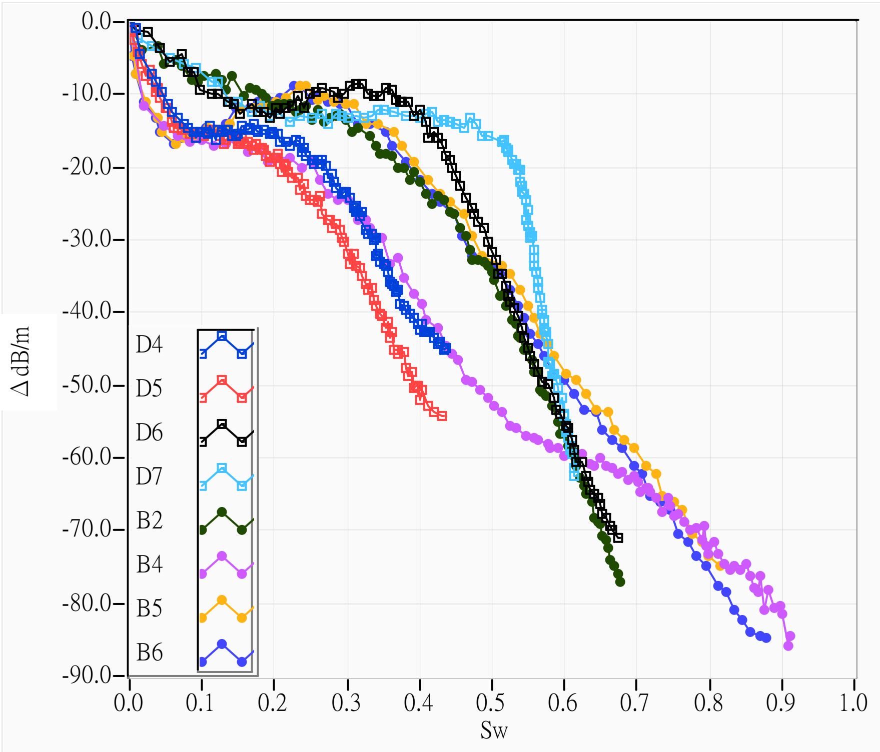

Fig. 6-14b Plots of Energy Attenuations against S_w using 1GHz SPR on B- and D-series Concrete Specimens

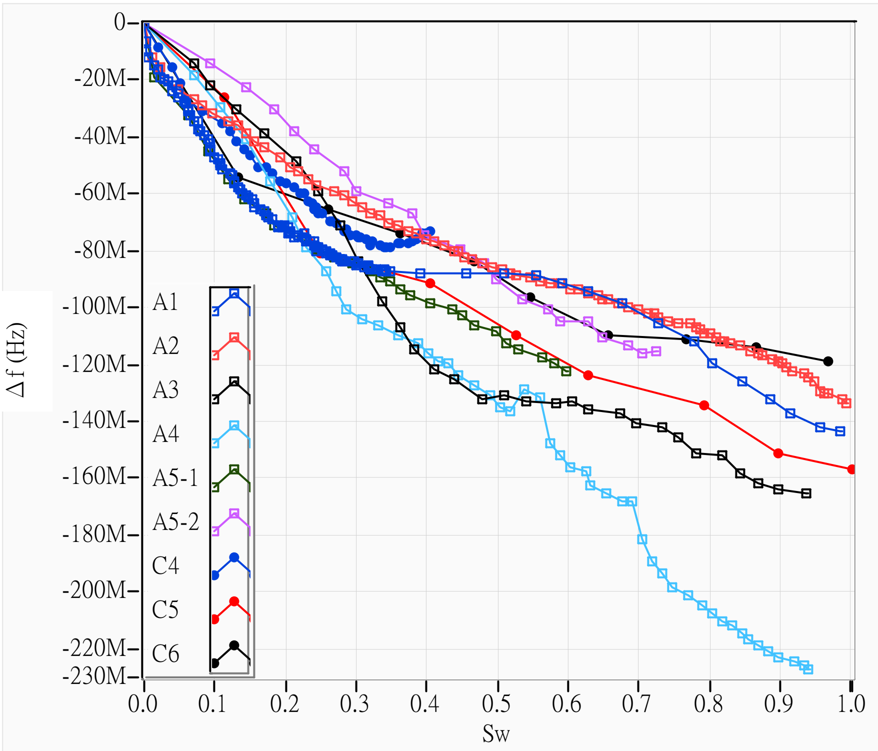

Fig. 6-15a Plots of Peak Frequency against S_w using 1GHz SPR on A- and C-series Concrete Specimens

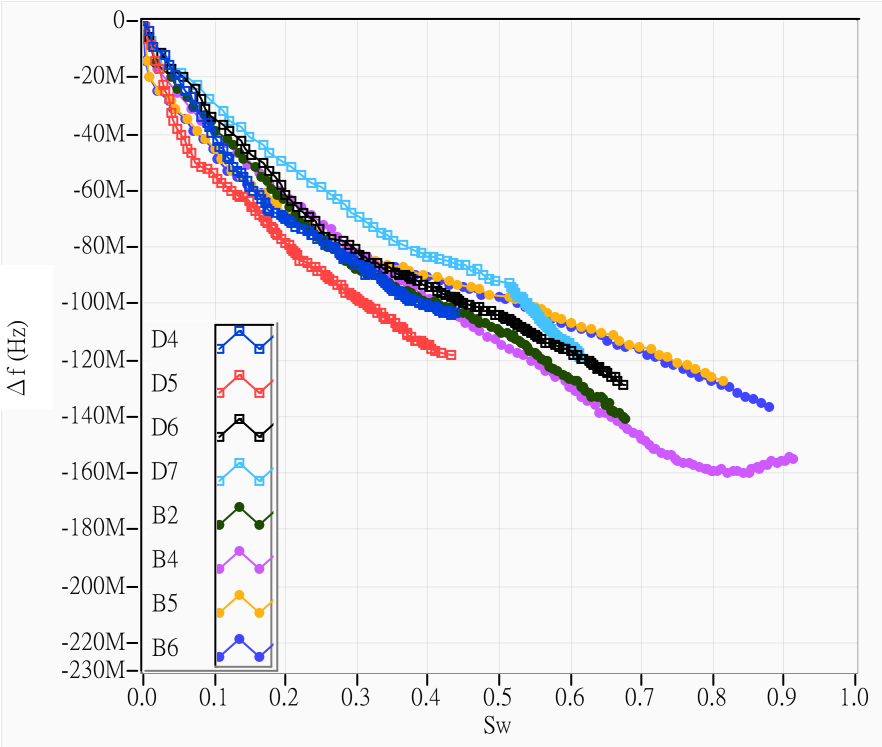

Fig. 6-15b Plots of Peak Frequency against S_w using 1GHz SPR on B- and D-series Concrete Specimens

With increasing S_w for all specimens, the energy attenuations (Fig. 6-14) are larger, whereas the peak frequencies (Fig. 6-15) drift to lower values. In general, the energy attenuations in B- and D-series are larger than those of A- and C-series but this trend is not observable in the drift of peak-frequencies.

Table 6-4 reports the sets of values obtained from the tests of EM wave properties, porosity, UPV and ISAT. The specimens in A- and C-series possess smaller UPV values (inferring a weaker compressive strength) and a faster rate of water absorption in ISAT (inferring a larger permeability) than the B- and D-series.

Table 6-4 Summary of Real Permittivity, Energy Attenuation and Peak-frequency drift detected by SPR on Concrete Specimens of Different Groups of Aggregate to Cement (A/C) Ratios

A/C ratio	Specimen designation *	EM wave properties determined by SPR: Real permittivity		Signal attenuation (dB)		Peak frequency (MHz)		Porosity (%) measured by		S_w after the permeation test runs	Ultra- sonic pulse velocity (m/s) at oven-dried state (Grade) ***	ISAT values (mL/m^2/s) at 10 min (Grade) ****
		at oven-dried state	after the test runs	at oven-dried state	after the test runs	at oven-dried state	after the test runs	Gravimetric method	MIP**			
6:1	A1	4.1	5.3	6.5	-1.6	662	519	13.6	11.48	0.98	2530 (P)	0.94 (H)
	A2	4.1	5.3	5.7	-1.6	655	521	16.3	14.67	0.68	2665 (P)	1.26 (H)
	A3	4.3	5.4	7.5	-2.7	658	492	17.5	17.84	1.00	3100 (Q)	1.4 (H)
	A4	4.2	5.2	7.0	-5.2	658	430	16.8	13.14	0.94	2940 (P)	1.35 (H)
	A5-1	5	5.6	4.7	0.7	654	531	16.6	14.97	0.94	2450 (P)	0.89 (H)
	A5-2	4.4	5.1	8.1	6.1	657	541	15.4	12.76	0.60	2790 (P)	0.74 (H)
6:1	C4	3.7	4.3	4.6	0	694	615	14.2	11.96	0.40	3510 (Q)	0.74(H)
	C5	4.0	5.6	6.7	-1.1	679	522	14.1	10.50	0.98	3380 (Q)	0.68(H)
	C6	3.7	5.2	5.1	0.1	691	572	13.6	10.89	1.00	3295 (Q)	0.59(H)
4.3:1	D4	4.5	5.7	5.5	-1.3	684	579	17.1	12.13	0.44	4460 (G)	0.62(H)
	D5	3.9	5.0	6.3	-2.2	695	576	19.9	11.61	0.43	4430 (G)	0.56(H)
	D6	4.0	5.1	7.6	-3.3	672	542	16.6	12.71	0.67	4310 (G)	0.60(H)
	D7	4.0	5.0	8.1	-1.3	680	561	17.3	16.34	0.61	4390 (G)	0.86(H)
3:1	B2	4.2	6.1	7.0	-5.0	664	522	16.5	13.03	0.68	3750 (G)	0.35(A)
	B4	4.3	6.2	5.5	-7.4	668	513	15.9	12.21	0.96	3440 (Q)	0.34(A)
	B5	4.1	6.4	7.1	-4.2	669	542	17.4	11.80	0.91	3440 (Q)	0.34(A)
	B6	4.1	6.6	7.1	-5.7	669	532	22.0	12.19	0.82	3490 (Q)	0.25(A)

* Specimens B1, C1 to C3 are excluded since the shapes of concrete cannot be formed due to too small a water to cement ratio; No experiment was conducted on cube B3. Specimens D1 to D3 are not included in this table since they were the only air-cured specimens, while all other specimens reported in this table are water-cured.

** MIP: Mercury Intrusion Porosimetry (measures gel and capillary pores effectively but not macro-pores)

*** Grades for Ultra-sonic pulse velocity

E: Excellent (Above 4575m/s)
G: Good (3660-4575m/s)
Q: Questionable (3060-3660m/s)
P: Poor (2135-3050m/s)
VP: Very Poor (Below 2135m/s)
(Source: http://www.mint.gov.my/PRODUCTS/BTI/nde/Ndt_Concrete_details.html)

**** Grades for permeability/absorption/diffusion

L: Low permeability/absorption/diffusion (Concrete Society 1987)
A: Average permeability/absorption/diffusion (Concrete Society 1987)
H: High permeability/absorption/diffusion (Concrete Society 1987)

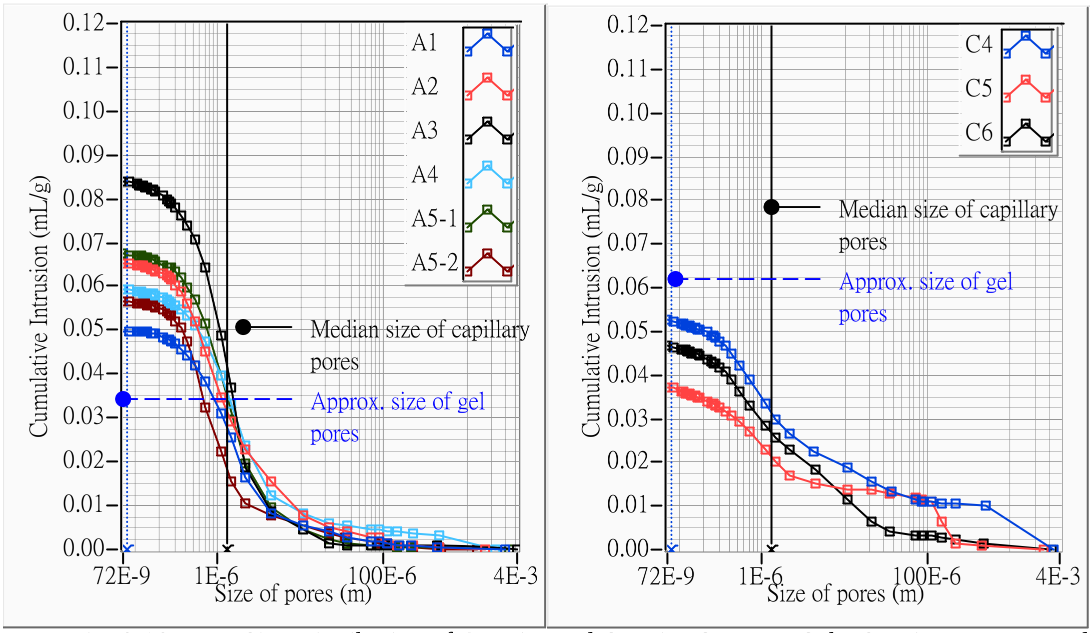

Fig. 6-16a Pore Size Distribution of A-series and C-series Concrete Cube Specimens Measured by Mercury Intrusion Porosimetry (MIP) Method

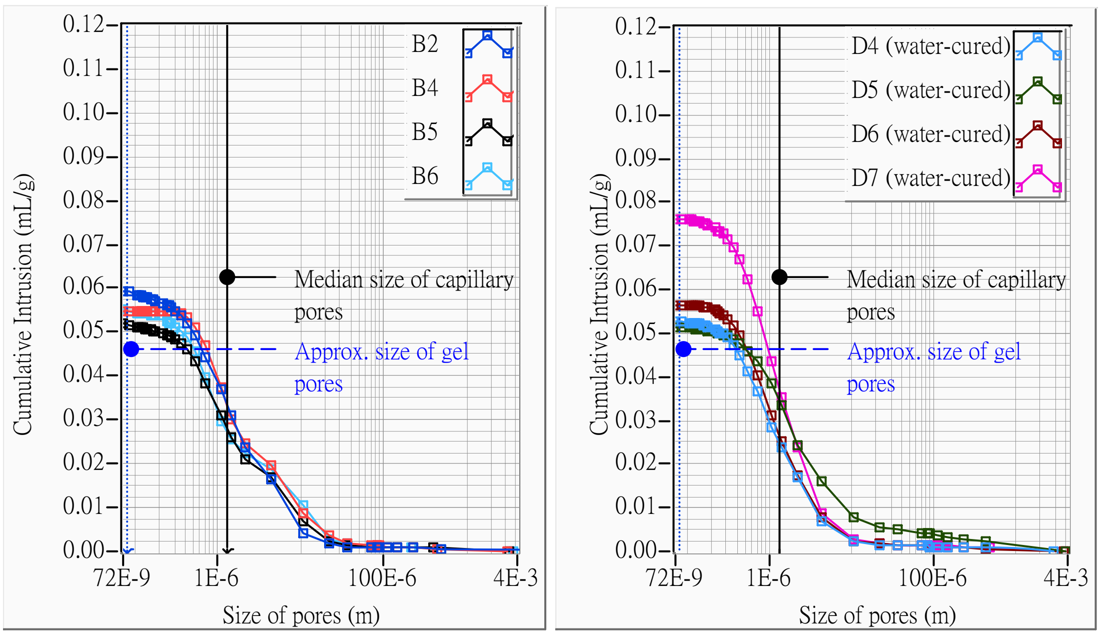

* Size of capillary pore: diameter 1.3μm median size (Glasser, 1992)
** Size of gel pore: less than 2-3nm diameter (Neville, 1995)
*** The figure at the right is the same as Fig.6-10

Fig. 6-16b Pore Size Distribution of B-series and D-series Concrete Specimens Measured by Mercury Intrusion Porosimetry (MIP) Method

The effects of various A/C ratios are reflected in the measurement of the overall porosity using gravimetric method, whereas those of various curing history were revealed by the pore size distribution using the MIP, as depicted in Fig. 6-16. It is also noted that the overall porosity values measured by the gravimetric method are larger (as shown in Fig. 6-17 and Fig. 6-18) and more sensible than that measured by the MIP in general, as reported in Table 6-3 and Table 6-4. This is attributed to the fact that MIP is effective in measuring the very small gel/capillary pores but not the relatively large macro-pores, whilst the gravimetric method determines a single and overall porosity value which covers most sizes of pore. This difference in the functions of these two methods is therefore complementary to each other.

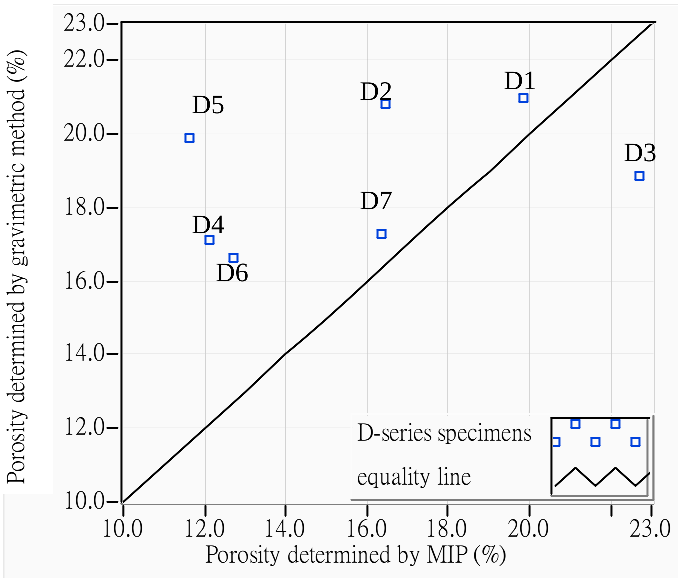

Remark: D1-D3 are air-cured specimens, whereas D4 to D7 are water-cured specimens

Fig. 6-17 Porosity Values determined by Gravimetric Method and Mercury Intrusion Porosimetry in D-series Concrete Specimens

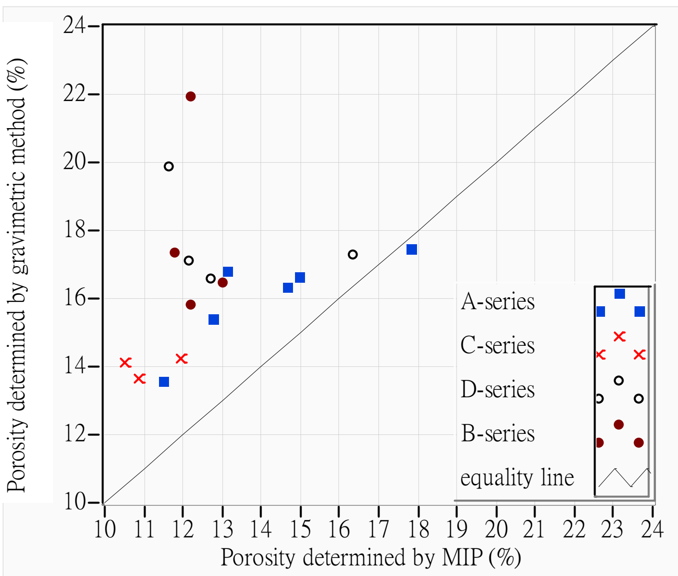

Fig. 6-18 Porosity Values determined by Gravimetric Method and Mercury Intrusion Porosimetry in all-series Specimens

The findings in this section have shown that concrete with a smaller A/C ratio possesses the following characteristics of material properties:

1. more porous (determined by the steeper curves in both $\Delta\varepsilon$' vs S_w and ΔdB/m vs S_w, as well as gravimetric method),
2. larger compressive strength (inferred by UPV values), and
3. less permeable (inferred by ISAT values)

6.4.4 SUMMARY OF FINDINGS

Table 6-5 summarizes the results and remarks qualitatively on the material properties in the respective series of concrete specimens. These properties include:

1. the real permittivity (ε') in the time domain,
2. the energy attenuation (dB/m) in the time domain,
3. the drift of the peak frequency in the frequency spectrum,
4. the porosity,
5. the volumetric fraction of gel and capillary pores in the pore size distribution,
6. the ultra-sonic pulse velocity (UPV), and
7. the initial surface absorption/permeability.

Table 6-5 Comments on the Values of the Measured Material Properties in Different Series of Concrete Specimens

<table>
<tr><th>Speci-men series (A/C ratio)</th><th>The measured material properties</th><th>Δε’</th><th>ΔdB</th><th>Δf</th><th>ϕ (by gravimet-ric method)</th><th>Volumetric fraction of gel and capillary pores (by MIP)</th><th>Grades of UPV</th><th>Surface absorption/ permeability</th></tr>
<tr><td rowspan="2">A (6:1)</td><td>Non compacted group</td><td colspan="2" rowspan="3">Smaller</td><td rowspan="6">Moderate</td><td rowspan="2">Moderate</td><td rowspan="2">The least to moderate</td><td rowspan="2">Poor</td><td rowspan="2">Most permeable</td></tr>
<tr><td>Well compacted group</td></tr>
<tr><td>C (6:1)</td><td>Well compacted and water-cured</td><td>The smallest</td><td>The least</td><td>Fair</td><td rowspan="3">Fairly permeable</td></tr>
<tr><td rowspan="2">D (4.3:1)</td><td>Water-cured group</td><td colspan="2" rowspan="3">Larger</td><td rowspan="3">Larger</td><td rowspan="3">Moderate</td><td rowspan="2">Good</td></tr>
<tr><td>Non compacted group</td></tr>
<tr><td>B (3:1)</td><td>Well compacted and water-cured</td><td>Good to Fair</td><td>Least permeable</td></tr>
<tr><td>D (4.3:1)</td><td>Air-cured group</td><td colspan="5">The largest</td><td>Good</td><td>Most permeable</td></tr>
</table>

ε’: Real permittivity
dB: Energy level
f: Peak frequency
φ: Porosity determined by the MIP and the gravimetric method

Table 6-5 has shown to be very successful in characterizing the concrete specimens treated with different methods of curing and prepared with different aggregate to cement ratios in this series of experiments.

6.5 SUMMARY AND DISCUSSION

This chapter details a series of experiments to characterize the pore structures/systems of concrete by a number of EM wave properties (i.e. $\Delta\varepsilon$', ΔdB/m and Δf) and other physical properties (PSD, porosity, UPV and ISAT), based on well-established methods. The pore structures of these concrete specimens were made to vary by controlling curing history, different aggregate to cement ratios, water to cement ratios and degree of compaction. In this series of experiments, the constitutive relationships between the three coupled pairs of EM wave properties (i.e. $\Delta\varepsilon$' vs S_w, ΔdB/m vs S_w and Δf vs S_w) were determined. These relationships are found to be able to characterize the pore structure of concrete. The most promising characterization is to identify the fast- and slow- climbing regions separated by the two demarcation points in the plots of $\Delta\varepsilon$' vs S_w. These demarcation points are termed *transition moisture content* at low S_w and *critical S_w* at high S_w. These two demarcation points are analogous to those identified in the soils in Chapter 8, and few previous studies on concrete by Soutsos et al. (2001), soil by Wang and Schmugge (1980) and sandstone by Knight and Nur (1987a) discussed in Chapters 2 and 3. Further interpretation of the fast-climbing and slow-climbing regions observed in concrete and in soil will be jointly elaborated in Section 8.4.2 and Section 10.3.1.

Most importantly, the findings reported in this chapter only characterize the effects of those gel pores and inter-connected capillary pores but not the macro-pores (such as honeycombs). It was observed that the measured EM wave properties are functions of curing history and aggregate to cement ratios, but not the water to cement ratios nor degree of compaction. This observation is attributed to the facts that

1. Air-cured concrete has a larger volumetric fraction of gel pores and inter-connected capillary pores than water-cured concrete does, and
2. Concrete with larger aggregate to cement ratios has larger values of porosity and specific surfaces.

The sets of results reported in this chapter provide the unique fingerprints of two characterization models described in Chapter 10 and form a technical basis to investigate real-life concrete components (i.e. walls, slabs and beams) to determine their water content, mix ratio and degree of curing.

7. EXPERIMENTS TO CHARACTERIZE ASPHALT BY DETERMINATION OF THE ELECTROMAGNETIC WAVE PROPERTIES USING THE CYCLIC MOISTURE VARIATION TECHNIQUE (CMVT)

7.1 INTRODUCTION

This chapter devises an experimental technique and results of determination of bulk dielectric properties and porosities within asphalt by Ground Penetrating Radar (GPR) with three different antenna frequencies. The method is based on simultaneous measurement of changes of the real part of complex permittivity (abbreviated as real permittivity/ε'), energy attenuation (expressed in dB/m scale) and peak-frequency drift during cyclic variations of the water content within these materials contained in a large sealed steel tank. A so-called cyclic moisture variation technique (CMVT) subjects these porous materials to a series of changes from partially saturated states to a fully saturated state via cycles of water-permeation and dewatering processes. This CMVT allows the porosities of porous materials (i.e. buried underneath the ground or highway pavements.) to be determined in field conditions with the use of water as an *enhancer* or a *tracer* to allow easy detection and differentiation of amounts of water/moisture in these materials by GPR. The porosity of asphalt can be obtained nondestructively using the CMVT and fitting the data into the Complex Refractive Index Model (CRIM) described in Section 2.5.4B. Two advantages are offered by this method. Firstly, it does not involve disturbance of the test materials associated with the traditional means of laboratory testing methods on cored samples. Secondly, it tests a large amount of material, but not on samples with very small mass extracted from the ground. The latter is usually the case in the traditional laboratory tests and is often shrouded in varying degrees of uncertainty.

7.2 DESIGN AND CONSTRUCTION OF EXPERIMENTAL RIG

The experimental rig consists of a 1.49m cubic metal tank which accommodates different strata/layers of materials as shown in Fig. 7-4. Four pieces of 8mm thick transparent acrylic sheets were placed at the four corners of the metal tank to create four triangular empty spaces at each corner which allowed access to and visual inspection of the material profile (Fig. 7-1 and 7-2). Two strata of asphalt and sub-grade soil (to be investigated in Chapter 8) were constructed as shown in Fig. 7-4. Antenna arrangements during each of the experiments are shown in Fig. 7-3. All the joints of the box were properly sealed to ensure that water did not leak during the experiments.

Fig. 7-1 Overview of the Experimental Rig of Asphalt Pavement Experiment

Fig. 7-2 Water Permeation by Sprinkling at the top in Experiment #1

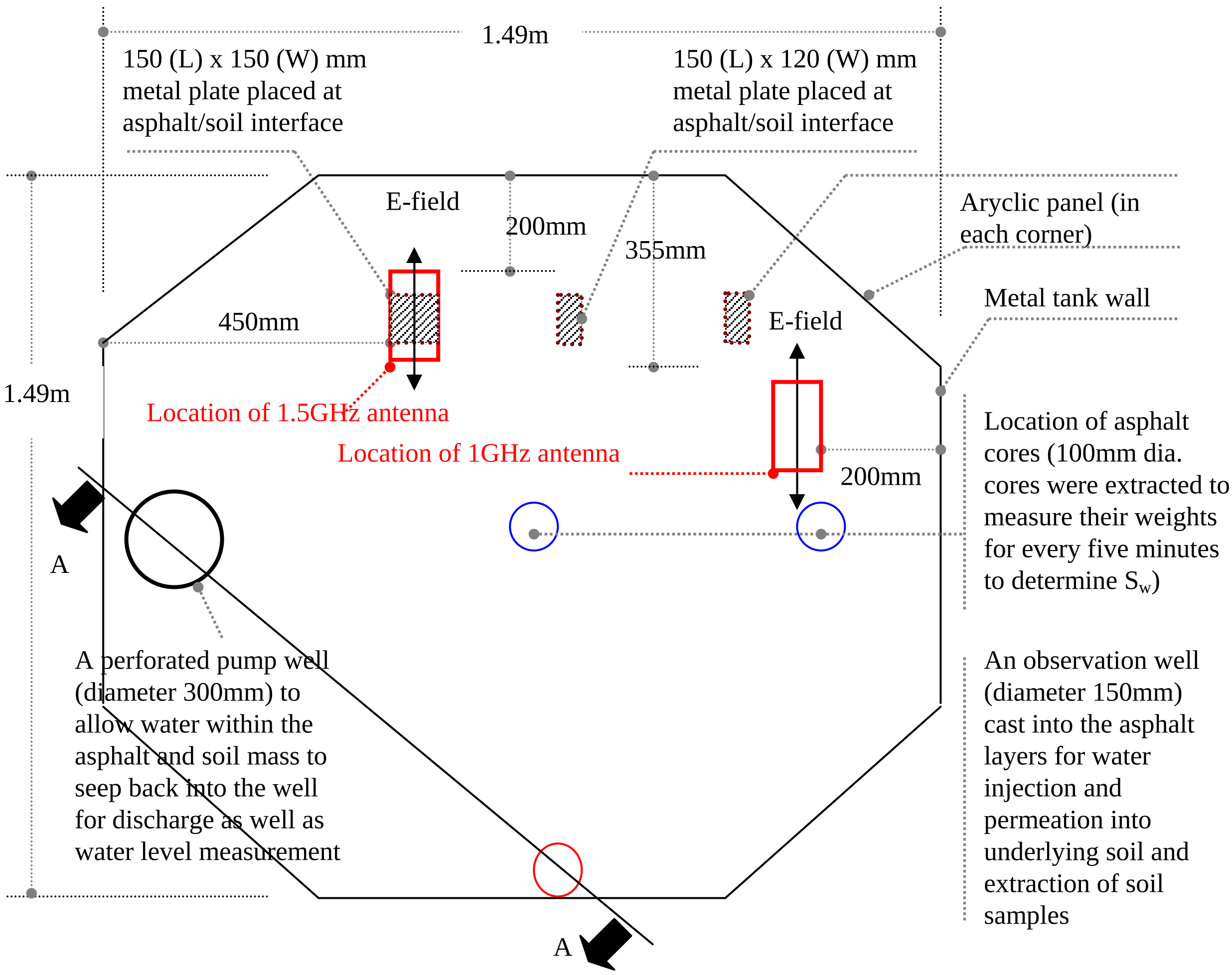

Fig. 7-3a Plan of the Experimental Rig and the Designated Positions of Antennas in Experiment #1

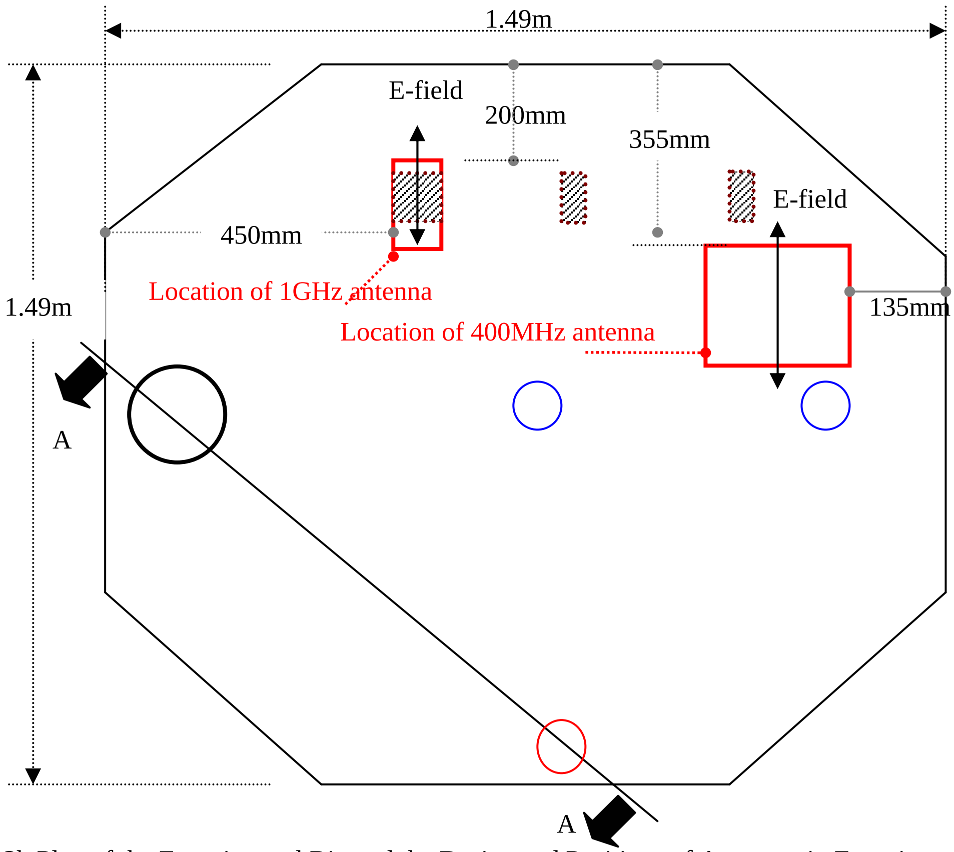

Fig. 7-3b Plan of the Experimental Rig and the Designated Positions of Antennas in Experiment #2 and #3

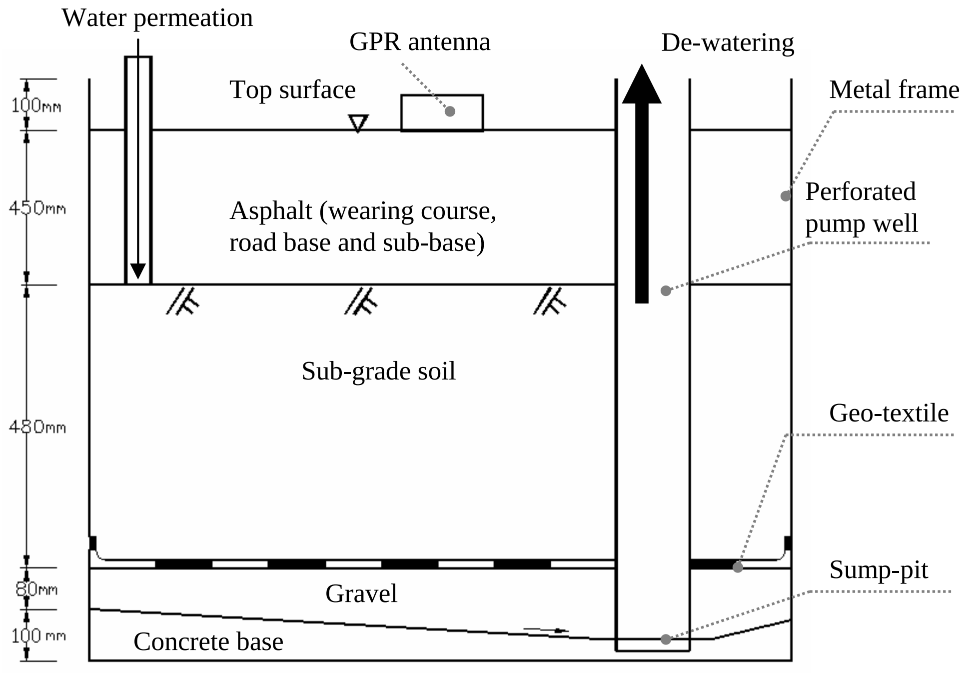

Fig. 7-4 Section A-A of the Asphalt Pavement

A series of three coordinated experiments was conducted according to the arrangement of the radar antennas as listed in Table 7-1 and depicted in Fig. 7-3. The three radar antennas have different depth ranges. For instance, the penetration depth of the 400 MHz antenna is to the bottom of the tank which is about 1.0 metres below the exposed top asphalt surface. Metal plates were also placed at the interface boundaries to help depth calibration.

Table 7-1 Combinations of GPR antennas and the Encompassed Ranges of Material Strata in each Experiment

<table>
<tr><th>Experiment</th><th>400MHz GPR</th><th>1GHz GPR</th><th>1.5GHz GPR</th></tr>
<tr><td>#1</td><td>not used</td><td colspan="2">range encompasses entire depth of top asphalt</td></tr>
<tr><td>#2</td><td rowspan="2">range encompasses entire depth of top asphalt and soil underneath</td><td rowspan="2">range encompasses entire depth of top asphalt</td><td>not used</td></tr>
<tr><td>#3</td><td>not used</td></tr>
</table>

In each experiment, a cyclic variation of moisture content in the asphalt and the sub-grade soil within the tank was carried out in two consecutive stages, i.e. permeation and de-watering stages. In the permeation stage, water was either sprayed on top of the mass at a typical constant rate of 0.06m^3/hr (in experiment #1, as shown in Fig. 7-8), or by direct water injection through a pre-installed tube down to the asphalt/soil interface at two constant rates of $0.098m^3/hr$ and $0.147m^3/hr$ in experiment #2 (as depicted in Fig. 7-9) and #3 (as depicted in Fig. 7-10). After saturation of the entire asphalt and soil mass, the water that seeped out of the mass was collected by the perforated pump well and discharged by pumping. During this de-watering stage, the water table was lowered progressively until the water stopped seeping.

The so-called Two-way transit time (TTT) and changes in water level inside the pump well were monitored frequently (i.e. every five seconds), simultaneously and continuously for up to 13 hours covering both stages in these experiments. TTT is the time required for a radar pulse to travel from the emitting antenna to the reflecting interface and back to the receiving antenna (i.e. traveling back and forth from the asphalt layer).

Two asphalt cores were retrieved and weighed every five minutes to measure their degree of water saturation throughout the experiments. Likewise, soil samples (i.e. the soil texture X described in Chapter 8) were retrieved by a boring auger and weighed to measure the degrees of water saturation (S_w) of these samples at both commencement and completion of each experiment.

Table 7-2 lists the materials incorporated in the fabrication of the model asphalt road section contained in the metal tank. The general practice covering both materials and workmanship of a normal asphalt road’s construction was followed. However, compaction by wheeled rollers cannot be performed due to the relatively small size of the rig. A motorized vibration tamping plate was used as a replacement. For each individual layer reported in Table 2, the material properties (such as porosity) at all locations are assumed not to vary locally since the materials in each layer were from the same origin, same time of placing and the same method of treatment.

Table 7-2 Description of Materials used in the Experimental Rig

Element	Function	Thickness (variation)	Nominal size of aggregate
Wearing course (asphalt)	Provide skid resistance	50mm±2mm	20mm
Road base (asphalt)	Spread loading of vehicle evenly	195mm±2mm	28mm
Sub-base (asphalt)	Spread loading of vehicle evenly	195mm±2mm	40mm
Sub-grade soil (texture X described in Ch.8)	Simulate actual site condition	480mm±2mm	Sandy size (see PSD in Fig. 8-1)
Geo-textile	Avoid clogging of sub-grade to gravel layer	-	-
Gravel	Provide an effective drainage layer	100mm approx.	20mm
Concrete	Provide a laid-to-fall solid base for diversion of water to the sump pit	100mm approx.	20mm

7.3 INSTRUMENTATION AND GPR ANTENNA FREQUENCIES

These experiments have benefited from the use of both the JRC radar system and GSSI radar system with three different operating radar antennae frequencies, i.e. 400MHz, 1GHz and 1.5GHz described in Chapter 4. The data obtained at these three frequencies allow the investigation of dielectric dispersion of asphalt and soil mass at different S_w, as predicted by Debye's (1929) model described in Section 2.5.3, as well as the comparison with the experimental results by Shang and Umana (1999).

A strain-gauge based pressure measuring device was installed inside the perforated pump well. It monitored the change of hydro-static water level throughout the experiments, at the same instant GPR measurements were performed, so that the S_w of the bulk mass at any moment can be estimated in Section 7.4.1. Its calibration detail has been discussed in Section 4.5.

As discussed in Section 3.4.2, the antenna frequency of the GPR is selected by compromising both the acceptable depth of penetration and the acceptable depth resolution as listed in Table 7-3. This table summarizes the velocities of EM wave propagation and the returned nominal peak frequencies of GPR waveforms with different antenna frequencies (i.e. 400 MHz, 1 GHz and 1.5 GHz) in both dry and saturated states. In these experiments, the 1GHz and 1.5GHz GPRs can penetrate the full thickness of the top asphalt layer (i.e. around 440mm) whilst the 400MHz GPR encompassed a depth covering the entire specimen section. The returned radar wave frequency spectra and the returned nominal peak frequencies of the three GPR antenna frequencies were illustrated in Fig. 7-5 (after processing with the five data processing techniques described in Chapter 5) in the dry and the saturated state respectively of the materials tested (i.e. asphalt and soil). In particular, the multiple side lobes found in the 400MHz frequency spectra as shown in Figure 7-5 were caused by the multiple reverberation/ringing effects in the time-domain. These effects are attributed to the limited size of the tank and the large footprints covered by the 400MHz GPR antenna as depicted in Figure 7-3b.

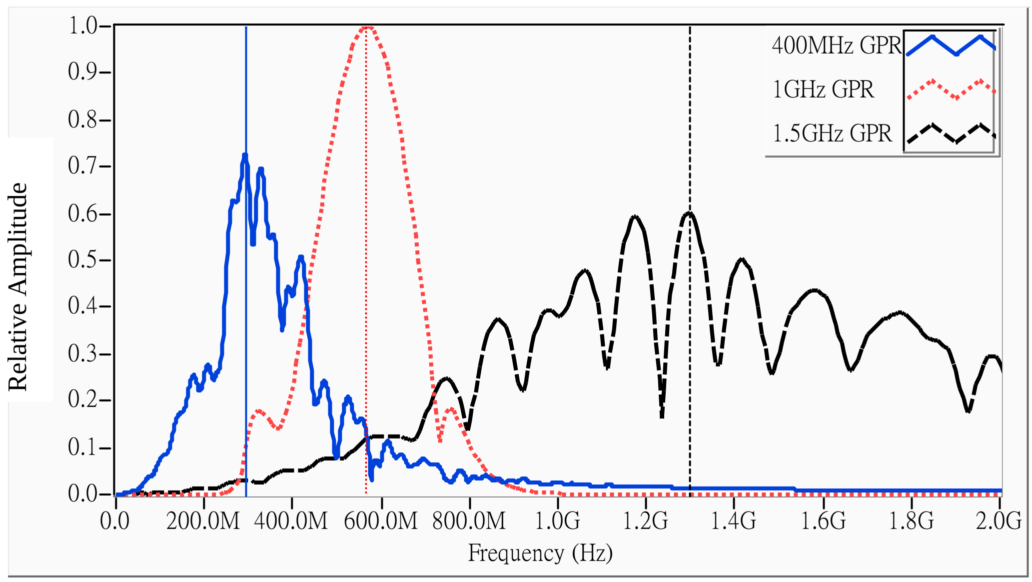

Fig. 7-5a Frequency Spectra of the Returned Radar Wave Signals for 400MHz (with a 250MHz to 450MHz band-pass filter), 1GHz (with a 300MHz to 750MHz band-pass filter) and 1.5GHz (with a 1GHz to 2GHz band-pass filter) Antennae in the Dry State

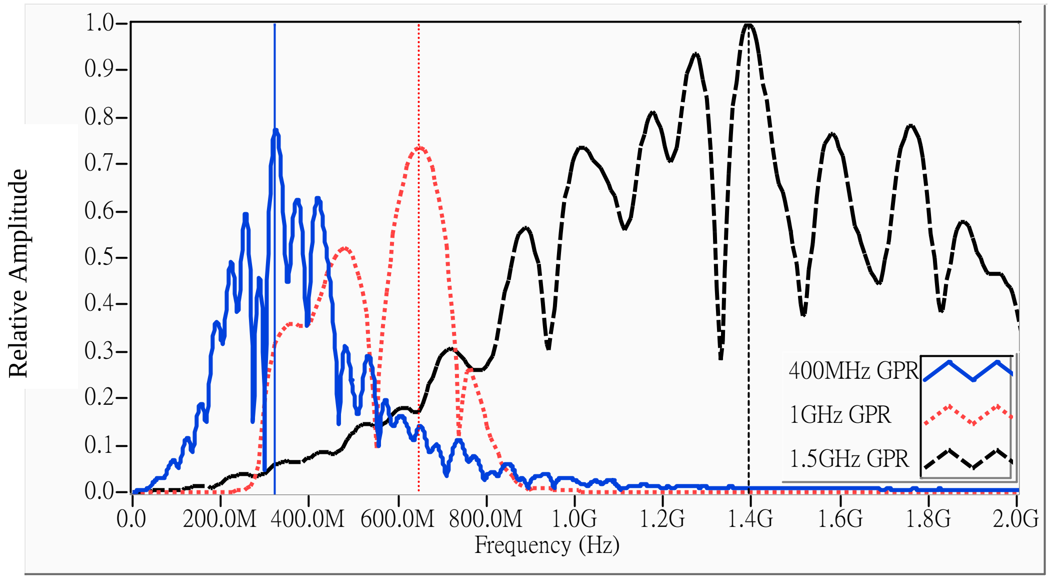

Fig. 7-5b Frequency Spectra of the Returned Radar Wave Signals for 400MHz (with a 250MHz to 450MHz band-pass filter), 1GHz (with a 300MHz to 750MHz band-pass filter) and 1.5GHz (with a 1GHz to 2GHz band-pass filter) Antennae in the Saturated State

According to Table 7-3 and Fig. 7-5, there are two contributing factors to yield better vertical resolution: a larger ε' (i.e. low propagation velocity) and a larger returned centre frequency. For instance in Table 7-3, the depth resolution of 400MHz GPR ranges from 100mm in the dry state to 78mm in the saturated state. When two interfaces (such as the asphalt/soil interface and the rising water table in the experimental rig) are separated within a distance which is no less than the corresponding range of the depth resolution (i.e. 100mm/78mm), the reflections produced by these interfaces appear to mingle together in the waveform/radargram. In other words, these reflections cannot be distinguished by one-quarter of the nominal wavelength corresponding to the nominal frequencies of the GPR antennae.

Table 7-3 Depth Resolutions (calculated according to one-forth of nominal wavelength) obtained in the Dry and Saturated States of Asphalt Specimen

Nominal/centre frequencies of the GPR antennae		**400MHz**	**1GHz**	**1.5GHz**
Dry state	Propagation velocity of GPR wave (v)	0.129 m/ns	0.134 m/ns	0.143 m/ns
	Returned nominal/characteristic peak frequency (determined from the frequency spectrum)	323 MHz	645 MHz	1.39 GHz
	Nominal/characteristic wavelength λ (=v/f)	400mm	208mm	103mm
	Depth resolution (one quarter of λ)	**100mm**	**52mm**	**26mm**
Saturated state	Propagation velocity of GPR wave (v)	0.0916 m/ns	0.117 m/ns	0.121 m/ns
	Returned nominal/characteristic peak frequency (determined from the frequency spectrum)	292MHz	567MHz	1.30 GHz
	Nominal/characteristic wavelength λ (=v/f)	313mm	206mm	92mm
	Depth resolution (one quarter of λ)	**78mm**	**52mm**	**23mm**

7.4 FINDINGS AND DATA ANALYSIS

The schematic diagram depicted in Fig. 7-6 summarizes the hierarchy and conceptual data flow of data analysis described at five different levels.

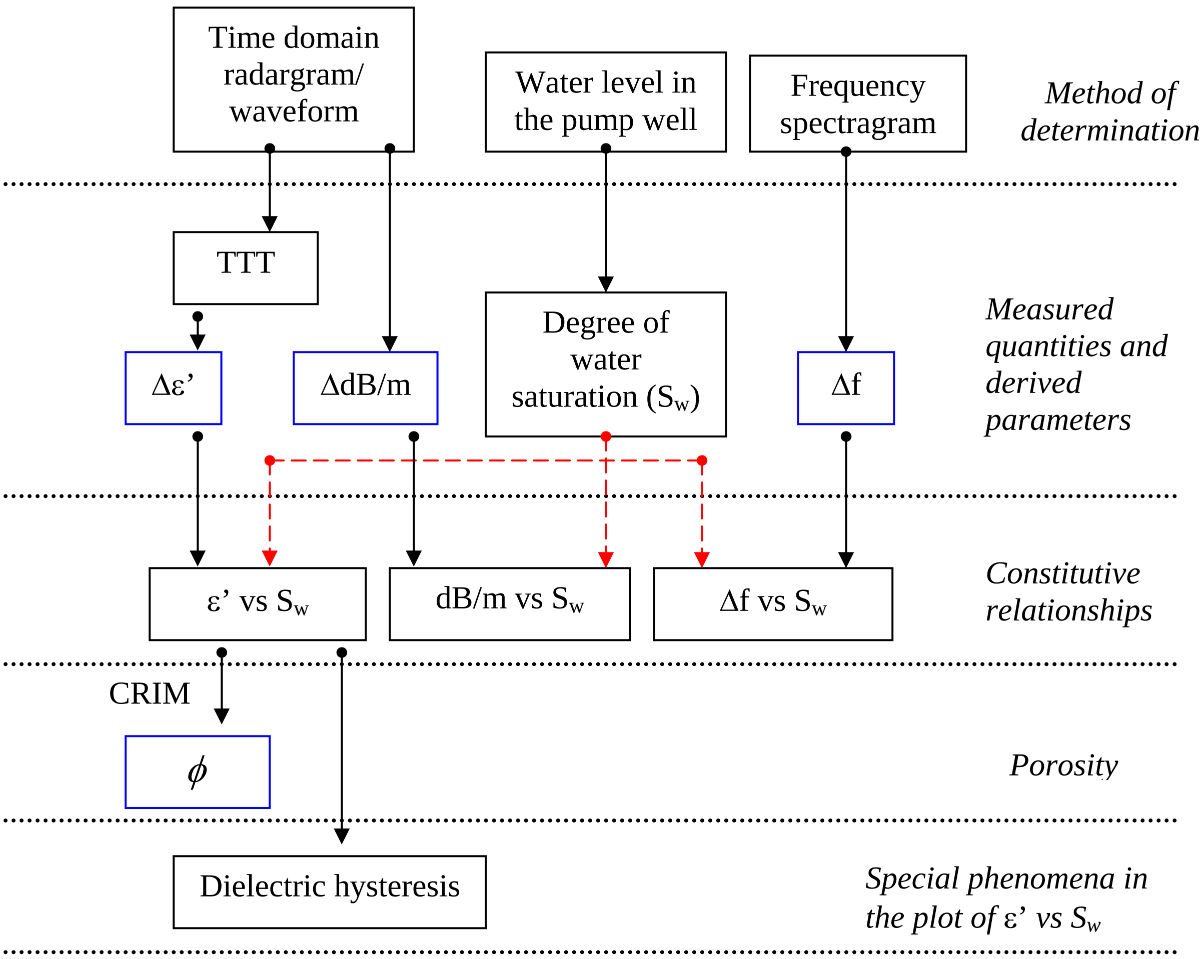

TTT: Two way transit time of radar wave from antenna to the base interface (ns)
ε': Real permittivity (see Section 7.4.3)
dB: Energy attenuation (see Section 7.4.4)
Δf: Change of peak-frequency at partially saturated state relative to peak-frequency at dry state (see Section 7.4.5)
ϕ: Porosity (see Section 7.4.3)
CRIM: Complex Refraction Index Model (see Section 7.4.3)
Remark: The values of material properties determined in the blue boxes were used in the characterization models constructed in Chapter 10

Fig. 7-6 Schematic Diagram of Hierarchy and Conceptual Data Flow of Different Methods of Data Analysis in the Experiments on Asphalt Pavement

7.4.1 ASSUMPTION OF OVERALL AND SINGLE DEGREE OF WATER SATURATION

During the permeation and de-watering processes, the water distribution or the degrees of water saturation were differential along the entire profile of the specimens. This case is different to the homogeneous water distribution found in most previous studies using EMCTL. The entire profile in this experimental setup consisted of a dry zone, a partially saturated zone, a capillary fringe and a fully saturated zone during both the permeation and de-watering stages (Bevan et al. 2003), as depicted in Fig. 7-7. An overall and single S_w was assumed to represent the differential S_w along the entire profile of soil masses at a particular instant, as if it would be essentially representing a homogeneous sample mass with evenly distributed water contents. This overall and single S_w (denoted by S_w afterwards for simplicity) was used to pair with the real permittivity determined from the TTTs which are the ray-path averages of the reflections from the base interface of soil specimens.

During both the permeation and de-watering stages, the intermediate S_w at any moment of the experiments were determined by adopting the methods and equations described in Section 6.4.1A which rely on water level measurement. In this chapter, this measurement is carried out by recording the water levels in the pump well through the strain-gauge based pressure gauge, as described in Section 4.5.

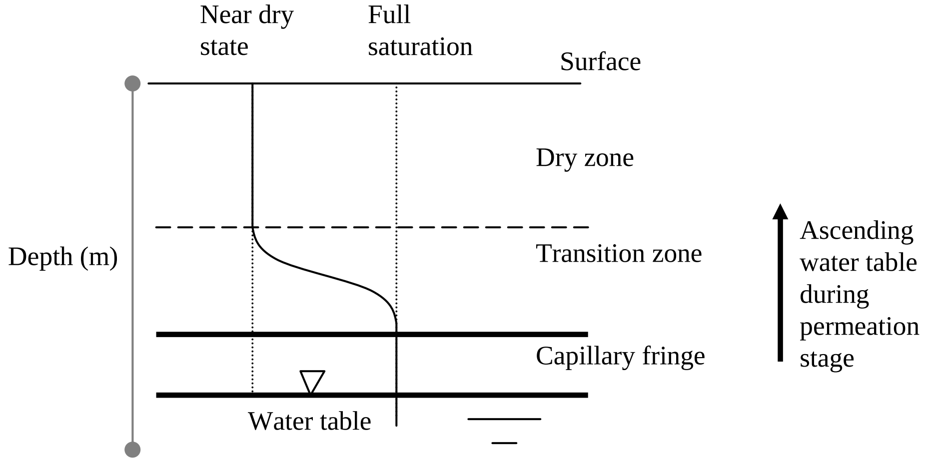

Fig. 7-7a Hypothetical Water Distribution at Various Depths of the Specimen during the Permeation Stages

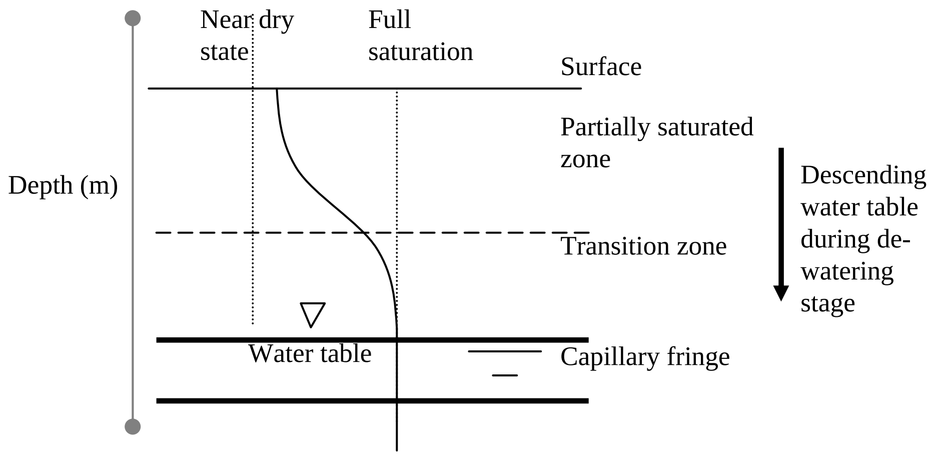

Fig. 7-7b Hypothetical Water Distribution at Various Depths of the Specimen during the De-watering Stages

This assumption of the overall and single S_w was also adopted in the modeling process by Chan and Knight (1999). In this work, a so-called 'global' water content or water saturation was used to model a 'myriad of combinations' of heterogeneous layers, in which there existed different individual water contents and saturations in each layer.

7.4.2 RADARGRAMS

Cyclic variation of moisture content is the essence of the experimental design, in which moisture content was allowed to change at prescribed settings. During the entire CMVT performed in each experiment, radargrams were obtained by stacking and aligning the waveforms to depict the lateral changes of the reflected signals. For example, the radargrams of the 1GHz and 1.5GHz GPR obtained in experiment #1 are shown in Fig. 7-8a and Fig. 7-8b respectively. Hydro-static water head levels in the pump well (i.e. the water table within the mass) are plotted in Fig. 7-8c. Note must be taken that Fig. 7-8a, Fig. 7-8b and Fig. 7-8c have been aligned with the same time axis (i.e. elapsed time) so that the events depicted by the radargrams can be directly correlated with those depicted with the hydro-static water level. The amplitudes of reflection shown in the radargrams (Fig. 7-8a and Fig. 7-8b) are encoded based on the color chart at the upper right corner of each radargram (i.e. from white (positive) to black (negative) respectively).

The three 1GHz radargrams produced in all these experiments are basically presenting similar results, as shown in Fig. 7-8a, Fig. 7-9a and Fig.7-10a. The only exception is the longer or shorter periods of permeation, saturation and de-watering which were dependent on the controlled rate of water permeation and the initial saturation levels of the material.

It is noted that experiment #2 lagged nine days behind experiment #1, and experiment #3 lagged behind experiment #2 by nine hours only. So experiment #2 and #3 can be treated as belonging to the same cycle of CMVT, whilst experiment #1 cannot. Between these experiments, the rig materials (i.e. asphalt and sub-grade soil) were exposed to open air and were subjected to evaporation and drying. The tank materials in experiment #2 were allowed to dry for a far longer period of time (i.e. nine days) compared to the same materials in experiment #3 (i.e. nine hours) before water permeation was started. Due to a greater amount of water retained in the rig materials at the commencement of experiment #3 compared to experiment #1 and #2, the initial S_w values for each of the rig materials in experiment #3 were found to be higher than those found in experiment #1 and #2.

Experiment #1

In the radargrams, the white lines at 6.5ns (as in Fig. 7-8a) and 5.8ns (as in Fig. 7-8b) represent the location of the asphalt/soil interface (i.e. 440mm below the top exposed surface) detected by 1GHz and 1.5GHz GPR. Their locations remained constant from the start, up to 6 hours and 42 minutes; however, their TTT values differ in these GPR frequencies. This discrepancy is a result of the different ε' perceived by the two antenna frequencies as predicted by the dielectric dispersion behaviour in Debye's (1929) model which was discussed in Section 2.5.3. The soil and gravel interface could not be detected as the depth of this interface (i.e. about 1m below the top exposed surface) exceeded the limited depth range of both the 1GHz and 1.5GHz radar systems.

As time progressed and when the water table rose above the asphalt/soil interface (i.e. after 6 hours and 42 minutes), the reflection from the rising water table was clearly observable and was indicated by an inclined white line. Simultaneously, the TTT from the asphalt/soil interface was lengthened continuously until the water level rose to the top, as shown in Fig. 7-8c. After saturation, de-watering started and the entire process was reversed.

Experiment #2 and #3

In Experiment #2 and #3, the 400MHz GPR was used to detect both asphalt/soil interface at about 440mm deep (i.e. reflection amplitude in negative polarity since $\varepsilon_{asphalt} < \varepsilon_{soil}$) and the soil/gravel interface at about 1m deep (i.e. reflection amplitude in negative polarity since $\varepsilon_{concrete\ base} < \varepsilon_{soil}$) as shown in Fig. 7-9 and Fig. 7-10.

For example in the radargrams produced in experiment #2, the white lines at 6.3ns (Fig. 7-9a for 1GHz) and 7.2ns (Fig. 7-9b for 400MHz) represent the location of the asphalt/soil interface. Their location remained constant from the start, up to 1 hour and 39 minutes but with different TTT values. This discrepancy is a result of the different ε' perceived by the two antenna frequencies, as explained previously. As time elapsed and when the water table rose above the asphalt/soil interface (i.e. after 1 hour and 39 minutes), the reflection from the rising water table was identified and was indicated by an inclined white line. Simultaneously, the TTT from the asphalt/soil interface was lengthened continuously until the water level rose to the top, as shown in Fig. 7-9c and Fig. 7-10c.

As shown in Fig. 7-9b, the black line at 19.8ns represents the soil/gravel interface at the bottom of the rig. Its TTT value continued to increase from 19.8ns initially to a maximum value (i.e. 25.3ns) at the saturation stage throughout the entire water permeation process. After saturation, de-watering started and the entire process was reversed.

Experiment #1 (by 1GHz and 1.5GHz antenna, permeation from ground level)

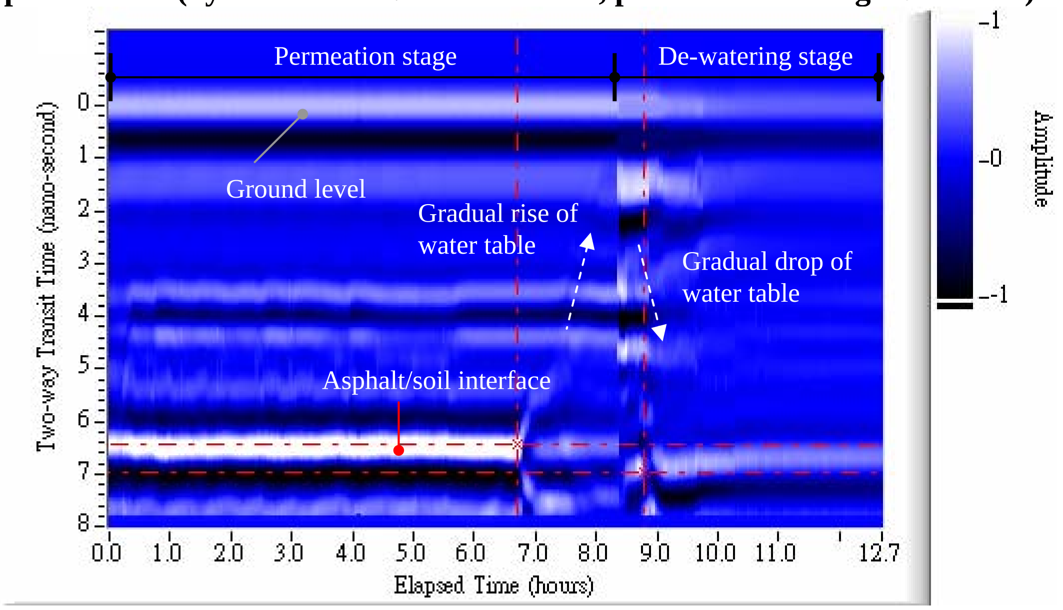

Figure 7-8a Radargram Using 1GHz GPR system obtained at Experiment #1

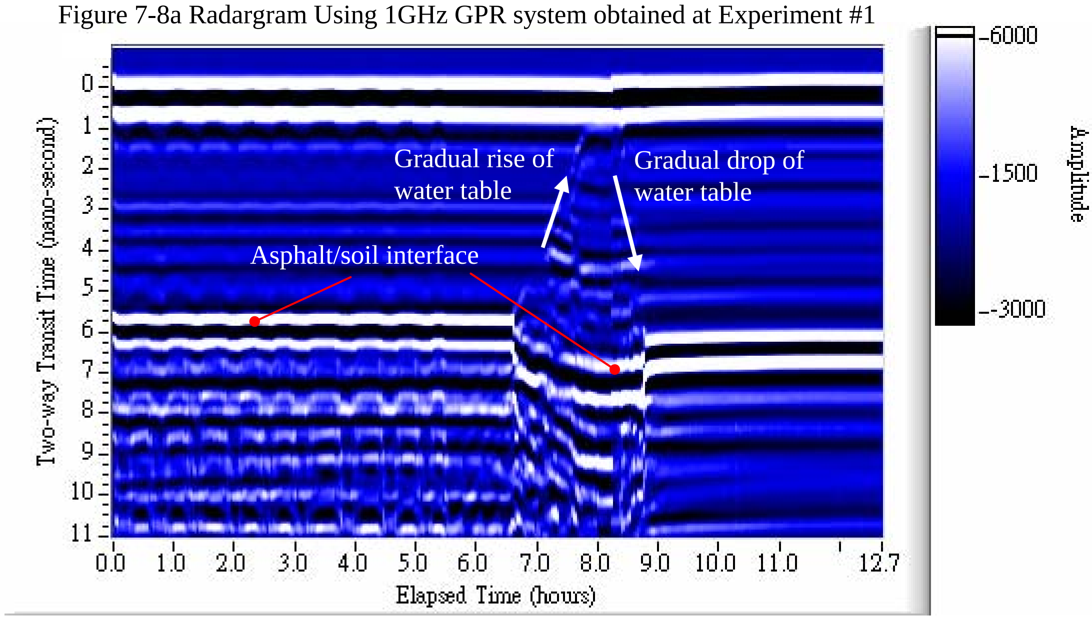

Figure 7-8b Radargram Using 1.5GHz GPR system obtained at Experiment #1

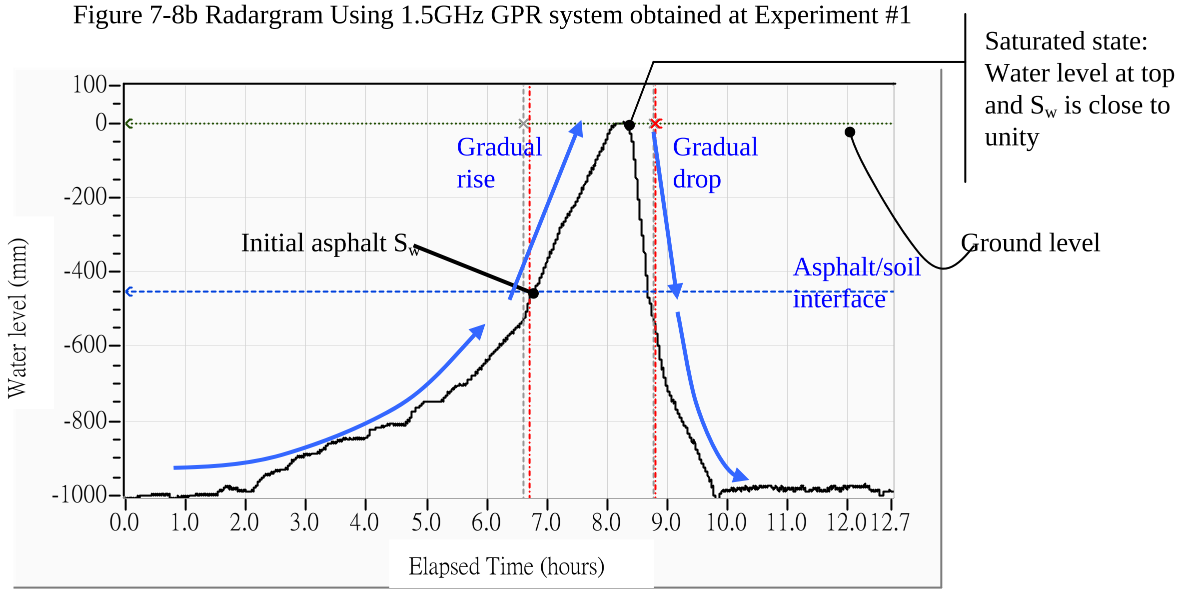

Figure 7-8c Water Level in the Pump Well in Experiment #1
(sprinkling/permeation rate: 0.06 m^3/hour and de-watering rate: 0.24 m^3/hour)

Experiment #2 (by 1GHz and 400MHz antenna, permeation from bore-hole)

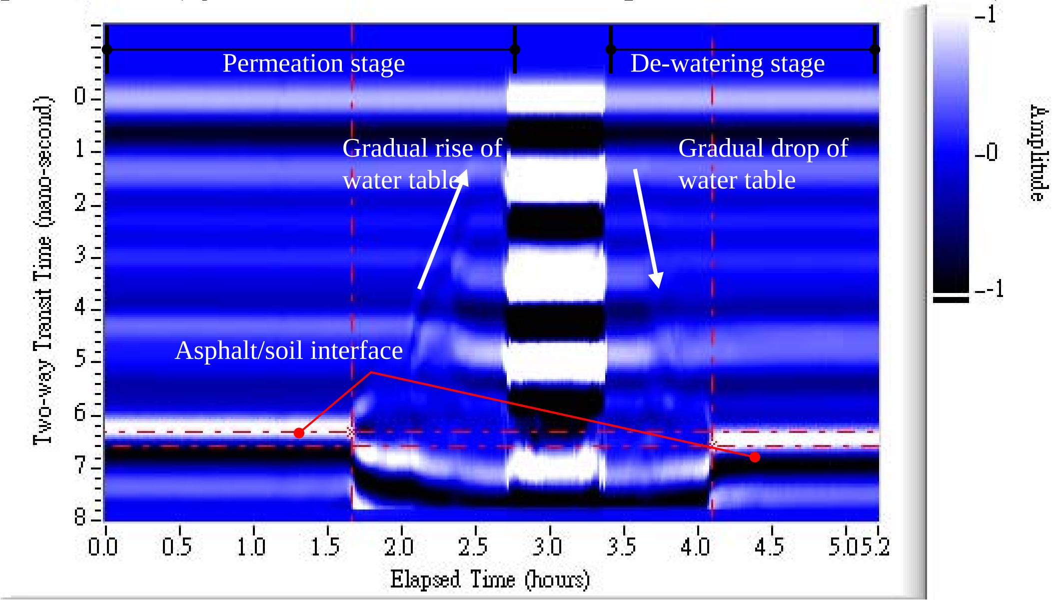

Fig. 7-9a 1GHz GPR Radargram in Experiment #2

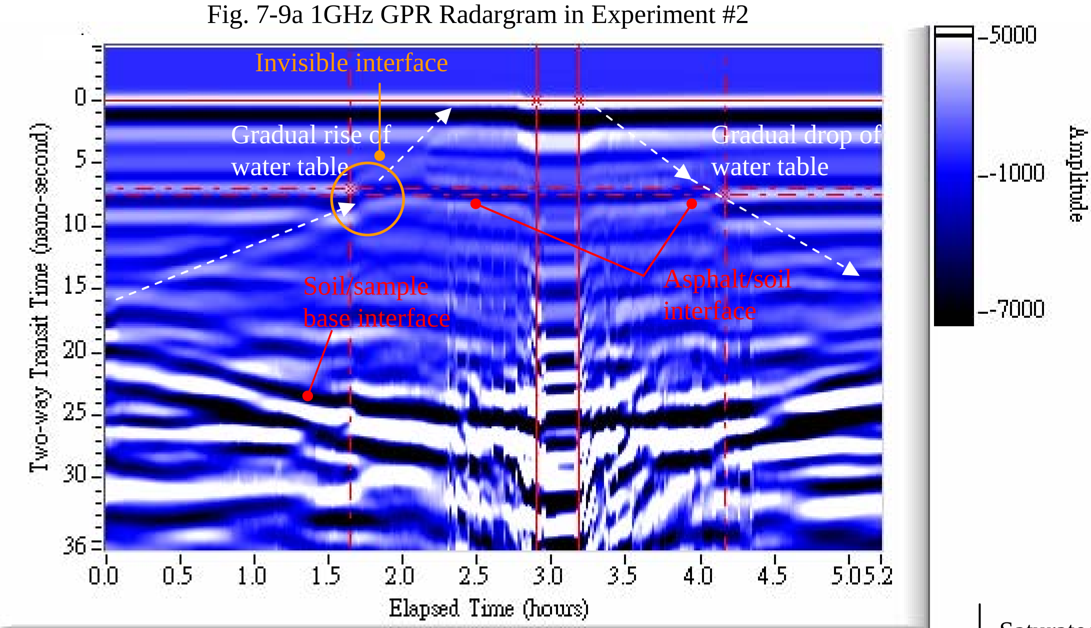

Fig. 7-9b 400MHz GPR Radargram in Experiment #2

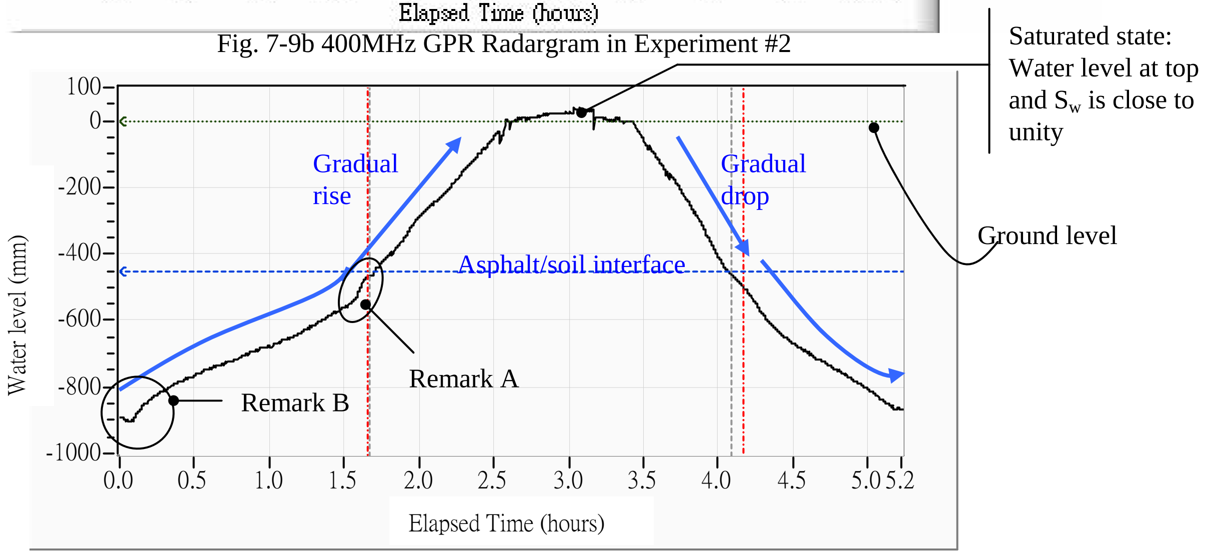

Figure 7-9c Water Level in the Pump Well in Experiment #2

(Water injection/permeation rate: 0.098 m^3/hour and de-watering rate 0.116m^3/hour)

Remark A: Abrupt increase of slope due to much permeable layer due to loose compaction at the asphalt/soil interface;

Remark B: Abrupt increase of slope due to the permeable nature of gravel section at the bottom as shown in Fig. 7-4

Experiment #3 (by 1GHz and 400MHz antenna, percolation from bore-hole)

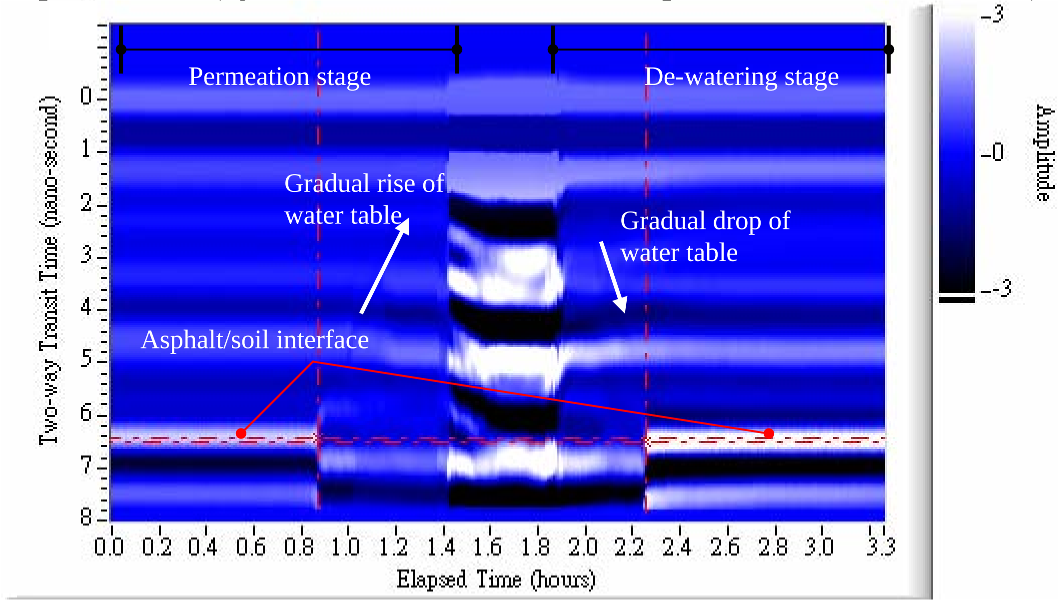

Fig. 7-10a 1GHz GPR Radargram in Experiment #3

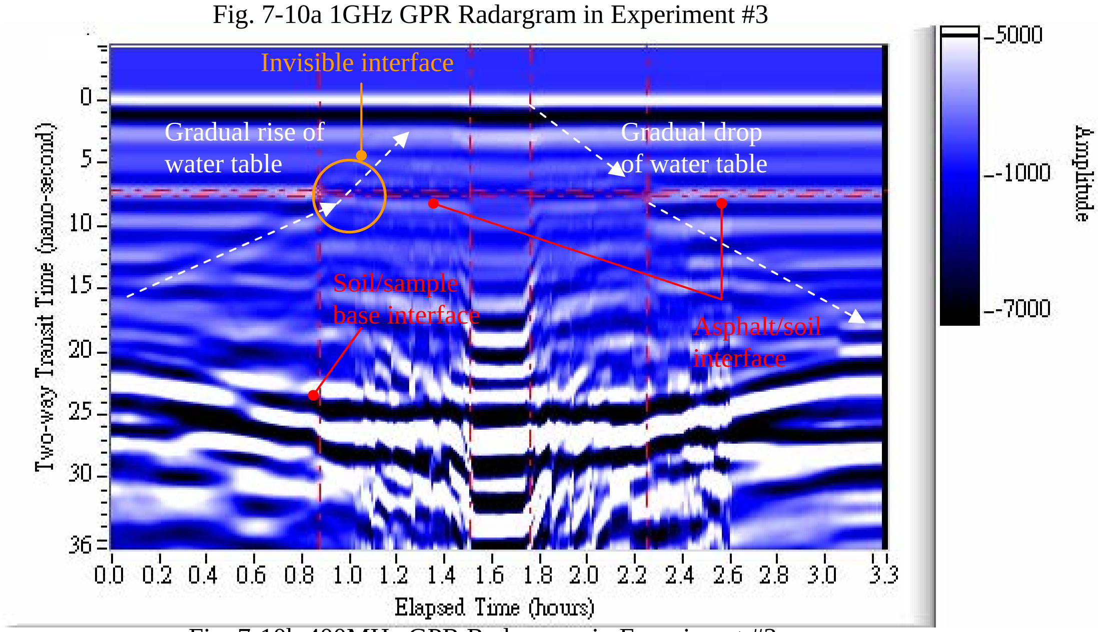

Fig. 7-10b 400MHz GPR Radargram in Experiment #3

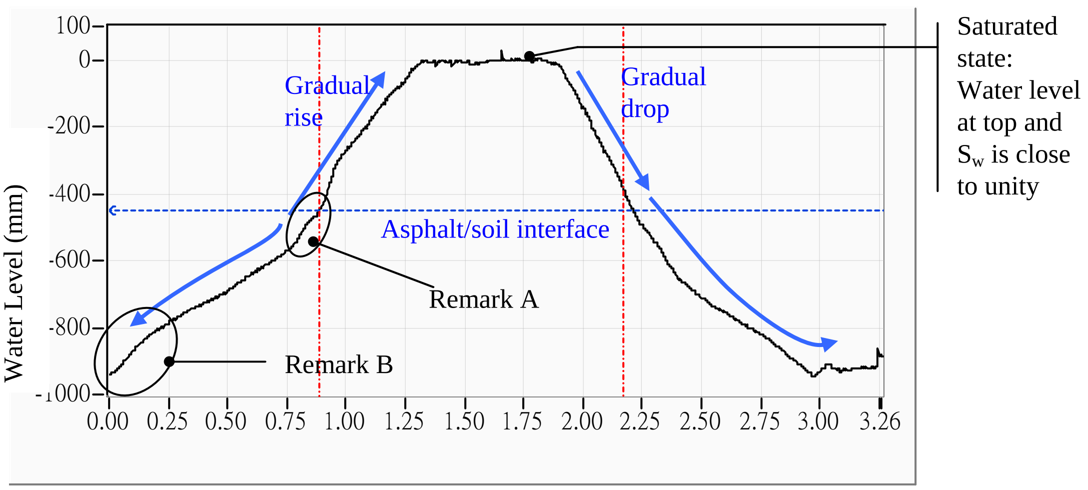

Fig.7-10c Water Level in the Pump Well in Experiment #3

(Water injection/permeation rate: 0.147 m^3/hr and de-watering rate 0.149m^3/hr)

Remark A: Abrupt increase of slope due to much permeable layer due to loose compaction at the asphalt/soil interface;

Remark B: Abrupt increase of slope due to the permeable nature of gravel section at the bottom as shown in Fig. 7-4

In all radargrams, invisible interfaces/dis-continuities of the reflection of asphalt/soil interface at the moment of the water table ascending above/descending below the asphalt/soil interface were found solely in the 400MHz radargrams (Fig. 7-9b and Fig. 7-10b). This was due to the smallest frequency which reduced the depth resolution, based on the principle as explained in Table 7-3. In general, there are two contributing factors to yield better depth resolution: higher ε' and higher centre frequency. In experiments #2 and #3 in which the lowest frequency 400MHz GPR was used, the vertical resolution was calculated in theory to range from 68mm at dry state and 77mm at saturated state according to Table 7-3. The reflection from the asphalt/soil interface was therefore not clear enough to be distinguished between the rising water table and the asphalt/sub-grade interface. This phenomenon vanished and therefore the reflections of the asphalt/soil interface became observable after the water table was adequately separated from the asphalt/soil interface.

7.4.3 CONSTITUTIVE RELATIONSHIPS BETWEEN REAL PERMITTIVITY AND DEGREES OF WATER SATURATION

ε' was plotted against S_w for all experiments and all three GPR frequencies, as shown in Fig. 7-11. ε' of a material with a small porosity, such as asphalt, increased smaller than that of a high porosity, such as soil. For highly porous sub-grade soil (i.e. texture X), pores occupy a large fraction of the total volume and the ε' increased from 16 to nearly 30, covering the entire range of S_w as depicted in Fig. 8-8 and Fig. 8-9. The findings of the sub-grade soil are not discussed in this chapter but in Chapter 8.

The data pairs of ε' and S_w at various frequencies were fitted using the CRIM (i.e. Eq. [2.5-21] and Eq. [2.5-22]) to obtain the values of porosity which governs the gradient of the CRIM's curve as shown in Fig. 7-11. These values were determined according to the coefficients of the second order CRIM equation, in which the process was described in Section 2.5.4B. For a material with a porosity less than 10%, the CRIM curve exhibits itself as a near-straight line. In Fig. 7-11, the determined porosity values from the fitted data at three GPR frequencies are 7.2% (400MHz permeation), 4.3% (400MHz de-watering), 2.3% (1GHz permeation) and 6.5% (1.5GHz permeation) as summarized in Table 7-4. This deviation should be due to the sensitivity of equipment between the JRC and GSSI systems. For the same range of S_w, the GSSI radar system (equipped with 400MHz and 1.5GHz antenna) detects a wider range of ε’, and hence gives a larger curve gradient and a larger porosity than the JRC radar system (equipped with 1GHz antenna) does. The actual porosity determined by gravimetric measurement according to BS EN 12697-8:2003 is 4.1% which is smaller than the values obtained in the GSSI system but larger than the JRC system. The deviation is thought to be caused by the inherent uncertainties exhibited during the CRIM fitting process, such as the selection of exponent 0.5 which assumes isotropic orientation of material packing, as well as geometrical factors, as discussed in Section 2.5.4B. The uncertainty analysis can be referred to Appendix K4.

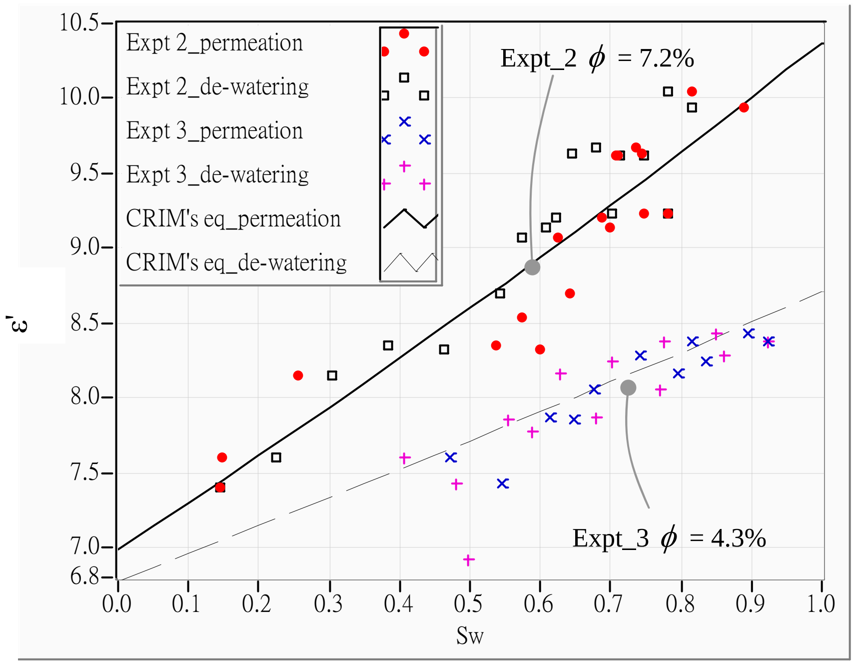

Figure 7-11a Plot of ε’ against Sw in Asphalt using 400MHz GPR

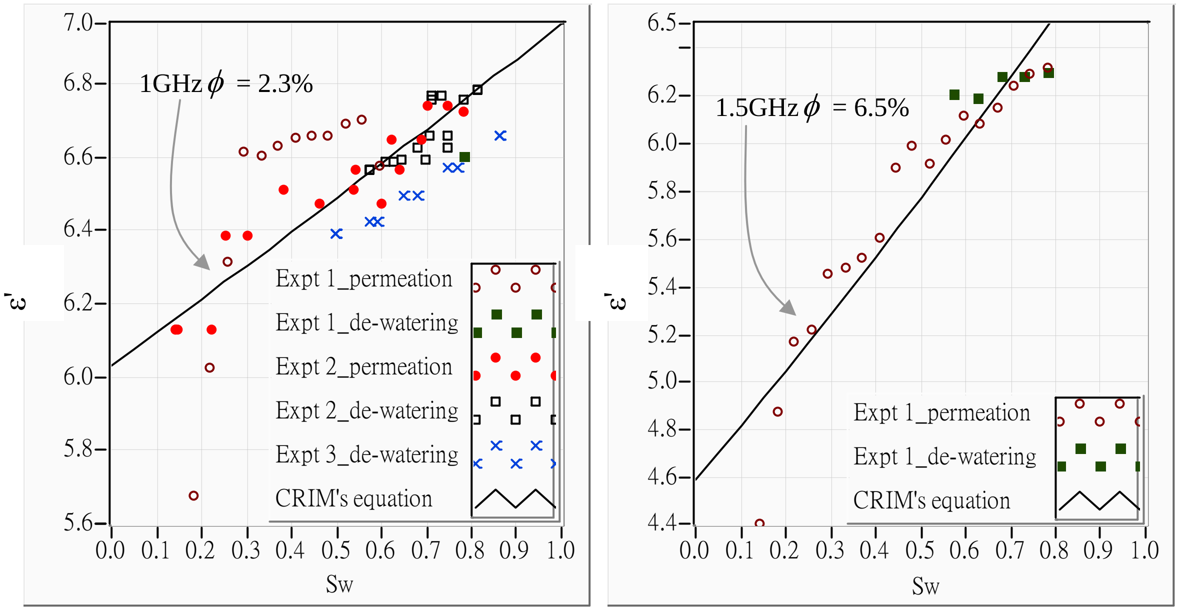

Remark: No data was available for 1GHz GPR in expt #3 at the permeation stage

Figure 7-11b Plot of ε' against Sw in Asphalt using 1GHz (left) and 1.5GHz (right) GPRs

In both experiment #2 and #3, data scattered significantly and logically into three bands of values of ε' according to the adopted GPR centre frequencies. The band at 400MHz possesses the greatest values of ε', followed by the smaller values achieved at 1GHz and the smallest at 1.5GHz. This phenomenon is attributed to the dielectric dispersion along the frequency spectrum depicted in the Debye's (1929) model introduced in Section 2.5.3 or 3.3.3, and is substantiated by the experimental findings reported by Shang and Umana (1999) reported in Section 2.3.

7.4.4 CONSTITUTIVE RELATIONSHIPS BETWEEN ENERGY ATTENUATION AND DEGREES OF WATER SATURATION

Values of reflected amplitudes from the asphalt/soil interface were used to determine the energy attenuation (dB/m) caused by increasing/decreasing S_w within the asphalt layer, using Eq. [5-2] described in Chapter 5. Following the same fashion to couple ε' with S_w described in Section 7.4.3, the values of dB/m were paired with the respective S_w as depicted in Fig. 7-12.

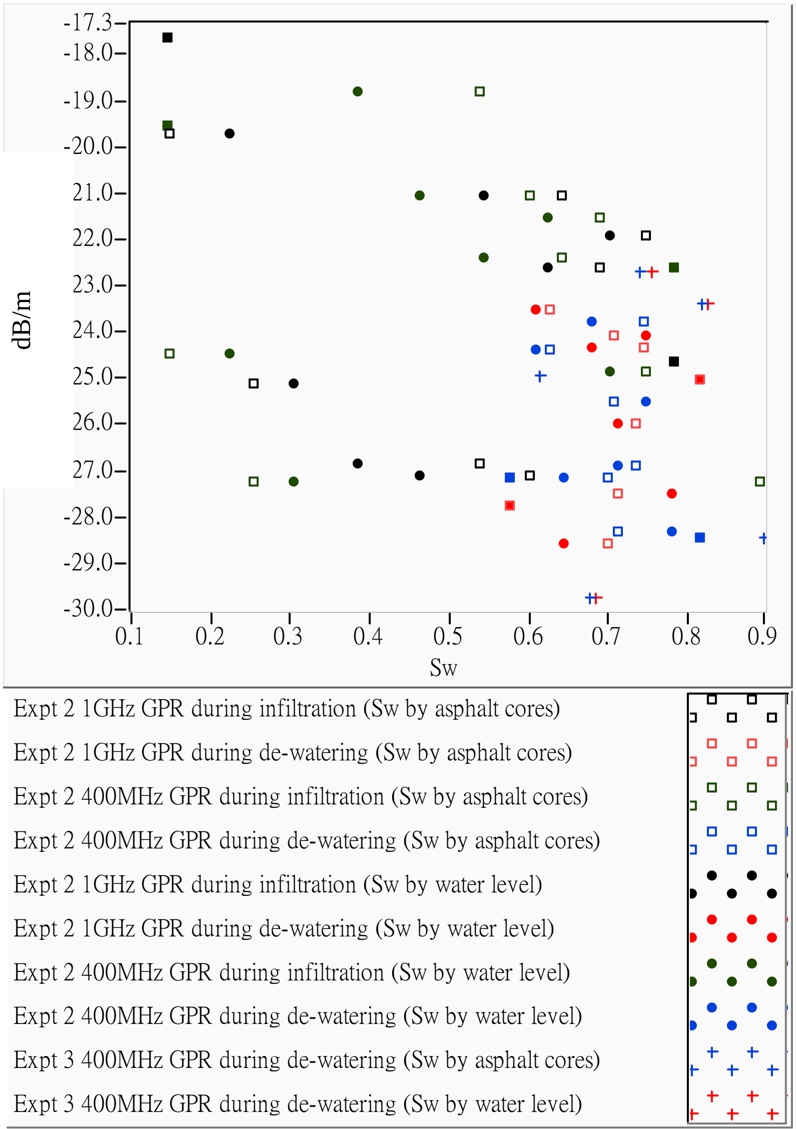

Fig. 7-12 Plot of Energy Attenuation against S_w in Asphalt

The energy attenuation is found to be larger at higher S_w in general because the larger water contents attenuate more reflected strengths than low water contents.

However, the ε' data is not well correlated with S_w data so that the general fitting process is not appropriate. It is considered that the dispersive data are caused by the presence of significant system noise when the amplitudes of the extracted peaks of reflections were determined. This noise is found to produce a fluctuated set of data on the detected energy attenuation (i.e. amplitude of a waveform) as shown in Fig. 7-12 than the detected TTT/ε' (i.e. timing of a waveform) as shown in Fig. 7-11 or the drift of the peak frequencies as depicted in Fig. 7-15.

Despite the values of energy attenuation being more dispersive than that of ε' and peak frequency, the limit can be determined to range from -7.9 to -13.4dB. This range of data determined by the 1GHz GPR will be further used in the characterization model described in Chapter 10.

7.4.5 CONSTITUTIVE RELATIONSHIPS BETWEEN FREQUENCY SPECTRUM AND DEGREES OF WATER SATURATION

Time-domain waveforms in each experiment were transformed to frequency spectra in the frequency domain as shown in Fig. 7-13. These spectra were achieved by carrying out the five data processing techniques described in Chapter 5. In all experiments, the peak-frequency drift is observed during the permeation stages (i.e. increasing S_w, as shown in Fig.7-14), and is restored to its original path during the de-watering stages. This indicates that the value of peak frequency is a function of water saturation/bulk water content possessed in asphalt.

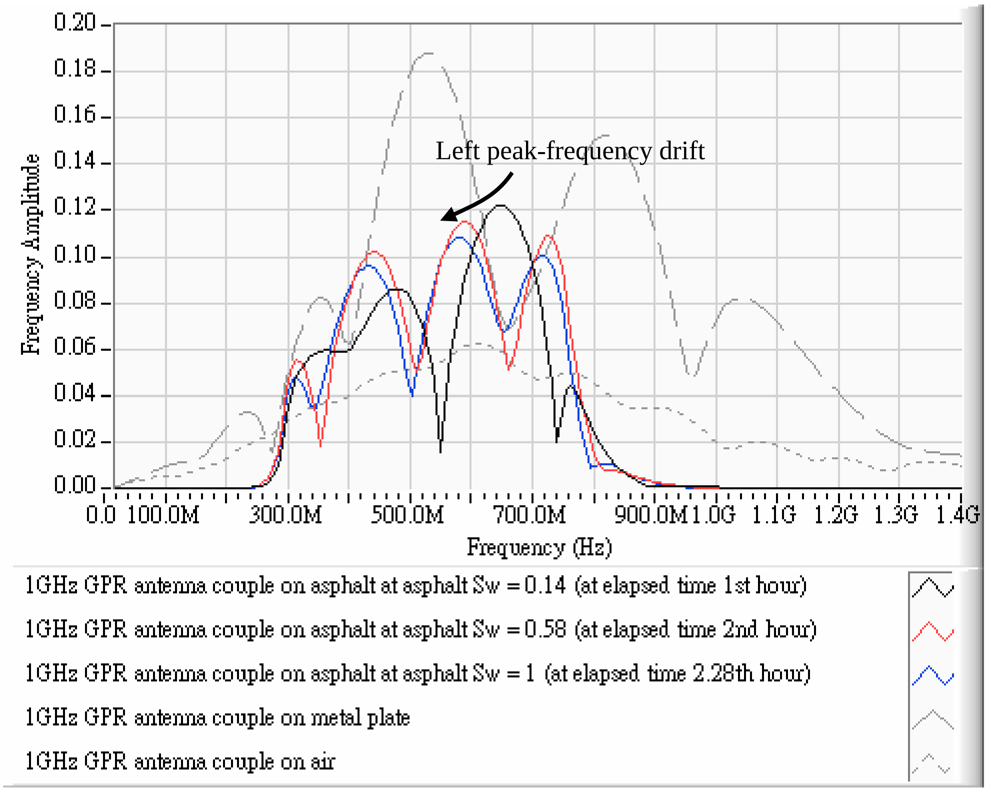

Fig. 7-13 A Number of Selected Frequency Spectra obtained using 1GHz Antenna and processed with a 300-750MHz band-pass filter

To make the variation of the peak frequencies immediately apparent, the frequency spectra transformed from the time-domain waveforms obtained in each soil texture were stacked and aligned to create sets of a so-called *spectragrams*. This transformation process was detailed in Chapter 5. Each spectragram depicts the stacked frequency spectra over elapsed time obtained in each soil specimen. An example is shown in Fig. 7-14 for 400MHz GPR used in experiment #2. A full set of 2-D plots obtained in all experiments are depicted in Appendix H2.

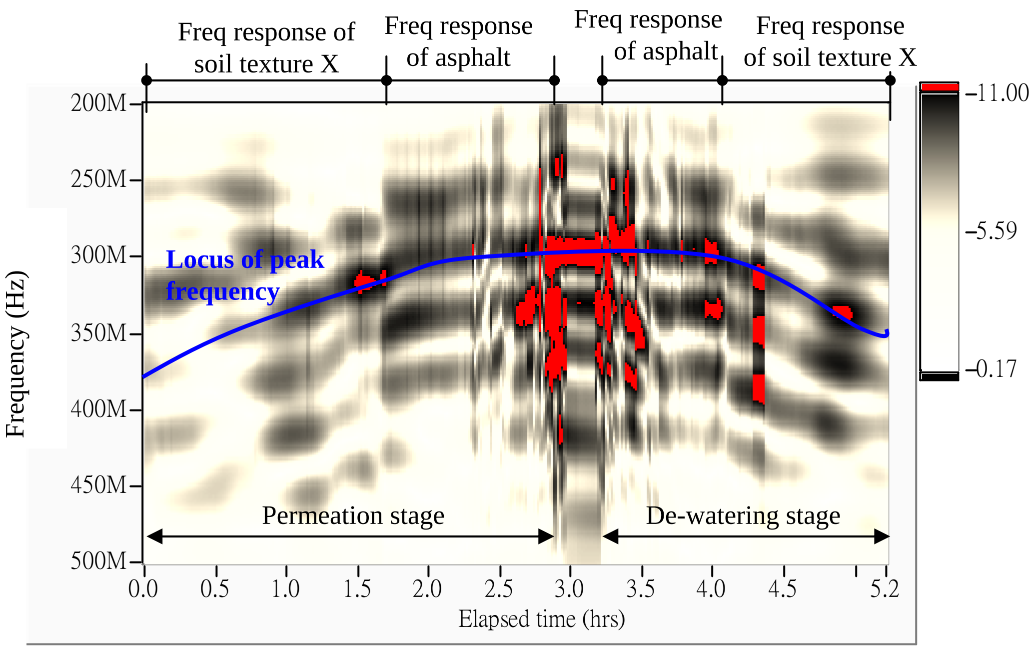

Remark: the time axis is the same as that in Fig.7-7

Fig.7-14 Spectragram obtained in Experiment #2 using 400MHz Antenna with a 250MHz to 450MHz band-pass filter)

The locus/trajectory of the 2-D plots of peak frequency over the elapsed time (as seen in Fig. 7-14 as an example) was traced to determine and quantify the peak-frequency drift. In each spectrum, the value of peak frequency is extracted and is plotted against the respective S_w.

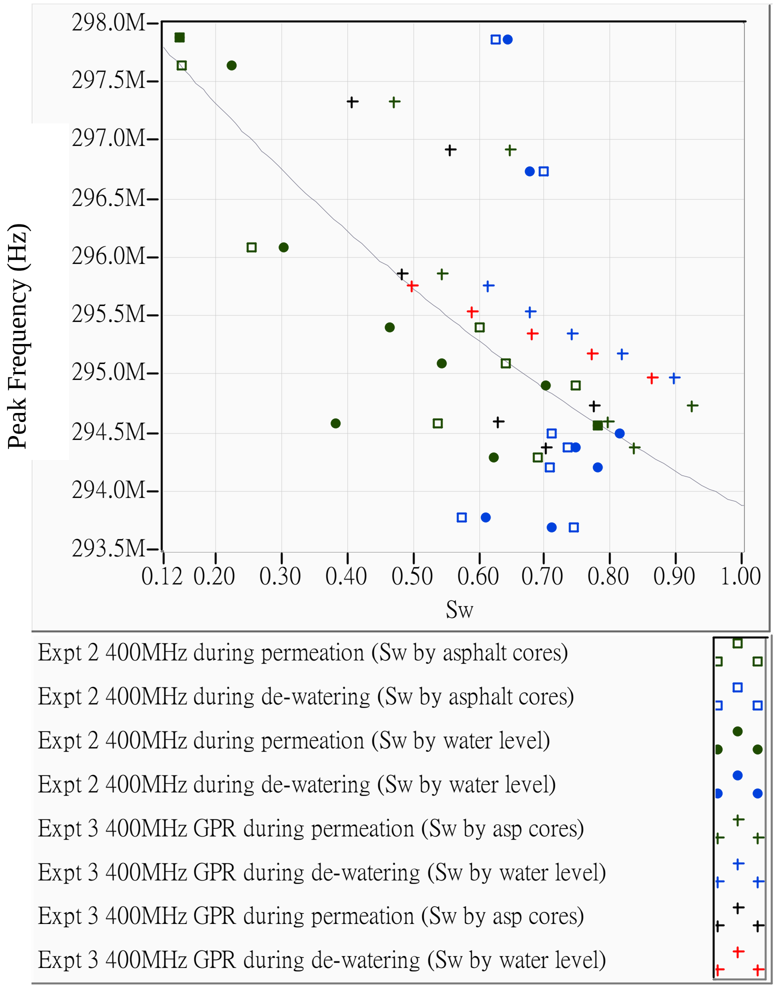

Fig.7-15a Peak-Frequencies determined by 400MHz GPR in Experiment #2 and #3

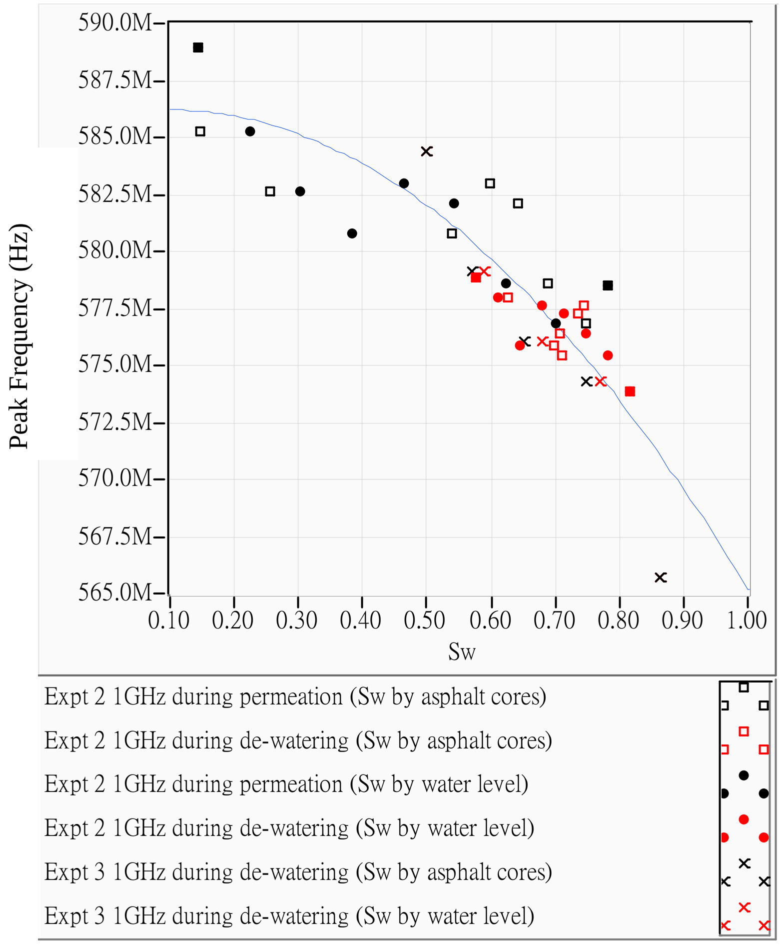

Remark: Data obtained in experiment #1 is not included

Fig.7-15b Peak-Frequencies determined by 1GHz GPR in Experiment #2 and #3

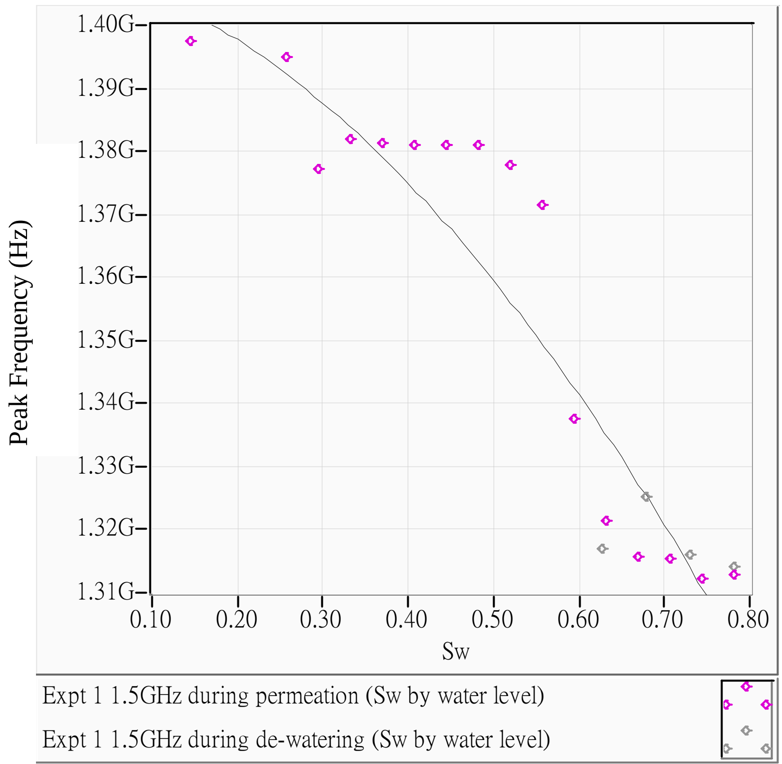

Fig.7-15c Peak-Frequencies determined by 1.5GHz GPR in Experiment #1

The maximum and minimum peak frequencies plotted in Fig. 7-15 are tabulated in Table 7-4. These values are correspondent to the range of peak frequencies which can be obtained in the dry and saturated states.

7.5 SUMMARY OF FINDINGS

Table 7-4 summarizes the ranges of ε', energy attenuation and peak frequencies, as well as the porosities and coefficients of correlation determined in the three coordinated experiments, via the fitting process of CRIM. These values are extracted from Fig. 7-11, Fig. 7-12 and Fig. 7-15.

Table 7-4 Summary of Findings in the Experiments on Asphalt Pavement

Experiment		**#1**		**#2**		**#3**	
GPR nominal frequencies		1GHz	1.5GHz	1GHz	400MHz	1GHz	400MHz
Range of ε'	Fig. 7-11	5.68 to 6.71	4.41 to 6.32	6.13 to 6.79	7.4 to 10.05	6.39 to 6.66	6.18 to 8.43
Correlation coefficient of the plot of ε' vs S_w		0.54	0.95	0.95	0.94	0.99	0.86
Range of energy attenuation (dB/m)	Fig. 7-12	N/A	N/A	-17.6 to -28.6	-18.8 to -28.4	N/A	-22.7 to -29.7
Range of peak frequency (Hz)	Fig. 7-15	N/A	1.312G to 1.422G	573.88Mto 588.96M	293.68M to 297.88M	565.69 G to 584.4G	294.37M to 297.34M
Porosity according to CRIM	Fig. 7-11	2.3%	6.5%	2.3%	7.2%	2.3%	4.3%

Remark: The uncertainty analysis of real permittivity and porosity are referred to Appendices K2, K3 and K4.

The four material properties of asphalt determined by the 1GHz GPR listed in Table 7-4 will be further used in the two characterization models described in Chapter 10.

7.6 SUMMARY AND DISCUSSION

The CMVT described in this chapter measures the changes in the real permittivities, the energy attenuations and the peak frequencies by varying the degrees of water saturation of asphalt. This experimental study concludes that measuring the real permittivity and the degree of water saturation of materials can yield the porosity of the asphalt and soil by a multitude of frequencies (i.e. 400MHz, 1GHz and 1.5GHz). The porosity was obtained through curve-fitting the data pairs of real permittivities and degree of water saturation to the well established Complex Refractive Index Model (CRIM). The determinations of material properties are possible only if the real permittivity and the degree of water saturation can be determined accurately, either in laboratory or field conditions. However, the transition moisture content and critical S_w in the plots of real permittivity and degree of water saturation found in concrete (Chapter 6) and soil (Chapter 8) are not observed in asphalt. This is presumably attributed to the small ranges of the observable changes of real permittivity, as well as the small specific surface which does not absorb bound water at any state of S_w. The latter reduces the contribution of real permittivity by restricting the electro-static motions of water inside the particles within the fine-grained contents of soil, as well as within the gel and capillary pores of air-cured concrete.

The effects of different mix types of asphalt layer composition, such as the base course and the wearing course, were found to be independent of the real permittivity. These findings are in agreement with the work carried out by Shang and Umana (1999), as described in Section 2.3. Shang and Umana's (1999) work suggests that the presence of water and the EM frequency are the only two important factors to govern the real and imaginary parts of dielectric permittivities of asphalt, whereas mix type, bulk density and asphalt cement content are not. This may be attributed to similar values of specific surface (i.e. normally in the order of 10^{-2} to 1 m^2/g) in the solid components of these mix types.

Furthermore, the frequency range (i.e. approximately 300MHz to 10GHz) of dielectric dispersion identified by Shang and Umana (1999) was found to be in the same frequency range (i.e. 400MHz to 1.5GHz) reported in the experimental findings in this chapter. For the latter, dielectric dispersion was found at every state of degree of water saturation, such that the real permittivity identified in the 400MHz GPR are the largest, followed by 1GHz GPR and the smallest using the 1.5GHz GPR. However, a word of caution must be stated that the method adopted by Shang and Umana (1999) is EMCTL, in which its frequency content does not entail the wide frequency band as found in the case of GPR systems. Hence the dispersion in asphalt found in this research is comparable, but not the same type as identified by Shang and Umana (1999).

Correct ranging of buried features such as anomalies, structural discontinuities and the thickness of the asphalt layers in highway pavement condition surveys require the knowledge of accurate real permittivities of the materials which are themselves functions of moisture content, as well as the adopted GPR frequencies. This knowledge of real permittivity determines the propagation velocity of EM GPR wave, and hence is a crucial factor of accurate ranging of the buried features.

Underneath the asphalt layers in these experiments, the data obtained from the well-graded sub-grade soil (or named as soil texture X in Chapter 8) will be shown in Chapter 8 to possess a far greater range of ε', energy attenuation, peak-frequency drift and value of porosity than that of asphalt. In Chapter 8, the strength of CMVT will be further elaborated through experimenting soil specimens of various textures to demonstrate the function and central role of water to differentiate these porous materials.

8. EXPERIMENTS TO CHARACTERIZE SOIL OF VARIOUS TEXTURE BY DETERMINATION OF THE ELECTROMAGNETIC WAVE PROPERTIES USING THE CYCLIC MOISTURE VARIATION TECHNIQUE (CMVT)

8.1 INTRODUCTION

This chapter describes the experimental technique and results of the determination of the bulk dielectric properties, porosities and permeabilities within a range of soil textures with a 1GHz Ground Penetrating Radar (GPR), without disturbing the test material associated with the traditional means of laboratory testing methods on cored samples. The soil specimens include ten different textures, ranging from coarse-grained soil (such as coarse sand and gravel) to fine-grained soil (such as fine sand and silty sand). This method is based on simultaneous tracking and measurement of changes of real permittivity during cyclic variations of the water content within these soils. The so-called cyclic moisture variation technique (CMVT) was pioneered in order to subject different soil specimens to a series of changes from a partially saturated state to a fully saturated state via a cycle of water-permeation and dewatering processes. With *differential* water distribution in the soil specimens, this CMVT allows the soil porosities and permeabilities to be determined, with water being used as an ‘enhancer’ or a ‘tracer’. Values of soil porosities were obtained using the CMVT and the data of real permittivity and degree of water saturation was fitted into the well-established Complex Refractive Index Model (CRIM). Values of soil permeabilities were also obtained through applying the Kozeny-Carmen model. Whilst performing the tests, critical degree of water saturation and some hysteresis of these materials were also observed. The former refers to the transition from fast-climbing to slow-climbing real permittivity during the permeation stages. The latter illustrates that the path-ways depicting the water-ingress and the water-egress processes did not follow the same path in the plot of the real permittivity versus the degree of water saturation (S_w) during the water-permeation and -de-watering stages. Both these phenomena are attributed to the bound/capillary water trapped in the transition zone and capillary fringe over the differential water distribution.

The different soil types are classified differently in various scientific disciplines, such as civil engineering, geology, soil science and agriculture. In civil engineering/geology, the determination of particle size distribution (PSD) of a soil sample is considered to be the most common and fundamental test method to classify soil according to the respective sizes of the composition (i.e. gravel, sand, silt and clay). The respective size fraction determined by the PSD allows engineers/geologists to characterize the soil texture, as well as to predict relevant engineering/geological properties of the soil. However, the PSD, as well as other traditional laboratory methods are not only tedious but also time-consuming to perform and the results obtained are often inaccurate. The inaccurate results are not only due to errors in the sampling process in which the original physical states of the sampled materials have been disturbed, but also due to the fact that laboratory tests cannot accurately simulate the same in-situ ground conditions of the original material. The test results are then viewed with varying degrees of uncertainty.

The rationale of the CMVT advocated in this chapter is similar to the CMVT devised in Chapter 7. In particular, this chapter highlights the advantages to be gained from determining the two engineering/geological properties (i.e. the porosities and permeabilities) of soil by continuously measuring the changes in the EM wave properties of the bulk mass of in-situ materials as the water content changes. This method was applied to a larger mass of material than either the traditional EM methods such as EMCTL, TDR and PDP described in Section 2.6, or traditional soil laboratory tests, such as specific gravity, hydrometer test, permeability test.

A series of coordinated experiments were conducted to characterize soil of different textures. This work was accomplished by analyzing the following relationships and phenomena of various material properties possessed by soil of different textures:

a. Benchmarking the positions of curves by recognizing the constitutive relationship between ε' and the respective degree of water saturation (S_w),
b. Curve-fitting the data in (a) into the Complex Refractive Index Model (CRIM) to obtain the soil porosity as described in Section 2.5.4B,
c. Predicting the soil permeability determined by the Kozeny-Carmen's model (Kozeny, 1927; Carmen, 1956) as described in Section 3.2.5.6,
d. Recognizing the constitutive relationship between the amplitude of reflection from a specific interface and the respective degree of water saturation, and
e. Recognizing the constitutive relationship between the 'peak frequency drift' in frequency spectra/spectragram and the respective degree of water saturation.

8.2 EXPERIMENTAL RIG AND THE STUDIED MATERIAL

The poorly-graded soil specimens A to I were sorted by a series of mechanical sieves of different mesh sizes, as shown in Fig. 8-1. These specimens range from coarse-grained soil (such as gravel) to fine-grained soil (such as silt). In these soil specimens, the distribution of grain size constitutes the bulk soil structure. Smaller grains fill in the voids formed between large grains and this packing of soil particles is known as a ‘poly-dispersed’ state, as depicted in Fig. 3.2-8. The divisions of the specimens are shown in Table 8-1 and the respective PSD presented graphically in Fig. 8-1.

Table 8-1 Texture and Composition of Soil Specimens

Soil Specimen Ref.	**Percentage of**				**Specimen Thickness (mm)**	**Description**	**Description in short form in Chapter 8 and 10 ****	**Grading characteristic**	**Specific Gravity**	**Nominal diameter d_{50} (mm)**	**Specific Surface *****	
	Gravel	**Sand**	**Silt**	**Clay**							**cm^{-1}**	**m^2/g**
A	0	54	40	6	165	Sandy SILT	Silt	Poorly graded	2.59	0.07	-	
B	0	75	17	8	160	Very silty, clayey SAND	Sand		2.61	0.34		
C	0	84	12	4	183	Silty, clayey SAND			2.60	0.70	1232	0.048
D	24	57	12	7	182	Silty, clayey, very gravelly SAND			2.62	1.38	1810	0.071
E	79	12	8	1	140	Slightly clayey, silty, sandy GRAVEL	Gravel		2.59	2.61	467	0.018
F	79	9	11	1	180				2.60	3.95	611	0.024
G	76	11	12	1	145				2.61	5.33	669	0.026
H	73	12	14	1	185	Slightly clayey, silty, sandy GRAVEL			2.59	6.87	731	0.028
I	67	15	17	1	170	Slightly clayey, very silty, sandy GRAVEL			2.59	10.18	824	0.032
X*	40	37	19	4	480	Slightly clayey, very silty, gravelly SAND	-	Well-graded	2.63	1.36	734	0.029

* Specimen X is the sub-grade soil under the asphalt layer in the asphalt pavement described in Ch. 7.

** The full descriptions of the poorly-graded soil specimens were made according to BS 5930:1981. These descriptions were simplified and represented as ‘sand’, ‘silt’ and ‘gravel’ in Chapter 8 and 10 for convenience.

*** Specific surface (in m^2/m^3) is computed by determining the ratio of surface area to volume of nominal size d_{50} of soil grains (see Eq. [3.2-3]), specific surface (in m^2/g) is calculated by dividing the specific surface (in m^2/m^3) by the specific gravity times the density of water.

**** Clay minerals: kaolin according to X-ray diffraction test
Sand minerals: quartz, feldspar and biotite according to visual identification

Experiments were repeatedly conducted for soil specimens A to I and X. The maximum thicknesses of the soil specimens A to I and X was chosen to be approximately 185mm and 450mm respectively by design after some calculations which entail the maximum ε' of the soil, as suggested in Section 4.3.2.2. These thicknesses fit the limit of penetration depth covering the 1GHz and 400MHz antennae when the soil specimens were saturated.

A geo-textile sheet was laid to serve as a filtering membrane to prevent clogging of the gravel drainage layer by the washing of very fine-grained soil particles. Each of the poorly-graded soil specimens A to I (of slightly varying thickness from 140mm to 185mm) was introduced to the test cell without compaction to maintain a loose packing condition so that a uniform and un-stratified soil profile was constructed, as shown in Fig. 8-2. The well-graded soil specimen X (480mm in thickness) was introduced into the test tank with compaction by a motorized vibration tamping plate on the first half layer (i.e. the first 240mm thick of soil) and on the second half layer (i.e. the second 240mm thick of soil) of the soils in the test tank as shown in Fig. 8-3 (which is the same as Fig. 7-4).

Among the poorly-graded soil specimens, soil specimen X is the well-graded sub-grade soil used in the typical asphalt road section which was described in detail in Chapter 7. Its PSD was found to be quite evenly distributed in the class of size fraction depicted in Fig. 8-1 and shown in Table 8-1. The experimental rig for testing this specimen is the same as the one used in the asphalt pavement experiment as depicted in Fig. 8-3.

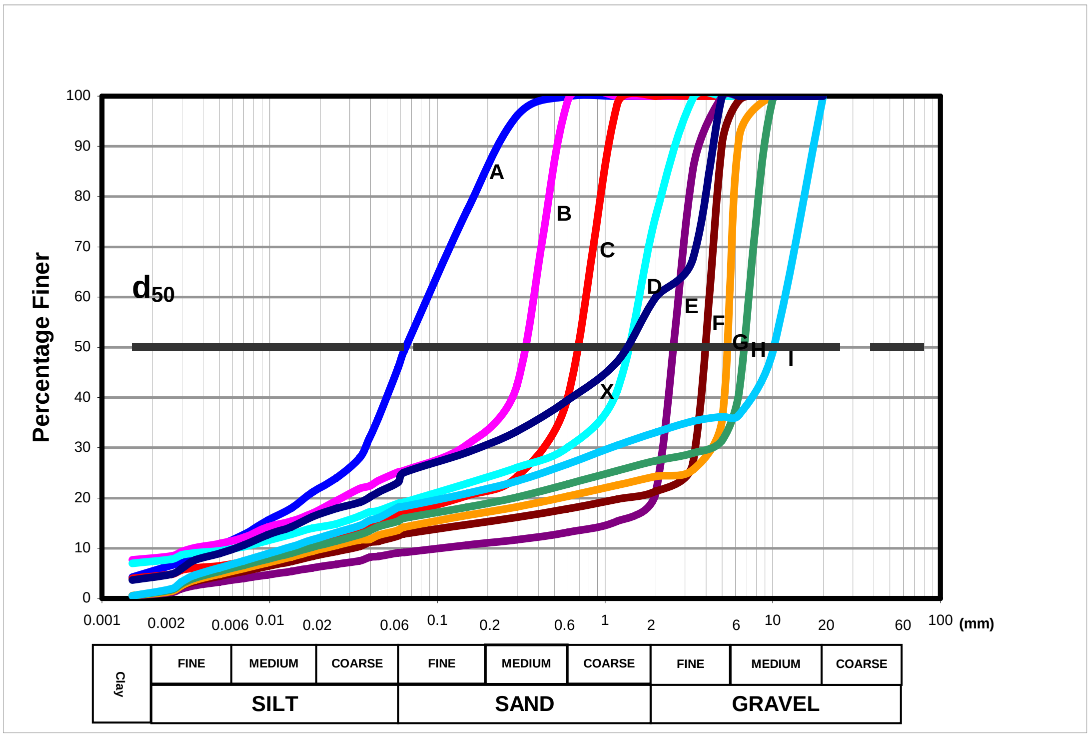

Fig. 8-1 Particle Size Distribution of the Studied Soil Specimens

In each experiment, a cyclic variation of moisture content in the soil specimens was performed and the processes weredivided into four stages,

1. The Initial Dry and Static Stage: Initially and without water injection, the antenna was coupled to the soil and background data was acquired for five minutes.

2. The Permeation Stage: Water was injected via a pre-installed PVC tube which was installed through soil layer and extended to the gravel drainage layer, as shown in Fig. 8-2a. Water was then allowed to fill the cell (for specimens A to I) and tank (for specimen X) from bottom-up direction at a specified constant rate.

3. The Saturation Stage: Sufficient time was then allowed to maintain each tested soil specimen at a saturated or near-saturated state.

4. The De-watering Stage: The original pipework during permeation was reversed and re-configured to allow de-watering of each tested specimen to take place as illustrated in Fig. 8-2b and Fig. 8-3. Free water was drained under a controlled discharge condition through the valve installed at the bottom of the cell (for specimens A to I as in Fig. 8-2b) or through the pump well (in the tank experiment for specimen X as in Fig. 8-3/Fig. 7-4) at the same rate as that in permeation.

The two-way transit time (TTT) of the returned wave from the base interfaces A, B and C was continuously monitored and recorded by the GPRs at all stages. The TTT is the time required for a radar pulse to travel from the emitting antenna to the reflecting interface and travel back to the receiving antenna (i.e. traveling twice the specimen thickness). Since soil samples were only extracted during the saturated state and after the de-watering processes, there was no disruption of the radar measurement process during the permeation and de-watering processes.

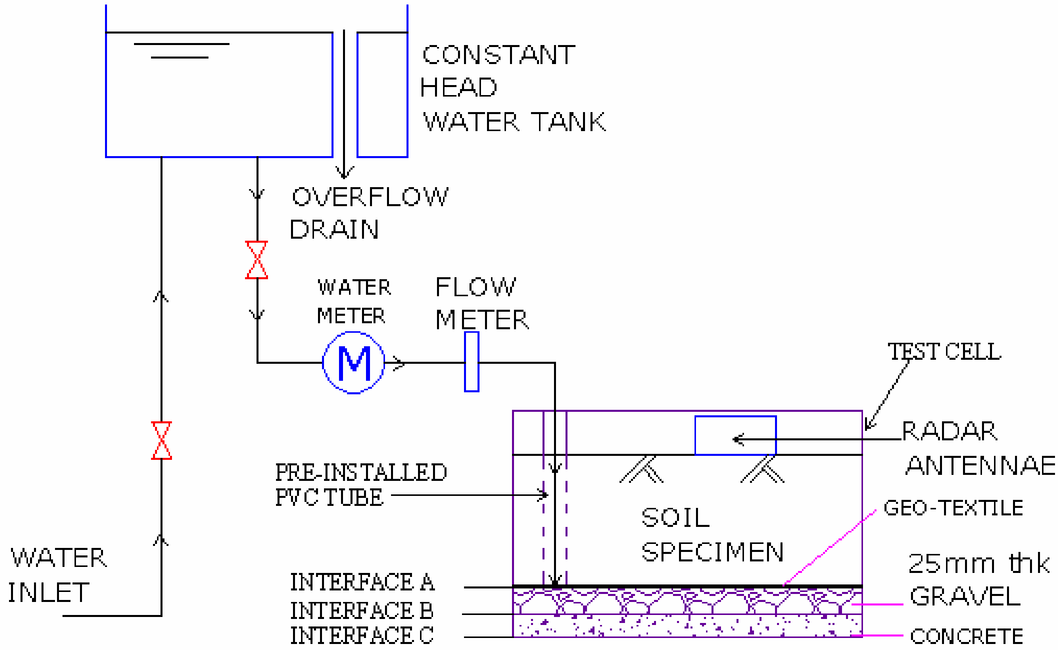

Remark: Drawing not to scale

Fig.8-2a Schematic Diagram of Permeation Setup (for experiments in soil specimens A to I)

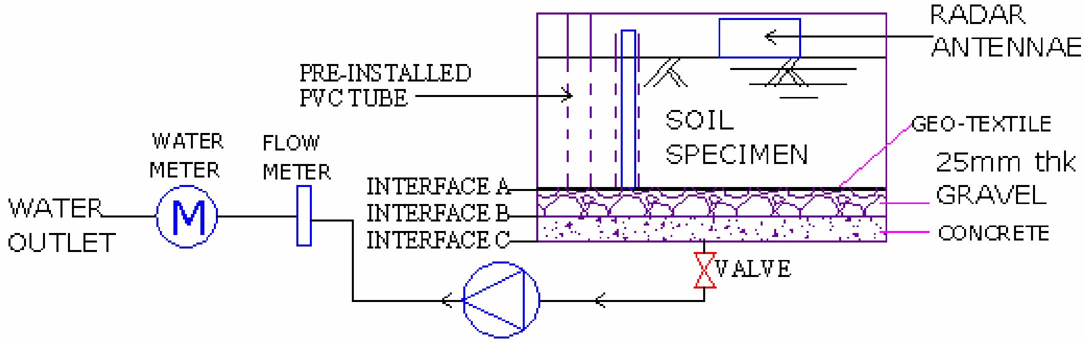

Remark: Drawing not to scale

Fig.8-2b Schematic Diagram of De-watering Setup (for experiments in soil specimens A to I)

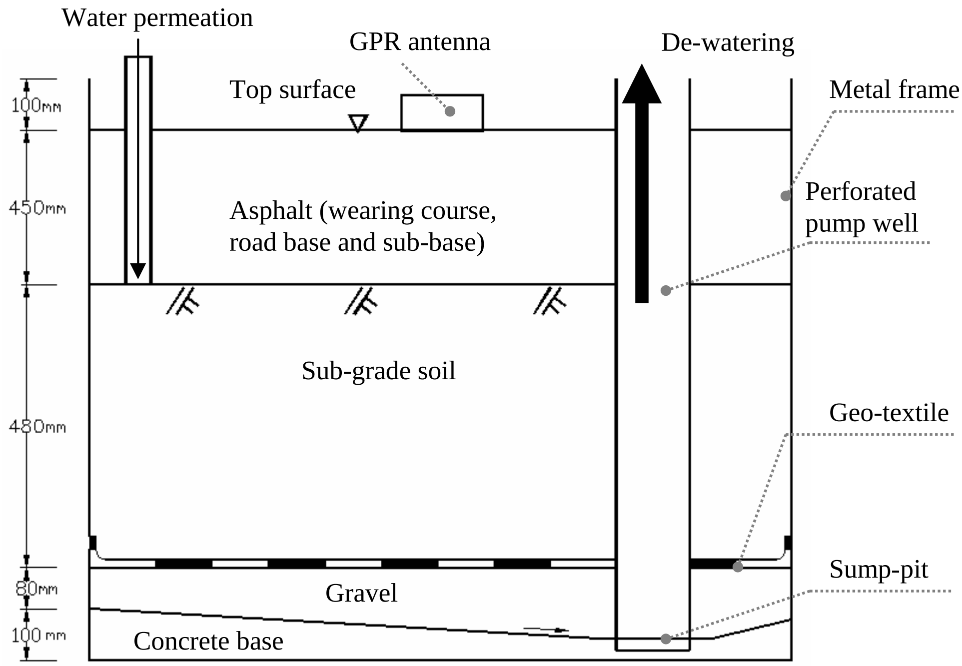

Remark: 1. this figure is identical to Fig. 7-4
2. the dimensions of the length and width are not shown in this figure

Fig. 8-3 Schematic Diagram of Permeation and De-watering Setups (for soil specimens X)

The method of determination of S_w was based on the assumption made in the asphalt pavement experiment described in Section 7.4.1. In this assumption, an overall and single S_w was assumed to represent the differential S_w along the entire profile of soil masses at a particular instant, as if it would be essentially representing a homogeneous sample mass with evenly distributed water content.

For each experiment, the values of S_w during the permeation stages were determined by interpolating the initial S_w (i.e. nearly zero) and the fully saturated S_w (i.e. unity). The values of S_w during the de-watering stages were obtained by interpolating the fully saturated S_w (i.e. unity) and the final S_w. The final S_w was determined by extracting and weighing the soil samples. Since the permeation and de-watering facilities were designed to permeate and pump at a constant rate through meticulous control by flowmeter and water meter (accurate to 0.001 m^3), the interpolations carried out in both stages were assumed to be linear. These values of S_w were paired with the EM wave properties determined under the same elapsed time, as described in the data analysis in Section 8.4.2 to 8.4.5 and 8.4.6.

8.3 INSTRUMENTATION AND GPR ANTENNA FREQUENCIES

These experiments have benefited from the use of both the 1GHz JRC radar system for specimens A to I and the GSSI 400MHz radar system for specimen X, as described in Chapter 4.

Table 8-2 summarizes the velocities of EM wave propagation and the returned nominal peak frequencies of GPR waveforms (see a similar table by Jol, 1995) with different antenna frequencies (i.e. 400MHz and 1 GHz) in both the dry and the saturated states. In these experiments, the GPRs have covered a penetration depth encompassing the full thickness of the soil specimens described in Table 8-1 even when the specimens were saturated. The returned radar wave frequency spectra and the returned nominal peak frequencies of the three GPR antennae were acquired by the five data processing techniques described in Chapter 5. These techniques transform the time-domain waveforms into spectra in the frequency domain, as illustrated in Fig. 8-4 in both the dry and the saturated state respectively.

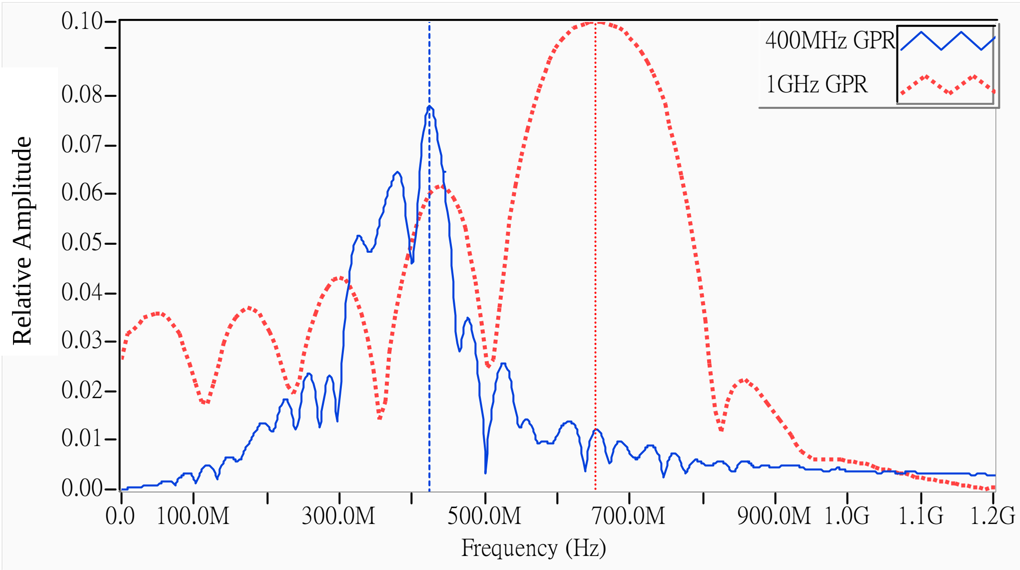

Fig.8-4a Frequency Spectra of the Returned Radar Wave Signals for 400MHz (processed with a 250-450MHz low-pass filter) and 1GHz (processed with a 800MHz low-pass filter) Antennae in the Dry State (returned peak frequencies were identified at 423.44MHz and 653.12MHz

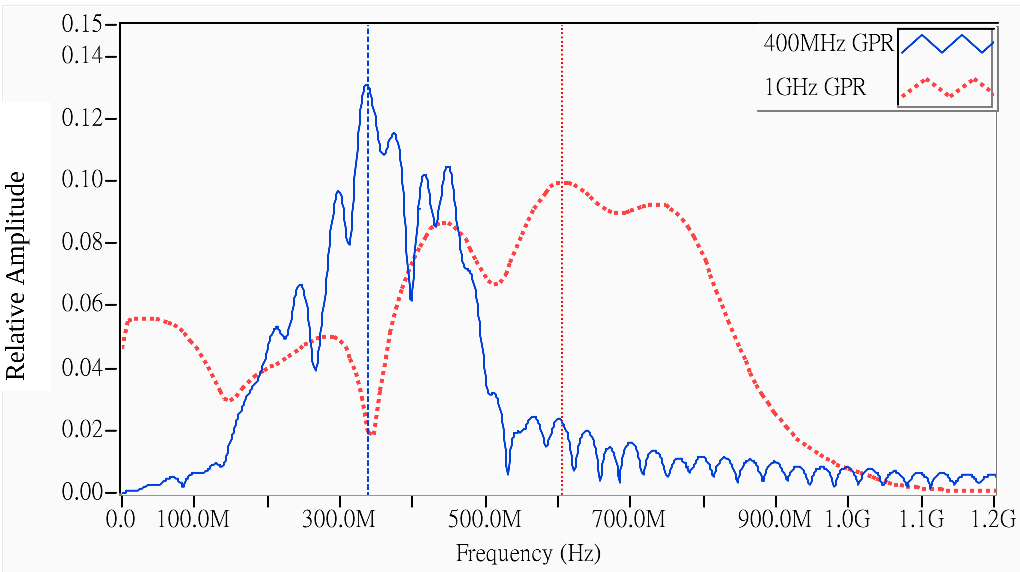

Fig.8-4b Frequency Spectra of the Returned Radar Wave Signals for 400MHz (processed with a 250-450MHz low-pass filter) and 1GHz (processed with a 800MHz low-pass filter) Antennae in the Saturated State (returned peak frequencies were identified at 337.5MHz and 605.91MHz respectively)

Table 8-2 Depth Resolutions calculated according to the Propagation Velocity of GPR Wave and the Returned Nominal Peak Frequency obtained in the Frequency Spectra in both Dry and Partially Saturated States of Soil with Soil Texture A and X using the Two Different GPR Antenna frequencies 400MHz and 1GHz

Nominal/Center frequencies of the GPR antennae		**400MHz**	**1GHz**
Soil specimens (details are shown in Table 8-1)		**X**	**A**
At initial state	Propagation velocity of GPR wave (v)	0.072 m/ns with S_w = 0.55	0.161 m/ns with S_w = 0
	Returned nominal/characteristic peak frequency (determined from the frequency spectrum)	423MHz	653MHz
	Nominal/characteristic wavelength λ (=v/f)	170mm	247mm
	Depth resolution (one quarter of λ)	**43mm**	**62mm**
At saturated state	Propagation velocity of GPR wave (v)	0.058 m/ns (S_w = 1)	0.049m/ns (S_w = 1)
	Returned nominal/characteristic peak frequency (determined from the frequency spectrum)	338MHz	606MHz
	Nominal/characteristic wavelength λ (=v/f)	171mm	81
	Depth resolution (one quarter of λ)	**43mm**	**20mm**

According to Table 8-2 and Fig. 8-4, a better depth resolution is yielded by a larger ε' (i.e. a lower propagation velocity in the case of 1GHz GPR). With a larger ε' at the saturated state, the depth resolution of the 1GHz GPR can be enhanced from 62mm with a small ε' at the dry state to 20mm.

When the spacing of the two interfaces is less than the respective ranges of the depth resolution, the reflections produced by these interfaces will appear to mingle together and are difficult to resolve. As a result, the interfaces A, B and C shown in Fig. 8-2 cannot be resolved in the radargrams, as illustrated in Fig. 8-6 and Fig. 8-7. Hence these interfaces are collectively represented as 'the base interface' in subsequent discussion.

8.4 FINDINGS AND DATA ANALYSIS

The schematic diagram in Fig. 8-5 depicts the hierarchy and conceptual data flow of different methods of data analysis.

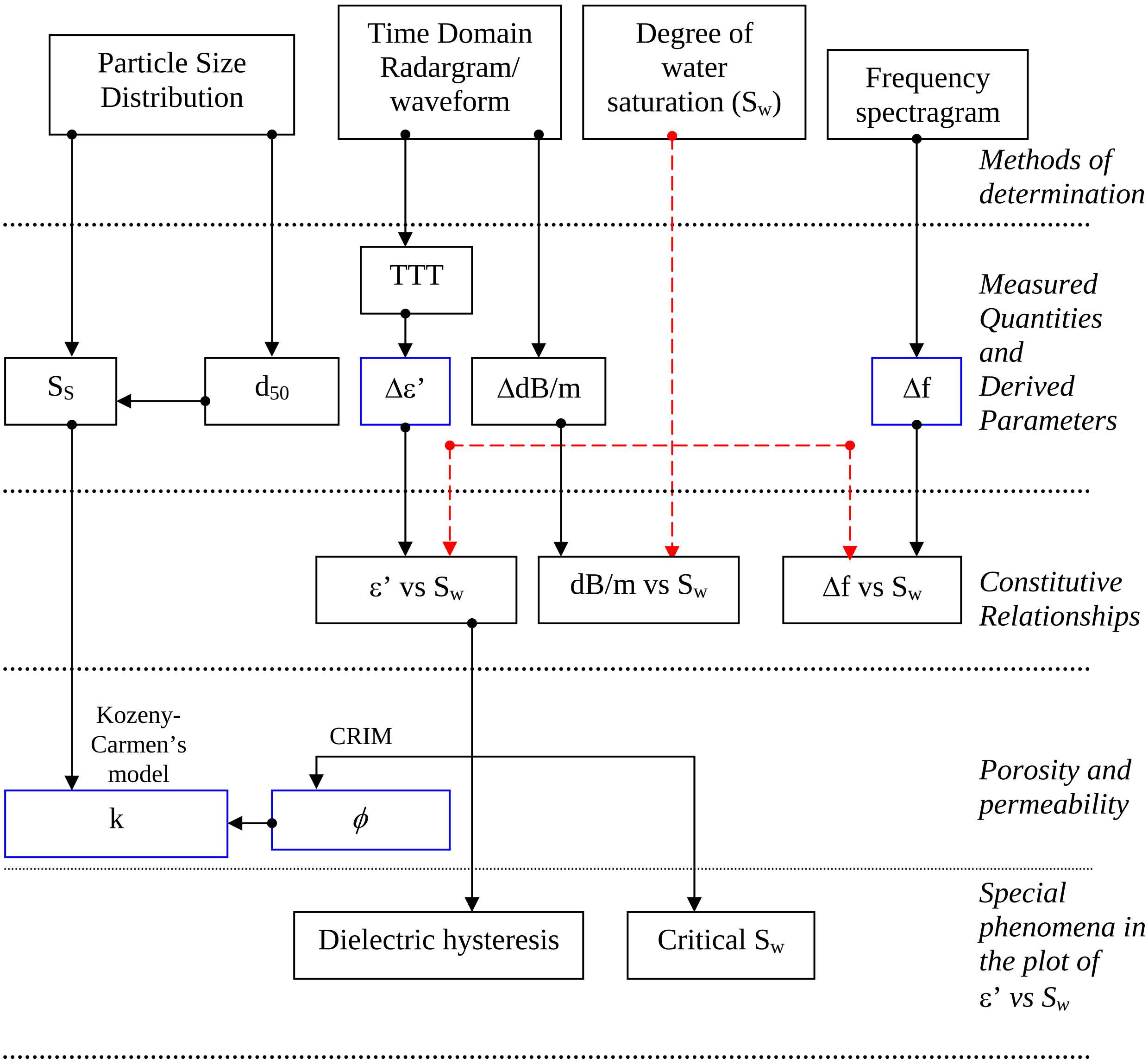

TTT: Two-way transit time of radar wave from antenna to the base interface (ns)
S_S: Specific Surface (m^2/m^3or m^2/g) (see Table 8-1)
d_{50}: Nominal diameter of soil specimen (mm) (see Table 8-1)
ε': Real permittivity (see Section 8.4.2)
dB: Energy attenuation (see Section 8.4.5)
Δf: Change of peak-frequency at partially saturated state relative to peak-frequency at dry state (see Section 8.4.6)
ϕ: Porosity (see Section 8.4.3)
k: Coefficient of permeability (m/s) (see Section 8.4.4)
CRIM: Complex Refraction Index Model (see Section 2.5.4B)
Kozeny-Carmen's Model (see Section 3.2.5.6)
Remark: the values of material properties determined in the blue boxes are to be used in the characterization models constructed in Chapter 10

Fig. 8-5 Schematic Diagram of Hierarchy and Conceptual Data Flow of Different Methods of Data Analysis in the Soil Experiments

For the determination of S_w, the details described in Section 7.4.1 were followed.

8.4.1 RADARGRAMS

During the entire process of CMVT performed in each experiment, the respective waveforms were obtained, stacked and aligned to produce radargrams for all soil specimens. Two examples of radargrams of fine-grained (i.e. specimen B) soil and coarse-grained (i.e. specimen H) soil are presented in Fig. 8-6 and Fig. 8-7 respectively. A full set of radargrams obtained in the experiments on all soil specimens are given in Appendix I. The amplitudes of the reflected waves shown in the radargrams in Fig. 8-6 and Fig. 8-7 are encoded based on the colour chart shown in the upper right corner of each radargram (i.e. from white positive, to black negative, respectively).

In these radargrams, the black lines (highlighted by dotted yellow arrows) at 6.1ns (as in Fig. 8-6), and 5.8ns (as in Fig. 8-7) correspond to the TTT required to travel the respective distances between the antenna to the base interface (i.e. the distance depends on the soil thickness described in Table 8-1). During the initial static stage of the experiment, the black lines in the radargram (as shown in Fig. 8-6 respectively) are static.

As time progressed in the permeation stage whilst a significant amount of water permeated and raised the transition zone to a higher level, the reflection from this rising transition zone was clearly observable. This transition zone was indicated by an inclined white line (highlighted by solid yellow arrows in the radargrams). During the same stage, the TTT, which corresponds to the reflections of the base interface, was lengthened gradually and remained static when the water level rose to the top of the soil layer (i.e. during the saturation stage). After saturating the specimens for a sufficient period of time, de-watering started and in theory, the black line should climb up to restore the descending trend in the permeation stage. However, this characteristic was not observed in the finest soil of specimens A, B and C (i.e. nominal size d_{50} is smaller than 0.699mm and their major texture up to that of medium sand as shown in Table 8-1).

To examine the presence and absence of restoration of TTT during de-watering stage more closely, two representative radargrams of soil specimen B and H are shown in Fig. 8-6 and Fig. 8-7 respectively. For the former, de-watering started after 40 minutes and from this moment onwards, the black line started to climb up slightly and remained static throughout the rest of the experiments. The slight 'climb-up' is attributed to the ease of drainage of water within the permeable gravel layer as shown in Fig. 8-2b. In fact, free water could not be discharged within the soil layer in this soil specimen. As a result, neither TTT and hence, nor ε' decreased in these soil specimens (i.e. A, B and C) during the respective de-watering stages.

This indicates that the fine-grained soil holds water more tightly than coarse-grained soil. This discrepancy is attributed to the reasons that

1. coarse-grained soil possesses a considerable volume of macroscopic or inter-aggregate pores which drain very rapidly and remain air-filled after drainage (Hillel, 1980) , and

2. fine-grained soil possesses a far larger specific surface, greater wilting point, and more dominating volumes of micro-pores in the overall pore size distribution than

coarse-grained soil. The associated physical behaviour is discussed in Section 3.2.5.2. For soil specimen X, radargrams in Fig. 7-9b and Fig. 7-10b are referred.

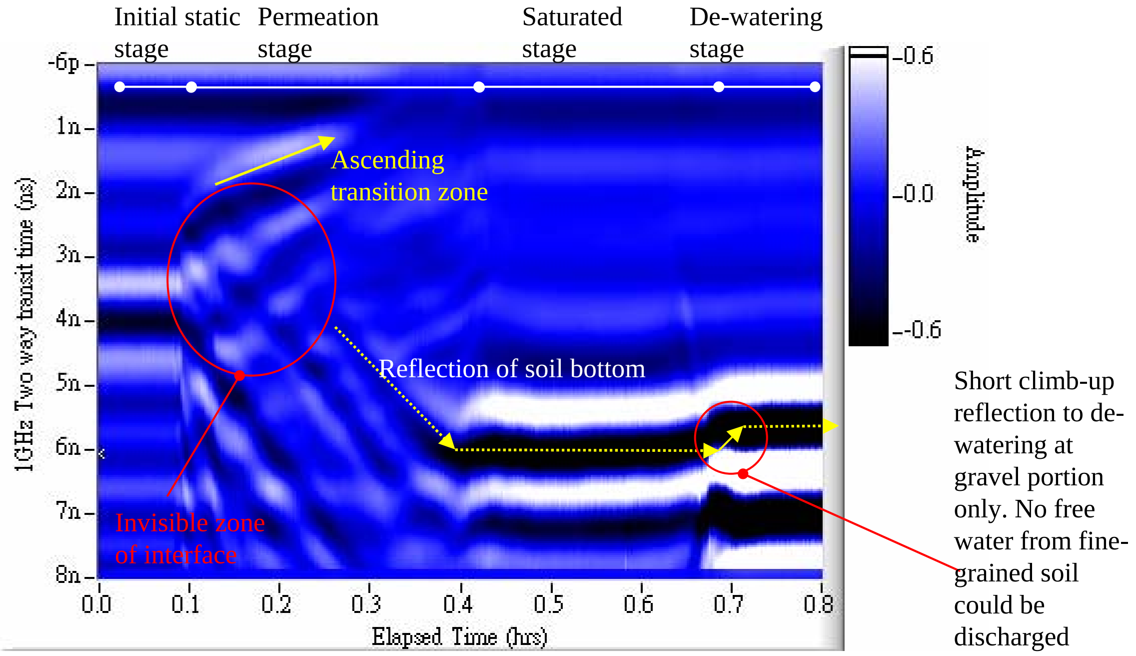

Fig. 8-6 Radargram of Soil Specimen B using 1GHz GPR

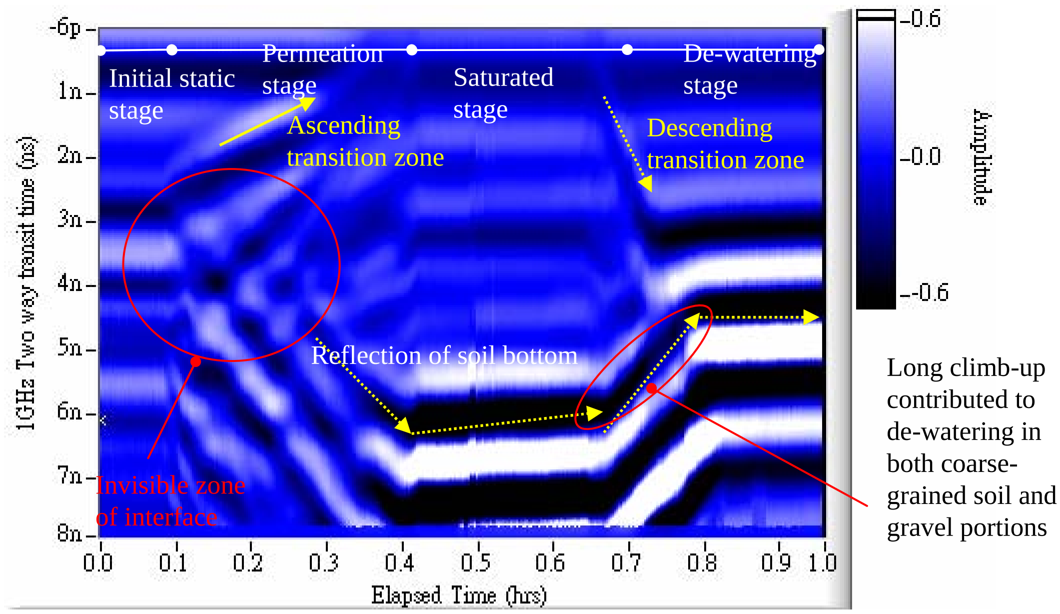

Fig. 8-7 Radargram of Soil Specimen H using 1GHz GPR

In each radargram obtained from each soil specimen, a so-called ‘Invisible Zone of Interface’ was commonly found at the instant of the transition zone ascending above the base interface (Bevan et al., 2003). Within this zone, the reflection of the base interface and the rising water table/transition zone were irresolvable and became invisible as shown in Fig. 8-6 and Fig. 8-7. This is attributed to the limits of depth resolution (one-forth of the wavelength) governed by the returned GPR frequencies and the EM wave propagation velocity as explained in Section 8.3 and Table 8-2.

8.4.2 CONSTITUTIVE RELATIONSHIP BETWEEN REAL PERMITTIVITY AND DEGREE OF WATER SATURATION

The ε' of these soil specimens was plotted against the respective S_w, as shown in Fig. 8-8 and 8-9. The S_w at a particular instant is assumed to represent the differential S_w along the entire profile of the soil specimens, as if it would be essentially representing a homogeneous sample mass with evenly distributed water content. Details of these assumptions are the same and can be referred to Section 7.4. Several important observations about the relationship between ε' and S_w in these figures are made and summarized as follows:

A. DEPENDENCE OF REAL PERMITTIVITY ON SOIL TEXTURE AT DIFFERENT DEGREES OF WATER SATURATION

With the variation of S_w, the silt specimen A possesses the greatest value of ε'. It is followed by the sand specimens B, C and D which entails the intermediate range of ε'. Finally, the gravel specimens E, F, G, H and I possesses the smallest range of ε'. This observation suggests that soil of smaller particle size (i.e. larger porosity and larger specific surface) attains higher values of ε' than soil of larger particle size (i.e. small porosity and smaller specific surface), given the same S_w. However, it must be cautious that same S_w does not imply same water content possessed in all soil specimens because the porosities of each specimen are different.

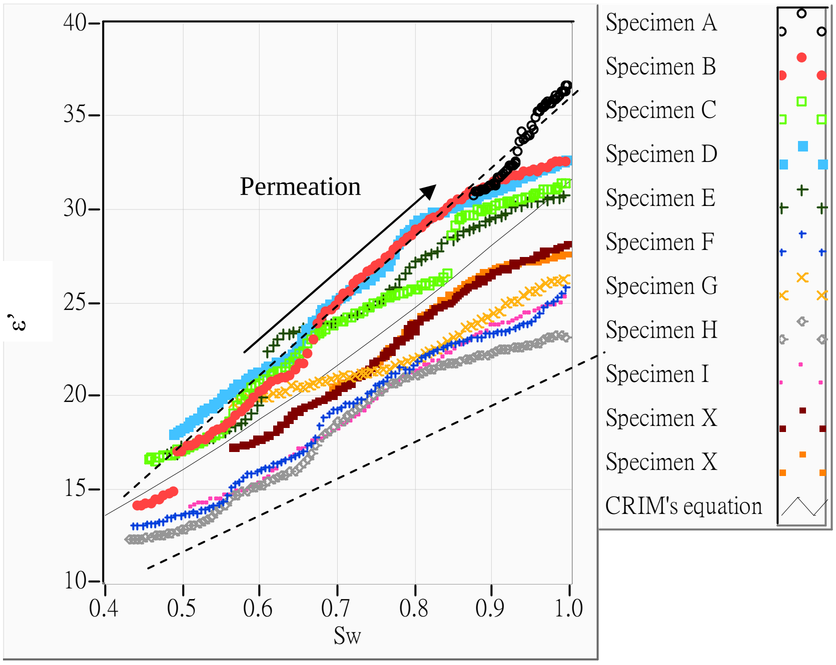

Fig. 8-8 Plots of ε' against S_w of Soil Specimens during the Permeation Stages

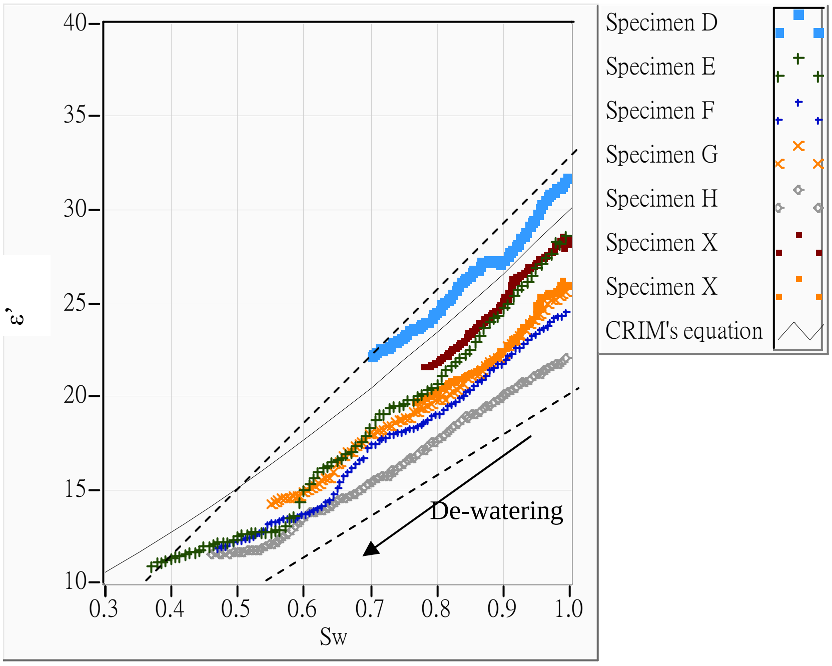

Fig. 8-9 Plots of ε' against S_w of Soil Specimens during the De-watering Stages

The relative positions of soil specimen X in the plots of ε' vs S_w (as shown in Fig. 8-8 and Fig. 8-9) are sandwiched between the soil specimens of sandy and gravelly texture. This characteristic can be explained by its well-graded size distribution depicted in the PSD graph as shown in Fig. 8-1. In other words, the poorly-graded soil serves as multiple fingerprints (denoting mainly the sandy and gravelly textures) to bench-mark the boundaries exhibited in ε' vs S_w.

B. CRITICAL DEGREE OF WATER SATURATION DURING THE PERMEATION STAGES

The curves in the plots of ε' vs S_w of most soil specimens (except specimen G) show a clear transition from an initially fast-climbing segment to a finally slow-climbing segment. For each of these soil specimens, these two segments are separated by a *turning point*, as annotated in the example (i.e. specimen X) illustrated in Fig. 8-10 which is extracted from Fig. 8-8. The critical S_w is designated as the water content corresponding to the *turning point*, after which the marginal increase of ε' was reduced with increasing S_w.

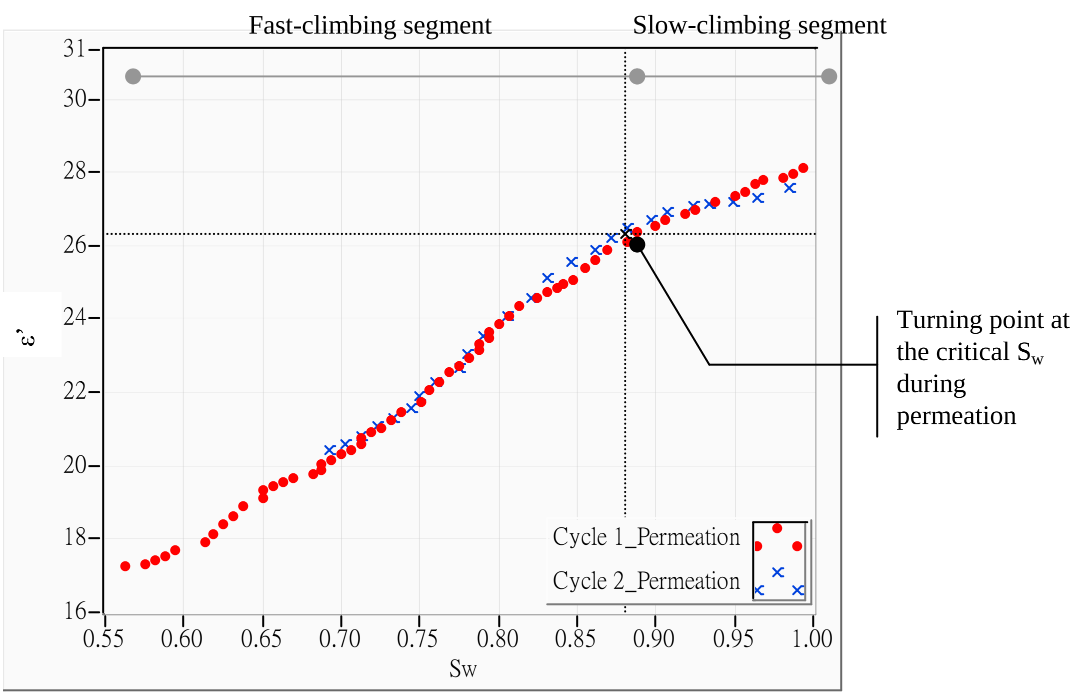

Remark: The data is extracted from Fig. 8.7a

Fig. 8-10 Turning Point/Critical S_w in the Plots of ε' against S_w in Soil Specimen X using 400MHz GPR during the Permeation stage

In the macroscopic scale of water distribution exhibited in each of these experiments, a transition zone and a capillary fringe exist along the soil profile, as illustrated in Fig. 8-11. These two zones contained bound and capillary water which was physically absorbed in the soil capillaries. When these water molecules are subject to an externally applied electrical field, their motion is limited by electrostatic interaction with clay particles/minerals (Huisman et al., 2003; West et al., 2003). As a result, the response to polarization of this bound and capillary water is smaller than that of free water (Saarenketo, 1998; West et al., 2003).

At the beginning of each experiment, water permeated from the bottom of the specimen to form and raise a water table, capillary fringe and transition zone progressively. According to the hypothetical distribution of water depicted in Fig. 8-11, the transition zone and capillary fringe at an early saturation (i.e. at the moment of lower transition zone and smaller overall S_w in Fig. 8-11a) are *smaller* than those approaching the final saturation (i.e. at the moment of higher transition zone and larger overall S_w in Fig. 8-11b). Since bound and capillary water (instead of free water) are the sources of wetting in the transition zone and capillary fringe, the volume of bound and capillary water possessed in the early saturation is *smaller* than that in the final saturation. Hence the response to polarization (measured by real permittivity) was reduced marginally at high S_w, as depicted in Fig. 8-10.

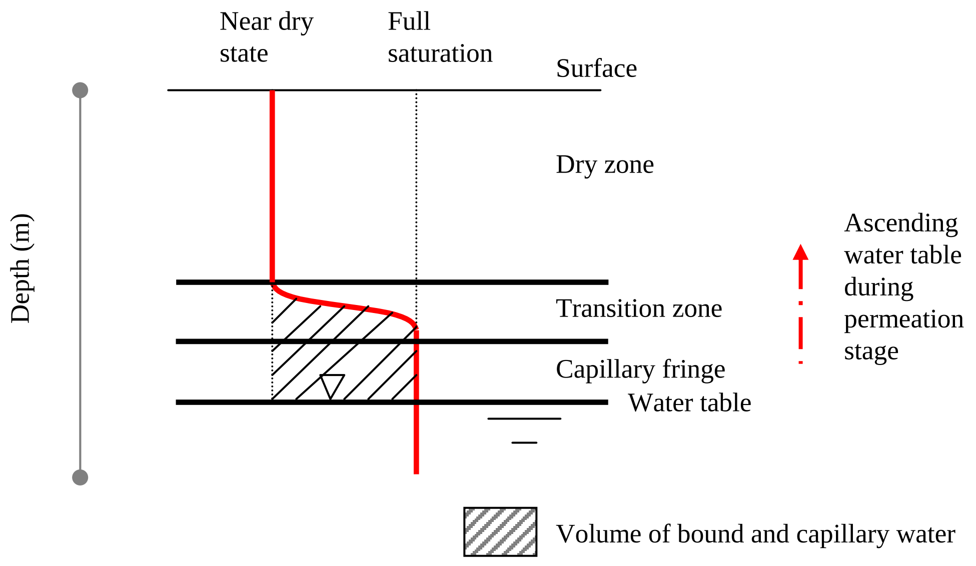

Fig. 8-11a Hypothetical and Differential Distribution of Water at Early Saturation during the Permeation Stage

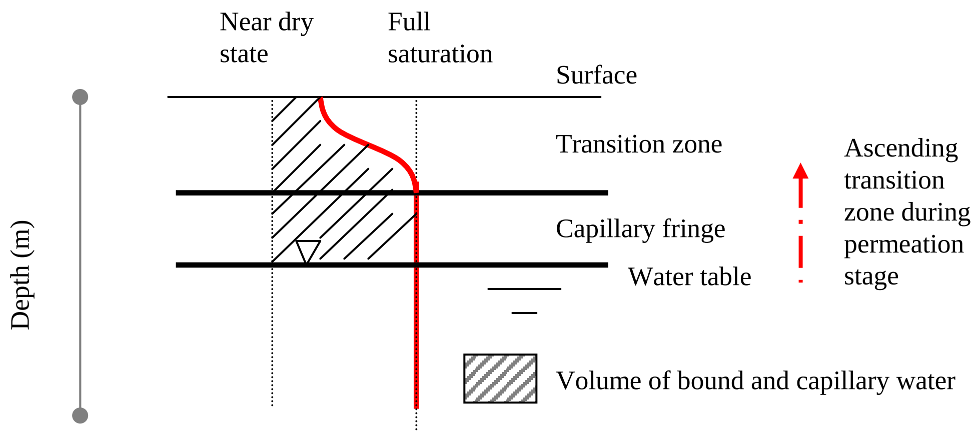

Fig. 8-11b Hypothetical and Differential Distribution of Water approaching the Final Saturation during the Permeation Stage

In the microscopic scale, this reduced response of polarization at high S_w can also be due to the loss of connectivity in gas pockets (Knight and Nur, 1987a) as discussed in Section 3.2.5.7C. This happens when the surface layers of soil particles are absorbing water (i.e. S_w increases progressively), the capacitance of the water-gas mixture increases and the thickness of the gas pockets decrease. When a *critical* S_w is reached, the capacitance in the gas phase of the pores is considered to be 'short-circuit' and contributes to a smaller capacitance value which reduces the increase of real permittivity at high S_w. However, a note of caution must be made in that the theory provided by Knight and Nur (1987a) is based on a microscopic and relatively homogeneous distribution of water in small-sized sandstone samples, using a dielectric cell operating in kHz and MHz frequency ranges, but not at the GHz level adopted in GPR and in this research. Nevertheless, it is believed that both macroscopic and microscopic factors affected the reduced responses to polarization at high S_w, but quantitative analysis and differentiation between these two factors are not well-understood.

C. INVISIBLE ZONE OF THE BASE INTERFACE

The measurements of ε' at $S_w<0.4$ are generally not achievable due to the limitation of depth resolution which creates the invisible zone of interface shown in the radargrams of Fig. 8-6 and Fig. 8-7. Therefore for all soil specimens, only a limited number of the pairs of ε' and S_w can be plotted as shown in Fig. 8-8 and Fig. 8-9 because the reflection interface cannot be found in the radargrams.

D. HYSTERESIS IN THE PLOTS OF REAL PERMITTIVITY VS DEGREE OF WATER SATURATION

The data obtained during the de-watering stages is found to pursue a different pathway to that obtained during the permeation stages (Fig. 8-8 and Fig. 8-9) in all soil specimens. This phenomenon is known as hysteresis and will be further discussed in Chapter 9.

The characterization of soil texture by means of the plots of ε' and S_w was shown to be successful. The data of these plots will be further utilized in soil texture characterization in terms of porosity and permeability in subsequent sub-sections.

8.4.3 CONSTITUTIVE RELATIONSHIP BETWEEN THE PREDICTED SOIL POROSITY (DETERMINED BY CRIM) AND SOIL TEXTURE

The values of porosity for each soil specimen (as shown in Fig. 8-12) were obtained through curve-fitting the data pairs of ε' and S_w (plotted in Fig. 8-8 and Fig. 8-9) into the CRIM and subsequently determining the coefficient of CRIM as a second order equation, as described in Section 2.5.4B. These values were further paired up with the respective nominal particle size (i.e. d_{50}) of each soil specimen tabulated in Table 8-1. Fig. 8-12 indicates that the porosities of the five gravel specimens E to I are the smallest in value and the least in variation, followed by the larger values and a wider variation achieved in the sand specimens B to D. The silt specimen A possesses the largest value of porosity. This description is summarized in Table 8-3.

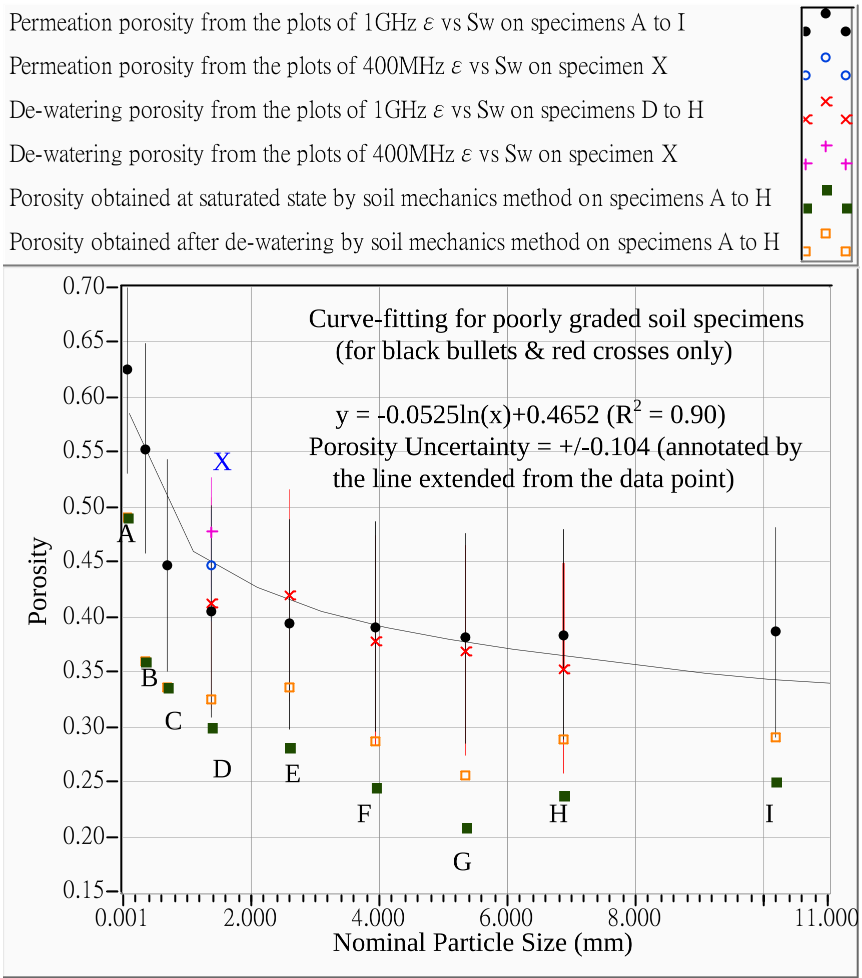

Remark:

* The lines extended from the black bullets & red crosses are the range of uncertainties. The uncertainty analysis is referred to Appendix K4.

** The horizontal axis represents the nominal particle size obtained at d_{50}

Fig. 8-12 Porosities obtained by Fitting Pairs of Real Permittivity and Degree of Water Saturation into the CRIM (during both the permeation and de-watering stages) and by the Soil Mechanics Method (after both the saturation stage and de-watering stage)

Table 8-3 Comment on the Values and Range of Values of Soil Porosity in Three Groups of Textures

SOIL SPECIMEN	FITTED VALUES OF POROSITY	RANGE OF VALUES OF POROSITY
GRAVEL	Smallest	Least
SAND	Medium	Medium
SILT	Largest	N/A (since not enough data)

The slow-climbing segment in some data pairs of ε' and S_w at high S_w exhibit a flatter gradient (i.e. particularly those values larger than the *critical* S_w which separate the turning slopes of curves as explained in Section 8.4.2B). This segment is also found in many other studies, such as the segment of high S_w described in Section 3.2.5.7C. The data in this segment is found not to agree with the CRIM curve which possesses an ever-increasing gradient (segment of intermediate S_w described in

Section 3.2.5.7B). The CRIM is therefore applied only within a range of intermediate S_w and before the critical S_w is reached.

The porosities obtained by CRIM were found to be larger than those of the independent measurement using the soil mechanics method (BS1377-2:1990) by an average value of 0.125, as depicted in Fig. 8-12. These differences are attributed to (1) the uncertainties of assuming the isotopic geometry of each mixture component which then corresponds to the application of square roots on ε', ε_A', ε_w' and ε_s' in CRIM; (2) the experimental uncertainties in measuring S_w. The former refers to the uncertainties led by the effect of the loose packing of the soil on the assumption of the isotropic geometry of soil grains. The latter refers to the difficulties in determining an accurate S_w. These difficulties are due to two attributes. Firstly, a full degree of water saturation (S_w = 1) was assumed when the specimens were merely in a nearly-saturated state when the water table ascended to the top. Secondly, the accuracies of moisture content determination (and hence enabling S_w determination) after the de-watering stage were affected by the process of extracting the surface samples, which might not be representative of the differential distribution of water along the soil section. Furthermore, the uncertainty of S_w is the most dominant one among the uncertainties of all other variables, such as thickness of samples and determination of ε' in CRIM. Despite these uncertainties, the porosity values obtained through CRIM are able to serve as an indicator of the actual porosity values of each soil texture. An error analysis of the computation of porosity using CRIM is referred to Appendix K4.

8.4.4 CONSTITUTIVE RELATIONSHIP BETWEEN THE PREDICTED SOIL PERMEABILITY AND SPECIFIC SURFACE

The values of permeability (as in Fig. 8-13) of each soil specimen are estimated via the Kozeny-Carmen's model (Kozeny, 1927; Carmen, 1956) (i.e. Eq. [3.2-6]), when porosity (by fitting with the CRIM) and specific surface (from Eq. [3.2-3]) are known. Subsequently, the permeability values were further paired with the corresponding specific surface of each soil specimen and plotted in Fig. 8-13 and reported in Table 8-4. In Fig. 8-13, the five gravel specimens E to I possess the largest permeability values, followed by the smaller values achieved in sand specimens C and D. Within these gravel and sand specimens, the increases of soil specific surface (i.e. finer soil specimens) correspond to the decrease of the soil permeabilities.

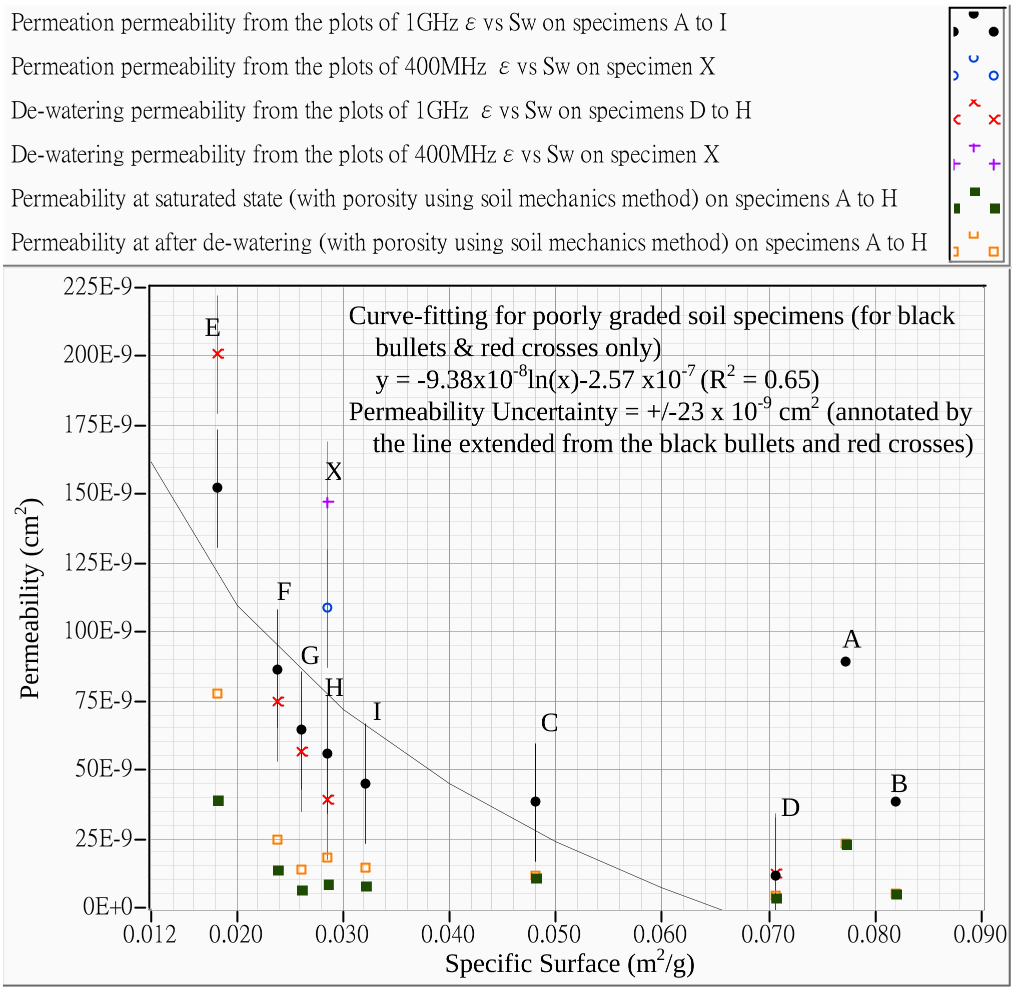

Remarks:
* Data of specimens A and B should be excluded in the fitted curve.
** Specific surface (in m^2/m^3) is computed by determining the ratios of surface area to volume of nominal sizes d_{50} of soil grains (Eq. [3.2-3], specific surface (in m^2/g) is calculated by dividing the specific surface (in m^2/m^3) by the specific gravity times the density of water.
*** The lines extended from the black bullets & red crosses are the range of uncertainties. The uncertainty analysis is referred to Appendix K4.

Fig. 8-13 Permeabilities determined by ε' (using 400MHz and 1GHz GPRs) and Specific Surface Area using Kozeny-Carmen model (Kozeny 1927, Carmen 1956)

However, both soil specimens of the finest texture, specimens A and B, do not agree with the fitted curve in Fig. 8-13, whilst they follow successfully a fitted curve in porosity as depicted in Fig. 8-12 previously. This failure in agreement with the predicted trend of Fig. 8-13 is attributed to the breakdown of hydraulic radius's theory described in Kozeny-Carmen's model (Kozeny, 1929; Carmen, 1956), as well as the violation of assuming a spherical grain when specific surfaces are approximated (i.e. Eq. [3.2-3]). For the former, this model fails to describe structured soil bodies (Hillel, 1980) like fissured fine particles in silt/clay and can be applied only in spherical/near-spherical soil grains. For the latter, the assumption of a spherical/near-spherical shape for soil specimens C to I is not valid for the finest specimens A and B. Therefore the values of permeability obtained in these two finest soil specimens (i.e. A and B) are not valid and should be excluded in Fig. 8-13.

In general, the values of these values of permeability for specimens C to I and X are found to be in good agreement with the published and well-known values, such as those reported by Freeze and Cherry (1979). The traditional constant/falling head permeability tests were not carried out because these tests require additional packing of the soil specimen, which disturbs the loose packing state as explained in Section 8.2.

The differences in the measured permeability during permeation and de-watering stages are attributed to the errors of the validity of Kozeny-Carmen's equation, porosity estimation using CRIM and specific surface estimation using Eq. [3.2-3]. The dominant source of uncertainty is the unknown specific surface of the small fraction (8% maximum) of the unknown clay minerals. The computed uncertainty of permeability is +/-23 x 10^{-9} cm^2 according to Appendix K5.

8.4.5 CONSTITUTIVE RELATIONSHIP BETWEEN ENERGY ATTENUATION AND DEGREE OF WATER SATURATION

Values of reflected amplitudes obtained from the reflection of the base interface were used to determine the energy attenuation (measured by dB/m) within various soil specimens, using Eq. [5-2]. However, this determination suffers from the *differential*, but *un-traceable* and *un-controllable* signal transmission control (STC) (i.e. an automatic gain setting) at different TTT of reflections along the time-axis built in the JRC and the GSSI radar system, as discussed in Section 5.1.2.

The typical ranges of TTT (for example, from 2ns to 2.5ns) for concrete/asphalt from the interface reflections are far smaller than those (for example, from 2ns to 7ns) for soil because of a far smaller amount of water permeation in concrete/asphalt than in soil. Hence, the effects of the *differential* STC on the amplitude of the base interface reflections are not obvious. The determination of energy attenuation for concrete and asphalt was successful, as reported in Chapter 6 and Chapter 7, but not for soil.

8.4.6 CONSTITUTIVE RELATIONSHIP BETWEEN PEAK-FREQUENCY DRIFT AND DEGREE OF WATER SATURATION

Time-domain waveforms obtained in each experiment were transformed to the frequency domain in terms of frequency spectra as shown in Fig. 8-14. These spectra were obtained by carrying out the five data processing techniques described in Chapter 5. In each spectrum, drift of the peak in the frequency axis was observed during the permeation stages and for coarse specimen D to I, this drift was reversed during the de-watering stages. This phenomenon indicates that the values of the peak frequencies obtained from the reflected waveforms are a function of water saturation/water content possessed in soil.

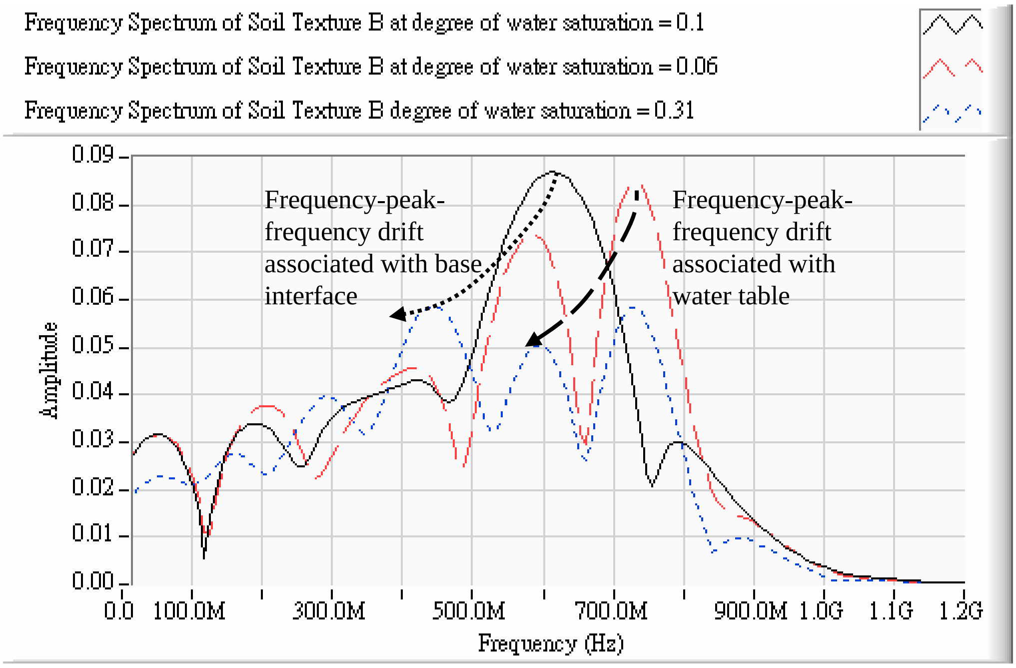

Fig. 8-14 A Number of Frequency Spectra obtained using 1GHz GPR on Soil Specimen B at different S_w and processed with a 750MHz low-pass filter at different S_w

It must be cautious that the peak-frequency drift associated with the base interface may not be the strongest amongst those associated with other reflections in the frequency spectra. In fact, the peak-frequency associated with the transition zone/water table was found to be usually the strongest in the spectra (such as with soil specimen B at S_w = 0.06 in Fig. 8-14), presumably because of its larger dielectric contrast compared to that of the base interface.

To make the variation of the peak frequencies immediately apparent, the frequency spectra transformed from the time-domain waveforms obtained in each soil specimen were stacked and aligned to create sets of a so-called *spectragrams*. This transformation process was detailed in Chapter 5. Each spectragram depicts the stacked frequency spectra over elapsed time obtained in each soil specimen. Fig. 8-15 to Fig. 8-17 depict the three examples of experiments on soil specimens B (poor-graded and very silty, clayey sand), H (poorly-graded and slightly clayey, silty, sandy gravel) and X (well-graded and slightly clayey, very silty, gravelly sand), using the two GPR frequencies. A full set of these spectragrams obtained from all specimens are given in Appendix H3.

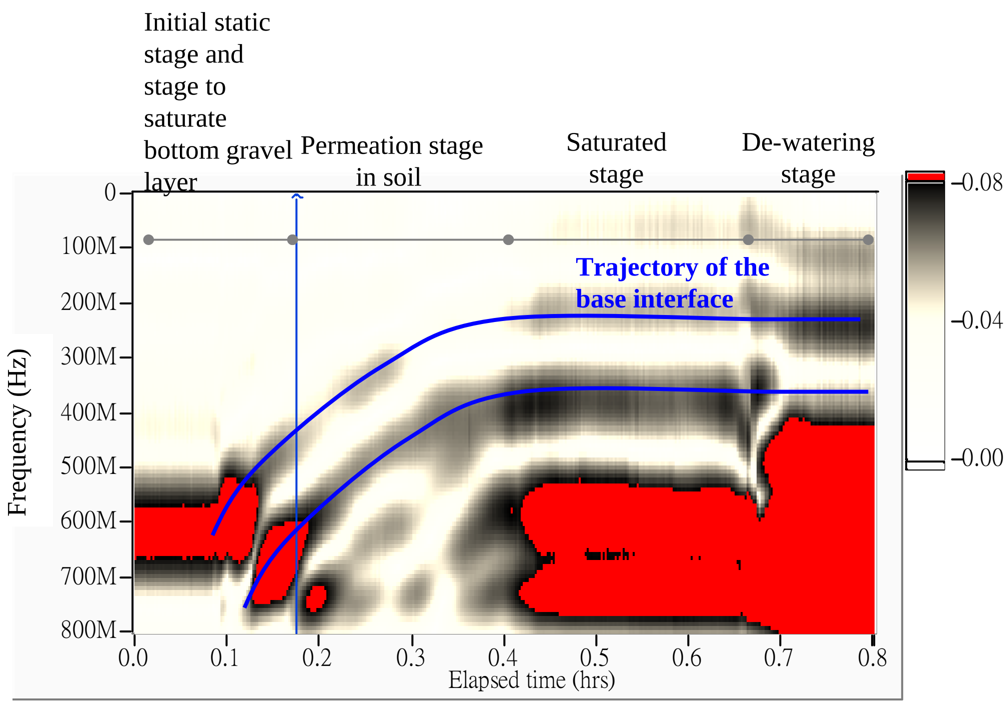

Fig. 8-15 Spectragram obtained in Soil Specimen B using 1GHz GPR and processed with a 750MHz low-pass filter

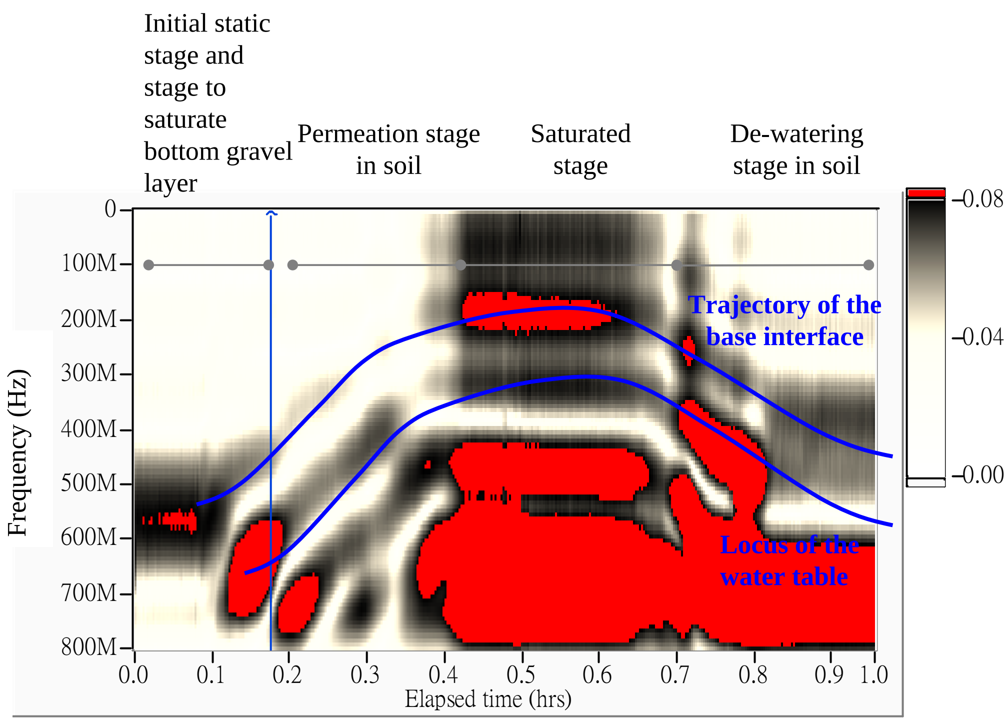

Fig. 8-16 Spectragram obtained in Soil Specimen H using 1GHz GPR and processed with a 750MHz low-pass filter

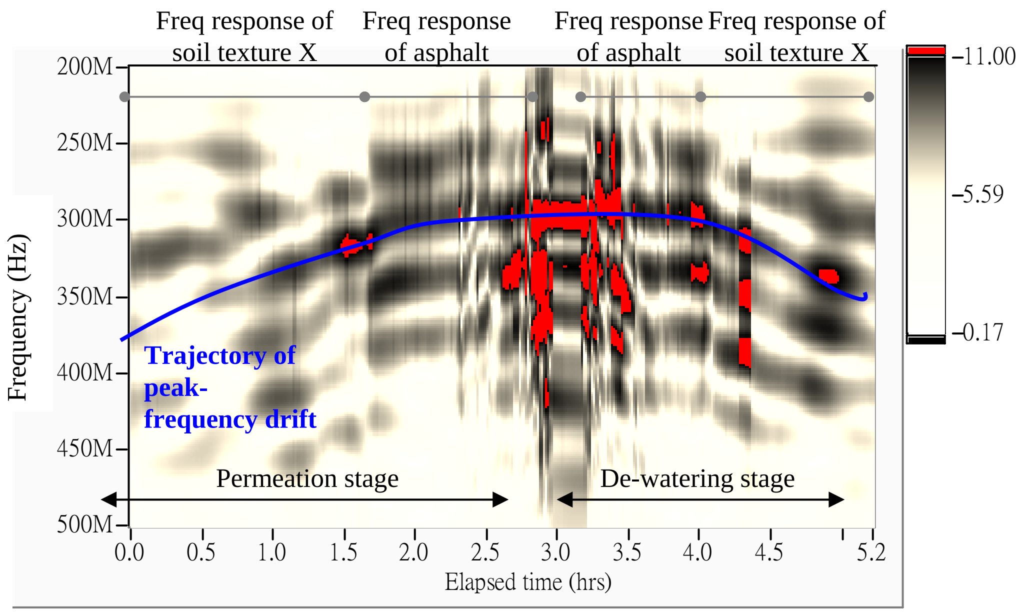

Remark: this figure is identical to Fig.7-12

Fig. 8-17 Spectragram obtained in Soil Specimen X using 400MHz GPR and processed with a 250MHz to 450MHz band-pass filter

The locus/trajectory of the spectragram (as shown in Fig. 8-15, Fig. 8-16 and Fig. 8-17) was traced to determine and quantify the drift of peak-frequency. In each spectrum, the values of peak frequency were extracted and were plotted against the elapsed time (as shown in Fig. 8-18) and respective S_w (as shown in Fig. 8-19). Fig. 8-18 covers the peak-frequency drift over the entire permeation process. The peak-frequency drift during the permeation and de-watering stages of soil specimens was extracted to plot against the S_w, as shown in Fig. 8-19.

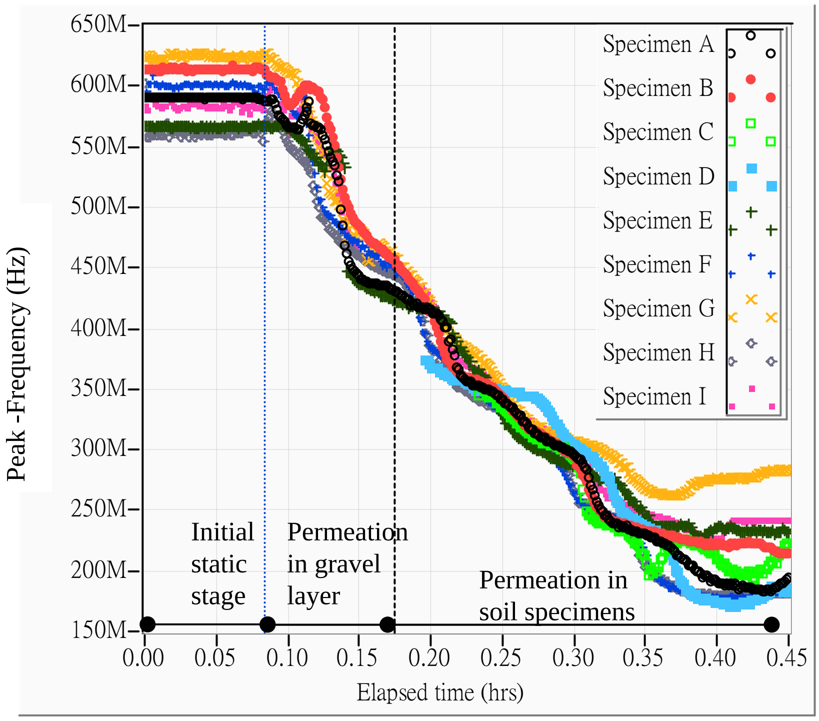

Fig. 8-18 Plots of Peak Frequency against elapsed time using 1GHz GPR (soil specimens A to I) during the Permeation Stages

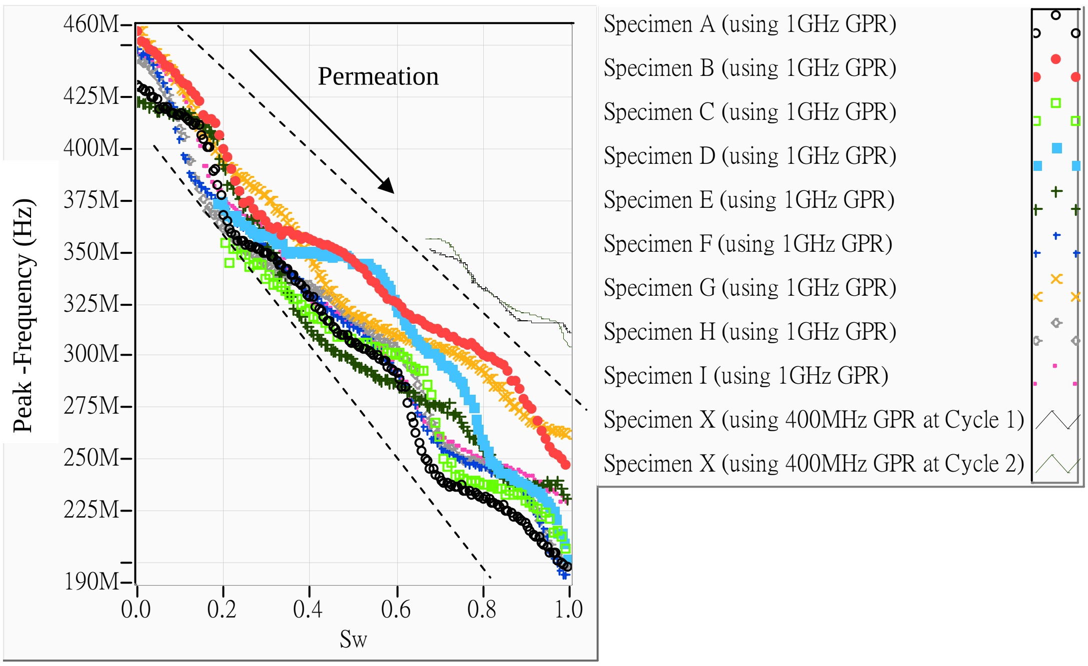

Fig. 8-19a Plots of Peak Frequency against S_w using 1GHz GPR (soil specimens A to I) and 400MHz GPR (soil specimen X in Experiment #2 and #3 described in Ch.7) during the Permeation Stages

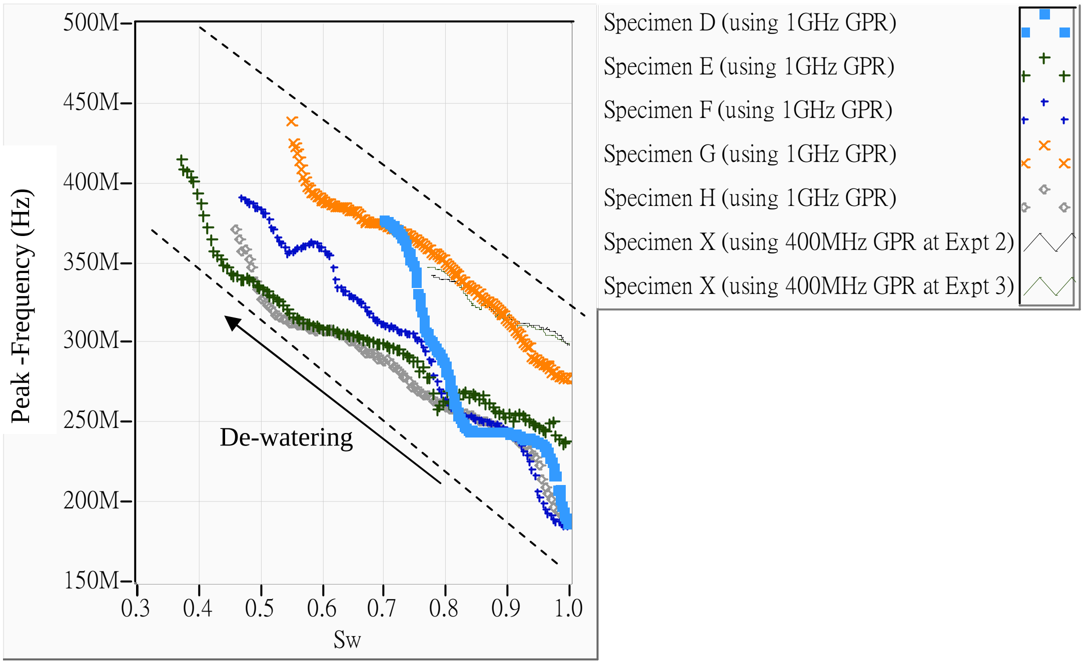

Fig. 8-19b Plots of Peak Frequency against S_w using 1GHz GPR (soil specimen A to I) and 400MHz GPR (soil specimen X in Experiment #2 and #3 described in Ch.7) during the De-watering Stages

Fig. 8-19 depicts clearly the changes of peak frequency as a function of S_w in different soil specimens. However, these plots can be used to estimate the respective S_w in soil but are unable to differentiate different textures among the poorly-graded soils.

8.5 SUMMARY OF FINDINGS

Table 8-4 summarizes a condensed set of fundamental engineering/geological properties of all studied soil textures obtained in this chapter. These properties include:

1. Specific surface,
2. Critical S_w obtained during permeation stage,
3. Porosity and,
4. Permeability.

Table 8-4 Values of Specific Surface Area, Porosity and Permeability in the Soil Specimens

Soil specimen Ref.	**Specific surface***		**Critical S_w obtained during the permeation stages**		**Porosity**			
					Permeation		**De-watering**	
	cm^{-1}	**m^2/g**	400M	1G	400M	1G	400M	1G
A	-		--	0.97	--	0.63	--	N
B				0.88		0.55		
C	1232	0.048		0.87		0.45		
D	1810	0.071		0.80		0.41		0.41
E	467	0.018		0.79		0.39		0.42
F	611	0.024		0.81		0.39		0.38
G	669	0.026		NA		0.38		0.37
H	731	0.028		0.78		0.38		0.35
I	824	0.032		0.78		0.40		-
X	734	0.029	0.88	-	0.45	-	0.48	-

Soil specimen Ref.	**Specific surface***		**Permeability ($x10^{-8}cm^2$)**			
			Permeation		**De-watering**	
	cm^{-1}	**m^2/g**	400M	1G	400M	1G
A	-		--	E	--	N
B				E		
C	1232	0.048		3.8		
D	1810	0.071		1.2		1.2
E	467	0.018		15.2		20.1
F	611	0.024		8.6		7.5
G	669	0.026		6.4		5.7
H	731	0.028		5.6		3.9
I	824	0.032		4.5		--
X	734	0.029	10.8	N	14.7	--

-- : No tests were performed.

NA: Not available since no critical S_w can be defined in the curves in Fig.8b

N: Not available since water could not be drained in the fine soil specimens A, B and C

E: Values are excluded because Kozeny-Carmen's model fails to be applied to soils with a large fraction of silt and clay content.

Remark: The uncertainty analysis of porosity and permeability is referred to Appendices K4 and K5.

Table 8-5 summarizes the EM wave properties of soils obtained through the waveform analysis in both time and frequency domains. These properties include the real permittivity and the peak-frequency drift in the spectragram.

Table 8-5 Summary of Findings in the Experiments of Soil Specimens

Freq.	**Soil specimens**	ε'		Peak frequency (Hz) associated with the base interface	
		At dry state	At saturated state	At dry state	At saturated state
1G	A	3.5	36.7	430.6M	197.7M
	B	3.5	32.6	456.9M	247.4M
	C	4.6	31.4	354.4M	260.1M
	D	3.9	32.7	375.1M	201.7M
	E	5.5	30.7	423.6M	230.7M
	F	4.6	25.8	448.1M	194.0M
	G	4.8	26.2	457.2M	262.0M
	H	2.1	23.2	443.7M	197.8M
	I	2.7	25.2	447.3M	229.1M
400M	X	N/A	28.6	NA	304.6M

Remark: The uncertainty analysis of porosity and permeability is referred to Appendices K2.

The values of the engineering/geological properties (i.e. porosity and permeability) described in Table 8-4 have successfully characterized the ten studied soil specimens used in this series of experiments. These sets of values will be used as a basis of the bench-marking the signature of poorly-graded soil textures (A to I), and finger-printing the well-graded soil specimen X in the two characterization models described in Ch. 10.

8.6 SUMMARY AND DISCUSSION

This experimental study demonstrates the strengths of the *cyclic moisture variation technique* (CMVT) to measure non-invasively the changes in the three electromagnetic radar properties due to the variation of the materials' moisture content. This technique does not require coring samples nor the use of other methods such as EMCTL and TDR which only work for a small mass of samples. The experimental study concludes that the simultaneous tracking of the real permittivities and the degree of water saturation of materials can be used to characterize the texture (i.e. gravel/sand/silt) of soil according to the respective:

1. curves corresponding to each poorly-graded gravel/sand/silt in the plots of real permittivity vs degree of water saturation.
2. values of porosity according to the fitting process of Complex Refractive Index Model (CRIM), and
3. values of permeability according to the computation by Kozeny-Carmen's model.

The findings from the first characteristic clarify the confusion and inconsistency reported from some studies: whether the dielectric properties of soil are texture-dependent, as explained in Section 2.7.1A. For the second characteristic, the porosities obtained by CRIM are found to be larger than those of the independent measurement using the soil mechanics method by an average value of 0.125, and serve as indicators of the actual values. For the last characteristic, the values of permeability obtained by the Kozeny-Carmen's model were found to be in good agreement with the well-known and published characteristic values for these soil textures, as reported in Section 3.5.2. However, the energy attenuation and peak-frequency drift were found not to be able to differentiate and characterize soil textures. The former cannot even be determined due to the automatic gain setting pre-determined in the GPR system. The latter is found not to depend on soil texture, despite it demonstrating a strong dependence on the increase/decrease of water content possessed in all soil specimens during CMVT.

The CMVT created a differential distribution of water along the soil depth, in which different degrees of water saturation and states of water (i.e. bound/free) are related to the existence of a dry zone, transition zone, capillary fringe and water table. In particular, the existence of a transition zone and capillary fringe is the major cause of the existence of a critical S_w found during permeation, as well as the dielectric hysteresis which will be reported in Chapter 9.

The findings reported in this chapter form a technical basis to provide a better in-situ characterization of soil textures, than reliance only on retrieving disturbed soil samples for soil laboratory tests as entailed in traditional civil engineering practice. For the in-situ soil texture characterization, the laboratory CMVT can be replicated in the field, alongside a traditional in-situ pump well test in a quasi-steady state situation. The details of a hypothetical implementation of field CMVT will be described in Chapter 11. In addition, the findings in this chapter also provide sets of data in the unified constitutive models described in Chapter 10.

9. DIELECTRIC HYSTERESIS OF SOIL AND ASPHALT

9.1 INTRODUCTION

Dielectric hysteresis is observed whilst plotting real permittivity against degree of water saturation in the data obtained in the experiment for asphalt (in Ch. 7) and soil specimens A to I, X (in Ch.8). This data consists of pairs of values of ε' determined using 400MHz and 1GHz radar systems and S_w of the tank material when subjected to the CMVT. The up-hill climbing portion of the curve (i.e. permeation) and the down-hill descending portion of the curve (i.e. de-watering) for soil (i.e. with a wide range of texture) and asphalt (i.e. wearing course, road base and sub-base) are found to pursue different pathways. The plots shown in Chapter 7 and Chapter 8 depict these dielectric hysteresis loops exhibited by the data in a fuzzy way. In this chapter, this data is re-arranged by tracing the trajectories of some data pairs of ε' and S_w in Fig. 8-8 and Fig. 8-9 to make these hysteresis loops more apparent.

9.2 DIELECTRIC HYSTERESIS OF SOIL

The real permittivity obtained in the permeation stages using the 1GHz GPR are significantly larger than those obtained in the de-watering stages, given the same S_w as depicted in Fig. 9-1. In particular, there is some correspondence and similarity between the dielectric hysteresis loops identified in the experiments described in this chapter (i.e. between S_w = 0.4 to 1) and those obtained by Knight and Nur (1987a) (i.e. between S_w = 0.1 to 0.9), as discussed in Section 3.2.5.8.

Since the water in soil specimens A, B and C was unable to be drained due to its small particle size, as well as the presence of clay minerals as explained in Section

8.4.1, hysteresis of these finer textured soils cannot be observed and is therefore not included in Fig. 9-1 and Fig. 9-2.

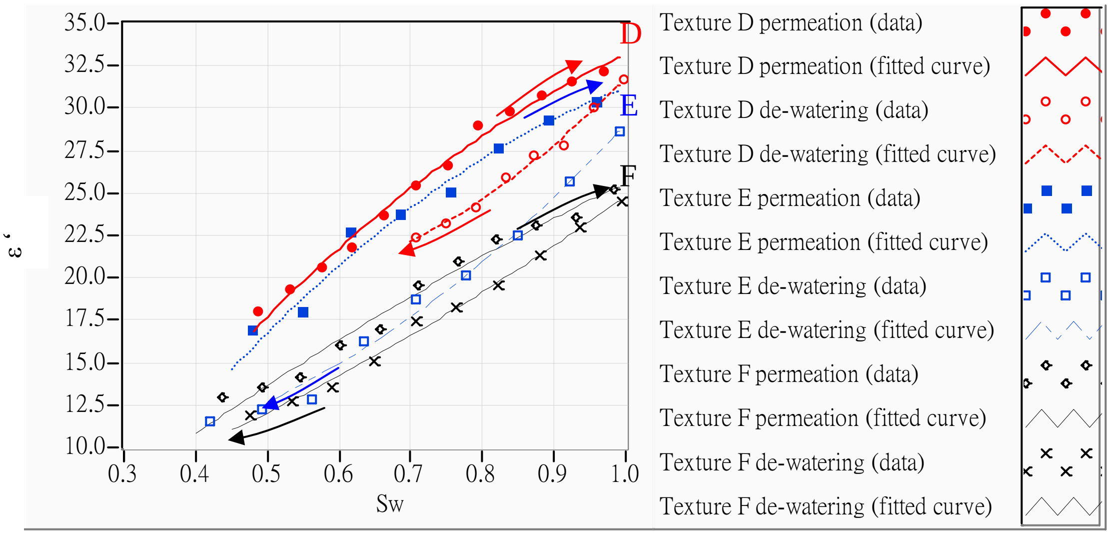

Remark: The fitted curves in this Figure were extracted from the data in Fig. 8-8 and Fig. 8-9

Fig.9-1 Dielectric Hysteresis of Soil Specimens D, E and F under CMVT using 1GHz GPR

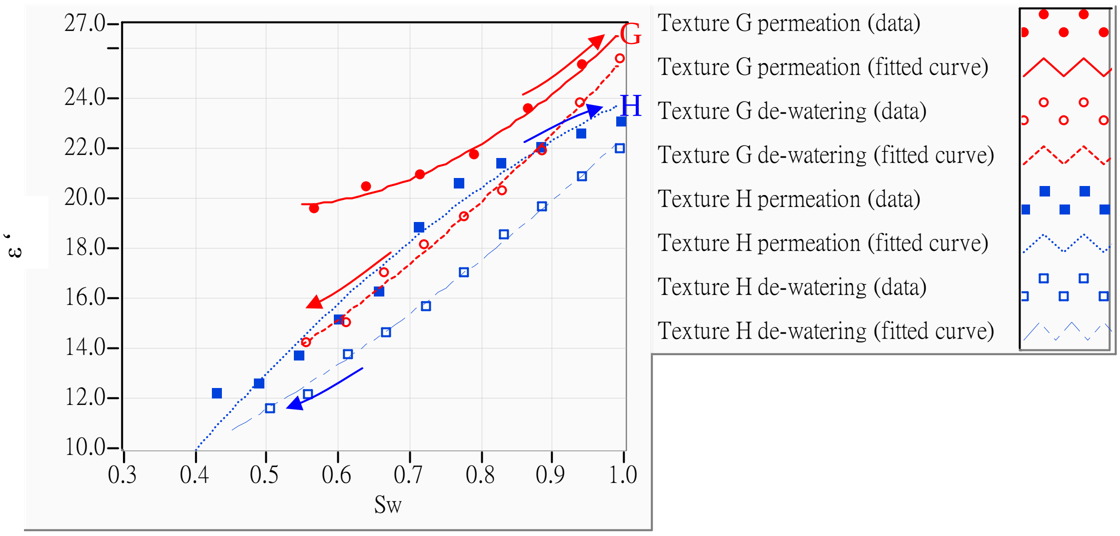

Remark: The fitted curves in this Figure were extracted from the data in Fig. 8-8 and Fig. 8-9

Fig.9-2 Dielectric Hysteresis of Soil Specimens G and H under CMVT using 1GHz GPR

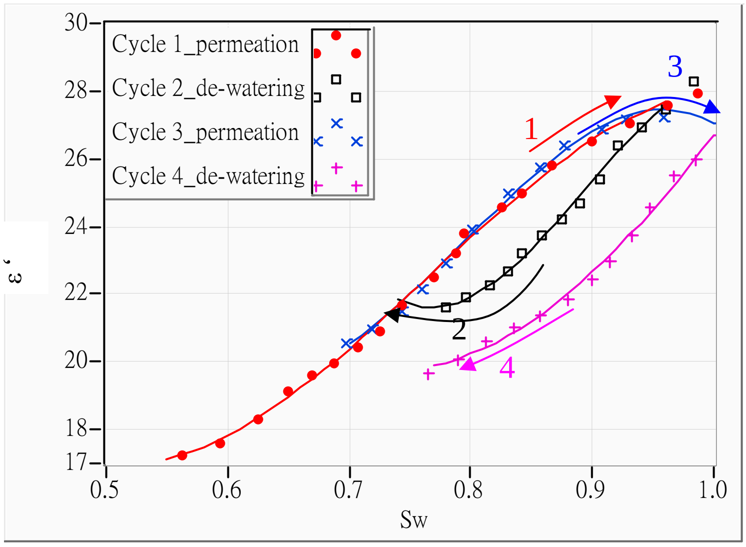

Remark:

1. The fitted curves in this Figure were extracted from the data in Fig. 8-8 and Fig. 8-9.
2. Cycle 1, 2 and Cycle 3, 4 refer to Experiment #2 and #3 described in Ch. 7 respectively.

Fig.9-3 Dielectric Hysteresis of Soil Specimens X under CMVT using 400MHz GPR

9.3 DIELECTRIC HYSTERESIS OF ASPHALT

A similar trend of behaviour regarding the respective sequential dielectric hysteresis loops was also found in asphalt. In Fig. 9-4, the second dielectric hysteresis loop (i.e. Experiment #3) is found to have shifted to lower dielectric values compared to the first loop (Experiment #2). The down-hill descending pathway of the first loop is found to have flipped over that of the ascending climbing portion of the same loop (when 400MHz was used). This flipping-over phenomenon repeated itself for the second dielectric hysteresis loop also (when 400 MHz was also used). However, this curve pattern could also be due to the uncertainty of the measured ε’ as the variation of ε’ was found to be within a very small range.

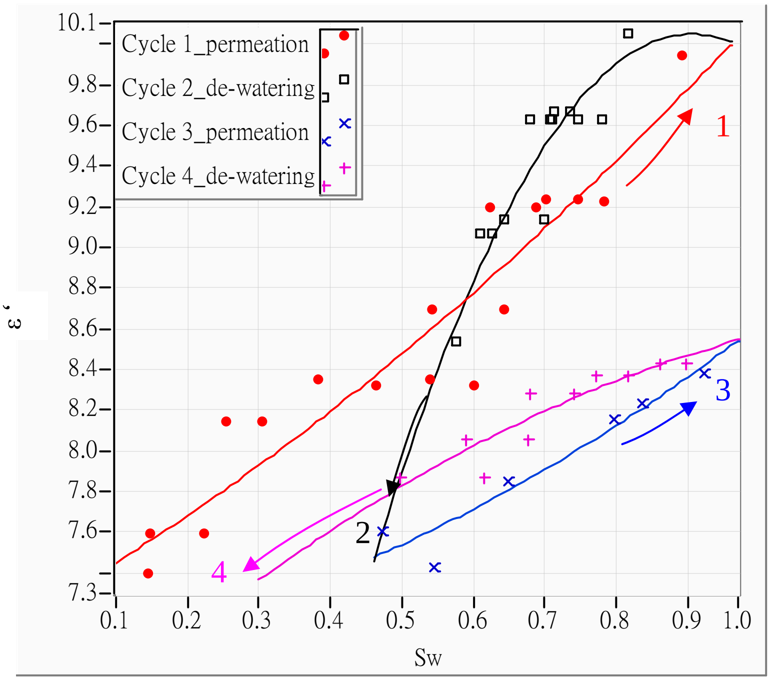

Remark:

1. The fitted curves in this Figure were extracted from the data in Fig. 7-11a
2. Cycle 1, 2 and Cycle 3, 4 refer to Experiment #2 and #3 described in Ch. 7 respectively.

Fig. 9-4 Dielectric Hysteresis of Asphalt under CMVT using 400MHz GPR

9.4 INVESTIGATION INTO SOURCES CAUSING DIELECTRIC HYSTERESIS

The hysteresis loops depicted in the previous figures can only be caused by either the material properties or the operational characteristics of the permeation and pumping facilities. To isolate these two possible sources and the origin of the observed dielectric hysteresis, an experiment was carried out with water alone (i.e. without the inclusion of any material in the test cell). In this experiment, the setup and the procedure were the same as shown in Fig. 8-2.

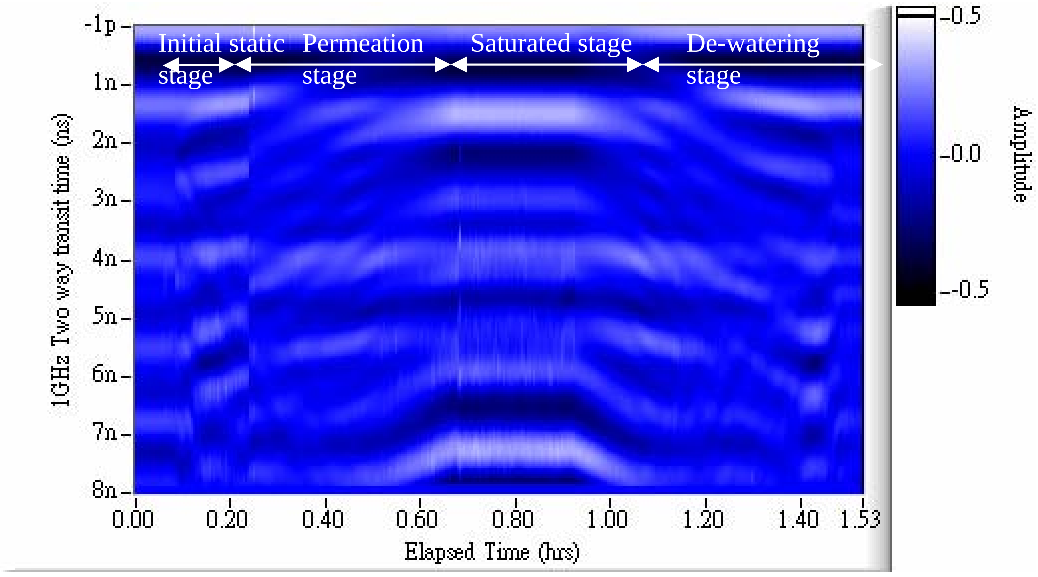

Fig. 9-5 Symmetric Pattern of Reflections in the Radargram obtained in a CMVT Experiment (without soil in the test cell)

The radargram obtained from this experiment shows a perfect symmetry between both permeation and de-watering stages, as shown in Fig. 9-5. No hysteresis was observed in this radargram as a result. Hence the hysteresis loops reported in previous figures are proved to be caused by the effects of the material (i.e. soil and asphalt) and their interaction with water, and not the permeation and pumping facilities.

9.5 CAUSES OF THE OBSERVED DIELECTRIC HYSTERESIS IN SOIL

The observed hysteresis exhibited in the curves of ε' and S_w in soil is probably attributed to the macroscopic and microscopic water distribution:

1. Macroscopic scale of water distribution

In the macroscopic scale of water distribution, the hysteresis loops can be attributed to the effect of bound and capillary water trapped in the transition zone and capillary fringe depicted in Fig. 9-6. According to this figure, the volume of soil in the transition region during the permeation stage is much *smaller* than that found during the de-watering stage. It follows that the volume of bound and capillary water (represented by the areas under the broken lines in Fig. 9-6) contained during the permeation stages should be *smaller* than that contained during the de-watering stages. For the case of a *smaller* volume of bound and capillary water, the response to externally imposed polarization (measured by real permittivity) is *greater* during the permeation stages than the de-watering stages. This is because the polarization ability of bound and capillary water is restricted by the electro-static interaction and motion governed by the fine-grained portion of soil (Huisman et al., 2003; West et al., 2003), as explained in Section 8.4.2B. Hence the real permittivity of the soil is *smaller* during the de-watering than the permeation stages and exhibits hysteresis loops in the curves of ε' and S_w. These remarks are tabulated and summarized in Table 9-1.

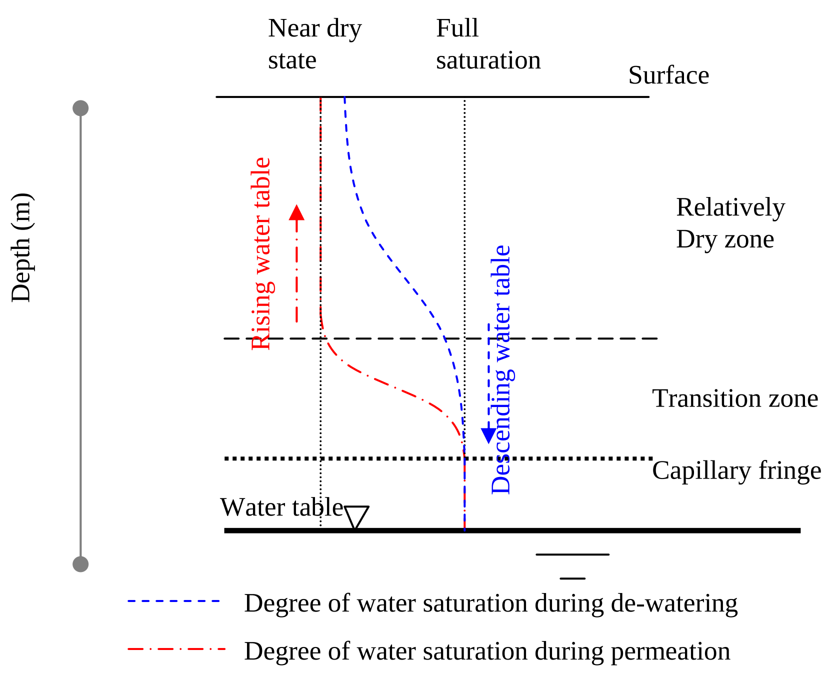

Fig. 9-6 Hypothetical Water Distribution at Various Depths of the Specimens during Permeation and De-watering Stages in CMVT

Table 9-1 Comparison of a Number of Material Properties under the same S_w during both Permeation and De-watering stages

In the transition zone	**Permeation stage**	**De-watering stage**
Volume of soils	smaller	Larger
Volume of bound/capillary water	smaller	Larger
Response to polarization	greater	smaller
Value of real permittivity	greater	smaller

2. Microscopic effect of water-filling and -emptying inside the soil capillaries

In the microscopic scale, a similar hysteresis was also reported by Knight and Nur (1987a) in sandstones during the imbibition and drainage stages using frequency ranging from kHz to MHz. Knight and Nur (1987a) attributed this hysteresis to the water-filling (vapor absorption/imbibition) and -emptying (evaporation/drainage) of the central pore volume. This theory was based on a model describing water adsorption in the capillaries of silica gel proposed by Foster (1932), as described in Section 3.2.5.8. This explanation was based on the experimental results on small-sized samples (with relatively homogeneous water distribution), but not in large-sized specimens (with differential macroscopic water distribution) investigated in this research. However, this theory is considered still valid to explain the dielectric hysteresis observed in these plots since the processes of water-filling and -emptying should have happened in the micro-scale of soil particles.

It is believed that both macroscopic and microscopic factors affected the dielectric hysteresis but quantitative analysis and differentiation between these two factors are not well-understood.

9.6 SUMMARY AND DISCUSSION

From the experimental data, it has been clearly shown that the real permittivity obtained during the de-watering stages can be very different to that determined during the permeation stages, given the same S_w. The phenomenon is known as dielectric hysteresis.

For both soil and asphalt, their shapes and patterns exhibited in the hysteresis loops are found to be quite different. Yet, there is not enough evidence from data to support the idea that these shapes and patterns are unique for the respective material. In asphalt, no apparent literature has reported this type of dielectric hysteresis. Hence, no similar phenomenon can corroborate this phenomenon and there still exists some reservations whether the dielectric hysteresis behaviour of asphalt found in this investigation is real or only exhibit uncertainties of real permittivity.

Dielectric hysteresis (or in essence wetting and drying) was only documented in a handful of studies, such as Knight and Nur (1987a) as described in Section 3.2.5.8. However, a special remark should also be made that the work of Knight and Nur (1987a) was conducted using guided EMCTL (Electromagnetic Coaxial Transmission Line) on a small sample size (i.e. 5.1cm diameter and 0.48cm thickness) of sandstone of small porosity (i.e. 7%), and within a low frequency range (i.e. 10 kHz to 1 MHz). In this research, the following differences are remarked compared to Knight and Nur's (1987a) work:

- a larger volume of soil samples and asphalt samples compared to the traditional guided EMCTL method and TDR/PDP described in Section 2.6, hence a differential distribution of water was created,
- a larger range of porosities (i.e. range from approximately 6% in asphalt and 45% in soil), and
- higher electromagnetic frequencies (i.e. 400MHz and 1GHz) and un-guided EM wave method (i.e. GPR)

Dielectric hysteresis loops reported in this chapter show that the past history of soil wetness/dryness possesses a kind of 'memory' effect associated with the permeation/de-watering cycles. In these series of experiments, all tested soil specimens possess a certain amount of fine particles. It follows that the past history of soil wetness/dryness, as well the presence of fine particles in soil, will exhibit dielectric hysteresis. In other words, this hysteresis may therefore be important in the characterization of fine grained soil, which is based on observing the differences in magnitude of ε' obtained during permeation and de-watering stages, given the same S_w. However, this research has not ventured deeper into the characterization of fine fractions by observing dielectric hysteresis, which is believed to be a worthwhile challenge for future research.

10. ESTABLISHMENT AND FORMULATION OF THE UNIFIED CONSTITUTIVE MODELS TO CHARACTERIZE THE THREE POROUS CONSTRUCTION MATERIALS

10.1 INTRODUCTION

This chapter devises and advocates the use of a number of unified constitutive models (UCMs) to characterize the three porous construction materials (i.e. concrete, asphalt and soil). The establishment and formulation of these models are based on sets of determined values of material properties obtained from sets of coordinated experiments described in Chapter 6 to Chapter 8. These material properties can be divided into two separate categories (i.e. the electromagnetic wave properties and the engineering/geological properties). The former refers to the real permittivity, the energy attenuation and the peak-frequency drift of the returned EM waves. The latter refers to porosity and permeability. The methods to determine the values of the material properties in each of these materials are summarized in Table 10-1.

Table 10-1 Methods to Determine the Electromagnetic Radar Properties and the Engineering/Geological Properties in Concrete, Asphalt and Soil Specimens

<table>
<tr><th colspan="2" rowspan="2">Material property</th><th colspan="3">Methods of determination of the material properties</th></tr>
<tr><th>Concrete</th><th>Asphalt</th><th>Soil</th></tr>
<tr><td rowspan="3">Electro-magnetic wave properties (determined by the 1GHz JRC radar)</td><td>Real permittivity (ε’)</td><td colspan="3">Two-way-transit-time of the reflections of reference interfaces</td></tr>
<tr><td>Energy attenuation (ΔdB/m)</td><td>Reduction in amplitude of the back wall reflection in the time domain returned waves</td><td>Reduction in amplitude of the reflection of interface in the time-domain returned waves</td><td>Not available due to differential and un-traceable automatic gain setting by the radar system (as described in Section 8.4.5)</td></tr>
<tr><td>Peak-frequency drift (Δf)</td><td colspan="3">Frequency spectrum transformed from the time-domain returned waves</td></tr>
<tr><td rowspan="2">Engineering/ geological properties</td><td>Porosity, Pore size distribution</td><td>Gravimetric method and mercury intrusion porosimetry test</td><td colspan="2">Curve-fitting of CRIM using the data of real permittivity and degree of water saturation</td></tr>
<tr><td>Permeability</td><td>Correlation with Initial Surface Absorption Test (ISAT)</td><td>Published data</td><td>Estimation using the Kozeny Carmen model</td></tr>
</table>

10.2 NOTES OF CAUTION OF THE UNIFIED CONSTITUTIVE MODELS

In devising the UCMs, two notes of cautions have been made and are described as follows:

10.2.1 FREQUENCY-DEPENDENT CHARACTERISTICS ON THE THREE EM WAVE PROPERTIES

It is well-known that the three EM wave properties are frequency-dependent. In these UCMs, the experimental data was obtained and determined based on a radar system with a nominal/characteristic frequency of 1GHz. Hence, the values of the EM wave properties in these UCMs cannot directly be applied when other nominal frequencies are used.

10.2.2 EFFECTS OF THICKNESS VARIATION OF THE SPECIMENS ON PEAK-FREQUENCY DRIFT

The thicknesses of the specimens vary according to the design of the experimental rigs of concrete, asphalt and soil. These thickness variations do not pose any problem on the determination of real permittivity and energy attenuation, since the effect of thickness variation of the specimen is fully considered and incorporated during the computation processes, as shown in Eq. [5-1] and Eq. [5-2]. However, this advantage found in the real permittivity and the energy attenuation does not apply to the peak-frequency drift. This is because the transformation from time-domain waveforms to frequency spectra do not involve the consideration of specimen thickness. Therefore remarks have to be made about the thickness variation for the models which involve the peak-frequency drift for clarification purposes.

10.3 CONSTITUTIVE RELATIONSHIP OF THE THREE ELECTROMAGNETIC WAVE PROPERTIES AND DEGREE OF WATER SATURATION IN THE THREE POROUS CONSTRUCTION MATERIALS

Fig. 10-1, Fig. 10-2 and Fig. 10-4 depict the constitutive relationship as sets of plots ($\Delta\varepsilon'$ vs S_w, ΔdB/m vs S_w and Δf vs S_w) obtained from air-cured concrete (as reported in Chapter 6), water-cured concrete (as reported in Chapter 6), asphalt (as reported in Chapter 7), as well as soil of gravelly, sandy and silty textures (as reported in Chapter 8).

10.3.1 REAL PERMITTIVITY VS DEGREE OF WATER SATURATION

The curves obtained in the air-cured concrete and the soil, of a range of textures, exhibit a similar pattern as shown in Fig. 10-1. This similar pattern refers to the initial and final slow-climbing regions that are separated by the fast-climbing region at intermediate S_w. The demarcation points found between the three regions are termed the *transition moisture contents* and the *critical S_w*. The existence of these demarcation points can also be found in some studies reported in the discussions in Section 3.2.5.7.

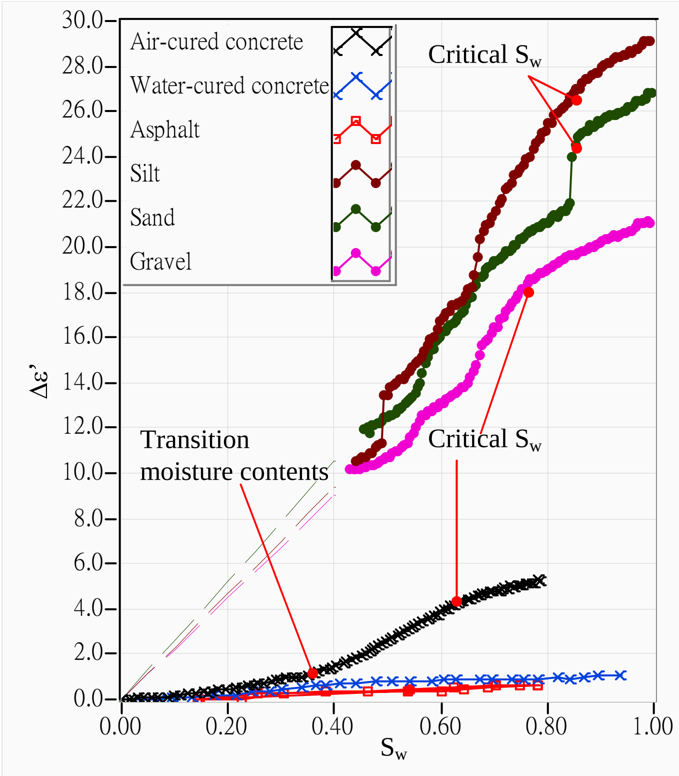

Remark:

1. Data of concrete, asphalt and soil are extracted from Fig. 6-9, Fig. 7-11b (left) and Fig. 8-8 respectively
2. The broken lines are hypothetical connections from the initial state to the lowest attainable Δε' and S_w. No data along these broken lines was available due to un-resolvable interfaces between the ascending transition zone and the base interface of the experimental rig of soil, as explained in Section 8.4.2C.

Fig. 10-1 Plots of Real Permittivity and Degree of Water Saturation in Concrete, Asphalt and Soil Specimens Using 1GHz Radar

The similarity of the plots of ε' vs S_w in the air-cured concrete and the soil (i.e. the presence of the two demarcation points) are thought to be due to similar pore structures/systems possessed in these materials. The pore structures of these materials and their behaviour exhibited in the plots of ε' vs S_w are summarized in Table 10-2.

Table 10-2 Pore Structures/Systems and Curves of the Plots of ε' and S_w in various Porous Construction Materials

Material	**Pore structures/systems**	**Characteristics of the curves of the plots between ε' vs S_w**
Air-cured concrete	Mainly *inter-connected* and relatively large volume of capillary pores (in µm scale) and gel pores (in nm scale) compared to water-cured concrete	Slow-climbing at low S_w and high S_w but fast-climbing at intermediate S_w.
Soil	Mainly *inter-connected* micro-pores (µm scale), capillary pores (in µm to mm scale) and macro-pores (in mm to cm scale)	
Water-cured concrete	Mainly *isolated* macro-pores (mm scale), a relatively small volume of gel pores (mm scale) and capillary pores (in µm scale) compared to air-cured concrete	Relatively gradual increase of ε' over the entire range of S_w
Asphalt	Mainly *inter-connected* macro-pores (in mm scale)	

➢ Slow-climbing regions at high and low S_w in air-cured concrete and soil

The slow-climbing regions at the small S_w and the very high S_w exhibited in *air-cured concrete* and *soil* indicate the reduced ability of water molecules to respond to polarizations driven by an external EM field. This phenomenon is due to the restricted electro-static motion of the solid particles (Huisman et al., 2003 and West et al. 2003). Hence their contributions to real permittivity in these regions of S_w are smaller than those of the fast-climbing region. This phenomenon is attributed to both the macroscopic and microscopic distribution of water contained in the *air-cured concrete* and the *soil* specimens.

In macroscopic scale of water distribution, this phenomenon is tale-tell signs of the volume of bound and capillary water existed in the transition zone and capillary fringe during the permeation stages, but not the de-watering stages. During the permeation stages, the transition zone and capillary fringe, and hence volume of bound and capillary water at an early instant (i.e. at intermediate S_w) were smaller than that at the final instant approaching saturation (i.e. at high S_w). Hence the contribution of real permittivity at an early instant is larger than that at the final instant. The S_w between these two instants demarcates the fast-climbing and the slow-climbing regions, and is known as critical S_w. Detailed discussions of the related theories are referred to Section 8.4.2B.

In microscopic scale of homogeneous water distribution, this phenomenon is attributed to the interaction of water in building-up of mono-layers of bound water over the solid surface (Knight, 1991) in the region of low S_w, and related to loss of connectivity in the gas pockets in the region of high S_w (Knight and Nur, 1987a). Detailed discussions of the related theories are referred to Section 3.2.5.7 and 8.4.2B.

In the cases of *water-cured concrete* and *asphalt*, the fast/slow-climbing regions and therefore the demarcation points (i.e. '*transition moisture contents*' and the '*critical* S_w') do not exist, as depicted in Fig. 10-1. Their absence corresponds to the gradual increase of ε' and only a narrow range of ε' over the entire S_w exists. This implies that these materials possess little pore space/small specific surface for water saturation, and therefore only allow for a small range of ε'. As a result, the fast/slow-climbing curve characteristics and the associated phenomena of bound/free water exhibited in *soil* and *air-cured concrete* do not exist, as depicted in Fig. 10-1.

- Fast-climbing region at the intermediate S_w in all materials

In the fast-climbing region of the intermediate S_w, water is effectively in its free state. This free water allows the formation of water-solid grain capacitors and water-gas capacitors (Knight and Nur, 1987a) which enhance the overall polarizability. Hence the effects of free water on real permittivity are more remarkable than those of bound water.

10.3.2 ENERGY ATTENUATION VS DEGREE OF WATER SATURATION

In the plots of the energy attenuation and S_w depicted in Fig. 10-2, the curves of the air-cured concrete possess both the demarcation points. In particular, the S_w correspondent to the two demarcating points found in the plot of energy attenuations (Fig. 10-2) have similar values to those identified in the plot of real permittivity (Fig. 10-1). This correspondence is possibly attributed to the similar effect of bound and capillary water and free water posed on both real permittivity and energy attenuation, as discussed in Section 10.3.1. For soils of various textures, regrettably no data was available due to un-traceable and differential automatic gain setting by the radar system, as explained in Section 5.1.2 and Section 8.4.5.

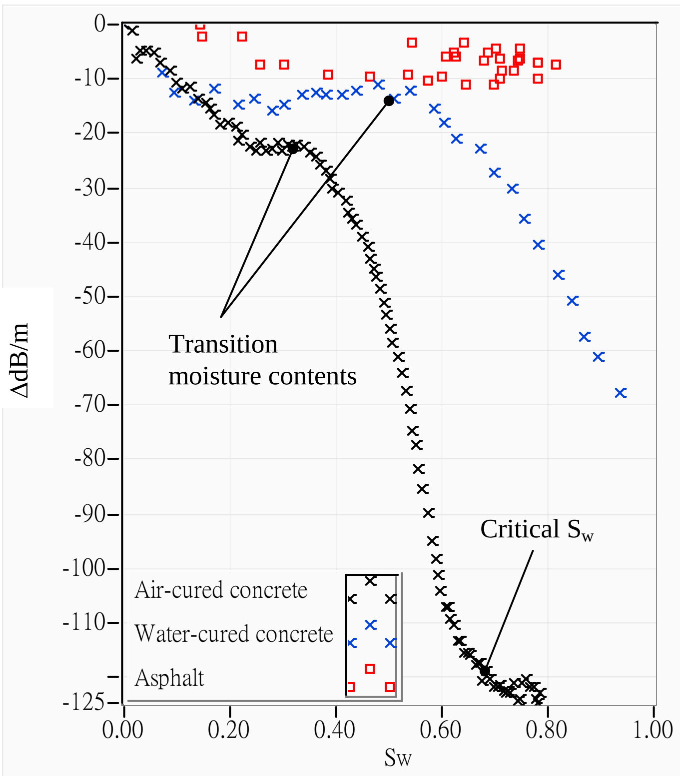

Remark: Data of concrete and asphalt are extracted from Fig. 6-10, Fig. 6-14 and Fig. 7-12 respectively

Fig. 10-2 Plots of Energy Attenuation and Degree of Water Saturation in Concrete and Asphalt Specimens Using 1GHz Radar

Due to the existence of these demarcation points at similar value of S_w in both plots of real permittivity and energy attenuation, it can be deduced that these sharp changes are governed by the same physical phenomena and justifications (i.e. the building-up of mono-layers of bound water, free water, water-solid grain and water-gas capacitors, gas pockets, as discussed in the previous paragraphs). However, such demarcation points are not found in the plot of peak-frequency drift, as shown in Fig. 10-4.

10.3.3 PEAK-FREQUENCY DRIFT VS DEGREE OF WATER SATURATION

The amount of water possessed in the porous materials was found to affect peak-frequency drift of the studied materials. Fig. 10-4 shows that dramatic decreases in magnitude of peak-frequency are found in all concrete and soil specimens, whereas the decrease of peak-frequency in asphalt is relatively small. An experiment (the same as the one described in Section 9.4) was conducted to investigate the effect of free water on the peak-frequency drift so that this effect can be compared to those in concrete, asphalt and soil. In this experiment (termed '*air-experiment*'), the rig design, setup, data acquisition and analysis are the same as those described in Chapter 8, except that no soil was introduced into the test cell. The radargram and the spectragram obtained from this experiment are depicted in Fig. 10-3a and Fig. 10-3b.

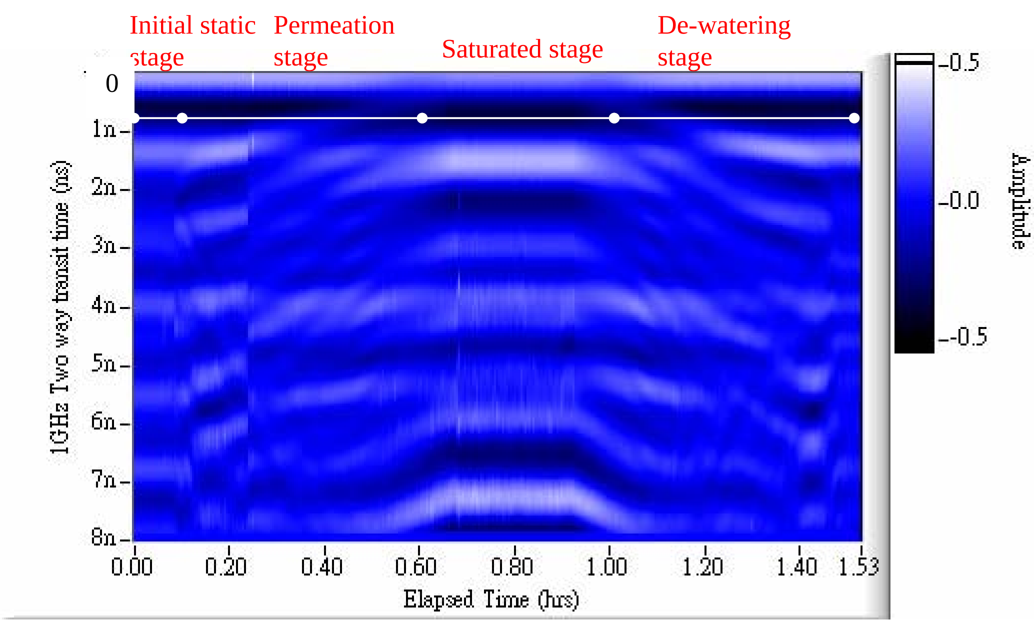

Fig. 10-3a Symmetric Pattern of Reflections in the Radargram obtained in a CMVT Experiment (without soil in the test cell)

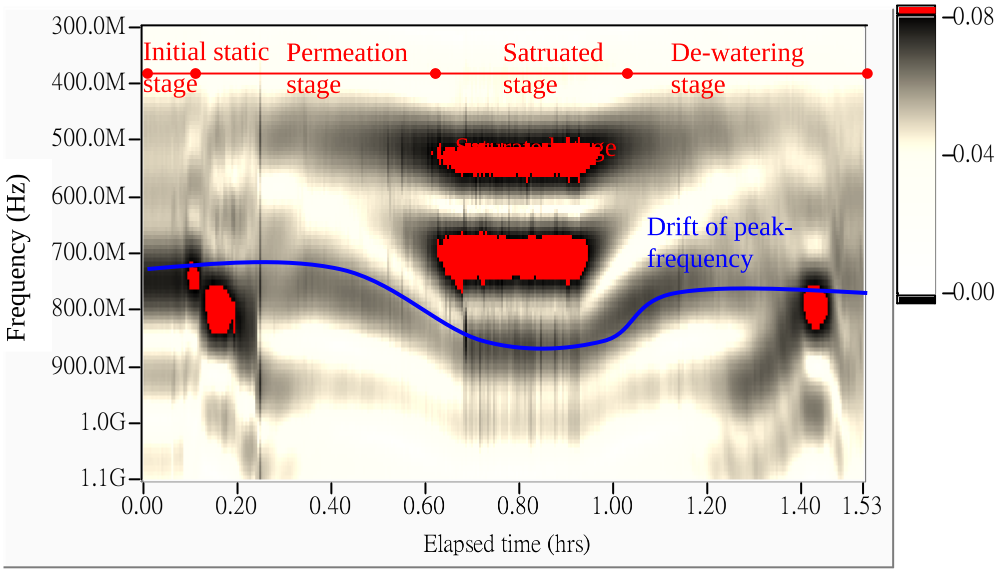

Fig. 10-3b Symmetric Pattern of Frequency Spectra in the Spectragram obtained under CMVT Experiment (without soil in the test cell) and processed with a 2GHz low-pass filter

In contrast to the results obtained in the experiments on concrete, asphalt and soil described in Chapter 6 to Chapter 8, the peak-frequency in the air-experiment increases with an increasing amount of free water, as shown in Fig. 10-3b. The peak-frequency was increased during the permeation stage and was restored back to the original value during the de-watering stage, as depicted in Fig. 10-3b.

Each of the trajectories obtained in the studied porous materials and in air obtained during the permeation stage was tracked and plotted in Fig. 10-4. This figure indicates that the decreases in magnitude of peak-frequency of concrete and soil are the largest, followed by a smaller decrease with asphalt, whereas the peak-frequency of free water increases.

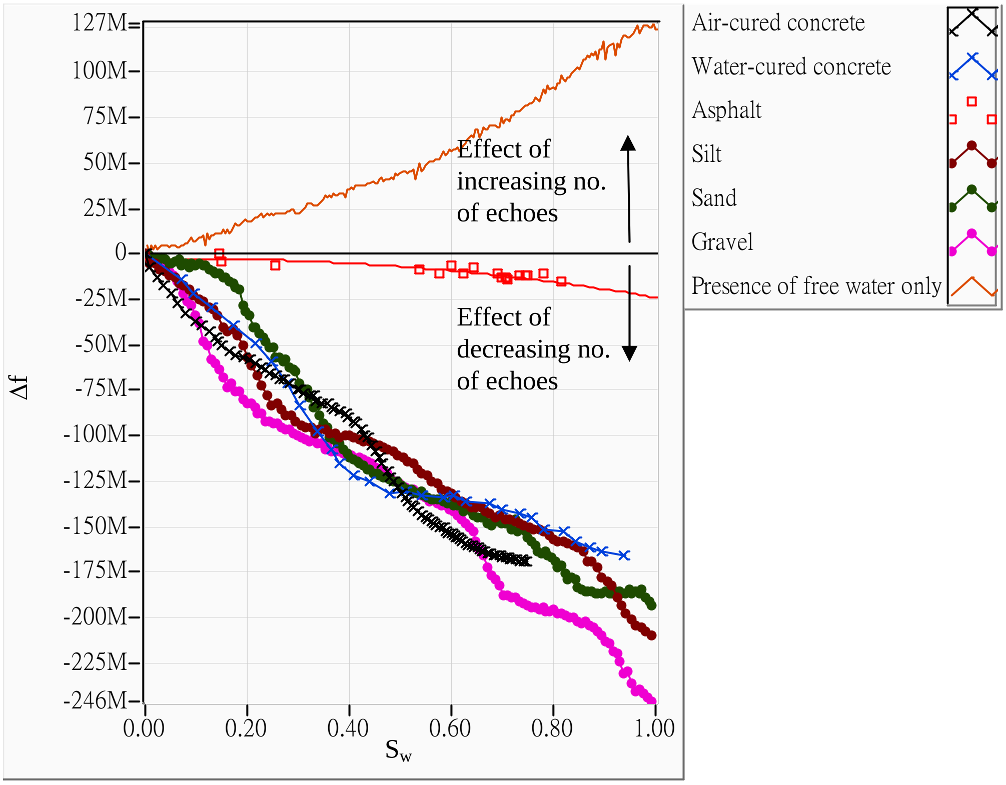

Remark: Data of concrete, asphalt and soil is extracted from Fig. 6-15, Fig. 7-15b and Fig. 8-18 respectively, whereas data of free water is extracted from that obtained in the permeation stage in the spectragram shown in Fig. 10-4.

Fig. 10-4 Plots of Peak-frequency Drift and Degree of Water Saturation in Concrete, Asphalt and Soil Specimens Using 1GHz Radar during the Permeation Stages

Table 10-3 The Effects of Number of Echoes in Waveforms on the Drift of Peak-Frequency in Experiments on Different Porous Construction Materials during both Permeation and De-watering Stages

Stage	**Materials**	**Time required to separate the echoes in time-domain waveforms**	**Number of multiple echoes**	**Peak-frequency**
Permeation	Concrete Asphalt Soil	longer	decrease	Smaller
	Air (only free water was present)	shorter	increase	Larger
De-watering	Concrete Asphalt Soil	shorter	increase	Larger
	Air (only free water was present)	longer	decrease	smaller

When concrete, asphalt and soil were wetted during the permeation stages, real permittivity was increased because of water permeation; hence the time separating these echoes was further separated and the number of multiple echoes in the waveforms was decreased, and the behaviour was reversed in the air-experiment.

These characterizatics are summarized in Table 10-3 and explained in the simulated results described in Section 5.2.3.

10.4 UNIFIED CONSTITUTIVE MODELS BASED ON ELECTROMAGNETIC WAVE PROPERTIES (REAL PERMITTIVITY, ENERGY ATTENUATION AND PEAK-FREQUENCY DRIFT)

Table 10-4 reports the largest values of the three EM wave properties identified in the experiments on concrete, asphalt and soil as described in Chapter 6, 7 and 8 respectively. These values are determined when the materials were at the saturated or the near-saturated state.

Table 10-4 The Largest Values of Real Permittivity, Energy Attenuation and Peak-frequency Drift Determined in the Experiments on Concrete, Asphalt and Soil Specimens Using the 1GHz Radar

Material		The largest real permittivity $\Delta\varepsilon'$ (At 1GHz)	The largest energy attenuation ΔdB/m	The largest peak-frequency drift Δf (MHz)
Concrete	Air-cured	+6.2	-138.9	-228
	High A/C ratio	+1.7	-81.7	-166
	Low A/C ratio	+2.4	-85.8	-160
Asphalt	Wearing course, base course	+1.1	-11	-23
Soil texture	Silt	+33.2	-	-233
	Sand	+29.1	-	-210
	Gravel	+25.2	-	-254

Remarks:

1. The largest $\Delta\varepsilon'$, ΔdB/m and Δf correspond to a saturated or nearly saturated state of the material. The positive/negative signs of the values are relative to the values obtained in the initial dry state of the material.
2. A/C: Aggregate to cement ratio, high A/C ratio refers to 6:1, and low A/C ratio refers to 4.3:1 and 3:1.
3. The values of energy attenuation (or signal attenuation) in soil were not determined due to the differential, un-traceable and un-controllable gain setting of the GPR systems, as described in Section 5.1.2 and Section 8.4.5.
4. The energy attenuation and the drifts of peak-frequency of concrete, asphalt and soil are determined with sample thickness of 150mm, 450mm and 140-182mm respectively.

The data reported in Table 10-4 were used to assign the material to their rightful regions entailed in the UCM #1 which provides a means to characterize the three construction materials, as depicted in Fig. 10-5.

The UCMs devised and reported in this section are established and formulated to depict the properties of the three porous construction materials from purely using the EM wave properties alone. Presentations of the models are in the form of the triangular diagram (Fig. 10-5), as well as 2D and 3D contour plots (Fig. 10-6 to 10-10).

In UCM #1, a less porous material occupies a region at the bottom left hand corner, whereas a more porous material occupies to the region in the direction of the arrow. $\Delta\varepsilon'$, ΔdB/m and Δf increase in magnitude along the direction of the arrow. The ultimate boundaries designated for a particular material as marked with different colours correspond to the values of the maximum change in values of the material properties at their saturated or near-saturated state, as reported in Table 10-4.

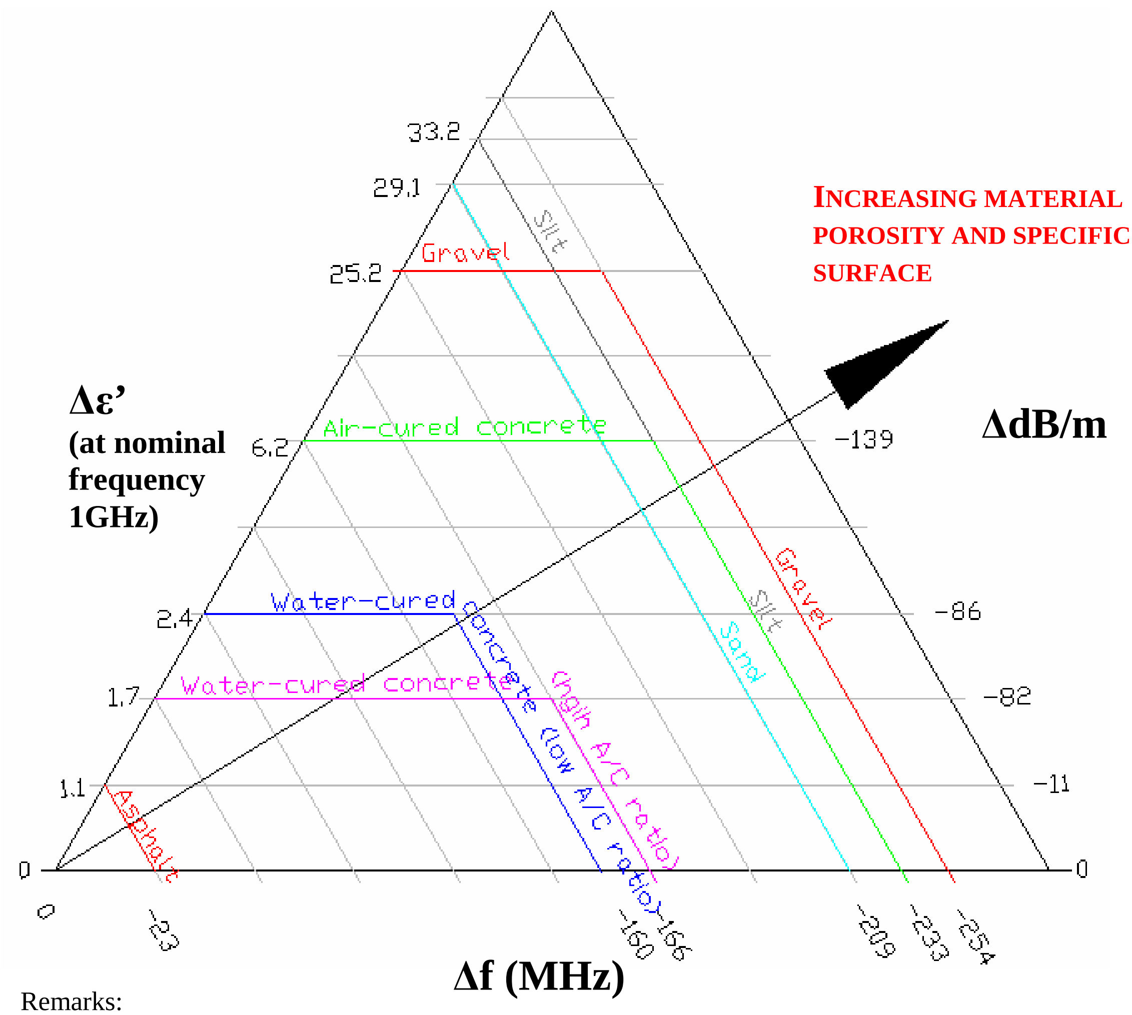

Remarks:

1. The methods to determine these values are according to Table 10-1, whereas the values of the experimental findings are summarized in Table 10-4.
2. The propagation of the ultimate boundary of a material (along the arrow) describes a wetting process from the point at initial dry state (i.e. the bottom left of the triangular diagram) to the saturated state (i.e. the ultimate boundaries marked with different colours). In this process the position of these ultimate boundaries are governed by the material porosities which vary significantly.
3. A/C ratio: Aggregate to cement ratio
4. The values of the peak-frequency drift of concrete, asphalt and soil are determined with sample thickness of 150mm, 450mm and 140-182mm respectively.
5. The value of material properties in each axis are in an arbitrary scale.

FIG. 10-5 Unified Constitutive Model #1: Real Permittivity, Energy Attenuation and Peak-Frequency Drift of Concrete, Asphalt and Soil Specimens Using 1GHz Radar

Similar ultimate boundaries can also be plotted in a three dimensional diagram as shown in UCM #2, as depicted in Fig. 10-6. These three dimensional contour plots are also used to depict the progressive changes of the EM wave properties due to increasing S_w in air-cured concrete (UCM #3), soil (UCM #4), water-cured concrete

(UCM #5) and asphalt (UCM #6).

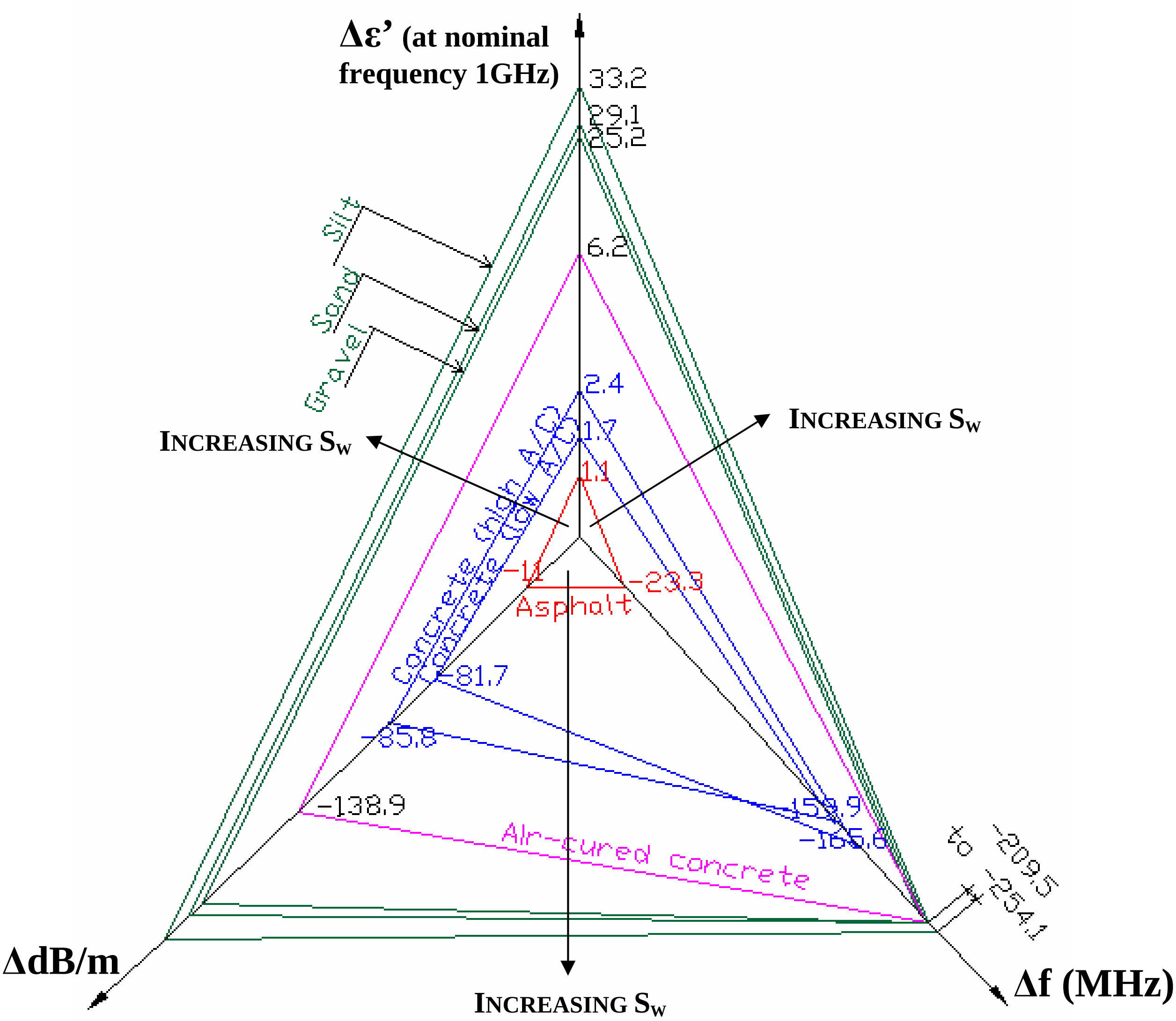

Remarks:
1. The methods to determine these values are according to Table 10-1, whereas the values of the experimental findings are summarized in Table 10-4.
2. The propagation of the ultimate boundary of a material (pointing outward from the axes) describes a wetting process from the point at initial dry state (i.e. the bottom left of the triangular diagram) to the saturated state (i.e. the ultimate boundaries marked with different colours). In this process the position of these ultimate boundaries are governed by the material porosities which vary significantly.
3. A/C ratio: Aggregate to cement ratio
4. The values of the peak-frequency drift of concrete, asphalt and soil are determined with sample thickness of 150mm, 450mm and 140-182mm respectively.
5. The values of material properties in each axis are in an arbitrary scale.

Fig. 10-6 Unified Constitutive Model #2: Real Permittivity, Energy Attenuation and Peak-Frequency Drift of Concrete, Asphalt and Soil Specimens Using 1GHz Radar

The 3D plots from Fig. 10-7 to 10-10 depict the fact that the variations of $\Delta\varepsilon'$, ΔdB/m and Δf expand as S_w increases along the direction of the arrows. These plots are successful in depicting the demarcation points associated with the slow-climbing regions at small S_w and very high S_w, as illustrated by the contrast amongst highly and less dense contour lines for air-cured concrete and soil. On the other hand, the less dense contour lines for well-cured concrete and asphalt indicate that these demarcation points do not exist.

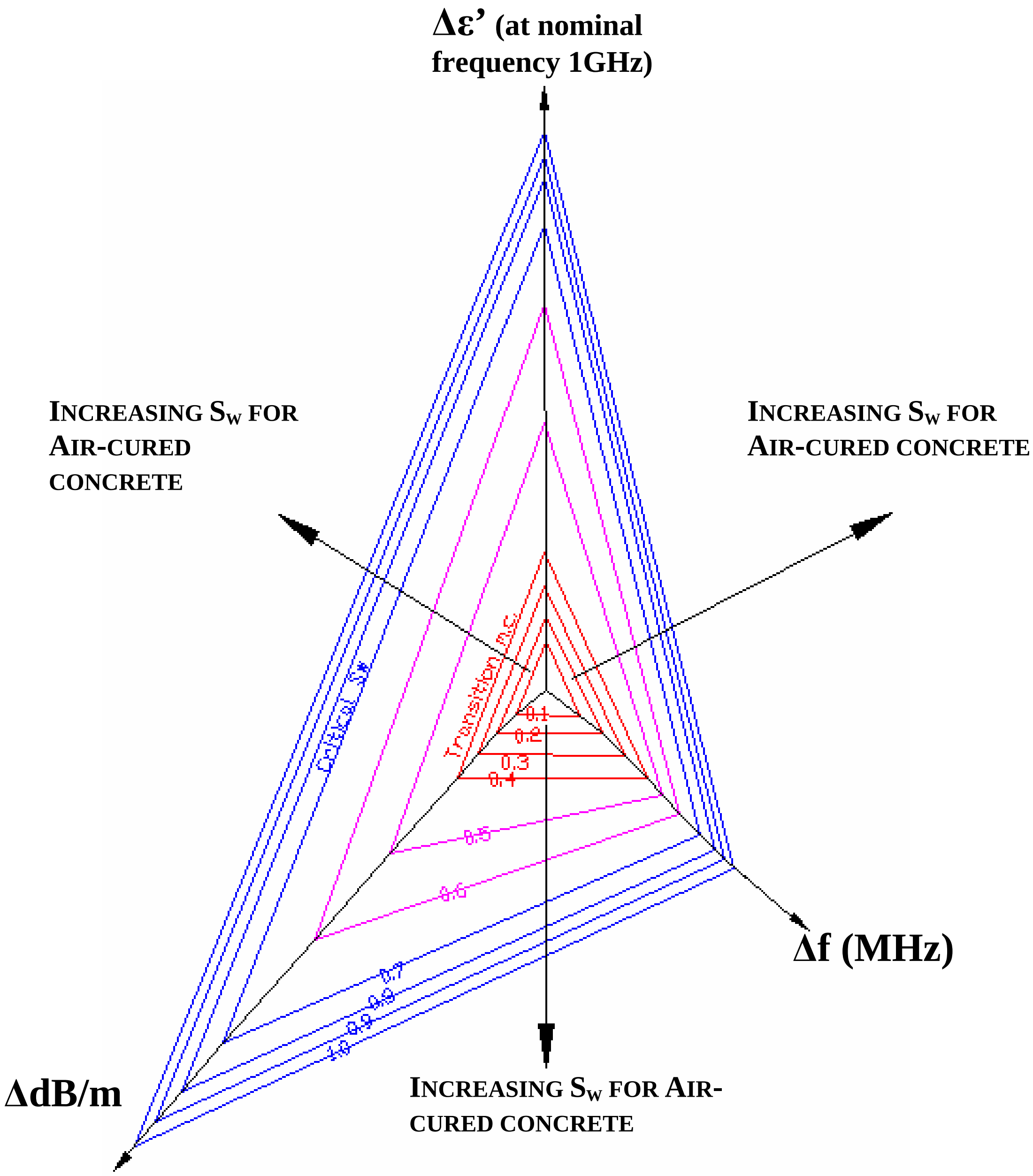

Remarks:
1. The methods to determine these values are according to Table 10-1, whereas the values of the experimental findings are summarized in Table 10-4.
2. The propagation of the ultimate boundary of a material (pointing outward from the axes) describes a wetting process from the point at initial dry state (i.e. the bottom left of the triangular diagram) to the saturated state (i.e. the ultimate boundaries marked with different colours). In this process the position of these ultimate boundaries are governed by the material porosities which vary significantly.
3. A/C ratio: Aggregate to cement ratio
4. The values of the peak-frequency drift of concrete, asphalt and soil are determined with sample thickness of 150mm, 450mm and 140-182mm respectively.
5. The values of material properties in each axis are in an arbitrary scale.

Fig. 10-7 Unified Constitutive Model #3: Real Permittivity, Energy Attenuation and Peak-Frequency Drift of Air-cured Concrete Specimens Using 1GHz Radar

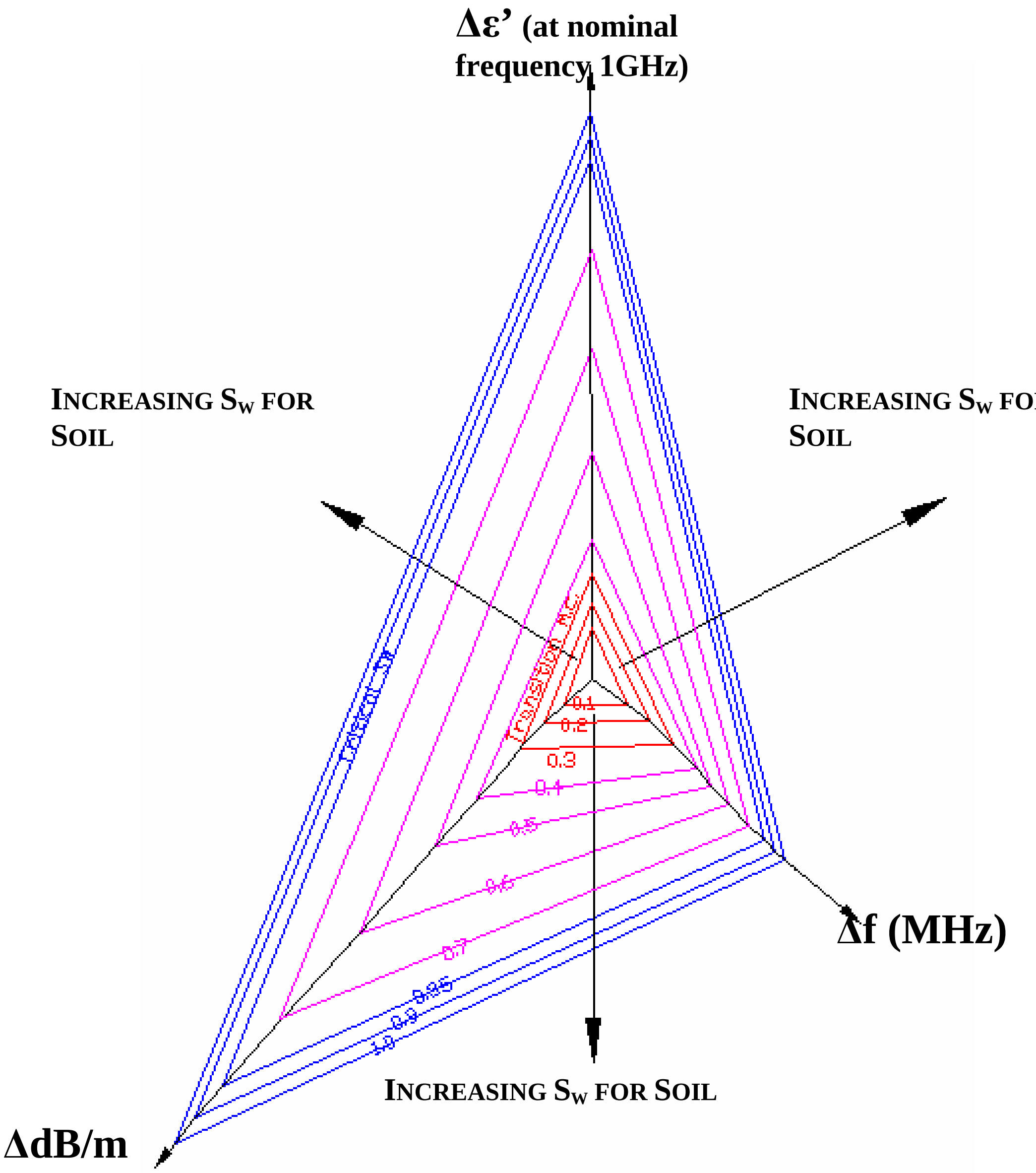

Remarks:

1. The methods to determine these values are according to Table 10-1, whereas the values of the experimental findings are summarized in Table 10-4.
2. The propagation of the ultimate boundary of a material (pointing outward from the axes) describes a wetting process from the point at initial dry state (i.e. the bottom left of the triangular diagram) to the saturated state (i.e. the ultimate boundaries marked with different colours). In this process the position of these ultimate boundaries are governed by the material porosities which vary significantly.
3. A/C ratio: Aggregate to cement ratio
4. The values of the peak-frequency drift of concrete, asphalt and soil are determined with sample thickness of 150mm, 450mm and 140-182mm respectively.
5. The values of material properties in each axis are in an arbitrary scale.

Fig. 10-8 Unified Constitutive Model #4: Real Permittivity, Energy Attenuation and Peak-Frequency Drift of Soil Specimens Using 1GHz Radar

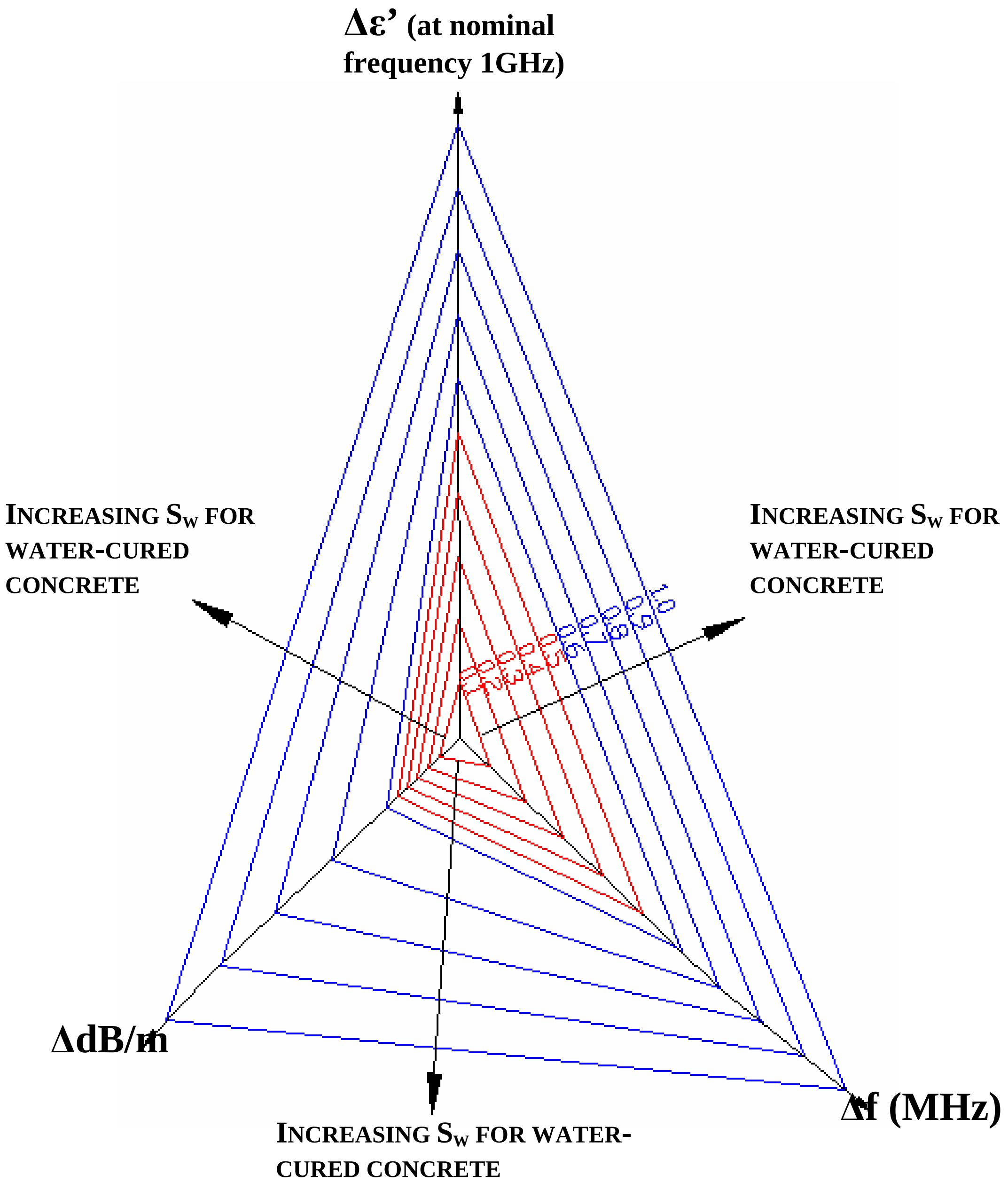

Remarks:
1. The methods to determine these values are according to Table 10-1, whereas the values of the experimental findings are summarized in Table 10-4.
2. The propagation of the ultimate boundary of a material (pointing outward from the axes) describes a wetting process from the point at initial dry state (i.e. the bottom left of the triangular diagram) to the saturated state (i.e. the ultimate boundaries marked with different colours). In this process the position of these ultimate boundaries are governed by the material porosities which vary significantly.
3. A/C ratio: Aggregate to cement ratio
4. The values of the peak-frequency drift of concrete, asphalt and soil are determined with sample thickness of 150mm, 450mm and 140-182mm respectively.
5. The values of material properties in each axis are in an arbitrary scale.

FIG. 10-9 Unified Constitutive Model #5: Real Permittivity, Energy Attenuation and Peak-Frequency Drift of Water-cured Concrete Specimens Using 1GHz Radar

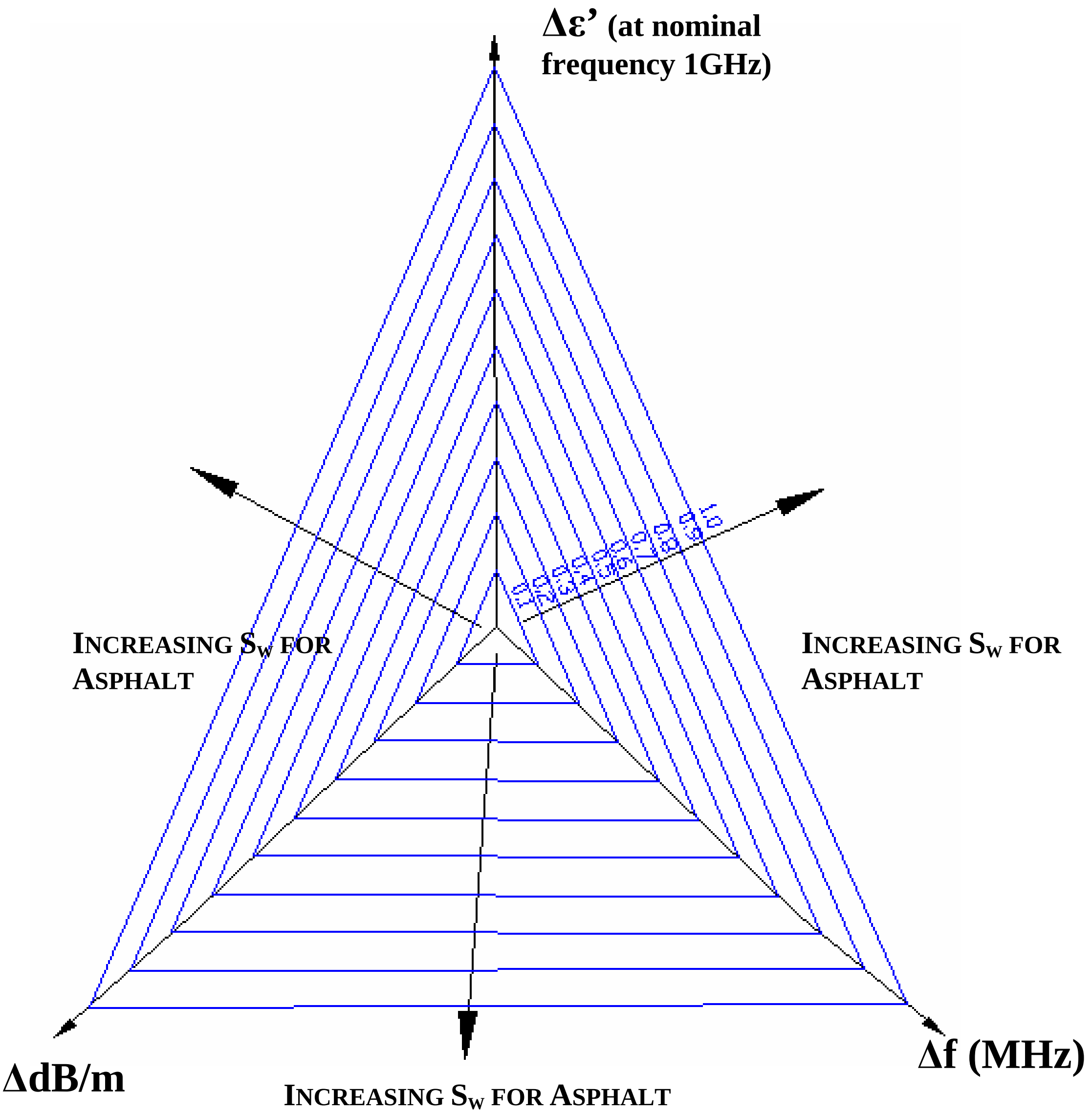

Remarks:

1. The methods to determine these values are according to Table 10-1, whereas the values of the experimental findings are summarized in Table 10-4.
2. The propagation of the ultimate boundary of a material (pointing outward from the axes) describes a wetting process from the point at initial dry state (i.e. the bottom left of the triangular diagram) to the saturated state (i.e. the ultimate boundaries marked with different colours). In this process the position of these ultimate boundaries are governed by the material porosities which vary significantly.
3. A/C ratio: Aggregate to cement ratio
4. The values of the peak-frequency drift of concrete, asphalt and soil are determined with sample thickness of 150mm, 450mm and 140-182mm respectively.
5. The values of material properties in each axis are in an arbitrary scale.

FIG. 10-10 Unified Constitutive Model #6: Real Permittivity, Energy Attenuation and Peak-Frequency Drift of Asphalt Specimens Using 1GHz Radar

10.5 UNIFIED CONSTITUTIVE MODEL BASED ON REAL PERMITTIVITY, POROSITY AND PERMEABILITY

The HUCM was established and formulated to integrate the real permittivity (ε') and the two engineering/geological properties of the three porous construction materials. The real permittivity is defined at the saturated or near-saturated state of the materials. The engineering/geological properties refer to the porosity and the permeabilities. The three properties described in HUCM were determined by the methods summarized in Table 10-1. Table 10-5 reports the largest values of the real permittivity, the estimated porosity and the estimated coefficient of permeability identified in the experiments on concrete, asphalt and soil as reported in Chapters 6, 7 and 8 respectively.

Table 10-5 Values of Real Permittivity, Energy Attenuation and Peak-frequency Drift Determined in the Experiments on Concrete, Asphalt and Soil Specimens Using the 1GHz Radar

Material		The largest real permittivity $\Delta\varepsilon'$ (at 1GHz) obtained in the experiments	Porosity (%)	Coefficient of permeability (m/s)
Concrete	Air-cured	+6.2	18.9-21	$> 10^{-10}$
	High A/C ratio	+1.7	13.6-17.5	$> 10^{-10}$
	Low A/C ratio	+2.4	15.9-19.9	10^{-12} to 10^{-10}
Asphalt	Wearing course, base course	+1.1	2.3	10^{-5}
Soil	Silt	+33.2	63	N/A
	Sand	+29.1	41-55	12-38 (x10^{-6})
	Gravel	+25.2	35-42	39-201 (x10^{-6})

Remarks:
1. Values of $\Delta\varepsilon'$, porosity and sand/gravel permeability are obtained from Section 6.5, 7.5 and 8.5.
2. A/C: Aggregate to cement ratio, high A/C ratio refers to 6:1, and low A/C ratio refers to 4.3:1 and 3:1.
3. The largest real permittivity is obtained when the material is in a saturated or nearly saturated state.
4. The porosities of each group of material are the average values of all specimens in that group.
5. The values of permeability of concrete are inferred from the Initial Surface Absorption Test according to the Concrete Society (1987). Hence they do not represent the true coefficients of permeability obtained from actual experiment.
6. The value of permeability of asphalt is based on characteristic values.
7. The value of permeability of silt is not available due to the break-down of the Kozeny-Carmen's model to model the structured soil bodies (Hillel, 1980) such as fissured fine particles in silt/clay, as explained in Section 8.4.4.

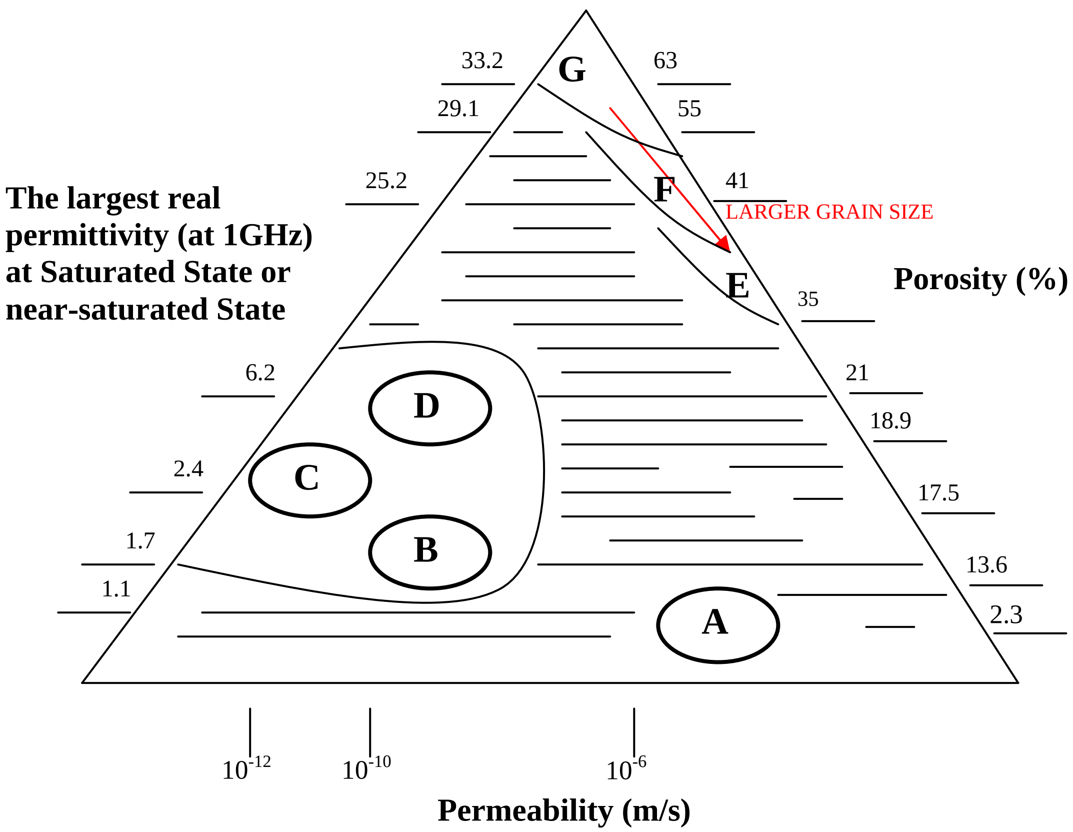

A. Asphalt (base course, wearing course)
B. Water-cured concrete (higher aggregate to cement ratio)
C. Water-cured concrete (lower aggregate to cement ratio)
D. Air-cured concrete due to the effect of water
E. Gravel
F. Sand
G. Silt

Remarks:
1. The methods to determine these values are according to Table 10-1 and experimental findings from Chapter 6 to Chapter 8,
2. The values of material properties in each axis are in an arbitrary scale.
3. The porosities of soils E, F and G are obtained from the Complex Refractive Index Model (CRIM) and exhibit a certain degree of errors compared to the real values, as explained in Section 8.4.3.
4. The coefficients of permeability of concrete are inferred from the ISAT results and do not represent the true coefficients of permeability obtained from actual experiment

Fig. 10-11 Unified Constitutive Model #7: Ultimate Real Permittivity, Porosity and Permeability of Concrete, Asphalt and Soil Specimens

In the UCM #7, the region of air-cured concrete (denoted by 'D') possesses the largest values of all three material properties, presumably due to its dominant volume of gel pores and inter-connected capillary pores. Water-cured concrete of low A/C ratio (denoted by region C) has a larger value of ultimate real permittivity and is more porous, but less permeable than those of a high A/C ratio (denoted by region B).

To the upper apex of the UCM #7, soils of various textures possess the largest values of the three material properties. Within this group, gravel (as denoted by region E) possess the smallest porosity and the smallest ultimate real permittivity, followed by the larger values in sand (denoted by region F), and the largest in silt (denoted by region G). This order is reversed in the case of permeability. The three material properties characterized in this model are shown to be governed by the soil textures. These orders show that the soil of finer texture is more porous and possesses larger values of real permittivity, but less permeable than those of coarse texture. For clay (of various types) in the family of soil, it would have been expected to occupy a position which has a larger porosity and smaller permeability than that occupied by silt. However, clay was not incorporated in these models because experiment on pure clay was not possible.

The values of the ultimate real permittivity and the porosity of asphalt are found to be the smallest amongst all the studied materials, but it is very permeable and is in the same order as gravel. The sub-divisions of each asphalt layer (i.e. wearing course, base course and sub-base) are not able to be characterized from this model, because of their very similar pore structure/systems.

In this model, the real permittivity and the porosity manifested in a tied relationship (i.e. an increase/decrease of one property always leads to an increase/decrease of another). However, a material with high porosity/high real permittivity does not necessarily imply high permeability, as shown in the cases of silt. This phenomenon is presumably attributed to the fact that porosity and real permittivity of a material are functions of their volume of pores, whereas permeability is governed by the connectivity of these pores. For asphalt which possesses a small volume of inter-connected pores, the material is found to be less porous and possess smaller real permittivity, but more permeable than air-cured concrete and soils.

10.6 SUMMARY AND DISCUSSION

This chapter establishes and formulates seven Unified Constitutive Models to characterize the three porous construction materials (concrete, asphalt and soil). These models are separated into two categories: purely EM wave properties and hybrid properties (i.e. real permittivity and engineering properties) by using three electromagnetic wave properties and two engineering/geological properties.

UCM #1 to #6 have been constructed relying on the three EM wave properties: real permittivity, energy attenuation and peak-frequency drift. These models characterize the porous construction materials by the sole determination of the three EM wave properties using the 1GHz GPR/SPR (described in Chapter 4) and a range of signal processing techniques (described in Chapter 5), as well as effective CMVT (described in Chapter 6 to Chapter 8). The greatest advantage of this characterization is that they were purely constructed using GPR/SPR instrumentation, but do not rely on traditional laborious laboratory tests on other physical properties of the material such as porosity, specific surface, permeability, and so on.

UCM #7 has been constructed using the largest real permittivity, the porosity and the permeability. The ultimate real permittivity refers to the maximum values of real permittivity attained by the materials. This model successfully demonstrates the relationship and interaction between real permittivity (as one of the most important EM wave properties) and the two important engineering/geological properties (as two of the most fundamental physical properties). In particular, a number of the engineering/geological properties were determined via a dielectric mixing model (i.e. CRIM in Section 2.5.4B) and a hydro-geological model (i.e. Kozeny-Carmen's model in Section 3.2.5.6), instead of following the traditional laboratory methods (i.e. specific gravity, falling/constant head permeability tests). With the successful application of these non-traditional methods, the determination of the engineering/geological properties shows great potential in the application of these instrumentations and models in real-life field investigations.

The models established and formulated in this chapter enhance the basic understanding of the material properties and their interactions with the pore structures/systems of the three studied materials in both EM wave and traditional engineering/geological perspectives. Also through these models, the effects of water are accentuated that it plays the most critical role in the characterization methodologies.

11. METHODOLOGY FOR THE FUTURE FIELD APPLICATION OF CYCLIC MOISTURE VARIATION TECHNIQUE (CMVT)

11.1 INTRODUCTION

The laboratory CMVT has shown to be very useful in the experiments and the unified constitutive models described in the previous chapters on characterizing the EM wave properties and the engineering properties of soil and asphalt. A step further would be to extend and implement the laboratory CMVT to an in-situ CMVT for field application. This chapter demonstrates the methods to carry out the in-situ CMVT based on a hypothetical scenario. The interpretation of the data analysis is based on the model data achieved according to the laboratory CMVT described in the previous chapters.

11.2 METHODOLOGY

This in-situ modified CMVT method can be carried out alongside a traditional in-situ pump well test in a quasi-steady state situation by following the procedures as follows, as well as the plan and schematic diagram shown in Fig.11-1 and Fig. 11-2.

1. Install pump well(s) and observation wells,
2. Measure the level of water table by piezometer installed in the observation wells prior to the start of pumping,
3. Start to pump from the pump well at a constant rate to draw-down the transition zone/capillary fringe/water table such that the depression zone (formed by the water table and created by pumping) produces hydraulic gradients/profiles over a large area, as shown in Fig. 11-2,
4. Traverse GPRs repeatedly using both the mono-static and bi-static antennae (with

Common Mid Point method) along the prescribed radial directions of a pump well in a fixed period of time,

5. Simultaneously measure the level of the water table and soil moisture by piezometer and Time Domain Reflectometry (TDR) respectively.

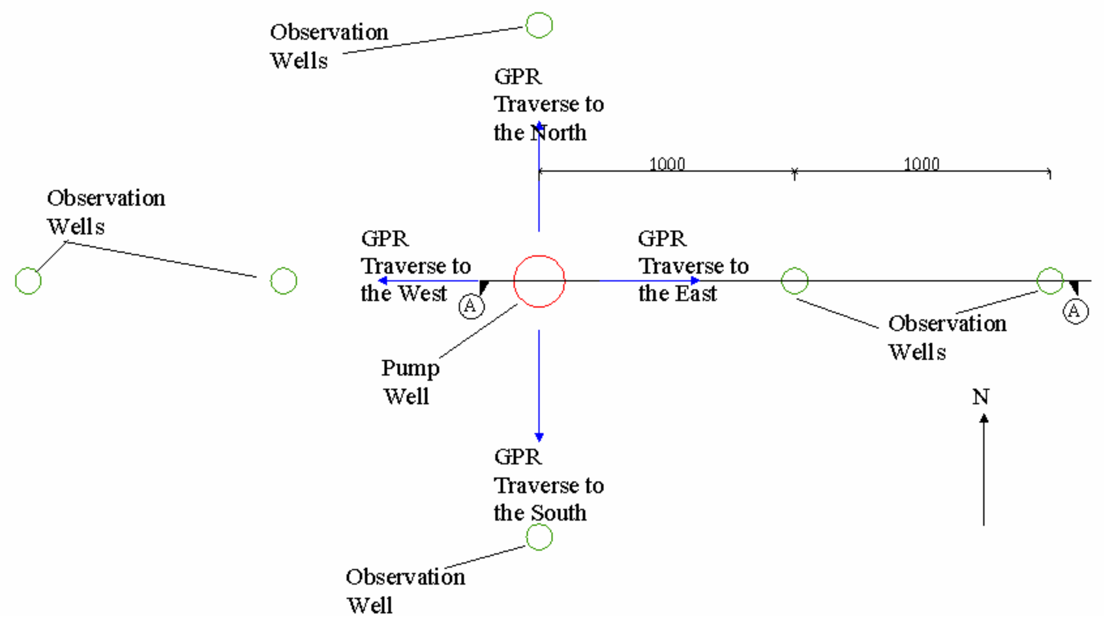

Fig.11-1 Plan of Pump Well, Observation Well and GPR Traverses

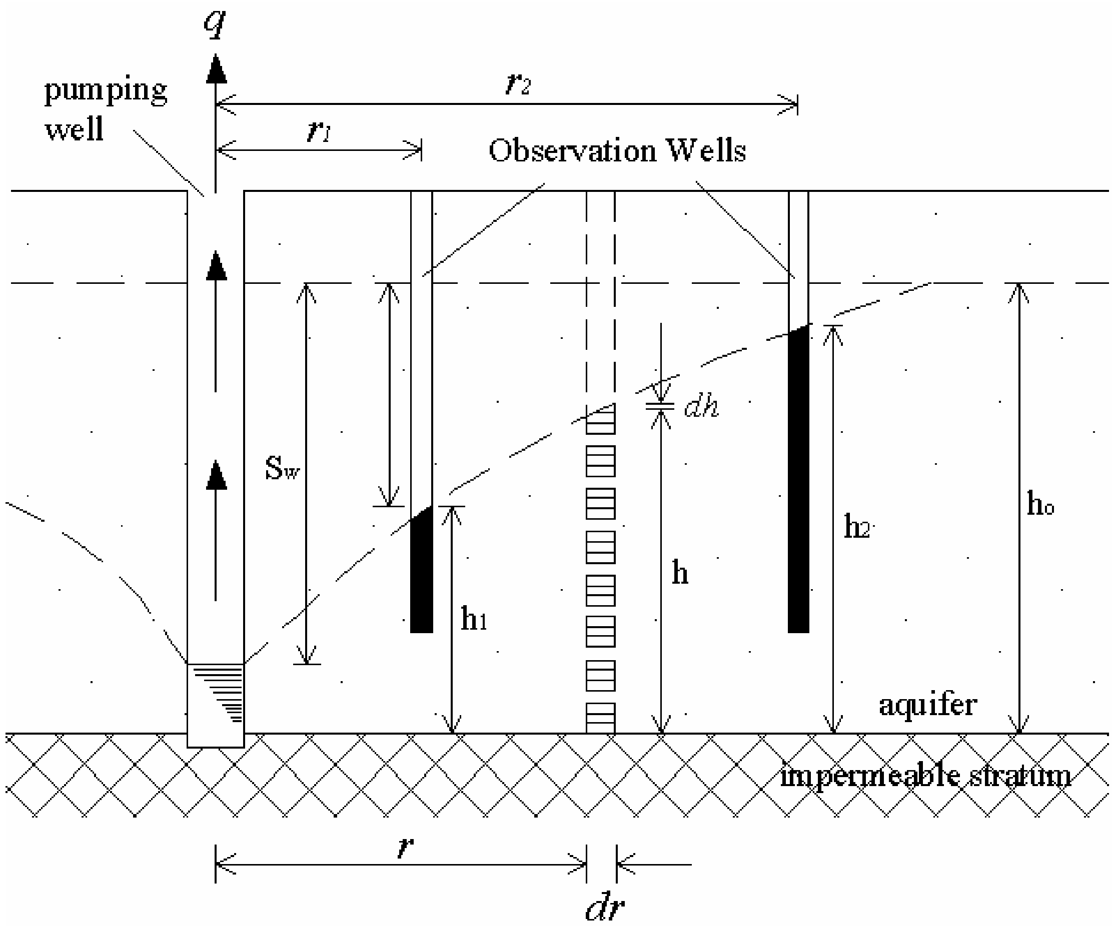

Fig.11-2 Section A-A of Fig.11-1: Hydraulic Gradient and Depression Zone in a In-situ Pump Well Test (Source: Whitlow, 2001)

11.3 DISCREPANCY IN CARRYING OUT FIELD CMVT AND LABORATORY CMVT

Though in-situ CMVT and laboratory CMVT have shown to be practical and convincing in the soil characterization in the field scale and laboratory scale respectively, a word of caution must be given in terms of two practical difficulties in recreating the ‘tank conditions’ used in the laboratory CMVT. Firstly, the boundaries are impermeable because of constructing a so-called ‘tank condition’ (i.e. impermeable tank walls and the tank bottom). Therefore, a nearly saturated state with a very high S_w (i.e. close to one) can be achieved, which may not be possible in field conditions. Secondly, with the provision of the pump and efficient drainage facilities within the tank, a very low S_w can be achieved. However in in-situ CMVT, such a wide range of S_w of the in-situ material may not be attained normally because of the difficulties in achieving this ideal 'tank condition'.

In addition, a number of field conditions must be satisfied to perform a successful application of CMVT in-situ, namely:

1. sufficient permeability in the soil mass,
2. existence of a high water table,
3. recognizable water table and the vadose zone in the radargram,
4. the effectiveness of the pumping facilities, and
5. a sufficient depth of penetration assessed by multi-frequency GPR systems.

11.4 SUMMARY AND DISCUSSION

The hypothetical experimental setup advocated in this chapter is also similar to the field studies reported by Endres et al. (2000) and Bevan et al. (2003). However, these two studies monitor continuously and investigate the changes of the soil transition zones through draw-down and recovery of the water content in an aquifer using GPR, which is different to the objective of soil characterization in this research.

This field CMVT offers a promising minimally invasive near-surface geo-physical technique to characterize the sub-surface soil texture of multi-layered strata and some of its material properties. It is likely that the disturbance to the ground is minimal and only involves the installation of a pump well (or in some cases several pump wells) and a number of observation wells.

Another advantage is the simplicity of the field setup. Since the entire setup of the in-situ CMVT works alongside the traditional pump well test, the additional effort required is proper operation of the GPR system, appropriate data processing technique and manipulation of the dielectric models to be fitted by experimental data. The latter includes the well-established CRIM and Kozeny-Carmen's model that relate a number of soil properties from both dielectric and engineering/geological perspectives. This method offers a comparative advantage over the traditional sample retrieval processes so that the material properties of large soil mass can be obtained and extensive coring can be avoided. However, it must be accepted that the uncertainties of the determined material properties using such methods shall be taken into account, as governed in Appendices K4 and K5.

12. LIMITATIONS OF CURRENT RESEARCH AND RECOMMENDATIONS FOR FUTURE RESEARCH

A number of limitations of this research and recommendations for future research are listed as follows:

1. The experiments detailed in this research were mainly laboratory-based in which the specimens were prepared in well-controlled conditions and therefore relatively homogeneous conditions can be ensured (e.g. particulate materials such as soils can be meticulously sieved and mixed to form the designated grade of soils wanted). As a result, heterogeneities of the porous materials (soils, asphalt, etc.) which are likely to be the norm and can be commonly found in the field were not encountered in this research. However, application and extension of the laboratory based CMVT to large scale field investigations should be explored using the methodology proposed in Ch.11.

2. The undesignated regions (as exhibited in the unified constitutive models illustrated in Ch. 10) not yet mapped to a particular material should be filled to cover these porous materials: such as rocks, timber, bricks, concrete of various mix ratios and containing different admixtures (e.g. pulverized fuel ash) and soils of various textures/mineralogy which were not investigated in this research. The methodology of characterizing and incorporating these materials into the models should follow those presented in Ch. 6, 7 and 8.

3. Ranging and characterization of deeper subsurface (in the order of tens of metres) often require antennae of much lower frequency (e.g. 25, 50 and 100Mz). These antennae frequency are higher than those adopted in this research (i.e. 400, 1000

and 1500MHz). Since radars of lower EM frequencies are not available, the extension to the characterization of the porous materials in lower EM frequencies should be explored, using similar methodology (i.e. CMVT) and lower-frequency GPR antennae.

4. Continuous monitoring of water content in both fresh and mature concrete using EM wave can be used as a useful diagnostic tool to perform the following functions (if used appropriately):

   - Maturity of concrete and the progress of cement hydration and strength development (provided the amount of water during mixing and curing are carefully controlled)

   - Detection of leakage of water into concrete walls and slabs (as a result of leakage of piped services) or the evaluation of the effectiveness of water-proof membranes applied over concrete etc. (contrast between areas of varying water content exhibits itself as differences in the real permittivity and energy attenuation through known concrete thicknesses)

13. CONTRIBUTIONS TO KNOWLEDGE

Knowledge of the behaviour of and interaction between pore structures/systems and water in concrete, asphalt and soil has been extended through the establishment and formulation of a number of unified constitutive models. These models describe the performance of the studied porous material from the electromagnetic perspective. This research has also devised a novel testing technique called Cyclic Moisture Variation Technique (CMVT) which allows easy differentiation and characterization of porous construction materials which are otherwise difficult to be differentiated when relatively dry.

13.1 ESTABLISHMENT AND FORMULATION OF THE UNIFIED CONSTITUTIVE MODELS

In this research, the three porous construction materials (concrete, asphalt and soil) have been characterized using CMVT and successfully assigned to their respective rightful positions/regions within the devised unified constitutive models. These models have been established and formulated according to the selected sets of data of material properties obtained through a series of experiments according to the changes of degrees of water saturation within these materials. These chosen material properties comprise the three electromagnetic (EM) wave properties and the two traditional engineering/geological properties. The former refers to the real permittivity, the energy attenuation and the peak-frequency drift of the returned EM waveforms, whereas the latter refers to the porosity and the permeability of the material. These chosen data sets of material properties constitute the unique ‘fingerprints’ to bench-mark and characterize the studied porous materials into different regimes of the models.

The different pore structures/systems of these porous construction materials manifest themselves as different curves in the plots of real permittivity (ε') vs degree of water saturation (S_w), as well as the plots of energy attenuation vs degree of water saturation (S_w). This characterization is based on identification of clear demarcations of the three regions exhibited in these curves:

1. a region of slow-climbing to fast-climbing at low S_w,
2. a fast-climbing region at intermediate S_w, and
3. another region of slow-climbing at very high S_w.

For highly porous material with inter-connected pores (in micro-meter and nano-meter sizes) such as those in soil of various textures and in air-cured concrete, the demarcation of regions are clearly observable and vary according to material texture. For less porous material with relatively small volume of these inter-connected pores such as water-cured concrete and asphalt, these demarcations are not clearly identified and defined. The existence of these two slow-climbing regions at both low and high S_w is attributed to both the differential water distribution within the transition zone and capillary fringe, as well as microscopic water distribution in the capillaries of fine particles. The fast-climbing region is attributed to the dominant effects of essentially free water which is relatively free to respond to polarization by an external EM field.

In formulating these unified constitutive models, the effects of a number of key variables/factors appropriate to each material were studied. In concrete, these variables/factors are curing history, aggregate to cement ratios, water-to-cement ratios and degree of compaction. In asphalt, the effects of different compositions (of different asphalt mixes) of the wearing course, base course and road base were the studied variables. In soil, ten different textures ranging from gravel to sandy silt were the studied factors. Some of these variables/factors were found to affect the three electromagnetic (EM) wave properties and the two traditional engineering/geological properties, and some did not. The effects of these variables/factors on the material properties are 'mapped' to corresponding regions in the unified constitutive models.

To date, no attempt was aware to report on characterizing the three studied materials: i.e. porous concrete, asphalt and soil, in such a unified approach from the EM perspective. This research is believed to represent a first attempt and has made a useful contribution to the understanding of the pore structures/systems and their effects on the electromagnetic behaviour/phenomena exhibited in these materials.

13.2 PIONEERING WORK IN THE USE OF A NOVEL CYCLIC MOISTURE VARIATION TECHNIQUE (CMVT) WITH DIFFERENTIAL WATER DISTRIBUTION

The CMVT is based on tracking continuously the changes of the real permittivity as degree of water saturation within the studied material change: i.e. from partially saturated states to a fully saturated state, and vice versa, through cycles of water-permeation and dewatering processes. This method does not require extensive retrieval of samples (in terms of amounts and places of extraction of material samples). The technique exploits the use of water as an enhancer or a tracer to allow detection and differentiation of these materials. The technique also allows a great mass of in-situ material properties to be determined with differential distribution of water, in contrast to only a small mass of material with homogeneous distribution of water. The latter only exist in laboratory condition and can only be tested either by the conventional Electromagnetic Coaxial Transmission Line (EMCTL) method and the Time Domain Reflectometry (TDR), or the traditional engineering tests on other physical properties. Thus the CMVT adopted in this research is more closed to the real condition in field and more realistic than the conventional EMCTL and TDR method.

During the implementation of CMVT, dielectric hysteresis in the plots between ε' and S_w was observed generally when asphalt and soil specimens were wetted and dried through various cycles of permeation and de-watering processes and vice versa. This hysteresis is possibly attributed to the differences in volume of bound and capillary water within the transition zone and the capillary fringe of the materials during the permeation and de-watering stages.

Due to the limitation of time, this research has not ventured deeper into the field implementation and application of CMVT nor detailed a study of dielectric hysteresis. However, the work embodied in this research should be able to pave the way for further study in the future. In particular, the large scale characterization of sub-surface material could be a very promising area for further investigation.

14. CONCLUSION

This research is recognized, as far as the author is aware, the first study of its kind (i.e. in terms of the technique of characterizing concrete, asphalt and soils by embodying an inter-disciplinary approach and using electromagnetic wave and engineering/geological properties).

The major experimental findings are summarized as follows:

1. The three studied porous materials (i.e. concrete, soil and asphalt) were differentiated and characterized by their unique curves exhibited in the plots of real permittivity/energy attenuation/peak-frequency drift against degrees of water saturation,

2. For **concrete**, both the changes of real permittivity and energy attenuation (under the effect of increasing water saturation) were dependent on curing history and aggregate to cement ratios, but not the water-to-cement ratios nor degree of compaction.

3. For asphalt and soils, data fitting into the Complex Refractive Index Model (CRIM) (with a multitude of frequencies 400MHz, 1GHz and 1.5GHz) produced a good fit and yield porosity values of 0.04 for **asphalt** and porosity values ranging from 0.38 to 0.63 for the **soil** specimens. These values for the soil specimens were found to be larger than the independent measurements of soil test by an average value of 0.13.

4. For **asphalt**, dielectric dispersion was observed at the frequencies 400MHz, 1GHz and 1.5GHz, such that at every state of degrees of water saturation, the values of real permittivity at lower frequency are larger than those of higher frequency.

5. The curves in the plots of the real permittivity against the degrees of water saturation of **soils** were found to be able to characterize and benchmark each individual gap-graded soil texture (i.e. gravel, sand or silt),

6. The curves in the plots of the real permittivity against the degree of water saturation in both the air-cured **concrete** and **soil** specimens were found to exhibit clearly a fast-climbing region at intermediate S_w and a slow-climbing region at very high degrees of water saturation, which indicates the similarity of pore structure possessed in these materials, and

7. Dielectric hysteresis was observed in both the **soil** and **asphalt** specimens (this is attributed to the different distribution of water possessed in these materials during the wetting and drying cycles).

With these experimental findings,, this research is believed to have made the following contributions:

1. the establishment and formulation of a number of unified constitutive models (using purely EM wave properties, as well as hybrid models using EM wave and other material/engineering properties) to characterize the three porous construction materials.

2. pioneering the use of a novel Cyclic Moisture Variation Technique (CMVT) and

3. the design, assembly and development of an effective instrumentation system and analysis software to allow the effective implementation of the CMVT. Such hard- and soft-ware are pivotal to the success of this research.

For most researchers and practitioners in the field of GPR/SPR, the presence of water in subsurface porous materials is usually considered undesirable because of significant EM wave attenuation. However, this research has turned this drawback into a useful characterization technique of the three porous construction materials. Without the help of water which possesses a remarkably large real permittivity, this characterization would not have been possible, especially when these materials are relatively dry. The approach advocated here in this research has marked a milestone of alternative thinking of the role of water in GPR material research.

The important role of water to the CMVT is similar to the instrumental use of the so-called '*intravenous contrast*' in a medical diagnostic technique. The injection and subsequent tracing the where-about of the '*intravenous contrast*' allows the visualization of the conditions of human internal organs using high energy radiographic imaging. Likewise, the CMVT allows the visualization the internal conditions (such as pores etc.) of concrete, asphalt and soils using non-invasive radar ranging.

It is also believed that the unified constitutive models, the experimental techniques and the related theories devised and developed in this research will constitute the fundamental basis for large-scale characterization of most porous materials found in the areas of building, civil engineering and geophysics. This research has also paved the way for further development of field radar terrestrial investigation of the earth, and perhaps extra-terrestrial and geophysical investigations: satellites (such as our Moon) and even planets (such as the Mars).

15. REFERENCES

Alharthi, A. and Lange, J. Soil Water Saturation: Dielectric Determination. *Water Resources Research*, 1987, 23(4), 591-595.

Al-Qadi, I.L. and Lahouar, S. Ground Penetrating Radar: State of the Practice for Pavement Assessment. *Materials Evaluation*, 2004, 759-763.

Al-Qadi, I.L. and Lahouar, S. Measuring Layer Thickness with GPR – Theory to Practice. *Construction and Building Materials*, in press, 2005.

Al-Qadi, I.L. Loulizim A., Haddad, R. and Riad, S. Correlations between Concrete Dielectric Properties and its Chloride Content. 7th International Conference on Structural Faults and Repair. 1997, 2, 423-429.

Arulanandan, K., and Mitchell, J.K. Low Frequency Dielectric Dispersion of Clay-electrolyte Systems. *Clay and Clay Minerals*, 1967, 16, 337-351.

ASTM D6432-99. *Standard Guide for Using the Surface Ground Penetrating Radar Method for Subsurface Investigation*, 1999.

Baher, H. *Analog & Digital Signal Processing*, 2nd Ed. John Wiley & Sons Ltd., 2001.

Baver, L.D., Gardener, W.H. and Gardener, W.R. W.R. *Soil Physics*, 4th Ed., John Wiley & Sons, Inc. 1972.

Beek, V. A. *Dielectric Properties of Young Concrete*. Ph.D. Thesis, Delft University, 2000.

Bell, F.G. *Engineering Properties of Soils and Rocks*. Blackwell Science, 4th Ed., 2000, 454.

Bevan, M.J., Endres, A.L., Rudolph, D.L. and Parkin, G.. The Non-invasive Characterization of Pumping-induced Dewatering using Ground Penetrating Radar. *Journal of Hydrology*, 2003, 281, 55-69.

Beyon, J.Y. *LabView Programming, Data Acquisition and Analysis*. Prentice Hall, 2001.

Binda L., Lenzi G. and Saisi A. NDE of Masonry Structures: Use of Radar Tests for the Characterisation of Stone Masonries. *NDT&E International*, 1998, 31(6), 411-419.

Birchak, J.R., Gardner, C.G., Hipp, J.E. and Victor, J.M. High Dielectric Constant Microwave Probes for Sensing Soil Moisture. *Proc. IEEE*, 1974, 62(1), 93-98.

Brisco, B, Pultz, T.J., Brown, R.J., Topp, G.C., Hares, M.A. and Zebchuk, W.D. Soil Moisture Measurement Using Portable Dielectric Probes and Time Domain Reflectometry. *Water Resources Research*, 1992, 28(5), 1339-1346.

Böttcher, C.J.F. and Bordewijk, P. *Theory of Electric Polarization*, Vol. II, 1973.

Bourbie, T. and Zinszner, B. Saturation Methods and Attenuation Versus Saturation Relations in Fontainebleu Sandstone. 54th Annual International Meeting, *Society of Exploration Geophysics*, Expanded Abstract, 1984, 344-350.

Brisco, B., Pultz, T.J., Brown, R.J., Topp, G.C., Hares, M.A. and Zebchuk, W.D. Soil Moisture Measurement Using Portable Dielectric Probes and Time Domain Reflectometry. *Water Resources Research*, 1992, 28(5), 1339-1346.

Brown, W.F. *Dielectrics, in Encyclopedia of Physics*. Springer-Verlag, New York, 1956.

Bruggeman, D.A.G. Berechnung Verschiedener Physikallischer Konstanten von Heterogenen Substanzen: *Ann Phys.*, 1935, 24, 634-664.

BS1377-2:1990. *Methods of test for soils for civil engineering purposes. Classification tests*, 1990.

BS1881-111:1983. *Testing Concrete: Method of Normal Curing of Test Specimens (20^{o}C Method)*. 1983.

BS1881-114:1983. *Testing Concrete: Methods for determination of density of hardened concrete*. 1983.

BS1881-208:1996. *Recommendations for the determination of the Initial Surface Absorption of Concrete*. 1996.

BS5930:1981 - *Code of Practice for Site Investigation*, 1981.

BS7591-1:1992. *Porosity and Pore Size Distribution of Materials – Part 1: Method of Evaluation by Mercury Porosimetry*. 1992.

BS EN 12697-8:2003. *Bituminous mixtures – Test methods for hot mix asphalt – Part 8: Determination of void characteristics of bituminous specimens*. 2003.

Bungey, J.H., Millard, S.G. and Shaw, M.R. Radar Assessment of Post-tensioned Concrete. *7th International Conference on Structural Faults and Repair,* 1997, 331-339.

Bungey, J. Some Recent Developments in Civil Engineering NDT in the UK. *Insight*, 2003, 45(12), 796-799.

Büyüköztürk, O. Imaging of concrete structures. *NDT&E International*, 1998, 31(4), 233-243.

Carmen, P.C. *Flow of Gases through Porous Media*. Academic Press Inc, 1956.

Chan, C.Y. and Knight, R.J. Determining Water Content and Saturation from Dielectric Measurements in Layered Materials. *Water Resources Research*, 1999, 35(1), 85-93.

Chugani, M.L., Samant, A.R. and Cerna, M. *LabVIEW: Signal Processing*. Prentice Hall PTR, U.S.A., 1998.

Cole, K. and Cole, R. Dispersion and Absorption in Dielectrics; I: Alternating Current Characteristics. *Journal of Chemical Physics*, 1941, 9, 341-351.

Concrete Society. Permeability Testing of Site Concrete: A Review of Methods and Experience. *Concrete Society Technical Report No. 31*, 1987.

Concrete Society. Guidance on Radar Testing of Concrete Structures. *Concrete Society Technical Report 48*, 1997.

Corcoran, K. Personal Communication, Geophysical Survey System Inc. 2005.

Daniels, D.J. Eds. *Ground Penetrating Radar*, 2nd Ed. The Institution of Electrical Engineers. London, 2004.

Davis, J.L. and Annan, A.P. Ground-Penetrating Radar for High-Resolution Mapping of Soil and Rock Stratigraphy. *Geophysical Prospecting*, 1989, 37, 531-551.

Davis, J.L., Topp, G. C. and Annan, A.P. Electromagnetic Detection of Soil Water Content: Progress Report II. *Remote Sensing and Soil Moisture and Ground Water, Workshop Proceedings*, 1976, 96-109.

De Loor, G.P. The Effect of Moisture on the Dielectric Constant of Hardened Portland Cement Paste. *Applied Science Res.*, 1961, 9, 297-308.

De Loor, G.P. The Dielectric Properties of Wet Materials. *IEEE Transactions on Geoscience and Remote Sensing*, 1983, GE-21, 3, 364-369.

Debye P. *Polar Molecules*. Chemical Publication Company 1929.

Dobson M.C., Ulaby, F.T., Hallikainen, M.T. and El-Rayes, M.A. Microwave Dielectric Behavior of Wet Soil – Part II: Dielectric Mixing Models. *IEEE Transactions on Geoscience and Remote Sensing*, 1985, GE-23(1), 35-46.

Emerson, W.W. The Structure of Soil Crumbs. *Journal of Soil Science*. 1959, 10, 235-244.

Endres, A.L. and Knight, R. A Theoretical Treatment of the Effect of Microscopic Fluid Distribution on the Dielectric Properties of Partially Saturated Rocks. *Geophysical Prospecting*. 1992, 40, 307-324.

Endres, A.L., Clement, W.P. and Rudolph, D.L. Ground Penetrating Radar Imaging of an Aquifer during a Pumping Test. *Ground Water*, 2000, 38, 566-576.

Foster, G.. The Sorption of Condensable Vapours by Porous Solids, Part I: The Application of the Capillary Theory. *Trans. Faraday Society*, 1932, 28, 645-657.

Freeze, R.A. and Cherry, J.A. *Ground Water*, Prentice Hall, 1979.

Garrouch, A.A. and Sharma, M.M. The influence of clay content, salinity, stress, and wettability on the dielectric properties of brine-saturated rocks: 10Hz to 10MHz. *Geophysics*, 1994, 59, 909-517.

Glasser, F.P. The Pore Structure of Paste in Concrete. *Cement and Concrete Research*, 1992, 20(2), 227-284.

Gorur, K., Smit, M.K. and Wittmann, F.H. Microwave Study of Hydrating Cement Paste at Early Age. *Cement and Concrete Research*, 1982, 12, 447-454.

Grote, K., Hubbard, S. and Rubin, Y. GPR Monitoring of Volumetric Water Content in Soils applied to Highway Construction and Maintenance. *The Leading Edge*, 2002, 482-485.

Gu, P. and Beaudoin, J.J. Dielectric Behaviour of Hardened Cementitious Materials. *Advances in Cement Research*. 1997, 9(33), 1-8.

Hall, P.G., and Rose, M.A. Dielectric Properties of Water Adsorbed by Kaolinite Clays. *J. Chem. Soc. Faraday Trans.*, 1978, 74, 1221-1233.

Hallikainen, M.T., Ulaby, F.T., Dobson M.C., El-Rayes, M.A. and Wu, L.K. Microwave Dielectric Behavior of Wet Soil – Part I: Empirical Models and Experimental Observations. *IEEE Transactions on Geoscience and Remote Sensing*, 1985, GE-23(1), 25-34.

Hanai, T. Dielectric Theory on the Interfacial Polarization for Two-phase Mixtures. *Bull. Inst. Chem Res*, 1961, 39, 341-367.

Hasted, J.B. *Aqueous Dielectrics*. Chapman and Hall, London 1973.

Herkelrath, W.N., Hamburg, S.P., Murphy, F. Automatic, Real-Time Monitoring of Soil Moisture in a Remote Field Area with Time Domain Reflectometry. *Water Resources Research*, 1991, 27(5), 857-864.

Hilhorst, M.A., Dielectric Characterisation of Soil. Ph.D. Thesis, Wageningen Agricultural University, 1998.

Hillel, D. *Fundamental of Soil Physics*. Academic Press, 1980.

Hillel, D. *Environmental Soil Physics*. Academic Press, 1998.

Hipp, J.E. Soil Electromagnetic Parameters as a Function of Frequency, Soil Density and Soil Moisture. *Proc. IEEE*, 1974, 62, 98-103.

Hoekstra, P. and Delaney, A. Dielectric Properties of Soils at UHF and Microwave Frequencies. *Journal of Geophysical Research*, 1974, 79(11), 1699-1708.

http://www.mint.gov.my/PRODUCTS/BTI/nde/Ndt_Concrete_details.html

Hubbard, S.S., Rubin, Y. and Majer, E. Ground-penetrating-radar-assisted saturation and permeability estimation in bimodal system. *Water Resources Research*, 1997, 33(5), 971-990.

Hubbard, S., Grote K., Rubin, Y. Mapping volumetric soil water content of a California Vineyard using High-frequency GPR ground wave data. *The Leading Edge*, 2002, 552-559.

Huisman, J.A., Hubbard, S.S., Redman, J.D. and Annan, A.P. Measuring Soil Water Content with Ground Penetrating Radar: A Review. *Vadose Zone Journal*, 2003, 2:476-491.

Irving, J. and Knight, R. J. Removal of Wavelet Dispersion from Ground-penetrating Radar Data. *Geophysics*, 2003, 68(3), 960-970.

Ishizaki, L., Komarneni, S. and Nanko, M. *Porous Materials: Process Technology & Applications*. Kluwer Academic Publisher, 1998.

Jol, H.M. Ground Penetrating Radar Antennae Frequencies and Transmitter Powers Compared for Penetration Depth, Resolution and Reflection Continuity. *Geophysical Prospecting*, 1995, 43, 693-709.

Kääriäinen, H., Rudolph, M., Schaurich, D., Tulla, K. and Wiggenhauser, H. Moisture Measurements in Building Materials with Microwaves. *NDT&E International*, 2001, 34, 389-394.

Keller, G.V. *Rock and Mineral Properties, in Nabighian,* M.N., Ed., Electromagnetic Methods in Applied Geophysics. Society of Exploration Geophysics, 1987.

Keller, G.V. and Licastro, P.H. Dielectric Constant and Electrical Resistivity of Natural State Cores. *U.S. Geol. Surv. Bull.*, 1959, 1052-H, 257-285.

Kenyon, W.E. Texture Effects on Megaherz Dielectric Properties of Calcite Rock Samples. *J. Appl. Phys.*, 1984, 55, 3153-3159.

Klein, J.D., and Sill, W.R. Electrical Properties of Artificial Clay-bearing Sandstone. *Geophysics*, 1982, 47, 1593-1605.

Knight, R.J. Hysteresis in the Electrical Resistivity of Partially Saturated Sandstones. *Geophysics*, 1991, 56(12), 2139-2147.

Knight, R. and Nur, A. Geometrical Effects in the Dielectric Response of Partially Saturated Sandstones. *The Log Analyst*, 1987a, 28, 513-519.

Knight, R.J., and Nur, A. The Dielectric Constant of Sandstones, 60kHz to 4 MHz. *Geophysics*, 1987b, 52, 644-654.

Knight, R.J. and Nolen-Hoeksema, R. A laboratory study of the dependence of elastic wave velocities on pore scale fluid distribution, *Geophysics Research Letter*, 1990, 17, 1529-1532.

Knoll, M.D. *A Petrophysical Basis for Ground-Penetrating Radar and Very Early Time Electromagnetics*. Ph.D. Thesis, The University of British Columbia, 1996.

Kowalsky, M.B., Dietrich, P., Teutsch, G. and Rubin, Y. Forward Modelling of Ground-Penetrating Radar Data Using Digitized Outcrop Images and Multiple Scenarios of Water Saturation. *Water Resources Research*, 2001, 37(6), 1615-1625.

Kozeny, J. Über kapillare Leitung des Wassers im Boden. *Sb. Akad. Wiss. Wien, Math-naturw. Kl.* Abt. IIa, 1927, 136, 271-306.

Kutrubes, D.L. Dielectric Permittivity Measurements of Soils Saturated with Hazardous Fluids. *M.Sc. Thesis*, 1986, Colorado School of Mines.

Lange, J.N. Microwave Properties of Saturated Reservoirs. *Geophysics*, 1983, 48, 367-375.

Li., C., Tercier, P. and Knight, R. Effect of Sorbed oil on the Dielectric Properties of sand and clay. *Water Resources Research*, 2001, 37(6) 1783-1793.

Lichtenecker, K. and Rother, K. *Physics Zeitschrift*, 1937, 255.

Lockhart, N.C. Electrical Properties and Surface Characteristics and Structure of Clays, I, Swelling Clays. *J. Colloid Interface Sci.*, 1980a, 74, 509-519.

Lockhart, N.C. Electrical Properties and Surface Characteristics and Structure of Clays, II, A Nonswelling Clay. *J. Colloid Interface Sci.*, 1980b, 74, 520-529.

Longeron, D.G., Argaud, M.J. and Feraud, J.P. Effect of Overburden Pressure and the Nature and Microscopic Distribution of Fluids on Electrical Properties of Rock Samples. *SPE Format. Eval.*, 1989, 4, 194-202.

Looyenga, H. Dielectric Constant of Mixtures. *Physica*, 1965, 31, 401-406.

Lowell, S., Shields, J.E., Thomas, M.A. and Thommes, M. *Characterization of Porous Solids and Powders: Surface Area, Pore Size and Density*. Kluwer Academic Publishers, 2004.

Lu Q., and Sato M., Estimation of hydraulic property of an unconfined aquifer by GPR, *10th International Conference on GPR*, Delft, Netherlands, 2004, 715-718.

Lunt, I.A., Hubbard, S.S. and Rubin, Y. Soil Moisture Content Estimation using Ground-penetrating Radar Reflection Data. *Journal of Hydrology*, 2005, 307, 254-269.

Maierhofer, Ch. and Wöstmann, J. Investigation of Dielectric Properties of Brick Materials as a Function of Moisture and Salt Content Using a Microwave Impulse Technique at Very High Frequencies. *NDT & E International*, 1998, 31(4), 259-263.

Mala Geoscience Web-page, *http://www.malags.com/*

Marshall T.J. and Holmes J.W. *Soil Physics*. Cambridge University Press, London, 1979.

Marshall, T.J., Holmes, J.W. and Rose, C.W. *Soil Physics*. Cambridge University Press, London, 1996.

Martinez, A. and Byrnes, A.P. Modeling Dielectric-constant values of Geologic Materials: An Aid to Ground-Penetrating Radar Data Collection and Interpretation. website: 'http://citeseer.csail.mit.edu/472934.html', 2001.

McCann, D.M. and Forde, M.C. Review of NDT methods in the assessment of concrete and masonry structures. *NDT&E International*, 2001, 34, 71-84.

McCarter, W.J. and Curran, P.N. The Electrical Response Characteristics of Setting Cement Paste. *Magazine of Concrete Research*, 1984, 36, 42-49.

Millard, S.G., Shaari, A. and Bungey, J.H. Frequency Characteristics of GPR Antennas. *Insight*, 2001, 43(7), 450-457.

Nakashima, Y., Zhou, H. and Sato, M., Estimation of groundwater level by GPR in an area with multiple ambiguous reflections, *Journal of Applied Geophysics*, 47, 241-249, 2001.

Neville, A.M. *Properties of Concrete*, 4^{th} Ed. and Final Ed. Harlow, Longman Group, 1995.

Okrasinski, T.A., Koerner, R.M., and Lord, A.E., Jr. Dielectric Constant Determination of Soils at L Band Microwave Frequencies. *Geotechnical Testing J.*, 1979, 1, 134-140.

Olhoeft, G.R. Electrical Properties from 10-3 to 109 Hz, Physics and Chemistry: in Banavar, J.R., Koplik, J., and Winkler, K.W., Eds. Physics and Chemistry of Porous Media II. *Am. Inst. of Phys. Conf. Proc.*, 1987, 154, 281-298.

Olhoeft, G.R. and Strangway, D.W. Dielectric Properties of the First 100 meters of the Moon. *Earth and Planetary Science Letters*, 1975, 24, 394-404.

Oota, S., Fujiwara, T., Matsuyama, K. and Kanemoto, Y. Evaluation of Concrete Strength using Radar Method on Structures. *Symposium of Non-Destructive Testing on Civil Engineering*, 2000, 549-557.

Peplinski N.R., Ulaby, F.T. and Dobson M.C. Dielectric Properties of Soils in the 0.3-1.3GHz Range. *IEEE Transactions on Geoscience and Remote Sensing*, 1995, 33(3), 803-807.

Perez-Pena, M., Roy, D.M., Bhalla, A.S. and Cross, L.E. Dielectric Properties of Densified Hardened Cementitous Materials. *Cement and Concrete Research*, 1986, 16, 951-965.

Poley, J.Ph., Nooteboom, J.J. and de Waal, P.J. Use of V.H.F. Dielectric Measurements for Borehole Formation Analysis. *The Log Analyst*, 1978, 19, 8-30.

Reynolds, J.M. *An Introduction to Applied and Environmental Geophysics*. England, John Wiley & Sons Ltd, 1997.

Robinson, D.A. Personal Communication, Stanford University, 2005.

Roth, K., Schulin, R., Flühler and Attinger, W. Calibration of Time Domain Reflectometry for Water Content Measurement Using Composite Dielectric Approach. *Water Resources Research*, 1990, 26**(**10), 2267-2273.

Rust, A.C., Russell, J.K. and Knight, R.J. Dielectric Constant as a Predictor of Porosity in Dry Volcanic Rocks. *Journal of Volcanology and Geothermal Research*, 1999, 91, 79-96.

Saarenketo, T. Electrical Properties of Water in Clay and Silty Soils. *Journal of Applied Geophysics*, 1998, 40, 73-88.

Schmugge, T., Blanchard, B., Burk, J. Paris and Wang, J. Report on the April, 1974 soil moisture flights. *NASA TN-D8199*, 1976.

Scott, J.J., Carroll, R.D., and Cunningham, D.R. Dielectric Constant and Electrical Conductivity Measurements of Moist Rock: A New Laboratory Method. *J. Geophy. Res.*, 1967, 72, 5105-5115.

Sen, P.N. The Dielectric and Conductivity Response of Sedimentary Rocks. *SPE Paper 9379*, 1980.

Sen, P.N., Scala, C. and Cohen, M.H. A Self-explanatory Model for Sedimentary Rocks with Application to the Dielectric Constant of Fused Glass Beads. *Geophysics*, 1981, 46(5), 781-795.

Sen, P.N. and Chew, W.C. The Frequency Dependent Dielectric and Conductivity Response of Sedimentary Rock. *Journal of Microwave Power*, 1983, 18, 95-105.

Shang, J.Q. and Umana, J.A. Dielectric Constant and Relaxation Time of Asphalt Pavement Materials. *Journal of Infrastructure System*, 1999, 5(4), 135-142.

Shaw, M.R., Millard, S.G., Houlden, M.A. Austin, B.A. and Bungey, J.H. A Large Diameter Transmission Line for the Measurement of the Relative Permittivity of Construction Materials. *British Journal of NDT*, 1993, 35(12), 696-704.

Shaw, M.R. The Permittivity and Conductivity of Concretes at Ground-Penetrating Radar Frequencies. Advances in Cement Research, 1998, 10(4), 187-194.

Sheets, K.R. and Hendrickx, J.M.H. Noninvasive Soil Water Content Measurement Using Electromagnetic Induction. *Water Resources Research*, 1995, 31(10), 2401-2409.

Shen, L.C., Savre, W.C., Price, J.M., and Athavale, K. Dielectric Properties of Reservoir Rocks at Ultra-high Frequencies. *Geophysics*, 1985, 50, 692-704.

Sherman, M.M. The Calculation of Porosity from Dielectric Constant Measurements: A Study Using Laboratory Data. *The Log Analyst*, 1986, 27, 15-24.

Sihvola, A.H. *Electromagnetic mixing formulas and applications*. Institution of Electrical Engineers. London, 1999.

Smith-Rose, R.L. The Electrical Properties of Soils for Alternating Currents at Radio Frequencies. *Proc. Royal Soc.* London, 1933, 140, 359-377.

Smith-Rose R.L. The Electrical Properties of Soil at Frequencies up to 100MHz; with a note on the resistivity of ground in the United Kingdom. *Proc. Phys. Soc. London*, 1935, 47, 923.

Soutsos, M.N., Bungey, J.H., Millard, S.G., Shaw, M.R. and Patterson, A. Dielectric Properties of Concrete and Their Influence on Radar Testing. *NDT&E International*, 2001, 34, 419-425.

Strangway, D.W. Mineral Magnetism: in *Mining Geophysics* Vol. II (theory): Society of Exploration Geophysics, 1972, 437-445.

Taherian, M.R., Kenyon, W.E., and Safinya, K.A. Measurement of the Dielectric Response of Water-saturated Rocks. *Geophysics*, 1990, 55, 1530-1541.

Taylor, M.A. and Arulanandan, K. Relationships between Electrical and Physical Properties of Cement Pastes. *Cement and Concrete Research*, 1974, 4, 881-897.

Topp, G. C., Davis, J.C. and Annan, A.P. Electromagnetic Determination of Soil Water Content: Measurements in Coaxial Transmission Lines. *Water Resources Research*, 1980, 16(3), 574-582.

Ulaby, F.T. *Fundamentals of Applied Electromagnetics*. New Jersey, Prentice Hall, 2001.

Ulaby, F.T., Bengal, T.H., Dobson, M.C., East, J.R., Garvin, J.B. and Evans, D.L. Microwave Dielectric Properties of Dry Rocks. *IEEE Transactions on Geoscience and Remote Sensing*, 1990, 28(3), 325-336.

Vaughan, C.J. Ground-penetrating Radar Surveys used in Archaeological Investigations. *Geophysics*, 1986, 51(3), 595-604.

Von Hippel A. ed. *Dielectric Materials and Applications*. Cambridge, Technology Press of MIT, 1995.

Wang, J.R. The Dielectric Properties of Soil-water Mixtures at Microwave Frequencies. *Radio Science*, 1980, 15(5), 977-985.

Wang, J.R. and Schmugge, T.J. An Empirical Model for the Complex Dielectric Permittivity of Soils as a Function of Water Content. *IEEE Transactions on Geoscience and Remote Sensing*, 1980, GE-18(4), 288-295.

Wensink, W.A. Dielectric Properties of Wet Soils in the Frequency Range 1-3000MHz. *Geophysical Prospecting*, 1993, 41, 671-696.

West, L.J. and Handley, K. Radar Frequency Dielectric Dispersion in Sandstone: Implications for Determination of Moisture and Clay Content. *Water Resources Research*, 2003, 39(2), 1026-1037.

Whitlow, R. *Basic Soil Mechanics,* 4th Ed. Prentice Hall, 2001.

Wilson, J. and Whittington, H. Variations in the Electrical Properties of Concrete with Change in Frequency, *IEE Proceedings Part A.* 1990, 137, 246-254.

Winslow D. and Liu D. The Pore Structure of Paste in Concrete. *Cement and Concrete Research*, 1990, 20(2), 227-235.

Wittmann, F.H. and Schlude, F. Microwave Absorption of Hardened Cement Paste. *Cement and Concrete Research*, 1975, 5, 63-71.

Xu, T. and McMechan, G.A. GPR Attenuation and its Numerical Simulation in 2.5 Dimensions. Geophysics, 1997, 62, 403-414.

Yilmaz, O. and Doherty, S.M. *Seismic Data Processing – Investigations in Geophysics*, no.2. Tulsa, Oklahoma, Society of Exploration Geophysics, 1987.

Yin, H. Acoustic Velocity and Attenuation of Rocks-isotropy, Intrinsic Anisotropy, and Stress-induced Anisotropy. Ph.D. Dissertation, Stanford University, 1993.

Young, J.F., Mindess, S., Gray, R.J. and Bentur, A. *The Science and Technology of Civil Engineering Materials*. New Jersey, Prentice Hall, 1998.

Zeng, X. and McMechan, G.A. GPR Characterization of Buried Tanks and Pipes. *Geophysics*, 1997, 62(3), 797-806.

APPENDIX A: SUMMARY OF LITERATURE STUDIES ON DIELECTRIC PROPERTIES WITH OTHER PHYSICAL PROPERTIES OF CONCRETE

Summary of some Studies on Dielectric Properties and Physical Properties of Concrete using Electro-magnetic Coaxial Transmission Line method

Physical properties correlated with dielectric properties	Studies	System type	Frequency range	Materials
Water Saturation/ Water content	De Loor (1961)	EMCTL	0.1 to 10MHz, 3GHz, 3.75GHz, 7.45GHz and 9.375GHz	Hardened Portland cement paste
	Shaw et al. (1993)	EMCTL	1MHz to 1.5GHz	Concrete
	Gu and Beaudoin (1997)	EMCTL	1MHz to 1.5GHz	Concrete
	Shaw (1998)	EMCTL	Up to 1GHz	Concrete
	Soutsos et al. (2001)	EMCTL	10MHz to 1GHz	Concrete with Ordinary Portland Cement (OPC), cement replacements like pulverized fuel ask (PFA) and ground granulated blast furnace slag (GGBS)
	Maierhofer and Wöstmann (1998)	Radar, with horn antennae	7GHz	Concrete, hollow brick, solid brick, sand-lime brick
	Binda et al. (1998)	Radar (Mono-static antennae)	500MHz, 900MHz and 1GHz	Stone and brick masonry
	Kääriäinen (2001)	Bore-hole antennae	8-16.5GHz, 0.5GHz in step	Concrete, sand and gravel
Water to cement ratio	*Perez-Pena et al. (1986)*	*EMCTL*	*1kHz to 2MHz*	*Hardened cementituous materials*
	Gorur et al. (1982)	*EMCTL*	*Not indicated*	*Hydrating cement paste*
	Wilson and Whittington (1990)	*EMCTL*	*1MHz to 100MHz*	*Concrete*
	McCarter and Curran (1984).	*EMCTL*	*1kHz*	*Cement paste*
	Taylor and Arulananda (1974),	*EMCTL*	*10MHz to 50MHz*	*Cement paste*
	Wittmann and Schlude (1975)	*EMCTL*	*8.5GHz to 12.2GHz*	*Cement paste*
	Gu and Beaudoin (1997)	EMCTL	1MHz to 1.5GHz	Cement paste
	Soutsos et al. (2001)	EMCTL	10MHz to 1GHz	Concrete with Ordinary Portland Cement (OPC), cement replacements like pulverized fuel ask (PFA) and ground granulated blast furnace slag (GGBS)

Physical properties correlated with dielectric properties	Studies	System type	Frequency range	Materials
Mix Design	Soutsos et al. (2001)	EMCTL	10MHz to 1GHz	Concrete with Ordinary Portland Cement (OPC), cement replacements like pulverized fuel ask (PFA) and ground granulated blast furnace slag (GGBS)
Porosity	Gu et al. (1997)	EMCTL	1MHz to 1.5GHz	Cement paste
	Oota (2000)	Radar (Bi-static antennae)	800MHz	Concrete
Salt concentration	Maierhofer and Wöstmann (1998)	Radar, with horn antennae	7GHz	Concrete, hollow brick, solid brick, sand-lime brick
Cement replacement, Cement strength	Shaw (1998)	EMCTL	Up to 1GHz	Concrete
Aggregate type	Shaw (1998)	EMCTL	Up to 1GHz	Concrete
Structural grouting	Bungey et al. (1997)	Radar	900MHz, 1GHz	Post-tensioned concrete
Strength	Oota (2000)	Radar (Bi-static antennae)	800MHz	Concrete
	Beek (2000)	Dielectric probe	1MHz to 1GHz.	Young concrete
Chloride content	Al-Qadi (1997)	EMCTL	0.1MHz to 40MHz	Concrete

Remarks:
1. EMCTL stands for Electromagnetic Coaxial Transmission Line
2. the works highlighted in *italic* font is reported by Gu et al. (1997).

APPENDIX B SUMMARY OF LITERATURE STUDIES ON DIELECTRIC PROPERTIES WITH OTHER PHYSICAL PROPERTIES OF SOIL

Summary of some Studies on Dielectric Properties and Physical Properties of Soil using Electro-magnetic Coaxial Transmission Line method

Relevant sub-sections	Physical properties correlated with dielectric constant	Studies	Frequency range	Materials
2.1	Water content/ water saturation	Simith-Rose (1933)	100 kHz - 10 MHz	Natural soils
		Keller and Licastro (1959)	50 Hz - 30 MHz	Rocks
		Scott et al. (1967)	100 Hz - 1 MHz	Natural soils and rocks
		Lundien (1971)	10 MHz - 1.5 GHz	Natural soils
		Birchak et al. (1974)	4 GHz - 6 GHz	Clay and crushed limestone
		Hipp (1974)	30 MHz - 4 GHz	Natural soils
		Hoekstra and Delaney (1974)	100 MHz - 26 GHz	Natural soils
		Poley et al. (1978)	1.5kHz -2.4 GHz	Sandstones and carbonates
		Hall and Rose (1978)	200 Hz - 1 GHz	Clays
		Okrasinski et al. (1979)	390 MHz - 1.5 GHz	Natural soils
		Topp et al. (1980)	20 MHz - 1 GHz	Glass beads and natural soils
		Wang (1980)	*1.4 – 5 GHz*	*Sand and Clay*
		Wang and Schmugge (1980)	1.4 GHz - 5 GHz	Natural soils
		Lange (1983)	100 MHz - 1 GHz	Glass beads and natural soils
		Dobson (1985)	*1.4 - 18 GHz*	*Sandy loam, silty clay and silty loam*
		Knight and Nur (1987)	60 kHz - 4 MHz	Sandstones
		Olhoeft (1987)	0.001 Hz - 1 GHz	Sand-clay mixtures
		Wensink (1993)	*1 - 3GHz*	*Natural soils*
		Knoll (1996)	*100kHz to 10MHz*	*Natural soils*
		Saarenketo (1998)	*30MHz to 3GHz*	*Clay and Silty soils*
		West et al. (2003)	*300MHz to 1000MHz*	*Clean medium to fine-grained sandstone*
2.2	Surface area	Lange (1983)	100 MHz - 1 GHz	Glass beads and natural soils
		Knight and Nur (1987)	60 kHz - 4 MHz	Sandstones
		Peplinski et al. (1995)	*0.3-1.3GHz*	*Natural soil*
		Li et al. (2001)	*100kHz -10MHz*	*Sand and clay*
	Lithology	Lundien (1971)	10 MHz - 1.5 GHz	Natural soils
		Poley et al. (1978)	1.5kHz -2.4 GHz	Sandstones and carbonates
	Grain size	Klein and Sill (1982)	0.01 Hz - 1 kHz	Glass bead-clay mixtures
	Grain geometry /geometry	Sen et al. (1981)	1.1 GHz	Sintered glass beads
		Kenyon (1984)	500 kH - 1.3 GHz	Carbonates
		Shen et al. (1985)	800 MHz - 1.2 GHz	Sedimentary rocks

Relevant sub-sections	Physical properties correlated with dielectric constant	Studies	Frequency range	Materials
2.4	Porosity	Poley et al. (1978)	1.5kHz -2.4 GHz	Sandstones and carbonates
		Okrasinski et al. (1979)	390 MHz - 1.5 GHz	Natural soils
		Sen et al. (1981)	1.1 GHz	Sintered glass beads
		Lange (1983)	100 MHz - 1 GHz	Glass beads and natural soils
		Kenyon (1984)	500 kH - 1.3 GHz	Carbonates
		Sherman (1986)	1.1 GHz	Sandstones and limestones
		Shen et al. (1985)	800 MHz - 1.2 GHz	Sedimentary rocks
		Knight and Nur (1987)	60 kHz - 4 MHz	Sandstones
		Olhoeft (1987)	0.001 Hz - 1 GHz	Sand-clay mixtures
		Knoll (1996)	*100kHz to 10MHz*	*Natural soils*
		Rust et al. (1999)	*0.01 – 10MHz*	*Volcanic rocks*
2.4.4	Clay content	*Wang (1980)*	*1.4 – 5 GHz*	*Sand and Clay*
		Wang and Schmugge (1980)	1.4 GHz - 5 GHz	Natural soils
		Olhoeft (1987)	0.001 Hz - 1 GHz	Sand-clay mixtures
		Klein and Sill (1982)	0.01 Hz - 1 kHz	Glass bead-clay mixtures
		Wensink (1993)	*1 - 3GHz*	*Natural soils*
		Peplinski et al. (1995)	*0.3-1.3GHz*	*Natural soil*
		Knoll (1996)	*100kHz to 10MHz*	*Natural soils*
		Li et al. (2001)	*100kHz -10MHz*	*Sand and clay*
		West et al. (2003)	*300MHz to 1000MHz*	*Clean medium to fine-grained sandstone*
	Clay microstructure	Arulanandan and Mitchell (1967)	30 Hz - 100 kHz	Clay
		Hall and Rose (1978)	200 Hz - 1 GHz	Clays
		Lockhart (1980a, 1980b)	10 Hz - 100 kHz	Clays
	Cation exchange	Lockhart (1980a, 1980b)	10 Hz - 100 kHz	Clays
-	Bulk density	Lundien (1971)	10 MHz - 1.5 GHz	Natural soils
		Hipp (1974)	30 MHz - 4 GHz	Natural soils
		Hallikainen et al. (1985)	1.4 GHz - 18 GHz	Natural soils
		Kutrubes (1986)	500 kHz - 1 GHz	Natural soils
		Ulaby, et al. (1990)	*0.5-18GHz for real part, 1.6-16GHz for imaginary part of dielectric permittivity*	*Rocks*
		Olhoeft and Strangway (1975)	*100MHz to 9GHz*	*Rocks from the Moon*
		Rust, et al. (1999)	*0.01 – 10MHz*	*Volcanic rocks*
-	Pore fluid content	Sen et al. (1981)	1.1 GHz	Sintered glass beads
	Rock Mineralogy	*Ulaby (1990)*	*0.5-18GHz for real part, 1.6-16GHz for imaginary part of dielectric permittivity*	*Rocks*

Relevant sub-sections	Physical properties correlated with dielectric constant	Studies	Frequency range	Materials
-	Salinity	Arulanandan and Mitchell (1967)	30 Hz - 100 kHz	Clay
		Klein and Sill (1982)	0.01 Hz - 1 kHz	Glass bead-clay mixtures
		Dobson (1985)	*1.4 - 18 GHz*	*Sandy loam, silty clay and silty loam*
-	Fluid composition	Hallikainen et al. (1985)	1.4 GHz - 18 GHz	Natural soils
		Kutrubes (1986)	500 kHz - 1 GHz	Natural soils
-	Temperature	*Olhoeft and Strangway (1975)*	*100MHz to 9GHz*	*Rocks from the Moon*
-	No specific correlations investigated	Taherian et al. (1990)	10 MHz - 1.3 GHz	Sandstones and carbonates

Remark: the works highlighted in *italic* font is newly added in this research.

Source: Knoll 1996 (re-arranged to summarize in terms of physical properties)

APPENDIX C THE FIVE ESSENTIAL VIRTUAL INSTRUMENTS IN THE LABVIEW DATA ACQUISITION PROGRAM

Four stages /VIs for data acquisition	Input	Values (default value in DAcqPs)	Functions
1. AI Config	Input limits	higher limit +1V, lower limit -1V	Maximum and minimum threshold of the voltage of the specified analog input channels
	Device	1	Device is the assigned device number to the DAQ device during configuration.
	Channels	1	Channels specify the set of analog input channels. The order of the channels in the scan list defines the order in which the channels are scanned during an acquisition.
	Buffer size	200k	Buffer size is the number of scans held by each buffer.
2. Conditional Retrieval	Trigger channel	1/2/3	A channel is selected to display the start of waveform in the waveform graph.
	Trigger slope	rising/ falling	The rising/falling option decides to display the start of waveform at the positive/negative slope of the wave in trigger channel.
	Trigger level	0.25V	The trigger level decides when trigger channel starts to trigger
	Pre-trigger scans	100	To fully ensure that no waveforms miss in the prescribed time window (scans to read at a time), 100 samples before the triggered point are acquired additionally.
	Hysteresis	0.1V	Hysteresis specifies the window that the signal must leave to meet the retrieval conditions.
3. AI Start	Scan rate	250k samples per second	The maximum scan rate of the NI DAQ board used is 250k samples per second. Channels specified in Table 4-1 share the sampling rate if they are in function at the same time.
4. AI Read/Write	Scan backlog	4	Scan backlog is the amount of data remaining in the buffer after this VI completes.
	Scans to read at a time	1024 scans	It determines how many sample points acquired in a complete waveform. It is designed to be 1024 to cope with the number of bits for subsequent FFT analysis.

* AI Clear is not included.

APPENDIX D COMPUTATION OF THE RE-SCALING FACTOR OF THE JRC RADAR SYSTEM

For radar EM wave traveling at the commonly known speed of light (299,792,458 meter per second) in air, the stepped down factor is computed according to the following calculation and data summarized in the below table.

$$\text{Distance} = \text{Velocity x Time}$$

$$\text{2 x distance from metal plate and antenna} = \text{Speed of light} \times \frac{\text{No. of sample points}}{\text{scan rate x calibrated stepped down factor}}$$

$$d = 2.997 \times 10^8 \text{ m/s} \times \frac{Y_d}{125\text{k} \times \text{stepped down factor}}$$

$$\text{Calibrated stepped down factor} = \frac{2.997 \times 10^8\, Y_d}{125\text{k} \times d}$$

where the physical meanings of ‘d’ and ‘Y_d’ in a particular waveform at a particular separation distance are represented in Fig. 4-5 and Fig. 4-10. The value of the re-scaling down factor is averaged in the table below.

Determination of the Re-scaling Factor built in the JRC Radar System

Distance from the position of antenna to the position of metal plate (d)	No. of sample points from the arbitrary zero to the position of metal plate (Y_d)	Stepped down factor (dimension-less)
0.20	148.31	517915.5
0.25	167.43	518924.6
0.30	190.00	516697.6
0.35	215.71	519088
0.40	238.23	517257.5
0.45	257.73	517271.6
0.50	278.78	517873.2
0.55	301.07	519580.4
0.60	322.78	518280.7
0.65	345.21	518240.4
0.70	365.89	516008.5
0.75	387.06	517161.6
0.80	408.34	523136.6
0.85	431.71	520390.8
0.90	451.85	505065
0.95	474.75	497075.1
1.00	495.40	506879.5
Average		**515697 (+/-1000)**

APPENDIX E1 THEORETICAL TIME-ZERO IN THE WAVEFORMS CAPTURED BY THE JRC RADAR SYSTEM

Determination of the Theoretical Time-zero in the Waveforms of 1GHz JRC Radar System

JRC 1GHz GPR antenna						
Distance from the position of antenna to the position of metal plate (d)	Theoretical Travel time at air		The measured difference from the metal plate reflection to the anchor peak of the waveform****		Time difference *****	
	T_d (ns) **	T_d' (Sample points) ***	A_d (ns)	A_d'(Sample points)	T_d - A_d (ns)	T_d' - A_d' (Sample points)
0.20	1.3	86	1.3	85	0.0	+1
0.25	1.7	107	1.6	104	0.1	+3
0.30	2.0	129	2.0	126	0.0	+3
0.35	2.3	150	2.4	152	0.1	-2
0.40	2.7	172	2.7	175	0.0	-3
0.45	3.0	193	3.0	194	0.0	-1
0.50	3.3	215	3.3	215	0.0	-0
0.55	3.7	236	3.7	238	0.0	-2
0.60	4.0	258	4.0	259	0.0	-1
0.65	4.3	279	4.4	282	-0.1	-3
0.70	4.7	301	4.7	302	0.0	-1
0.75	5.0	322	5.0	324	0.0	-2
0.80	5.3	344	5.4	345	-0.1	-1
0.85	5.7	365	5.7	368	0.0	-3
0.90	6.0	387	6.0	388	0.0	-1
0.95	6.3	408	6.4	411	-0.1	-3
1.00	6.7	430	6.7	432	0.0	-2
Average					-0.02	-0.88

* The labels d, Y_d, and A_d are referred to Fig. 4-5.

** The theoretical travel time through air presented in nano-second is calculated by

$$v_a = \frac{2d}{T_d} = \frac{c}{\sqrt{\varepsilon_a}} \Rightarrow T_d = \frac{2d}{c}$$

where v is the radar wave propagation velocity in air (i.e. 2.997 x 10^8 m/s), d is the distance from the position of antenna to the position of metal plate, T_d is the traveled time in air, c is the traveling speed of light and ε is the real permittivity of air (i.e. unity).

*** The theoretical travel time through air in number of sample points (T_d') is calculated by
Theoretical travel time = T_d x 125k/sec (sampling rate of the digital interface) x 515697 (re-scaling factor)

**** The data are determined from the radargrams in Fig. 4-4.

***** The differences between T_a and A_d are the rightful position of theoretical time-zero in a waveform, which is measured by shifting to left (+ve sign) or right (-ve sign) of the position of the anchor peak in a waveform.

APPENDIX E2 THEORETICAL TIME-ZERO IN THE WAVEFORMS CAPTURED BY THE GSSI RADAR SYSTEM

Determination of the Theoretical Time-zero in the Waveforms of
400MHz and 1.5GHz Radar Systems

GSSI 400MHz GPR antenna						
Designated distance from the position of antenna to the position of metal plate (d)	Theoretical Travel time at air		The measured difference from the metal plate reflection to the anchor peak of the waveform****		Time difference *****	
	T_d (ns) **	T_d' (Sample points) ***	A_d (ns)	A_d'(Sample points)	T_d - A_d	T_d' - A_d' (Sample points)
600	4.0	68	3.9	66	0.1	+2
1000	6.7	114	6.5	111	0.2	+3
1500	10.0	171	9.6	164	0.4	+7
2000	13.3	228	12.7	217	0.6	+11
Average					+0.33	+5.64
GSSI 1.5GHz GPR antenna						
Designated distance from the position of antenna to the position of metal plate (d)	Theoretical Travel time at air		The measured difference from the metal plate reflection to the anchor peak of the waveform****		Time difference *****	
	T_d (ns) **	T_d' (Sample points) ***	A_d (ns)	A_d' (Sample points)	T_d - A_d	T_d' - A_d' (Sample points)
600	4.0	137	3.9	134	0.1	3
1000	6.7	228	6.5	221	0.2	7
1500	10.0	342	9.9	338	0.1	4
2000	13.3	455	13.0	445	0.3	10
Average					+0.18	+5.96

* The labels d, Y_d, and A_d are referred to Fig. 4-10.

** The theoretical travel time through air presented in nano-second is calculated by

$$v_a = \frac{2d}{T_d} = \frac{c}{\sqrt{\varepsilon_a}} \Rightarrow T_d = \frac{2d}{c}$$

where v is the radar wave propagation velocity in air (i.e. 2.997 x 10^8 m/s), d is the distance from the position of antenna to the position of metal plate, T_d is the traveled time in air, c is the traveling speed of light and ε is the real permittivity of air (i.e. unity).

*** The theoretical travel time through air in number of sample points (T_d') is calculated by
Theoretical travel time for 400MHz antenna = T_d x1.71x 10^{10} samples /sec (sampling rate)
Theoretical travel time for 1.5GHz antenna = T_d x3.41 x10^{10} samples /sec (sampling rate)

**** The data are determined from the radargrams in Fig. 4-8 (for 400MHz) and Fig. 4-9 (for 1.5GHz).

***** The differences between T_a and A_d are the rightful position of theoretical time-zero in a waveform, which is measured by shifting to left (+ve sign) or right (-ve sign) of the position of the anchor peak in a waveform.

APPENDIX F THE FRONT PANELS AND THE BLOCK DIAGRAM OF THE IN-HOUSED DEVELOPED DATA ACQUISITION PROGRAM IN LABVIEW ENVIRONMENT

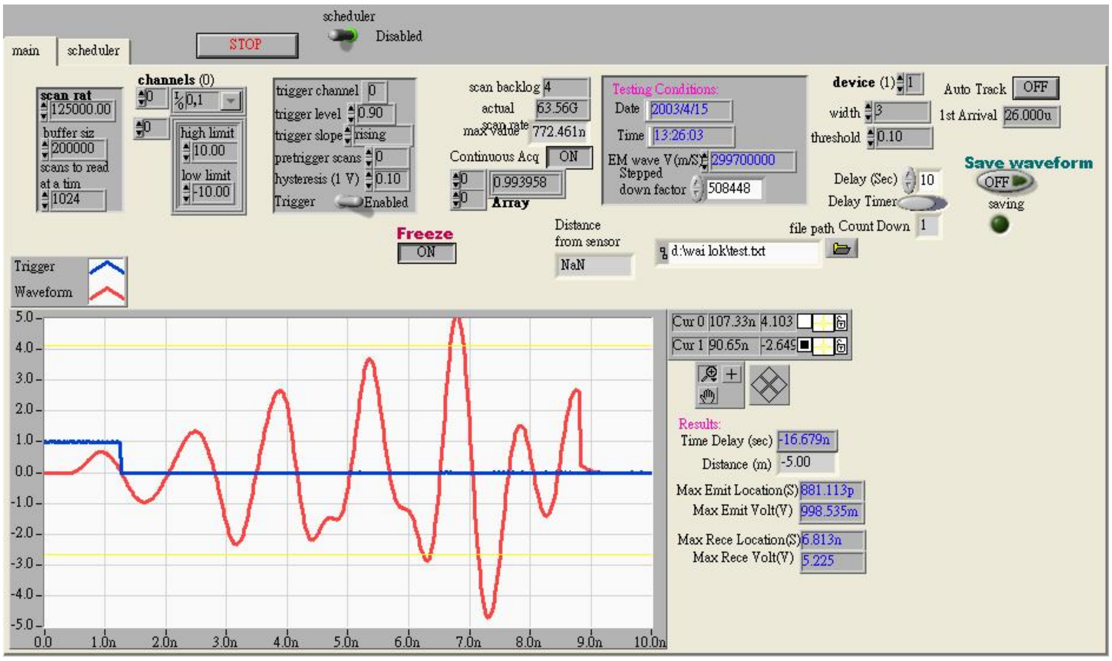

Front panel (1) of the In-housed developed Data Acquisition Program constructed in LabVIEW Environment

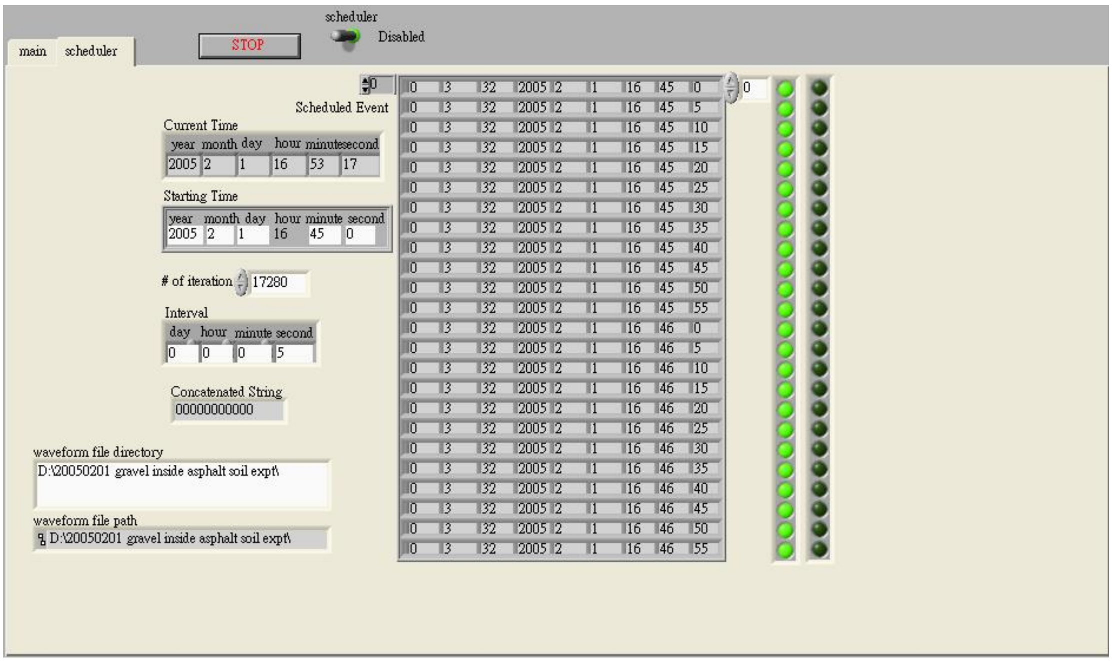

Front Panel (2) of the In-housed developed Data Acquisition Program constructed in LabVIEW Environment

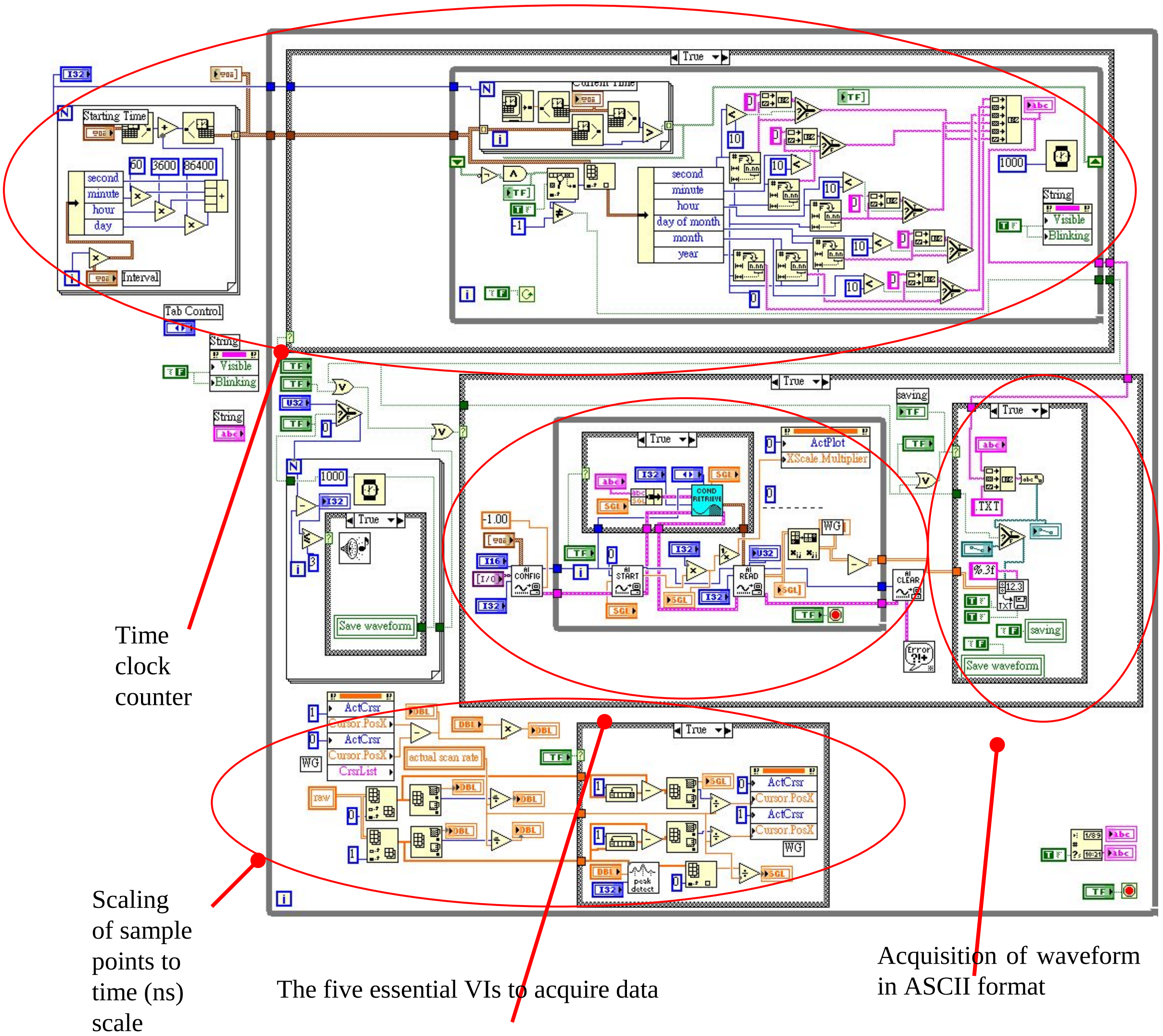

Block diagram of the In-housed developed Data Acquisition Program constructed in LabVIEW Environment

APPENDIX G

APPENDIX G PHOTOS OF EACH SIDE OF CONCRETE SPECIMENS AFTER TEST RUNS

Remarks:
1. The line drawn on the surface of concrete indicates the wetting front after each test run,
2. The arrows at the right indicates the direction of water permeation
3. The capital letters at the upper left hand corner indicate the faces of concrete specimens (A, B, C and D are in clockwise direction, with face A on top)

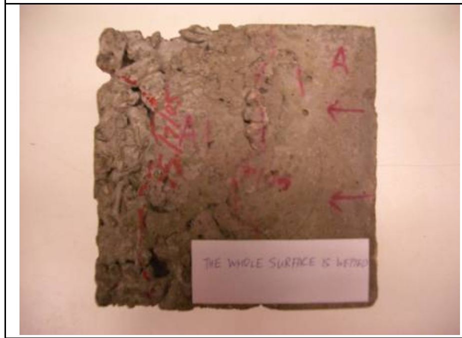	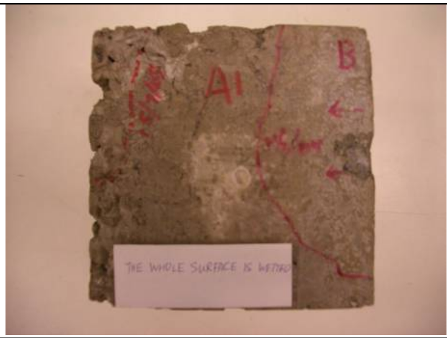	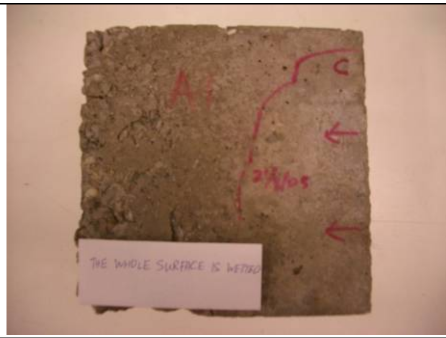	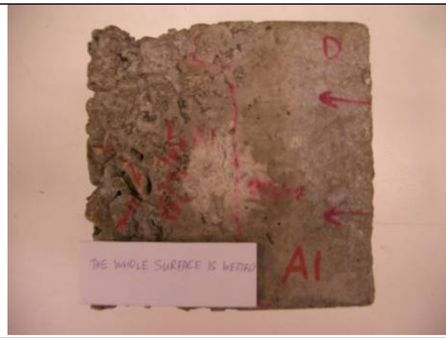
A1 Face A	A1 Face B	A1 Face C	A1 Face D
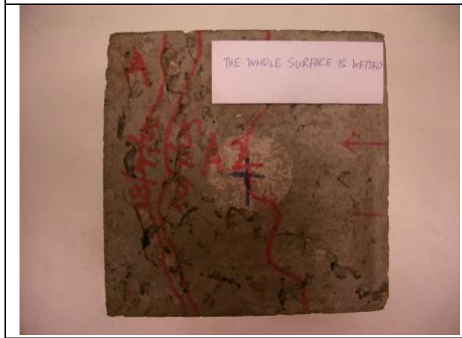			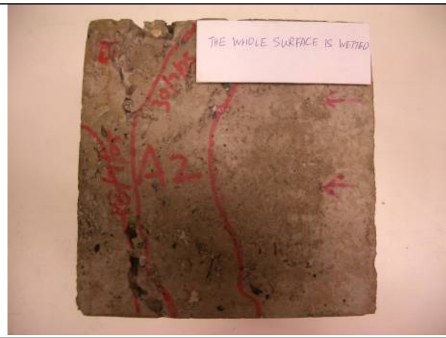
A2 Face A	A2 Face B	A2 Face C	A2 Face D

		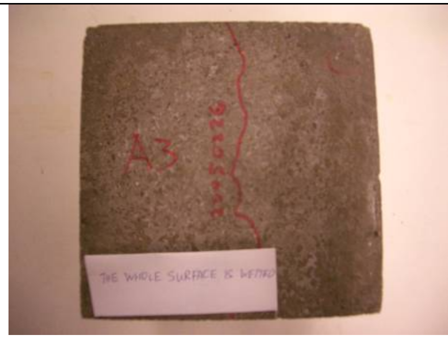	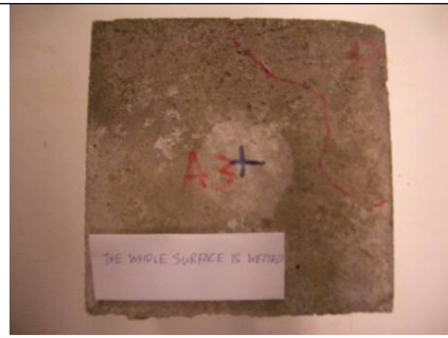
A3 Face A	A3 Face B	A3 Face C	A3 Face D
	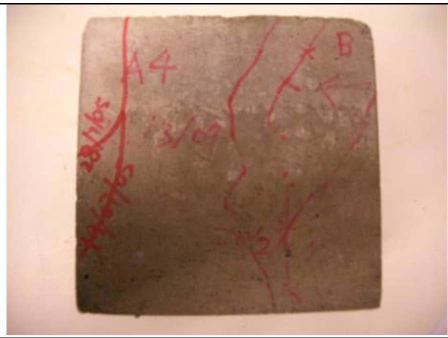	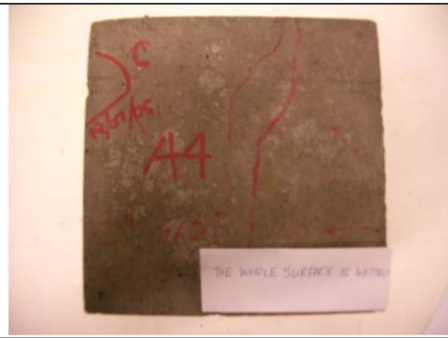	
A4 Face A	A4 Face B	A4 Face C	A4 Face D
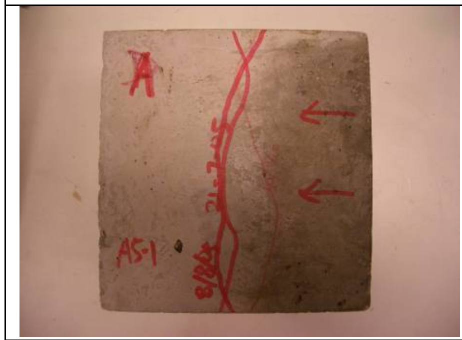	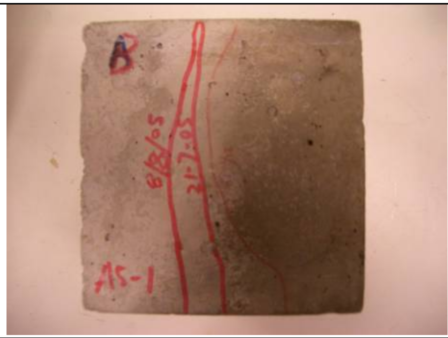		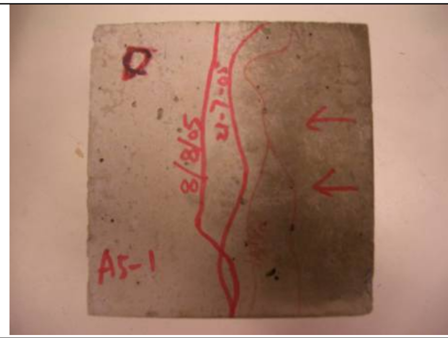
A5-1 Face A	A5-1 Face B	A5-1 Face C	A5-1 Face D

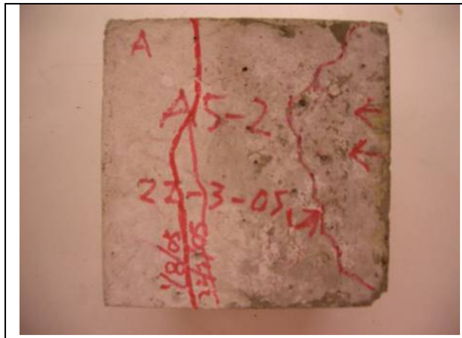		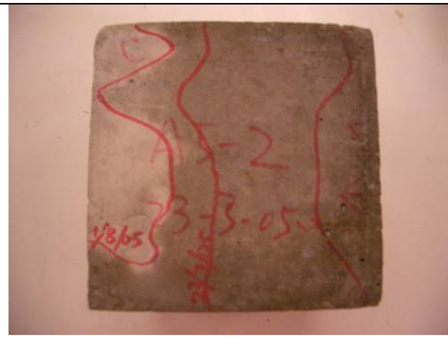	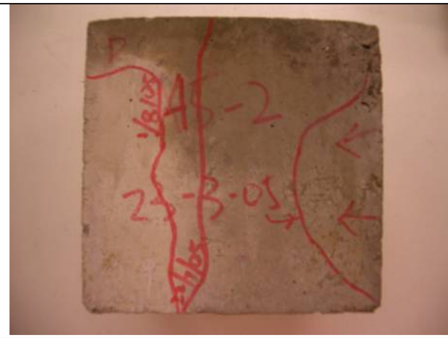
A5-2 Face A	A5-2 Face B	A5-2 Face C	A5-2 Face D
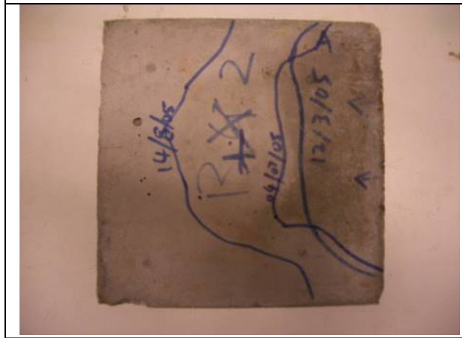	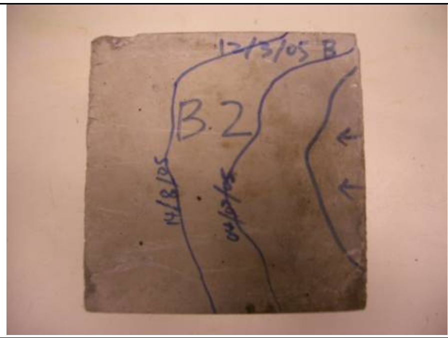	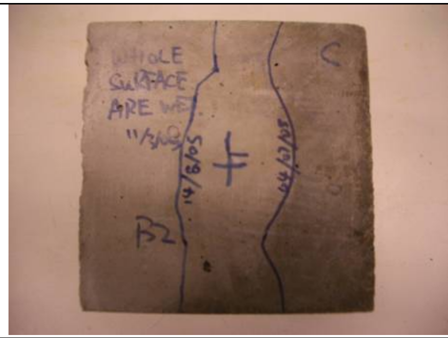	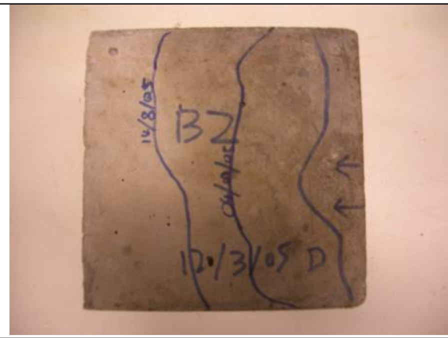
B2 Face A	B2 Face B	B2 Face C	B2 Face D
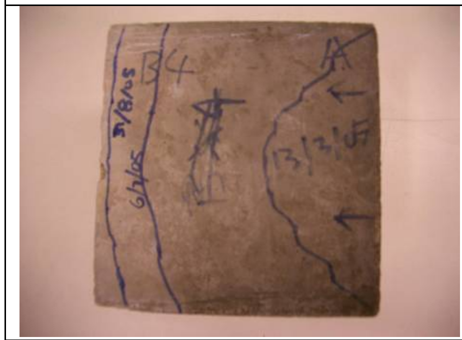		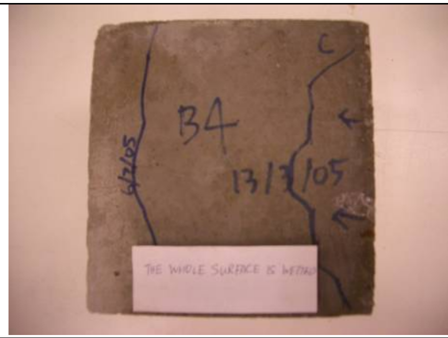	
B4 Face A	B4 Face B	B4 Face C	B4 Face D

	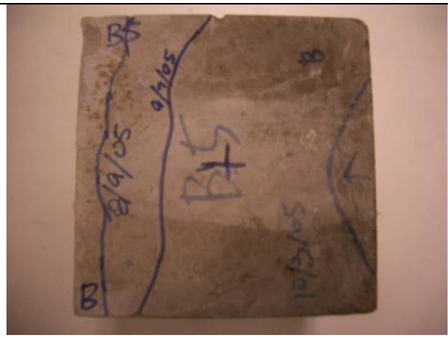	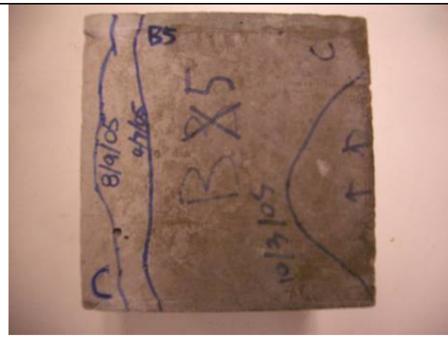	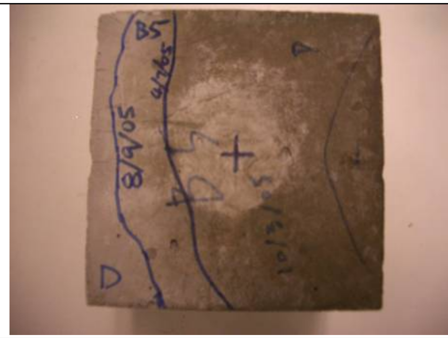
B5 Face A	B5 Face B	B5 Face C	B5 Face D
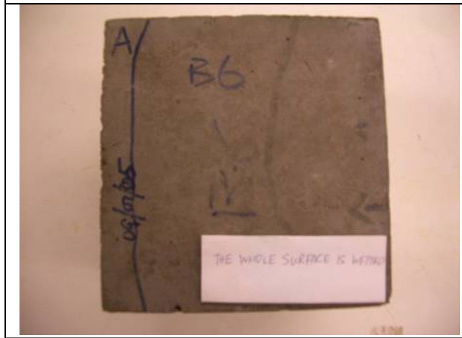	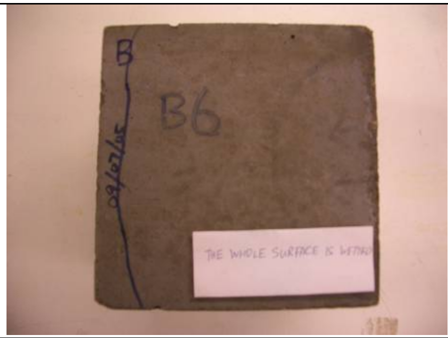	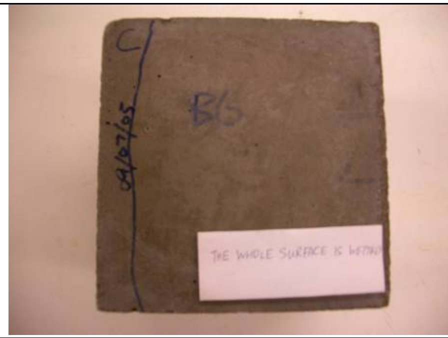	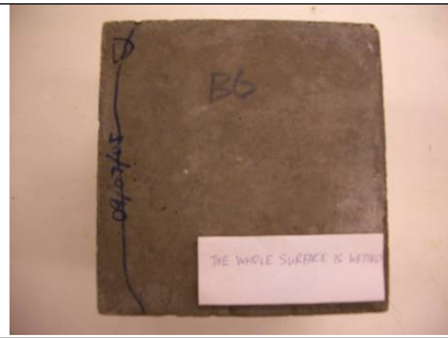
B6 Face A	B6 Face B	B6 Face C	B6 Face D
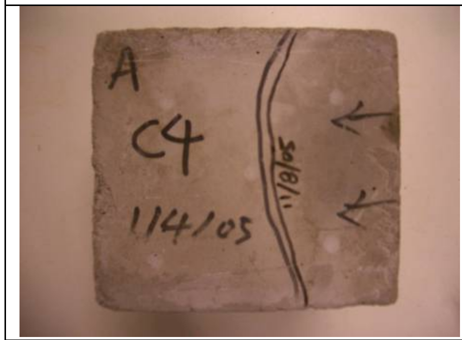		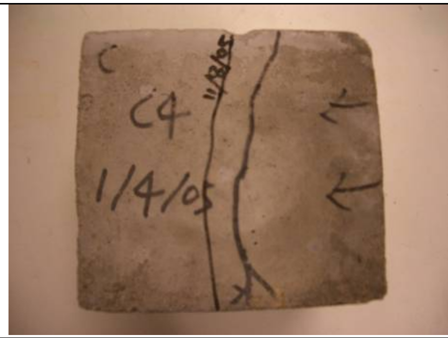	
C4 Face A	C4 Face B	C4 Face C	C4 Face D

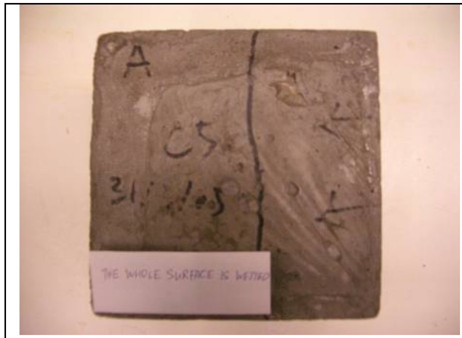

C5 Face A

C5 Face B

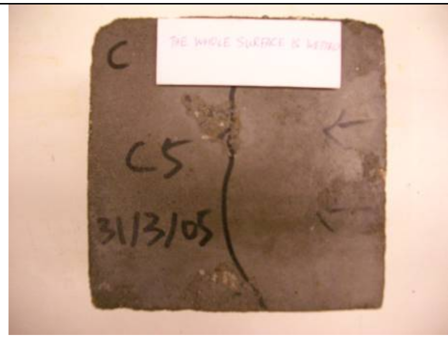

C5 Face C

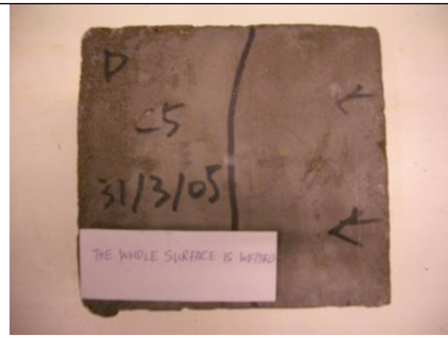

C5 Face D

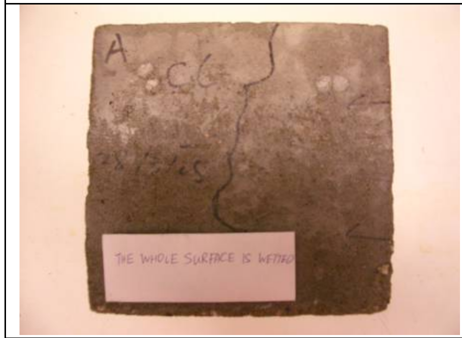

C6 Face A

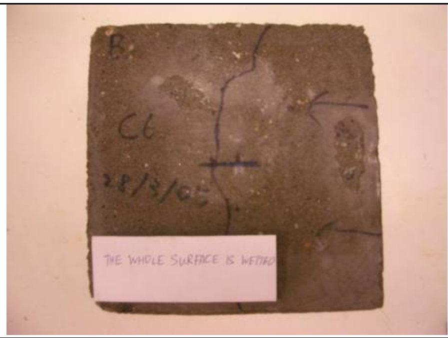

C6 Face B

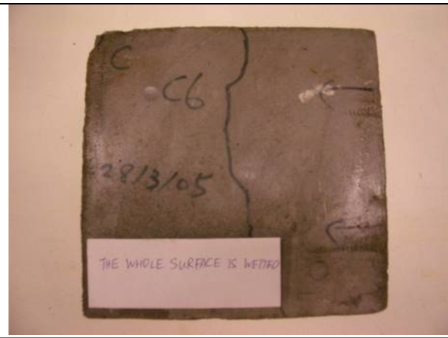

C6 Face C

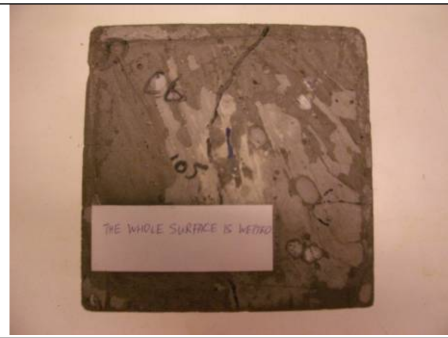
C6 Face D

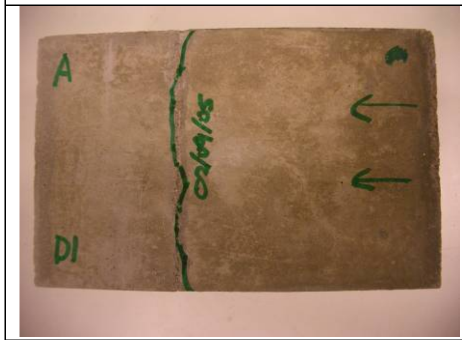

D1 Face A

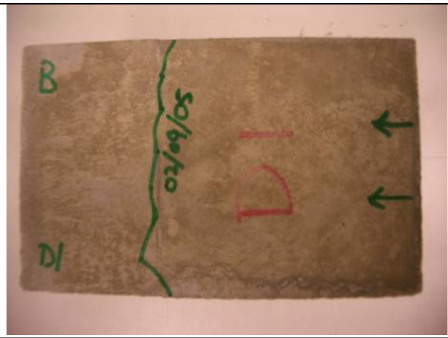

D1 Face B

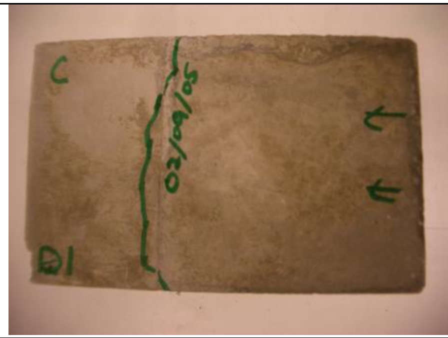

D1 Face C

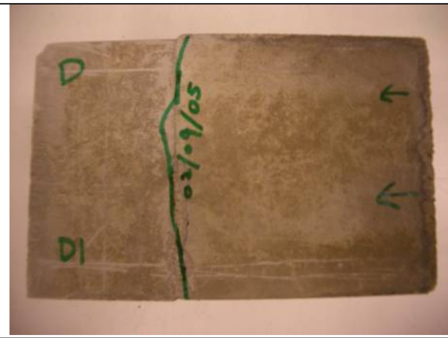

D1 Face D

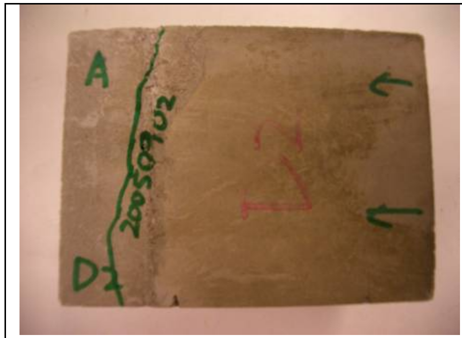	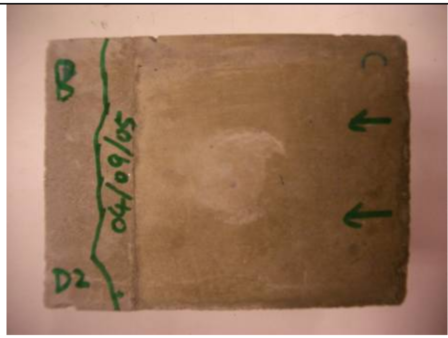	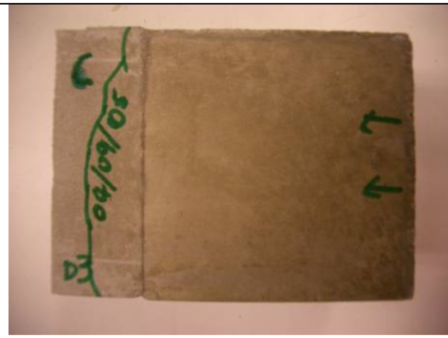	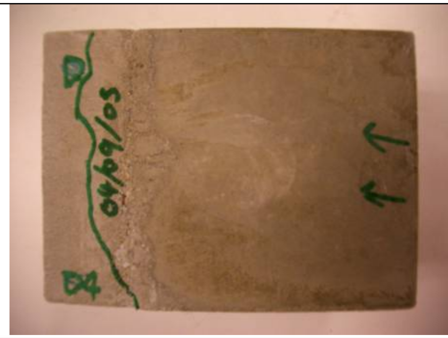
D2 Face A	D2 Face B	D2 Face C	D2 Face D
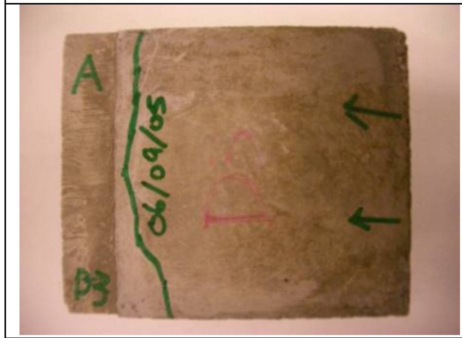	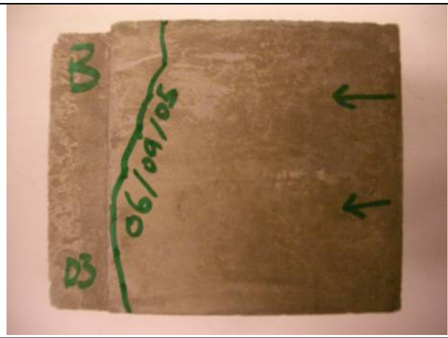		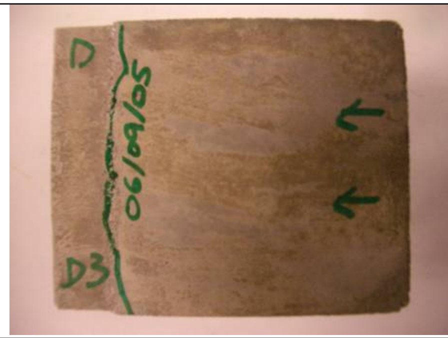
D3 Face A	D3 Face B	D3 Face C	D3 Face D
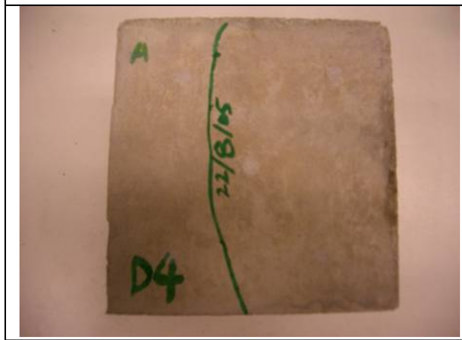	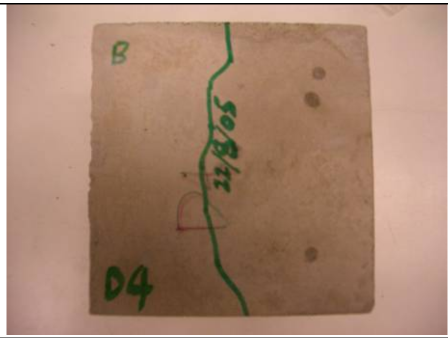	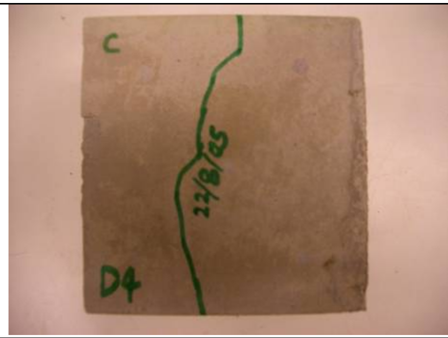	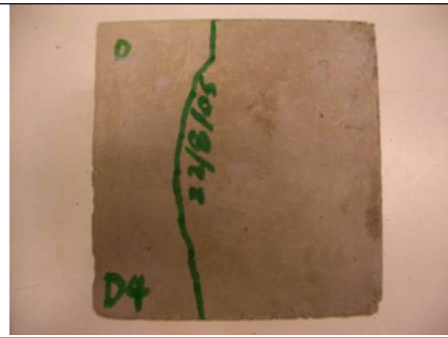
D4 Face A	D4 Face B	D4 Face C	D4 Face D

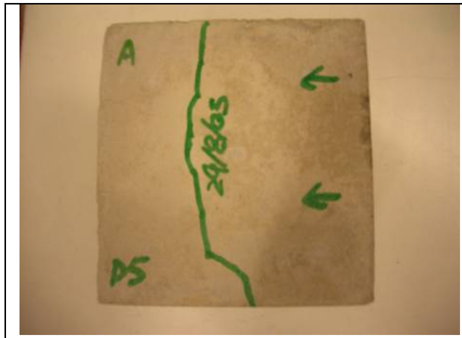

D5 Face A

D5 Face B

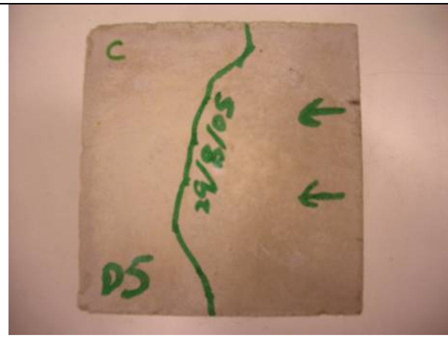

D5 Face C

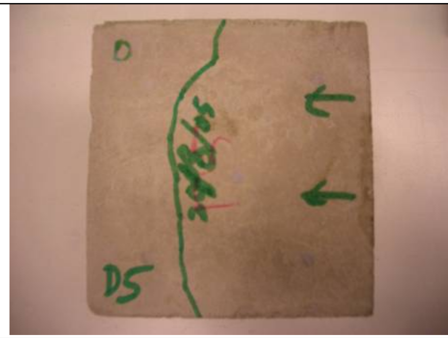

D5 Face D

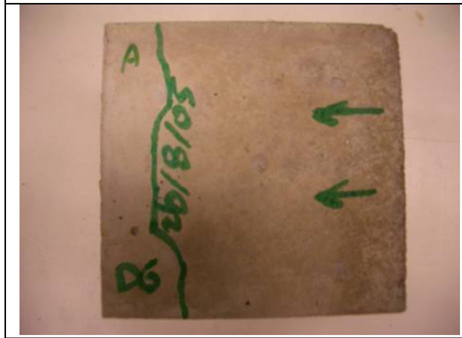

D6 Face A

D6 Face B

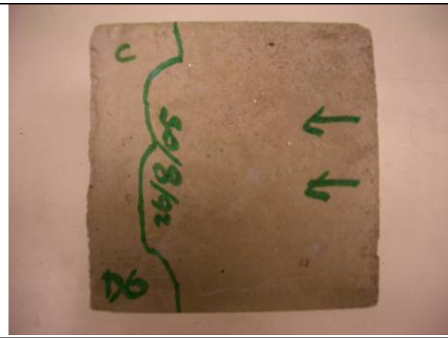

D6 Face C

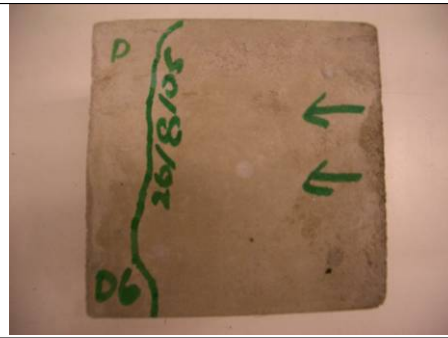

D6 Face D

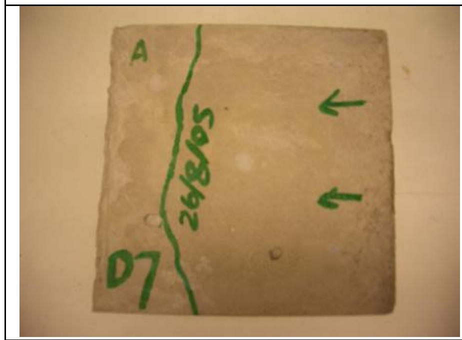

D7 Face A

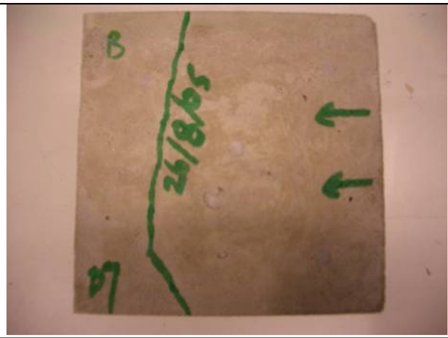

D7 Face B

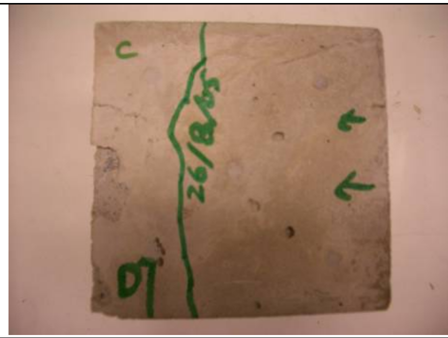

D7 Face C

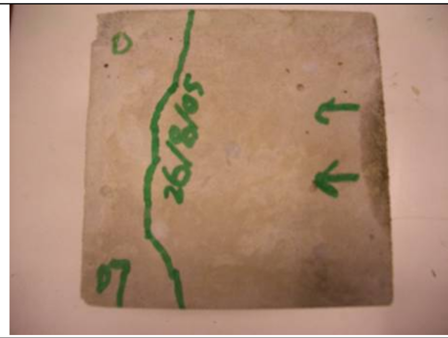

D7 Face D

APPENDIX H1 FREQUENCY SPECTRAGRAMS OF CONCRETE SPECIMENS

General remark: The blue lines indicate the peak-frequency drift.

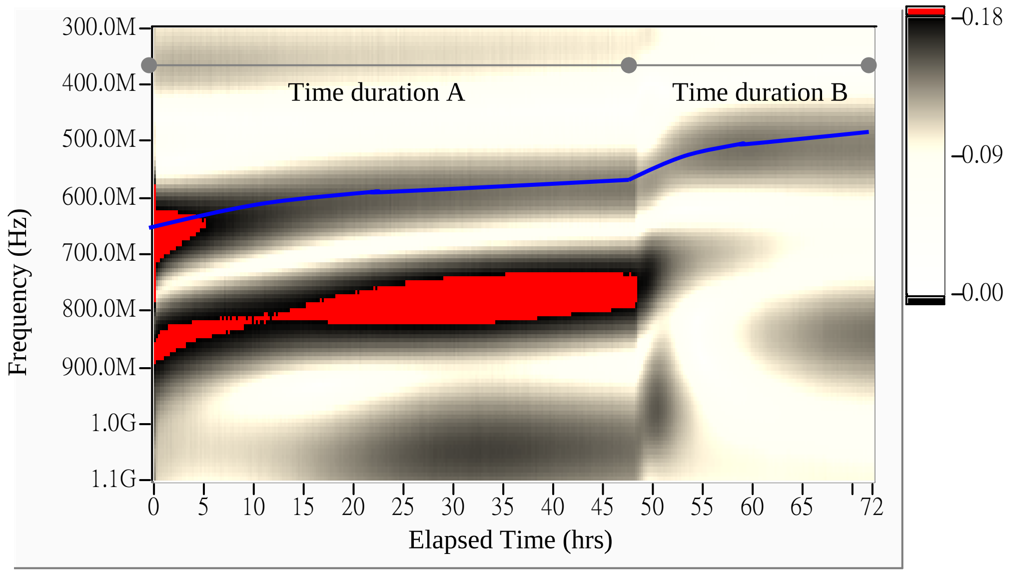

Remark:
Time duration A: 1.5m constant water head during the first 48 hrs
Time duration B: 200kPa pneumatic pressure exerted on 1.5m constant water head during the final 24hrs

Spectragram obtained in A1 using 1GHz SPR and processed with a 2GHz low-pass filter

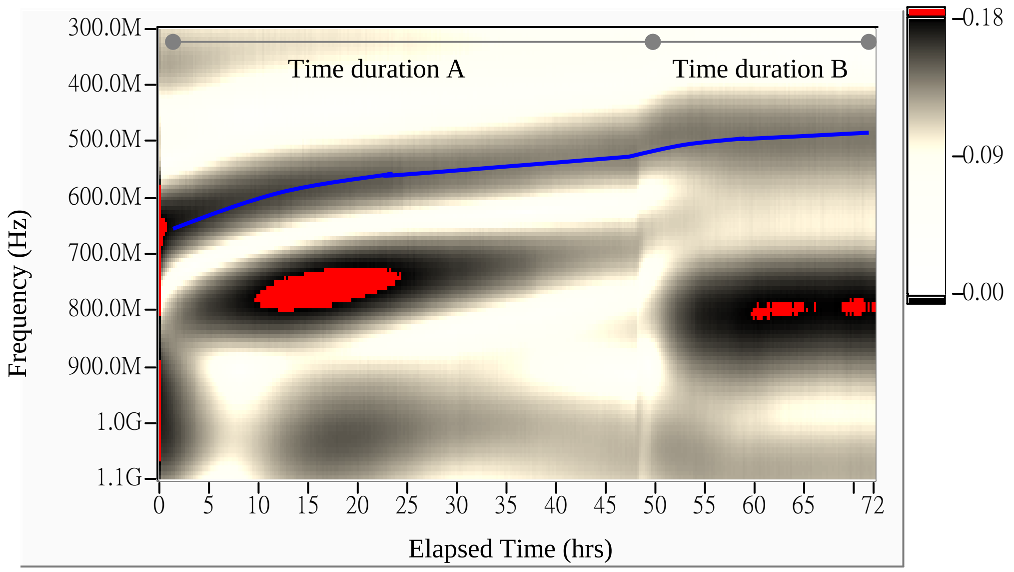

Remark:
Time duration A: 1.5m constant water head during the first 48 hrs
Time duration B: 200kPa pneumatic pressure exerted on 1.5m constant water head during the final 24hrs

Spectragram obtained in A2 using 1GHz SPR and processed with a 2GHz low-pass filter

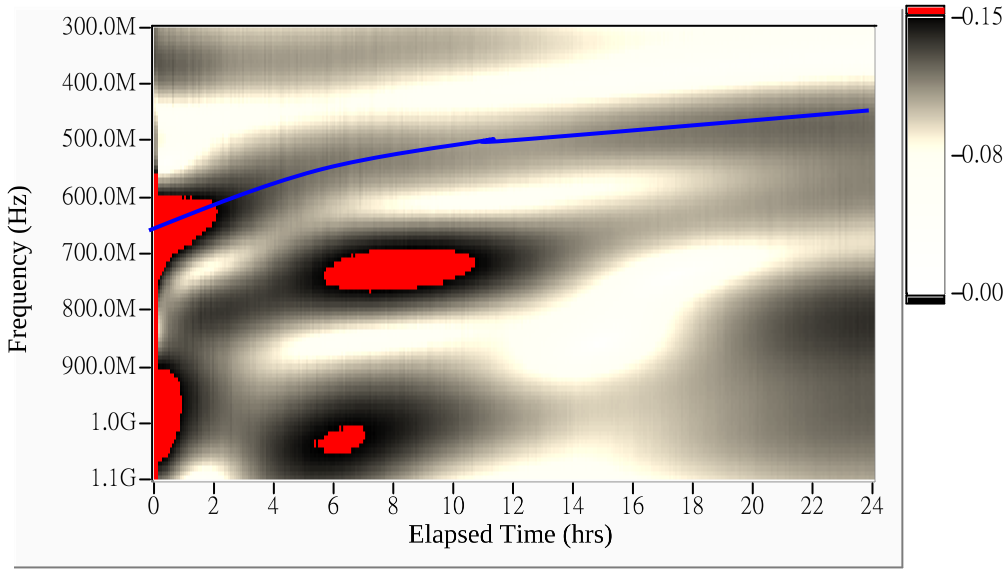

Spectragram obtained in A3 using 1GHz SPR and processed with a 2GHz low-pass filter

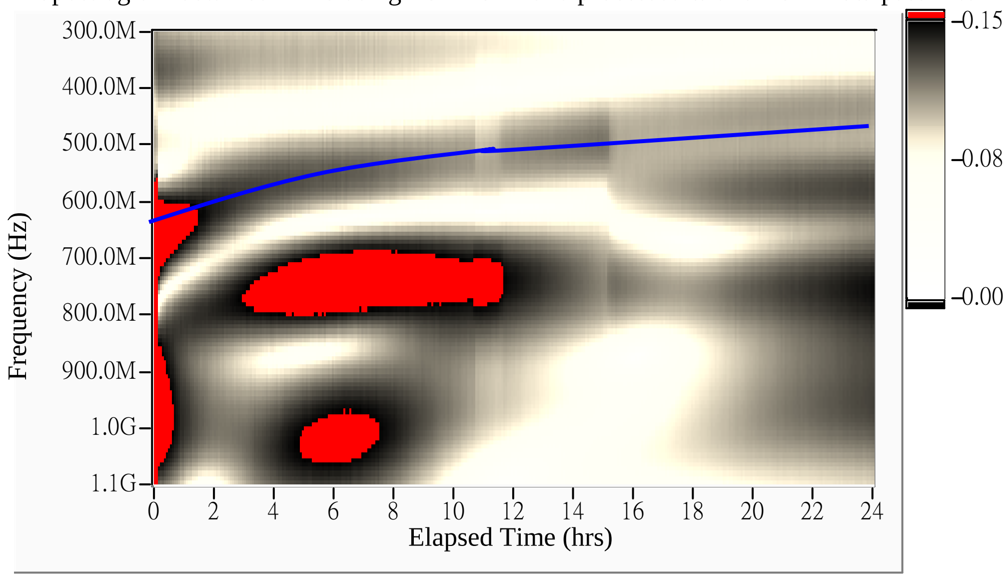

Spectragram obtained in A4 using 1GHz SPR and processed with a 2GHz low-pass filter

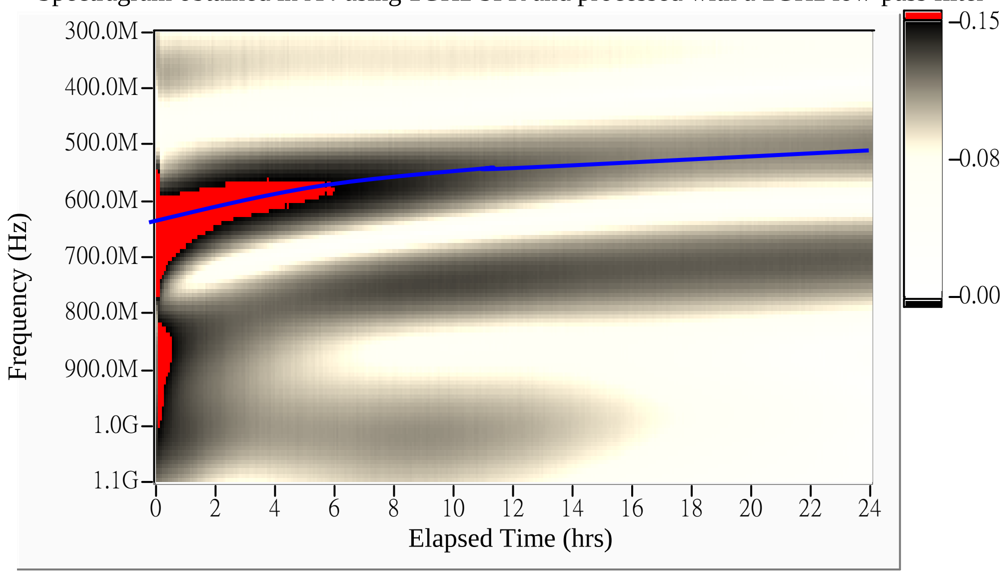

Spectragram obtained in A5-1 using 1GHz SPR and processed with a 2GHz low-pass filter

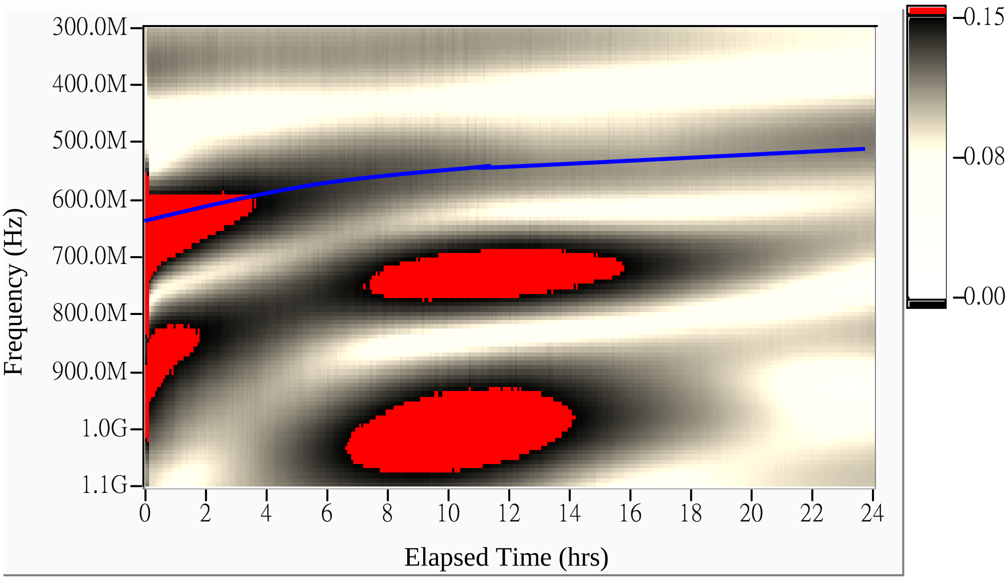

Spectragram obtained in A5-2 using 1GHz SPR and processed with a 2GHz low-pass filter

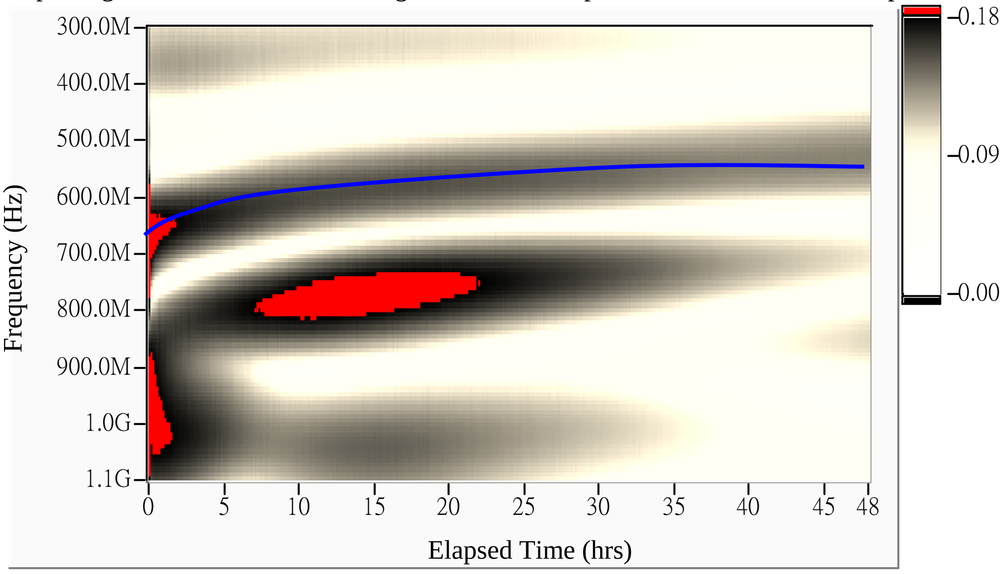

Spectragram obtained in B2 using 1GHz SPR and processed with a 2GHz low-pass filter

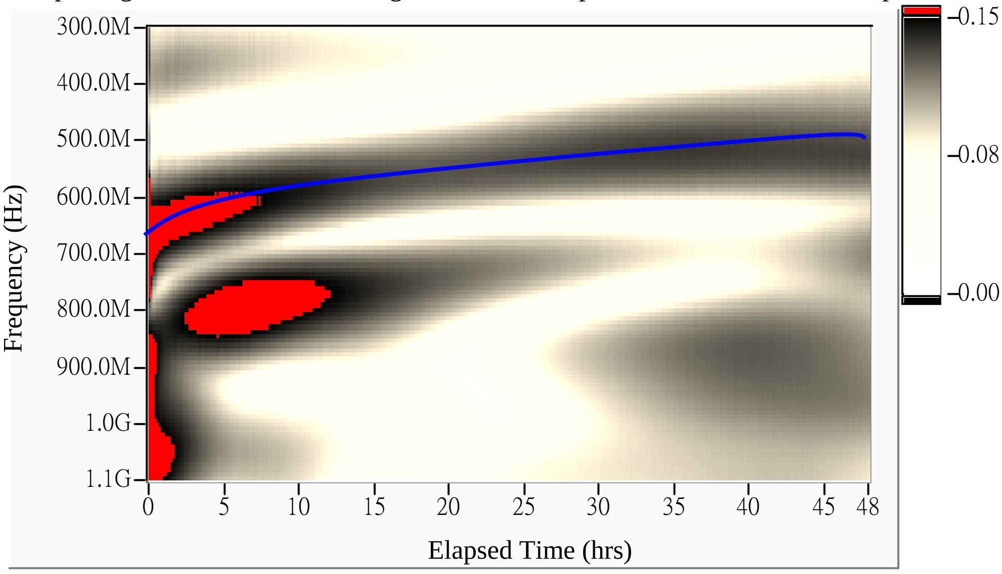

Spectragram obtained in B4 using 1GHz SPR and processed with a 2GHz low-pass filter

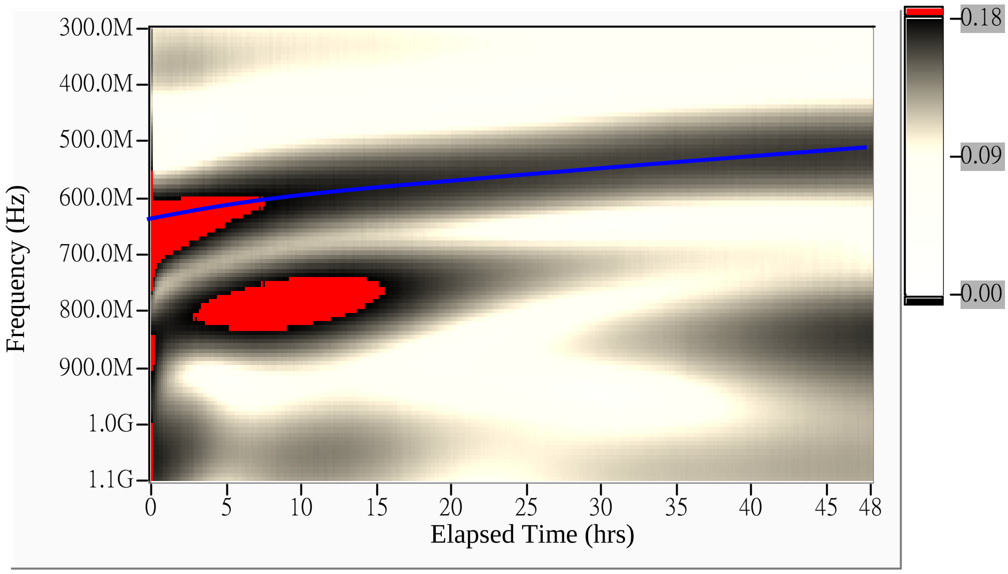

Spectragram obtained in B5 using 1GHz SPR and processed with a 2GHz low-pass filter

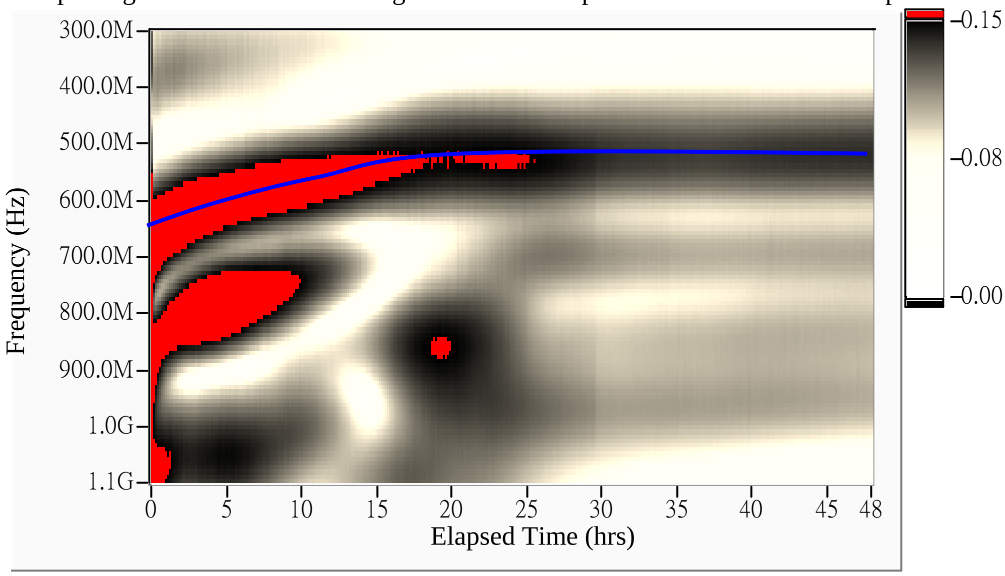

Spectragram obtained in B6 using 1GHz SPR and processed with a 2GHz low-pass filter

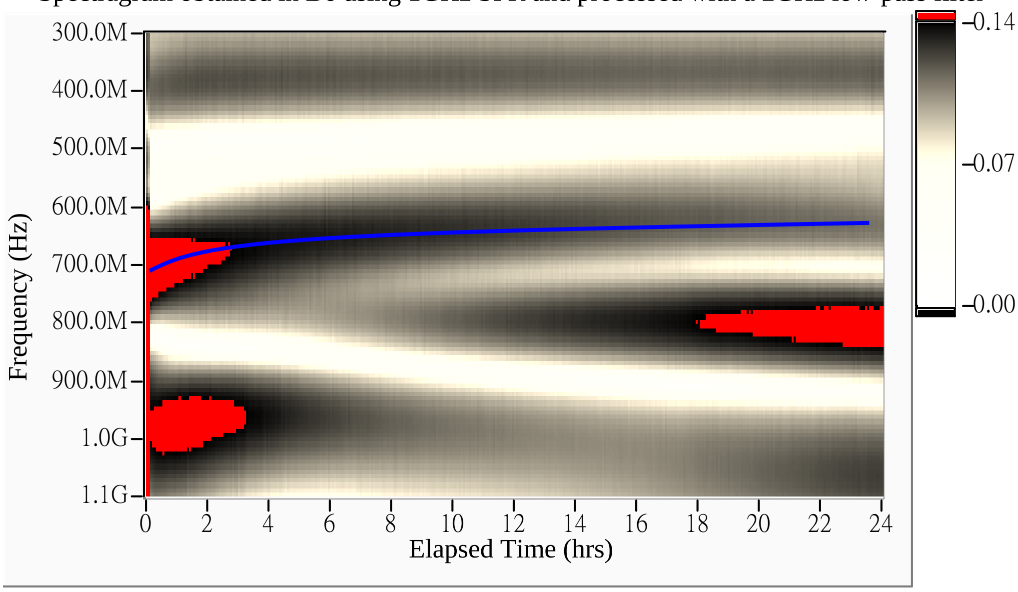

Spectragram obtained in C4 using 1GHz SPR and processed with a 2GHz low-pass filter

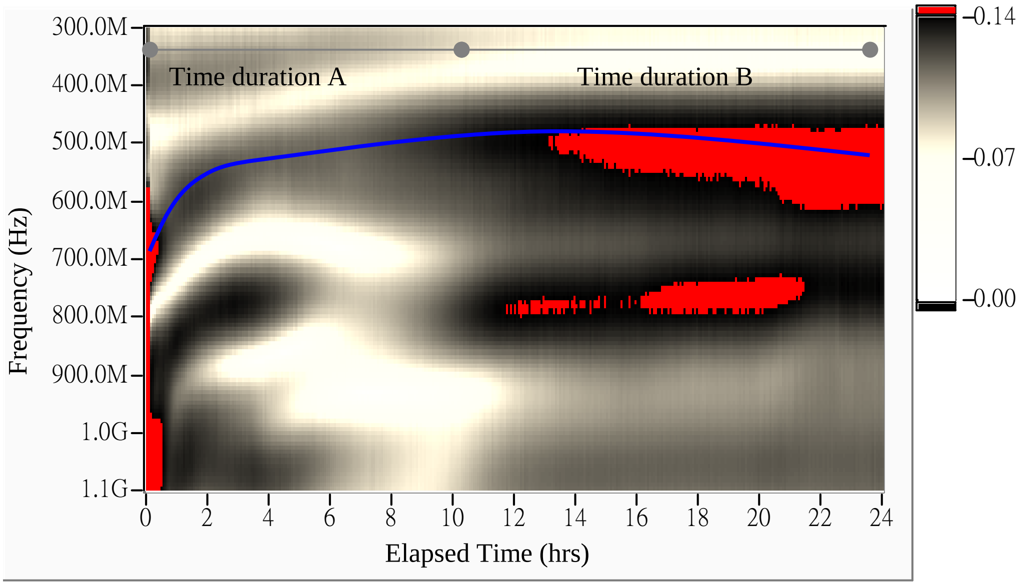

Remark:
Time duration A: The specimen was not saturated yet in this duration
Time duration B: The specimen was saturated in this duration

Spectragram obtained in C5 using 1GHz SPR and processed with a 2GHz low-pass filter

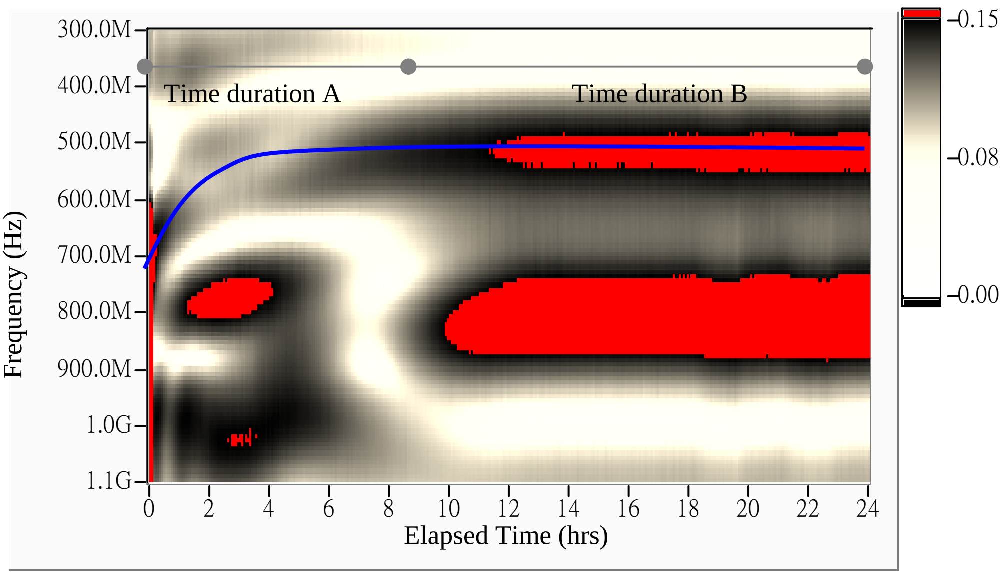

Remark:
Time duration A: The specimen was not saturated yet in this duration
Time duration B: The specimen was saturated in this duration

Spectragram obtained in C6 using 1GHz SPR and processed with a 2GHz low-pass filter

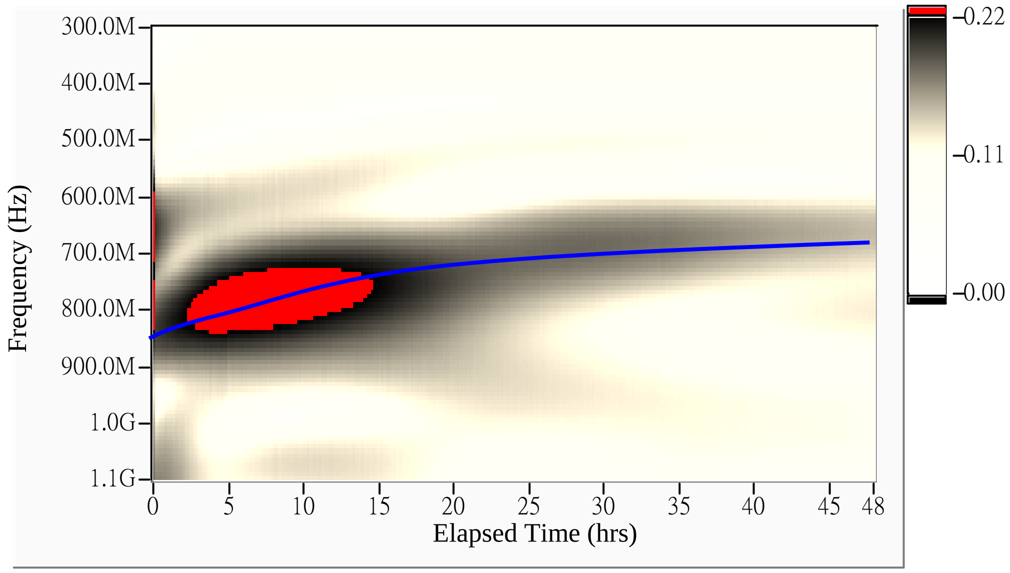

Spectragram obtained in D1 using 1GHz SPR and processed with a 2GHz low-pass filter

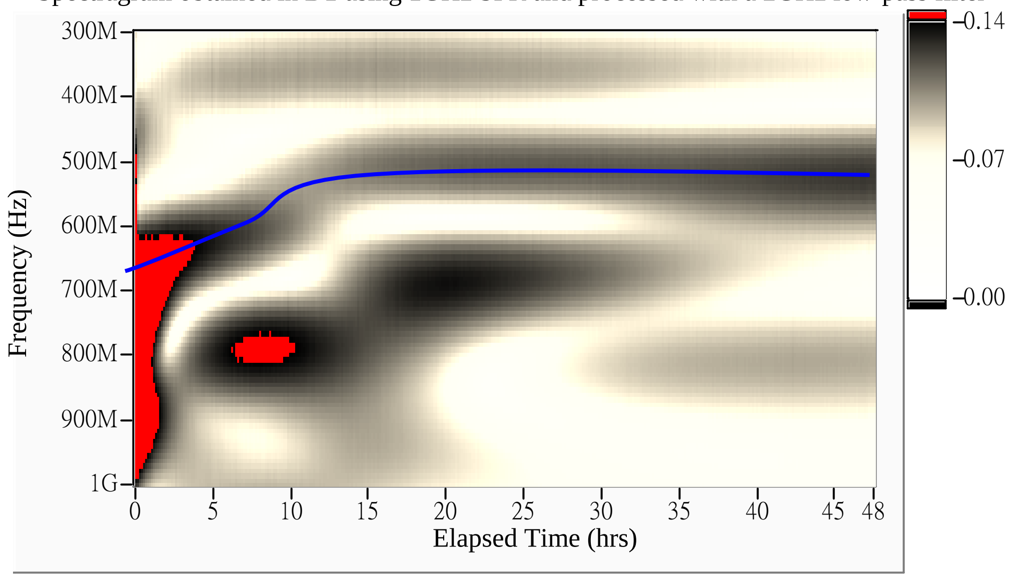

Spectragram obtained in D2 using 1GHz SPR and processed with a 2GHz low-pass filter

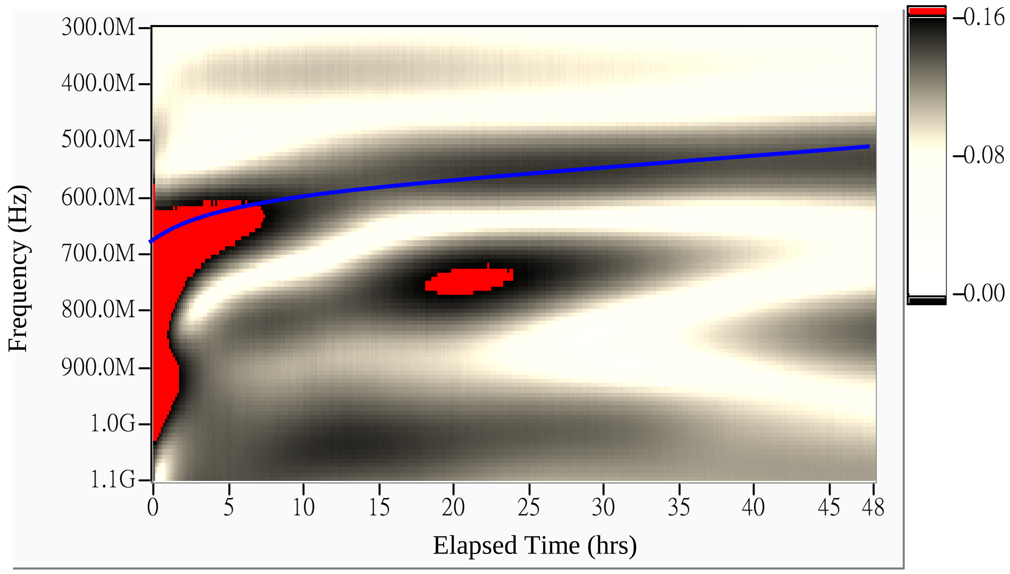

Spectragram obtained in D3 using 1GHz SPR and processed with a 2GHz low-pass filter

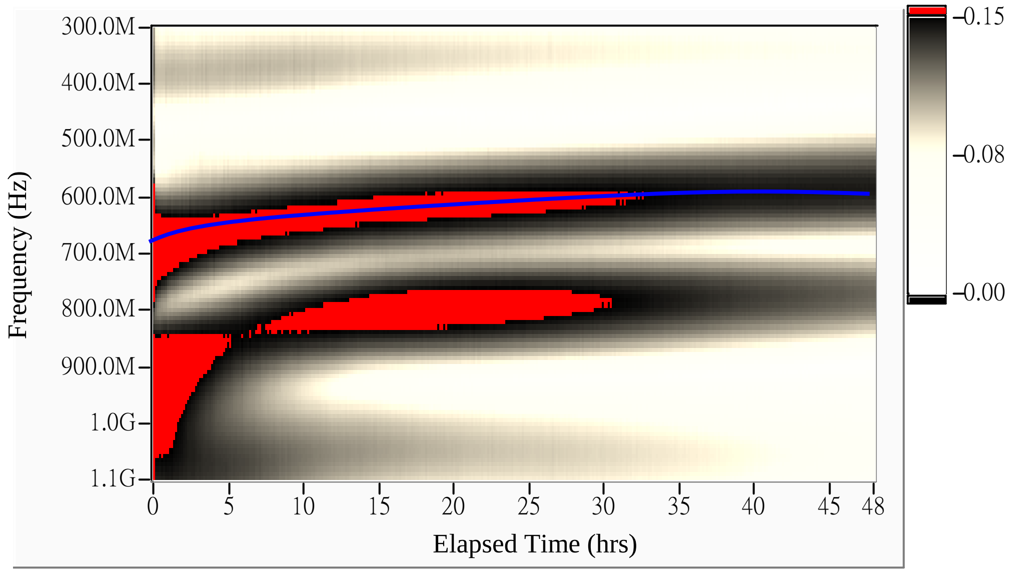

Spectragram obtained in D4 using 1GHz SPR and processed with a 2GHz low-pass filter

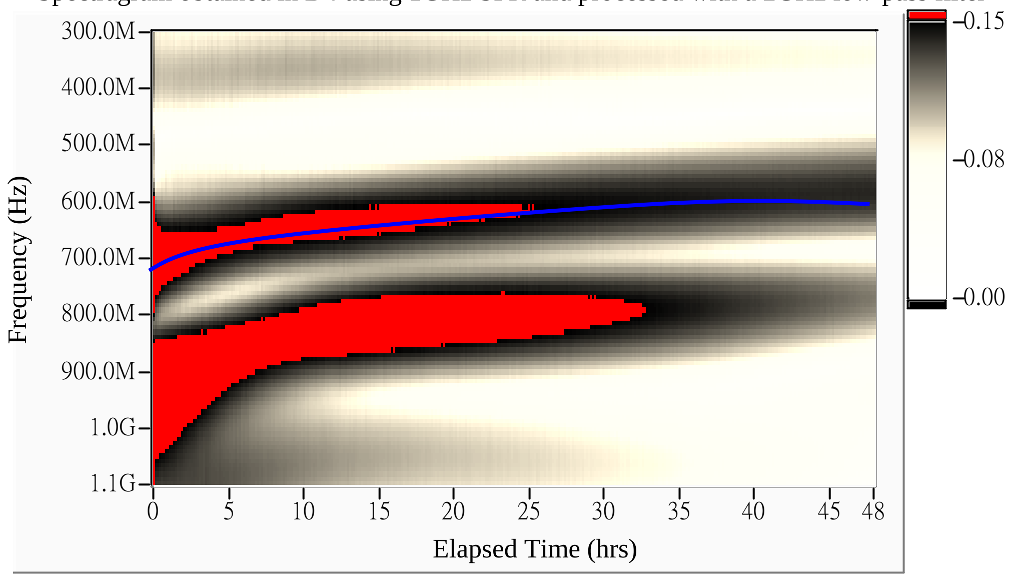

Spectragram obtained in D5 using 1GHz SPR and processed with a 2GHz low-pass filter

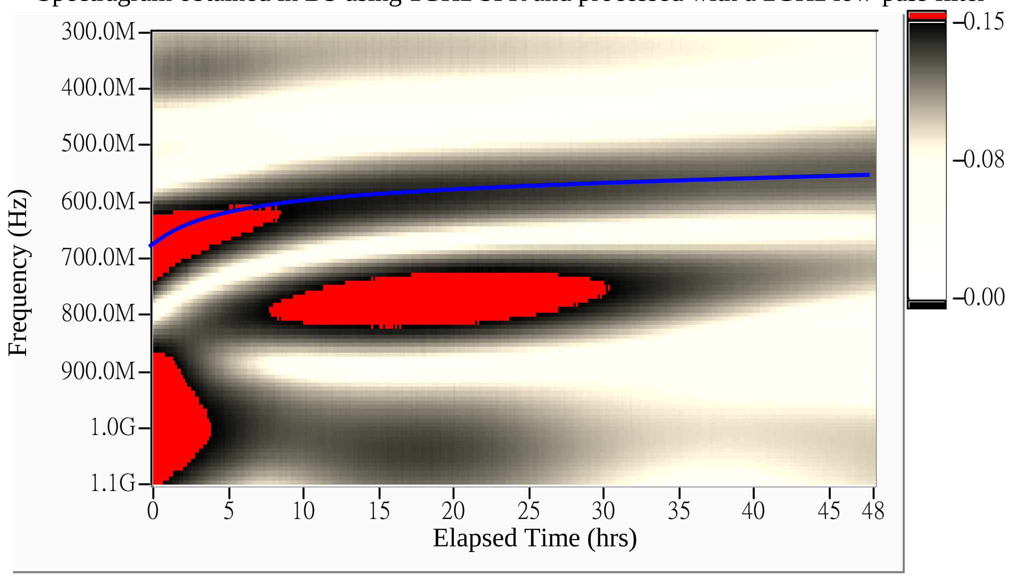

Spectragram obtained in D6 using 1GHz SPR and processed with a 2GHz low-pass filter

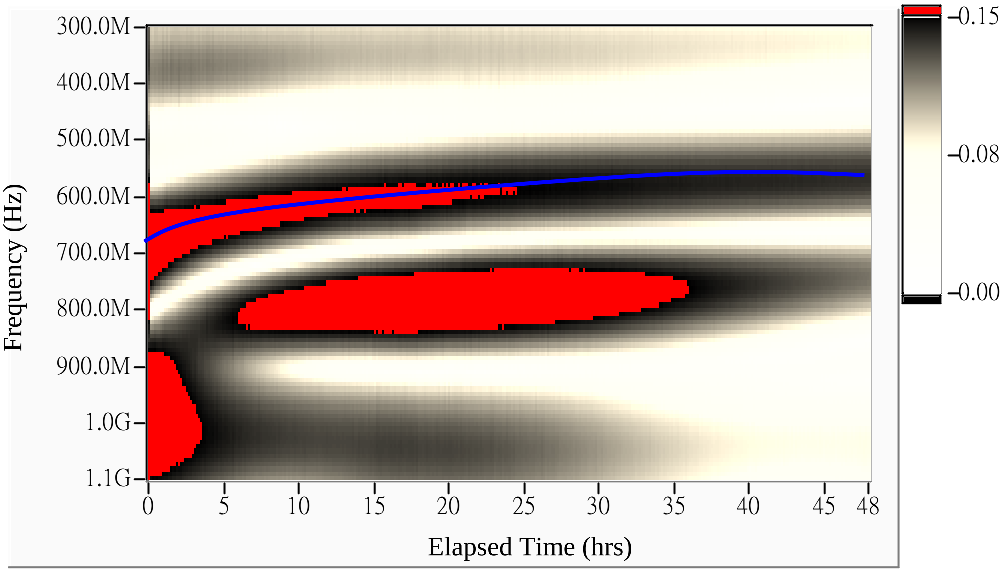

Spectragram obtained in D7 using 1GHz SPR and processed with a 2GHz low-pass filter

APPENDIX H2 FREQUENCY SPECTRAGRAMS OF ASPHALT SPECIMENS

General remark: The blue lines indicate the peak-frequency drift.

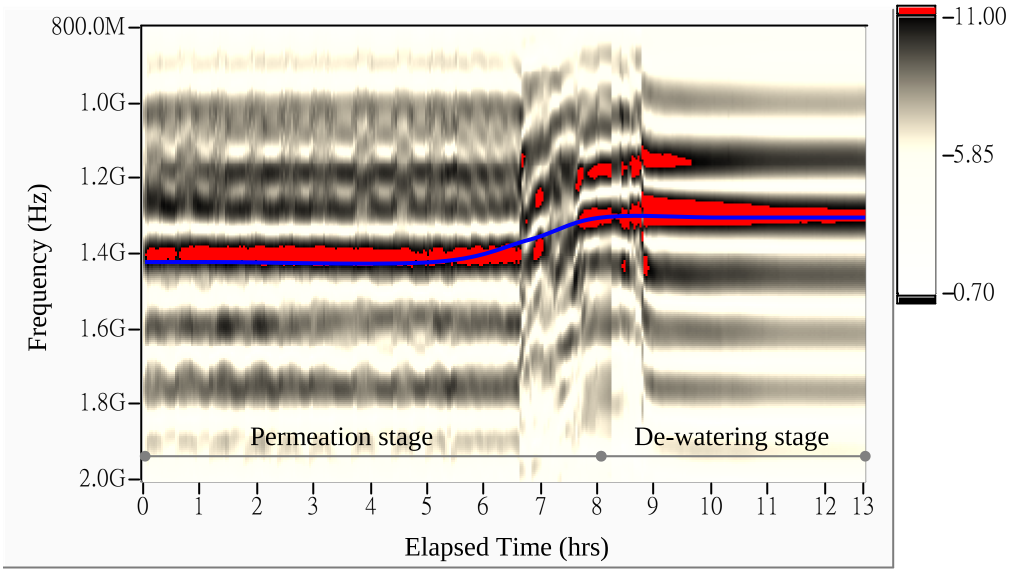

Spectragram obtained in Experiment #1 using 1.5GHz antenna and processed with a 1G to 2GHz band-pass filter

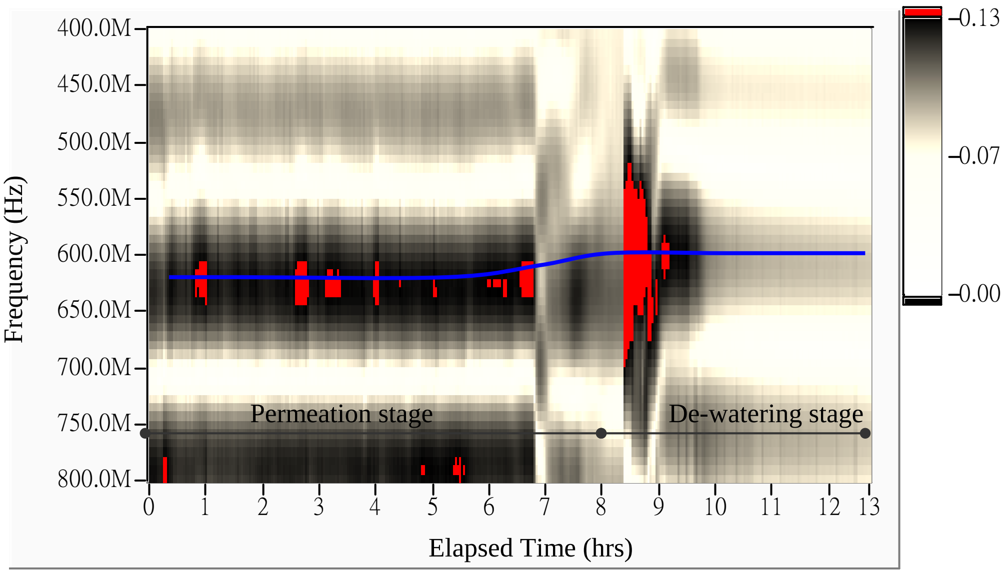

Spectragram obtained in Experiment #1 using 1GHz antenna and processed with a 300M to 750MHz band-pass filter

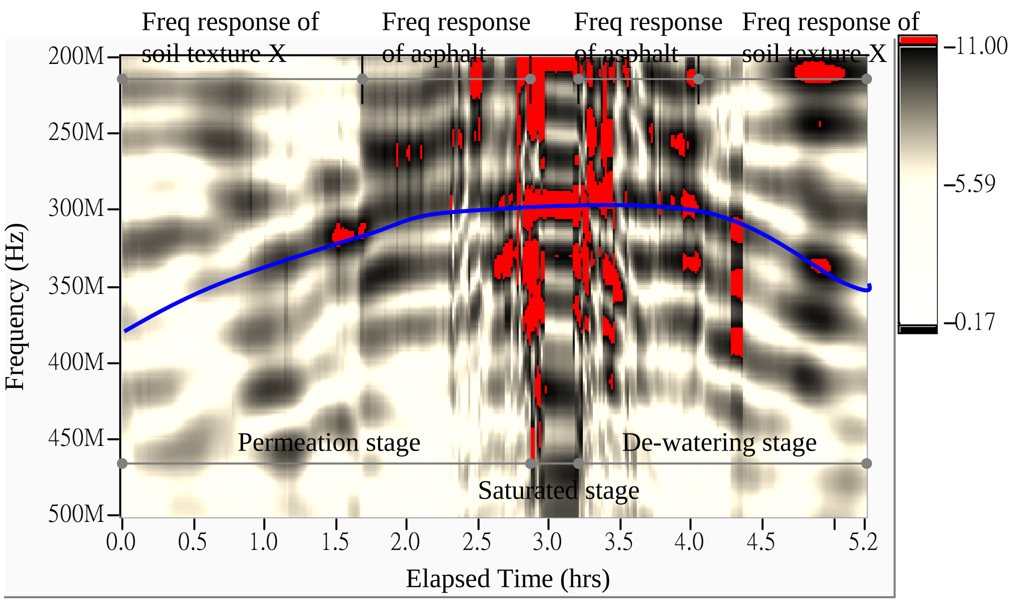

Spectragram obtained in Experiment #2 using 400MHz antenna and processed with a 250M to 450MHz band-pass filter

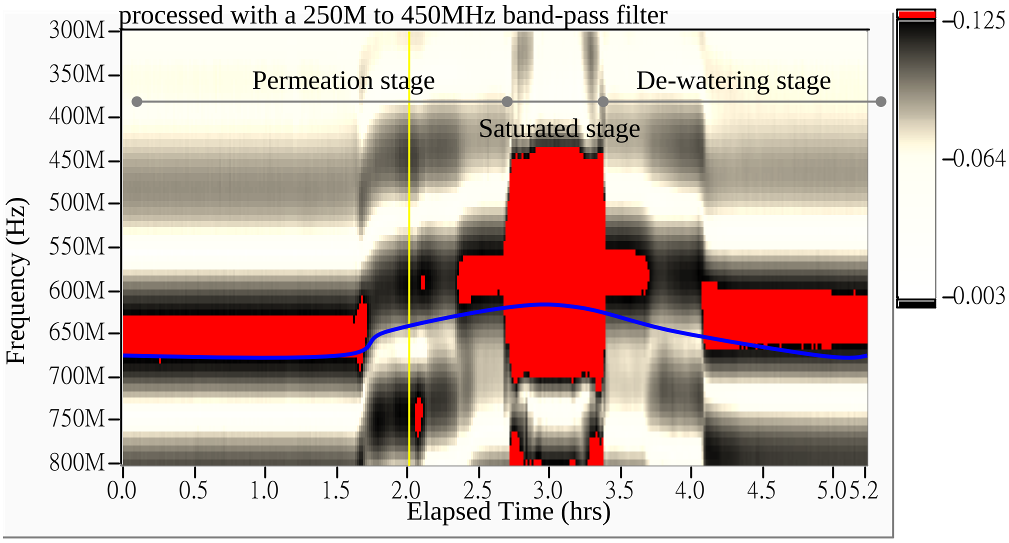

Spectragram obtained in Experiment #2 using 1GHz antenna and processed with a 300M to 750MHz band-pass filter

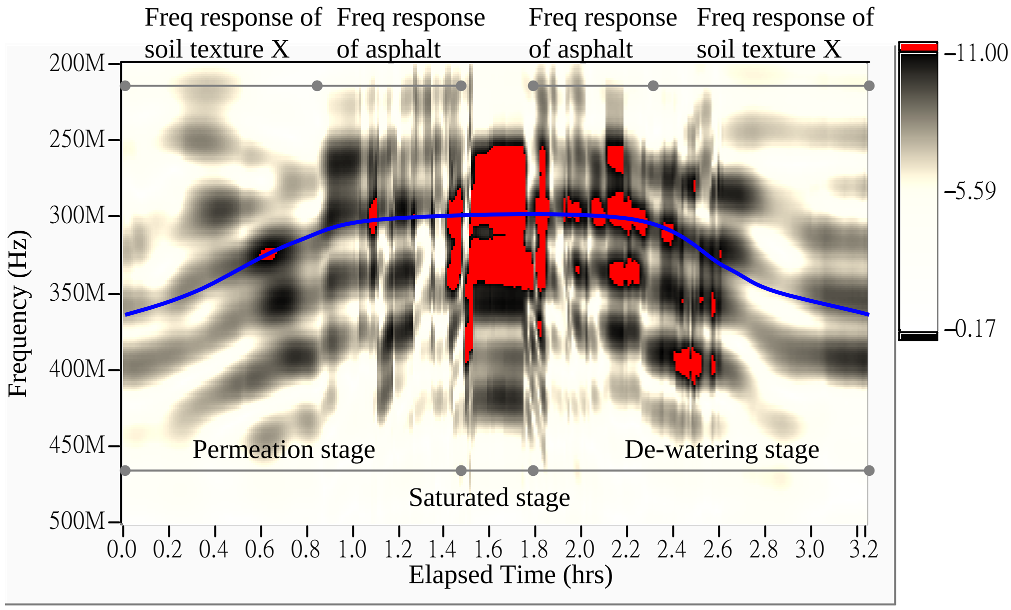

Spectragram obtained in Experiment #3 using 400MHz antenna and processed with a 250M to 450MHz band-pass filter

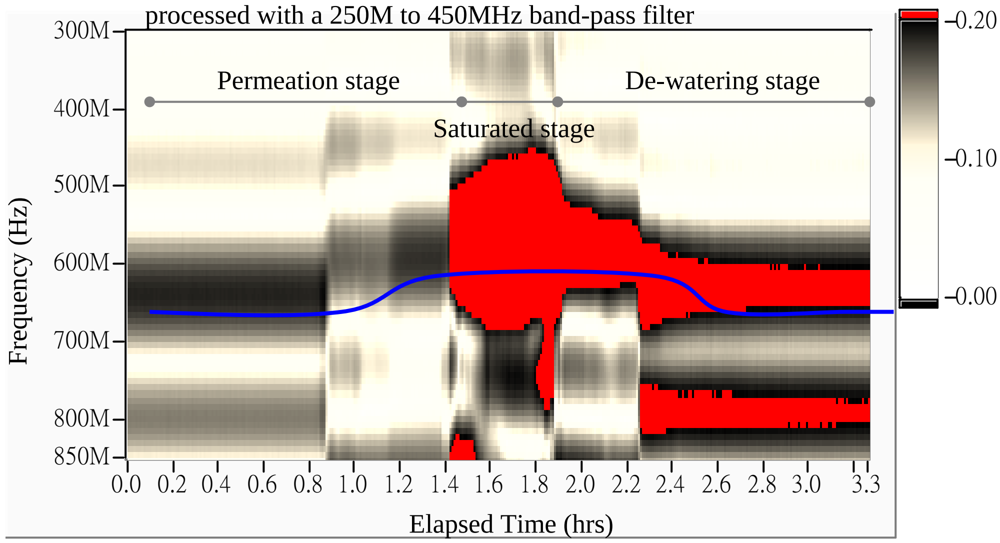

Spectragram obtained in Experiment #3 using 1GHz antenna and processed with a 300M to 750MHz band-pass filter

APPENDIX H3 FREQUENCY SPECTRAGRAMS OF SOIL SPECIMENS

General remarks:

1. The blue lines indicate the peak-frequency drift.
2. The vertical blue line in each spectragram indicates an instant in the elapsed time separating the initial static stage & stage to saturate bottom gravel layer, as well as the permeation stage to soil specimens.

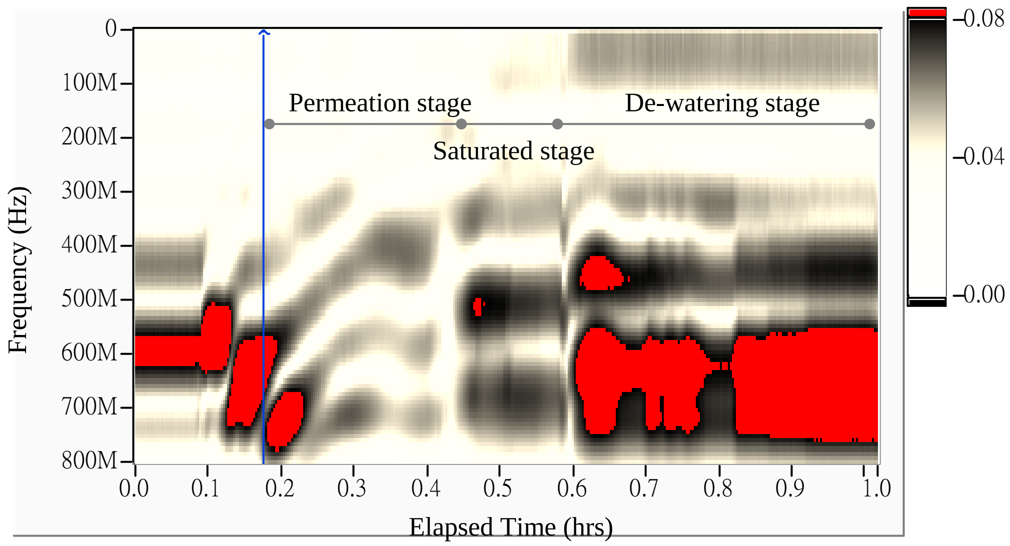

Spectragram obtained in Soil Specimen A using 1GHz antenna and processed with a 750MHz low-pass filter

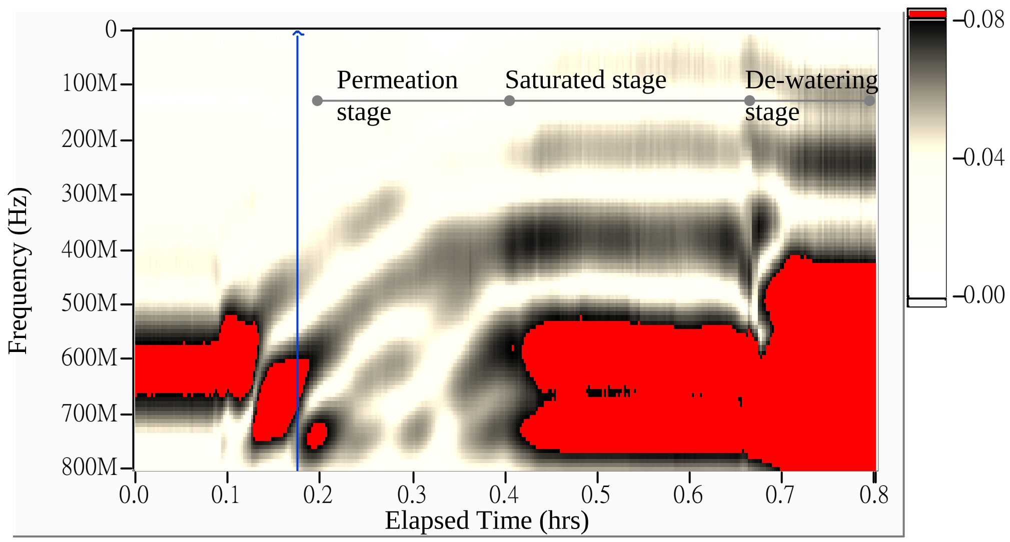

Spectragram obtained in Soil Specimen B using 1GHz antenna and processed with a 750MHz low-pass filter

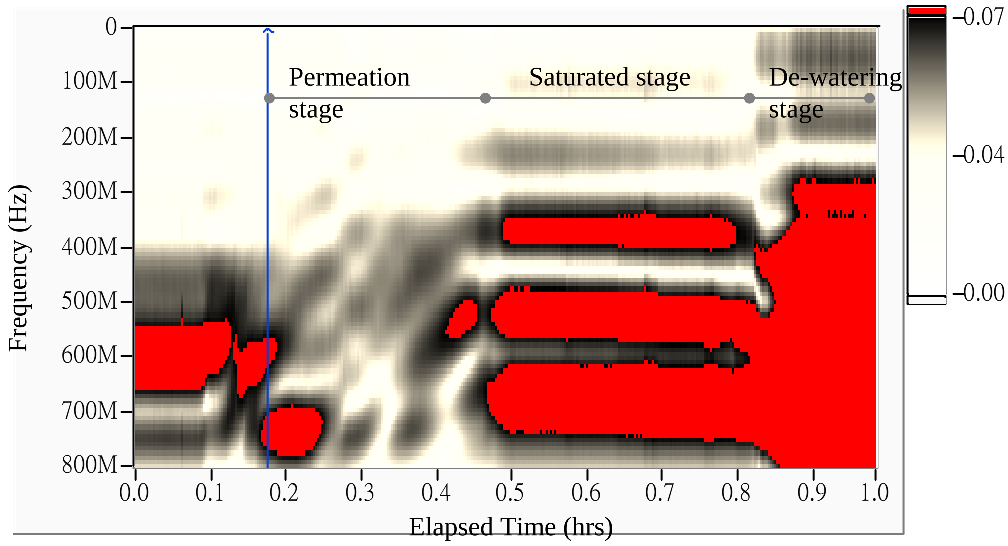

Spectragram obtained in Soil Specimen C using 1GHz antenna and processed with a 750MHz low-pass filter

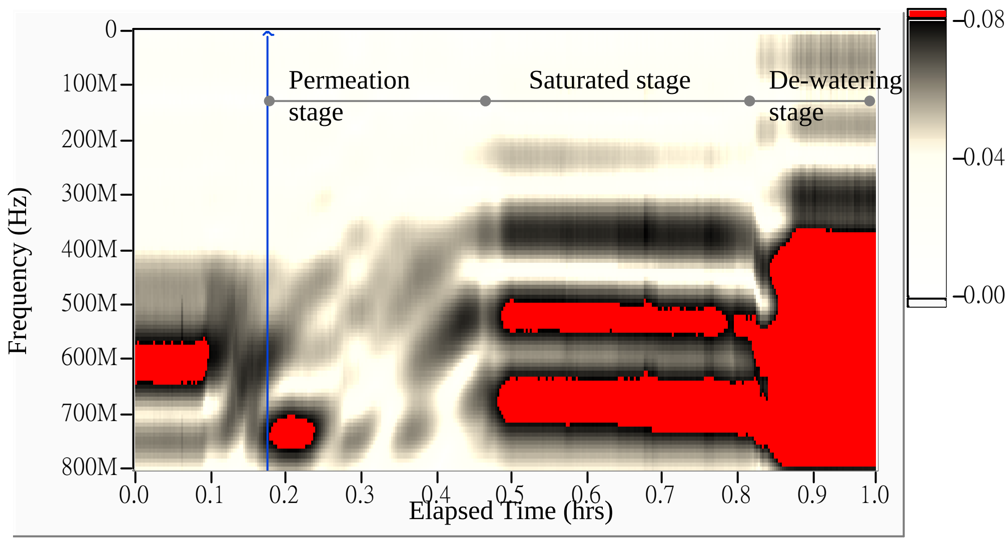

Spectragram obtained in Soil Specimen D using 1GHz antenna and processed with a 750MHz low-pass filter

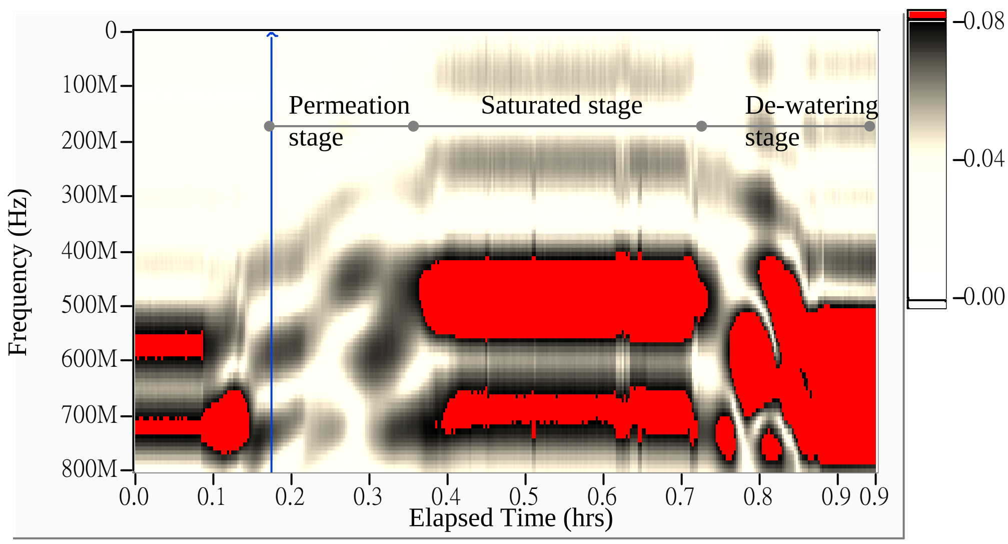

Spectragram obtained in Soil Specimen E using 1GHz antenna and processed with a 750MHz low-pass filter

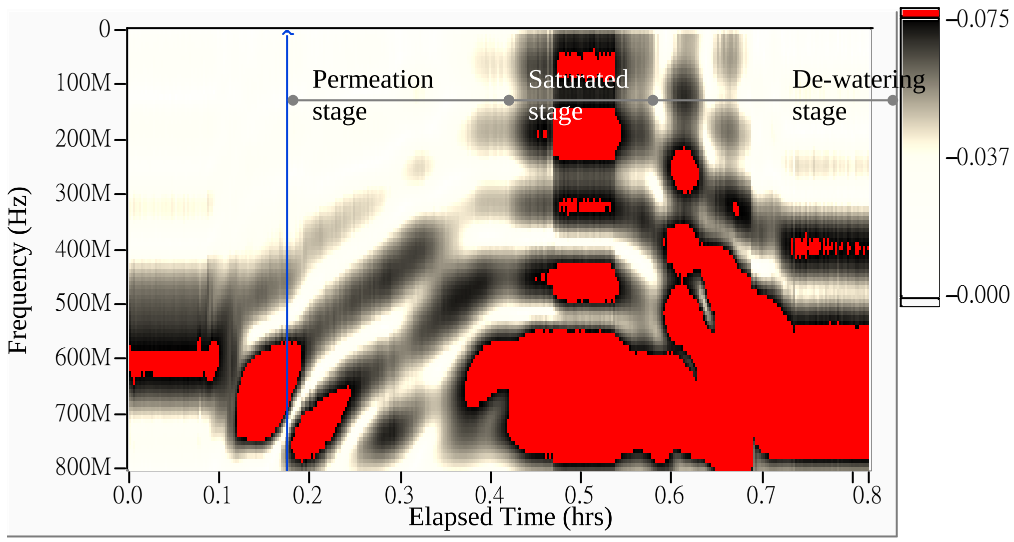

Spectragram obtained in Soil Specimen F using 1GHz antenna and processed with a 750MHz low-pass filter

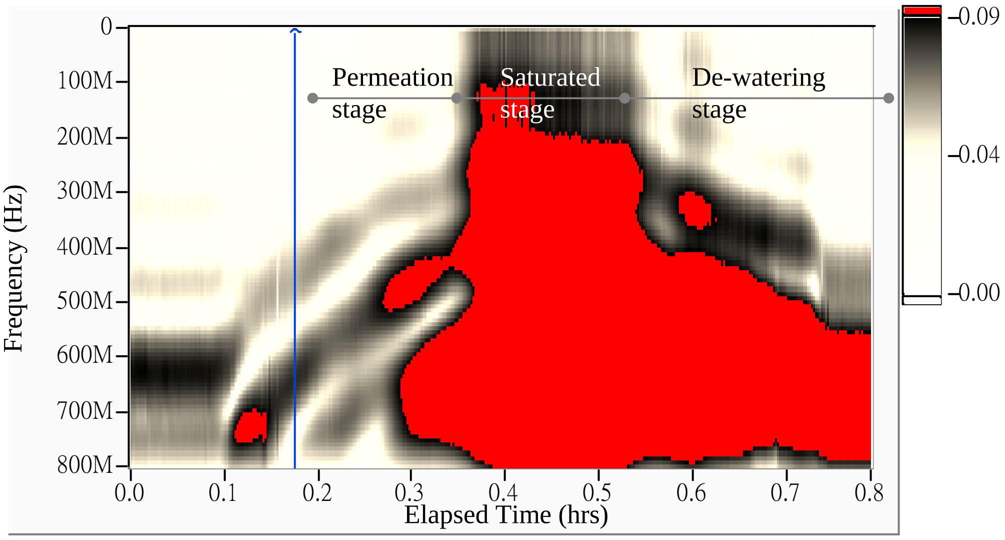

Spectragram obtained in Soil Specimen G using 1GHz antenna and processed with a 750MHz low-pass filter

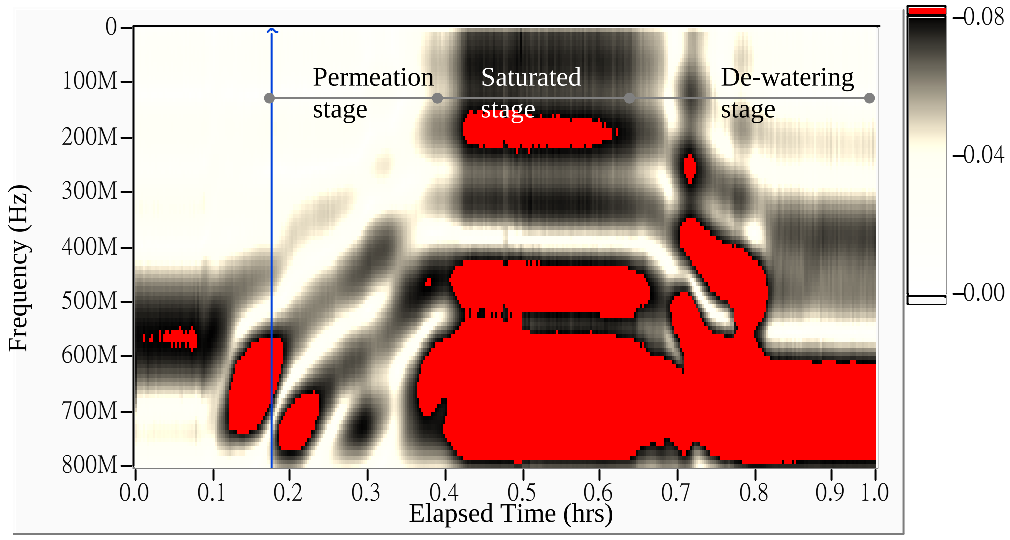

Spectragram obtained in Soil Specimen H using 1GHz antenna and processed with a 750MHz low-pass filter

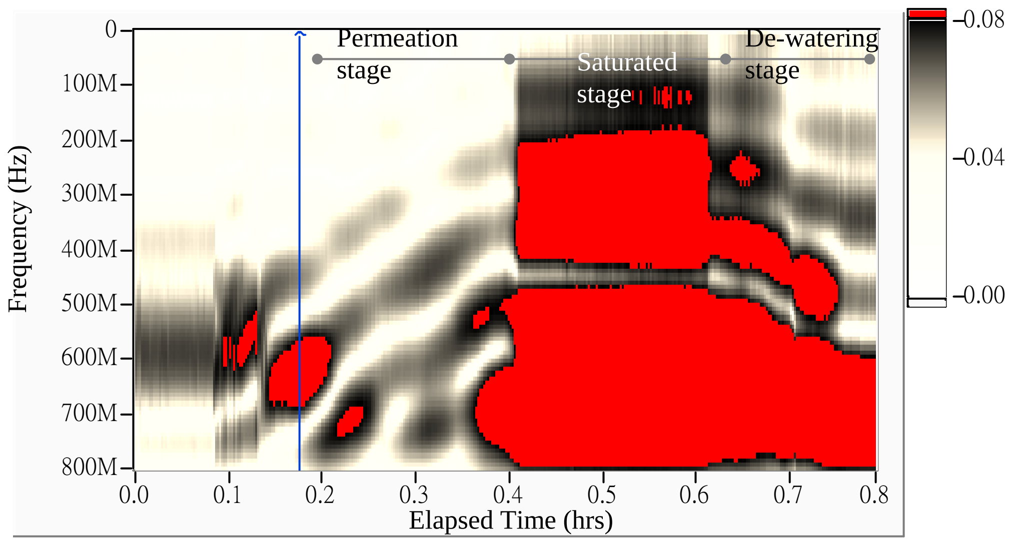

Spectragram obtained in Soil Specimen I using 1GHz antenna and processed with a 750MHz low-pass filter

APPENDIX I RADARGRAMS OF SOIL SPECIMENS

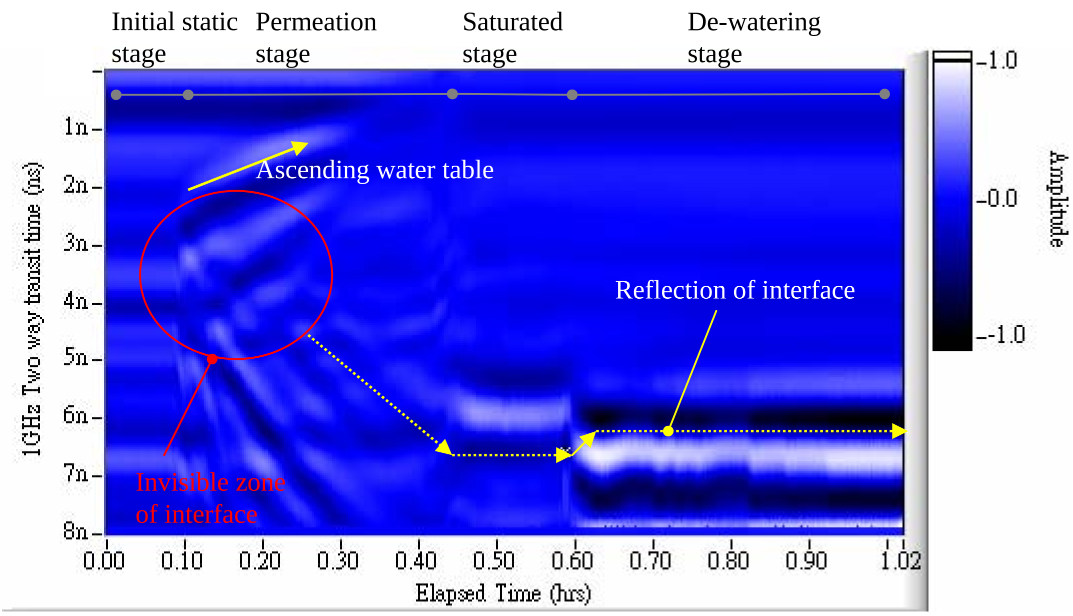

1GHz Radargram of Soil Texture A

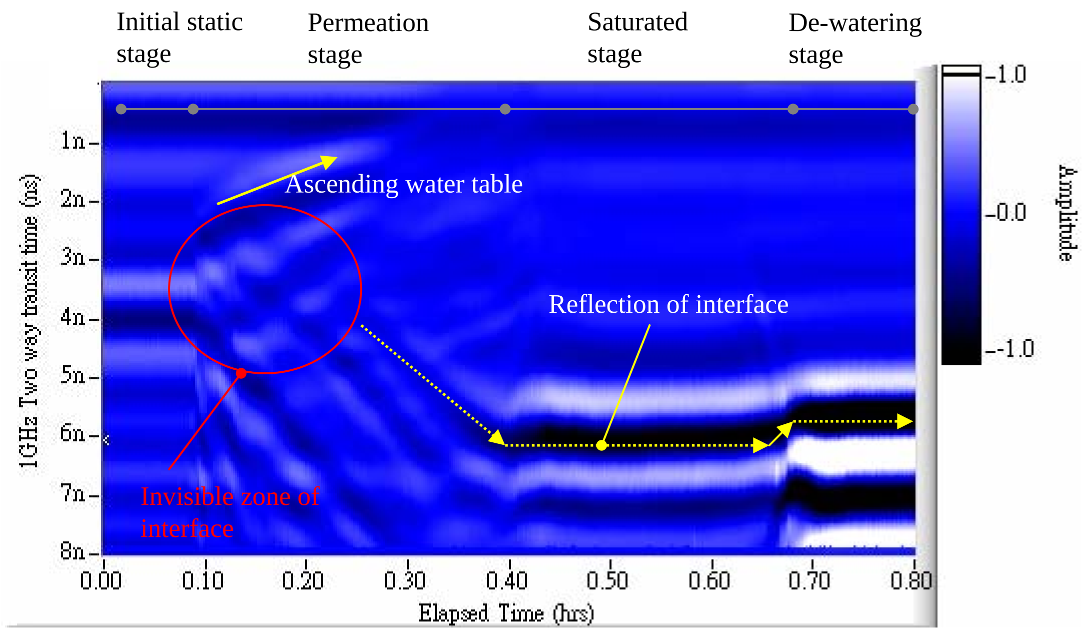

1GHz Radargram of Soil Texture B

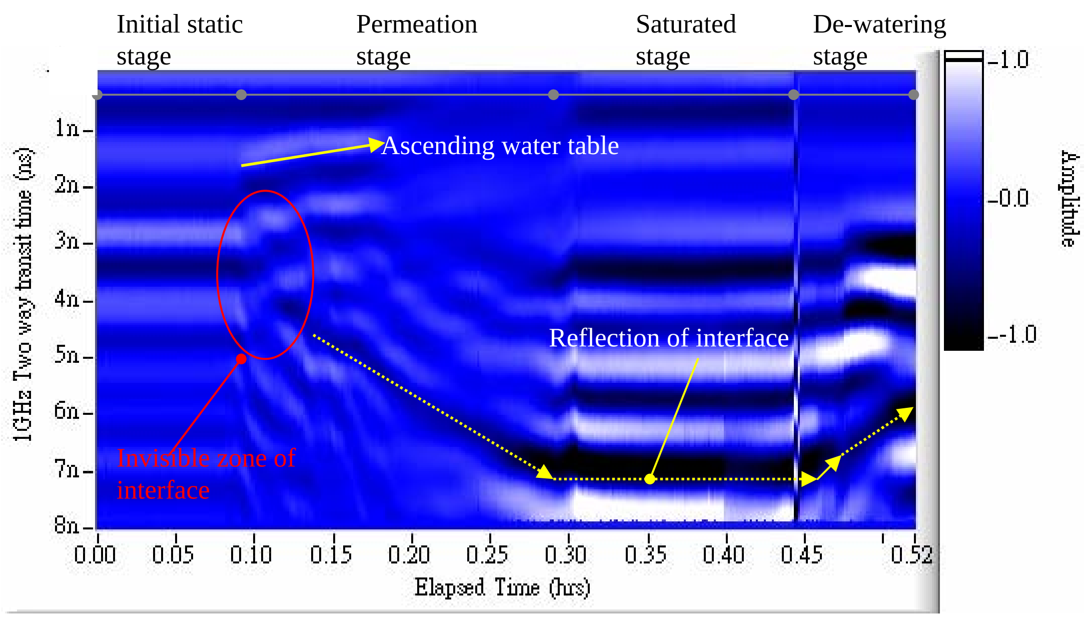

1GHz Radargram of Soil Texture C

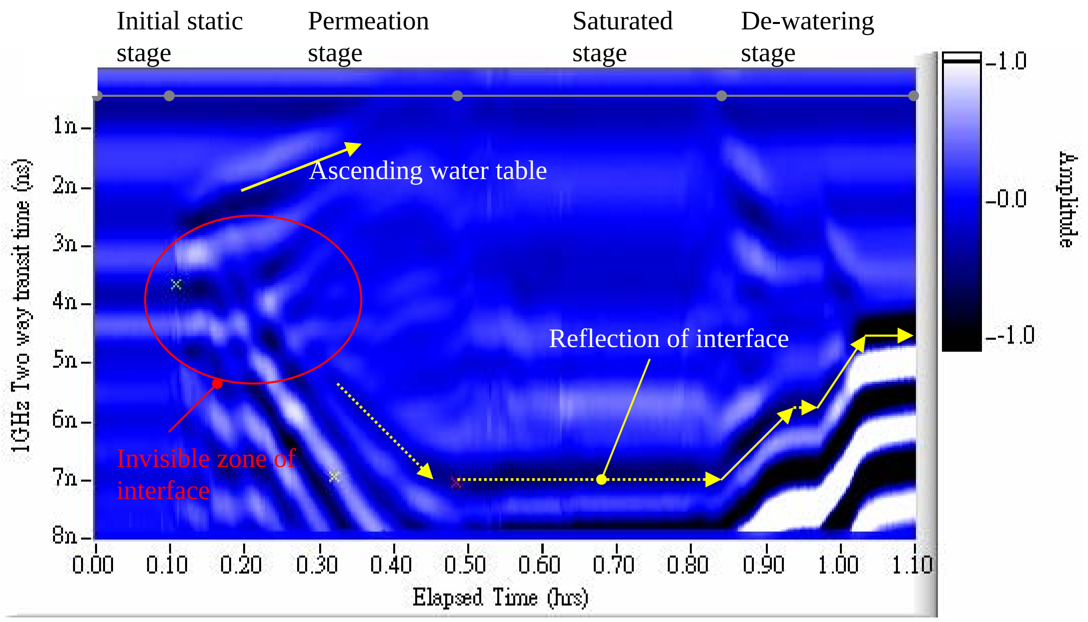

1GHz Radargram of Soil Texture D

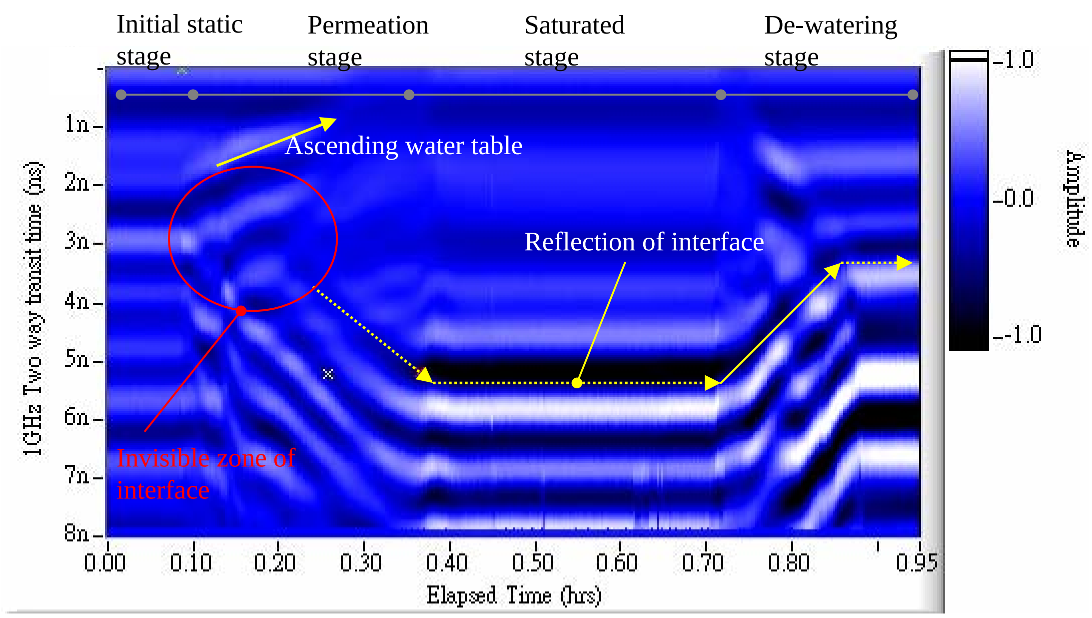

1GHz Radargram of Soil Texture E

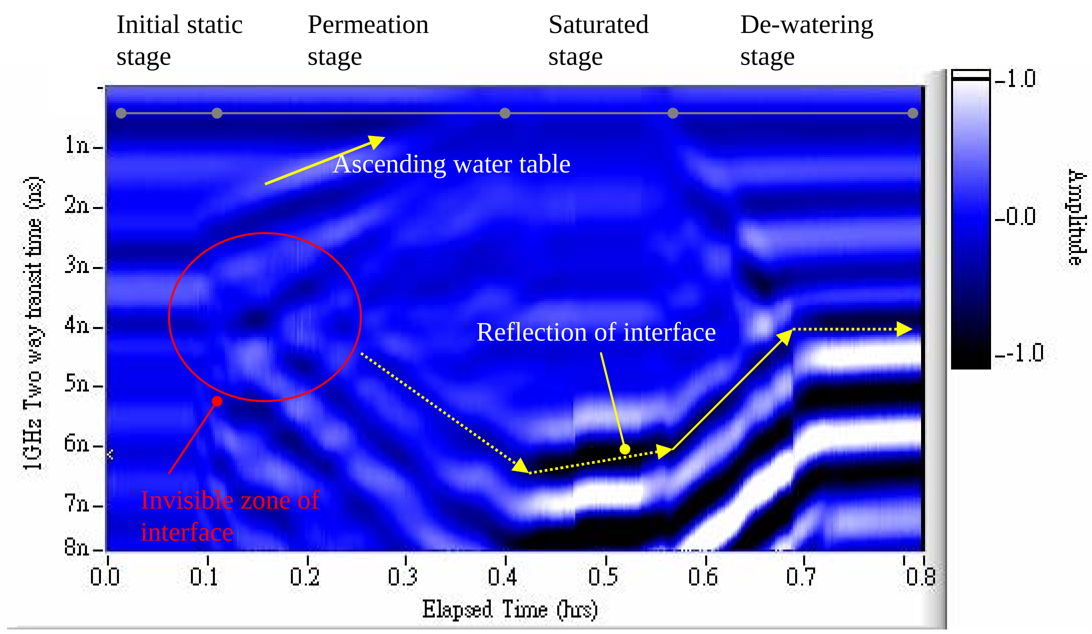

1GHz Radargram of Soil Texture F

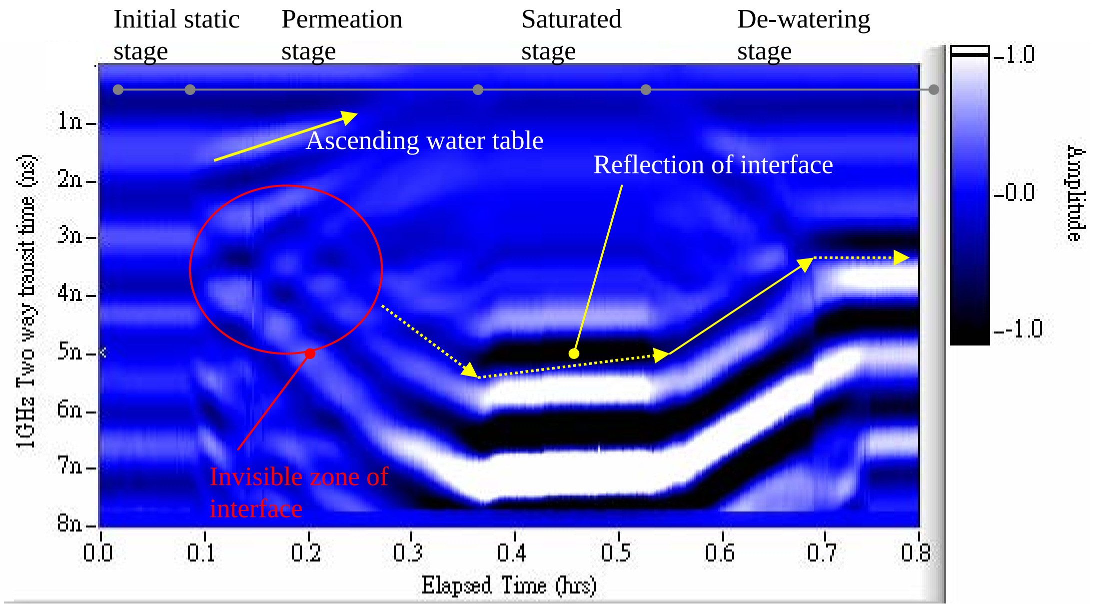

1GHz Radargram of Soil Texture G

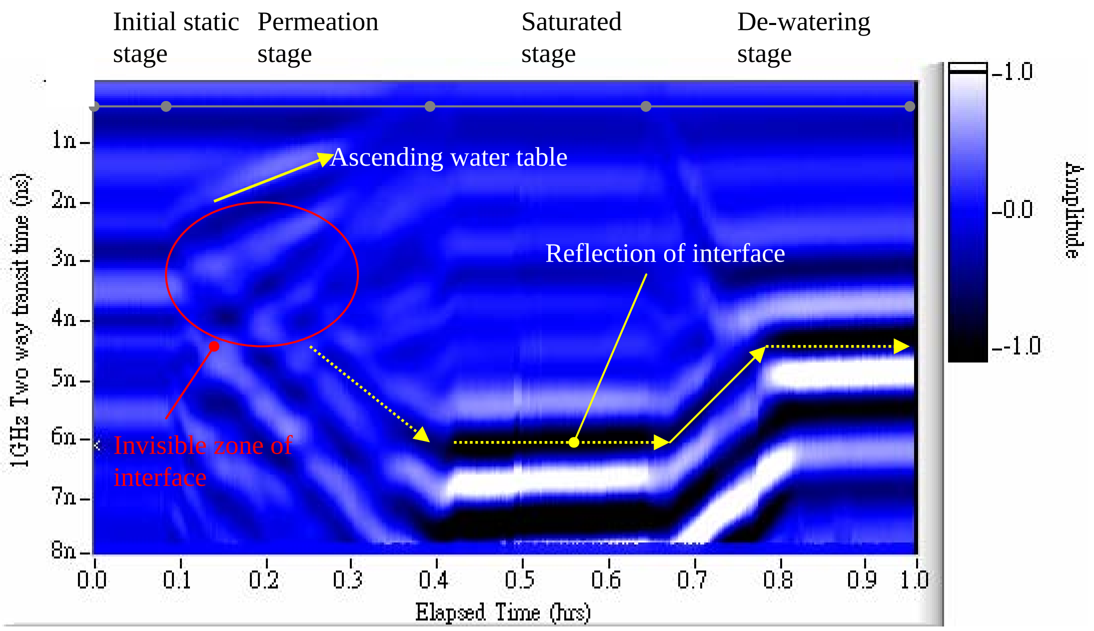

1GHz Radargram of Soil Texture H

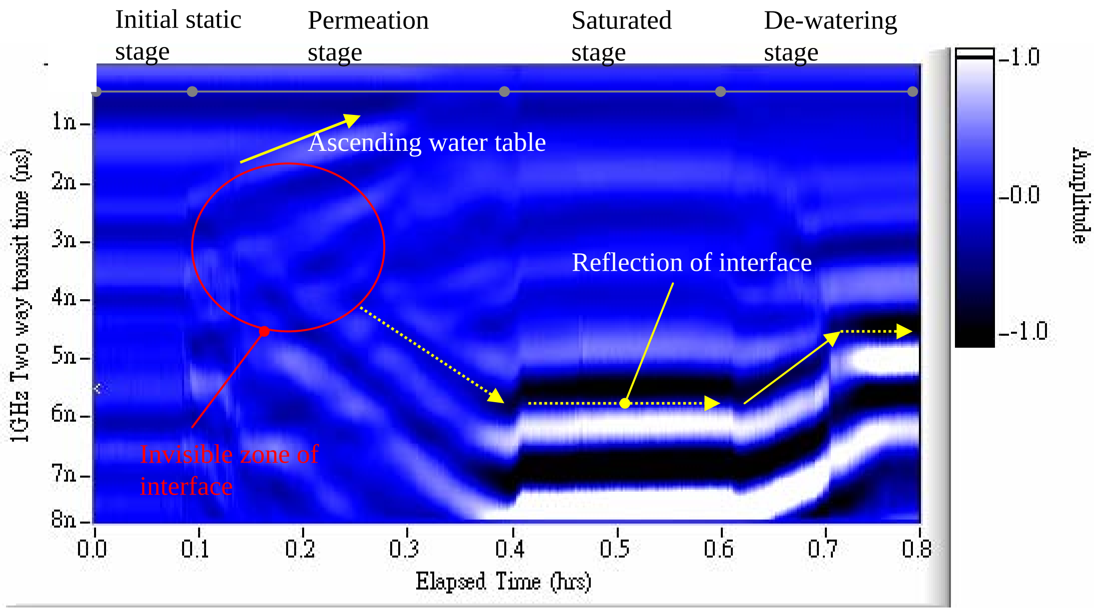

1GHz Radargram of Soil Texture I

APPENDIX J PHOTO COLLECTION

Experiment on Concrete (Chapter 6)

Overview of the Experiments on Concrete Specimen

The Cored Sample from Concrete Specimens for Mercury Intrusion Porosimetry (MIP) Test

Slump test of fresh-made Concrete

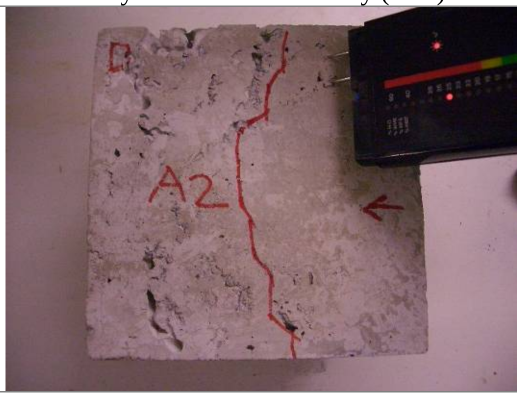

Determination of the Wetting Front after Test Runs using a Protimeter

Experiments on Asphalt Pavement (Chapter 7)

Overview of the Experiments on Asphalt Pavement

Overview of the Experiments on Asphalt Pavement

The Constant Head Water Tank

Asphalt Cores Extracted from the Asphalt Pavement

Experiments on Soil (Chapter 8)

Overview of the Experiments on Soil Specimens

Overview of the Experiments on Soil Specimens

Sieved Soil Specimens

Specific Gravity Test on Soil Specimens

APPENDIX K1 FLOW OF UNCERTAINTY ANALYSIS (FOLLOWING ISO GUIDE 17025)

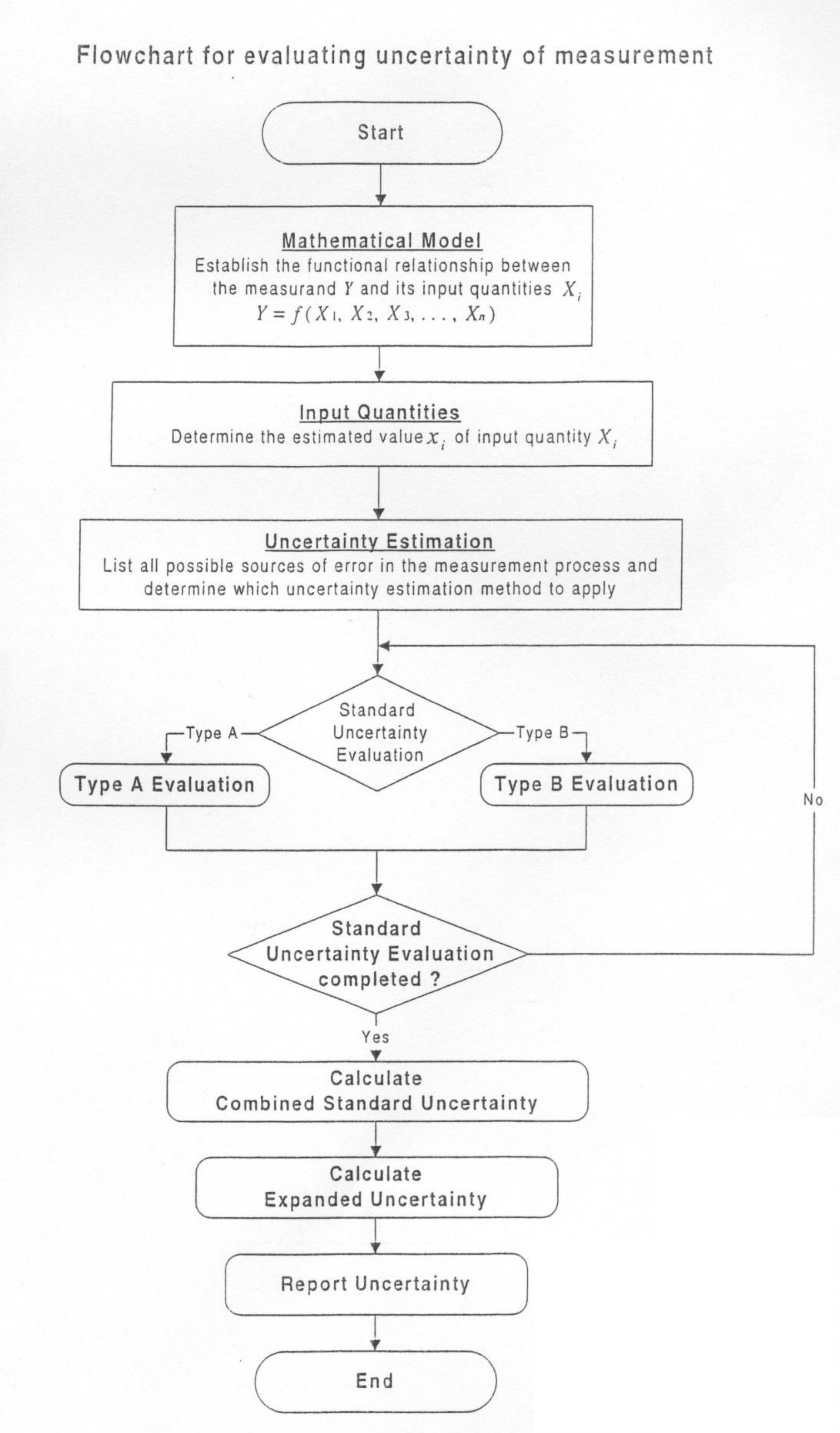

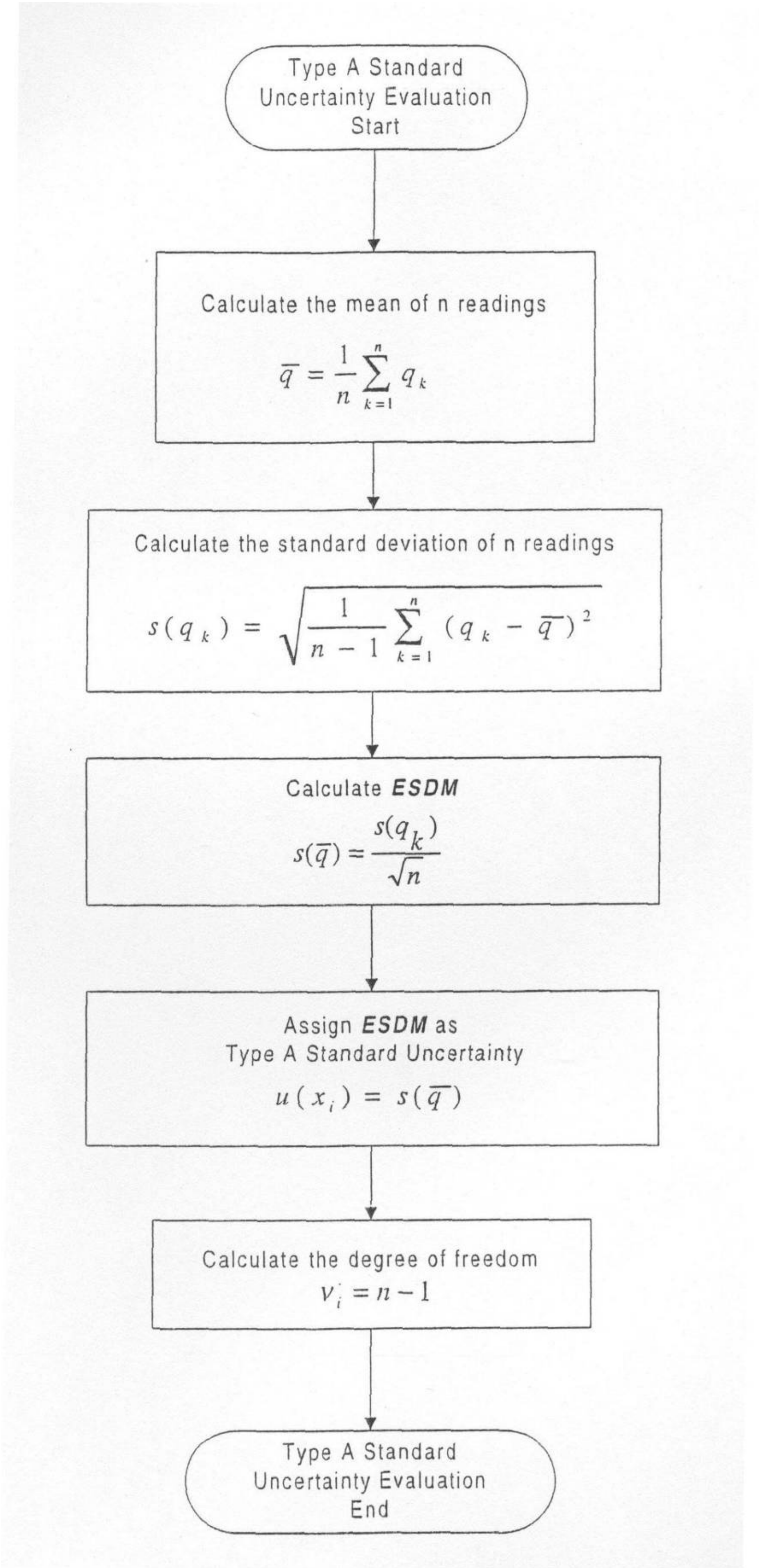
Type A Standard
Uncertainty Evaluation
Start
Calculate the mean of n readings
$\overline{q} = \frac{1}{n}\sum_{k=1}^{n} q_k$
Calculate the standard deviation of n readings
$s(q_k) = \sqrt{\frac{1}{n-1}\sum_{k=1}^{n}(q_k - \overline{q})^2}$
Calculate **ESDM**
$s(\overline{q}) = \frac{s(q_k)}{\sqrt{n}}$
Assign **ESDM** as
Type A Standard Uncertainty
$u(x_i) = s(\overline{q})$
Calculate the degree of freedom
$\nu_i = n - 1$
Type A Standard
Uncertainty Evaluation
End

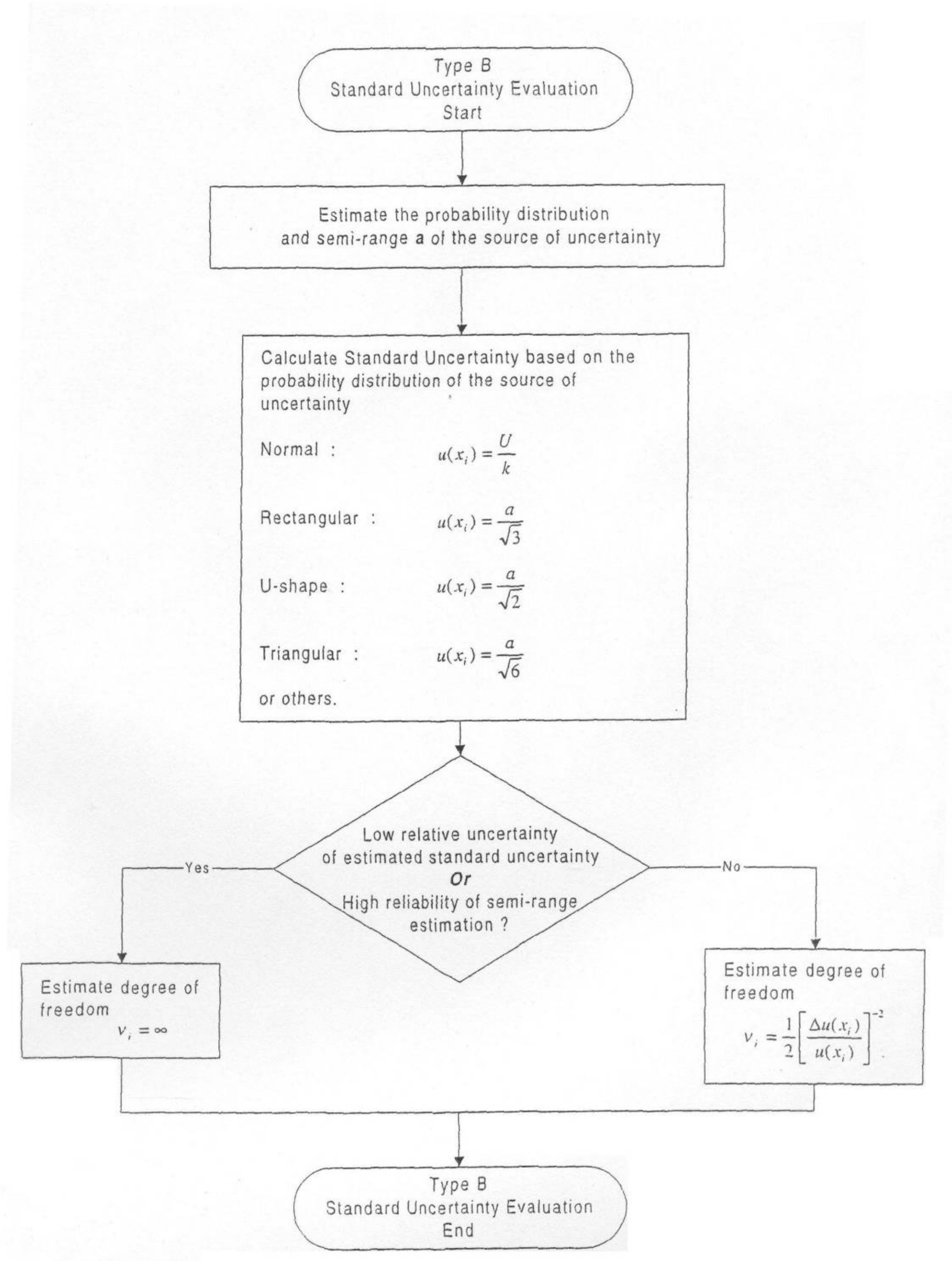
Type B
Standard Uncertainty Evaluation
Start
Estimate the probability distribution
and semi-range a of the source of uncertainty
Calculate Standard Uncertainty based on the probability distribution of the source of uncertainty
Normal : $u(x_i) = \frac{U}{k}$
Rectangular : $u(x_i) = \frac{a}{\sqrt{3}}$
U-shape : $u(x_i) = \frac{a}{\sqrt{2}}$
Triangular : $u(x_i) = \frac{a}{\sqrt{6}}$
or others.
Low relative uncertainty
of estimated standard uncertainty
Or
High reliability of semi-range
estimation ?
Yes
No
Estimate degree of freedom
$\nu_i = \infty$
Estimate degree of freedom
$\nu_i = \frac{1}{2}\left[\frac{\Delta u(x_i)}{u(x_i)}\right]^{-2}$
Type B
Standard Uncertainty Evaluation
End

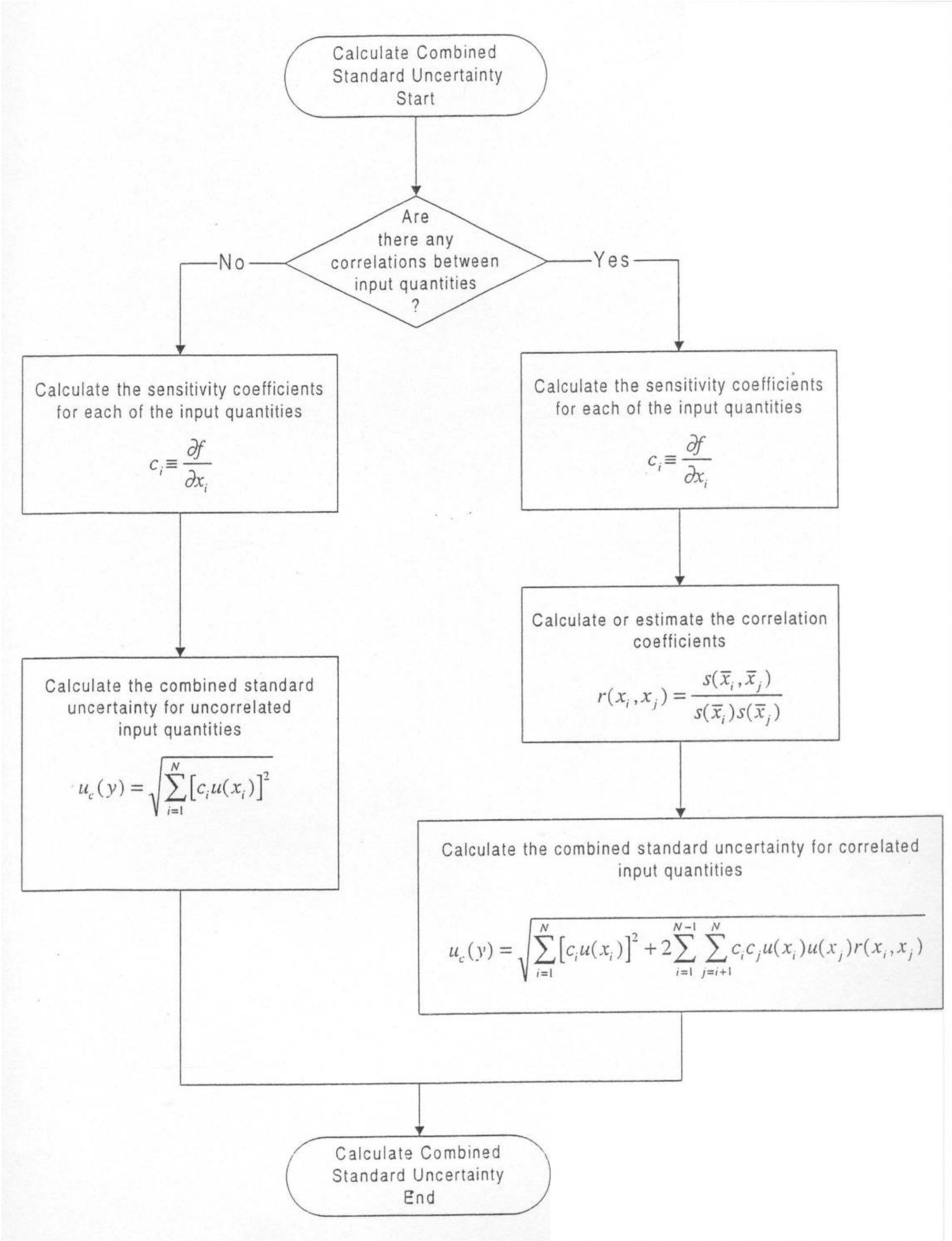
Calculate Combined
Standard Uncertainty
Start
Are
there any
correlations between
input quantities
?
No
Yes
Calculate the sensitivity coefficients
for each of the input quantities
$c_i \equiv \frac{\partial f}{\partial x_i}$
Calculate the sensitivity coefficients
for each of the input quantities
$c_i \equiv \frac{\partial f}{\partial x_i}$
Calculate or estimate the correlation
coefficients
$r(x_i, x_j) = \frac{s(\bar{x}_i, \bar{x}_j)}{s(\bar{x}_i)s(\bar{x}_j)}$
Calculate the combined standard
uncertainty for uncorrelated
input quantities
$u_c(y) = \sqrt{\sum_{i=1}^{N} [c_i u(x_i)]^2}$
Calculate the combined standard uncertainty for correlated
input quantities
$u_c(y) = \sqrt{\sum_{i=1}^{N} [c_i u(x_i)]^2 + 2\sum_{i=1}^{N-1} \sum_{j=i+1}^{N} c_i c_j u(x_i) u(x_j) r(x_i, x_j)}$
Calculate Combined
Standard Uncertainty
End

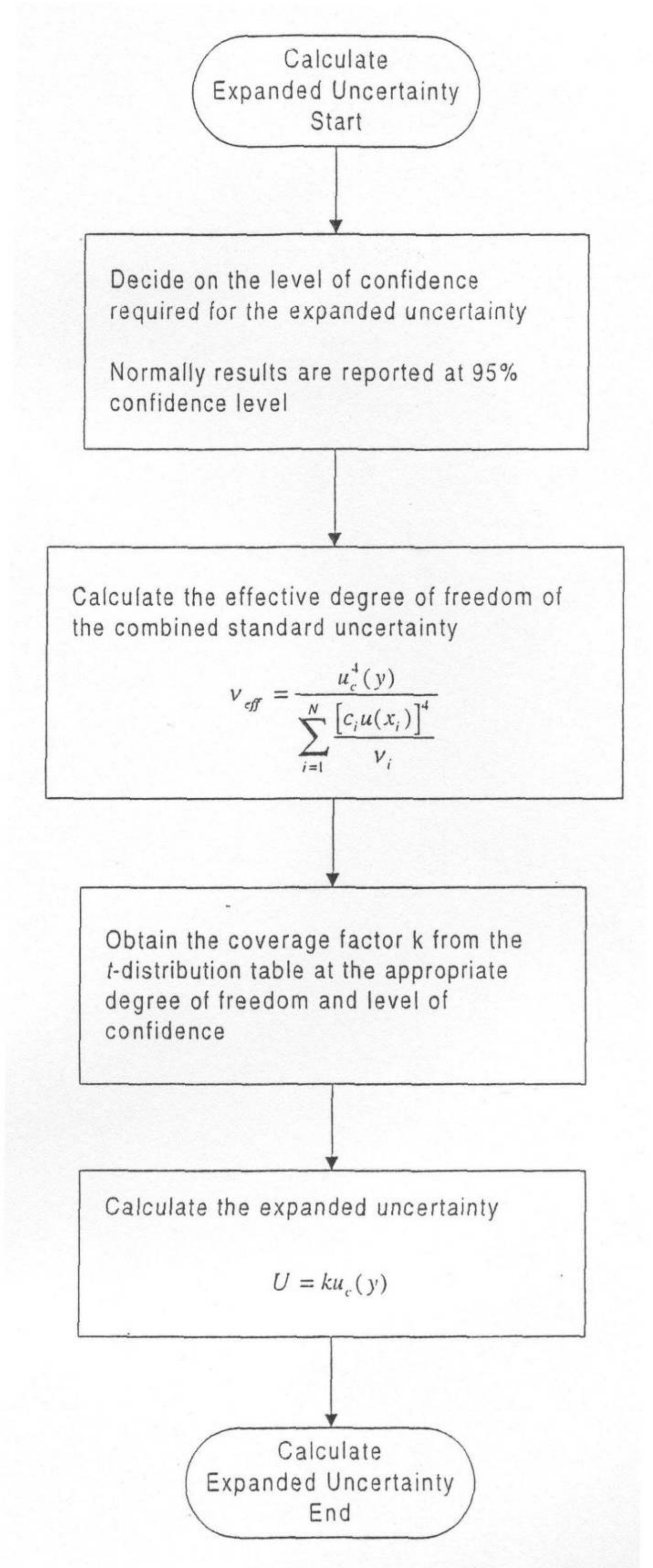
Calculate Expanded Uncertainty Start
Decide on the level of confidence required for the expanded uncertainty
Normally results are reported at 95% confidence level
Calculate the effective degree of freedom of the combined standard uncertainty
$$\nu_{eff} = \frac{u_c^4(y)}{\sum_{i=1}^{N} \frac{\left[c_i u(x_i)\right]^4}{\nu_i}}$$
Obtain the coverage factor k from the t-distribution table at the appropriate degree of freedom and level of confidence
Calculate the expanded uncertainty
$$U = k u_c(y)$$
Calculate Expanded Uncertainty End

APPENDIX K2A UNCERTAINTY ANALYSIS OF REAL PERMITTIVITY USING 1GHZ JRC RADAR SYSTEM

(A) Mathematical model in ε’ determination

$$\varepsilon' = (\frac{cT}{2D})^2 \;=>\; \varepsilon' = (\frac{c \times \dfrac{P}{F \times 125 \times 10^3}}{2D})^2 \text{ ....Eq. (1)}$$

where
c is the speed of light which is a constant,
D is the thickness measured by measuring tape,
T is Two-way Transit Time (TTT),
P is the number of sample point in the time axis,
F is the re-scaling time factor. Since the original time base acquired from the output interface of JRC radar is in the order of milli-second but not in the original nano-second, a ‘re-scaling factor’ for the waveforms was established to obtain an accurate two-way-transit-time (TTT) of reflections in time-domain, and
125k is the sampling rate of the hardware interface (i.e. National Instrument 6013 board)

(B) Sensitivity Coefficients

- by derivative of material thickness measured by measuring tape according to Eq. [1],

$$c_d = \frac{\partial \varepsilon'}{\partial D} = (\frac{cP}{2F \times 125 \times 10^3})^2 \frac{\partial}{\partial D}(\frac{1}{D^2}) = -(\frac{c^2 P^2}{2 \times (125 \times 10^3)^2 F^2 D^3}) = \mathbf{-20.86}$$

for D = 0.45m (for example, thickness of asphalt), F = 515697 (dimension-less),
P = 419, dimension-less (number of sample points which is equivalent to 6.5ns traveled in 450mm thick asphalt layer).

- by derivative of the re-scaling factor (F) according to Eq. [1],

$$c_F = \frac{\partial \varepsilon'}{\partial F} = (\frac{cP}{2D \times 125 \times 10^3})^2 \frac{\partial}{\partial F}(\frac{1}{F^2}) = -(\frac{c^2 P^2}{2 \times (125 \times 10^3)^2 D^2 F^3}) = \mathbf{-1.821 \times 10^{-5}}$$

for D = 0.45m (for example, thickness of asphalt), F = 515697 (dimension-less),
P = 419, dimension-less (number of sample points which is equivalent to 6.5ns traveled in 450mm thick asphalt layer).

- by derivative of the sample points (P) according to Eq. [1],

$$c_P = \frac{\partial \varepsilon'}{\partial P} = (\frac{c}{2DF \times 125 \times 10^3})^2 \frac{\partial}{\partial P}(P^2) = \frac{c^2 P}{2D^2 F^2 \times (125 \times 10^3)^2} = \mathbf{0.0224}$$

for D = 0.45m (for example, thickness of asphalt), F = 515697 (dimension-less),
P = 419, dimension-less (number of sample points which is equivalent to 6.5ns traveled in 450mm thick asphalt layer).

(C1) Standard uncertainty for the depth measurement by measuring tape:

1. ***Calibration uncertainty***,

$$\mu_{cal-tape} = \frac{a_{cal-tap}}{k_{cal-tap}} \text{ ….. [Type B]}$$

where $a_{cal\text{-}tap}$ is the uncertainty obtained from the calibration certificate,
$k_{cal\text{-}tap}$ is the coverage factor used in the calibration certificate, which is 1.96.

2. Standard uncertainty of the ***resolution***,

$$\mu_{res-tape} = \frac{a_{res-tap}}{\sqrt{3}} \text{ ….. [Type B]}$$

where $a_{res\text{-}tap}$ is the resolution of the semi-range of the measuring tape.
(Remark: $\sqrt{3}$ is adopted as the probability distribution for general application.)

3. Standard uncertainty of the ***randomness***,

$$\mu_{ran-tape} = \frac{M_{SD-tape}}{\sqrt{n}} \text{ ….. [Type A]}$$

where $M_{SD\text{-}tape}$ is the standard deviation of repeated measurements and n is the number of repeated measurements.

4. Standard uncertainty in ***thermal expansion***,

$$\mu_{thermal-tape} = \frac{0.5x10^{-4}}{\sqrt{3}} \text{ ….. [Type B]}$$

Note: the interval for thermal expansion coefficient of measuring tape = +/-$0.5x10^{-4}/^{o}C$.
This uncertainty is negligible since the value is too small.

(C2) Standard uncertainty for the measurement of re-scaling factor:

1. ***Calibration uncertainty*** of the re-scaling factor,

$$\mu_{cal-F} = \frac{a_{cal-F}}{k_{cal-F}} \text{ ….. [Type B]}$$

where $a_{cal\text{-}F}$ is the uncertainty obtained from the calibration certificate,
$k_{cal\text{-}F}$ is the coverage factor used in the calibration certificate, which is 1.96.

2. Experimental uncertainty of ***randomness***,

$$\mu_{ran-F} = \frac{M_{SD-F}}{\sqrt{n}} \text{ ..... [Type A]}$$

where M_{SD-F} is the standard deviation of repeated measurements and n is the number of repeated measurements.

(C3) Standard uncertainty for the measurement of sampling points:

1. ***Calibration uncertainty*** of the sampling points,

$$\mu_{cal-P} = \frac{a_{cal-P}}{k_{cal-P}} \text{ ..... [Type B]}$$

where a_{cal-P} is the uncertainty obtained from the calibration certificate,
k_{cal-P} is the coverage factor used in the calibration certificate, which is 1.96.

2. Experimental uncertainty of ***randomness***,

$$\mu_{ran-P} = \frac{M_{SD-P}}{\sqrt{n}} \text{ ..... [Type A]}$$

where M_{SD-P} is the standard deviation of repeated measurements and n is the number of repeated measurements.

(D1) Combined standard uncertainty of the measuring tape from C1:

$$\sum \mu_d^2 = \mu_{cal-tape}^2 + \mu_{ran-tape}^2 + \mu_{res-tape}^2$$

(D2) Combined standard uncertainty of the measurement of re-scaling factor from C2:

$$\sum \mu_F^2 = \mu_{cal-F}^2 + \mu_{ran-F}^2$$

(D3) Combined standard uncertainty of the measurement of sample points from C3:

$$\sum \mu_P^2 = \mu_{cal-P}^2 + \mu_{ran-P}^2$$

(E) Combined uncertainty U_c,

$$U_c = \sqrt{(c_d \sum \mu_d)^2 + (c_F \sum \mu_F)^2 + (c_P \sum \mu_P)^2}$$

(F) Expanded Uncertainty U_e,

$$U_e = kU_c$$

For student's distribution in statistics for 95% confidence, the coverage factor k is 2.

APPENDIX K WORKSHEET OF UNCERTAINTY ANALYSIS OF REAL PERMITTIVITY DETERMINED BY JRC RADAR SYSTEM

Source of Error		Unit	Type	S.D.	S.D.	Semi-range *	Semi-range (point)	rm	a	μ_i	$\Sigma\mu_i^2$	c_i	c_i^2	$c_i^2\Sigma\mu_i^2$
Material thickness 'D'	Calibration uncertainty of the measuring tape (according to Cal. Cert)	m	B	-	-	0.002	-	-	1.96	1.02E-03				
	Resolution of the measuring tape (according to Cal. Cert)	m	B	-	-	0.0005	-	-	1.73205	2.89E-04				
	Repeatability of measuring tape readings	m	A	7.47E-05	-	-	-	10	3.16228	2.36E-05	1.13E-06	-20.8642	435.3148	0.0005
1GHz Radar re-scale factor 'F'	Calibration uncertainty	-	B	-	-	-	1440	-	1.96	7.35E+02				
	Randomness of TTT readings	-	A	-	903.5	-	-	10	3.16228	2.86E+02	6.21E+05	-1.82E-05	3.32E-10	0.0002
1GHz Radar sample point 'P'	Calibration uncertainty	-	B	-	-	-	0.5	-	1.96	2.55E-01				
	Randomness of sample point readings	-	A	-	0.64	-	-	60	7.74597	8.32E-02	7.20E-02	0.0224	5.02E-04	3.6128E-05

Input Constants

F=	515697	re-scaling factor
P=	386.77	no. of sample points in the waveform to travel in the material layers, = TTT x re-scaling factor x sampling rate (125x10³)
c=	3.00E+08	speed of light
T=	6.00E-09	TTT = P/(F x sampling rate (125x10³))
D=	0.2	thickness of specimen

c_d =	-202.5000
c_F =	-1.82E-05
c_P =	0.0224

Summation	
$U_c = \sqrt{\sum (c_i u_i)^2}$	0.0271
k	2
U_e=kU_c	**0.0541**
U_e (after round up)	**0.05**

Note :

a	=	distribution	Uc	=	combined uncertainty
rm	=	no. of repetitive measurement	Ue	=	expanded uncertainty
μ_i	=	standard uncertainty	k	=	coverage factor
$\Sigma\mu_i$	=	combined standard uncertainty	Type	=	A (statistical) or B (probability/semi-range)
ci	=	sensitivity coefficient	TS	=	time window's resolution
			S.D.	=	standard deviation

Remark : Uncertainties are calculated at 95 % confidence level.

APPENDIX K3A UNCERTAINTY ANALYSIS OF REAL PERMITTIVITY USING 400MHZ AND 1.5GHZ GSSI RADAR SYSTEMS

(A) Mathematical model in ε' determination

$$\varepsilon' = (\frac{cT}{2D})^2 \text{ ....Eq. (1)}$$

where
c is the speed of light which is a constant,
D is the thickness measured by measuring tape and
T is Two-way Transit Time (TTT)

(B) Sensitivity Coefficient

- by derivative of material thickness measured by measuring tape according to Eq. [1]

$c_d = \frac{\partial \varepsilon'}{\partial D} = (\frac{cT}{2})^2 \frac{\partial}{\partial D}(\frac{1}{D^2}) = -(\frac{c^2T^2}{2D^3}) =$ **-20.86** for D = 0.45m (thickness of asphalt)

- by derivative of the Two-way Transit Time (TTT) measured by the radar system according to Eq. [1]

$c_T = \frac{\partial \varepsilon'}{\partial T} = (\frac{c}{D})^2 \frac{\partial}{\partial T}(T^2) = 2T(\frac{c}{D})^2 =$ **5.78×10^9** for T = 6.5ns (traveling time in asphalt)

(C1) Standard uncertainty for the depth measurement by measuring tape:

1. ***Calibration uncertainty***,

$$\mu_{cal-tape} = \frac{a_{cal-tap}}{k_{cal-tap}} \text{ ..... [Type B]}$$

where $a_{cal-tap}$ is the uncertainty obtained from the calibration certificate,
$k_{cal-tap}$ is the coverage factor used in the calibration certificate, which is 1.96.

2. Standard uncertainty of the ***resolution***,

$$\mu_{res-tape} = \frac{a_{res-tap}}{\sqrt{3}} \text{ ..... [Type B]}$$

where $a_{res-tap}$ is the resolution of the semi-range of the measuring tape.
(Remark: $\sqrt{3}$ is adopted as the probability distribution for general application.)

3. Standard uncertainty of the ***randomness***,

$$\mu_{ran-tape} = \frac{M_{SD-tape}}{\sqrt{n}} \text{ ….. [Type A]}$$

where $M_{SD\text{-}tape}$ is the standard deviation of repeated measurements and n is the number of repeated measurements.

4. Standard uncertainty in ***thermal expansion***,

$$\mu_{thermal-tape} = \frac{0.5x10^{-4}}{\sqrt{3}} \text{ ….. [Type B]}$$

Note: the interval for thermal expansion coefficient of measuring tape = +/-0.5x10^{-4}/^{o}C. This uncertainty is negligible since the value is far smaller than other uncertainties.

(C2) Standard uncertainty for the measurement of two-way transit time (TTT):

1. ***Calibration uncertainty***

$$\mu_{cal-T} = \frac{a_{cal-T}}{k_{cal-T}} \text{ ….. [Type B]}$$

where $a_{cal\text{-}T}$ is the uncertainty obtained from the calibration certificate,
$k_{cal\text{-}T}$ is the coverage factor used in the calibration certificate, which is 1.96.

2. Experimental uncertainty of ***resolution***,

$$\mu_{res-T} = \frac{TR}{\sqrt{3}} \text{ ….. [Type B]}$$

where TR =	Time window of the waveform
	Number of sample points of the waveform

(Remark: $\sqrt{3}$ is adopted as the probability distribution for general application.)

3. Experimental uncertainty of ***randomness***,

$$\mu_{ran-T} = \frac{M_{SD-T}}{\sqrt{n}} \text{ ….. [Type A]}$$

where $M_{SD\text{-}T}$ is the standard deviation of repeated measurements and n is the number of repeated measurements.

(D1) Combined standard uncertainty of the measuring tape from C1:

$$\sum \mu_d^2 = \mu_{cal-tape}^2 + \mu_{res-tape}^2 + \mu_{ran-tape}^2$$

(D2) Combined standard uncertainty of the measurement of two-way transit time from C2:

$$\sum \mu_T^2 = \mu_{cal-T}^2 + \mu_{res-T}^2 + \mu_{ran-T}^2$$

(E) Combined uncertainty U_c,

$$U_c = \sqrt{(c_d \sum \mu_d)^2 + (c_T \sum \mu_T)^2} \ ,$$

(F) Expanded Uncertainty U_e,

$$U_e = kU_c$$

For student’s distribution in statistics for 95% confidence, the coverage factor k is 2.

APPENDIX K3B: WORKSHEET OF UNCERTAINTY ANALYSIS OF REAL PERMITTIVITY DETERMINED BY GSSI RADAR SYSTEM

Source of Error		Unit	Type	S.D.	S.D.	TS	Time	Semi-range	rm	a	μ_i	$\Sigma \mu_i^2$	c_i	c_i^2	$c_i^2 \Sigma \mu_i^2$
Material thickness 'D'	Calibration uncertainty of the measuring tape (according to Cal. Cert)	m	B	-	-	-		0.002	-	1.96	1.02E-03				
	Resolution of the measuring tape (according to Cal. Cert)	m	B	-	-	-		0.0005	-	1.73205	2.89E-04				
	Repeatability of measuring tape readings	m	A	7.47E-05	-	-		-	10	3.16228	2.36E-05	1.13E-06	-20.8642	435.3147	0.0005
400MHz Radar TTT 'T'	Calibration uncertainty of TTT	s	B	-	-	-	1.00E-10		-	1.96	5.10E-11				
	Resolution of TTT (Time window: 40ns, No. of sample points: 512)	s	B	-	-	7.81E-11		-	-	1.73205	4.51E-11				
	Randomness of TTT readings	s	A	-	4.64E-12	-		-	60	7.74597	5.99E-13	4.64E-21	5.78E+09	3.34E+19	0.1548

$c_d =$ -20.8642

$c_T =$ 5.78E+09

Input Constants

c=	3.00E+08	speed of light
T=	6.50E-09	two-way transit time required to travel in asphalt layers
D=	0.45	thickness of asphalt

Summation	
$U_c = \sqrt{\sum (c_i u_i)^2}$	0.3941
k	2
$U_e = kU_c$	**0.7882**
U_e (after round up)	**0.8**

Note :
- a = distribution
- rm = no. of repetitive measurement
- μ_i = standard uncertainty
- $\Sigma\mu_i^2$ = combined standard uncertainty
- c_i = sensitivity coefficient
- U_c combined uncertainty
- U_e expanded uncertainty
- k coverage factor
- Type A (statistical) or B (probability/semi-range)
- TS time window's resolution
- S.D. standard deviation

Remark : Uncertainties are calculated at 95 % confidence level.

APPENDIX K4A UNCERTAINTY ANALYSIS OF POROSITY ESTIMATION BY COMPLEX REFRACTIVE INDEX MODEL

(A) Mathematical model in ε' determination by Complex Refractive Index Model (CRIM)

$$\sqrt{\varepsilon'} = S_w\phi(\sqrt{\varepsilon_w}') + (1-S_w)\phi(\sqrt{\varepsilon_A}') + (1-\phi)(\sqrt{\varepsilon_S}') \;\ldots\ldots[1]$$

where ε' , ε'_w , ε'_A, ε'_s = real permittivity of the bulk mass, water (81 at 100MHz at room temperature), air (1) and solid matters forming the soil particle matrix respectively, ϕ = porosity and θ_v = volumetric water content

$$\phi = \frac{\sqrt{\varepsilon'} - \sqrt{\varepsilon'_S}}{8S_w - \sqrt{\varepsilon'_S} + 1} \;\ldots\ldots[2]$$

$$\varepsilon' = (\frac{cT}{2D})^2 \;\Rightarrow\; \varepsilon' = (\frac{c \times \dfrac{P}{F \times 125 \times 10^3}}{2D})^2 \;\ldots\ldots[3]$$

where
c is the speed of light which is a constant,
D is the thickness measured by measuring tape,
T is Two-way Transit Time (TTT),
P is the number of sample point in the time axis,
F is the re-scaling time factor. Since the original time base acquired from the output interface of JRC radar is in the order of milli-second but not in the original nano-second, a 're-scaling factor' for the waveforms was established to obtain an accurate two-way-transit-time (TTT) of reflections in time-domain, and
125k is the sampling rate of the hardware interface (i.e. National Instrument 6013 board)

Inserting Eq. [3] into Eq. [2],

$$\phi = \frac{c\dfrac{P}{F \times 125 \times 10^3} - 2D\sqrt{\varepsilon'_S}}{2D(8S_w - \sqrt{\varepsilon'_S} + 1)} \;\ldots\ldots[4]$$

Eq. [4] is the mathematical model of this uncertainty analysis.

(B) Sensitivity Coefficients

- by derivative of ***material thickness*** (D) measured by measuring tape according to Eq. [4],

$$c_d = \frac{\partial \phi}{\partial D} = (\frac{cP}{2F \times 125 \times 10^3 \times (8S_w - \sqrt{\varepsilon'_S} + 1})\frac{\partial}{\partial D}(\frac{1}{D})$$

when S_w = 0, F = 515697, P = 2n x 125k x F = 129, ε_s = 2, D = 0.2m, c = 3 x 10^8 m/s

$$c_d = \frac{\partial \phi}{\partial D} = \left(\frac{3\times10^8\times129}{2\times515697\times125\times10^3\times(1-\sqrt{2})}\right)\left(-\frac{1}{0.2^2}\right) = \mathbf{18.117}$$

when S_w = 1, F = 515697, P = 6n x 125k x F = 387, ε_s = 2, D = 0.2m, c = 3 x 10^8 m/s

$$c_d = \frac{\partial \phi}{\partial D} = \left(\frac{3\times10^8\times387}{2\times515697\times125\times10^3\times(8-\sqrt{2}+1)}\right)\left(-\frac{1}{0.2^2}\right) = -2.968$$

The value obtained when S_w = 1 is rejected because it is smaller than the value obtained when S_w = 0. Therefore **c_d = 18.117**

- by derivative of the ***re-scaling factor*** (F) according to Eq. [4],

$$c_f = \frac{\partial \phi}{\partial F} = \left(\frac{cP}{2D\times125\times10^3\times(8S_w-\sqrt{\varepsilon_S'}+1}\right)\frac{\partial}{\partial D}\left(\frac{1}{F}\right)$$

when S_w = 0, F = 515697, P = 2n x 125k x F = 129, ε_s = 2, D = 0.2m, c = 3 x 10^8 m/s

$$c_f = \frac{\partial \phi}{\partial F} = \left(\frac{3\times10^8\times129}{2\times0.2\times125\times10^3\times(1-\sqrt{2})}\right)\left(-\frac{1}{515697^2}\right) = \mathbf{7.026\ x\ 10^{-6}}$$

when S_w = 1, F = 515697, P = 6n x 125k x F = 387, ε_s = 2, D = 0.2m, c = 3 x 10^8 m/s

$$c_f = \frac{\partial \phi}{\partial F} = \left(\frac{3\times10^8\times387}{2\times0.2\times125\times10^3\times(8-\sqrt{2}+1)}\right)\left(-\frac{1}{515697^2}\right) = -1.151\ x\ 10^{-6}$$

The value obtained when S_w = 1 is rejected because it is smaller than the value obtained when S_w = 0. Therefore **c_f = 7.026 x 10^{-6}**

- by derivative of the ***sample points*** (P) according to Eq. [1],

$$c_p = \frac{\partial \phi}{\partial P} = \frac{c}{2D\times125\times10^3\times F\times(8S_w-\sqrt{\varepsilon_S'}+1)}$$

when S_w = 0, F= 515697, ε_s = 2, D = 0.2m, c = 3 x 10^8 m/s

$$c_p = \frac{\partial \phi}{\partial P} = \frac{3\times10^8}{2\times0.2\times125\times10^3\times515697\times(1-\sqrt{2})} = \mathbf{0.0281}$$

when S_w = 1, F= 515697, ε_s = 2, D = 0.2m, c = 3 x 10^8 m/s

$$c_p = \frac{\partial \phi}{\partial P} = \frac{3\times10^8}{2\times0.2\times125\times10^3\times515697\times(8-\sqrt{2}+1)} = 1.534\ x\ 10^{-3}$$

The value obtained when S_w = 1 is rejected because it is smaller than the value obtained when S_w = 0. Therefore **c_p = 0.0281**

➢ by derivative of the ***degree of water saturation*** (S_w) according to Eq. [1],

Let u = $8S_w - \sqrt{\varepsilon_S^{'}} + 1$, $\frac{\partial u}{\partial S_w} = 8$, $\frac{\partial \phi}{\partial u} = -u^{-2}(\frac{cT - 2D\sqrt{\varepsilon_S^{'}}}{2D})$

$$c_{Sw} = \frac{\partial \phi}{\partial S_w} = \frac{\partial u}{\partial S_w} \times \frac{\partial \phi}{\partial u} = -8u^{-2}(\frac{cT - 2D\sqrt{\varepsilon_S^{'}}}{2D}) = -4(\frac{cT - 2D\sqrt{\varepsilon_S^{'}}}{Du^2})$$

when S_w = 0, T = 2ns, ε_s = 2, D = 0.2m, c = 3 x 10^8 m/s

$$c_{Sw} = \frac{\partial \phi}{\partial S_w} = \frac{-4(3 \times 10^8 \times 2 \times 10^{-9} - 2 \times 0.2\sqrt{2})}{0.2(1 - \sqrt{2})^2} = \mathbf{-4}$$

when S_w = 1, T = 6ns, ε_s = 2, D = 0.2m, c = 3 x 10^8 m/s

$$c_{Sw} = \frac{\partial \phi}{\partial S_w} = \frac{-4(3 \times 10^8 \times 6 \times 10^{-9} - 2 \times 0.2\sqrt{2})}{0.2(8 - \sqrt{2} + 1)^2} = -0.429$$

The value obtained when S_w = 1 is rejected because it is smaller than the value obtained when S_w = 0. Therefore **c_{Sw} = 0.4**

(C1) Standard uncertainty for the depth measurement by measuring tape:

1. ***Calibration uncertainty***,

$$\mu_{cal-tape} = \frac{a_{cal-tap}}{k_{cal-tap}} \text{ ….. [Type B]}$$

where $a_{cal-tap}$ is the uncertainty obtained from the calibration certificate,
$k_{cal-tap}$ is the coverage factor used in the calibration certificate, which is 1.96.

2. Standard uncertainty of the ***resolution***,

$$\mu_{res-tape} = \frac{a_{res-tap}}{\sqrt{3}} \text{ ….. [Type B]}$$

where $a_{res-tap}$ is the resolution of the semi-range of the measuring tape.
(Remark: $\sqrt{3}$ is adopted as the probability distribution for general application.)

3. Standard uncertainty of the ***randomness***,

$$\mu_{ran-tape} = \frac{M_{SD-tape}}{\sqrt{n}} \text{ ….. [Type A]}$$

where $M_{SD\text{-}tape}$ is the standard deviation of repeated measurements and n is the number of repeated measurements.

4. Standard uncertainty in ***thermal expansion***,

$$\mu_{thermal-tape} = \frac{0.5x10^{-4}}{\sqrt{3}} \text{ ….. [Type B]}$$

Note: the interval for thermal expansion coefficient of measuring tape = +/-0.5x10^{-4}/^{o}C. This uncertainty is negligible since the value is too small.

(C2) Standard uncertainty for the measurement of re-scaling factor:

1. ***Calibration uncertainty*** of the re-scaling factor,

$$\mu_{cal-F} = \frac{a_{cal-F}}{k_{cal-F}} \text{ ….. [Type B]}$$

where $a_{cal\text{-}F}$ is the uncertainty obtained from the calibration certificate,
$k_{cal\text{-}F}$ is the coverage factor used in the calibration certificate, which is 1.96.

2. Experimental uncertainty of ***randomness***,

$$\mu_{ran-F} = \frac{M_{SD-F}}{\sqrt{n}} \text{ ….. [Type A]}$$

where $M_{SD\text{-}F}$ is the standard deviation of repeated measurements and n is the number of repeated measurements.

(C3) Standard uncertainty for the measurement of sampling points:

1. ***Calibration uncertainty*** of the sampling points,

$$\mu_{cal-P} = \frac{a_{cal-P}}{k_{cal-P}} \text{ ….. [Type B]}$$

where $a_{cal\text{-}P}$ is the uncertainty obtained from the calibration certificate,
$k_{cal\text{-}P}$ is the coverage factor used in the calibration certificate, which is 1.96.

2. Experimental uncertainty of ***randomness***,

$$\mu_{ran-P} = \frac{M_{SD-P}}{\sqrt{n}} \text{ ….. [Type A]}$$

where M_{SD-P} is the standard deviation of repeated measurements and n is the number of repeated measurements.

(C3) Standard uncertainty for the measurement of degree of water saturation (S_w):

1. Experimental uncertainty of $\mathbf{S_w}$ **at oven dried state** by gravimetric method

$$\mu_{Sw(oven)} = \frac{a_{Sw(oven)}}{k_{Sw(oven)}} \text{ ….. [Type B]}$$

2. Experimental uncertainty of $\mathbf{S_w}$ **at saturated state** by gravimetric method

$$\mu_{Sw(saturated)} = \frac{a_{Sw(saturated)}}{k_{Sw(saturated)}} \text{ ….. [Type B]}$$

(D1) Combined standard uncertainty of the measuring tape from C1:

$$\sum \mu_d^2 = \mu_{cal-tape}^2 + \mu_{ran-tape}^2 + \mu_{res-tape}^2$$

(D2) Combined standard uncertainty of the measurement of re-scaling factor from C2:

$$\sum \mu_F^2 = \mu_{cal-F}^2 + \mu_{ran-F}^2$$

(D3) Combined standard uncertainty of the measurement of sample points from C3:

$$\sum \mu_P^2 = \mu_{cal-P}^2 + \mu_{ran-P}^2$$

(D3) Combined standard uncertainty of the measurement of sample points from C4:

$$\sum \mu_{Sw}^2 = \mu_{Sw(oven)}^2 + \mu_{Sw(saturated)}^2$$

(E) Combined uncertainty $\mathbf{U_c}$,

$$U_c = \sqrt{(c_d \sum \mu_d)^2 + (c_F \sum \mu_F)^2 + (c_P \sum \mu_P)^2 + (c_{Sw} \sum \mu_{Sw})^2}$$

(F) Expanded Uncertainty $\mathbf{U_e}$,

$$U_e = kU_c$$

For student’s distribution in statistics for 95% confidence, the coverage factor k is 2.

APPENDIX K4B: WORKSHEET OF UNCERTAINTY ANALYSIS OF THE COMPLEX REFRACTIVE INDEX MODEL (CRIM)

Source of Error		Unit	Type	S.D.	S.D.	Semi-range	Semi-range (point)	Semi-range of Sw	rm	a	μ_i	$\Sigma\mu_i^2$	c_i	c_i^2	$c_i^2\Sigma\mu_i^2$
Material thickness	Calibration uncertainty of the measuring tape (according to Cal. Cert)	m	B	-	-	0.002	-	-	-	1.960	1.02E-03				
	Resolution of the measuring tape (according to Cal. Ce	m	B	-	-	0.0005	-	-	-	1.732	2.89E-04				
	Repeatability of measuring tape readings	m	A	7.47E-05	-	-	-	-	10	3.162	2.36E-05	1.13E-06	18.1170	328.2257	3.69E-04
1GHz Radar re-scale factor	Calibration uncertainty	-	B	-		-	1440	-	-	1.960	7.35E+02				
	Randomness of TTT readings	-	A	-	903.50	-	-	-	10	3.162	2.86E+02	6.21E+05	7.03E-06	4.94E-11	3.07E-05
1GHz Radar sample point	Calibration uncertainty	-	B	-	-	-	0.5	-	-	1.960	2.55E-01				
	Randomness of sample point readings	-	A	-	0.64	-	-	-	60	7.746	8.32E-02	7.20E-02	-0.0281	7.90E-04	5.69E-05
Degree of water saturation (Sw)	Oven-dried state Sw (error due to sampling process)	-	A	-	-	-	-	0.005	-	1.732	2.89E-03				
	Saturated Sw (error due to sampling process)	-	A	-	-	-	-	0.02	-	1.732	1.15E-02	1.42E-04	-4.0000	1.60E+01	2.27E-03

c_d =	18.117
c_f =	7.03E-06
c_p =	-0.02810
c_{Sw} =	-4

Input Constants

F=	515697	re-scaling factor
c=	3.00E+08	speed of light

Summation	
$U_c = \sqrt{\sum (c_i u_i)^2}$	0.0522
k	2
$U_e = kU_c$	**0.1044**
U_e (after round u	**0.1**

Note :

a	=	distribution	U_c	combined uncertainty
rm	=	no. of repetitive measurement	U_e	expanded uncertainty
μ_i	=	standard uncertainty	k	coverage factor
$\Sigma\mu$	=	combined standard uncertainty	Type	A (statistical) or B (probability/semi-range)
c_i	=	sensitivity coefficient	TS	time window's resolution
			S.D.	standard deviation

Remark : Uncertainties are calculated at 95 % confidence level.

APPENDIX K5A UNCERTAINTY ANALYSIS OF PERMEABILITY ESTIMATION BY KOZENY CARMEN'S PERMEABILITY MODEL

(A) Mathematical model in ε' determination by Kozeny Carmen's Permeability Model

$$k = \frac{\phi^3}{cS_t^{\ 2}} = \frac{\phi^3}{5(1-\phi)^2 S_S^{\ 2}} \quad \text{.......[1]}$$

where k is the coefficient of permeability, ϕ = porosity and S_s is the specific surface of the soil.

(B) Sensitivity Coefficients

- by derivative of ***specific surface*** (S_S),

for S_S = 470 m^2/ m^3 (the smallest value of soil specimen), ϕ = 0.4,

$$c_{SS} = \frac{\partial k}{\partial S_S} = \frac{\phi^3}{5(1-\phi^2)}(-2)(\frac{1}{S_S^3}) = \frac{-2\phi^3}{5(1-\phi^2)S_S^3} = \mathbf{-2.935 \times 10^{-10}}$$

- by derivative of the ***porosity*** (ϕ),

for S_S = 470 m^2/ m^3 (the smallest value of soil specimen), ϕ = 0.4,
let x = ϕ^3, y = $5(1-\phi^2)S_S^2$,

$$c_p = \frac{\partial k}{\partial \phi} = \frac{x\partial y + y\partial x}{y^2} = \frac{15\phi^2(1-\phi^2)S_S^2 - 10\phi^4 S_S^2}{25(1-\phi^2)^2 S_S^4} = \mathbf{4.517 \times 10^{-7}}$$

(C1) Standard uncertainty for the porosity: the same as U_e in Appendix K4B.

(C2) Standard uncertainty for the specific surface:

$$\mu_{SS} = \frac{a_{SS}}{k_{SS}} \quad \text{..... [Type B]}$$

where a_{SS} is the uncertainty of the estimate of specific surface,
k_{SS} is the coverage factor used in the estimate, which is 1.96.

(D) Combined uncertainty U_c,

$$U_c = \sqrt{(c_P \sum \mu_P)^2 + (c_{SS} \sum \mu_{SS})^2}$$

(E) Expanded Uncertainty U_e,

$$U_e = kU_c$$

For student's distribution in statistics for 95% confidence, the coverage factor k is 2.

APPENDIX K5B: WORKSHEET OF UNCERTAINTY ANALYSIS OF THE KOZENY-CARMEN'S PERMEABILITY MODEL

Source of Error		Unit	Type	Clay fraction	Assumed clay specific surface *	Sand fraction	Computed sand specific surface	Semi-range of specific surface **	a	μ_i	$\Sigma\mu_i^2$	c_i	c_i^2	$c_i^2\Sigma\mu_i^2$
Porosity	Combined uncertainty	Refer to the uncertainty analysis in CRIM									0.1044	4.52E-07	2.04E-13	2.13E-14
Specific surface	approximation uncertainty for soil specimen	cm^{-1}	B	0.07	2.05E+07	0.93	1810	716737	1.96	3.66E+05	1.34E+11	-2.94E-10	8.61E-20	1.15E-08

Summation	
$U_c = \sqrt{\sum (c_i u_i)^2}$	1.15E-08
k	2
U_e=kU_c	**2.30E-08**

c_p = 4.517E-07

c_{SS} = -2.935E-10

* Assumed clay specific surface = $(800m^2/g)(2.56x10^6)/100$

** Semi-range of specific surface = (clay fraction x clay Ss + sand fraction x sand Ss - sand Ss)/2

Note :
- a = distribution
- rm = no. of repetitive measurement
- μ_i = standard uncertainty
- $\Sigma\mu$ = combined standard uncertainty
- c_i = sensitivity coefficient
- U_c = combined uncertainty
- U_e = expanded uncertainty
- k = coverage factor
- Type = A (statistical) or B (probability/semi-range)
- TS = time window's resolution
- S.D. = standard deviation

Remark : Uncertainties are calculated at 95 % confidence level.

APPENDIX K6A UNCERTAINTY ANALYSIS OF ENERGY ATTENUATION

(B) Mathematical model in determination of energy attenuation

$$\text{Energy attenuation expressed in dB/m} = (20x\log\frac{A_{reflection}}{A_{anchor}}) / \text{D}\ldots\ldots[1]$$

where $A_{reflection}$ = amplitude of the material interface, A_{anchor} = amplitude of reflection of the anchor peak, T = the thickness of the specimen.

(B) Sensitivity Coefficients

- by derivative of ***thickness*** (D),

for D = 0.2m, A_1 = 0.5V, A_2 = 0.2V,

$$c_T = \frac{\partial E}{\partial T} = \frac{-20}{0.2^2}\log(\frac{0.5}{0.2}) = \mathbf{-198.97}$$

- by derivative of amplitude of the materal interface ($A_{reflection}$),

for D = 0.2m, A_1 = 0.5V

$$c_{A1} = \frac{\partial E}{\partial A_1} = \frac{20}{T}\frac{\partial}{\partial A_1}(\log A_1 - \log A_2) = \frac{20}{T}(\frac{2.303}{A_1}) = \mathbf{460.6}$$

- by derivative of amplitude of the anchor peak (A_{anchor}),

for D = 0.2m, A_2 = 0.2V

$$c_{A2} = \frac{\partial E}{\partial A_1} = \frac{20}{T}\frac{\partial}{\partial A_1}(\log A_1 - \log A_2) = \frac{20}{T}(\frac{-2.303}{A_2}) = \mathbf{-1151.5}$$

(C1) Standard uncertainty for the depth measurement by measuring tape:

1. ***Calibration uncertainty***,

$$\mu_{cal-tape} = \frac{a_{cal-tap}}{k_{cal-tap}} \text{ ….. [Type B]}$$

where $a_{cal-tap}$ is the uncertainty obtained from the calibration certificate,
$k_{cal-tap}$ is the coverage factor used in the calibration certificate, which is 1.96.

2. Standard uncertainty of the ***resolution***,

$$\mu_{res-tape} = \frac{a_{res-tap}}{\sqrt{3}} \text{ ….. [Type B]}$$

where $a_{res\text{-}tap}$ is the resolution of the semi-range of the measuring tape.
(Remark: $\sqrt{3}$ is adopted as the probability distribution for general application.)

3. Standard uncertainty of the ***randomness***,

$$\mu_{ran-tape} = \frac{M_{SD-tape}}{\sqrt{n}} \quad \text{….. [Type A]}$$

where $M_{SD\text{-}tape}$ is the standard deviation of repeated measurements and n is the number of repeated measurements.

4. Standard uncertainty in ***thermal expansion***,

$$\mu_{thermal-tape} = \frac{0.5x10^{-4}}{\sqrt{3}} \quad \text{….. [Type B]}$$

Note: the interval for thermal expansion coefficient of measuring tape = +/-0.5x10^{-4}/^{o}C. This uncertainty is negligible since the value is too small.

(C2) Standard uncertainty for the energy attenuation:

1. Standard uncertainty of ***voltage resolution***,

$$\mu_{res-V} = \frac{M_{res-V}}{\sqrt{3}} \quad \text{….. [Type B]}$$

2. Standard uncertainty of ***voltage randomness***,

$$\mu_{ran-V} = \frac{M_{SD-V}}{\sqrt{n}} \quad \text{….. [Type A]}$$

(D1) Combined Standard Uncertainty of depth measurement

$$\sum \mu_D^2 = \mu_{cal-tape}^2 + \mu_{ran-tape}^2 + \mu_{res-tape}^2$$

(D2) Combined Standard Uncertainty of voltage amplitude

$$\sum \mu_{A1}^2 = \mu_{res-V}^2 + \mu_{ran-V}^2 \,;\; \sum \mu_{A2}^2 = \mu_{res-V}^2 + \mu_{ran-V}^2$$

(E) Combined uncertainty U_c,

$$U_c = \sqrt{(c_D \sum \mu_D)^2 + (c_{A1} \sum \mu_{A1})^2 + (c_{A2} \sum \mu_{A2})^2}$$

(F) Expanded Uncertainty U_e,

$$U_e = kU_c$$

For student’s distribution in statistics for 95% confidence, the coverage factor k is 2.

APPENDIX K6B WORKSHEET OF UNCERTAINTY ANALYSIS OF ENERGY ATTENUATION

Source of Error		Unit	Type	S.D.	S.D.	V	Semi-range	rm	a	μ_i	$\Sigma\mu_i^2$	c_i	c_i^2	$c_i^2\Sigma\mu_i^2$
Material thickness 'D'	Calibration uncertainty of the measuring tape (according to Cal. Cert)	m	B	-	-	-	0.01	-	1.96	5.10E-03				
	Resolution of the measuring tape (according to Cal. Cert)	m	B	-	-	-	0.0005	-	1.7321	2.89E-04				
	Repeatability of measuring tape readings	m	A	7.47E-05	-	-	-	10	3.1623	2.36E-05	2.61E-05	-199.0	3.96E+04	1.03
Voltage amplitude A1	Resolution of voltage amplitude	s	B	-	-	1.53E-04	-	-	1.7321	8.81E-05				
	Randomness of voltage amplitude readings	s	A	-	5.80E-03	-	-	60	7.746	7.49E-04	5.69E-07	460.6	2.12E+05	0.12
Voltage amplitude A2	Resolution of voltage amplitude	s	B	-	-	1.53E-04	-	-	1.7321	8.81E-05				
	Randomness of voltage amplitude readings	s	A	-	5.80E-03	-	-	60	7.746	7.49E-04	5.69E-07	-1151.5	1.33E+06	0.75

Summation	
$U_c = \sqrt{\sum (c_i u_i)^2}$	1.9085
k	2
$U_e = kU_c$	**3.8169**
U_e (after round up	**3.8**

$c_D =$	-199.0
$c_{A1} =$	460.6
$c_{A2} =$	-1151.5

Note :
- a = distribution
- rm = no. of repetitive measurement
- μ_i = standard uncertainty
- $\Sigma\mu$ = combined standard uncertainty
- c_i = sensitivity coefficient
- U_c combined uncertainty
- U_e expanded uncertainty
- k coverage factor
- Type A (statistical) or B (probability/semi-range)
- V Voltage
- S.D. standard deviation

Remark : Uncertainties are calculated at 95 % confidence level.

APPENDIX L JUSTIFICATION OF THE USE OF S_W IN LIEU OF θ_v AS A MEASURE OF MATERIAL WETNESS

Despite the mentioned difficulties of θ_v determination in Section 2.7.1C, the bulk θ_v in the soils tested can be indirectly determined using the TTT of the rising water table identified in the radargram during permeation, (as represented by the solid yellow line in Fig. A). The relationship for conversion of measured TTT to $S_{w(TTT)}$ and then to θ_v is shown in equation [1].

$$\theta_v = \phi S_{w(TTT)} = \phi\left(\frac{TTT_{\text{int}} - TTT_{dry}}{TTT_{sat} - TTT_{dry}}\right) \text{ ……...[1]}$$

where θ_v = bulk water content; ϕ = porosity; $S_{w(TTT)}$ = degrees of water saturation determined using TTT of water table;
TTT_{int} = two-way transit time of the water table at any intermediate moment
TTT_{dry} = two-way transit time of the water table at dry state
TTT_{sat} = two-way transit time of the water table at saturated state

It must be cautioned that the first equality in Eq. [1] (i.e. $\theta_v = \phi S_{w(TTT)}$) is a fundamental and well-known relationship, which is valid based on the assumption that water is able to penetrate every single pore space within the material.

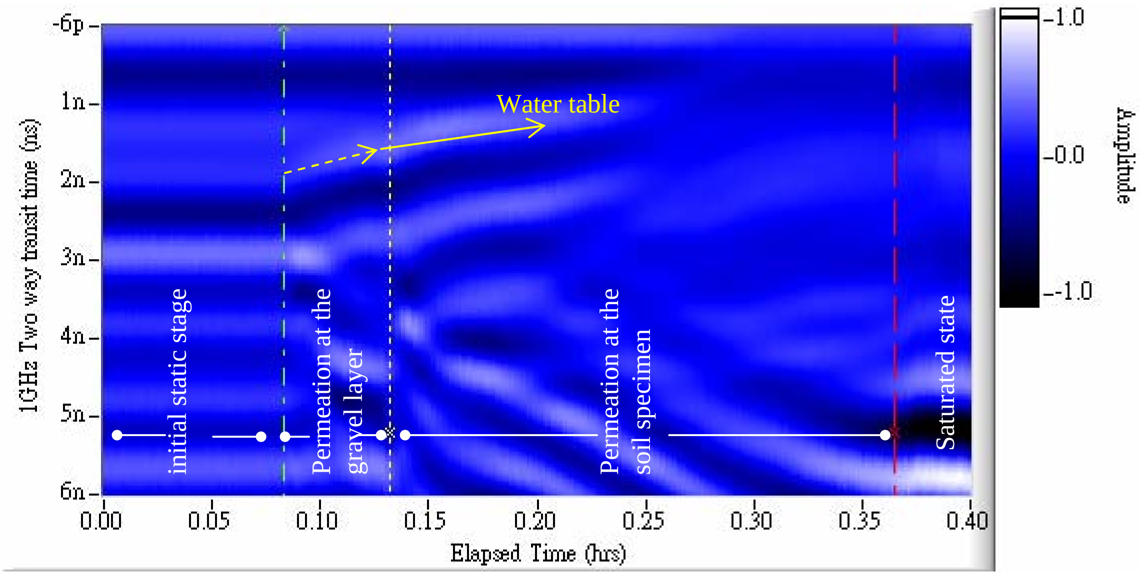

Fig. A Radargram of Soil Specimen E (permeation stage only) (the soil specimen type is referred to Ch.8)

Also in equation [1], the second equality (i.e. $S_{w(TTT)} = \frac{TTT_{\text{int}} - TTT_{dry}}{TTT_{sat} - TTT_{dry}}$), it is based implicitly on the assumption that if water losses or even gain (by leakage and/or evaporation/condensation) can be discounted, then the constant rate of water injection and the subsequent linearly rising water table will mean that S_w (and hence the θ_v added to the soil mass) will be largely represented by the corresponding rise in the radar detected water table (which also agrees with the visually observable water table) as shown in the radargram.

The black bullet points illustrated in Fig. B1 and B2 depict the relationship between S_w/θ_v derived from the water table measured by TTT (according to Eq. [1]) and the corresponding elapsed time, in which this relationship was the extracted TTT data obtained from Fig. A. The straight line refers to the intermediate S_w (obtained by interpolating the initial and saturated S_w, represented by the solid squares in Fig. B1 and B2), as described in Section 2.7.1C.

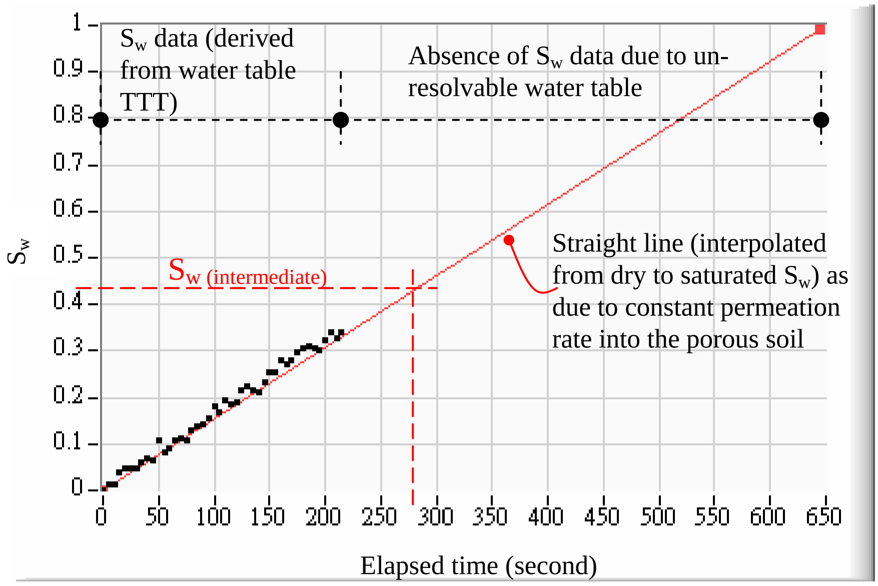

Fig. B1 Plot of S_w against elapsed time using equation 1 and interpolated S_w between the dry & saturated S_w in soil specimen E (the soil specimen type is referred to Ch.8)

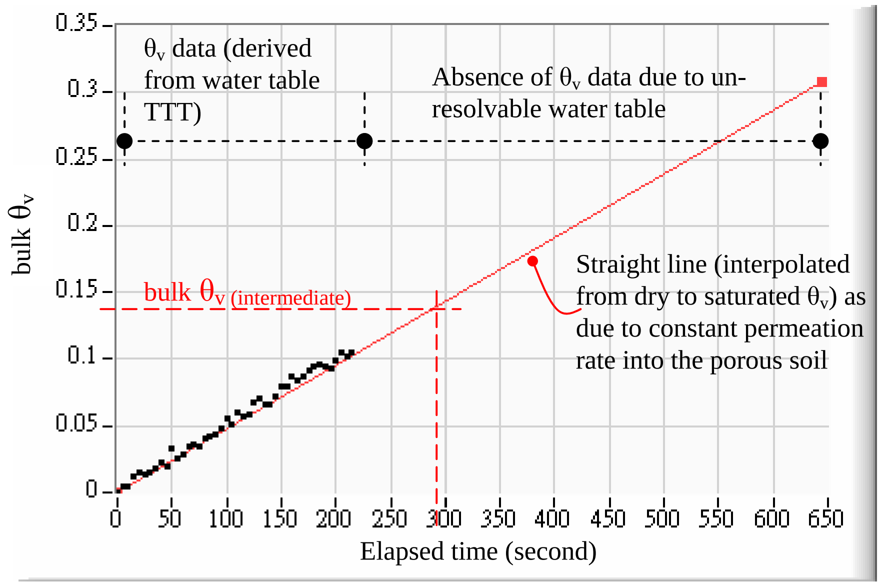

Fig. B2 Plot of θ_v against elapsed time using equation 1 and interpolated θ_v between the dry & saturated θ_v in soil specimen E (the soil specimen type is referred to Ch.8)

The close correlation between the actual S_w/θ_v and linearly fitted S_w/θ_v (as shown in Fig. B1 and B2), even with the absence of data points after $S_w>0.34$ or $\theta_v>0.11$ (due to un-resolvable water table in the radargram), justifies the use of S_w in lieu of θ_v and assumption suggested in Section 2.7.1C.

APPENDIX M ERRORS IN S_W ESTIMATION

Based on Fig. B1 and B2 (for specimen E only), the errors identified between the actual S_w/θ_v (the black bullet points) and the linearly fitted S_w/θ_v (the red line) for all experiments of the ten soil specimens were reported and represented by a histogram, as shown in Fig. C. From this figure, the root mean square difference (RMSD) of S_w exhibited in all experiments was found to be 0.03. Hence the measure of S_w reported in this thesis exhibits an uncertainty +/-0.03. Due to the small uncertainties of both S_w and ε' reported in this section, and appendices K2 & K3 respectively, the observation of the dielectric hysteresis reported in Chapter 9 is well-justified without significant errors.

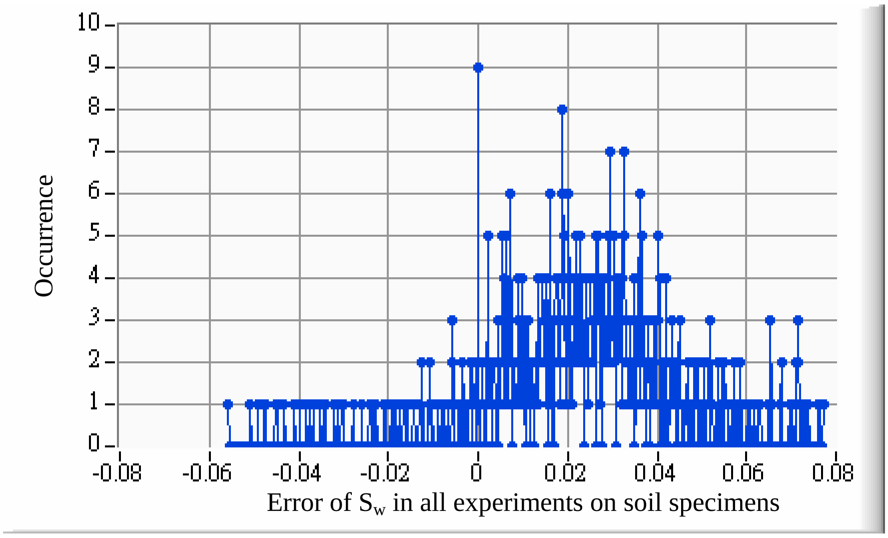

Fig. C Occurrence of Errors of S_w estimation in all specimens

No TTT data of water table was available during de-watering stage, since water table could not be clearly identified in most of the experiments. This is attributed to the unclear boundary between saturated and dry zones observed during de-watering stage than those observed during permeation stage.